



Journal of
Clinical Medicine

Special Issue Reprint

Diagnostic Imaging of Arthritis

Edited by
Iwona Sudol-Szopińska and Mihra Taljanovic

mdpi.com/journal/jcm



Diagnostic Imaging of Arthritis

Diagnostic Imaging of Arthritis

Editors

Iwona Sudoł-Szopińska
Mihra Taljanovic



Basel • Beijing • Wuhan • Barcelona • Belgrade • Novi Sad • Cluj • Manchester

Editors

Iwona Sudoł-Szopińska
National Institute of
Geriatrics, Rheumatology and
Rehabilitation
Warsaw
Poland

Mihra Taljanovic
University of Arizona
Tucson, AZ
USA

Editorial Office

MDPI
St. Alban-Anlage 66
4052 Basel, Switzerland

This is a reprint of articles from the Special Issue published online in the open access journal *Journal of Clinical Medicine* (ISSN 2077-0383) (available at: https://www.mdpi.com/journal/jcm/special_issues/Diagnostic_Imaging_Arthritis).

For citation purposes, cite each article independently as indicated on the article page online and as indicated below:

Lastname, A.A.; Lastname, B.B. Article Title. <i>Journal Name</i> Year , <i>Volume Number</i> , Page Range.
--

ISBN 978-3-0365-8876-6 (Hbk)

ISBN 978-3-0365-8877-3 (PDF)

doi.org/10.3390/books978-3-0365-8877-3

© 2023 by the authors. Articles in this book are Open Access and distributed under the Creative Commons Attribution (CC BY) license. The book as a whole is distributed by MDPI under the terms and conditions of the Creative Commons Attribution-NonCommercial-NoDerivs (CC BY-NC-ND) license.

Contents

Miriam Frenken, Benedikt Ostendorf, Ralph Brinks, Christoph Schleich, Lena M. Wilms, Stefan Vordenbäumen, et al. Proof-of-Concept Double-Blind Placebo-Controlled Trial Measuring Cartilage Composition in Early Rheumatoid Arthritis under TNF- α -Inhibitor Therapy Reprinted from: <i>J. Clin. Med.</i> 2023 , <i>12</i> , 2306, doi:10.3390/jcm12062306	1
Maria Sotniczuk, Anna Nowakowska-Płaza, Jakub Wroński, Małgorzata Wisłowska and Iwona Sudol-Szopińska The Clinical Utility of Dual-Energy Computed Tomography in the Diagnosis of Gout—A Cross-Sectional Study Reprinted from: <i>J. Clin. Med.</i> 2022 , <i>11</i> , 5249, doi:10.3390/jcm11175249	13
Andrea S. Klauser, Felix de-Koekoek, Christoph Schwabl, Christian Fink, Miriam Friede and Robert Csapo Intraobserver Assessment of Shear Wave Elastography in Tensor Fasciae Latae and Gluteus Maximus Muscle: The Importance of the Hip Abductor Muscles in Runners Knee Compared to Healthy Controls Reprinted from: <i>J. Clin. Med.</i> 2022 , <i>11</i> , 3605, doi:10.3390/jcm11133605	21
Sara Kamp Felbo, Mikkel Østergaard, Inge Juul Sørensen and Lene Terslev Ultrasound of the Heel Improves Diagnosis—Tender Entheses in the Heel Region Rarely Corresponds to Inflammatory Enthesitis in Patients with Peripheral Spondyloarthritis Reprinted from: <i>J. Clin. Med.</i> 2022 , <i>11</i> , 2325, doi:10.3390/jcm11092325	31
Jessica A. Martinez, Mihra S. Taljanovic, Andres A. Nuncio Zuniga, Betsy C. Wertheim, Denise J. Roe, Sima Ehsani, et al. Feasibility Trial to Evaluate Tendon Stiffness Obtained from Shear Wave Elastography Imaging as a Biomarker of Aromatase Inhibitor-Induced Arthralgias Reprinted from: <i>J. Clin. Med.</i> 2022 , <i>11</i> , 1067, doi:10.3390/jcm11041067	39
Monika Ostrowska, Emil Michalski, Piotr Gietka, Małgorzata Mańczak, Magdalena Posadzy and Iwona Sudol-Szopińska Ankle Magnetic Resonance Imaging in Juvenile Idiopathic Arthritis Versus Non-Juvenile Idiopathic Arthritis Patients with Arthralgia Reprinted from: <i>J. Clin. Med.</i> 2022 , <i>11</i> , 760, doi:10.3390/jcm11030760	51
Mateusz Kotecki, Piotr Gietka, Magdalena Posadzy and Iwona Sudol-Szopińska Radiographs and MRI of the Cervical Spine in Juvenile Idiopathic Arthritis: A Cross-Sectional Retrospective Study Reprinted from: <i>J. Clin. Med.</i> 2021 , <i>10</i> , 5798, doi:10.3390/jcm10245798	67
Monika Ostrowska, Piotr Gietka, Małgorzata Mańczak, Emil Michalski and Iwona Sudol-Szopińska MRI Findings in Hip in Juvenile Idiopathic Arthritis Reprinted from: <i>J. Clin. Med.</i> 2021 , <i>10</i> , 5252, doi:10.3390/jcm10225252	79
Mateusz Kotecki, Robert Gasik, Piotr Głuszko and Iwona Sudol-Szopińska Radiological Evaluation of Cervical Spine Involvement in Rheumatoid Arthritis: A Cross-Sectional Retrospective Study Reprinted from: <i>J. Clin. Med.</i> 2021 , <i>10</i> , 4587, doi:10.3390/jcm10194587	95

Tarimobo M. Otobo, Nele Herregods, Jacob L. Jaremko, Iwona Sudol-Szopinska, Walter P. Maksymowych, Arthur B. Meyers, et al. Reliability of the Preliminary OMERACT Juvenile Idiopathic Arthritis MRI Score (OMERACT JAMRIS-SIJ) Reprinted from: <i>J. Clin. Med.</i> 2021 , <i>10</i> , 4564, doi:10.3390/jcm10194564	107
Mirkamal Tolend, Andrea S. Doria, Arthur B. Meyers, Tore A. Larheim, Shelly Abramowicz, Julien Aguet, et al. Assessing the Reliability of the OMERACT Juvenile Idiopathic Arthritis Magnetic Resonance Scoring System for Temporomandibular Joints (JAMRIS-TMJ) Reprinted from: <i>J. Clin. Med.</i> 2021 , <i>10</i> , 4047, doi:10.3390/jcm10184047	125
Romain Gillet, François Zhu, Pierre Padoin, Aymeric Rauch, Gabriela Hossu, Pedro Augusto Gondim Teixeira, et al. MR Imaging Biomarkers for Clinical Impairment and Disease Progression in Patients with Shoulder Adhesive Capsulitis: A Prospective Study Reprinted from: <i>J. Clin. Med.</i> 2021 , <i>10</i> , 3882, doi:10.3390/jcm10173882	143
Daniel Baur, Christoph Schwabl, Christian Kremser, Mihra S. Taljanovic, Gerlig Widmann, Luca Maria Sconfienza, et al. Shear Wave Elastography of the Plantar Fascia: Comparison between Patients with Plantar Fasciitis and Healthy Control Subjects Reprinted from: <i>J. Clin. Med.</i> 2021 , <i>10</i> , 2351, doi:10.3390/jcm10112351	157
Edouard Germain, Charles Lombard, Fatma Boubaker, Mathias Louis, Alain Blum, Pedro Augusto Gondim-Teixeira, et al. Imaging in Hip Arthroplasty Management—Part 1: Templating: Past, Present and Future Reprinted from: <i>J. Clin. Med.</i> 2022 , <i>11</i> , 5465, doi:10.3390/jcm11185465	167
Iwona Sudol-Szopińska, Ewa Żelnio, Marzena Olesińska, Piotr Gietka, Sylwia Ornowska, Deborah Jane Power, et al. Update on Current Imaging of Systemic Lupus Erythematosus in Adults and Juveniles Reprinted from: <i>J. Clin. Med.</i> 2022 , <i>11</i> , 5212, doi:10.3390/jcm11175212	187
Charles Lombard, Pierre Gillet, Edouard Germain, Fatma Boubaker, Alain Blum, Pedro Augusto Gondim Teixeira, et al. Imaging in Hip Arthroplasty Management Part 2: Postoperative Diagnostic Imaging Strategy Reprinted from: <i>J. Clin. Med.</i> 2022 , <i>11</i> , 4416, doi:10.3390/jcm11154416	205
Jennifer S. Weaver, Ernest R. Vina, Peter L. Munk, Andrea S. Klauser, Jamie M. Elifritz and Mihra S. Taljanovic Gouty Arthropathy: Review of Clinical Manifestations and Treatment, with Emphasis on Imaging Reprinted from: <i>J. Clin. Med.</i> 2022 , <i>11</i> , 166, doi:10.3390/jcm11010166	243
Tetyana Gorbachova, Yulia V. Melenevsky, L. Daniel Latt, Jennifer S. Weaver and Mihra S. Taljanovic Imaging and Treatment of Posttraumatic Ankle and Hindfoot Osteoarthritis Reprinted from: <i>J. Clin. Med.</i> 2021 , <i>10</i> , 5848, doi:10.3390/jcm10245848	271
Charles Lombard, Pedro Teixeira, Edouard Germain, Gauthier Dodin, Mathias Louis, Alain Blum, et al. Elbow Stiffness Imaging: A Practical Diagnostic and Pretherapeutic Approach Reprinted from: <i>J. Clin. Med.</i> 2021 , <i>10</i> , 5348, doi:10.3390/jcm10225348	287



Article

Proof-of-Concept Double-Blind Placebo-Controlled Trial Measuring Cartilage Composition in Early Rheumatoid Arthritis under TNF- α -Inhibitor Therapy

Miriam Frenken ^{1,*}, Benedikt Ostendorf ², Ralph Brinks ², Christoph Schleich ¹, Lena M. Wilms ¹, Stefan Vordenbäumen ², Anja Müller-Lutz ¹, Jutta G. Richter ², Oliver Sander ², Gerald Antoch ¹, Matthias Schneider ², Xenofon Baraliakos ³, Daniel B. Abrar ^{1,†} and Philipp Sewerin ^{2,3,†}

¹ Department of Diagnostic and Interventional Radiology, Medical Faculty, University Hospital Düsseldorf, Heinrich-Heine-University Düsseldorf, 40225 Düsseldorf, Germany

² Department and Hiller Research Unit of Rheumatology, Medical Faculty, University Hospital Düsseldorf, Heinrich-Heine-University Düsseldorf, 40225 Düsseldorf, Germany

³ Rheumazentrum Ruhrgebiet, Medical Faculty, Ruhr-University Bochum, 44649 Herne, Germany

* Correspondence: miriam.frenken@med.uni-duesseldorf.de

† These authors contributed equally to this work.

Abstract: Low levels of delayed gadolinium-enhanced magnetic resonance imaging of cartilage (dGEMRIC) values are indicative of cartilage degeneration. Patients with early rheumatoid arthritis are known to have low dGEMRIC values due to inflammatory activity. The additional effect of biological disease-modifying antirheumatic drug (bDMARD) and conventional synthetic disease-modifying antirheumatic drug (csDMARD) treatment on cartilage status is still unclear. In this prospective, double-blinded, randomized proof-of-concept clinical trial, patients with early rheumatoid arthritis (disease duration less than 12 months from symptoms onset) were treated with methotrexate + adalimumab (10 patients: 6/4 (f/m)). A control group with methotrexate alone (four patients: 2/2 (f/m)) was used. Cartilage integrity in the metacarpophalangeal joints was compared using dGEMRIC at baseline, 12, and 24 weeks after treatment initiation. A statistically significant increase in dGEMRIC levels was found in the adalimumab group considering the results after 12 and 24 weeks of therapy ($p < 0.05$) but not in the control group (p : non-significant). After 24 weeks, a tendency towards increased dGEMRIC values under combination therapy was observed, whereas methotrexate alone showed a slight decrease without meeting the criteria of significance (dGEMRIC mean change: +85.8 ms [−156.2–+346.5 ms] vs. 30.75 ms [−273.0–+131.0 ms]; p : non-significant). After 24 weeks of treatment with a combination of methotrexate and adalimumab, a trend indicating improvement in cartilage composition is seen in patients with early rheumatoid arthritis. However, treatment with methotrexate alone showed no change in cartilage composition, as observed in dGEMRIC sequences of metacarpophalangeal joints.

Keywords: rheumatoid arthritis; therapeutics; articular cartilage; radiology; musculoskeletal system

Citation: Frenken, M.; Ostendorf, B.; Brinks, R.; Schleich, C.; Wilms, L.M.; Vordenbäumen, S.; Müller-Lutz, A.; Richter, J.G.; Sander, O.; Antoch, G.; et al. Proof-of-Concept Double-Blind Placebo-Controlled Trial Measuring Cartilage Composition in Early Rheumatoid Arthritis under TNF- α -Inhibitor Therapy. *J. Clin. Med.* **2023**, *12*, 2306. <https://doi.org/10.3390/jcm12062306>

Academic Editors:
Iwona Sudol-Szopińska,
Mihra Taljanovic and
Burkhard Möller

Received: 1 February 2023

Revised: 10 March 2023

Accepted: 14 March 2023

Published: 16 March 2023



Copyright: © 2023 by the authors. Licensee MDPI, Basel, Switzerland. This article is an open access article distributed under the terms and conditions of the Creative Commons Attribution (CC BY) license (<https://creativecommons.org/licenses/by/4.0/>).

1. Introduction

Rheumatoid arthritis (RA) is a chronic systemic autoimmune disease characterized by enduring joint inflammation resulting in a specific pattern of cartilage and bone damage and ultimately loss of joint function (1). The chronic, progressive nature of the disease leads to physical limitation, reduced quality of life, and higher mortality rates [1,2].

The pathomechanism of RA is not yet fully understood. However, inflammation of the synovial membrane, cytokine, and chemokine-induced cell migration into the joint space, and consecutive cartilage damage and bone erosions, appear to play a key role in the progression and maintenance of the disease [3].

Early detection, accurate monitoring, and a treat-to-target approach with disease-modifying antirheumatic drugs (DMARDs) are components of a modern treatment strategy that aims to control inflammation soon after diagnosis to prevent joint damage [4]. In the last two decades, the treatment of RA has been revolutionized by the development of biological disease-modifying antirheumatic drugs (bDMARDs). Adalimumab (ADA) as one of these is a TNF- α inhibitor approved for the treatment of patients who do not achieve clinical remission with conventional synthetic (cs) DMARDs (e.g., methotrexate, MTX) [5]. Beyond significant improvement in clinical activity already after 12 weeks [6], treatment with adalimumab also showed significantly less structural damage in conventional radiographs [7].

Magnetic resonance imaging (MRI) is more sensitive than conventional radiography in the detection of RA-related musculoskeletal alterations [8]. In 2003, the Outcome Measures in Rheumatology Clinical Trials (OMERACT) group introduced the RA MRI score (RAMRIS), a sum score that reflects the severity of synovitis, bone marrow edema, and erosions in the hand and wrist to determine the disease activity and to monitor therapy response [9]. Cartilage changes do not directly contribute to the score, although cartilage changes appear to be important in monitoring RA and are even more closely associated with physical impairment than bone damage [10], highlighting the importance of imaging procedures that focus on cartilage. Indirectly, however, cartilage damage was included in the RAMRIS in 2017 through joint space narrowing, which is a result of cartilage damage [11]. As joint space narrowing only detects an advanced state of cartilage damage, in which the cartilage thickness has already decreased, techniques to visualize early cartilage changes are urgently needed. Compositional MR imaging techniques are suitable for this purpose, among which gadolinium-enhanced MRI of cartilage (dGEMRIC) is the gold standard. This contrast agent-based MRI technique allows the detection of cartilage degeneration by revealing the loss of proteoglycans [12] and has the potential to predict joint space narrowing [13].

This highly effective MRI technique works by indirectly visualizing proteoglycans, indicating early cartilage changes [12]. After the application of a contrast agent, the negatively charged gadolinium diethylenetriamine pentaacetate anions (Gd-DTPA) enter the cartilage in an inverse relationship to the concentration of the negatively charged glycosaminoglycan side chains of the proteoglycans. A decrease in proteoglycan content in degenerated cartilage thus leads to an accumulation of paramagnetic gadolinium ions [14]. This increased gadolinium concentration results in an enhanced signal in T1-weighted sequences and a shortened T1 relaxation time in MR imaging, i.e., lower dGEMRIC values [15]. With dGEMRIC molecular cartilage, changes in early RA could already be detected at a time when morphological changes were not yet visible [16,17]. Nevertheless, data on cartilage composition for patients with RA under therapy are rare. Recently, a stable cartilage composition was reported with MTX therapy in patients with RA over 6 months [18]. On the other hand, the effect of TNF- α inhibitors on cartilage quality still remains unclear.

Therefore, our aim was to conduct a proof-of-concept prospective study on the effect of TNF- α inhibitor treatment on cartilage integrity in newly diagnosed RA patients based on dGEMRIC assessment of finger joints.

2. Materials and Methods

2.1. Study Population

The study was approved by the local ethics committee (approval number MO-LKP-719) and was conducted in line with the Declaration of Helsinki. Written informed consent was obtained from all participants individually. All patients were diagnosed for having RA and all had to fulfill the American College of Rheumatology (ACR)/European League Against Rheumatism (EULAR) 2010 classification criteria [19]. The symptom duration was not allowed to be >12 months. Any treatment with cs- or b-DMARDs including methotrexate was not allowed prior to study inclusion. Furthermore, the use of prednisolone for the last 4 weeks before study entry was not allowed. All subjects were ≥ 18 years of age.

Since previous work has shown that metacarpophalangeal MCP2 and MCP3 joints are more frequently affected in RA [20], these two joints were selected for study inclusion and imaging evaluation. Hence, as an inclusion criterion, all patients had to have at least one swollen or tender MCP2 or MCP3 joint in at least one hand. Patients were assigned to receive either MTX (15 mg oral MTX once weekly) alone or MTX + ADA (40 mg every 2 weeks) in a ratio of 2:1 by central block randomization.

2.2. MR Imaging

MRI of the dominantly affected hand was performed in all patients at baseline and at 12 and 24 weeks after the initiation of treatment in all patients. A 3T-MRI system (Magnetom Skyra syngo; Siemens Healthineers, Erlangen, Germany) was used. Subjects were imaged in a prone position with the hand extended over the head and the palm facing down ('superman position'). For anatomical imaging, a coronal short tau inversion recovery (STIR) sequence of the hand and the wrist, a T1-weighted turbo spin echo (TSE) sequence, a T1-weighted VIBE, and two T1-weighted sequences with two different flip angles (8 and 26°) were acquired before injection of a contrast agent. A gadolinium-based MR contrast agent was applied intravenously (0.4 mL/kg body weight of Gd-DTPA2, Magnevist; Schering). After contrast agent injection, a coronal VIBE, a TSE, and a transversal SE-sequence with fat suppression were applied. The sequence parameters were selected according to a previous study and are adapted to the Magnetom Skyra syngo 3T-MRI [12] (Table 1). Morphological images of the hand were acquired. Additionally, the cartilage integrity of MCP2 and MCP3 joints was monitored by the evaluation of compositional MRI using dGEMRIC. To achieve high-resolution images with thin sections and a small FOV, the hand was placed in a dedicated receive-only 16-channel high-resolution hand coil (3T Tim Coil, Siemens Healthineers). According to previous studies, there was a delay of 40 min between the application of the contrast agent and the dGEMRIC sequence [21]. A three-dimensional dual-flip-angle gradient-echo sequence was used for T1 mapping [21]. Flip angles were defined at 5° and 26°. Ten sagittal slices with a thickness of 2 mm and a FoV of 90 × 53.5 mm were positioned perpendicular to the joint spaces. Motion correction was applied to the MCP joint of each patient to reduce movement-related artifacts using STROKETOOL (Frechen, Germany) before image analysis [22].

Table 1. Detailed sequence parameters.

Sequence/Parameter	STIR	T1 TSE	T1 VIBE	T1 FLIP	T1 VIBE	T1 TSE	T1 TSE fs	T1
Contrast agent	no	no	no	no	yes	yes	yes	yes
Orientation	coronal	coronal	coronal	coronal	coronal	coronal	transversal	sagittal
TE/TR [ms/ms]	31/ 5560	27/ 862	5.8/ 1.9	5.8/ 1.9	5.8/ 1.9	27/ 862	16/ 702	4.56/ 15
Flip angle [°]	120	150	8	8 + 26	8	150	90	5 + 26
Slice thickness [mm]	2.5	2.5	3	3	3	2.5	2.5	2
FoV [mm × mm]	130 × 130	140 × 140	140 × 140	140 × 140	140 × 140	140 × 140	120 × 120	90 × 53.5
Number of images	1	1	1	2	1	1	1	2
Basic resolution	448	512	128	128	128	512	384	384
Number of acquired slices	17	17	10	10	10	17	20	10

STIR: short tau inversion recovery; TSE: turbo spin echo; VIBE: volumetric interpolated breath-hold examination; Fs: fat-suppressed; TE: echo time; TR: repetition time; FoV: field of view.

2.3. Image Analysis

Molecular imaging to visualize cartilage composition was performed using dGEMRIC on MCP2 and MCP3 joints. dGEMRIC is represented by the T1 map after injection of the contrast agent. Two separate regions of interest (ROI) were placed in the phalangeal and metacarpal cartilage of the MCP joints. Gradient echo sequences with a flip angle of 8° served as anatomical references for the algorithm by which the ROI were automatically placed in each cartilage zone [23]. Within these ROI, dGEMRIC values were recorded (T1 (in milliseconds)). A mean dGEMRIC value of MCP 2 and MCP 3, proximal and distal cartilage layer, respectively, was calculated per patient and per examination time point. To complement our results, morphologic imaging was assessed in the form of the RAMRIS. MR images were analyzed by consensus by two physicians trained in musculoskeletal imaging (CS, radiologist with 8 years of experience, and PS, rheumatologist with 8 years of experience) to assess subscores for synovitis, erosion, and edema in the hand and wrist.

2.4. Statistical Analysis

Statistical analysis was performed using R (Version 3.6.0, 64-bit). The mean, median, first and third quartile, minimum, and maximum for dGEMRIC values were calculated as descriptive statistics (listed in Table 2). To investigate whether treatment with ADA results in a difference in cartilage composition after 6 months of therapy, we performed two calculations. First, the change in dGEMRIC values in the MCP2 and MCP3 joints was calculated separately for each of the two treatment arms including all three study time points (baseline, 12 weeks, and 24 weeks after treatment initiation). Second, the Wilcoxon rank sum test was used to directly compare the difference in dGEMRIC values between baseline and 24 weeks after therapy initiation in both study arms (ADA + MTX or placebo + MTX). *p*-values below 0.05 were considered to be significant.

Table 2. dGEMRIC values at baseline (t_0) and change in dGEMRIC values after 24 weeks (t_2) compared to baseline.

Pooled MCP2 and MCP3 dGEMRIC Values	Adalimumab		Control Group	
	t_0	$\Delta(t_2 - t_0)$	t_0	$\Delta(t_2 - t_0)$
Min.	390	−156.20	380.2	−273.00
1st Qu.	428.5	31.62	473.2	−97.88
Median	513.0	75.88	616.0	9.50
Mean	523.7	85.78	585.5	−30.75
3rd Qu.	614.8	141.60	676.2	76.62
Max.	647.8	346.50	803.2	131.00

MCP2/3: metacarpophalangeal joint of digit 2/3; dGEMRIC: delayed gadolinium-enhanced MRI of cartilage; MTX: methotrexate.

3. Results

3.1. Patient Population

Initially, a total of 20 patients were included as a proof-of-concept scenario (11 females/9 males, mean age: 45.8 years). All patients received at least one MRI scan. Despite reminder letters, three patients appeared only for the first MRI appointment (3 males: 1 × ADA + MTX group, 2 × control group). Three others received two MRI examinations and did not attend the final appointment (3 females: 2 × ADA + MTX group, 1 × control group). This resulted in 14 remaining patients, 10 allocated to the ADA + MTX group (6 females/4 males, mean age: 44.9 years) and 4 to the control group (2 females/2 males, mean age: 46.7 years).

3.2. Descriptive Statistics

Descriptive statistics of pooled MCP2 and MCP3 dGEMRIC values at baseline (t_0) and the change in dGEMRIC values after 24 weeks (t_2) compared to baseline are listed in Table 2. Furthermore, the evaluation of RAMRIS can be found in Table 3 and the decrease in RAMRIS values without significant differences in change is displayed in Figure 1 (median change over 24 weeks: ADA-MTX group: -5.8 ; control group: -1.0 , p : non-significant).

Table 3. RAMRIS values at baseline (t_0), after 12 weeks (t_1), after 24 weeks (t_2) in both treatment groups.

RAMRIS			
Adalimumab	t_0	t_1	t_2
Max.	75	70	57
Median	32.18	31.50	27.90
Min.	10	8	8
Control group			
Max.	29	28	28
Median	22.00	20.00	18.67
Min.	17	14	12

RAMRIS: rheumatoid arthritis magnetic resonance imaging score; MTX: methotrexate.

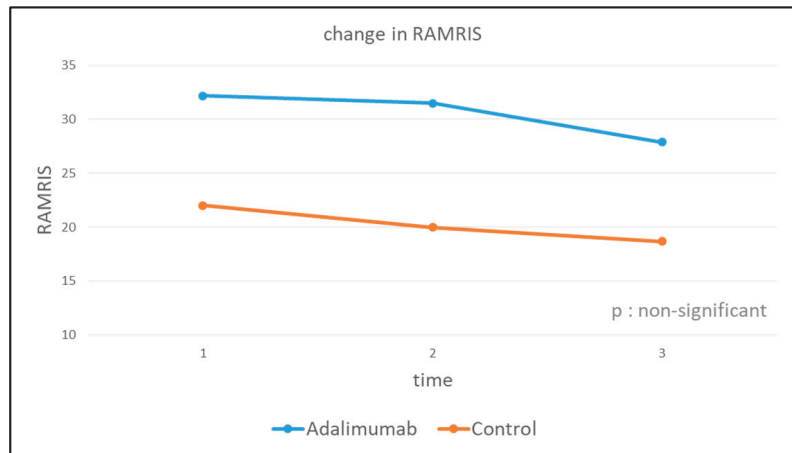


Figure 1. Change in RAMRIS between baseline and 24-week follow-up in both treatment arms. There was no significant difference in change between both treatment arms (p : non-significant).

3.3. Cartilage Integrity (dGEMRIC)

First, dGEMRIC values increased significantly in the ADA-MTX group (median change over 24 weeks: 75.88 ms, $p < 0.05$). In contrast, only a minimal, non-significant increase in dGEMRIC values was observed in the control group (median change over 24 weeks: 9.50 ms, p : non-significant) (Figure 2).

Second, in the direct comparison of the two treatment arms, there was a tendency for a greater increase in dGEMRIC values under adalimumab (ADA + MTX) than in the control group (placebo + MTX) which, however, did not meet the criteria for statistical significance (ADA + MTX group: dGEMRIC mean change 85.8 ms, range -156.2 – 346.5 ms; control group: dGEMRIC mean change -30.75 ms, range -273.0 – 131.0 ms; p : non-significant) (Figure 3). An example of dGEMRIC visualized cartilage of an early RA patient treated with adalimumab plus MTX is shown in Figure 4.

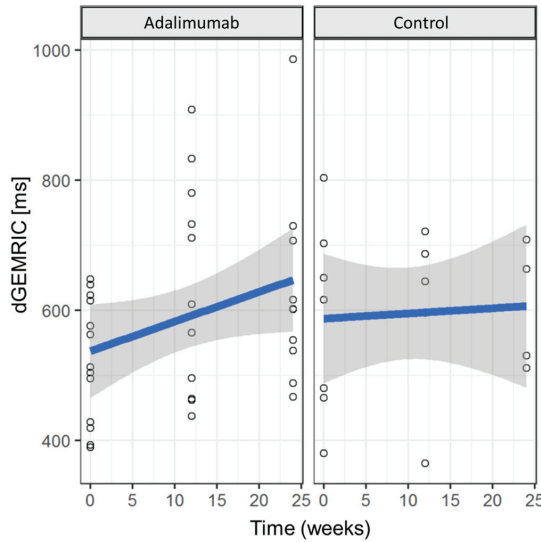


Figure 2. Change in cartilage quality over time. Change in dGEMRIC values in ms for both treatment groups over time with consideration of intermediate results (baseline, 12-week, and 24-week follow-up). There is strong statistical evidence of an increase in dGEMRIC values over time under adalimumab ($p < 0.05$), whereas the control group shows only a slight increase without statistical evidence (p : non-significant).

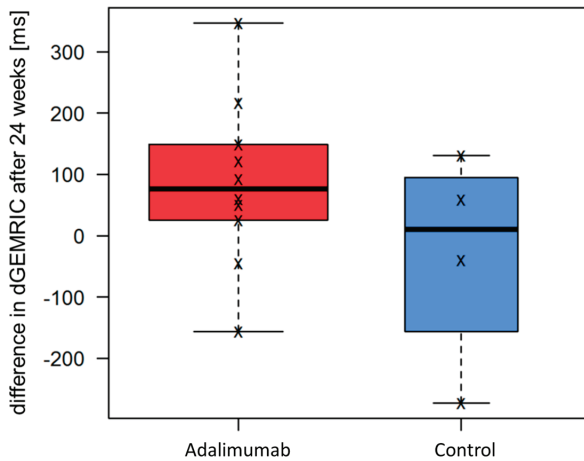


Figure 3. Change in cartilage quality in both treatment arms. The figure shows the difference in delayed gadolinium-enhanced MR imaging of cartilage (dGEMRIC) values in ms between baseline and 24-week follow-up in both treatment groups. Greater dGEMRIC values imply higher cartilage quality. Under adalimumab plus methotrexate (MTX), there was a—yet not significant—tendency for a greater increase in dGEMRIC values, suggesting a slight improvement in cartilage quality compared to the MTX monotherapy of the control group.

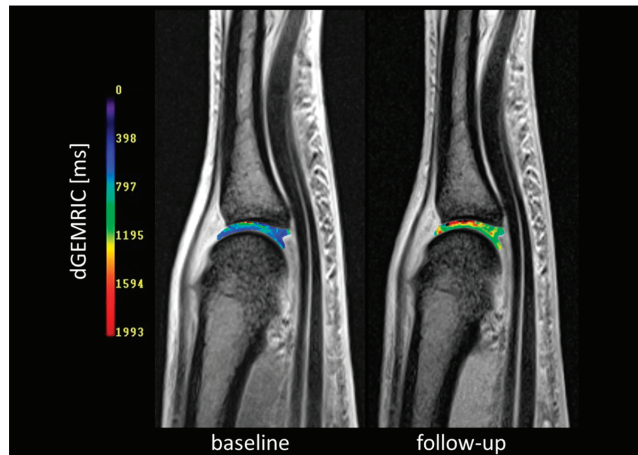


Figure 4. Cartilage composition of the MCP3 joint at baseline and after therapy. Fusion of morphological images with dGEMRIC maps demonstrating cartilage composition of the MCP3 joint at baseline and after 24 weeks of adalimumab plus MTX therapy (follow-up). Blue indicates cartilage damage and red indicates healthy cartilage. After therapy dGEMRIC values have increased (change from blue to green), indicating cartilage regeneration.

4. Discussion

An early start of a disease-modifying therapy and achieving early remission are two of the basic principles of the therapy concept for RA [4]. Early treatment significantly improves the long-term outcome and is therefore an important principle of the EULAR recommendations [4]. In this double-blind, placebo-controlled, proof-of-concept clinical trial, the effect of adalimumab in combination with MTX vs. MTX monotherapy on joint cartilage integrity of MCP2 and MCP3 in patients with early RA was examined with compositional MRI of the cartilage by using dGEMRIC [24]. To the best of our knowledge, this is the first trial evaluating the effect of adalimumab therapy on the cartilage in the finger joints.

Our main finding was that adalimumab added to MTX therapy leads to a significant increase in dGEMRIC values, which continuously improved over time, taking into account the measurements after 12 and 24 weeks, which was not observed in the group treated with MTX without adalimumab. These results indicate that controlling inflammation with adalimumab may lead to an improvement in cartilage quality, which is impaired by the underlying inflammatory disease (RA) [11]. In addition, the baseline to endpoint comparison alone, 6 months after initiation of therapy, showed a trend in cartilage improvement under ADA + MTX. However, compared with the control treatment arm, placebo + MTX, this change was not statistically relevant, possibly due to the fact that the number of patients who could be recruited was lower than expected.

The results of this study are in line with Beals et al., who documented reduced cartilage damage under bDMARD therapy using infliximab [25]. In this study, the results even suggest that, under therapy with bDMARDs, not only a reduction of cartilage damage but even a slight regeneration seems possible. The slightly different results between our study and the results of Beals et al. might be due to the different cartilage measurement MRI techniques (DCE-MRI vs. dGEMRIC) or due to the rather unlikely effect of the different bDMARDs used in both studies. Moreover, it has to be mentioned that the study populations also differ since our study aimed at very early, cs- and bDMARD naïve RA patients as compared to patients with a diagnosis of RA for at least 6 months in the study by Beals et al. However, both studies support the assumption of a positive effect of TNF- α -inhibitors on cartilage integrity in RA. Whether the effect of the TNF α inhibitor in

this study can be explained predominantly by a direct influence on the cartilage matrix or by a general decrease in inflammation, which indirectly has a positive effect on the cartilage, is still unclear. In addition to compositional imaging with dGEMRIC, the RAMRIS based on morphological imaging and sensitivity to change in joint inflammation and damage has been evaluated. The decreasing RAMRIS values in both treatment groups showed no significant difference in change, suggesting that next to the decreasing inflammation, a direct effect of TNF- α -inhibitors on cartilage might be responsible for the positive compositional cartilage changes under adalimumab. The results of this study are in contrast with the only further study that investigated the effect of bDMARDs on cartilage using dGEMRIC. Tiderius et al. investigated knee joints in 7 chronic RA patients and found cartilage deterioration after 22 weeks [26]. A possible explanation is that patients with early RA respond better to bDMARDs than patients at a more advanced stage of the disease, which again supports the current treatment principle of early and treat-to-target (T2T) therapy. Another potential explanation is a difference in sensitivity to bDMARDs between different joints. This theory can be supported by findings that point out a difference in cartilage regeneration between knee and ankle joints. Kuettner and Cole showed that cartilage cells in the knee synthesize fewer proteoglycans in reaction to damage than do cartilage cells in the ankle, suggesting a lower capacity for repair and regeneration [27]. Furthermore, the results of Kuettner and Cole indicated an increased degree of cartilage surface disorder with increasing body weight. In our cohort, however, there were no significant differences with respect to body weight.

Recently, the suitability of MRI for therapy monitoring using the control parameter bone edema has been questioned, as superiority of the MRI-guided treat-to-target group compared to the conventionally guided group could not be demonstrated [28]. This study explicitly focused on cartilage quality measured by dGEMRIC, which can only be assessed by MRI. Compositional cartilage imaging is expected to detect cartilage damage at an early stage [13]. As this may be a sign of progressive RA, which should be treated as early as possible [11], we still consider MRI a valuable diagnostic tool, especially since cartilage changes might be a more sensitive control parameter than bone marrow edema.

This study has some strengths. It is a double-blinded, placebo-controlled, clinical trial and the first published report of the compositional ability of MRI to depict cartilage regeneration in RA. This is important since the exclusion of the assessment of cartilage in previous clinical trials was an obstacle to the acceptance of MRI as a substitute for radiography [29]. However, the use of MRI is preferable as previous studies have shown that cartilage loss is at least as relevant to the long-term outcome as bone erosion [29]. One of the further strengths of this study is the use of dGEMRIC for cartilage imaging, as until recently, the MRI technique dGEMRIC was considered the reference standard to evaluate extracellular matrix components of hyaline cartilage [21].

Limitations of this study include manually selected ROI for dGEMRIC measurement in the MCP finger joints instead of automatically algorithm-based ROI. Due to the small size of the MCP joint and the resulting low contrast, automated cartilage recognition is not yet reliable enough to be used in study situations. Manual evaluation by an experienced radiologist was therefore preferred, despite the possible human interference factor. For future studies, the increased automated evaluation of clinical image data should be pursued. Another limitation of the current study was that the observations were based on a small number of patients. Only patients with early rheumatoid arthritis, i.e., with an onset of symptoms less than 12 months ago, were included in this patient group. These patients are relatively difficult to enroll, as the path from first symptom to the rheumatological diagnosis is often time-consuming. In addition, some of these patients start therapy with DMARDs, which was an exclusion criterion for the study. Recruitment of the patients was therefore only possible through close cooperation with the local outpatient clinic and doctors from primary care. To validate the changes in finger joint cartilage measured in patients with early rheumatoid arthritis in this proof-of-concept scenario, future studies with larger patient cohorts are recommended.

5. Conclusions

In conclusion, this study suggests that in patients with early RA, Adalimumab plus MTX tends to improve cartilage composition after 24 weeks. The results point out that TNF- α -inhibitors may induce cartilage regeneration in early RA and thus slow down or even prevent the development of joint damage, while this is not the case for patients treated with MTX alone. Furthermore, compositional MR imaging is proving to be a valuable tool for assessing inflammation to detect early cartilage damage in RA.

Author Contributions: Conceptualization, P.S., C.S., B.O. and M.S.; methodology, B.O. and R.B.; software, R.B. and A.M.-L.; validation, P.S., D.B.A. and S.V.; formal analysis, C.S., O.S. and M.F.; investigation, L.M.W., S.V., J.G.R. and A.M.-L.; resources, D.B.A., O.S. and J.G.R.; data curation, R.B. and M.F.; writing—original draft preparation, M.F.; writing—review and editing, M.F., P.S., C.S. and G.A.; visualization, R.B. and M.F.; supervision, P.S. and X.B.; project administration, M.F., D.B.A. and P.S.; funding acquisition, M.S. and B.O. All authors have read and agreed to the published version of the manuscript.

Funding: AbbVie Deutschland GmbH & Co. KG; Max-Planck-Ring 2; 65205 Wiesbaden provided the study medication and financed the study. M.F., L.M.W., and D.B.A. were supported by a research grant from the medical faculty of the University of Dusseldorf.

Institutional Review Board Statement: The study was conducted according to the guidelines of the Declaration of Helsinki and approved by the Institutional Ethics Committee of the Heinrich-Heine University of Dusseldorf (reference number: MO-LKP-719).

Informed Consent Statement: Informed consent was obtained from all subjects involved in the study.

Data Availability Statement: Data and evaluation scripts can be provided by the authors upon reasonable request.

Acknowledgments: The authors thank Erika Rädisch for assistance with the MRI measurements.

Conflicts of Interest: The authors declare no conflict of interest.

References

1. Lee, D.M.; Weinblatt, M.E. Rheumatoid arthritis. *Lancet* **2001**, *358*, 903–911. [[CrossRef](#)] [[PubMed](#)]
2. Tobon, G.J.; Youinou, P.; Saraux, A. The environment, geo-epidemiology, and autoimmune disease: Rheumatoid arthritis. *J. Autoimmun.* **2010**, *35*, 10–14. [[CrossRef](#)] [[PubMed](#)]
3. McInnes, I.B.; Schett, G. Pathogenetic insights from the treatment of rheumatoid arthritis. *Lancet* **2017**, *389*, 2328–2337. [[CrossRef](#)]
4. Combe, B.; Landewe, R.; Daien, C.I.; Hua, C.; Aletaha, D.; Alvaro-Gracia, J.M.; Bakkers, M.; Brodin, N.; Burmester, G.R.; Codreanu, C.; et al. 2016 update of the EULAR recommendations for the management of early arthritis. *Ann. Rheum. Dis.* **2017**, *76*, 948–959. [[CrossRef](#)]
5. den Broeder, A.; van de Putte, L.; Rau, R.; Schattenkirchner, M.; Van Riel, P.; Sander, O.; Binder, C.; Fenner, H.; Bankmann, Y.; Velagapudi, R.; et al. A single dose, placebo controlled study of the fully human anti-tumor necrosis factor-alpha antibody adalimumab (D2E7) in patients with rheumatoid arthritis. *J. Rheumatol.* **2002**, *29*, 2288–2298.
6. Huang, F.; Zhang, F.C.; Bao, C.D.; Tao, Y.; Gu, J.R.; Xu, J.H.; Zhu, P.; Xu, H.J.; Zhang, Z.Y.; Zhao, D.B.; et al. [Adalimumab plus methotrexate for the treatment of rheumatoid arthritis: A multi-center randomized, double-blind, placebo-controlled clinical study.]. *Zhonghua Nei Ke Za Zhi* **2009**, *48*, 916–921. [[PubMed](#)]
7. Takeuchi, T.; Yamanaka, H.; Ishiguro, N.; Miyasaka, N.; Mukai, M.; Matsubara, T.; Uchida, S.; Akama, H.; Kupper, H.; Arora, V.; et al. Adalimumab, a human anti-TNF monoclonal antibody, outcome study for the prevention of joint damage in Japanese patients with early rheumatoid arthritis: The HOPEFUL 1 study. *Ann. Rheum. Dis.* **2014**, *73*, 536–543. [[CrossRef](#)]
8. American College of Rheumatology Rheumatoid Arthritis Clinical Trials Task Force Imaging, G.; Outcome Measures in Rheumatology Magnetic Resonance Imaging Inflammatory Arthritis Working, G. Review: The utility of magnetic resonance imaging for assessing structural damage in randomized controlled trials in rheumatoid arthritis. *Arthritis Rheumatol.* **2013**, *65*, 2513–2523. [[CrossRef](#)]
9. Ostergaard, M.; Peterfy, C.; Conaghan, P.; McQueen, F.; Bird, P.; Ejbjerg, B.; Shnier, R.; O'Connor, P.; Klarlund, M.; Emery, P.; et al. OMERACT rheumatoid arthritis magnetic resonance imaging studies. Core set of MRI acquisitions, joint pathology definitions, and the OMERACT RA-MRI scoring system. *J. Rheumatol.* **2003**, *30*, 1385–1386.
10. Aletaha, D.; Funovits, J.; Smolen, J.S. Physical disability in rheumatoid arthritis is associated with cartilage damage rather than bone destruction. *Ann. Rheum. Dis.* **2011**, *70*, 733–739. [[CrossRef](#)]

11. Ostergaard, M.; Peterfy, C.G.; Bird, P.; Gandjbakhch, F.; Glinatsi, D.; Eshed, I.; Haavardsholm, E.A.; Lillegraven, S.; Boyesen, P.; Ejbjerg, B.; et al. The OMERACT Rheumatoid Arthritis Magnetic Resonance Imaging (MRI) Scoring System: Updated Recommendations by the OMERACT MRI in Arthritis Working Group. *J. Rheumatol.* **2017**, *44*, 1706–1712. [[CrossRef](#)] [[PubMed](#)]
12. Miese, F.; Buchbender, C.; Scherer, A.; Wittsack, H.J.; Specker, C.; Schneider, M.; Antoch, G.; Ostendorf, B. Molecular imaging of cartilage damage of finger joints in early rheumatoid arthritis with delayed gadolinium-enhanced magnetic resonance imaging. *Arthritis Rheumatol.* **2012**, *64*, 394–399. [[CrossRef](#)] [[PubMed](#)]
13. Owman, H.; Ericsson, Y.B.; Englund, M.; Tiderius, C.J.; Tjornstrand, J.; Roos, E.M.; Dahlberg, L.E. Association between delayed gadolinium-enhanced MRI of cartilage (dGEMRIC) and joint space narrowing and osteophytes: A cohort study in patients with partial meniscectomy with 11 years of follow-up. *Osteoarthr. Cartil.* **2014**, *22*, 1537–1541. [[CrossRef](#)] [[PubMed](#)]
14. Bashir, A.; Gray, M.L.; Burstein, D. Gd-DTPA²⁻ as a measure of cartilage degradation. *Magn. Reson. Med.* **1996**, *36*, 665–673. [[CrossRef](#)] [[PubMed](#)]
15. Crema, M.D.; Roemer, F.W.; Marra, M.D.; Burstein, D.; Gold, G.E.; Eckstein, F.; Baum, T.; Mosher, T.J.; Carrino, J.A.; Guermazi, A. Articular cartilage in the knee: Current MR imaging techniques and applications in clinical practice and research. *Radiographics* **2011**, *31*, 37–61. [[CrossRef](#)]
16. Schleich, C.; Muller-Lutz, A.; Sewerin, P.; Ostendorf, B.; Buchbender, C.; Schneider, M.; Antoch, G.; Miese, F. Intra-individual assessment of inflammatory severity and cartilage composition of finger joints in rheumatoid arthritis. *Skelet. Radiol.* **2015**, *44*, 513–518. [[CrossRef](#)]
17. Muller-Lutz, A.; Schleich, C.; Sewerin, P.; Gross, J.; Pentang, G.; Wittsack, H.J.; Antoch, G.; Schneider, M.; Ostendorf, B.; Miese, F. Comparison of quantitative and semiquantitative dynamic contrast-enhanced MRI with respect to their correlation to delayed gadolinium-enhanced MRI of the cartilage in patients with early rheumatoid arthritis. *J. Comput. Assist. Tomogr.* **2015**, *39*, 64–69. [[CrossRef](#)]
18. Sewerin, P.; Muller-Lutz, A.; Abrar, D.B.; Odendahl, S.; Eichner, M.; Schneider, M.; Ostendorf, B.; Schleich, C. Prevention of the progressive biochemical cartilage destruction under methotrexate therapy in early rheumatoid arthritis. *Clin. Exp. Rheumatol.* **2019**, *37*, 179–185.
19. Aletaha, D.; Neogi, T.; Silman, A.J.; Funovits, J.; Felson, D.T.; Bingham, C.O., 3rd; Birnbaum, N.S.; Burmester, G.R.; Bykerk, V.P.; Cohen, M.D.; et al. 2010 rheumatoid arthritis classification criteria: An American College of Rheumatology/European League Against Rheumatism collaborative initiative. *Ann. Rheum. Dis.* **2010**, *69*, 1580–1588. [[CrossRef](#)]
20. Frize, M.; Ogungbemile, A. Estimating rheumatoid arthritis activity with infrared image analysis. *Stud. Health Technol. Inform.* **2012**, *180*, 594–598.
21. Miese, F.R.; Ostendorf, B.; Wittsack, H.J.; Reichelt, D.C.; Mamisch, T.C.; Zilkens, C.; Lanzman, R.S.; Schneider, M.; Scherer, A. Metacarpophalangeal joints in rheumatoid arthritis: Delayed gadolinium-enhanced MR imaging of cartilage—A feasibility study. *Radiology* **2010**, *257*, 441–447. [[CrossRef](#)] [[PubMed](#)]
22. Miese, F.; Kropil, P.; Ostendorf, B.; Scherer, A.; Buchbender, C.; Quentin, M.; Lanzman, R.S.; Blondin, D.; Schneider, M.; Bittersohl, B.; et al. Motion correction improves image quality of dGEMRIC in finger joints. *Eur. J. Radiol.* **2011**, *80*, e427–e431. [[CrossRef](#)] [[PubMed](#)]
23. Mori, V.; Sawicki, L.M.; Sewerin, P.; Eichner, M.; Schaarschmidt, B.M.; Oezel, L.; Gehrmann, S.; Bittersohl, B.; Antoch, G.; Schleich, C. Differences of radiocarpal cartilage alterations in arthritis and osteoarthritis using morphological and biochemical magnetic resonance imaging without gadolinium-based contrast agent administration. *Eur. Radiol.* **2018**, *29*, 2581–2588. [[CrossRef](#)]
24. Miese, F.R.; Ostendorf, B.; Wittsack, H.J.; Reichelt, D.C.; Kropil, P.; Lanzman, R.S.; Mamisch, T.C.; Zilkens, C.; Jellus, V.; Quentin, M.; et al. Cartilage quality in finger joints: Delayed Gd(DTPA)(2)-enhanced MRI of the cartilage (dGEMRIC) at 3T. *Rofo* **2010**, *182*, 873–878. [[CrossRef](#)] [[PubMed](#)]
25. Beals, C.; Baumgartner, R.; Peterfy, C.; Balanescu, A.; Mirea, G.; Harabagiu, A.; Popa, S.; Cheng, A.; Feng, D.; Ashton, E.; et al. Magnetic resonance imaging of the hand and wrist in a randomized, double-blind, multicenter, placebo-controlled trial of infliximab for rheumatoid arthritis: Comparison of dynamic contrast enhanced assessments with semi-quantitative scoring. *PLoS ONE* **2017**, *12*, e0187397. [[CrossRef](#)]
26. Tiderius, C.J.; Sandin, J.; Svensson, J.; Dahlberg, L.E.; Jacobsson, L. Knee cartilage quality assessed with dGEMRIC in rheumatoid arthritis patients before and after treatment with a TNF inhibitor. *Acta Radiol.* **2010**, *51*, 1034–1037. [[CrossRef](#)]
27. Kuettner, K.E.; Cole, A.A. Cartilage degeneration in different human joints. *Osteoarthr. Cartil.* **2005**, *13*, 93–103. [[CrossRef](#)]
28. Moller-Bisgaard, S.; Horslev-Petersen, K.; Ejbjerg, B.; Hetland, M.L.; Ornbjerg, L.M.; Glinatsi, D.; Moller, J.; Boesen, M.; Christensen, R.; Stengaard-Pedersen, K.; et al. Effect of Magnetic Resonance Imaging vs Conventional Treat-to-Target Strategies on Disease Activity Remission and Radiographic Progression in Rheumatoid Arthritis: The IMAGINE-RA Randomized Clinical Trial. *JAMA* **2019**, *321*, 461–472. [[CrossRef](#)]
29. Peterfy, C.; Emery, P.; Tak, P.P.; Ostergaard, M.; DiCarlo, J.; Otsa, K.; Navarro Sarabia, F.; Pavelka, K.; Bagnard, M.A.; Gylvin, L.H.; et al. MRI assessment of suppression of structural damage in patients with rheumatoid arthritis receiving rituximab: Results from the randomised, placebo-controlled, double-blind RA-SCORE study. *Ann. Rheum. Dis.* **2016**, *75*, 170–177. [[CrossRef](#)]

Disclaimer/Publisher's Note: The statements, opinions and data contained in all publications are solely those of the individual author(s) and contributor(s) and not of MDPI and/or the editor(s). MDPI and/or the editor(s) disclaim responsibility for any injury to people or property resulting from any ideas, methods, instructions or products referred to in the content.



Article

The Clinical Utility of Dual-Energy Computed Tomography in the Diagnosis of Gout—A Cross-Sectional Study

Maria Sotniczuk ^{1,*}, Anna Nowakowska-Plaza ², Jakub Wroński ², Małgorzata Wisłowska ²
and Iwona Sudol-Szopińska ¹

¹ Department of Radiology, National Institute of Geriatrics, Rheumatology and Rehabilitation, 02-637 Warsaw, Poland

² Department of Rheumatology, National Institute of Geriatrics, Rheumatology and Rehabilitation, 02-637 Warsaw, Poland

* Correspondence: m.sotniczuk@gmail.com

Abstract: Dual-energy computed tomography (DECT) is an imaging technique that detects monosodium urate (MSU) deposits. This study aimed to assess the clinical utility of DECT in the diagnosis of gout. A total of 120 patients with clinical suspicion of gout who underwent DECT were retrospectively enrolled. The sensitivity and specificity of DECT alone, American College of Rheumatology (ACR)/European Alliance of Associations for Rheumatology (EULAR) classification criteria without DECT, and ACR/EULAR criteria with DECT were assessed. Additionally, an analysis of gout risk factors was performed. When artifacts were excluded, any MSU volume provided the best diagnostic value of DECT (AUC = 0.872, 95% CI 0.806–0.938). DECT alone had a sensitivity of 90.4% and specificity of 74.5%. Although ACR/EULAR criteria without DECT provided better diagnostic accuracy than DECT alone (AUC = 0.926, 95% CI 0.878–0.974), the best value was obtained when combining both (AUC = 0.957, 95% CI 0.924–0.991), with 100% sensitivity and 76.6% specificity. In univariate analysis, risk factors for gout were male sex, presence of tophi, presence of MSU deposits on DECT, increased uric acid in serum (each $p < 0.001$), and decreased glomerular filtration rate (GFR) ($p = 0.029$). After logistic regression, only increased serum uric acid ($p = 0.034$) and decreased GFR ($p = 0.018$) remained independent risk factors for gout. Our results suggest that DECT significantly increases the sensitivity of the ACR/EULAR criteria in the diagnosis of gout.

Keywords: gout; dual-energy computed tomography; monosodium urate crystals

Citation: Sotniczuk, M.; Nowakowska-Plaza, A.; Wroński, J.; Wisłowska, M.; Sudol-Szopińska, I. The Clinical Utility of Dual-Energy Computed Tomography in the Diagnosis of Gout—A Cross-Sectional Study. *J. Clin. Med.* **2022**, *11*, 5249. <https://doi.org/10.3390/jcm11175249>

Academic Editors: Marco Sebastiani and Eugen Feist

Received: 2 August 2022

Accepted: 4 September 2022

Published: 5 September 2022

Publisher's Note: MDPI stays neutral with regard to jurisdictional claims in published maps and institutional affiliations.



Copyright: © 2022 by the authors. Licensee MDPI, Basel, Switzerland. This article is an open access article distributed under the terms and conditions of the Creative Commons Attribution (CC BY) license (<https://creativecommons.org/licenses/by/4.0/>).

1. Introduction

Gout is the most common inflammatory arthritis, and its prevalence is increasing in Western societies [1]. The inflammation is caused by the deposition of monosodium urate (MSU) crystals in and around joints [2]. An increased risk of developing gout is associated with male sex, obesity, hyperuricemia, and a diet rich in purines [3]. A gout attack presents as a sudden, painful swelling of the joint, usually the first metatarsophalangeal or ankle joint. Chronic gout leads to joint destruction and the formation of tophi in soft tissues [1,2].

The gold standard for the diagnosis of gout is a visualization of the presence of negatively birefringent MSU crystals under polarizing microscopy in a sample of aspirated synovial fluid from an affected joint. However, this is an invasive procedure and can be difficult to perform, especially in small joints. Moreover, false negative results can occur due to low concentrations of crystals in the early stage of the disease [2]. The search for MSU crystals can also be negative in the case of extra-articular gout involvement.

The 2015 American College of Rheumatology (ACR)/European Alliance of Associations for Rheumatology (EULAR) gout classification criteria are often used in clinical trials [4]. This scoring system includes clinical criteria and laboratory and imaging findings. Imaging modalities that can facilitate the diagnosis of gout and are included in

ACR/EULAR criteria are plain radiography (presence of typical bone erosions), ultrasound (presence of a “double contour” sign), and dual-energy computed tomography (DECT).

DECT, which has become more popular over the last few years, enables the detection and quantification of MSU crystal deposition in joints, tendons, and periarticular soft tissue. DECT does not require a contrast agent; instead, it uses tissue-specific attenuation. Data are acquired at 80 kV and 140 kV and analyzed using a two-material decomposition algorithm designed for gout that color-codes urate [4–6]. A positive scan is defined as the presence of color-coded MSU depositions at articular or periarticular sites. Nail-bed, submillimeter-sized, skin, motion, menisci, costal cartilage, and vessels should be excluded as artifacts [4,7,8]. DECT has a sensitivity of 79–93% and a specificity of 75–90% [9–12]. Nevertheless, false-negative results are considered common in patients with a recent onset of gout [13,14].

The aim of this study was to assess the diagnostic value of DECT in patients with clinical suspicion of gout. Additionally, an analysis of gout risk factors was performed.

2. Materials and Methods

Patients who were hospitalized in the reference center for rheumatic disease from January 2018 until February 2021 due to clinical suspicion of gout and underwent DECT were retrospectively enrolled in the study. The study was approved by the institutional ethics board (KBT-1/2/2022). Patients with no medical history available (electronic or paper) were excluded from the study.

The following data were also collected: patient characteristics (age, sex, and BMI), comorbidities (hypertension, diabetes, chronic kidney disease, kidney stones, psoriasis, hypothyroidism, dyslipidemia, obesity [defined as BMI ≥ 30 kg/m²], and inflammatory rheumatic conditions, such as rheumatoid, psoriatic, and unspecified arthritis, other spondyloarthropathies, and connective tissue diseases), laboratory findings (serum uric acid level, uric acid in urine, 24 h urine collection, creatinine and glomerular filtration rate (GFR), C-reactive protein, and full lipid profile), presence of tophi, and history of urate-lowering therapy. Data from imaging findings included in the database were: the presence of typical erosions on X-ray and MSU deposits on DECT (with their location and volume).

For DECT, a dual-energy scanner (Siemens Somatom Definition AS 128-slices) with voltage of 80/140 kV was used. All examinations were reconstructed using bone algorithm 0.75 mm slices. Software program syngo.via 4.6.6 Siemens Healthineers (Warsaw, Poland) was used for post-processing with a “gout” preset. The MSU crystals were color-coded green. DECT was considered positive based on the automatically calculated result checked by two experienced radiologists who excluded possible artifacts. The DECT analysis was performed by radiologists blinded to clinical and laboratory findings.

Due to the lack of synovial fluid examination in all patients, in our study, we used clinical diagnosis of gout as the diagnostic gold standard. The clinical diagnosis of gout was made by two rheumatologists (attending physician and independent expert) based on patients’ symptoms, history of gout risk factors and comorbidities, physical examination, and laboratory and imaging findings. Additionally, all patients were retrospectively analyzed using the 2015 ACR/EULAR gout classification criteria—both with and without taking into account the DECT results.

Statistical Analysis

For each of the diagnostic methods (DECT alone, ACR/EULAR classification criteria without DECT, and ACR/EULAR classification criteria with DECT), the sensitivity and specificity were calculated, and the receiver operating characteristic (ROC) curves were obtained with the calculation of the area under the curve (AUC). The compliance of the data with the normal distribution was assessed using the Shapiro–Wilk test. The significance of the observed differences between the two groups was assessed using the Student’s *t*-test for variables with a normal distribution, the Mann–Whitney U test for variables without a

normal distribution, and the chi-square test or Fisher’s exact test (for tables with values less than 5) for categorical variables. In multivariate analysis, logistic regression analysis was used. Statistical significance was set at $p < 0.05$. Statistical analysis was performed using Statistica 13.3 software (StatSoft Polska, Kraków, Poland).

3. Results

A total of 120 patients (84 men and 36 women) were enrolled in the study. Out of them, 88 (73.3%) patients had more than one anatomical area scanned with DECT. Overall, 318 anatomical areas were examined, and 180 (57%) were positive for MSU crystals on DECT (Table 1).

Table 1. Anatomical areas examined by dual-energy computed tomography.

Anatomical Areas	Total	Positive for MSU Crystals
Hands	79	30 (38%)
Feet and ankles	141	95 (67%)
Knees	59	35 (59%)
Shoulders	6	5 (83%)
Elbows	33	15 (45%)
Total	318	180 (57%)

MSU: monosodium urate.

Feet and ankles, followed by knees, were the most common sites for MSU depositions. Examples of DECT scans positive for MSU crystals in a foot and ankle and in a knee are presented in Figures 1 and 2, respectively.

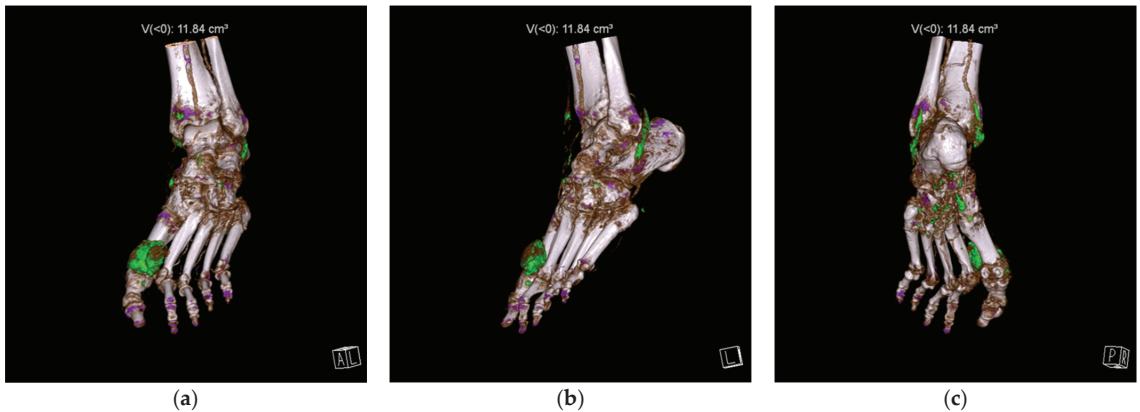


Figure 1. Dual-energy computed tomography 3D reconstruction of a foot positive for monosodium urate (MSU) crystals (color-coded green) in anterior (a), lateral (b), and posterior (c) views. The MSU deposits are present around the first metatarsophalangeal joint (a,b) and around multiple tendons in the ankle and foot (b,c). Volume of the MSU deposits was automatically calculated (11.84 cm³).

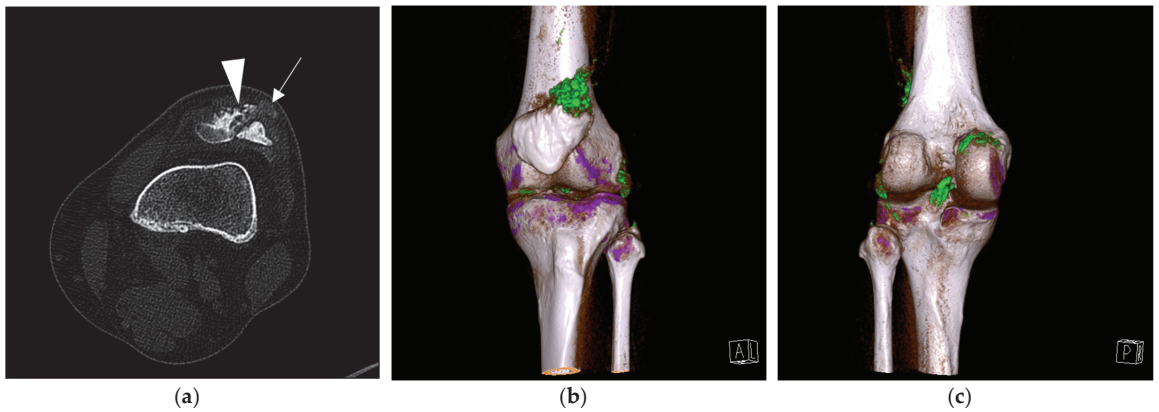


Figure 2. Gout in a knee. (a) Computed tomography scan shows erosions (arrowhead) and a possible tophus (arrow) at the lateral aspect of the patella base. (b) Dual-energy computed tomography 3D reconstruction confirms monosodium urate (MSU) deposits (color-coded green) in this location. (c) Dual-energy computed tomography 3D reconstruction shows MSU deposits in the posterior compartment of the knee.

A total of 73 (58%) patients were finally clinically diagnosed with gout. Patient characteristics are presented in Table 2, and gout diagnostic features are presented in Table 3.

Table 2. Patients’ characteristics.

Patient Characteristics	Gout (n = 73)	Without Gout (n = 47)	Difference
Age (mean, ±SD)	55.4 (±12.1)	52.9 (±14.4)	ns
Sex—male (n, %)	61 (83.6%)	23 (48.9%)	p < 0.001
Obesity (n, %)	33(45.2%)	18(38.3%)	ns
Hypertension (n, %)	39 (53.4%)	26 (55.3%)	ns
Type 2 diabetes (n, %)	13 (17.8%)	7 (14.9%)	ns
Dyslipidemia (n, %)	40 (54.8%)	23 (48.9%)	ns
Kidney stones (n, %)	3 (4.1%)	3 (6.4%)	ns
Chronic kidney disease (n, %)	18 (24.7%)	8 (17%)	ns
Rheumatic conditions			
- Arthritis, rheumatoid, or unspecified (n, %)	7 (9.6%)	14 (29.8%)	p = 0.005
- Psoriasis or psoriatic arthritis (n, %)	6 (8.2%)	6 (12.8%)	ns
- Other spondyloarthritis (n, %)	10 (13.7%)	7 (14.9%)	ns
- Connective tissue disease (n, %)	4 (5.6%)	4 (8.5%)	ns
- Calcium pyrophosphate dihydrate deposition (n, %)	0	3 (6.4%)	-
- Infection arthritis (n, %)	1 (1.4%)	1 (2.1%)	ns
Hypothyroidism (n, %)	1 (1.4%)	4 (8.5%)	ns
Alcohol dependency (n, %)	1 (1.4%)	1 (2.1%)	ns
Myeloproliferative syndrome (n, %)	1 (1.4%)	0 (0%)	-

DECT detected MSU deposits in 96 (80%) patients. The optimal cut-off point for the MSU volume was calculated to be 0.05 cm³ (AUC = 0.779, 95% CI 0.692–0.866). However, after radiological assessment, 18 positive DECT results were evaluated as artifacts (mainly nails and menisci). Examples of artifacts are presented in Figure 3.

Table 3. Patients' gout diagnostic features.

Gout Diagnostic Features	Gout (n = 73)	Without Gout (n = 47)	Difference
Uric acid in serum, mg/dL (mean, ±SD)	8.1 (±2.2)	6.1 (±2.3)	<i>p</i> < 0.001
Elevated uric acid in serum (n, %)	46 (63%)	16 (34%)	<i>p</i> = 0.002
Uric acid in 24 h urine collection, g/24 h (median, min, max)	0.46 (0.18, 1.2)	0.41 (0.29, 0.82)	ns
Excessive uric acid in urine (n, %)	4 (5.5%)	1 (2.1%)	ns
Tophus (n, %)	12 (16.4%)	0 (0%)	-
Features of gout in X-ray (n, %)	21 (28.8%)	3 (6.4%)	<i>p</i> = 0.003
Positive DECT result (n, %)	68 (93.2%)	28 (59.6%)	<i>p</i> < 0.001
- True deposits in DECT (n, %)	66 (90.4%)	12 (25.5%)	<i>p</i> < 0.001
- Artifacts in DECT (n, %)	48 (65.8%)	25 (53.2%)	ns
Diagnosis of gout according to ACR/EULAR criteria before DECT (n, %)	54 (74%)	4 (8.5%)	<i>p</i> < 0.001
Diagnosis of gout according to ACR/EULAR criteria after DECT (n, %)	73 (100%)	11 (23.4%)	<i>p</i> < 0.001
Uric-acid-lowering treatment (n, %)	41 (56.2%)	11 (23.4%)	<i>p</i> < 0.001

DECT: dual-energy computed tomography, ACR/EULAR: American College of Rheumatology/European Alliance of Associations for Rheumatology.



Figure 3. Dual-energy computed tomography of a foot with artifacts present in nailbeds (arrows) and skin (arrowhead).

The best diagnostic value of DECT, after artifacts exclusion, was obtained with any MSU volume (AUC = 0.872, 95% CI 0.806–0.938), with a DECT sensitivity of 90.4% and specificity of 74.5%.

The 2015 ACR/EULAR gout classification criteria without DECT provided better diagnostic accuracy than DECT alone, with 74% sensitivity and 91.5% specificity (AUC = 0.926, 95% CI 0.878–0.974). The best diagnostic value was obtained with the ACR/EULAR criteria taking into account DECT results, with 100% sensitivity and 76.6% specificity (AUC = 0.957, 95% CI 0.924–0.991). In the studied group, DECT enabled a gout diagnosis in 19 additional patients and the exclusion of gout in 3 patients. ROC curves of the gout diagnostic tools are presented in Figure 4.

The following risk factors for gout were identified in a univariate analysis: male sex, presence of tophi, presence of MSU deposits on DECT, increased uric acid in serum (each *p* < 0.001), and decreased GFR (*p* = 0.029). After logistic regression, only increased serum uric acid (*p* = 0.034) and decreased GFR (*p* = 0.018) remained independent risk factors for gout.

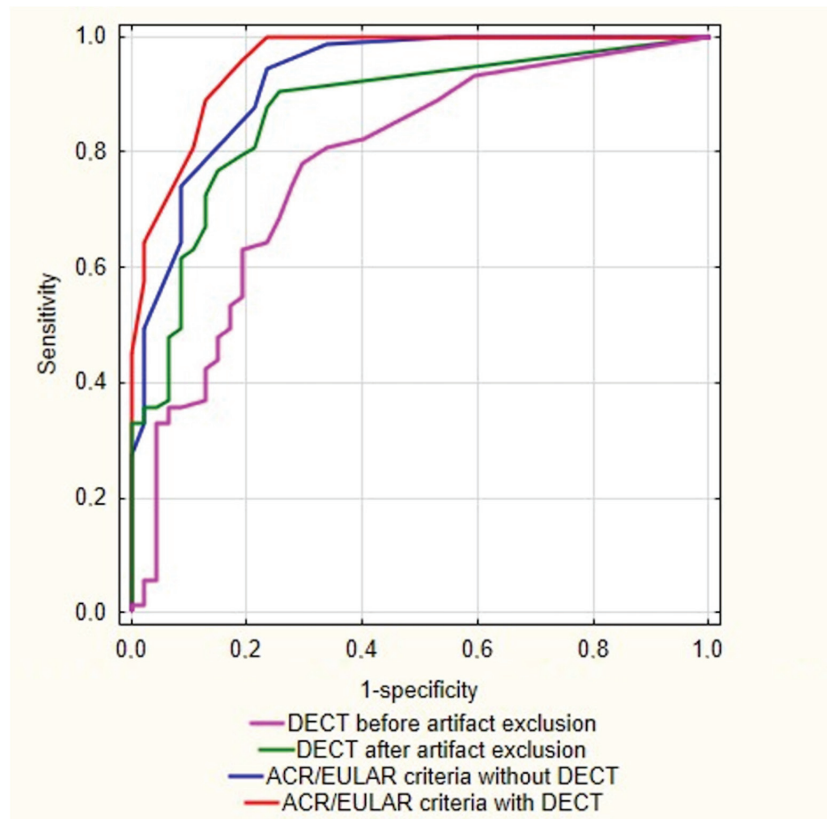


Figure 4. Receiver operating curves of the different gout diagnostic tools. DECT: dual-energy computed tomography, ACR: American College of Rheumatology, EULAR, European Alliance of Associations for Rheumatology.

4. Discussion

This cross-sectional study showed that the detection of MSU crystals on DECT can significantly improve gout diagnosis. We found that DECT alone has a sensitivity of 90.4% and a specificity of 74.5%, which is consistent with the results of previous studies [9–12]. However, DECT should not be used alone without consideration of other gout features. In our study, the best diagnostic accuracy was obtained with the 2015 ACR/EULAR gout classification criteria including DECT, with 100% sensitivity and 76.6% specificity. This is in line with a previous study by Gamala et al., who found that DECT has an additive value in ACR/EULAR gout classification criteria [15].

To the best of our knowledge, this is the first study to assess the relationship between the volume of MSU deposits on DECT and the diagnosis of gout. After DECT artifacts were excluded, any positive MSU result provides the best diagnostic value, regardless of the size of the deposit. However, if there is no possibility of the manual exclusion of artifacts by the radiologist, the cut-off value of 0.05 cm³ provides the best diagnostic value.

The artifact identification is executed subjectively and requires a large amount of experience. In our study, the most challenging step was the differentiation of small amounts of MSU deposits (sometimes as little as 0.01 cm³) from artifacts. This could give false-positive results. Although there are studies that have attempted to optimize DECT post-processing settings to reduce artifacts, additional studies are needed to improve the automatic elimination of all artifacts [6–8,16–19].

Our study also showed the need for more reliable gout diagnosis in patients with suspected gout. Primary care physicians often prescribe uric-acid-lowering drugs to patients with suspected gout due to hyperuricemia associated with arthralgia. In this study, 11 (23.4%) patients without gout were taking urate-lowering treatment. It cannot be unequivocally assessed whether this was due to an overtreatment or observation of patients in remission due to the dissolution of MSU crystals after uric-acid-lowering treatment. The use of the 2015 ACR/EULAR criteria in conjunction with DECT resulted in drug withdrawal in these patients. Other inflammatory joint diseases should be taken into account in the differential diagnosis. We found significantly more autoimmune arthritis among patients in whom gout was excluded than in patients with confirmed gout (29.8% vs. 9.6%) (Table 2).

Risk factors for gout are well-studied and include male sex, obesity, chronic kidney disease, hypertension, diabetes, and hyperuricemia [20,21]. In our study, only increased serum uric acid ($p = 0.034$) and decreased GFR ($p = 0.018$) remained independent risk factors for gout in multivariate analysis, probably due to the small sample size.

Our study has several other limitations. The first limitation is the lack of data on the onset of symptoms. We obtained some false-negative DECT results, which are likely due to the examination taking place at an early disease stage, when the MSU crystals did not have time to be deposited in the joints [13]. Secondly, ultrasound results were not included in our analysis. Finally, the major limitation is the fact that none of the patients had synovial fluid tested for MSU crystals. Although this is theoretically the gold standard for gout diagnosis, the synovial fluid aspiration procedure is invasive and technically difficult to perform in the joints most commonly affected by gout, and false negative results can occur due to low concentrations of crystals in the early stage of the disease. Therefore, gout in everyday clinical practice is diagnosed clinically.

5. Conclusions

DECT proved to be a helpful tool in the diagnosis of gout in a real-world setting, significantly increasing the sensitivity of the 2015 ACR/EULAR criteria. DECT could therefore be beneficial for patients with suspected gout by providing an earlier diagnosis and treatment. Both clinicians and radiologists should be aware of possible artifacts that can lead to false-positive results. As such, DECT should not be used alone as a diagnostic tool.

Author Contributions: Conceptualization, M.S., M.W. and I.S.-S.; methodology, M.S. and A.N.-P.; validation, J.W.; formal analysis, J.W.; investigation, M.S. and A.N.-P.; resources, I.S.-S.; data curation, J.W.; writing—original draft preparation, M.S., A.N.-P. and J.W.; writing—review and editing, M.W. and I.S.-S.; visualization, J.W.; supervision, I.S.-S.; project administration, M.S.; funding acquisition, N/A. All authors have read and agreed to the published version of the manuscript.

Funding: This research received no external funding.

Institutional Review Board Statement: The study was conducted according to the guidelines of the Declaration of Helsinki, and approved by the Institutional Bioethics Committee of the National Institute of Geriatrics, Rheumatology and Rehabilitation (protocol code KBT-1/2/2022, February 2022).

Informed Consent Statement: Patient consent was waived due to the retrospective study design, which was based on medical records.

Data Availability Statement: The data underlying this article will be shared upon reasonable request to the corresponding author.

Conflicts of Interest: The authors declare no conflict of interest.

References

1. Kuo, C.F.; Grainge, M.J.; Zhang, W.; Doherty, M. Global epidemiology of gout: Prevalence, incidence and risk factors. *Nat. Rev. Rheumatol.* **2015**, *11*, 649–662. [[CrossRef](#)] [[PubMed](#)]
2. Sudol-Szopińska, I.; Afonso, P.D.; Jacobson, J.A.; Teh, J. Imaging of gout: Findings and pitfalls. A pictorial review. *Acta Reumatol. Port.* **2020**, *45*, 20–25. [[PubMed](#)]
3. Zhang, Y.; Chen, C.; Choi, H.; Chaisson, C.; Hunter, D.; Niu, J.; Neogi, T. Purine-rich foods intake and recurrent gout attacks. *Ann. Rheum. Dis.* **2012**, *71*, 1448–1453. [[CrossRef](#)]
4. Neogi, T.; Jansen, T.L.; Dalbeth, N.; Fransen, J.; Schumacher, H.R.; Berendsen, D.; Brown, M.; Choi, H.; Edwards, N.L.; Janssens, H.J.; et al. 2015 Gout Classification Criteria: An American College of Rheumatology/European League against Rheumatism collaborative initiative. *Arthritis Rheumatol.* **2015**, *67*, 2557–2568. [[CrossRef](#)]
5. Teh, J.; McQueen, F.; Eshed, I.; Plagou, A.; Klauser, A. Advanced imaging in the diagnosis of gout and other crystal arthropathies. *Semin. Musculoskelet. Radiol.* **2018**, *22*, 225–236. [[CrossRef](#)]
6. Jeon, J.Y.; Lee, S.W.; Jeong, Y.M.; Baek, H.J. The effect of tube voltage combination on image artefact and radiation dose in dual-source dual-energy CT: Comparison between conventional 80/140 kV and 80/150 kV plus tin filter for gout protocol. *Eur. Radiol.* **2019**, *29*, 1248–1257. [[CrossRef](#)] [[PubMed](#)]
7. Mallinson, P.I.; Coupal, T.; Reisinger, C.; Chou, H.; Munk, P.L.; Nicolaou, S.; Ouellette, H. Artifacts in dual-energy CT gout protocol: A review of 50 suspected cases with an artifact identification guide. *AJR Am. J. Roentgenol.* **2014**, *203*, W103–W109. [[CrossRef](#)] [[PubMed](#)]
8. Carr, A.; Doyle, A.J.; Dalbeth, N.; Aati, O.; McQueen, F.M. Dual-energy CT of urate deposits in costal cartilage and intervertebral disks of patients with tophaceous gout and age-matched controls. *AJR Am. J. Roentgenol.* **2016**, *206*, 1063–1067. [[CrossRef](#)]
9. Ogdie, A.; Taylor, W.J.; Weatherall, M.; Fransen, J.; Jansen, T.L.; Neogi, T.; Schumacher, H.R.; Dalbeth, N. Imaging modalities for the classification of gout: Systematic literature review and meta-analysis. *Ann. Rheum. Dis.* **2015**, *74*, 1868–1874. [[CrossRef](#)]
10. Spermon, J.; Dijke, C.V. Dual energy CT: Added value in gouty arthritis. *JBR-BTR* **2013**, *96*, 34–37. [[CrossRef](#)]
11. Girish, G.; Melville, D.M.; Kaeley, G.S.; Brandon, C.J.; Goyal, J.R.; Jacobson, J.A.; Jamadar, D.A. Imaging appearances in gout. *Arthritis* **2013**, *2013*, 673401. [[CrossRef](#)]
12. Mallinson, P.I.; Reagan, A.C.; Coupal, T.; Munk, P.L.; Ouellette, H.; Nicolaou, S. The distribution of urate deposition within the extremities in gout: A review of 148 dual-energy CT cases. *Skelet. Radiol.* **2014**, *43*, 277–281. [[CrossRef](#)] [[PubMed](#)]
13. Jia, E.; Zhu, J.; Huang, W.; Chen, X.; Li, J. Dual-energy computed tomography has limited diagnostic sensitivity for short-term gout. *Clin. Rheumatol.* **2018**, *37*, 773–777. [[CrossRef](#)] [[PubMed](#)]
14. Lee, J.S.; Seo, W.J. What is the diagnostic value of dual-energy computed tomography in patients with clinical diagnosis of gout? *Adv. Rheumatol.* **2021**, *61*, 40. [[CrossRef](#)] [[PubMed](#)]
15. Gamala, M.; Jacobs, J.W.G.; van Laar, J.M. The diagnostic performance of dual energy CT for diagnosing gout: A systematic literature review and meta-analysis. *Rheumatology* **2019**, *58*, 2117–2121. [[CrossRef](#)]
16. Park, E.H.; Yoo, W.H.; Song, Y.S.; Byon, J.H.; Pak, J.; Choi, Y. Not All Green Is Tophi: The Importance of Optimizing Minimum Attenuation and Using a Tin Filter to Minimize Clumpy Artifacts on Foot and Ankle Dual-Energy CT. *AJR Am. J. Roentgenol.* **2020**, *214*, 1335–1342. [[CrossRef](#)] [[PubMed](#)]
17. Strobl, S.; Kremser, C.; Taljanovic, M.; Gruber, J.; Stofferin, H.; Bellmann-Weiler, R.; Klauser, A.S. Impact of Dual-Energy CT Postprocessing Protocol for the Detection of Gouty Arthritis and Quantification of Tophi in Patients Presenting with Podagra: Comparison with Ultrasound. *AJR Am. J. Roentgenol.* **2019**, *213*, 1315–1323. [[CrossRef](#)]
18. Dubief, B.; Avril, J.; Pascart, T.; Schmitt, M.; Loffroy, R.; Maillefert, J.F.; Ornetti, P.; Ramon, A. Optimization of dual energy computed tomography post-processing to reduce lower limb artifacts in gout. *Quant. Imaging Med. Surg.* **2022**, *12*, 539–549. [[CrossRef](#)]
19. Pascart, T.; Budzik, J.F. Dual-energy computed tomography in crystalline arthritis: Knowns and unknowns. *Curr. Opin. Rheumatol.* **2022**, *34*, 103–110. [[CrossRef](#)]
20. Singh, J.A.; Reddy, S.G.; Kundukulam, J. Risk factors for gout and prevention: A systematic review of the literature. *Curr. Opin. Rheumatol.* **2011**, *23*, 192–202. [[CrossRef](#)]
21. Dehlin, M.; Jacobsson, L.; Roddy, E. Global epidemiology of gout: Prevalence, incidence, treatment patterns and risk factors. *Nat. Rev. Rheumatol.* **2020**, *16*, 380–390. [[CrossRef](#)] [[PubMed](#)]



Article

Intraobserver Assessment of Shear Wave Elastography in Tensor Fasciae Latae and Gluteus Maximus Muscle: The Importance of the Hip Abductor Muscles in Runners Knee Compared to Healthy Controls

Andrea S. Klauser ^{1,†}, Felix de-Koekoek ^{1,†}, Christoph Schwabl ^{1,*}, Christian Fink ², Miriam Friede ³ and Robert Csapo ⁴

¹ Radiology Department, Medical University Innsbruck, Anichstrasse 35, 6020 Innsbruck, Austria; andrea.klauser@i-med.ac.at (A.S.K.); felix.de-koekoek@tirol-kliniken.at (F.d.-K.)

² Gelenkpunkt—Sport- und Gelenkchirurgie Innsbruck, 6020 Innsbruck, Austria; info@gelenkpunkt.com

³ Fachhochschule Kärnten Gemeinnützige Privatstiftung, 9020 Klagenfurt am Wörthersee, Austria; m.friede@fh-kaernten.at

⁴ Centre for Sport Science and University Sports, University of Vienna, 1010 Wien, Austria; robert.csapo@univie.ac.at

* Correspondence: christoph.schwabl@i-med.ac.at

† These authors contributed equally to this work.

Citation: Klauser, A.S.; de-Koekoek, F.; Schwabl, C.; Fink, C.; Friede, M.; Csapo, R. Intraobserver Assessment of Shear Wave Elastography in Tensor Fasciae Latae and Gluteus Maximus Muscle: The Importance of the Hip Abductor Muscles in Runners Knee Compared to Healthy Controls. *J. Clin. Med.* **2022**, *11*, 3605. <https://doi.org/10.3390/jcm11133605>

Academic Editors: Mihra Taljanovic and Kevin L Garvin

Received: 17 March 2022

Accepted: 20 June 2022

Published: 22 June 2022

Publisher's Note: MDPI stays neutral with regard to jurisdictional claims in published maps and institutional affiliations.



Copyright: © 2022 by the authors. Licensee MDPI, Basel, Switzerland. This article is an open access article distributed under the terms and conditions of the Creative Commons Attribution (CC BY) license (<https://creativecommons.org/licenses/by/4.0/>).

Abstract: Background: Iliotibial band syndrome (ITBS) represents one of the most common running related injuries. The pathophysiology is postulated to be caused by excessive ITB tension, impingement and irritation of soft tissues at the lateral femoral epicondyle. However, direct evidence has yet to be found and the multifactorial etiology is under discussion. The purpose was to evaluate stiffness of ITB, gluteus maximus (GM) and tensor fasciae latae (TFL) muscles using shear wave elastography (SWE). Methods: In 14 patients with clinically verified ITBS and 14 healthy controls, three SWE measurements each of ITB, GM and TFL in both legs was performed to determine measurement reliability and between-group and -leg differences. Results: The mean value of ITB was 12.8 m/s with ICC of 0.76, whereas the values measured in the GM were 3.02 m/s with an ICC of 0.87. No statistically significant difference in controls compared to patients were found ($p = 0.62$). The mean value of TFL was 5.42 m/s in healthy participants, compared to 3.89 m/s patients with an ICC of 0.98 ($p = 0.002$). Conclusion: Although SWE showed no difference in ITB stiffness, significant differences for TFL muscle stiffness in runner's knee was found, suggesting that the hip abductor muscles might play a bigger role in the pathophysiology of ITBS. We aimed to implement baseline values for stiffness assessments and prove reliability for further prospective studies of SWE in runner's knee.

Keywords: sonoelastography; iliotibial band syndrome; ultrasonography; runners knee; hip muscles; tensor fasciae latae; gluteus maximus

1. Introduction

Iliotibial band syndrome (ITBS) (i.e., runner's knee) is characterized by lateral knee pain and represents one of the most common running related injuries, affecting up to 10% of all active runners [1]. It is a non-traumatic overuse injury caused by repeated flexion and extension of the knee leading to irritation in the structures around the knee [2]. Orchard et al. [3] described an impingement zone occurring at 30° of knee flexion during foot strike and the early stance phase of running. During this impingement period in the running cycle, eccentric contraction of the tensor fascia latae muscle and of the gluteus maximus muscle causes the leg to decelerate, generating tension in the iliotibial band, leading to irritation of the underlying soft tissues at the level of the lateral femoral epicondyle [4,5]. ITBS is usually diagnosed on the basis of a detailed history and physical examination [6].

However, direct evidence with objective imaging criteria must still be investigated.

Shear wave elastography (SWE) generated by ultrasound is an innovative ultrasound imaging-based technique facilitating the quantitation of tissue elasticity by measuring the propagation velocity of US shear waves in the tissues of interest. Pilot experiments have demonstrated the feasibility of SWE measurements of ITB in 16 healthy volunteers [7].

As a relatively new imaging technique, SWE allows for a quick, non-invasive quantitative assessment of tissue stiffness [8–11].

In contrast to strain/compression sonoelastography, where mechanical tissue compression is needed, SWE uses an acoustic radiation force pulse sequence to generate shear waves, which propagate perpendicular to the US beam, causing transient displacements.

The distribution of shear wave velocities at each pixel is directly related to the shear modulus, an absolute measure of the tissue's elastic properties.

Shear-wave elastography is considered to be more objective, quantitative, and reproducible than compression sonoelastography, and as many studies have showed, SWE seems to have a promising role in determining the severity of disease in various musculoskeletal tissues including tendons, muscles, nerves, fascias and ligaments [8–10,12,13].

In addition, MRI is also a suitable method to evaluate the ITB and especially the surrounding structures for differential diagnosis. On MRI, the ITB is a hypointense, flat, linear structure in the lateral hip, thigh, and knee. In the absence of pathology, there should be no adjacent edema or significant intrasubstance signal changes. On MRI, the normal ITB will typically be of a thickness of about 1 to 3 mm at the level of the lateral femoral epicondyle, consistent with sonographic findings [1,14,15]. Nevertheless, the thickening of the ITB has been reported inconsistently in both MRI and US, therefore an independent imaging marker is desirable [16].

The aim of the study was to define baseline values and to prove the reliability of three SWE-based measurements each of ITB, TFL and GM and to compare results of patients clinically diagnosed with ITB-syndrome with a healthy control group. We hypothesized that SWE elastic moduli would be significantly higher in participants diagnosed with ITBS.

2. Materials and Methods

All participants gave their informed consent for inclusion before they participated in the study. The study was conducted in accordance with the Declaration of Helsinki, and the protocol was approved by the Institutional Review Boards (IRBs) of our institution (EK Nr: 1090/2018).

The dependent variables were the stiffness of the ITB, TFL and GM as measured by SWE. The independent variable was the presence of ITBS.

2.1. Participants

14 patients (mean age $32.6 \pm 6.6/m$; $f = 7:7$) with verified ITBS and 14 healthy volunteers (median age $26.1 \pm 5.2/m$; $f = 7:7$) with no statistically relevant difference in age were recruited during 2018–2019. ITBS was verified through clinical examination by an experienced orthopedic surgeon and functional tests were used for differential diagnosis including the Noble, Ober and Thomas tests, which were positive in all of the included patients [17–19]. In addition, MRI scans were performed to test the presence of edema and exclude other injuries (e.g., lateral meniscal tear) potentially causing similar symptoms [20]. Patients presenting with such secondary injuries were excluded from the study. A history of precedent lower extremity pain or injuries in the last six months as well as severe injuries (e.g., fractures), surgeries at any time, BMI > 30 or physiotherapy because of ITBS in the last 12 months were further criteria for exclusion. Previous medication was no exclusion criteria.

Participants in the control group had to be healthy and physically active (physical activity > 150 min/week) with no history of ITBS (Global Recommendations on Physical Activity for Health, 2009. World Health Organization. Geneva, Switzerland. Available online: <http://www.who.int/ncds/prevention/physical-activity/en/> accessed on 13 July

2018). One of the *participants* from the healthy group had a lateral meniscus tear in his dominant leg, which was one of our exclusion criteria. This participant's data were removed from analysis; therefore, the analysis was conducted on a sample of 14 patients with ITBS and 13 healthy participants.

2.2. US Examination

To obtain SWE images, participants lay relaxed supine on an examination bed with their backs slightly raised and knees rested on a support cushion (hip angle 140–150°, knee angle ~90°). US images were obtained in the sagittal and frontal plane, respectively, in both legs in three locations: proximally, above the tensor fasciae latae (2 cm proximal of the greater trochanter of the femur in the direction of the anterior superior iliac spine) and gluteus maximus muscles (4.5 cm proximal of the greater trochanter of the femur in the direction of the highest point on the iliac crest), and distally above the ITB (2 cm proximal of the lateral femoral epicondyle).

An ultrasound SWE system (Aixplorer Supersonic Imagine, Aix-en-Provence, France) with a 50 mm linear array transducer (SL 18-5, Supersonic Imagine, France) was used with settings in the musculoskeletal mode. The frequency was 18 MHz, and the SWE option was penetration mode with an opacity of 85%. The preset was adjusted to a depth of 1 cm for the iliotibial tract and 3 cm for the gluteal muscles with an elastic scale < 600 kPa. The color scale used in the shear modulus (in kPa) showed the lowest values in blue to the highest values in red. The size of regions of interest (ROI) had to be at least 3 × 10 mm in order to cover the ITB and 50 × 30 mm in order to cover the gluteal muscles. The Q-Box™ diameter was defined by the thickness of the ITB and the muscles, respectively. The Q-Box™ was traced manually to include a maximum of the muscles in order to avoid the muscle-tendon junction and fasciae and to downsize it in order to measure the very thin ITB.

During measurements, an ultrasound gel was applied between the skin and the transducer to avoid skin deformation. The midpoint of the transducer was placed perpendicularly on the skin's surface on the ITB and muscle fibers with a light pressure and then the SWE mode was activated to examine the shear wave modulus [21]. During the acquisition of the SWE mode, the transducer was kept motionless for about 5–8 s [22]. Image quality was closely monitored throughout the measurements. When the color in the ROI was uniform and the structure of the ITB and the muscle fibers visible, the images were frozen and then put on the Q-Box™ to obtain the shear wave modulus from the system and stored for SWE analysis (kPa, m/s) [23]. For this purpose, the probe was held aligned along the long axes of the GM (axial transducer positioning) and TFL (longitudinal transducer positioning) muscle fibers and at the distal ITB (longitudinal transducer positioning), before regions of interest were manually drawn on frozen images (Figures 1–3). In the ITB, care was taken to leave out hyperechoic lines due to cortical bone to avoid potential bias. Three measurements were obtained in each location by freezing and unfreezing and acquiring new images each time with consecutive manual ROI placement in order to prove intraobserver reliability. Shear wave velocities and shear moduli were obtained by a single observer with five years of experience in MSK US and SWE in three locations: Two measurements were performed at the hip level, at approximately 50% of the distance between the anterior superior iliac spine and the greater trochanter of the femur to assess the TFL and the GM muscles, followed by a distal measurement of the ITB obtained 2 cm proximally of the level of the lateral femoral epicondyle. The three measurements were used to calculate intra-observer variability and the mean of the three measurements was used for further statistical analysis. Shear wave velocities are given in m/s.

Note that only TFL and GM and not the gluteus medius muscle were measured, because they contribute fibres to the ITB. The gluteus medius muscle has no direct attachment to the ITB, therefore we did not perform measurements [14,24].

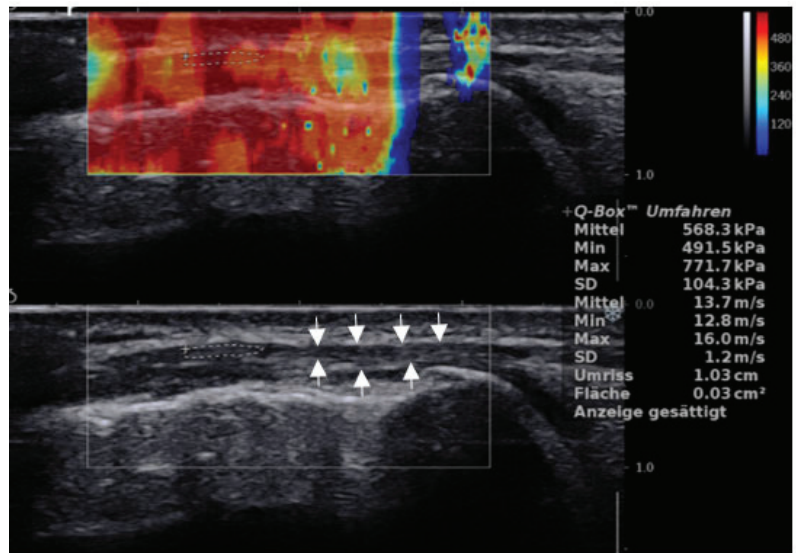


Figure 1. Longitudinal scan of the ITB. ROI shows measurement 2 cm proximal of the femoral condyle in a 29-year-old male patient with ITBS. Note: B mode US shows hypochoic thickening and irregularity of the ITB (between arrows) with a mean of 13.7 m/s.

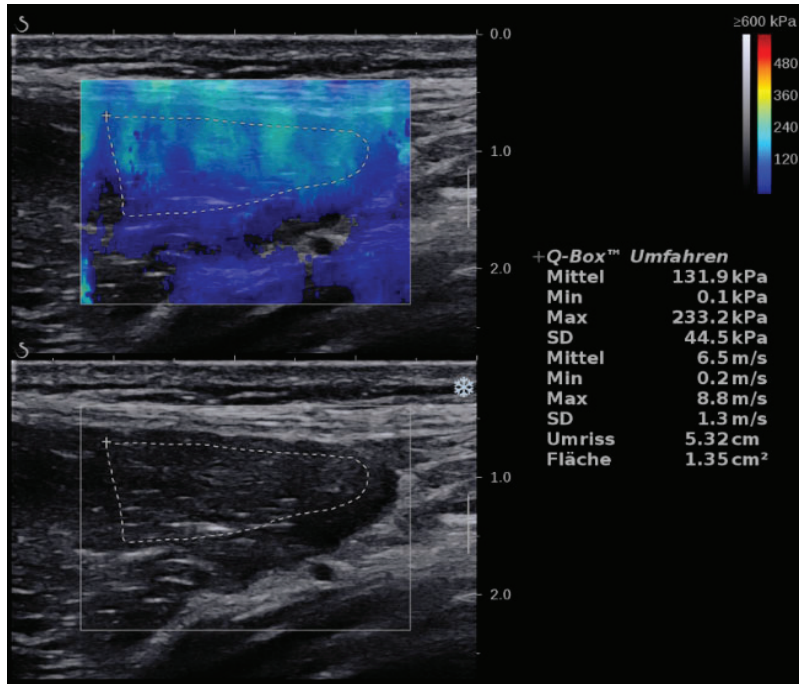


Figure 2. Longitudinal scan of the TFL muscle showing SWE and B-mode with a mean of 6.5 m/s. (the same patient with ITBS as in Figure 1).

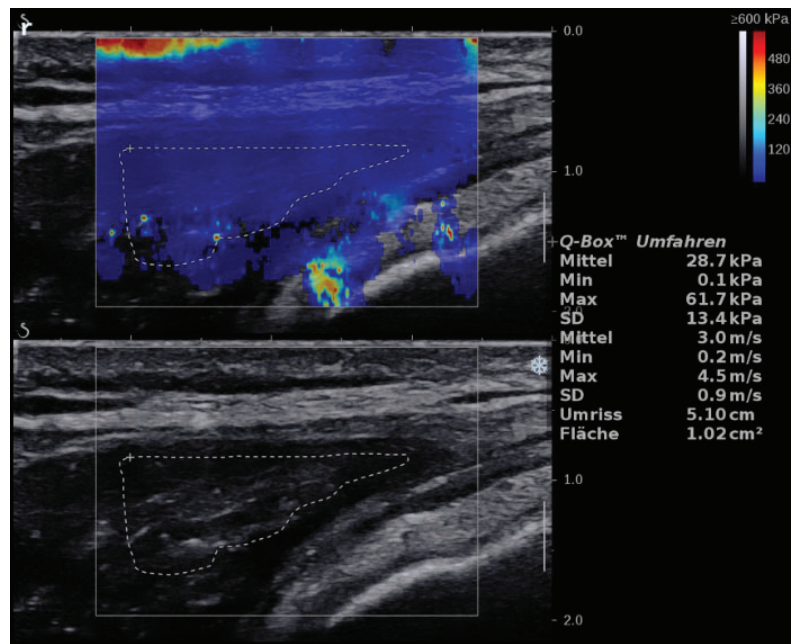


Figure 3. Axial scan of the GM muscle showing SWE and B-mode. (the same patient with ITBS as in Figure 1).

2.3. Statistical Analysis

The sample size was determined through a priori power analysis ($\alpha = 0.05$, $1 - \beta = 0.8$, $dz = 1$) based on previously published data of ITB stiffness [7].

For statistical analyses, we used SPSS version 25 (© IBM). Intraclass correlation coefficients (ICC's) were calculated using a two-way mixed effects models to quantify absolute agreement of measurements [25]. Typical errors of measurement were calculated by dividing standard deviation of (maximum) difference scores by the square root of two [26]. In addition, the minimal detectable change (MDC) was calculated as: $1.96 \times \text{standard error of the mean (SEM)} \times \sqrt{2}$ [27].

Differences in tissue stiffness, as reflected by measures of shear wave propagation velocity (m/s) were tested for significance by means of factorial MANOVA's and a two-way mixed ANOVA considering measures obtained in the ITB, GM and TFL as dependent variables, "leg" (affected/non dominant versus non-affected/dominant) as within- and "group" (patient versus control group) as between-participant factors, respectively. Box's test was used to test the assumption of homogeneity of co-variances. For significant differences, Pearson's coefficient was calculated through n^2 -conversion [28].

A p -value less than 0.05 was declared as statistically relevant.

3. Results

3.1. ITB

ITB showed a mean of 13.24 ± 2.24 m/s (coefficient of variation (CV): 16.92%) in healthy participants and failed to reach statistically significant differences in comparison with the mean of the diseased legs (12.36 ± 2.92 m/s (CV 23.62%)), ($P = 0.62$), (Figure 1). Neither the differences between dominant/non-dominant as well as diseased/non-diseased legs were statistically relevant ($p > 0.2$).

ITB showed a good intra-observer reliability with an ICC of 0.76 (0.63–0.85). SEM ranged from 0.43 to 0.56. MDC ranged from 1.19 to 1.55.

3.2. TFL

TFL values were significantly higher in healthy participants with a mean of 5.42 ± 2.25 m/s (CV: 41.51%) compared with a mean of 3.89 ± 1.92 m/s (CV: 49.36%) in diseased legs ($p = 0.002$, $r = 0.41$), (Figure 2). Intraobserver reliability was excellent with an ICC of 0.98 (0.96-0.99). SEM ranged from 0.43 to 0.75. MDC ranged from 1.19 to 2.08.

3.3. GM

GM mean SWE values failed to reach statistically significant differences with a mean of 2.9 ± 0.95 m/s (CV: 32.76%) in healthy participants and a mean of 3.14 ± 1.73 m/s (CV: 55.10%) in diseased legs ($p = 0.26$), (Figure 3). Intraobserver reliability showed an ICC of 0.87 (0.80-0.92). SEM ranged from 0.18 to 0.33. MDC ranged from 0.50 to 0.91. The TFL/GM ratio was significantly higher in the healthy group compared to the patient's group ($p = 0.049$, $r = 0.41$), (Figure 4).

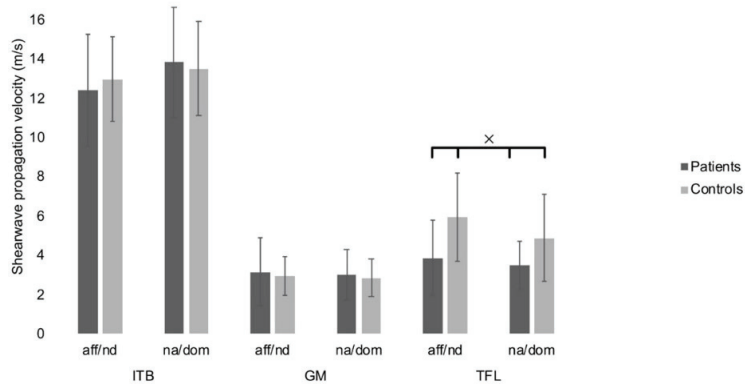


Figure 4. Baseline data of shear wave propagation velocity. Bars and error bars represent the means and standard deviations measured in the iliotibial band (ITB), gluteus maximus (GM) and tensor fasciae latae (TFL) muscles. Results are separately shown for the affected or non-dominant (aff/nd) and non-affected or dominant (na/dom) limbs, respectively. Note the significant difference between patients and healthy participants in the TFL (between cross).

4. Discussion

We were able to show in our study that there are no statistically significant differences in SWE values between the patient group with ITBS and the healthy control group. These findings are in line with a recent study examining ITBS and hip abductors using SWE, where no statistical differences in ITB SWE values were found in patients with verified ITBS before and after physiotherapy [29]. This was the first study to apply SWE in ITBS, however reliability data were not referenced in detail. Therefore, the goal of this study was to show that baseline SWE values are reproducible and can, therefore, be used in further studies to assess runners knee. The current hypothesis concerning the etiology of the ITBS is that excessive tone in the ITB leads to the compression of underlying fat tissue and consequently, to inflammation and pain [30].

Another study examining the effect of muscle fatigue using EMG in females with ITBS, however, suggests that the hip abductors of patients suffering from ITBS do not show lower maximum strength but demonstrate less resistance to fatigue than those of healthy runners. Therefore, the study suggested implementing a gluteus medius endurance training regime in a runner's rehabilitation program [31]. In agreement with this study, a more recent study has identified a number of kinematic differences between injured and healthy runners that were consistent across injured subgroups; pelvic drop was found to be the most important predictor variable [32]. This finding might be in line with our results, supporting the hypothesis that muscular deficits (i.e., hip abductor weakness) might lead to improper posture during the stance phase of the gait cycle (i.e., pelvic drop and valgus collapse),

resulting in excessive ITB strains and inflammation. Hence, in many cases, appropriate strength training might represent the first line of treatment and should be considered before more invasive treatment options, such as the injection of local steroids or even surgery are contemplated [33]. It would be of interest to test SWE in ITBS patients in order to test the hypothesis that insufficient hip abductor tone is involved in the pathogenesis of the syndrome. In another study applying SWE, the group of Tateuchi et al. [7] used a transversal scanning plane to investigate the effect of angle and moment of hip and knee joints on ITB stiffness. They noted a ceiling effect of measurements obtained in the longitudinal plane. No such ceiling effect was observed in our study, which may be explained by the newer generation equipment used.

Limitations

Although data collection was standardized to minimize influencing factors, we have several limitations to mention. First, the ITB is a very thin aponeurotic fascia lying above the cortical bone which represents a challenge in the acquisition of SWE measurements. This often results in saturated values (Figure 1). However, we performed three measurements each, in order to get reproducible values, which mainly did not result in saturated values. Nevertheless, it is questionable if this fact was leading to the lack of statistical differences between patients and controls. Future studies in the ITB should consider using a gel pad. Additionally, subjacent/adjacent edema usually observed in patients suffering from ITBS could contribute to lower SWE speed values [34]. We didn't compare the thickness of the ITB between groups, which is also a limitation of our study. Perhaps there could be a correlation between thickened ITB and lower speed values. Second, measurements obtained in the ITB are influenced by the resting tension of muscles inserting into it. While all study participants were instructed to fully relax the examined extremity during the US examination, it cannot be excluded that involuntary contraction of GM or the TFL muscles may have introduced bias into ITB SWE measurements. Furthermore, we are aware that stiffness values measured in a relaxed state do not necessarily reflect the conditions during physical activity.

A recent study by Besomi et al. [35] showed different values in ITB stiffness, but in contrast to our study, the ITB was measured more proximally, resulting in different values and appearance. We have decided to measure the ITB at the insertion, as this is also where changes also in the b-mode of patients may occur.

A further limitation is that we did not examine a healthy runners group. This refers to healthy participants without ITBS symptoms with a self-reported weekly training volume of at least 20 km. Training may induce changes in the shear modulus and therefore lead to different baseline values.

A recent SWE study provided evidence that the muscles of active runners exhibit an increased stiffness that can be beneficial to their athletic performance [36]. Increased muscle stiffness in runners might lead to false negative SWE values as compared to healthy volunteers. Moreover, another very recent study showed that women with genu varum alignment exhibit higher ITB strain during weight-bearing, which could be related to a higher incidence of ITBS in women [37]. This was unknown to us prior to this study's subject selection and therefore not evaluated and should be addressed in further studies.

A further limitation is the relatively small study population, which limits statistical power and may have contributed to the differences in the mean values between the study groups. In this study we had good intra-observer reproducibility, but unfortunately no inter-observer reproducibility was evaluated as the measurements were carried out by only one radiologist, which represents a further limitation.

5. Conclusions

SWE is an evolving imaging modality recently available on higher frequency ultrasound transducers which enabled us to obtain reliable quantitative measurements of tissue stiffness of ITB, TFL and GM. SWE showed no difference in ITB stiffness, whereas a sig-

nificant difference for TFL muscle stiffness was found, suggesting that the hip abductor muscles might play a bigger role in the pathophysiology of ITBS. Our study summarizes SWE values with good intraobserver variability, and can serve as a background for further longitudinal studies of stiffness assessments in runners knee.

Author Contributions: Conceptualization, A.S.K., F.d.-K., C.S., C.F., M.F. and R.C.; Data curation, A.S.K., F.d.-K., C.F., M.F. and R.C.; Formal analysis, A.S.K., F.d.-K., C.S. and R.C.; Funding acquisition, R.C.; Investigation, A.S.K., F.d.-K., C.F., M.F. and R.C.; Methodology, A.S.K., F.d.-K., C.S. and C.F.; Project administration, A.S.K., C.S. and R.C.; Resources, A.S.K. and M.F.; Software, A.S.K.; Supervision, A.S.K. and R.C.; Validation, A.S.K., C.S. and R.C.; Visualization, A.S.K., F.d.-K. and C.S.; Writing—original draft, A.S.K., F.d.-K., C.S. and R.C.; Writing—review & editing, A.S.K., F.d.-K. and C.S. All authors have read and agreed to the published version of the manuscript.

Funding: This research received no external funding.

Institutional Review Board Statement: All participants gave their informed consent for inclusion before they participated in the study. The study was conducted in accordance with the Declaration of Helsinki, and the protocol was approved by the Institutional Review Boards (IRBs) of our institution (EK Nr: 1090/2018).

Informed Consent Statement: Informed consent was obtained from all participants involved in the study.

Conflicts of Interest: The authors declare that they have no conflict of interest.

References

1. Fairclough, J.; Hayashi, K.; Toumi, H.; Lyons, K.; Bydder, G.; Phillips, N.; Best, T.M.; Benjamin, M. The functional anatomy of the iliotibial band during flexion and extension of the knee: Implications for understanding iliotibial band syndrome. *J. Anat.* **2006**, *208*, 309–316. [[CrossRef](#)] [[PubMed](#)]
2. Van der Worp, M.P.; van der Horst, N.; de Wijer, A.; Backx, F.J. Nijhuis-van der Sanden MW. Iliotibial band syndrome in runners: A systematic review. *Sports Med.* **2012**, *42*, 969–992. [[CrossRef](#)] [[PubMed](#)]
3. Orchard, J.; Fricker, P.A.; Abud, A.T.; Mason, B.R. Biomechanics of Iliotibial Band Friction Syndrome in Runners. *Am. J. Sports Med.* **1996**, *24*, 375–379. [[CrossRef](#)] [[PubMed](#)]
4. Baker, R.L.; Fredericson, M. Iliotibial Band Syndrome in Runners: Biomechanical Implications and Exercise Interventions. *Phys. Med. Rehabil. Clin. N. Am.* **2016**, *27*, 53–77. [[CrossRef](#)] [[PubMed](#)]
5. Taunton, J.E.; Ryan, M.B.; Clement, D.B.; McKenzie, D.C.; Lloyd-Smith, D.R.; Zumbo, B.D. A retrospective case-control analysis of 2002 running injuries. *Br. J. Sports Med.* **2002**, *36*, 95–101. [[CrossRef](#)]
6. Magrum, E.; Wilder, R.P. Evaluation of the Injured Runner. *Clin. Sports Med.* **2010**, *29*, 331–345. [[CrossRef](#)]
7. Tateuchi, H.; Shiratori, S.; Ichihashi, N. The effect of angle and moment of the hip and knee joint on iliotibial band hardness. *Gait Posture* **2015**, *41*, 522–528. [[CrossRef](#)]
8. Sandrin, L.; Tanter, M.; Gennisson, J.-L.; Catheline, S.; Fink, M. Shear elasticity probe for soft tissues with 1-D transient elastography. *IEEE Trans. Ultrason. Ferroelectr. Freq. Control* **2002**, *49*, 436–446. [[CrossRef](#)]
9. Taljanovic, M.S.; Gimber, L.H.; Becker, G.W.; Latt, L.D.; Klauser, A.S.; Melville, D.M.; Gao, L.; Witte, R.S. Shear-Wave Elastography: Basic Physics and Musculoskeletal Applications. *RadioGraphics* **2017**, *37*, 855–870. [[CrossRef](#)]
10. Baur, D.; Schwabl, C.; Kremser, C.; Taljanovic, M.; Widmann, G.; Sconfienza, L.; Sztankay, J.; Feuchtner, G.; Klauser, A. Shear Wave Elastography of the Plantar Fascia: Comparison between Patients with Plantar Fasciitis and Healthy Control Subjects. *J. Clin. Med.* **2021**, *10*, 2351. [[CrossRef](#)]
11. Abu-Awwad, A.; Faur, C.I.; Tudoran, M.; Petrescu, P.H.; Motoc, A.; Grigoras, M.L.; Tudoran, C.; Ghiga, I.L.; Patrascu, J.M.; Popa, A.; et al. Evaluation of Normal and Pathological Patellar Tendon by Real-Time Shear Wave Elastography. *Orthop. Rheumatol. Open Access J.* **2021**, *18*, 555982. [[CrossRef](#)]
12. Garra, B.S. Imaging and Estimation of Tissue Elasticity by Ultrasound. *Ultrasound Q.* **2007**, *23*, 255–268. [[CrossRef](#)] [[PubMed](#)]
13. Gatz, M.; Bejder, L.; Quack, V.; Schradang, S.; Dirrichs, T.; Tingart, M.; Kuhl, C.; Betsch, M. Shear Wave Elastography (SWE) for the Evaluation of Patients with Plantar Fasciitis. *Acad. Radiol.* **2020**, *27*, 363–370. [[CrossRef](#)] [[PubMed](#)]
14. Flato, R.; Passanante, G.J.; Skalski, M.R.; Patel, D.B.; White, E.; Matcuk, G.R. The iliotibial tract: Imaging, anatomy, injuries, and other pathology. *Skelet. Radiol.* **2017**, *46*, 605–622. [[CrossRef](#)]
15. Mansour, R.; Yoong, P.; Mckean, D.; Teh, J. The iliotibial band in acute knee trauma: Patterns of injury on MR imaging. *Skelet. Radiol.* **2014**, *43*, 1369–1375. [[CrossRef](#)] [[PubMed](#)]
16. Jiménez Díaz, F.; Gitto, S.; Sconfienza, L.M.; Draghi, F. Ultrasound of iliotibial band syndrome. *J. Ultrasound* **2020**, *23*, 379–385. [[CrossRef](#)]

17. Hariri, S.; Savidge, E.T.; Reinold, M.M.; Zachazewski, J.; Gill, T.J. Treatment of recalcitrant iliotibial band friction syndrome with open iliotibial band bursectomy: Indications, technique, and clinical outcomes. *Am. J. Sports Med.* **2009**, *37*, 1417–1424. [[CrossRef](#)] [[PubMed](#)]
18. Harvey, D. Assessment of the flexibility of elite athletes using the modified Thomas test. *Br. J. Sports Med.* **1998**, *32*, 68–70. [[CrossRef](#)]
19. Lavine, R. Iliotibial band friction syndrome. *Curr. Rev. Musculoskelet. Med.* **2010**, *3*, 18–22. [[CrossRef](#)]
20. Ekman, E.F.; Pope, T.; Martin, D.F.; Curl, W.W. Magnetic Resonance Imaging of Iliotibial Band Syndrome. *Am. J. Sports Med.* **1994**, *22*, 851–854. [[CrossRef](#)]
21. Payne, C.; Watt, P.; Cercignani, M.; Webborn, N. Reproducibility of shear wave elastography measures of the Achilles tendon. *Skelet. Radiol.* **2018**, *47*, 779–784. [[CrossRef](#)] [[PubMed](#)]
22. Zhang, Z.J.; Fu, S.N. Shear Elastic Modulus on Patellar Tendon Captured from Supersonic Shear Imaging: Correlation with Tangent Traction Modulus Computed from Material Testing System and Test-Retest Reliability. *PLoS ONE* **2013**, *8*, e68216. [[CrossRef](#)] [[PubMed](#)]
23. Zhou, J.; Yu, J.; Liu, C.; Tang, C.; Zhang, Z. Regional Elastic Properties of the Achilles Tendon Is Heterogeneously Influenced by Individual Muscle of the Gastrocnemius. *Appl. Bionics Biomech.* **2019**, *2019*, 8452717. [[CrossRef](#)] [[PubMed](#)]
24. Huang, B.K.; Campos, J.C.; Peschka, P.G.M.; Pretterklieber, M.L.; Skaf, A.Y.; Chung, C.B.; Pathria, M.N. Injury of the Gluteal Aponeurotic Fascia and Proximal Iliotibial Band: Anatomy, Pathologic Conditions, and MR Imaging. *RadioGraphics* **2013**, *33*, 1437–1452. [[CrossRef](#)] [[PubMed](#)]
25. Koo, T.K.; Li, M.Y. A Guideline of Selecting and Reporting Intraclass Correlation Coefficients for Reliability Research. *J. Chiropr. Med.* **2016**, *15*, 155–163. [[CrossRef](#)]
26. Hopkins, W.G. Measures of Reliability in Sports Medicine and Science. *Sports Med.* **2000**, *30*, 1–15. [[CrossRef](#)]
27. Nair, P.M.; Hornby, T.G.; Behrman, A.L. Minimal Detectable Change for Spatial and Temporal Measurements of Gait After Incomplete Spinal Cord Injury. *Top. Spinal Cord Inj. Rehabil.* **2012**, *18*, 273–281. [[CrossRef](#)]
28. Lakens, D. Calculating and reporting effect sizes to facilitate cumulative science: A practical primer for t-tests and ANOVAs. *Front Psychol.* **2013**, *4*, 863. [[CrossRef](#)]
29. Friede, M.C.; Klauser, A.; Fink, C.; Csapo, R. Stiffness of the iliotibial band and associated muscles in runner's knee: Assessing the effects of physiotherapy through ultrasound shear wave elastography. *Phys. Ther. Sport* **2020**, *45*, 126–134. [[CrossRef](#)]
30. Strauss, E.; Kim, S.; Calcei, J.G.; Park, D. Iliotibial Band Syndrome: Evaluation and Management. *J. Am. Acad. Orthop. Surg.* **2011**, *19*, 728–736. [[CrossRef](#)]
31. Brown, A.M.; Zifchock, R.A.; Lenhoff, M.; Song, J.; Hillstrom, H.J. Hip muscle response to a fatiguing run in females with iliotibial band syndrome. *Hum. Mov. Sci.* **2019**, *64*, 181–190. [[CrossRef](#)] [[PubMed](#)]
32. Bramah, C.; Preece, S.J.; Gill, N.; Herrington, L. Is There a Pathological Gait Associated With Common Soft Tissue Running Injuries? *Am. J. Sports Med.* **2018**, *46*, 3023–3031. [[CrossRef](#)] [[PubMed](#)]
33. Noble, C.A. Iliotibial band friction syndrome in runners. *Am. J. Sports Med.* **1980**, *8*, 232–234. [[CrossRef](#)] [[PubMed](#)]
34. Davis, L.C.; Baumer, T.G.; Bey, M.J.; Van Holsbeeck, M.T. Clinical utilization of shear wave elastography in the musculoskeletal system. *Ultrasonography* **2019**, *38*, 2–12. [[CrossRef](#)] [[PubMed](#)]
35. Besomi, M.; Nava, G.T.D.A.; Hoorn, W.V.D.; Hug, F.; Vicenzino, B.; Hodges, P.W. Influence of transducer orientation on shear wave velocity measurements of the iliotibial band. *J. Biomech.* **2021**, *120*, 110346. [[CrossRef](#)] [[PubMed](#)]
36. Miyamoto, N.; Hirata, K.; Inoue, K.; Hashimoto, T. Muscle Stiffness of the Vastus Lateralis in Sprinters and Long-Distance Runners. *Med. Sci. Sports Exerc.* **2019**, *51*, 2080–2087. [[CrossRef](#)]
37. Kim, D.Y.; Miyakawa, S.; Ms, T.F.; Takemura, M. Sex Differences in Iliotibial Band Strain under Different Knee Alignments. *PM&R* **2019**, *12*, 479–485.



Article

Ultrasound of the Heel Improves Diagnosis—Tender Entheses in the Heel Region Rarely Corresponds to Inflammatory Enthesitis in Patients with Peripheral Spondyloarthritis

Sara Kamp Felbo ^{1,2,*}, Mikkel Østergaard ^{1,2}, Inge Juul Sørensen ¹ and Lene Terslev ^{1,2}

¹ Copenhagen Center for Arthritis Research, Center for Rheumatology and Spine Diseases, Centre of Head and Orthopaedics, Rigshospitalet, 2600 Glostrup, Denmark

² Department of Clinical Medicine, University of Copenhagen, 2200 Copenhagen, Denmark

* Correspondence: sarahelenakamp@gmail.com

Abstract: Enthesitis is a key pathology in spondyloarthritis (SpA), but diagnosis may be clinically challenging. The objective of this study was to investigate the prevalence of ultrasound enthesitis lesions in tender entheses in the heel region in patients with peripheral SpA. In 27 patients with tenderness upon palpation at the Achilles tendon or the plantar fascia insertion, ultrasound assessment of the affected enthesitis was performed using greyscale and color Doppler mode. Images were evaluated using the Outcome Measures in Rheumatology (OMERACT) scoring system for enthesitis, scoring presence/absence of hypoechoogenicity, thickening, calcifications/enthesophytes, and erosions, and color Doppler activity semi quantitatively from 0 to 3. A total enthesitis sum score was calculated. A second examiner scanned 10 patients for inter-reader reliability. Ultrasound signs of inflammatory enthesitis (thickening/hypoechoogenicity and/or Doppler activity) were found in 48%, and 19% showed Doppler activity—all in the Achilles enthesitis. Inflammatory pathologies other than enthesitis (e.g., tendinitis, arthritis, bursitis) were identified in 26% of tender heels. The ultrasound OMERACT scoring system for enthesitis lesions showed excellent intra- and inter-reader agreement in a clinical setting. In conclusion, less than 50% of clinically tender entheses are related to inflammatory enthesitis when assessed by ultrasound. Ultrasound is useful for diagnosing other pathologies that may explain tenderness in the area.

Keywords: ultrasound; enthesitis; spondyloarthritis

Citation: Felbo, S.K.; Østergaard, M.; Sørensen, I.J.; Terslev, L. Ultrasound of the Heel Improves Diagnosis—Tender Entheses in the Heel Region Rarely Corresponds to Inflammatory Enthesitis in Patients with Peripheral Spondyloarthritis. *J. Clin. Med.* **2022**, *11*, 2325. <https://doi.org/10.3390/jcm11092325>

Academic Editors:
Fabio Cacciapaglia and
François Jamar

Received: 28 December 2021

Accepted: 20 April 2022

Published: 21 April 2022

Publisher's Note: MDPI stays neutral with regard to jurisdictional claims in published maps and institutional affiliations.



Copyright: © 2022 by the authors. Licensee MDPI, Basel, Switzerland. This article is an open access article distributed under the terms and conditions of the Creative Commons Attribution (CC BY) license (<https://creativecommons.org/licenses/by/4.0/>).

1. Introduction

Enthesitis, inflammation at the insertion of tendon, capsule, or ligament into the bone, is a key pathology in spondyloarthritis (SpA) diseases including psoriatic arthritis (PsA) [1–3]. It is defined as a key domain for assessing disease activity and response to treatment [4,5]. Objective findings of enthesitis involvement may be scarce, as both clinical examination and biochemical parameters may be normal. Therefore, diagnosis and evaluation of disease activity typically rely on a characteristic medical history and patient-reported symptoms. Imaging has shown to be valuable in detecting enthesitis involvement and is more sensitive than clinical examination for assessing inflammation at entheses [3–5]. Imaging may be used in both diagnosis and assessment of disease activity [6]. However, imaging studies of enthesitis have shown great discrepancies in the association between clinical findings and findings of inflammation by ultrasound where inflammatory changes may be seen in asymptomatic entheses and where symptomatic entheses may display no inflammatory changes [7,8].

The Outcome Measures in Rheumatology (OMERACT) Ultrasound Working Group has defined and validated the elementary lesions for enthesitis both in static images and in patients [1,2]. Enthesis thickening, hypoechoogenicity, and Doppler activity are inflam-

matory lesions with Doppler activity indicating active inflammation. Bone erosions and enthesophytes/calcifications are structural lesions.

We have previously found a poor correlation between tender joints and signs of inflammation by ultrasound in patients with established psoriatic arthritis [9]. The aim of this study was to investigate the association between clinically tender Achilles and plantar fascia entheses in patients with peripheral SpA and ultrasound signs of inflammation. Furthermore, we aimed to describe if other findings can explain clinically tender entheses.

2. Materials and Methods

2.1. Patients and Clinical Evaluation

Patients with SpA according to the ASAS criteria [10] who presented with tender Achilles tendon insertion or plantar fascia insertion at the calcaneus when evaluated by their treating rheumatologist were referred to the ultrasound clinic for assessment and potential inclusion in the study. If several tender entheses were present, the most tender on clinical examination was selected. The study was approved by the local ethics committee (J. no. H-16035123).

Clinical evaluation included counts of tender (68) and swollen (66) joints, tender entheses (according to Spondyloarthritis Research Consortium of Canada (SPARCC)), and a global evaluation of disease activity on a visual analog scale (VAS) by the patient's usual rheumatologist and a measure of the level of C-reactive protein (CRP). Patients filled out the health assessment questionnaire (HAQ) and a global evaluation of disease activity (Pt global) and pain (Pt Pain) on a visual analog scale (VAS) (0–100).

2.2. Ultrasound Examination and Scoring

Ultrasound was performed the same day as the clinical examination, with a GE Logiq[®] E9 machine, version R5 (Milwaukee, WI, USA) with a 6–15 MHz linear transducer, in greyscale (GS) and color Doppler (CD) modality. For CD, the frequency, pulse repetition frequency (PRF), and gain were set according to published guidelines [11] with a Doppler frequency of 7.5 MHz and a PRF of 0.4 MHz. The same settings were used for all patients. Tender entheses were examined in longitudinal and transverse planes and patients were positioned according to the European League Against Rheumatism (EULAR) guidelines [12] in the prone position and the foot in a neutral position. Enthesitis of the tender entheses was scored using the OMERACT enthesitis scoring system for presence/absence of thickening, hypoechogenicity, calcifications/enthesophytes, and erosions and semi quantitatively 0–3 for CD activity ≤ 2 mm from the bony cortex [2,13]. Each lesion was scored separately and, subsequently, a sum score (0–7) was calculated by summing the binary scores (0/1) of thickening, hypoechogenicity, calcifications/enthesophytes and erosions, and the 0–3 score for color Doppler activity. All examinations were performed by one examiner (SKF, 5 years of musculoskeletal ultrasound experience) and 10 patients were also examined by a second examiner on the same day (LT, >20 years of experience) for inter-reader agreement. Stored images were re-read by the first examiner after 3 weeks for intra-reader agreement.

2.3. Statistics

Descriptive statistics are presented as numbers (percentages) for binary variables and as medians (interquartile ranges) for continuous variables. Inter- and intra-reader agreement, as well as the agreement between clinical and ultrasound findings of enthesitis, was evaluated using Cohen's Kappa and prevalence and bias-adjusted Kappa (PABAK) [14] for binary outcomes, weighted Kappa (squared weights) for ordinal outcomes, and intraclass correlation coefficient (ICC) for sum scores. Kappa values of 0–0.20 were considered as slight agreement, 0.21–0.40 as fair, 0.41–0.60 as moderate, 0.61–0.80 as good, and 0.81–1.00 as excellent [15]. Findings at Achilles entheses vs. fascia plantaris were compared by Fischer's exact test or Mann–Whitney U test, as appropriate (post hoc analyses). The significance level was set to $p < 0.05$. Statistical analyses were performed with R, version 3.6.1.

3. Results

3.1. Population Characteristics

Twenty-seven patients with peripheral SpA and tender entheses were included. Fourteen (52%) of the tender entheses were at the Achilles tendon insertion and 13 (48%) were at the plantar fascia insertion. PsA according to the CASPAR criteria could additionally be classified in 15 (56%) of the patients. Patients were a median (interquartile range) of 49 (38–56) years old, 59% were male and the median disease duration was 2 (0–6) years. The population characteristics for the cohort are shown in Table 1. The patients' global pain scores (VAS 0–100) were high with a median (IQR) of 63 (41–73). We found no statistically significant differences in population characteristics between patients with PsA and other SpA (data not shown).

Table 1. Population characteristics for all patients and patients with tender Achilles and plantar fascia entheses, respectively.

	All n = 27	Achilles n = 14	Fascia Plantaris n = 13	Difference	
	No/Median (%/IQR)	No/Median (%/IQR)	No/Median (%/IQR)	OR (95% CI)/ Difference in Medians (95% CI) ¹	p
Age (years)	49 (38–56)	50 (39–57)	44 (37–52)	3 (–9–14)	0.56
Sex (male)	16 (59)	8 (57)	8 (62)	1.2 (0.2–7.3)	1
PsA	15 (56)	8 (57)	7 (54)	1.1 (0.2–6.7)	1
Enthesis—Achilles	14 (52)	14 (100)	0 (0)	-	-
Enthesis—Plantar fascia	13 (48)	0 (0)	13 (100)	-	-
Disease duration (years)	2 (0.25–6)	1 (0–6)	2 (1–6)	–1 (–4–3)	0.42
CRP (mg/L)	3.5 (1.5–6.8)	4.4 (1.6–7.8)	2.8 (1.8–4.7)	1.0 (–1.8–4.5)	0.54
TJC (0–68)	1 (0–11)	2 (0–11)	1 (0–8)	0 (–2–4)	0.75
SJC (0–66)	0 (0–0)	0 (0–0)	0 (0–0)	0 (0–0)	0.64
SPARCC (0–16)	2 (1–4)	3 (1–4)	2 (1–2)	0 (–1–2)	0.40
DAS28-CRP	2.5 (2.1–3.0)	2.3 (2–2.8)	2.6 (2.3–3.3)	–0.3 (–0.8–0.3)	0.18
Physician global VAS (0–100)	27 (14–42)	30 (23–70)	17 (12–36)	13 (–5–36)	0.15
HAQ (0–3)	0.88 (0.50–1.20)	0.75 (0.38–1.38)	0.88 (0.75–1.13)	–0.25 (–0.75–0.38)	0.38
Pt. global VAS (0–100)	72 (52–78)	71 (19–78)	72 (53–78)	–4 (–33–13)	0.68
Pt. pain VAS (0–100)	63 (41–73)	65 (38–79)	59 (47–67)	5 (–25–21)	0.70

CI: Confidence Interval, CRP: C-reactive protein, DAS28-CRP: Disease Activity Score in 28 joints using C-reactive protein, HAQ: Health Assessment Questionnaire, IQR: Interquartile range, OR: Odd ratio, Pt.: Patient, PsA: Psoriatic arthritis, SJC: Swollen Joint Count, SPARCC: Spondyloarthritis Research Consortium of Canada enthesitis index, TJC: Tender Joint Count, VAS: Visual Analogue Scale. ¹ OR (95% CI) by Fisher's exact test for binary variables, difference in medians (95% CI) by Mann–Whitney U test for continuous variables.

3.2. Ultrasound Findings and Agreement

Ultrasound findings and the difference in findings between Achilles tendon and plantar fascia entheses are presented in Table 2 and image examples in Figure 1. One or more ultrasound signs of enthesitis (structural or inflammatory lesions) could be found in 19 (70%) of the tender entheses. Greyscale inflammatory ultrasound signs of enthesitis (thickening or hypoechogenicity) were found in 13 (48%) entheses, and 5 (19%) of all entheses, 38% of entheses with greyscale signs of inflammation showed CD activity. The most common inflammatory sign of enthesitis was thickening (13 (48%) of entheses), which was numerically somewhat more frequent at the plantar fascia (7 (54%)) compared to at the Achilles tendon (6 (43%)), while hypoechogenicity was seen in 12 (44%) of the entheses (6 (43%) Achilles entheses, 6 (46%) plantar fascia entheses). CD activity was seen only at

the Achilles tendon (5 (36%) Achilles entheses, OR = 0, $p = 0.04$). Structural lesions were found in 44% of all entheses. Enthesophytes/calcifications were the most common lesion (12 (44%)) while erosions were more seldomly seen (4 (15%)). Both types of structural lesions (enthesophytes/calcifications and erosions) were statistically significantly more frequent at the Achilles tendon enthesis compared to the plantar fascia enthesis (OR for enthesophytes/calcifications 0.03, $p < 0.001$, for erosions 0.00, $p = 0.098$). No statistically significant differences were found in ultrasound lesions between patients with PsA and other types of SpA (data not shown).

Table 2. Ultrasound findings and difference between findings at the Achilles and plantar fascia entheses.

	All <i>n</i> = 27	Achilles <i>n</i> = 14	Fascia Plantaris <i>n</i> = 13	Difference	
	No/Median (%/IQR)	No/Median (%/IQR)	No/Median (%/IQR)	OR (95% CI)/ Difference in Medians (95% CI) ¹	<i>p</i>
Elementary lesions					
Thickening	13 (48)	6 (43)	7 (54)	1.5 (0.3–9.2)	0.71
Hypoechoogenicity	12 (44)	6 (43)	6 (46)	1.1 (0.2–6.7)	1
Calcifications/Enthesophytes	12 (44)	11 (79)	1 (8)	0.0 (0.0–0.3)	<0.001
Erosions	4 (15)	4 (29)	0 (0)	0.0 (0.0–1.5)	0.10
CD (presence)	5 (19)	5 (36)	0 (0)	0.0 (0.0–1.0)	0.04
CD grade (positive only)	2 (2–2)	2 (2–2)	NA	-	-
Combined lesions					
Any inflammatory lesion ²	13 (48)	6 (43)	7 (54)	1.5 (0.3–9.2)	0.71
Any structural lesion ²	12 (44)	11 (79)	1 (8)	0.0 (0.0–0.3)	<0.001
Any inflammatory AND any structural lesion ²	6 (22)	5 (36)	1 (8)	0.2 (0.0–1.8)	0.17
Any inflammatory OR any structural lesion ²	19 (70)	12 (86)	7 (54)	0.2 (0.0–1.6)	0.10
Sum-score					
Sum-score (0–7) ³	1 (0.0–2.5)	1.5 (1–4)	1 (0–2)	1.0 (0.0–3.0)	0.09

CD: Color Doppler, CI: Confidence interval, IQR: Interquartile range, OR: Odds Ratio. ¹ OR (95% CI) by Fisher’s exact test for binary variables, difference in medians (95% CI) by Mann–Whitney U test for continuous variables. ² Inflammatory lesion = thickened and/or hypoechoogenic with/without CD activity. Structural lesion = enthesophytes and/or erosions. ³ Sum of binary scores (0/1) of thickening, hypoechoogenicity, calcifications/enthesophytes and erosions, and 0–3 score for color Doppler activity.

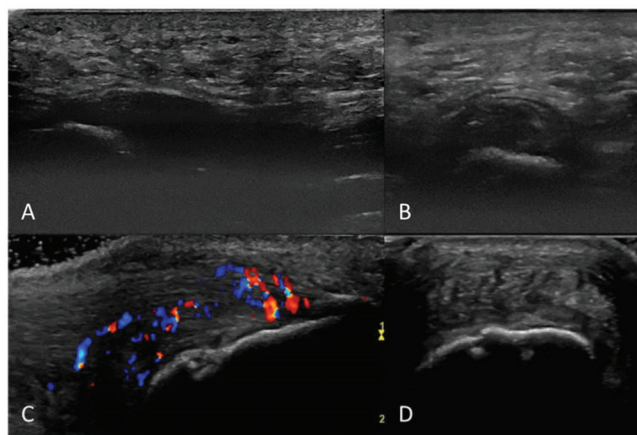


Figure 1. Greyscale images of the plantar fascia insertion with thickening and hypoechoogenicity in longitudinal (A) and transverse (B) plane, and the Achilles tendon insertion with thickening, hypoechoogenicity, color Doppler activity and enthesophyte in longitudinal plane (C) and greyscale image in transverse plane (D).

In patients with tender entheses that did not show any ultrasound inflammatory signs of enthesitis ($n = 14$), other possible explanations for tenderness could be found in 7 (50%) (tendinitis ($n = 2$), arthritis in the subtalar joint ($n = 2$), tenosynovitis of the tibialis posterior tendon ($n = 1$), retrocalcaneal bursitis ($n = 2$)). Findings in greyscale and CD are shown in Figure 2.

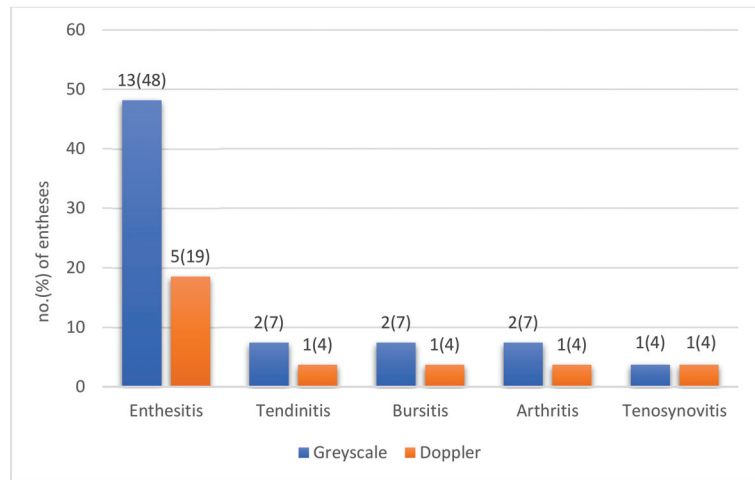


Figure 2. Ultrasound findings of inflammation in patients with spondyloarthritis (SpA) and tenderness at entheses in the heel region ($n = 27$) shown as no. (percentage) of tender entheses with presence of lesions in greyscale (blue) and color Doppler mode (orange).

Agreements between tenderness versus any ultrasound signs of enthesitis versus ultrasound inflammatory signs of enthesitis versus Doppler activity in the entheses and ultimately versus ultrasound enthesitis OR other explanatory pathology are shown in Table 3. Overall, an inflammatory explanation for tenderness (enthesitis or other inflammatory pathology) could be found by ultrasound in 20 (74%) of the heels with tender entheses.

Table 3. Agreement between enthesal tenderness and ultrasound signs of enthesitis.

	PEA	κ	PABAK
Tenderness vs. any US sign of enthesitis (inflammatory ¹ or structural ²)	70	0	0.41
Tenderness vs. any US inflammatory sign of enthesitis ¹	48	0	−0.04
Tenderness vs. US inflammatory enthesitis ¹ with Doppler activity	19	0	−0.63
Tenderness vs. any US inflammatory signs of enthesitis ¹ OR other explanatory pathology	70	0	0.41

κ : Cohens Kappa, PABAK: Prevalence Adjusted Bias Adjusted Kappa, PEA: Percent Exact Agreement, US: ultrasound. ¹ Hypoechoogenicity and/or thickening. ² Enthesophytes/calcifications and/or erosions.

Intra- and inter-reader agreements are shown in Table 4. Intra-reader agreement for all individual lesions was excellent (Cohens Kappa 0.93–1.00, PABAK 0.93–1.00), as was ICC for sum scores (0.99 (0.98–1.00)). Inter-reader agreement was marginally lower both for individual lesions (Cohen’s Kappa 0–1, PABAK 0.8–1.0) and for sum scores (ICC 0.98 (0.93–0.99)).

Table 4. Intra- and inter-reader agreements of ultrasound elementary lesions of enthesitis and sum score.

	Intrareader (n = 27)				Interreader (n = 10)			
	Prev. (%)	PEA (%)	κ	PABAK	Prev. (%)	PEA (%)	κ	PABAK
Thickened	48	100	1	1	20	100	1	1
Hypoechoogenicity	46	96	0.93	0.93	5	90	0	0.8
Erosions	15	100	1	1	20	100	1	1
Enthesophytes/Calcifications	44	100	1	1	60	100	1	1
Color Doppler presence	19	100	1	1	10	100	1	1
Color Doppler grade (0–3)	NA	96	0.97	NA	NA	100	1	NA
Inflammation ¹ yes/no	48	100	1	1	20	100	1	1
Structural ² yes/no	44	100	1	1	60	100	1	1
	ICC (95% CI)				ICC (95% CI)			
Ultrasound lesion Sum-score ³	0.99 (0.98–1.00)				0.98 (0.93–0.99)			

CI: Confidence Interval, ICC: Intraclass Correlation, κ: Cohens Kappa, PABAK: Prevalence Adjusted Bias Adjusted Kappa, PEA: Percent Exact Agreement, Prev.: Mean prevalence of the two reads. ¹ Inflammation = hypoechoogenicity and/or thickening with/without Color Doppler activity. ² Structural = enthesophytes and/or erosions. ³ Sum of the binary scores (0/1) of thickening, hypoechoogenicity, calcifications/enthesophytes and erosions, and the 0–3 score for color Doppler activity.

4. Discussion

In this cross-sectional study of tender heel entheses in 27 patients with SpA, only 48% were found to be related to ultrasound signs of inflammatory enthesitis and only 19% had signs of Doppler activity (active inflammation—all in the Achilles enthesitis). The lack of Doppler findings at the plantar fascia insertion may be explained by attenuation of the ultrasound by the heel fat pad, limiting the ability to detect Doppler activity. Therefore, greyscale signs of inflammation are of more importance here.

The most prevalent enthesitis lesion was thickening/hypoechoogenicity at the Achilles insertion and thickening at the plantar fascia insertion. In some of the tender entheses without ultrasound signs of enthesitis, we could identify other origins of the pain than enthesitis (subtalar synovitis, tenosynovitis and retrocalcaneal bursitis). Thus, this study underlines the value of ultrasound for establishing the origin of pain around the heel in patients with SpA, as the treatment options for enthesitis in SpA are different than for arthritis. Therefore, the presence or absence of different pathologies may impact clinical decision-making, optimizing the outcome for the individual patient.

The poor association between clinical symptoms at the enthesis level and objective signs of inflammatory activity by ultrasound has also been demonstrated by Michelsen et al. [16] who found a lack of association between clinical and US signs of enthesitis in a cohort of PsA patients focusing only on the Achilles tendon. They also found that the signs of active inflammation and structural changes were similar in patients with and without tender enthesitis, highlighting that clinical examination may have limited value as compared to ultrasound evaluation.

Structural lesions were found in 44% of the symptomatic entheses, with a much higher frequency in Achilles compared to plantar fascia entheses, and with calcifications/enthesophytes being the predominant findings. This is in line with the findings by Seven et al. [7] who found structural lesions to be the predominant lesion of lower limb entheses in an axial cohort of SpA patients initiating TNF alpha blocker treatment, irrespective of tenderness. They also found that these structural changes had no sensitivity to change. Enthesophytes are also a common finding in healthy controls and appear to be increasingly frequent with age [17]. The structural ultrasound lesions, therefore, seem to be unrelated to clinical entheses tenderness, and this challenges the usefulness of ultrasound structural lesions in the assessment of tender entheses. A longitudinal investigation of the

development of these lesions in patients with newly diagnosed SpA and control groups could, however, be interesting.

Strengths of our study are the use of the OMERACT consensus-based and validated ultrasound enthesitis definitions and scoring system and the excellent inter- and intra-reader agreements of the scoring system. A limitation is the small sample size, for both the study cohort and the inter-reader analyses, with only 10 patients included for the latter analyses. Another limitation is the lack of blinding and control group.

In conclusion, less than half of clinically tender entheses in the heel region had ultrasound signs of inflammatory enthesitis (greyscale) and 19% were Doppler positive. Ultrasound was able to identify other pathologies as the origin of the heel pain. Ultrasound assessment of tender entheses is helpful for correct diagnosis and treatment decisions.

Author Contributions: All authors designed the study and developed the study protocol. S.K.F. and L.T. performed the ultrasound examinations and scoring as described. S.K.F. performed analyses and wrote the first draft of the paper. All authors interpreted data, revised the manuscript, read, and approved the final manuscript. All authors have read and agreed to the published version of the manuscript.

Funding: This work was supported by research grants from The Danish Rheumatism Association (grant number A4199) and the Danish Psoriasis Association. The funding bodies did not play any role in the design; in the collection, analysis, and interpretation of data; in the writing of the manuscript; or in the decision to submit the manuscript for publication.

Institutional Review Board Statement: The study was conducted according to the guidelines of the Declaration of Helsinki and approved by the Ethics committee of the capital region in Denmark (journal no. H-16035123).

Informed Consent Statement: Informed consent was obtained from all subjects involved in the study.

Data Availability Statement: The datasets used and/or analyzed during the current study are available from the corresponding author on reasonable request.

Acknowledgments: We thank all participating patients as well as staff at Center for Rheumatology and Spine Diseases, Rigshospitalet-Glostrup.

Conflicts of Interest: The authors declare that they have no competing interest relevant to this manuscript.

References

1. Terslev, L.; Naredo, E.; Iagnocco, A.; Balint, P.V.; Wakefield, R.J.; Aegerter, P.; Aydin, S.Z.; Bachta, A.; Hammer, H.B.; Bruyn, G.A.; et al. Defining enthesitis in spondyloarthritis by ultrasound: Results of a Delphi process and of a reliability reading exercise. *Arthritis Care Res. (Hoboken)* **2014**, *66*, 741–748. [[CrossRef](#)] [[PubMed](#)]
2. Balint, P.V.; Terslev, L.; Aegerter, P.; Bruyn, G.A.W.; Chary-Valckenaere, I.; Gandjbakhch, F.; Iagnocco, A.; Jousse-Joulin, S.; Moller, I.; Naredo, E.; et al. Reliability of a consensus-based ultrasound definition and scoring for enthesitis in spondyloarthritis and psoriatic arthritis: An OMERACT US initiative. *Ann. Rheum. Dis.* **2018**, *77*, 1730–1735. [[CrossRef](#)] [[PubMed](#)]
3. D'Agostino, M.-A.; Said-Nahal, R.; Hacquard-Bouder, C.; Brasseur, J.-L.; Dougados, M.; Breban, M. Assessment of peripheral enthesitis in the spondylarthropathies by ultrasonography combined with power Doppler: A cross-sectional study. *Arthritis Rheum.* **2003**, *48*, 523–533. [[CrossRef](#)] [[PubMed](#)]
4. Lehtinen, A.; Taavitsainen, M.; Leirisalo-Repo, M. Sonographic analysis of enthesopathy in the lower extremities of patients with spondylarthropathy. *Clin. Exp. Rheumatol.* **1994**, *12*, 143–148. [[PubMed](#)]
5. Balint, P.V.; Kane, D.; Wilson, H.; McInnes, I.B.; Sturrock, R.D. Ultrasonography of enthesal insertions in the lower limb in spondyloarthropathy. *Ann. Rheum. Dis.* **2002**, *61*, 905–910. [[CrossRef](#)] [[PubMed](#)]
6. Mandl, P.; Navarro-Compan, V.; Terslev, L.; Aegerter, P.; van der Heijde, D.; D'Agostino, M.A.; Baraliakos, X.; Pedersen, S.J.; Jurik, A.G.; Naredo, E.; et al. EULAR recommendations for the use of imaging in the diagnosis and management of spondyloarthritis in clinical practice. *Ann. Rheum. Dis.* **2015**, *74*, 1327–1339. [[CrossRef](#)]
7. Seven, S.; Pedersen, S.J.; Østergaard, M.; Felbo, S.K.; Sørensen, I.J.; Døhn, U.M.; Terslev, L. Peripheral Enthesitis Detected by Ultrasonography in Patients with Axial Spondyloarthritis-Anatomical Distribution, Morphology, and Response to Tumor Necrosis Factor-Inhibitor Therapy. *Front. Med. (Lausanne)* **2020**, *7*, 341. [[CrossRef](#)] [[PubMed](#)]
8. Naredo, E.; Battle-Gualda, E.; Garcia-Vivar, M.L.; Garcia-Aparicio, A.M.; Fernandez-Sueiro, J.L.; Fernandez-Prada, M.; Giner, E.; Rodriguez-Gomez, M.; Pina, M.F.; Medina-Luezas, J.A.; et al. Power Doppler ultrasonography assessment of entheses in spondyloarthropathies: Response to therapy of enthesal abnormalities. *J. Rheumatol.* **2010**, *37*, 2110–2117. [[CrossRef](#)]

9. Felbo, S.K.; Wiell, C.; Ostergaard, M.; Poggenborg, R.P.; Boyesen, P.; Hammer, H.B.; Boonen, A.; Pedersen, S.J.; Juul Sorensen, I.; Madsen, O.R.; et al. Do tender joints in active psoriatic arthritis reflect inflammation assessed by ultrasound and magnetic resonance imaging? *Rheumatology* **2021**. [[CrossRef](#)]
10. Rudwaleit, M.; van der Heijde, D.; Landewe, R.; Akkoc, N.; Brandt, J.; Chou, C.T.; Dougados, M.; Huang, F.; Gu, J.; Kirazli, Y.; et al. The Assessment of SpondyloArthritis International Society classification criteria for peripheral spondyloarthritis and for spondyloarthritis in general. *Ann. Rheum. Dis.* **2011**, *70*, 25–31. [[CrossRef](#)] [[PubMed](#)]
11. Torp-Pedersen, S.T.; Terslev, L. Settings and artefacts relevant in colour/power Doppler ultrasound in rheumatology. *Ann. Rheum. Dis.* **2008**, *67*, 143–149. [[CrossRef](#)] [[PubMed](#)]
12. Moller, I.; Janta, I.; Backhaus, M.; Ohrndorf, S.; Bong, D.A.; Martinoli, C.; Filippucci, E.; Sconfienza, L.M.; Terslev, L.; Damjanov, N.; et al. The 2017 EULAR standardised procedures for ultrasound imaging in rheumatology. *Ann. Rheum. Dis.* **2017**, *76*, 1974–1979. [[CrossRef](#)] [[PubMed](#)]
13. Bruyn, G.A.; Iagnocco, A.; Naredo, E.; Balint, P.V.; Gutierrez, M.; Hammer, H.B.; Collado, P.; Filippou, G.; Schmidt, W.A.; Jousse-Joulin, S.; et al. OMERACT Definitions for Ultrasonographic Pathologies and Elementary Lesions of Rheumatic Disorders 15 Years on. *J. Rheumatol.* **2019**, *46*, 1388–1393. [[CrossRef](#)] [[PubMed](#)]
14. Byrt, T.; Bishop, J.; Carlin, J.B. Bias, prevalence and kappa. *J. Clin. Epidemiol.* **1993**, *46*, 423–429. [[CrossRef](#)]
15. Landis, J.R.; Koch, G.G. The measurement of observer agreement for categorical data. *Biometrics* **1977**, *33*, 159–174. [[CrossRef](#)] [[PubMed](#)]
16. Michelsen, B.; Diamantopoulos, A.P.; Soldal, D.M.; Hammer, H.B.; Kavanaugh, A.; Haugeberg, G. Achilles enthesitis defined by ultrasound is not associated with clinical enthesitis in patients with psoriatic arthritis. *RMD Open* **2017**, *3*, e000486. [[CrossRef](#)] [[PubMed](#)]
17. Guldberg-Moller, J.; Terslev, L.; Nielsen, S.M.; Konig, M.J.; Torp-Pedersen, S.T.; Torp-Pedersen, A.; Christensen, R.; Bliddal, H.; Ellegaard, K. Ultrasound pathology of the entheses in an age and gender stratified sample of healthy adult subjects: A prospective cross-sectional frequency study. *Clin. Exp. Rheumatol.* **2019**, *37*, 408–413. [[PubMed](#)]



Article

Feasibility Trial to Evaluate Tendon Stiffness Obtained from Shear Wave Elastography Imaging as a Biomarker of Aromatase Inhibitor-Induced Arthralgias

Jessica A. Martinez^{1,2,*}, Mihra S. Taljanovic^{3,4}, Andres A. Nuncio Zuniga⁵, Betsy C. Wertheim¹, Denise J. Roe^{1,6}, Sima Ehsani^{1,7}, Sao Jiralerspong^{1,7}, Jennifer Segar^{1,7} and Pavani Chalasani^{1,7}

- ¹ The University of Arizona Cancer Center, Tucson, AZ 85719, USA; bwertheim@uacc.arizona.edu (B.C.W.); droe@arizona.edu (D.J.R.); simaehsani@arizona.edu (S.E.); sjiral@arizona.edu (S.J.); segar@arizona.edu (J.S.); pchalasani@uacc.arizona.edu (P.C.)
 - ² Department of Nutritional Sciences, University of Arizona, Tucson, AZ 85719, USA
 - ³ Department of Medical Imaging and Orthopaedic Surgery, University of Arizona, Tucson, AZ 85719, USA; mihrat@radiology.arizona.edu
 - ⁴ Department of Radiology, University of New Mexico, Albuquerque, NM 87131, USA
 - ⁵ Department of Biomedical Engineering, University of Arizona, Tucson, AZ 85719, USA; aanuncio@arizona.edu
 - ⁶ Department of Epidemiology and Biostatistics, University of Arizona, Tucson, AZ 85719, USA
 - ⁷ Department of Medicine, University of Arizona, Tucson, AZ 85719, USA
- * Correspondence: jam1@arizona.edu

Citation: Martinez, J.A.; Taljanovic, M.S.; Nuncio Zuniga, A.A.; Wertheim, B.C.; Roe, D.J.; Ehsani, S.; Jiralerspong, S.; Segar, J.; Chalasani, P. Feasibility Trial to Evaluate Tendon Stiffness Obtained from Shear Wave Elastography Imaging as a Biomarker of Aromatase Inhibitor-Induced Arthralgias. *J. Clin. Med.* **2022**, *11*, 1067. <https://doi.org/10.3390/jcm11041067>

Academic Editor: Kevin L. Garvin

Received: 7 January 2022

Accepted: 16 February 2022

Published: 18 February 2022

Publisher's Note: MDPI stays neutral with regard to jurisdictional claims in published maps and institutional affiliations.



Copyright: © 2022 by the authors. Licensee MDPI, Basel, Switzerland. This article is an open access article distributed under the terms and conditions of the Creative Commons Attribution (CC BY) license (<https://creativecommons.org/licenses/by/4.0/>).

Abstract: Aromatase inhibitor-induced arthralgia (AIA) comprises significant, activity-limiting musculoskeletal symptoms, including joint pain, myalgia, and joint stiffness. We conducted a prospective feasibility study in postmenopausal women diagnosed with early-stage (0–3) hormone receptor positive (HR+) breast cancer who were candidates for treatment with adjuvant AI therapy ($n = 16$). Tendons of the hands and wrists and the median nerve were imaged using gray-scale and power Doppler ultrasound (US) and US SWE. Arthralgia symptoms were evaluated using the Breast Cancer Prevention Trial (BCPT) Symptom Checklist musculoskeletal subscale (MS) and the Western Ontario and McMaster Universities Osteoarthritis Index (WOMAC) pain and stiffness subscales. At baseline, there were significant differences in the SW velocities of tendons between dominant and nondominant hands. Increased velocity in 2 of 6 tendons and the median nerve was associated with greater pain at baseline, whereas slower velocity of the extensor digitorum tendon (suggesting decreased stiffness) was associated with a higher WOMAC stiffness score. Increased SW velocity (suggestive of increased stiffness) at baseline in the abductor pollicis longus tendon was associated with a worsening of all three pain and stiffness measures by 6 months. Future studies should evaluate SWE scores related to AIA outcomes in a larger sample size.

Keywords: aromatase inhibitors; breast cancer; shear wave elastography; ultrasound; joint pain; stiffness; arthralgia; aromatase inhibitor-induced arthralgia (AIA)

1. Introduction

Aromatase inhibitor-induced arthralgia (AIA) comprises significant, activity-limiting musculoskeletal symptoms, including joint pain, myalgia, and joint stiffness [1]. AIA can also include carpal tunnel syndrome (CTS) [2,3], tenosynovitis, and muscle weakness [4,5]. Symptoms can affect the spine as well as large and small joints of the upper and lower extremities [6,7]. The median time to develop initial AIA symptoms is 6 weeks, with peak symptoms reported at 6 months [8]; however, some women experience worsening symptoms up to 1–2 years post-initiation of an aromatase inhibitor (AI) [9,10]. Extended adjuvant AI therapy (10 years) has been shown to improve disease-free survival when compared to placebo in women who completed 5 years of standard AI therapy [11]. Given

the long duration of treatment, it is imperative to identify patients at risk for AIA in order to develop early interventions and improve quality of life and adherence to therapy. The development of biomarkers for AIA is an unmet clinical need which impacts a large patient population.

Previous studies have used Doppler ultrasound (US) to evaluate pathological changes of the tendons and joints associated with AIA. Our prior study suggested that women with AIA had non-significantly higher hyperemia and increased tenosynovial fluid relative to asymptomatic, age-matched controls using a Doppler US [12]. Similarly, Dizdar et al. showed that patients with AIA had significantly more fluid in the tendon sheaths and electrophysiologic findings of carpal tunnel syndrome relative to patients on AI without pain [4]. However, other studies using US and age-matched controls found no association between any US findings and AIA symptoms [13,14]. The inconsistency in relating US findings to AIA symptoms underscores the need for more sophisticated imaging techniques to better evaluate physiologic changes with AIA.

Shear wave elastography (SWE) is a novel imaging technique used to acquire a measure of tendon stiffness via shear acoustic waves of a focused ultrasonic beam [15]. In our prior case-control study, women with AIA had significantly faster SW velocities (suggesting stiffer tendons) than age-matched controls, determined by US SWE [12]. While this preliminary case-control study had a limited sample size, the finding of stiffer tendons with AIA was intriguing given that affected tendons have been shown to be softer than healthy normal tendons in other studies [16]. For example, Turkay et al. demonstrated that adult patients with de Quervain tenosynovitis had slower SW velocities (suggesting softer tendons) than healthy adults in the first extensor compartment of the hand [17]. Conversely, SWE studies of the median nerve in the assessment of carpal tunnel syndrome have shown increased SW velocities in patients relative to controls [18]. Other studies suggest that the relationship between pain and soft tissue stiffness on US SWE may vary by pathology. Breda et al. showed that patients with patellar tendinopathy had significantly increased SW velocities (suggesting increased tendon stiffness) compared to age-matched asymptomatic controls [19]. Hou et al. suggested that there was tendon softening on US SWE with rotator cuff disease [20]. Pan et al. showed a significant positive correlation between pain and increased SW velocities in patients with plantar fasciitis [21]. In the context of rheumatoid arthritis, muscle stiffness was not associated with muscle strength; however, that study did not evaluate tendon stiffness with imaging [22].

Here, in the context of an ongoing prospective study to evaluate the biomarkers of AIA in postmenopausal women, we evaluated tendon features of the hands and wrists using US SWE in a subset of patients. Tendon stiffness was evaluated at initiation and after 6 months of AI treatment. To our knowledge, this is the first study to use US SWE to associate tendon stiffness with AIA symptoms in breast cancer patients taking AI and to determine whether it is feasible to associate tendon stiffness at baseline with worsening AIA symptoms by 6 months.

2. Materials and Methods

2.1. Study Design

This study was embedded in an ongoing, single-arm, prospective clinical trial of patients with early-stage hormone receptor positive (HR+) breast cancer to evaluate and develop blood-based and imaging biomarkers of AIA. The trial was approved by our institutional review board and was conducted in accordance with the requirements of the provisions of the Declaration of Helsinki. All patients provided written informed consent. The trial was registered on clinicaltrials.gov (NCT03665077). All eligible patients completed their definitive treatment (surgery \pm radiation) and were recruited at the time of their medical oncologist visit, prior to initiation of anastrozole as adjuvant therapy. For this sub-study, US SWE images were captured at the initiation of their AI ($n = 16$) and after 6 months ($n = 9$). The US SWE component of this study was originally planned for all participants; however, the US instrument was no longer available for continuation of

SWE studies for reasons that were unrelated to the current study or the authors. Of the 16 patients with baseline SWE and questionnaire data, 14 had paired questionnaire data at 6 months.

2.2. Participants

Postmenopausal women diagnosed with early-stage (0–3) HR+ breast cancer who were candidates for treatment with adjuvant AI therapy were eligible for this trial. Exclusion criteria included prior breast cancer diagnosis, prior adjuvant or neo-adjuvant chemotherapy, prior endocrine therapy (AI or tamoxifen), history of rheumatoid arthritis or other autoimmune arthritis, daily NSAID use (other than baby aspirin), or any corticosteroids or immunosuppressive therapies.

2.3. BCPT-MS

The Breast Cancer Prevention Trial (BCPT) Symptom Checklist is a 42-item questionnaire validated in breast cancer survivors [23]. Here, we used the musculoskeletal subscale (BCPT-MS), which consists of the mean of responses to three questions addressing general aches and pains, joint pain, and muscle stiffness. The BCPT-MS subscale has been shown to be responsive to changes in AIA [24]. Scores range from 0–12, with higher scores representing worse symptoms.

2.4. WOMAC

The Western Ontario and McMaster Universities Osteoarthritis Index (WOMAC) is a 24-item instrument developed to assess pain, stiffness, and physical function in participants with osteoarthritis or AIA [25,26]. Here, we evaluated the pain (5 items) and stiffness (2 items) subscales using the 5-point Likert format (0 = none, 1 = mild, 2 = moderate, 3 = severe, and 4 = extreme). As discussed in Bellamy [25], for convenience and for comparison purposes to previous studies, total scores and each subscale were normalized to a range of 0–100.

2.5. Gray-Scale, Power Doppler, and Shear Wave Elastography (SWE) US Imaging and Scoring

All images were collected before and after the initiation of AI (baseline and 6 months). Real-time gray-scale and power Doppler US examination of the bilateral wrists were performed on a General Electric Logiq E9 machine using the 18–8 MHz linear hockey stick transducer as previously described [12]. Briefly, during gray-scale and power Doppler US examination, patients were seated with their hands resting on a small table placed between the examiner and the patient. All tendons and tendon sheaths were evaluated for the presence of a normal or increased synovial fluid complex on gray-scale evaluation and for the presence of active inflammation on power Doppler evaluation. Anatomical regions of interest included the abductor pollicis longus, extensor pollicis brevis, extensor digitorum tendon, extensor carpi ulnaris, flexor digitorum superficialis and flexor digitorum profundus tendons, and the median nerve.

SWE examinations of the bilateral wrists and scoring of these images were performed as previously described [12]. Briefly, a Siemens S3000 ACUSON US unit (Siemens Medical Systems) with a high-resolution (9–4 MHz) and 12-MHz linear transducers were used to optimize visualization of the examined regions and to accommodate depth. The tissue elasticity (degree of stiffness) was displayed on a color bar elastogram on the screen and expressed as SW velocities in m/s (scale: 0.5–20 m/s). A copious amount of US gel was also used to accommodate the depth. The anatomical regions of interest were collected along both long and short axes of the tendons/tendon sheaths.

To score SWE images, regions of interest (ROIs) were examined by a fellowship-trained musculoskeletal radiologist with more than 5 years of experience in US SWE imaging. ROIs contained the entire anatomical site of interest in each image. The B-mode images were co-registered with SW velocity color maps. The average SW velocity within each ROI was calculated using color map values and tabulated by a biomedical engineer. Each image

was captured and scored in triplicate. The code to generate ROI's is available on the public repository, GitHub.

2.6. Statistical Analysis

Baseline characteristics were summarized using the median and interquartile range (IQR) for continuous variables and proportions for categorical variables. Changes in symptom scores across time were tested using linear mixed-effects models, with time (interval since baseline) as a continuous variable, adjusted for the baseline symptom score, and clustered on the participant. Additional models further adjusted for age at baseline, BMI at baseline, and definitive therapy (mastectomy versus lumpectomy). For SWE data, the velocity at each image location (7 locations), axis (long or short), and side (dominant or non-dominant) was measured in triplicate and reported as the mean \pm SD or median (range). Changes in SW velocity across time were tested using linear mixed-effects models with time (interval since baseline) as a continuous variable, adjusted for transducer and baseline velocity (mean of the triplicate measures), clustered on the participant. The random-effect constant could not be reasonably estimated in 8 of the 28 models (one model for each location-axis-side combination), presumably due to the complexity of the model. Thus, a sensitivity analysis used the same models without clustering on the participant, and another sensitivity analysis did not adjust for the baseline velocity (but clustered on the participant). For the association between the baseline SW velocity and baseline symptoms, symptom scores were dichotomized into asymptomatic (score = 0) or symptomatic (score > 0) participants, and median velocities (mean of triplicate measures) were compared between these two groups using Wilcoxon rank-sum tests. Similar Wilcoxon rank-sum tests were used to compare the median baseline SWE velocity (mean of the triplicate measure) across groups of participants whose symptoms worsened or did not worsen between baseline and 6 months. No adjustments were made for multiple comparisons. Statistical analyses were conducted using Stata 17.0 (StataCorp, College Station, TX, USA).

3. Results

3.1. Participant Characteristics

The participants in the SWE subgroup were older adults with a median (IQR) age of 64.9 (63.5–71.5) years at enrollment (Table 1). Patients were enrolled shortly after diagnosis of their breast cancer. The Median (IQR) time between diagnosis and enrollment was 4.6 (3.3–6.3) months. Participants ranged from a healthy weight to obese, with a median (IQR) BMI of 25.9 (23.4–33.6) kg/m², and the majority were non-Hispanic white (87.5%). There were 15 participants classified as right-hand dominant, and one was left-handed. For their definitive treatments, 75% had lumpectomy, and 62.5% had adjuvant radiation. There were three participants with stage 0 breast cancer, 11 with stage I, and two with stage II. All patients were still adherent to their AI at 6 months.

3.2. Gray-Scale and Power Doppler Ultrasound (US)

There was no increased power Doppler signal to suggest active inflammation at baseline or after 6 months in any participants on the Power Doppler interrogation. Additionally, all anatomical sites appeared normal using Grayscale US.

3.3. Baseline Shear Wave (SW) Velocity

Mean \pm SD baseline SW velocities were compared between dominant versus nondominant sides in the long (Table 2a) and short (Table 2b) axes. The abductor pollicis longus had a significantly faster mean velocity, suggesting greater stiffness, on the dominant side (5.59 ± 2.46 m/s) relative to the non-dominant side (4.71 ± 2.14 m/s) in the long axis ($p = 0.020$), with no difference in the short axis.

Table 1. Baseline characteristics in the shear wave elastography cohort ($n = 16$).

Characteristic	Median (IQR) or n (%)
Age at enrollment (y)	64.9 (63.5–71.5)
Age at diagnosis (y)	64.4 (63.1–71.2)
Time since diagnosis (months)	4.6 (3.3–6.3)
BMI (kg/m^2)	25.9 (23.4–33.6)
Right-side dominant	15 (94%) ^a
Race/ethnicity	
Non-Hispanic white	14 (87.5%)
Hispanic	2 (12.5%)
Definitive breast surgery	
Mastectomy	4 (25.0%)
Lumpectomy	12 (75.0%)
Radiation	
No	6 (37.5%)
Yes	10 (62.5%)
Disease stage	
0	3 (18.8%)
I	11 (68.8%)
II	2 (12.5%)

^a Participants were contacted retroactively and asked about handedness. Four participants could not be reached and were classified as right-handed. Abbreviations: BMI: body mass index.

Table 2. (a) Baseline shear wave elastography velocity (m/s) for long axis: mean \pm SD^a. (b) Baseline shear wave elastography velocity (m/s) for short axis: mean \pm SD^a.

(a)			
Image Location	Dominant Side	Non-Dominant Side	p -Value
Abductor pollicis longus	5.59 \pm 2.46	4.71 \pm 2.14	0.020
Extensor carpi ulnaris	4.76 \pm 1.67	4.64 \pm 1.64	0.568
Extensor digitorum tendon	5.55 \pm 1.51	5.93 \pm 2.22	0.157
Extensor pollicis brevis	4.00 \pm 1.21	4.11 \pm 1.71	0.684
Flexor digitorum profundus	6.77 \pm 2.23	6.45 \pm 2.77	0.389
Flexor digitorum superficialis	6.09 \pm 1.59	6.47 \pm 1.99	0.162
Median nerve	5.56 \pm 2.08	6.18 \pm 1.70	0.020
(b)			
Image Location	Dominant Side	Non-Dominant Side	p -Value
Abductor pollicis longus	4.47 \pm 1.07	4.41 \pm 0.86	0.728
Extensor carpi ulnaris	4.42 \pm 0.62	4.33 \pm 0.69	0.342
Extensor digitorum tendon	5.03 \pm 0.99	4.91 \pm 1.29	0.548
Extensor pollicis brevis	4.72 \pm 0.71	4.29 \pm 0.95	0.007
Flexor digitorum profundus	4.53 \pm 0.67	5.18 \pm 1.30	<0.001
Flexor digitorum superficialis	4.51 \pm 0.82	4.97 \pm 1.43	0.045
Median nerve	5.02 \pm 1.31	5.21 \pm 1.49	0.413

^a Mixed-effects model adjusted for the transducer, clustered on the patient (no adjustments for multiple comparisons).

Differences between sides in the abductor pollicis longus at the baseline are illustrated for a representative patient (Figure 1a,b). There were no other differences in tendons by side in the long axis. There were differences in SW velocity by side in three of six tendons in the short axis: the extensor pollicis brevis (dominant: 4.72 \pm 0.71 m/s versus nondominant: 4.29 \pm 0.95 m/s; $p = 0.007$), flexor digitorum profundus (dominant: 4.53 \pm 0.67 m/s versus nondominant: 5.18 \pm 1.30 m/s; $p < 0.001$), and the flexor digitorum superficialis (dominant: 4.51 \pm 0.82 m/s versus nondominant: 4.97 \pm 1.43 m/s; $p = 0.045$). Additionally, the median nerve had a significantly slower mean velocity on the dominant side in the long axis (dominant: 5.56 \pm 2.08 m/s versus nondominant: 6.18 \pm 1.70 m/s; $p = 0.020$). Given these observed differences, all other results are stratified by side and axis.

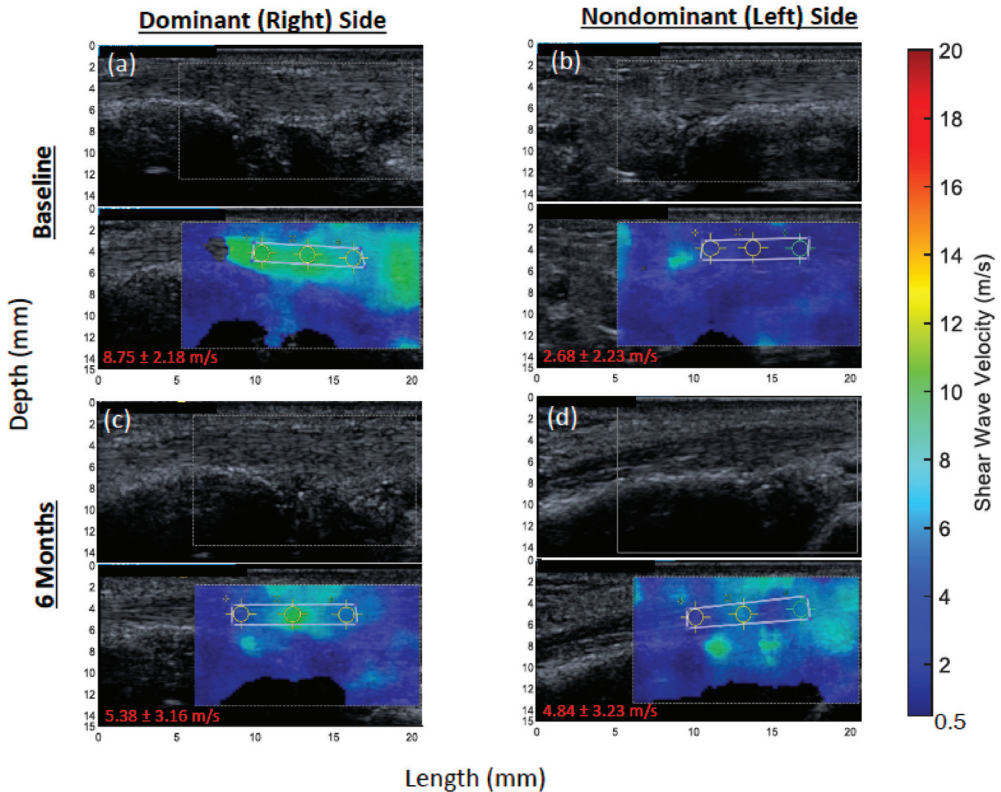


Figure 1. Representative shear wave elastography (SWE) images of the abductor pollicis longus (APL) tendon from a breast cancer patient initiating an aromatase inhibitor. Each elastogram (**bottom**) is displayed with its corresponding gray-scale image (**top**). Images were collected at the level of the wrist. At baseline, mean SW velocities were significantly faster on the dominant side relative to the nondominant in the long axis ($p = 0.020$). From baseline to 6 months, there was a significant reduction in SW velocity on the dominant side ($p = 0.027$) but not on the non-dominant side ($p = 0.849$). (a) APL tendon at baseline on dominant side. (b) APL tendon at baseline on non-dominant side. (c) APL tendon at 6 months on dominant side. (d) APL tendon at 6 months on non-dominant side. The shear wave velocity (mean \pm standard deviation) was measured in meters per second (m/s) and is presented on the lower left corner of each image.

3.4. Baseline Association between SW Velocity and Pain and Stiffness Scores

Median (IQR) SW velocities among symptomatic (score > 0) versus asymptomatic (score = 0) patients were compared for BCPT-MS (symptomatic, $n = 12$; asymptomatic, $n = 4$), WOMAC pain (symptomatic, $n = 5$; asymptomatic, $n = 11$), and WOMAC stiffness (symptomatic, $n = 9$; asymptomatic, $n = 7$). Patients that were symptomatic, as reported by the BCPT-MS, had a significantly faster median (range) SW velocity, suggesting greater stiffness, in the extensor carpi ulnaris (4.6 (3.3–4.9) versus 4.0 (2.7–4.3) m/s; $p = 0.008$ (nondominant side; short axis)) and the flexor digitorum profundus ((7.9 (4.8–9.9) versus 4.5 (2.7–6.8) m/s; $p = 0.020$ (dominant side; short axis)). Patients that were symptomatic using the BCPT-MS also had a faster median (range) SW velocity for the median nerve on the dominant side in both the long ((5.7 (4.2–9.2) versus 3.5 (2.5–5.8) m/s; $p = 0.030$) and short ((5.0 (4.0–7.7) versus 4.3 (3.8–4.6) m/s; $p = 0.042$) axes. The median SW velocity was not different in any other tendons for women with a score > 0 on the BCPT-MS at baseline on either side or in either axis. For women that were symptomatic on the WOMAC stiffness

subscale, the extensor digitorum tendon had a significantly slower median (range) SW velocity ((4.8 (3.0–5.6) versus 5.4 (4.7–7.1) m/s; $p = 0.009$ (nondominant side; short axis)). No other tendons nor the median nerve were related to a score > 0 on the WOMAC stiffness subscale at baseline. No tendons nor the median nerve were related to a score > 0 on the WOMAC pain subscale at baseline.

3.5. Change in SW Velocity

Changes in SW velocity from baseline to 6 months of AI treatment were calculated in the 9 participants that had paired images (Table 3). The abductor pollicis longus showed a significant decrease in SW velocity (suggestive of tendon softening) on the dominant side in the long axis (β -coefficient = -0.024 m/s; $p = 0.027$) but no change on the non-dominant side or on either side in the short axis. Differences in the abductor pollicis longus from baseline to 6 months in the long axis on both sides are illustrated for a representative patient (Figure 1). The extensor carpi ulnaris showed a significant decrease in SW velocity on the dominant side in the long axis (β -coefficient = -0.033 m/s; $p < 0.001$) but an increase in the short axis (β -coefficient = 0.006 m/s; $p = 0.040$). The flexor digitorum superficialis had a significant decrease in SW velocity in the long axis on both the dominant (β -coefficient = -0.024 m/s; $p = 0.014$) and non-dominant (β -coefficient = -0.020 m/s; $p = 0.038$) sides. The median nerve had a significant increase in SW velocity on the dominant side in both the long (β -coefficient = 0.031 m/s; $p = 0.002$) and short (β -coefficient = 0.018 m/s; $p = 0.009$) axes, but it had a significant decrease in velocity on the non-dominant side in the long axis (β -coefficient = -0.021 m/s; $p = 0.019$).

Table 3. Shearwave elastography change in velocity (m/s) over time (6 months): beta-coefficient (p -value)^a.

Image Location	Long Axis Dominant Side	Short Axis Dominant Side	Long Axis Non-Dominant Side	Short Axis Non-Dominant Side
Abductor pollicis longus	-0.024 (0.027)	0.002 (0.701)	0.002 (0.849)	-0.001 (0.797) ^b
Extensor carpi ulnaris	-0.033 (0.000)	0.006 (0.040) ^b	-0.000 (0.996)	0.002 (0.570) ^b
Extensor digitorum tendon	0.002 (0.817)	-0.006 (0.257)	0.004 (0.698)	-0.006 (0.363) ^b
Extensor pollicis brevis	0.006 (0.485)	0.007 (0.148) ^b	0.007 (0.507)	0.005 (0.458)
Flexor digitorum profundus	0.022 (0.084)	0.003 (0.329) ^b	0.012 (0.453)	-0.004 (0.351)
Flexor digitorum superficialis	-0.024 (0.014)	0.007 (0.138) ^b	-0.020 (0.038) ^b	-0.007 (0.332)
Median nerve	0.031 (0.002)	0.018 (0.009)	-0.021 (0.019)	0.016 (0.113)

^a Mixed-effects model with time (date) as a continuous variable, adjusted for baseline velocity (mean of three measures) and the transducer, clustered on the patient (no adjustments for multiple comparisons); ^b The random-effect constant could not be reasonably estimated. Significance was unchanged in the sensitivity analyses.

3.6. Association between Baseline SW Velocity and Worse Pain and Stiffness Scores at 6 Months

We then sought to determine whether baseline SW velocity predicted a worsening of pain and stiffness scores from baseline to 6 months (BCPT-MS ($n = 10$ worsening, $n = 4$ non-worsening); WOMAC pain ($n = 5$ worsening, $n = 9$ non-worsening); WOMAC stiffness ($n = 8$ worsening, $n = 6$ non-worsening)). The abductor pollicis longus had significantly faster median (range) SW velocities at baseline in women that had a worse BCPT-MS at 6 months relative to women with a non-worsening score ((5.1 (4.1–8.9) m/s versus 3.8 (2.8–4.5) m/s; $p = 0.024$) and in women with a worse WOMAC stiffness score at 6 months ((5.1 (4.0–8.9) m/s versus 4.2 (2.8–8.4) m/s; $p = 0.043$), both in the long axis on the dominant side. Women that had worsening WOMAC pain scores also had a non-significantly faster median (range) SW velocity in the abductor pollicis longus at baseline relative to women with a non-worsening score ((8.4 (4.3–8.8) m/s versus 4.5 (2.8–8.9) m/s; $p = 0.083$; long axis, dominant side). The only other anatomical site associated with questionnaire scores at 6 months was the flexor digitorum superficialis, which had a significantly faster median SW velocity in women with a worsening WOMAC stiffness score

relative to women with a non-worsening score ((6.7 (4.9–9.1) m/s versus 4.7 (4.1–6.0) m/s; $p = 0.008$ (long axis, dominant side)). There were no other significant differences in SW velocities at baseline for any anatomical sites with regard to worsening pain or stiffness scores at 6 months.

4. Discussion

This study was originally designed to determine whether baseline SW velocities (tendon stiffness) could predict whether or not women taking AI as their adjuvant therapy for breast cancer would develop AIA symptoms. However, our final sample size limited our ability to perform the appropriate statistical models that would allow for prediction of AIA. Despite this setback, our results suggest that increased SW velocity (suggestive of increased stiffness) at baseline in the abductor pollicis longus was associated with a worsening of all three pain and stiffness measures by 6 months. Additionally, an increased velocity in two of six tendons and the median nerve was associated with greater pain at baseline, whereas a slower velocity of the extensor digitorum tendon (suggestive of decreased stiffness) was associated with a greater WOMAC stiffness score. Furthermore, we identified important differences in SW velocity by the image axis and between dominant and non-dominant hands that can inform standardization procedures for SWE image collection in future studies.

At baseline, there were significant differences in SW velocity between dominant and non-dominant sides for four of six tendon sites as well as the median nerve. The greatest difference was observed for the abductor pollicis longus, which had a significantly faster median SW velocity, suggesting stiffer tendons, on the dominant side in the long axis (15.7% difference) than the non-dominant side. The abductor pollicis longus is responsible for facilitating movement and stabilization of the thumb, and the increased velocity in this tendon may be related to high use of the thumb, particularly on the dominant side. The extensor pollicis brevis had a faster median SW velocity on the dominant side than the non-dominant side but in the short axis only (9.1% difference). The flexor digitorum profundus and flexor digitorum superficialis both had significantly slower velocities on the dominant side than the non-dominant side in the short axis only (14.3% and 10.2% slower, respectively). The importance of evaluating these differences in SW velocities by side has been suggested in other studies for different tendons. For example, in athletes with unilateral patellar tendonitis, the more painful side was significantly more stiff than the less painful side (169% difference) and was significantly more stiff than the dominant side patellar tendon of controls (159% difference). However, there was no difference by side within the healthy control group [27]. Siu et al. showed that the Achilles tendon of the nondominant ankle was significantly stiffer in frequent exercisers than in infrequent exercisers, but there was no difference between exercise groups on the dominant side, and there were no within-person differences in stiffness between sides [28]. Coupepe' et al. also observed no difference in SW velocities of the patellar tendon between sides in healthy individuals [29]. A study by Hsiao et al. suggested that aging plays a significant role in the differences in SW velocities of the patellar tendon between sides, with older healthy individuals having a larger difference between sides (10.8% stiffer left side) than younger individuals (6.3% stiffer left side) [30]. Notably, the oldest group in the Hsiao study was on par with the current study. To our knowledge, there are no other studies that directly compare differences in SW velocities between dominant and non-dominant hands in the tendons of the hands and wrists. Whether the percent differences in SW velocities between sides observed in this study represent a clinically meaningful difference for arthralgias is unknown, particularly given that AIA presents bilaterally.

For some tendons (e.g., the Achilles tendon), it has consistently been shown that softer tendons are associated with symptomatic findings; however, the opposite has been observed in the rotator cuff and patellar tendon [19,31]. For the median nerve, faster SW velocities are associated with symptomatic findings, such as carpal tunnel syndrome [18]. Our previous work suggested that women on AI for treatment of their breast cancer that

reported pain in their hands and wrists had stiffer tendons than age-matched healthy women [12]. However, we were unable to determine whether stiffer tendons were a result of AI treatment in our previous study. Therefore, here, we sought to determine whether the degree of tendon stiffness changed with AI treatment or remained constant. To our knowledge, this is the first study to record changes in SW velocities of the tendons of hands and wrists over time in breast cancer patients on AI. There was a significant decrease in SW velocities in the long axis (suggesting tendon softening) for three of six tendons, but there was an increased velocity for one of six tendons in the short axis (suggesting tendon stiffening). There was also an increased SW velocity over 6 months for the median nerve in both the long and short axes but a decrease in the short axis on the non-dominant side. Overall, the magnitude of changes was greater in the dominant hand for all anatomical sites. However, absolute changes in velocity were very small (all < 1%) and may not be clinically relevant. Future studies with age-matched controls followed for an equal time are necessary to determine whether these small changes while on AI treatment over 6 months represent clinically meaningful changes in tendon stiffness or are indeed a result of AI treatment.

Several patients had elevated pain and stiffness at baseline quantified by the WOMAC and BCPT-MS questionnaires, prior to AI treatment. Therefore, we next sought to determine whether tendon stiffness at baseline was associated with these measures. There were two of six tendon sites that were significantly stiffer among patients with a BCPT-MS score > 0, and one of six was stiffer with a WOMAC stiffness score > 0. Interestingly, the median nerve had significantly faster velocities at baseline in both axes on the dominant side in women with a BCPT-MS score > 0. This is consistent with other studies noting a relationship between symptomatic findings and a stiffer median nerve [18]. Notably, at baseline, the median (IQR) questionnaire scores were very low: BCPT-MS, 0.83 (0.67–1.0); WOMAC stiffness, 12.5 (12.5–25). There was one person with a BCPT-MS score > 1.5 at baseline, which other studies have used as a cut-off for the development of AIA [24,32]. Additionally, using WOMAC, there was only one person with severe stiffness at baseline (the same person with BCPT-MS score > 1.5), three with moderate stiffness, and five with mild stiffness. Thus, while some women had symptoms present at baseline, only one person had scores equivalent to what is found with AIA. Future studies with a larger sample size should evaluate SW velocities in relationship to established AIA.

There were 14 patients that had both baseline SWE images and paired baseline to 6-month pain and stiffness questionnaire data. Higher SW velocity in the abductor pollicis longus at baseline was associated with a worsening of all three subscales. While the difference in baseline SW velocity only reached statistical significance for the BCPT-MS and WOMAC stiffness scores, there was a 185% higher SW velocity at baseline among women with higher WOMAC pain scores at 6 months for the abductor pollicis longus. While no other studies have demonstrated a relationship between SWE scores in the abductor pollicis longus and the development of AIA, this finding is consistent with a small study showing symptomatic findings on MRI in the abductor pollicis longus in two women that developed AIA [33]. Similarly, in a case study of a woman with AIA, the abductor pollicis longus showed thickening on US, and a diagnosis of tendinopathy was made [34]. In the current study, the only other tendon for which increased SW velocities at baseline were associated with AIA outcomes at 6 months was the flexor digitorum superficialis. The flexor tendons are supported by the transverse carpal ligament, which has been shown to have increased SW velocities with repetitive hand use prior to the onset of symptoms, such as in pianists [35]. Given that the flexor digitorum superficialis flexes both the middle and proximal phalanges, it may be the first to fail and possibly be representative for the hand. Notably, however, there was no difference at baseline in the flexor digitorum superficialis between symptomatic and asymptomatic patients, as measured by any pain or stiffness questionnaire. A 20-point change in the WOMAC pain and stiffness scores is considered the minimally clinically important difference [36]. Here, six of eight participants with worsening scores reached a 20-point increase on the WOMAC stiffness scale, and three of five participants reached it on the WOMAC pain scale. A larger sample size is needed to

evaluate the relationship between SW velocities and WOMAC pain and stiffness scores in order to determine clinically relevant differences in SW velocities based on these scales. Future studies should confirm whether SW velocities in the abductor pollicis longus predict AIA outcomes in breast cancer patients.

A critical weakness of our study is a small sample size ($n = 16$) with an even smaller paired baseline-to-post-treatment subset for the SWE component ($n = 9$). However, there were 14 patients with paired baseline SWE images and 6-month questionnaire data that allowed for generating hypotheses regarding the use of SWE as a predictive imaging biomarker of AIA, particularly for the abductor pollicis longus tendon. Given the small sample size, all results should be considered hypothesis-generating; many of the observed changes were small and need to be tested in a larger sample size. Despite the small sample size, we were still able to identify important differences between dominant and non-dominant hands in both the long and short axes that could inform image acquisition for future studies. The use of two separate transducers (9–4 MHz and 12 MHz) is also a limitation [37]. It is possible that some of the observed differences were due to the error introduced with a higher-frequency transducer. However, we adjusted for transducer in the analysis, obtained images in triplicate, and used the entire anatomical image—all of which increase confidence in our results. We were also limited in that the majority of women already had musculoskeletal symptoms (BCPT-MS) and stiffness (WOMAC stiffness) at baseline; however, all but one of these were mild to moderate. We initially projected that 50% of our population would develop AIA based on the BCPT-MS score of ≥ 1.5 [24]; however, only four of 14 (29%) participants reached that threshold at 6 months. Future studies should select patients with limited or no musculoskeletal symptoms at baseline or select scales with a wider range to better define the changes with AI treatment by SWE. Nonetheless, our prospective study design, including acquisition of the images in triplicate and use of the entire anatomical image to calculate SWE scores, has strengths which contribute an innovative technique to the literature.

5. Conclusions

In conclusion, we have shown that (1) it is feasible to recruit women with breast cancer not yet experiencing AI symptoms and to collect an SWE measurement at two timepoints, (2) this method of collecting SWE data is reproducible and that capturing SW velocity measurements of each tendon in triplicate is also feasible, (3) study procedures impose a low patient burden, (4) it is important to capture both dominant and non-dominant sides, and (5) we have refined the code to quantify SWE measurements. Furthermore, our results suggest that the abductor pollicis longus tendon could be an important anatomical site to predict AIA in breast cancer patients using US SWE. Given the small sample size, all findings should be considered as hypothesis-generating. Future studies should evaluate SW velocities related to pain and stiffness outcomes in a larger sample size. Future studies should also consider hand dominance and image acquisition along both axes when reporting clinical outcomes.

Author Contributions: Conceptualization, J.A.M. and P.C.; methodology, J.A.M., P.C. and M.S.T.; software, A.A.N.Z.; formal analysis, B.C.W. and D.J.R.; investigation, P.C., A.A.N.Z., M.S.T., S.E., S.J. and J.S.; resources, P.C.; data curation, B.C.W.; writing—original draft preparation, J.A.M.; writing—review and editing, J.A.M., P.C., M.S.T., B.C.W., A.A.N.Z., S.E. and S.J.; visualization, J.A.M., B.C.W. and A.A.N.Z.; supervision, J.A.M., P.C. and M.S.T.; project administration, J.A.M. and P.C.; funding acquisition, J.A.M. and P.C. All authors have read and agreed to the published version of the manuscript.

Funding: This research was funded by The University of Arizona Cancer Center, Clinical Research Oversight Counsel (CROC) grant.

Institutional Review Board Statement: The study was conducted according to the guidelines of the Declaration of Helsinki, and it was approved by the Institutional Review Board (or Ethics Committee) of The University of Arizona (protocol code: 1712078374A010, approved on 2 December 2020).

Informed Consent Statement: Informed consent was obtained from all subjects involved in the study.

Data Availability Statement: The data presented in this study are available on request from the corresponding author. The data are not publicly available due to containing information that could compromise the privacy of research participants.

Acknowledgments: The authors would like to thank Tracy L. Sheldon for the acquisition of the ultrasound images.

Conflicts of Interest: The authors declare no conflict of interest.

References

1. Park, S.-H.; Knobf, M.T.; Sutton, K.M. Etiology, Assessment, and Management of Aromatase Inhibitor-Related Musculoskeletal Symptoms. *Clin. J. Oncol. Nurs.* **2012**, *16*, 260–266. [[CrossRef](#)] [[PubMed](#)]
2. Sestak, I.; Sapunar, F.; Cuzick, J. Aromatase Inhibitor–Induced Carpal Tunnel Syndrome: Results From the ATAC Trial. *J. Clin. Oncol.* **2009**, *27*, 4961–4965. [[CrossRef](#)] [[PubMed](#)]
3. Spagnolo, F.; Sestak, I.; Howell, A.; Forbes, J.F.; Cuzick, J. Anastrozole-Induced Carpal Tunnel Syndrome: Results From the International Breast Cancer Intervention Study II Prevention Trial. *J. Clin. Oncol.* **2016**, *34*, 139–143. [[CrossRef](#)] [[PubMed](#)]
4. Dizdar, O.; Özçakar, L.; Malas, F.Ü.; Harputluoglu, H.; Bulut, N.; Aksoy, S.; Ozisik, Y.; Altundag, K. Sonographic and Electrodiagnostic Evaluations in Patients with Aromatase Inhibitor–Related Arthralgia. *J. Clin. Oncol.* **2009**, *27*, 4955–4960. [[CrossRef](#)] [[PubMed](#)]
5. Morales, L.; Pans, S.; Verschuere, K.; Van Calster, B.; Paridaens, R.; Westhovens, R.; Timmerman, D.; De Smet, L.; Vergote, I.; Christiaens, M.-R.; et al. Prospective Study to Assess Short-Term Intra-Articular and Tenosynovial Changes in the Aromatase Inhibitor–Associated Arthralgia Syndrome. *J. Clin. Oncol.* **2008**, *26*, 3147–3152. [[CrossRef](#)]
6. Presant, C.A.; Bosserman, L.; Young, T.; Vakil, M.; Horns, R.; Upadhyaya, G.; Ebrahimi, B.; Yeon, C.; Howard, F. Aromatase Inhibitor–Associated Arthralgia and/or Bone Pain: Frequency and Characterization in Non–Clinical Trial Patients. *Clin. Breast Cancer* **2007**, *7*, 775–778. [[CrossRef](#)]
7. Gaillard, S.; Stearns, V. Aromatase inhibitor-associated bone and musculoskeletal effects: New evidence defining etiology and strategies for management. *Breast Cancer Res.* **2011**, *13*, 205. [[CrossRef](#)]
8. Henry, N.L.; Giles, J.T.; Ang, D.; Mohan, M.; Dadabhoy, D.; Robarge, J.; Hayden, J.; Lemler, S.; Shahverdi, K.; Powers, P.; et al. Prospective characterization of musculoskeletal symptoms in early stage breast cancer patients treated with aromatase inhibitors. *Breast Cancer Res. Treat.* **2007**, *111*, 365–372. [[CrossRef](#)]
9. Howell, A. Results of the ATAC (Arimidex, Tamoxifen, Alone or in Combination) trial after completion of 5 years’ adjuvant treatment for breast cancer. *Lancet* **2005**, *365*, 60–62. [[CrossRef](#)]
10. Castel, L.D.; Hartmann, K.E.; Mayer, I.A.; Saville, B.R.; Alvarez, J.; Boomershire, C.S.; Abramson, V.G.; Chakravarthy, A.B.; Friedman, D.L.; Cella, D.F. Time course of arthralgia among women initiating aromatase inhibitor therapy and a postmenopausal comparison group in a prospective cohort. *Cancer* **2013**, *119*, 2375–2382. [[CrossRef](#)]
11. Goss, P.E.; Ingle, J.N.; Pritchard, K.I.; Robert, N.J.; Muss, H.; Gralow, J.; Gelmon, K.; Whelan, T.; Strasser-Weippl, K.; Rubin, S.; et al. Extending Aromatase-Inhibitor Adjuvant Therapy to 10 Years. *N. Engl. J. Med.* **2016**, *375*, 209–219. [[CrossRef](#)] [[PubMed](#)]
12. Martinez, J.A.; Taljanovic, M.S.; Witte, R.S.; Zuniga, A.A.N.; Wertheim, B.C.; Kwok, C.K.; Goldstein, B.A.; Roe, D.J.; Chalasani, P. Shear wave elastography detects novel imaging biomarkers of aromatase inhibitor–induced joint pain: A pilot study. *J. Ultrason.* **2021**, *21*, e1–e6. [[CrossRef](#)] [[PubMed](#)]
13. Shanmugam, V.K.; McCloskey, J.; Elston, B.; Allison, S.J.; Eng-Wong, J. The CIRAS study: A case control study to define the clinical, immunologic, and radiographic features of aromatase inhibitor-induced musculoskeletal symptoms. *Breast Cancer Res. Treat.* **2011**, *131*, 699–708. [[CrossRef](#)]
14. Henry, N.L.; Jacobson, J.; Banerjee, M.; Hayden, J.; Smerage, J.B.; Van Poznak, C.; Storniolo, A.M.; Stearns, V.; Hayes, D.F. A prospective study of aromatase inhibitor-associated musculoskeletal symptoms and abnormalities on serial high-resolution wrist ultrasonography. *Cancer* **2010**, *116*, 4360–4367. [[CrossRef](#)] [[PubMed](#)]
15. Sarvazyan, A.P.; Rudenko, O.; Swanson, S.D.; Fowlkes, J.; Emelianov, S. Shear wave elasticity imaging: A new ultrasonic technology of medical diagnostics. *Ultrasound Med. Biol.* **1998**, *24*, 1419–1435. [[CrossRef](#)]
16. Taljanovic, M.S.; Gimber, L.H.; Becker, G.W.; Latt, L.D.; Klausner, A.S.; Melville, D.M.; Gao, L.; Witte, R.S. Shear-Wave Elastography: Basic Physics and Musculoskeletal Applications. *RadioGraphics* **2017**, *37*, 855–870. [[CrossRef](#)] [[PubMed](#)]
17. Turkey, R.; Inci, E.; Aydeniz, B.; Vural, M. Shear wave elastography findings of de Quervain tenosynovitis. *Eur. J. Radiol.* **2017**, *95*, 192–196. [[CrossRef](#)]
18. Giambini, H.; An, K.-N. Ultrasound Elastography for Hand Soft Tissue Assessment. *Hand Clin.* **2021**, *38*, 119–128. [[CrossRef](#)]
19. Breda, S.J.; Van Der Vliet, A.; De Vos, R.-J.; Krestin, G.P.; Oei, E.H.G. The association between patellar tendon stiffness measured with shear-wave elastography and patellar tendinopathy—A case-control study. *Eur. Radiol.* **2020**, *30*, 5942–5951. [[CrossRef](#)]
20. Hou, S.W.; Merkle, A.N.; Babb, J.; McCabe, R.; Gyftopoulos, S.; Adler, R.S. Shear Wave Ultrasound Elastographic Evaluation of the Rotator Cuff Tendon. *J. Ultrason. Med.* **2016**, *36*, 95–106. [[CrossRef](#)]

21. Pan, W.; Zhou, J.; Lin, Y.; Zhang, Z.; Wang, Y. Elasticity of the Achilles Tendon in Individuals with and without Plantar Fasciitis: A Shear Wave Elastography Study. *Front. Physiol.* **2021**, *12*, 686631. [[CrossRef](#)] [[PubMed](#)]
22. Alfuraih, A.M.; Tan, A.L.; O'Connor, P.; Emery, P.; Wakefield, R.J. Muscle stiffness in rheumatoid arthritis is not altered or associated with muscle weakness: A shear wave elastography study. *Mod. Rheumatol.* **2020**, *30*, 617–625. [[CrossRef](#)] [[PubMed](#)]
23. Stanton, A.L.; Bernaards, C.A.; Ganz, P.A. The BCPT Symptom Scales: A Measure of Physical Symptoms for Women Diagnosed with or at Risk for Breast Cancer. *J. Natl. Cancer Inst.* **2005**, *97*, 448–456. [[CrossRef](#)] [[PubMed](#)]
24. Swenson, K.K.; Nissen, M.J.; Henly, S.; Maybon, L.; Pupkes, J.; Zwicky, K.; Tsai, M.L.; Shapiro, A.C. Identification of Tools to Measure Changes in Musculoskeletal Symptoms and Physical Functioning in Women with Breast Cancer Receiving Aromatase Inhibitors. *Oncol. Nurs. Forum* **2013**, *40*, 549–557. [[CrossRef](#)] [[PubMed](#)]
25. Bellamy, N.; Buchanan, W.W.; Goldsmith, C.H.; Campbell, J.; Stitt, L.W. Validation study of WOMAC: A health status instrument for measuring clinically important patient relevant outcomes to antirheumatic drug therapy in patients with osteoarthritis of the hip or knee. *J. Rheumatol.* **1988**, *15*, 1833–1840.
26. Chen, L.; Lin, C.-C.; Huang, T.-W.; Kuan, Y.-C.; Huang, Y.-H.; Chen, H.-C.; Kao, C.-Y.; Su, C.-M.; Tam, K.-W. Effect of acupuncture on aromatase inhibitor-induced arthralgia in patients with breast cancer: A meta-analysis of randomized controlled trials. *Breast* **2017**, *33*, 132–138. [[CrossRef](#)]
27. Zhang, Z.J.; Ng, G.Y.-F.; Lee, W.C.; Fu, A. Changes in Morphological and Elastic Properties of Patellar Tendon in Athletes with Unilateral Patellar Tendinopathy and Their Relationships with Pain and Functional Disability. *PLoS ONE* **2014**, *9*, e108337. [[CrossRef](#)]
28. Siu, W.-L.; Chan, C.-H.; Lam, C.-H.; Lee, C.-M.; Ying, M. Sonographic evaluation of the effect of long-term exercise on Achilles tendon stiffness using shear wave elastography. *J. Sci. Med. Sport* **2016**, *19*, 883–887. [[CrossRef](#)]
29. Couppe, C.; Kongsgaard, M.; Aagaard, P.; Hansen, P.; Bojsen-Moller, J.; Kjaer, M.; Magnusson, S.P. Habitual loading results in tendon hypertrophy and increased stiffness of the human patellar tendon. *J. Appl. Physiol.* **2008**, *105*, 805–810. [[CrossRef](#)]
30. Hsiao, M.-Y.; Chen, Y.-C.; Lin, C.-Y.; Chen, W.-S.; Wang, T.-G. Reduced Patellar Tendon Elasticity with Aging: In Vivo Assessment by Shear Wave Elastography. *Ultrasound Med. Biol.* **2015**, *41*, 2899–2905. [[CrossRef](#)]
31. Washburn, N.; Onishi, K.; Wang, J.H.-C. Ultrasound elastography and ultrasound tissue characterisation for tendon evaluation. *J. Orthop. Transl.* **2018**, *15*, 9–20. [[CrossRef](#)] [[PubMed](#)]
32. Shapiro, A.C.; Adlis, S.A.; Robien, K.; Kirstein, M.N.; Liang, S.; Richter, S.A.; Lerner, R.E. Randomized, blinded trial of vitamin D3 for treating aromatase inhibitor-associated musculoskeletal symptoms (AIMSS). *Breast Cancer Res. Treat.* **2016**, *155*, 501–512. [[CrossRef](#)] [[PubMed](#)]
33. Singer, O.; Cigler, T.; Moore, A.B.; Levine, A.B.; Hentel, K.; Belfi, L.; Do, H.T.; Mandl, L.A. Defining the aromatase inhibitor musculoskeletal syndrome: A prospective study. *Arthritis Care Res.* **2012**, *64*, 1910–1918. [[CrossRef](#)] [[PubMed](#)]
34. Martens, H.A.; Schroder, C.P.; van der Eerden, P.J.M.; Willemsse, P.H.B.; Posthumus, M.D. Severe disabling tendinopathy caused by anastrozole. *Rheumatology* **2007**, *46*, 1619–1621. [[CrossRef](#)]
35. Mhanna, C.; Marquardt, T.L.; Li, Z.-M. Adaptation of the Transverse Carpal Ligament Associated with Repetitive Hand Use in Pianists. *PLoS ONE* **2016**, *11*, e0150174. [[CrossRef](#)]
36. Tubach, F.; Ravaud, P.; Beaton, D.; Boers, M.; Bombardier, C.; Felson, D.T.; Van Der Heijde, D.; Wells, G.; Dougados, M. Minimal clinically important improvement and patient acceptable symptom state for subjective outcome measures in rheumatic disorders. *J. Rheumatol.* **2007**, *34*, 1188–1193.
37. O'Hara, S.; Zelesco, M.; Rocke, K.; Stevenson, G.; Sun, Z. Reliability Indicators for 2-Dimensional Shear Wave Elastography. *J. Ultrasound Med.* **2019**, *38*, 3065–3071. [[CrossRef](#)]



Article

Ankle Magnetic Resonance Imaging in Juvenile Idiopathic Arthritis Versus Non-Juvenile Idiopathic Arthritis Patients with Arthralgia

Monika Ostrowska ¹, Emil Michalski ^{1,*}, Piotr Gietka ², Małgorzata Mańczak ³, Magdalena Posadzy ⁴
and Iwona Sudot-Szopińska ¹

- ¹ Department of Radiology, National Institute of Geriatrics, Rheumatology and Rehabilitation, 02-637 Warsaw, Poland; monique.ostrowska@gmail.com (M.O.); sudolszopinska@gmail.com (I.S.-S.)
² Clinic of Pediatric Rheumatology, National Institute of Geriatrics, Rheumatology and Rehabilitation, 02-637 Warsaw, Poland; malgietka1@gmail.com
³ Department of Gerontology, Public Health and Didactics, National Institute of Geriatrics, Rheumatology and Rehabilitation, 02-637 Warsaw, Poland; m.manczak@op.pl
⁴ Indywidualna Praktyka Lekarska, Magdalena Posadzy, 61-426 Poznań, Poland; magdalenaposadzy@gmail.com
* Correspondence: emil.michalski.md@gmail.com; Tel.: +48-226-709192

Abstract: This retrospective case–control study aimed to evaluate whether Magnetic Resonance Imaging (MRI) enables differentiation of ankle arthritis in Juvenile Idiopathic Arthritis (JIA) from ankle arthralgia of unknown aetiology in patients clinically suspected of JIA. Forty-four children, at ages 5–16, who underwent MRI of the ankle from January 2016 to March 2021 for clinically suspected active ankle arthritis in the course of JIA were included. MRI findings in both groups—patients with the final diagnosis of JIA and without final diagnosis of JIA—were compared and scored. The sum of the scores of 22 ankle lesions in an individual patient (active, destructive and developmental), so-called the MRI summarized score, was calculated and tested in terms of the most optimal diagnosis of JIA. Interobserver agreement was calculated. Inflammatory features were seen on MRI in 38 out of all the included patients (86%). The most common lesions in both groups were effusion in the tibio-talar joint (68% in JIA and 64% in the arthralgia group) and effusion in subtalar joint (64% in JIA vs. 59% in the arthralgia group). In general, more lesions were identified in the JIA group than in non-JIA. However, only tenosynovitis was significantly more common in the JIA vs. non-JIA group ($p = 0.031$). The MRI summarized score did not allow for discrimination between ankle arthritis in JIA from non-JIA patients; the best levels of sensitivity (32%), specificity (91%), positive predictive value PPV (78%) and negative predictive value NPV (57%) were achieved only at the cut-off point of 10.

Keywords: juvenile idiopathic arthritis; ankle arthritis; magnetic resonance imaging; scoring

Citation: Ostrowska, M.; Michalski, E.; Gietka, P.; Mańczak, M.; Posadzy, M.; Sudot-Szopińska, I. Ankle Magnetic Resonance Imaging in Juvenile Idiopathic Arthritis Versus Non-Juvenile Idiopathic Arthritis Patients with Arthralgia. *J. Clin. Med.* **2022**, *11*, 760. <https://doi.org/10.3390/jcm11030760>

Academic Editor: François Jamar

Received: 23 November 2021

Accepted: 28 January 2022

Published: 30 January 2022

Publisher's Note: MDPI stays neutral with regard to jurisdictional claims in published maps and institutional affiliations.



Copyright: © 2022 by the authors. Licensee MDPI, Basel, Switzerland. This article is an open access article distributed under the terms and conditions of the Creative Commons Attribution (CC BY) license (<https://creativecommons.org/licenses/by/4.0/>).

1. Introduction

Juvenile idiopathic arthritis (JIA) is a heterogeneous group of chronic nonpyogenic inflammatory arthritides with persistent symptoms for at least 6 weeks that are present before the child is 16 years old [1–4]. It is the most common form of childhood arthritis [5–7]. In certain JIA subtypes, the disease is rapidly progressive, and if diagnosed with a delay and left untreated, may lead to structural damage and permanent impairment of physical function [8].

Joint damage in JIA results from synovitis with formation of pannus, which, in the so-called outside-in mechanism, destroys cartilage and bone, leading to subchondral erosions, inflammatory cysts, and ankylosis [6]. A similar inflammatory process, osteitis, starts within the subchondral bone marrow and, through the inside-out mechanism, first leads to subchondral cysts formation, with further evolution to erosions and hyaline cartilage damage [9–11]. Another location of disease, typical for the juvenile enthesitis-related arthritis (ERA) subtype of JIA, are tendons, ligaments, and capsule entheses with

inflammation (enthesitis) may lead to bone reaction with the formation of cysts and erosions and peri-enthesal soft tissue involvement [12]. Active inflammation may also concern tendons' sheaths; tenosynovitis may lead to secondary tendinitis with possible tendon tears. Lastly, inflammation of the intra- or extraarticular fat tissue is recognized as another important pathogenetic factor in rheumatology [13]. Early detection of all disease locations is important to assess the advancement of disease with disease progression and to adapt appropriate treatment [14].

After the knee, the ankle and foot are the joints most commonly affected by JIA [4,15]. Clinical symptoms most frequently include arthralgia, and/or joint edema, and/or tenderness. Differentiation between JIA-related and non-JIA pathologies remains challenging, since there are no specific clinical or laboratory findings enabling differentiation between JIA and traumatic, overused lesions, or septic, reactive, post-infectious, or even malignant lesions affecting the ankle or foot [16].

Magnetic Resonance Imaging (MRI) is considered to be the most sensitive imaging tool for the detection of synovitis as well as for the detection of cartilage lesions, bone erosions, and bone marrow pathologies [17–21]. Despite high sensitivity, the specificity of MRI findings remains problematic, since a number of other pathologies follow MRI patterns similar to JIA. The most common pathologies in JIA are thought to be effusions and synovitis. Most accurately joint effusions and synovitis are distinguished on postcontrast MRI images using gadolinium injection [1,22]. Since there is no evidence to date that gadolinium accumulation in the brain and kidneys is harmful to the human body [23,24], with hypothetical cumulative and long term effects of retained gadolinium, it warrants special attention while making decisions when performing contrast examination in children and young adults [25], and indicates the need to investigate the non-contrast MRI to assess inflammation in the pediatric population [23,24].

As it is often difficult to differentiate fluid and synovitis by MRI without intravenous administration of contrast, the term “effusion/synovial thickening” was introduced where these two inflammatory features are considered all together as a single item [25]. Other active inflammatory lesions that may be seen in children with JIA include osteitis, bursitis, enthesitis, myositis, and panniculitis. Destructive inflammatory lesions developing in the course of JIA include cysts, erosions, joint space narrowing, chondromalacia, ankylosis, and secondary osteoarthritis. Joint inflammation overlapping natural bone growth in juveniles may lead to growth disturbances and developmental disorders [9,10,15].

So far, there are only single papers describing active and destructive inflammatory lesions in the ankle in JIA, and they focus on primary findings [8,26]. This study aimed to evaluate the full spectrum of possible JIA-related pathologies in MRI, including active, destructive, and developmental lesions, and to test if MRI allows ankle arthritis in JIA to be differentiated from ankle arthralgia of unknown aetiology. It was hypothesized that non-contrast MRI of the ankle can differentiate between these two groups of patients.

2. Patients and Methods

2.1. Patients

This retrospective single-center study included 44 children aged 5–16 with clinically suspected active ankle arthritis who underwent MRI of the ankle from January 2016 to March 2021. For patients who underwent multiple ankle MRIs, only the first exam was included. Both MRI and clinical evaluations were performed in the authors' referential center for pediatric rheumatology.

On clinical evaluation children presented with ankle pain, swelling, tenderness, and/or limitation of movement associated with pain persisting more than 6 weeks [27].

Children with diagnoses other than inflammatory arthritis (e.g., tumour, trauma, septic arthritis, osteomyelitis, including chronic recurrent multifocal osteomyelitis), as well as children with the history of intraarticular corticosteroid injection or radionuclide synovectomy performed within the last six months were excluded.

The clinical data were collected, including demographic information concerning age and sex and the final diagnosis.

Parents or legal guardians of all patients gave informed consent to take part in the study. The study was performed in accordance with the Declaration of Helsinki and was approved by the local ethics committee (KBT-3/5/2018).

2.2. MRI Protocol and Interpretation of Imaging Features

MRI of the ankle was performed on a 1.5 Tesla system (Siemens Avanto) in a dedicated 8 channels coil. Patients were examined in a supine position. No sedation was used. Intravenous contrast agent was not used. The following sequences and planes were applied: T2-weighted (w), PD (Proton Density) and PD-w with fat saturation (FS) in axial plane, PD FS and T1-w in sagittal plane, and T2 TIRM (Turbo Inversion Recovery Magnitude) and PD-w in coronal plane. Sequences, planes of imaging, slice thickness, and the remaining technical information regarding the MRI examination are shown in Table 1.

Table 1. MRI acquisitions for ankle examination.

	Plane	TR	TE	ST (mm)	Gap (mm)	FoV (mm)	Matrix
Localiser	All	8.2	3.51	6.0	6.0	250 × 250	192 × 256
T2	Tra	7230	71	3.0	0.6	150 × 150	224 × 320
PD	Tra	2800	33	3.0	0.6	150 × 150	272 × 320
PD FS	Tra	2800	33	3.0	0.6	150 × 150	272 × 320
PD FS	Sag	2900	32	3.0	0.6	170 × 170	288 × 384
T1	Sag	666	11	3.0	0.6	170 × 170	240 × 320
T2 TIRM	Cor	4060	74	3.0	0.6	150 × 150	218 × 256
PD	Cor	3020	33	3.0	0.6	150 × 150	272 × 320

Cor, coronal; FOV, field of view; FS, fat saturation; Sag, sagittal; ST, slice thickness; TE, echo time; TR, repetition time; Tra-transverse; w, weighted.

The range of examination in all sequences covered the area from the tibiotalar joint to the metatarso-phalangeal (MTP) joints.

The following joints were covered: tibiotalar, subtalar, talonavicular, calcaneocuboid, “cuneocuboid joint”, naviculocuneiform (3 articulations), tarsometatarsal (Lisfranc joint; 5 articulations), and MTP joints. Bone marrow edema was assessed in the distal end of tibia and fibula, in talus, calcaneus, naviculare, medial, intermedium, and the lateral cuneiforms, cuboideum, proximal ends of the metatarsal bones 1–5.

The evaluated tendons included: tibialis anterior, extensor digitorum longus, extensor hallucis longus, tibialis posterior, flexor hallucis longus, flexor digitorum longus, peroneus longus, and peroneus brevis.

Out of all distal entheses, the entheses of the long extensors and long flexors of toes and halluces, and the forefoot in general, were not evaluated according to the study protocol for the ankle joint.

Entheses of the interosseous ligaments at the level of the ankle and midfoot and hindfoot entheses of the Achilles tendon and plantar fascia were included.

Two hindfoot bursae of the Achilles tendon and subcutaneous bursa of the heel were assessed.

Images were evaluated with the aim of identifying and scoring active, destructive, inflammatory lesions, as well as developmental lesions of the ankle and midfoot joint, listed in Table 2. MRI definitions for active and chronic inflammatory lesions were based on the Panwar et al. [25] and on the Arthritis Subcommittee of the European Society of Musculoskeletal Radiology (ESSR) recommendations [28].

Table 2. MRI scoring system for ankle joint arthritis.

	Inflammatory Features	Scoring
1	Effusion/synovial thickening	0: no intraarticular fluid 1: trace of fluid not distending the joint capsule/physiologic 2: mild: increased amount of fluid/synovial thickening mildly distending joint capsule 3: moderate to severe: increased amount of fluid/synovial thickening moderately to severely distending joint capsule
2	Bone marrow edema * #	0: no BME 1: discrete patchy BME 2: focal BME 3: diffuse BME
3	Tenosynovitis	0: no tenosynovitis 1: tenosynovitis 2: tenosynovitis with secondary tendinitis
4	Enthesitis of the tendons, plantar fascia, ligaments	0: no enthesitis 1: enthesitis—at least one of the entheses' inflammatory features is present: high signal and/or thickening of the enthesis and/or perientheseal soft tissue inflammation and/or BME in the bony part of the enthesis
5	Bursitis	0–1
6	Myositis	0–1
7	Juxtaarticular soft tissue inflammation	0–1
8	Kager's fat pad involvement	0–1
9	Fat tissue in tarsal tunnel involvement	0–1
10	Fat tissue in sinus tarsi involvement	0–1
11	Bone erosions	0–1
12	Cysts	0–1
13	Chondromalacia	0–1
14	Joint space narrowing	0–1
15	Physis involvement	0–1
16	Ankylosis	0–1
17	Osteophytes	0–1
18	Sclerotization	0–1
19	Avascular necrosis	0–1
22	Developmental disorders	0–1

* Bone area pertaining to Achilles and plantar fascia attachment belongs to the enthesitis domain; BME in physis pertain to physis involvement domain. # In case of different stages of BME seen in a given bone, the highest score is applied.

The term “effusion/synovial thickening” was introduced by Panwar et al. [25], defined as “an increased amount (greater than physiologic) of high signal intensity within the joint space distending the joint capsule on fluid sensitive sequences”. Bone marrow edema (BME) is of high signal on T2-w and PD-w images, and is best visualized by T2 FS or STIR/TIRM sequences, hypointense on T1w images [28]. Enthesis is hyperintense on T2 and PDw images, best visualized by T2 FS or STIR/TIRM sequences, and is hypointense

on T1w images. The bony part of an enthesis may show BME [28]. Bone erosions are sharply margined trabecular bone defects with disrupted cortical bone continuity, seen in at least two planes, with low signal intensity on T1-w images. When active (filled with active synovitis) they are of low signal on T1-w and high signal intensity on fluid sensitive sequences. Intraosseous cysts present as high signal intensity foci on T2-w images and low signal intensity on T1-w images, and they are better delineated compared with ill-defined areas of BME [28].

Remaining destructive lesions included: joint space narrowing, ankylosis, osteophytes, sclerotization, and avascular necrosis (AVN).

Developmental disorders included: bone remodeling, premature closure of physis, coalition, accessory bone, and Stieda process.

The images were independently evaluated and scored by two radiologists, both with 15 years of experience in MSK imaging (10 years in the rheumatological center), blinded to clinical and laboratory data.

All lesions in each ankle were scored in a binary way (0–1) except for effusions/synovial thickening and BME (scores 0–3) and tenosynovitis (scores 0–2). Final MRI diagnosis and the scorings for JIA-confirmed patients vs. patients without final diagnosis of JIA were established as a consensus. Results are included in Table 3.

Table 3. MRI results in JIA vs. non-JIA group.

	MRI Lesions and Scorings	JIA Confirmed Group <i>n</i> = 22	Non-JIA Group <i>n</i> = 22	<i>p</i>
1	Effusion/Synovial thickening tibio-talar joint			
	0	7 (32%)	8 (36%)	0.352
	1	9 (41%)	11 (50%)	
	2	3 (14%)	3 (14%)	
	3	3 (14%)	0 (0%)	
2	Effusion/Synovial thickening subtalar joint			
2	0	8 (36%)	9 (41%)	0.490
	1	7 (32%)	9 (41%)	
	2	5 (23%)	4 (18%)	
	3	2 (9%)	0 (0%)	
	3	BME tibia		
3	0	16 (73%)	19 (86%)	0.415
	1	5 (23%)	3 (14%)	
	2	1 (5%)	0 (0%)	
	3	0 (0%)	0 (0%)	
	4	BME fibula		
4	0	17 (77%)	20 (91%)	0.385
	1	4 (18%)	2 (9%)	
	2	1 (5%)	0 (0%)	
	3	0 (0%)	0 (0%)	

Table 3. Cont.

	MRI Lesions and Scorings	JIA Confirmed Group n = 22	Non-JIA Group n = 22	p
5	BME calcaneus/subtalar joint			
	0	15 (68%)	17 (77%)	0.547
	1	5 (23%)	5 (23%)	
	2	1 (5%)	0 (0%)	
3	1 (5%)	0 (0%)		
6	BME talus			
	0	15 (68%)	18 (82%)	0.433
	1	6 (27%)	4 (18%)	
	2	1 (5%)	0 (0%)	
3	0 (0%)	0 (0%)		
7	BME naviculare			
	0	16 (73%)	18 (82%)	0.347
	1	4 (18%)	4 (18%)	
	2	2 (9%)	0 (0%)	
3	0 (0%)	0 (0%)		
8	BME cuboideum			
	0	18 (82%)	17 (77%)	0.191
	1	2 (9%)	5 (23%)	
	2	2 (9%)	0 (0%)	
3	0 (0%)	0 (0%)		
9	BME cuneiform medial			
	0	18 (82%)	18 (82%)	0.565
	1	3 (14%)	4 (18%)	
	2	1 (5%)	0 (0%)	
3	0 (0%)	0 (0%)		
10	BME cuneiform intermedium			
	0	18 (82%)	18 (82%)	0.565
	1	3 (14%)	4 (18%)	
	2	1 (5%)	0 (0%)	
3	0 (0%)	0 (0%)		
11	BME cuneiform lateral			
	0	20 (91%)	18 (82%)	0.234
	1	1 (5%)	4 (18%)	
	2	1 (5%)	0 (0%)	
3	0 (0%)	0 (0%)		
12	BME base of MET1			
	0	20 (91%)	20 (91%)	0.513
	1	1 (5%)	2 (9%)	
	2	1 (5%)	0 (0%)	
3	0 (0%)	0 (0%)		

Table 3. Cont.

	MRI Lesions and Scorings	JIA Confirmed Group n = 22	Non-JIA Group n = 22	p
13	BME MET2			
	0	21 (95%)	21 (95%)	0.368
	1	0 (0%)	1 (5%)	
	2	1 (5%)	0 (0%)	
3	0 (0%)	0 (0%)		
14	BME MET3			
	0	21 (95%)	21 (95%)	0.368
	1	0 (0%)	1 (5%)	
	2	1 (5%)	0 (0%)	
3	0 (0%)	0 (0%)		
15	BME MET4			
	0	21 (95%)	21 (95%)	0.368
	1	0 (0%)	1 (5%)	
	2	1 (5%)	0 (0%)	
3	0 (0%)	0 (0%)		
16	BME MET5			
	0	21 (95%)	21 (95%)	0.368
	1	0 (0%)	1 (5%)	
	2	1 (5%)	0 (0%)	
3	0 (0%)	0 (0%)		
17	Enthesitis			
	0	21 (95%)	22 (100%)	0.660
1	1 (5%)	0		
18	Tenosynovitis			
	0	16 (73%)	22 (100%)	0.031
	1	4 (18%)	0 (0%)	
2	2 (9%)	0 (0%)		
19	Kager's fat pad inflammations			
	0	20 (91%)	22 (100%)	1
1	2 (10%)	0 (0%)		
20	Fat tissue inflammation in tarsal tunnel			
	0	21 (95%)	22 (100%)	1
1	1 (5%)	0 (0%)		
21	Fat tissue inflammation in sinus tarsi			
	0	21 (95%)	22 (100%)	1
1	1 (5%)	0 (0%)		
22	Juxtaarticular soft tissue inflammation			
	0	21 (95%)	22 (100%)	1
1	1 (5%)	0 (0%)		

Table 3. Cont.

	MRI Lesions and Scorings	JIA Confirmed Group n = 22	Non-JIA Group n = 22	p
24	Bursitis			0.469
	0	20 (91%)	22 (100%)	
	1	2 (9%)	0 (0%)	
25	Myositis			1
	0	22 (100%)	22 (100%)	
	1	0 (0%)	0 (0%)	
26	Cyst			1
	0	21 (95%)	22 (100%)	
	1	1 (5%)	0 (0%)	
27	Bone erosion			0.469
	0	20 (91%)	22 (100%)	
	1	2 (9%)	0 (0%)	
28	Chondromalacia			0.469
	0	20 (91%)	22 (100%)	
	1	2 (9%)	0 (0%)	
29	Joints space narrowing			0.469
	0	20 (91%)	22 (100%)	
	1	2 (9%)	0 (0%)	
30	Physis involvement			1
	0	22 (100%)	22 (100%)	
	1	0 (0%)	0 (0%)	
31	Ankylosis			1
	0	21 (95%)	22 (100%)	
	1	1 (5%)	0 (0%)	
32	Osteophytes			0.469
	0	20 (91%)	22 (100%)	
	1	2 (9%)	0 (0%)	
33	Sclerotization			1
	0	21 (95%)	22 (100%)	
	1	1 (5%)	0 (0%)	
34	AVN/OCD			1
	0	21 (95%)	22 (100%)	
	1	1 (5%)	0 (0%)	
35	Developmental lesions			0.410
	0	20 (91%)	17 (77%)	
	1	2 (9%)	5 (23%)	

In addition, the MRI summarized score was calculated as the sum of scores of all 22 ankle and foot lesions in an individual patient to test which value provides the most optimal diagnosis in terms of high sensitivity, specificity, and positive and negative predictive values. The results are presented in Table 4.

Table 4. Diagnostic value of the summarized MRI score as a predictor of JIA.

MRI Score	JIA	Non JIA	True Pos.	False Pos.	False Neg.	True Neg.	Sensitivity	Specificity	PPV	NPV
36	1	0	1	0	21	22	0.045	1.000	1.000	0.512
21	1	0	2	0	20	22	0.091	1.000	1.000	0.524
17	1	0	3	0	19	22	0.136	1.000	1.000	0.537
16	0	1	3	1	19	21	0.136	0.955	0.750	0.525
14	1	0	4	1	18	21	0.182	0.955	0.800	0.538
13	0	1	4	2	18	20	0.182	0.909	0.667	0.526
11	2	0	6	2	16	20	0.273	0.909	0.750	0.556
10	1	0	7	2	15	20	0.318	0.909	0.778	0.571
9	0	1	7	3	15	19	0.318	0.864	0.700	0.559
7	0	1	7	4	15	18	0.318	0.818	0.636	0.545
6	0	1	7	5	15	17	0.318	0.773	0.583	0.531
4	2	3	9	8	13	14	0.409	0.636	0.529	0.519
3	1	1	10	9	12	13	0.455	0.591	0.526	0.520
2	6	5	16	14	6	8	0.727	0.364	0.533	0.571
1	4	4	20	18	2	4	0.909	0.182	0.526	0.667
0	2	4	22	22	0	0	1.000	0.000	0.500	

Pos.—positive, neg.—negative.

2.3. Statistical Analysis

The MRI lesions are presented as numbers and percentages. The chi-squared test and a chi-squared test with Yates’ correction were used. The receiver operating characteristic (ROC) curve analysis was used to verify the discriminant ability of the MRI summarized score. The sensitivity, specificity, positive predictive value (PPV), and negative predictive value (NPV) of the created MRI score were calculated. The level of statistical significance was set at $p < 0.05$. Statistical analyses were performed with Statistica v. 13.1 (Dell Inc. 2016, Tulsa, OK, USA). Interobserver agreement was calculated using Cohen’s kappa coefficient. Kappa values below 0.20 were considered poor agreement, 0.21–0.40 fair, 0.41–0.60 moderate, 0.61–0.80 good, and 0.81–1.00 very good [29]. The final score was established by consensus.

3. Results

This study included 44 children with clinically suspected ankle arthritis in whom MRI of ankles and feet were performed between January 2017 and March 2021. The mean age of patients was 12.7 (range: 5–17) with female predominance (35 girls and 9 boys).

Out of 44 included patients, JIA was confirmed in 22 patients (50%) including 14 with oligoarthritis, 6 with undifferentiated JIA, 1 patient with systemic JIA, and 1 patient with the ERA subtype. In the remaining 22 (50%) patients, JIA was excluded.

The mean age of patients in the JIA group was 12.4 years (SD: 3.5); in the non-JIA group, the mean age was 12.9 (SD:2.5), and the difference was not significant ($p = 0.557$).

Regarding sex of the patients, the JIA group consisted of 18 females (82%) and 4 males (18%), whereas in the non-JIA group there were 17 females (77%) and 5 males (23%), and the difference was not significant ($p = 1$).

The duration of arthritis in JIA patients was from 5 to 144 months (mean 35.41 months), and in non-JIA patients the duration of symptoms was from 6 to 36 months (mean 17.6 months).

Separation of the patient population into JIA and non-JIA was performed by pediatricians after the analysis of all available data—clinical, laboratory, and imaging. MRI was

used to make a definitive diagnosis in many cases, in the light of non-conclusive clinical and blood tests.

On MRI only 6 children were lesions free, including 2 (4.5%) with JIA, and 4 (9.0%) in non-JIA group; $p = 0.380$. Inflammatory features were seen on MRI in 38 out of all the included patients (86%). Table 3 shows the frequency of MRI lesions in the JIA-confirmed vs. non-JIA groups in individual joints, tendon sheaths, bones, and entheses.

In general, more lesions were identified in the JIA group than in non-JIA.

The most common findings in both groups were effusion in the tibio-talar joint (68% in JIA, and 64% in the arthralgia group) and effusion in the subtalar joint (64% in JIA vs. 59% in the arthralgia non-JIA group). Tenosynovitis was the only lesion that was significantly more common in JIA vs. the non-JIA group ($p = 0.031$).

Regarding active inflammatory lesions, none of the non-JIA patients developed advanced active lesions (stages 2 or 3, depending on a lesion) and in none from the non-JIA group were the destructive lesions seen, whereas they were diagnosed in 12 out of 22 patients with JIA (55%). In none from the non-JIA group of patients the following lesions were seen: Kager's fat pad inflammation, fat tissue inflammation in tarsal tunnel and in sinus tarsi, juxtaarticular soft tissue inflammation, or bursitis.

There was a very good interobserver agreement for scoring all active and destructive items, except for 2 cases of effusion in the inferior talar joint. The percentage of agreement was 96%, and Cohen's kappa of agreement $\kappa = 0.947$ (95% CI: 0.875–1).

Since single MRI features were nonspecific for JIA (only the incidence of tenosynovitis was significantly higher in the JIA group), the MRI summarized score was calculated as the sum of the scores of an individual patient. The range of values of such an indicator ranged from 0 to 36 (Table 4). The more inflammatory features and the higher the score, the more likely the child has been diagnosed with JIA. However, even at a score of 16, a child was not diagnosed to have JIA, and specificity and PPV reached 100% with a score of 17 only.

The optimal cut-off point for the indicator appeared at the value of 10; at such a cut-off point, the best levels of sensitivity and specificity were obtained.

4. Discussion

This study showed that inflammatory features in the ankle and midfoot are frequently seen in MRI in children with a clinical diagnosis of arthritis, both with JIA as well without a final diagnosis of JIA. More lesions were identified in the JIA group than in non-JIA, but only tenosynovitis was significantly more common in the JIA vs. non-JIA group ($p = 0.031$). The MRI summarized score (a sum of all lesions' scores), was unhelpful in discriminating ankle arthritis in JIA from non-JIA patients; the best levels of sensitivity (32%), specificity (91%), PPV (78%), and NPV (57%) were achieved only at a cut-off point of 10.

Talonavicular joint synovitis is particularly overlooked in clinical assessment [3]. Even limiting the clinical evaluation to soft tissues, it appears that differentiation between synovitis and tenosynovitis can be challenging on the basis of clinical evaluation, because these structures are in close proximity and both may cause diffuse swelling and decreased function [8,22,30,31]. One study reported tenosynovitis on MRI in more than half of the patients, whereas no tendon involvement had been detected clinically [8]. This was also confirmed by ultrasound studies [3,32,33] which found that clinical examination has low positive predictive value for synovitis and tenosynovitis assessment.

There have been a number of studies on hip, hand, and wrist, and especially knee MRI in JIA, but still very few have been undertaken on the ankle joint [3], although it is the second most frequently affected joint in children [3,4]. MRI provides a more objective, detailed, and reproducible assessment of disease status compared to clinical examination alone [8]. It can reliably evaluate the extent of inflammation in patients with JIA, including the detection of synovitis, tenosynovitis, and enthesitis [8,31,32], and it has the advantage over ultrasound in depicting BME and in showing areas of joint inflammation poorly visualized by ultrasound, such as sinus tarsi, tarsal canal, interosseous ligaments, or the posterior recess of the tibiotalar joint.

In this study we aimed to analyze in MRI the distribution and advancement of inflammatory lesions in the ankle joints and to test if MRI allows ankle arthritis in JIA to be differentiated from ankle arthralgia of unknown aetiology.

According to the International League Against Arthritis (ILAR) classification of JIA, arthritis is the common feature of all JIA subtypes [3]. In this study arthritis joint effusion/synovial thickening was the most common lesion in both groups in the tibio-talar joint (68% in JIA vs. 64% in the arthralgia group) and in the subtalar joint (64% in JIA vs. 59% in arthralgia non-JIA group) (Figure 1). Surprisingly, the ILAR criteria do not include the involvement of other structures around the joint, such as tendon sheaths and entheses [3], or bone marrow or intraarticular or periarticular fat tissue. In this MRI evaluation, an exhaustive list of structures and tissues which potentially may be affected in the ankle joint were included.



Figure 1. Magnetic resonance imaging (MRI) of the left ankle of an 11-year-old boy with juvenile idiopathic arthritis (JIA). T2-weighted turbo inversion recovery magnitude (TIRM) images in axial (A,D), coronal (B), and sagittal PD-weighted planes (C). Bone marrow edema (BME) stage 2 in the cuboid bone (arrow in (A)). Effusion/synovial thickening stage 2 in the tibio-talar joint (arrow in (B)). Fat tissue in sinus tarsi involvement stage 1 (arrowhead in (B)). Enthesitis of the interosseous ligaments stage 1 (black asterisks in (B)). Kager's fat pad inflammation arrow in (C). Tenosynovitis of the flexor hallucis longus muscle tendon stage 1 arrow in (D).

In our study joint inflammation was more prevalent than tenosynovitis (69.7%) which is consistent with previous studies [8]. However, the study of Javadi et al. [8] included 46% patients with JIA receiving treatment before MRI, and 56% of the subjects received a gadolinium-based contrast agent. The tibiotalar joint was most frequently affected, like in

the current study (Figure 1). Synovitis was also more prevalent in MRI than tenosynovitis in the Phatak et al. study [26] that enrolled 55 consecutive children with disease durations of less than 5 years. The tibio-talar joint was again the most frequently affected. The prevalence of subtalar joint involvement for Phatak et al. was similar to that of other studies [34].

Whereas BME was the most common pathology in a study by Phatak et al. [26] that focused on midfoot involvement only in ERA patients, in the current work, it was the second, after effusion/synovial thickening most commonly diagnosed lesion in both analyzed groups, even more frequently in the non-JIA group (Figure 2).

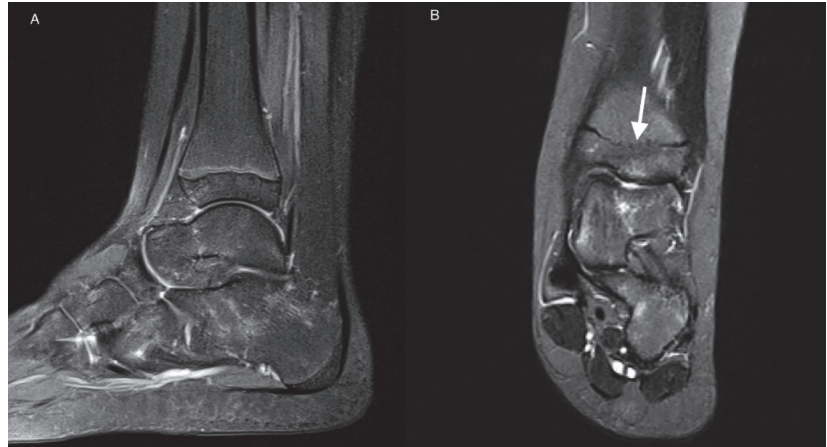


Figure 2. MRI of the left ankle of an 11-year-old girl with JIA. T2-weighted TIRM images in sagittal (A) and coronal (B) planes. Patchy BME (stage 1) in talus and calcaneus. Developmental disorder in the form of premature closure of physis (arrow).

Tenosynovitis was seen less frequently than synovitis and BME in the current study—in 27%, all with JIA. However, it was the only feature which was significantly more common in the JIA vs. non-JIA group ($p = 0.031$). Long flexors and long extensors of the toes, flexor hallucis longus, and peroneus complex sheaths were affected, with two cases of secondary tendon involvement of the tibialis posterior tendon and flexor hallucis longus tendon. Tenosynovitis was detected by Javadi et al. [8] in 39% of patients, also less frequently than synovitis, and the tibialis posterior tendon (39%) and peroneus complex (18%) were the most commonly involved.

In other studies, tenosynovitis was more common than ankle joint arthritis [32,35]. It has been found in up to 71% of JIA patients with symptomatic ankle inflammation [35]. Isolated tenosynovitis (without synovitis) was reported from 3.9% of ankles to up to 39% of ankles [32]. Again, tibialis posterior tendon was the most commonly affected in MRI [8], followed by the peroneus longus and brevis tendons [4].

Enthesitis was seen on MRI in only 1 patient with the ERA subtype of JIA, with the involvement of the interosseous ligaments (Figure 1). Enthesitis is considered the leading feature of juvenile spondyloarthropathies, pertaining to 3 subtypes of JIA according to ILAR classification: ERA, psoriatic arthritis, and undifferentiated arthritis. On clinical examination it was reported in even 80% of patients with ERA subtype, more commonly in juveniles than in adults [36], and involving mainly the hip, ankles, and feet [37]. Plantar fascia insertion (38%) and Achilles enthesitis (22%) were one of most frequently affected sites in a cohort of patients with ERA [38]. US and MRI are important in the verification of both symptomatic and asymptomatic enthesitis which may have value in classification of children with JIA into these subtypes [26]. However, enthesopathic lesions can also be seen in 14% of healthy children [39].

Phatak et al. [26] conducted research focused on tarsitis that is believed to be characteristic of ERA subtype of JIA and is considered specific to juvenile SpA. The authors diagnosed inflammatory lesions in midfoot in 54% of included children in MRI, in comparison to 43% of the cases diagnosed on clinical examination and 36% seen on ultrasound. Enthesitis was seen in 25% of the cases mainly in tibialis posterior, flexor hallucis longus, peroneus longus, tibialis anterior, and peroneus brevis tendons. They also reported peroneus longus inflammation and adjacent bone marrow edema in cuboid in 8 patients which is called the functional enthesitis [12]. In the current study there was only one case of enthesitis of the midfoot interosseous ligaments.

Fat tissue involvement in ankle MRI in JIA has not been reported so far. In the current study MRI showed involvement of fat tissue in 3 patients with JIA: the Kager’s fat pad in 2 patients (10%), in sinus tarsi in 1 (5%), and in the tarsal canal in 1 (5%) (Figure 1). In RA fat tissue is infiltrated by the same inflammatory cells as synovium and subchondral bone and may be responsible for cartilage and bone damage [13]. Similar studies are missing for JIA.

None of our 44 patients had myositis, a rare feature of JIA [40–42], or physis involvement. Destructive lesions were seen in single cases and in the JIA-confirmed group only (Table 3). Ankylosis, for example, was identified in only one patient in the talo-calcaneal joint (Figure 3). In a study by Phatak et al. [26], mentioned earlier, ankylosis tarsitis was diagnosed in 3 cases.

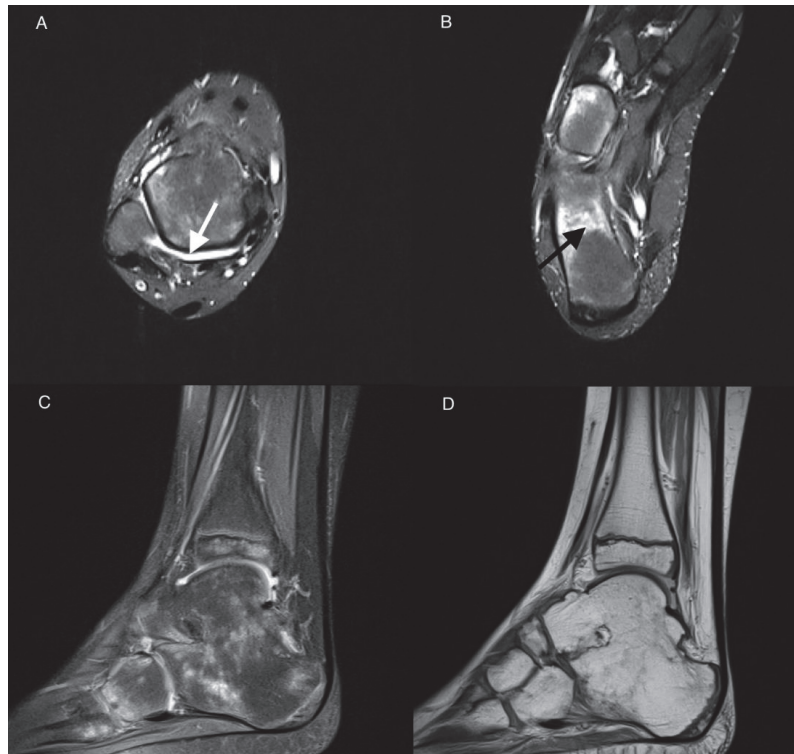


Figure 3. MRI of the right ankle of a 9-year-old boy with JIA. Axial T2-weighted TIRM images (A,B), sagittal PD with fat saturation (C), and sagittal PD-weighted image (D). Effusion/synovial thickening stage 2 in the tibio-talar joint (arrow). BME in numerous bones of the ankle and tarsum, the most advanced in calcaneus stage 3 (arrow in (B)). Tibio-talar joint space narrowing, tibio-calcaneal ankylosis, and osteophytes (C,D).

Developmental lesions were seen in both analyzed groups and were even more common in non-JIA (Table 4). In the JIA-confirmed group there were the Stieda process (1 patient) and premature closure of the distal physis of tibia and fibula (1 case) (Figure 2), and in non-JIA patients there were the Stieda process (2 cases), os trigonum (2 cases), and premature closure of the physis without features of past inflammation (1 case).

There was very high interobserver agreement for scoring all active and chronic items, except for 2 patients with effusion/synovial thickening in subtalar joint. Nevertheless, in the light of the propensity of the disease to involve the bone marrow, bone marrow lesions will especially require differentiation with edema-like signal changes representing residual hematopoietic marrow in the ankles and feet of healthy children. The latter are seen in up to 59% of patients younger than 16 years, are usually tiny, symmetrical, of fairly consistent pattern, are not associated with inflammatory features, and disappear with age [43,44]. However, the marrow pattern may be more extensive, confluent and may represent pathology; intensive focal or diffuse pattern of BME was observed in the JIA-only patients in the current study (Figures 1 and 3).

In summary, this paper confirms that diagnosis of ankle arthritis in the course of JIA is challenging. Contrary to adults, where a majority of the ankle arthropathies result in osteoarthritis and trauma with quite specific clinical and radiographic presentations [45,46], in the pediatric population diagnosis is often based on exclusion criteria. Inflammatory features in MRI were seen with comparable frequency in children with JIA and without a final diagnosis of JIA, and out of a number of analyzed inflammatory and destructive features, only tenosynovitis was significantly more common in the JIA.

According to our knowledge, a similar large number of inflammatory lesions of the ankle joint has been lately proposed by Panwar and the MRI in JIA OMERACT working group [25] as a part of the standardized whole body-MRI scoring system aimed at assessing disease activity in juvenile idiopathic arthritis. Whereas our scoring system was used to test if MRI may help to differentiate ankle arthritis in the JIA from other arthropathies within the ankle and foot. The MRI summarized score was calculated as the sum of scorings of all 22 ankle and midfoot lesions in an individual patient to test which value provides the most optimal diagnosis in terms of high sensitivity, specificity, and positive and negative predictive values. The cut-off 10 points of the proposed MRI summarized score may support the differential diagnosis with high sensitivity and specificity for JIA.

A limitation of the paper was omitting the intravenous contrast administration in order to differentiate with higher accuracy joint and tendon sheath effusion from synovitis and tenosynovitis, but this was part of the protocol. Another issue that could influence the findings was preselection of the patients, who might have been first referred by clinicians for ultrasound and not diagnosed further, in case of positive ultrasound exam. That could result in reduction of the spectrum of lesions seen on MRI with predominance of BME over soft tissue abnormalities; the latter are well seen by ultrasound. Also, a selection bias might have resulted in the lack of structural damage on MRI in majority of this population, which is usually diagnosed on radiographs. On the other hand, damage rarely occurs early in JIA, and the low prevalence in the current study may mirror natural course of JIA.

The main advantage of the paper is involvement in the analysis of a number of possible MRI features that might be identified in JIA patients in ankle and midfoot. The MRI summarized scoring system aimed to discriminate JIA from non-JIA patients was also created and tested.

5. Conclusions

The findings of the study confirm that MRI diagnosis of JIA remains challenging, and except for tenosynovitis, other MRI features are nonspecific for JIA. The MRI summarized score, as a sum of all lesions' scorings, also does not support discrimination between ankle arthritis in JIA from non-JIA patients with clinically suspected arthritis.

Author Contributions: Conceptualization, M.O. and I.S.-S.; Data curation, M.O., E.M., P.G., M.M. and I.S.-S.; Formal analysis, E.M., M.M., M.P. and I.S.-S.; Funding acquisition, M.O. and P.G.; Investigation,

I.S.-S.; Methodology, M.O., E.M. and I.S.-S.; Project administration, I.S.-S.; Resources, E.M., M.P. and I.S.-S.; Software, E.M. and M.M.; Supervision, I.S.-S.; Validation, M.O., E.M., M.P. and I.S.-S.; Visualization, I.S.-S.; Writing—original draft, M.O., E.M., P.G. and I.S.-S.; Writing—review & editing, M.O., E.M., P.G., M.M., M.P. and I.S.-S. All authors have read and agreed to the published version of the manuscript.

Funding: This research received no external funding.

Institutional Review Board Statement: The study was conducted according to the guidelines of the Declaration of Helsinki and approved by the Institutional Ethics Committee of the National Institute of Geriatrics, Rheumatology and Rehabilitation in Warsaw (KBT-3/5/2018).

Informed Consent Statement: Informed consent was obtained from all subjects involved in the study.

Conflicts of Interest: The authors declare no conflict of interest.

References

1. Hemke, R.; Kuijpers, T.W.; van der Berg, J.M.; Van Veenendaal, M.; Dolman, K.M.; Van Rossum, M.A.J.; Maas, M. The diagnostic accuracy of unenhanced MRI in the assessment of joint abnormalities in juvenile idiopathic arthritis. *Eur. Radiol.* **2013**, *23*, 1998–2004. [[CrossRef](#)] [[PubMed](#)]
2. Raveli, A.; Martini, A. Juvenile idiopathic arthritis. *Lancet* **2007**, *369*, 767–778. [[CrossRef](#)]
3. Pascoli, L.; Wright, S.; McAllister, C.; Rooney, M. Prospective evaluation of clinical and ultrasound findings in ankle disease in juvenile idiopathic arthritis: Importance of ankle ultrasound. *J. Rheumatol.* **2010**, *37*, 2409–2414. [[CrossRef](#)] [[PubMed](#)]
4. Peters, S.E.; Laxer, R.M.; Connolly, B.L.; Parra, D.A. Ultrasound—guided steroid tendon sheath injection in juvenile idiopathic arthritis: A 10-year single center retrospective study. *Pediatr. Rheumatol.* **2017**, *15*, 22–29. [[CrossRef](#)]
5. Lovell, D.J. Juvenile idiopathic arthritis: Clinical features. In *Primer on the Rheumatic Diseases*; Klippel, J.H., Stone, J.H., Crofford, L.J., White, P.F., Eds.; Springer: New York, NY, USA, 2008; pp. 142–148.
6. Argyropoulou, M.I.; Fanis, S.L.; Xenakis, T.; Efremidis, S.C.; Siamopoulou, A. The role of MRI in the evaluation of hip joint disease in clinical subtypes of juvenile idiopathic arthritis. *Br. J. Radiol.* **2002**, *75*, 229–233. [[CrossRef](#)]
7. Murray, J.G.; Ridley, N.T.F.; Mitchell, N.; Rooney, M. Juvenile chronic arthritis of the hip: Value of contrast enhanced MR imaging. *Clin. Radiol.* **1996**, *51*, 99–102. [[CrossRef](#)]
8. Javadi, S.; Kan, J.H.; Orth, R.C.; DeGuzman, M. Wrist and ankle MRI in patients with juvenile idiopathic arthritis: Identification of unsuspected multicompartmental tenosynovitis and arthritis. *Am. J. Roentgenol.* **2014**, *202*, 413–417. [[CrossRef](#)]
9. Sudoł-Szopińska, I.; Grochowska, E.; Gietka, P.; Plaza, M.; Pracoń, G.; Saied, F.; Walentowska-Janowicz, M. Imaging of juvenile idiopathic arthritis. Part II: Ultrasonography and MRI. *J. Ultrason.* **2016**, *16*, 237–251. [[CrossRef](#)]
10. Sudoł-Szopińska, I.; Znajdek, M.; Gietka, P.; Vasilevska-Nikodinovska, V.; Patrovic, L.; Salapura, V. Imaging of Juvenile Spondyloarthritis. Part II: Ultrasonography and Magnetic Resonance Imaging. *J. Ultrason.* **2017**, *17*, 176–181. [[CrossRef](#)]
11. Ostrowska, M.; Maśliński, W.; Prochorec-Sobieszek, M.; Nieciecki, M.; Sudoł-Szopińska, I. Cartilage and bone damage in rheumatoid arthritis. *Rheumatologia* **2018**, *2*, 111–120. [[CrossRef](#)]
12. Sudoł-Szopińska, I.; Kwiatkowska, B.; Prochorec-Sobieszek, M.; Maśliński, W. Enthesopathies and enthesitis. Part 1: Etiopathogenesis. *J. Ultrason.* **2015**, *15*, 72–84. [[CrossRef](#)] [[PubMed](#)]
13. Sudoł Szopińska, I.; Kontny, E.; Zaniewicz Kaniewska, K.; Prochorec Sobieszek, M.; Saied, F.; Maśliński, W. Role of inflammatory factors and adipose tissue in pathogenesis of rheumatoid arthritis and osteoarthritis. Part I: Rheumatoid adipose tissue. *J. Ultrason.* **2013**, *13*, 192–201. [[CrossRef](#)] [[PubMed](#)]
14. Malattia, C.; Damasio, M.B.; Basso, C.; Verri, A.; Magnaguagno, F.; Viola, S.; Gattorno, M.; Ravelli, A.; Toma, P.; Martini, A. Dynamic contrast-enhanced magnetic resonance imaging in the assessment of disease activity in patients with juvenile idiopathic arthritis. *Rheumatology* **2010**, *49*, 178–185. [[CrossRef](#)] [[PubMed](#)]
15. Sudoł-Szopińska, I.; Jans, L.; Jurik, A.G.; Hemke, R.; Eshed, I.; Boutry, N. Imaging features of the juvenile inflammatory arthropathies. *Sem. Musculosk. Radiol.* **2018**, *22*, 147–165.
16. Kim, K.H.; Kim, D.S. Juvenile idiopathic arthritis: Diagnosis and differential diagnosis. *Korean J. Pediatr.* **2010**, *53*, 931–935. [[CrossRef](#)]
17. Magni-Manzoni, S.; Malattia, C.; Lanni, S.; Ravelli, A. Advances and challenges in imaging in juvenile idiopathic arthritis. *Nat. Rev. Rheumatol.* **2012**, *8*, 329–336. [[CrossRef](#)]
18. Hemke, R.; Nusman, C.M.; van der Heijde, D.M.; Doria, A.S.; Kuijpers, T.W.; Maas, M.; van Rossum, M.A.J. Frequency of joint involvement in juvenile idiopathic arthritis during a 5-year follow-up of newly diagnosed patients: Implications for MR imaging as outcome measure. *Rheumatol. Int.* **2015**, *35*, 351–357. [[CrossRef](#)]
19. Gardner-Medwin, J.M.M.; Greg, I.; Karl, J. MRI in juvenile idiopathic arthritis and juvenile dermatomyositis. *Ann. N. Y. Acad. Sci.* **2009**, *1154*, 52–83. [[CrossRef](#)]
20. McKay, G.M.; Cox, L.A.; Long, B.W. Imaging juvenile idiopathic arthritis: Assessing the modalities. *Radiol. Technol.* **2010**, *81*, 318–327.

21. Gyls-Morin, V.M.; Graham, T.B.; Blebea, J.S.; Dardzinski, B.J.; Laor, T.; Johnson, N.D.; Oestreich, A.E.; Passo, M.H. Knee in early juvenile rheumatoid arthritis: MR imaging findings. *Radiology* **2001**, *220*, 696–706. [[CrossRef](#)]
22. McQueen, F.M. Magnetic resonance imaging in early inflammatory arthritis: What is its role? *Rheumatology* **2000**, *39*, 700–706. [[CrossRef](#)] [[PubMed](#)]
23. Kanda, T.; Nakai, Y.; Hagiwara, A.; Oba, H.; Toyoda, K.; Furui, S. Distribution and chemical forms of gadolinium in the brain: A review. *Br. J. Radiol.* **2017**, *90*, 20170115. [[CrossRef](#)] [[PubMed](#)]
24. Ranga, A.; Agarwal, Y.; Garg, K.J. Gadolinium based contrast agents in current practice: Risks of accumulation and toxicity in patients with normal renal function. *Indian J. Radiol. Imaging* **2017**, *27*, 141–147. [[CrossRef](#)] [[PubMed](#)]
25. Panwar, J.; Tolend, M.; Redd, B.; Srinivasalu, H.; Colbert, R.A.; Akikusa, J.; Appenzeller, S.; Carrino, J.A.; Herregods, N.; Jans, L.; et al. Consensus-driven conceptual development of a standardized whole body-MRI scoring system for assessment of disease activity in juvenile idiopathic arthritis: MRI in JIA OMERACT working group. *Semin. Arthritis Rheum.* **2021**, *51*, 1350–1359. [[CrossRef](#)] [[PubMed](#)]
26. Phatak, S.; Mohindra, N.; Zanwar, A.; Aggarwal, A. Prominent midfoot involvement in children with enthesitis-related arthritis category of juvenile idiopathic arthritis. *Clin. Rheumatol.* **2017**, *36*, 1737–1745. [[CrossRef](#)] [[PubMed](#)]
27. Petty, E.R.; Southwood, T.R.; Manners, P.; Baum, J.; Glass, D.N.; Goldenberg, J.; He, X.; Maldonado-Cocco, J.; Orozco-Alcala, J.; Prieur, A.-M.; et al. International League of Associations for Rheumatology classification of juvenile idiopathic arthritis: Second revision, Edmonton, 2001. *J. Rheumatol.* **2004**, *31*, 390–392.
28. Sudoł-Szopińska, I.; Jurik, A.G.; Eshed, I.; Lennart, J.; Grainger, A.; Østergaard, M.; Klausner, A.; Cotton, A.; Wick, M.C.; Maas, M.; et al. Recommendations of the ESSR arthritis subcommittee for the use of magnetic resonance imaging in musculoskeletal rheumatic diseases. *Semin. Musculoskelet Radiol.* **2015**, *19*, 396–411. [[PubMed](#)]
29. Landis, J.R.; Koch, G.G. The Measurement of Observer Agreement for Categorical Data. *Biometrics* **1977**, *33*, 159–174. [[CrossRef](#)]
30. Damasio, M.B.; Malattia, C.; Martini, A.; Tomà, P. Synovial and inflammatory diseases in childhood: Role of new imaging modalities in the assessment of patients with juvenile idiopathic arthritis. *Pediatr. Radiol.* **2010**, *40*, 985–998. [[CrossRef](#)]
31. Kan, J.H.; Graham, T.B. Combined pre-injection wrist and ankle MRI protocol and steroid joint injection in juvenile idiopathic arthritis. *Pediatr. Radiol.* **2011**, *41*, 1326–133228. [[CrossRef](#)]
32. Rooney, M.E.; McAlister, C.; Burns, J.F. Ankle disease in juvenile idiopathic arthritis: Ultrasound findings in clinically swollen ankles. *J. Rheumatol.* **2009**, *36*, 1725–1729. [[CrossRef](#)] [[PubMed](#)]
33. Remadios, D.; Martin, K.; Kaplan, G.; Mitchel, R.; Woo, P.; Rooney, M. Juvenile chronic arthritis: Diagnosis and management of tibio-talar and subtalar joint. *Br. J. Rheumatol.* **1997**, *36*, 1214–1217. [[CrossRef](#)] [[PubMed](#)]
34. Hendry, G.; Gardner-Medwin, J.; Watt, G.F.; Wooburn, J. A survey of foot problems in juvenile idiopathic arthritis. *Musculoskelet. Care* **2008**, *6*, 221–232. [[CrossRef](#)] [[PubMed](#)]
35. Tynjala, P.; Honkanen, V.; Lahdenne, P. Pediatric rheumatology. Intra-articular steroids in radiologically confirmed tarsal and hip synovitis of juvenile idiopathic arthritis. *Clin. Exp. Rheumatol.* **2004**, *22*, 643–648. [[PubMed](#)]
36. Tse, S.M.L.; Laxer, R.M. New advances in juvenile spondyloarthritis. *Nat. Rev. Rheumatol.* **2012**, *8*, 269–279. [[CrossRef](#)] [[PubMed](#)]
37. Aquino, M.R.; Tse, S.M.L.; Gupta, S.; Rachlis, A.C.; Stimec, J. Whole-body MRI in juvenile spondyloarthritis: Protocols and pictorial review of characteristic patterns. *Pediatr. Radiol.* **2015**, *45*, 754–762. [[CrossRef](#)]
38. Weiss, P.F.; Klink, A.J.; Behrens, E.M.; Sherry, D.D.; Finkel, T.H.; Feudtner, C.; Keren, R. Enthesitis in an inception of enthesitis-related arthritis. *Arthritis Care Res.* **2011**, *63*, 1307–1312. [[CrossRef](#)]
39. Poggenborg, R.P.; Eshed, I.; Ostergaard, M.; Sørensen, I.J.; Møller, J.M.; Madsen, O.R.; Pedersen, S.J. Enthesitis in patients with psoriatic arthritis, axial spondyloarthritis and healthy subjects assessed by “head-to-toe” whole-body MRI and clinical examination. *Ann. Rheum Dis.* **2015**, *74*, 823–829. [[CrossRef](#)]
40. Liu, S.W.; Velez, N.F.; Lam, C.E.; Femia, A.; Granter, S.R.; Townsend, H.B.; Vleugels, R.A. Dermatomyositis induced by anti-tumour necrosis factor in a patient with juvenile idio-pathic arthritis. *JAMA Dermatol.* **2013**, *149*, 1204–1208. [[CrossRef](#)]
41. Gietka, P.; Rutkowska-Sak, L.; Lisowska, B. Myositis in the course of the systemic form juvenile idiopathic arthritis. *Reumatologia* **2014**, *52*, 142–145. [[CrossRef](#)]
42. Lindehammar, H.; Lindvall, B. Muscle involvement in juvenile idiopathic arthritis. *Rheumatology* **2004**, *43*, 1546–1554. [[CrossRef](#)] [[PubMed](#)]
43. Pal, C.R.; Tasker, A.D.; Ostlere, S.J.; Watson, M.S. Heterogenous signal in bone marrow on MRI in children’s feet: A normal finding? *Skelet. Radiol.* **1999**, *28*, 274–287. [[CrossRef](#)] [[PubMed](#)]
44. Shabshin, N.; Schweitzer, M.E.; Morrison, W.B.; Carrino, J.A.; Keller, M.S.; Grissom, L.E. High-signal T2 changes of the bone marrow of the foot and ankle in children: Red marrow or traumatic changes? *Pediatr. Radiol.* **2006**, *36*, 670–676. [[CrossRef](#)] [[PubMed](#)]
45. Biz, C.; Golin, N.; De Cicco, M.; Maschio, N.; Fantoni, I.; Frizziero, A.; Belluzzi, E.; Ruggieri, P. Long-term radiographic and clinical-functional outcomes of isolated, displaced, closed talar neck and body fractures treated by ORIF: The timing of surgical management. *BMC Musculoskelet. Disord.* **2019**, *20*, 363. [[CrossRef](#)] [[PubMed](#)]
46. Belluzzi, E.; Olivotto, E.; Toso, G.; Cigolotti, A.; Pozzuoli, A.; Biz, C.; Trisolino, G.; Ruggieri, P.; Grigolo, B.; Ramonda, R.; et al. Conditioned media from human osteoarthritic synovium induces inflammation in a synoviocyte cell line. *Connect Tissue Res.* **2019**, *60*, 136–145. [[CrossRef](#)] [[PubMed](#)]

Article

Radiographs and MRI of the Cervical Spine in Juvenile Idiopathic Arthritis: A Cross-Sectional Retrospective Study

Mateusz Kotecki ^{1,*}, Piotr Gietka ², Magdalena Posadzy ³ and Iwona Sudoł-Szopińska ¹

¹ Department of Radiology, National Institute of Geriatrics, Rheumatology and Rehabilitation, 02-637 Warsaw, Poland; sudolszopinska@gmail.com

² Department of Pediatric Rheumatology, National Institute of Geriatrics, Rheumatology and Rehabilitation, 02-637 Warsaw, Poland; malgieta1@gmail.com

³ Individual Private Practice Magdalena Posadzy, 61-426 Poznan, Poland; magdalenaposadzy@gmail.com

* Correspondence: mateuszjankotecki@gmail.com; Tel.: +48-694-976-677

Abstract: Background: Juvenile idiopathic arthritis (JIA) is the most common rheumatic disease among children. In some patients, cervical spine arthritis remains a serious and chronic manifestation of JIA. The aim of this study was to assess the frequency of cervical spine lesions on radiographs and MRI in JIA patients with clinical signs of cervical spine involvement and to verify if with the addition of MRI, the use of radiographs could be abandoned. Methods: This retrospective study evaluated consecutive 34 children (25 girls; aged 6–18 years, median 15.5 years) with JIA and with clinical involvement of cervical spine. In each patient, both radiographs and MRI of the cervical spine were performed. Imaging findings were correlated with clinical and laboratory data. Results: The cervical spine was affected in 35% of patients. The most frequent lesions were subaxial subluxations (SAS; 24%), apophyseal joint ankylosis (9%), and C1/C2 joint lesions (9%). Anterior atlanto-axial subluxation (AAS) was diagnosed only by radiography, and most of the SAS were seen on radiography, whereas only a few on MRI. Reversely, C1/C2 soft tissue involvement were seen on MRI only. Cervical spine involvement was associated with raised ESR ($p = 0.012$) and CRP ($p = 0.014$). Conclusions: The cervical spine lesions are still frequent complication of JIA affecting up to 35% of JIA patients. Most of them develop serious complications, such as AAS and ankylosis. Despite advantages of MRI in terms of the imaging of the atlanto-axial region radiography shows superiority in diagnosis of AAS and SAS.

Citation: Kotecki, M.; Gietka, P.; Posadzy, M.; Sudoł-Szopińska, I. Radiographs and MRI of the Cervical Spine in Juvenile Idiopathic Arthritis: A Cross-Sectional Retrospective Study. *J. Clin. Med.* **2021**, *10*, 5798. <https://doi.org/10.3390/jcm10245798>

Academic Editor: Burkhard Möller

Received: 16 November 2021

Accepted: 8 December 2021

Published: 11 December 2021

Publisher's Note: MDPI stays neutral with regard to jurisdictional claims in published maps and institutional affiliations.



Copyright: © 2021 by the authors. Licensee MDPI, Basel, Switzerland. This article is an open access article distributed under the terms and conditions of the Creative Commons Attribution (CC BY) license (<https://creativecommons.org/licenses/by/4.0/>).

Keywords: cervical spine; juvenile idiopathic arthritis; atlanto-axial subluxation; radiography; magnetic resonance imaging

1. Introduction

Juvenile idiopathic arthritis (JIA) is a systemic inflammatory disease of poorly understood complex pathogenesis, influenced by genetic and environmental factors [1]. Recent classification divides JIA into seven subtypes: systemic onset JIA, oligoarthritis, rheumatoid factor (RF) positive polyarthritis, RF-negative polyarthritis, enthesitis-related arthritis (ERA), psoriatic arthritis (PsA), and undifferentiated arthritis (uA) [1]. It is the most commonly diseased spinal location that is affected by JIA in up to 77% of individuals [2]. According to the American College of Rheumatology (ACR) and recent studies, the real prevalence of cervical spine involvement may, however, be higher due to the subclinical course of the disease [3,4]. For example Kjellberg et al. [3] in a study on 82 children with JIA showed that 35% of them developed at least one radiographic lesion in cervical spine. In a recent study performed on 40 children with JIA, only 20% of patients had clinical symptoms, while in 62.5% the lesions were identified by cervical spine MRI [5]. Moreover, the cervical spine involvement is considered a poor prognostic factor by ACR [4]. There is a lack of studies which focus both on radiography and MRI in children.

The spectrum of spinal lesions in JIA is similar to adults with rheumatoid arthritis (RA) except for a higher occurrence of ankylosis and vertebral bodies or discs hypoplasia in juveniles [6,7]. The most common abnormalities include apophyseal joint ankylosis, C1/C2 arthritis, and anterior atlanto-axial sublaxations [6–8]. Compared to RA, erosions are found only occasionally [6–9]. Another peculiarity in JIA is vertebral bodies and intervertebral discs hypoplasia. Due to the natural joint laxity in children, the assessment of cervical instabilities and their differentiation with unstable pseudospondylolisthesis is challenging [7,9].

There is still no consensus whether to perform radiography or MRI for diagnosis of cervical spine involvement. Especially nowadays, when the prevalence of advanced cervical lesions should be less common in the era of biological treatment, the use of radiographs might be questioned. Radiography provides dynamic information on cervical spine alignment whereas it has low sensitivity for the detection of early inflammatory lesions. MRI enables imaging of complex atlanto-axial anatomy, inflammatory pannus, bone marrow edema and spinal cord lesions. Thus, the use of MRI may lead to early diagnosis of cervical spine arthritis. However, dynamic evaluation of the spine is not performed during MRI in majority of the centers. In radiography, another concern is radiation, whereas MRI is radiation-free. However, in younger children, to avoid motion artifacts sedation may be needed during MRI.

The majority of early lesions are reversible, but they may also progress to chronic irreversible abnormalities that will be seen on radiography, such as sublaxations and ankylosis [10].

The aim of this study was to assess frequency of cervical spine lesions on radiographs and MRI in a cohort of JIA patients with clinical signs of cervical spine involvement and to verify if with the addition of MRI, the use of radiographs could be abandoned.

2. Materials and Methods

The local institutional review board has accepted the study protocol (no. KBT-3/2/2018). The study was performed respecting the ethical principles of the Declaration of Helsinki.

Lateral radiographs and MRI of the cervical spine performed in children clinically suspected of the cervical spine arthritis from 1 January 2010 to 31 December 2019 were assessed retrospectively. At single rheumatology center at this time period 11,838 radiographs and 1267 MRIs of the cervical spine both in adults and children were performed. From this group after pairing studies (at least one MRI and one radiograph per patient), excluding more than one study set per a patient, cases with time interval between studies exceeding 60 days, excluding adults, and finally excluding diagnoses other than JIA, the study group amounted to 34 patients. Fifty-two children had a diagnosis other than JIA, and age and sex matching served as the control group (38 patients). The Figure 1 show a general summary of an inclusion process.

As the mentioned before, the study included 34 patients with JIA with a median age of 15.5 years (IQR 13.0–17.0) of which 25 were girls. Thirty-eight children with the diagnosis other than JIA were matched according to age and sex and served as a control group. No significant differences ($p > 0.05$) were found in the subject characteristics between both groups. This group included 3 children with juvenile systemic lupus erythematosus, 3 with juvenile scleroderma, 1 with borreliosis, and remaining 31 with numbness of upper extremity or cervical spine pain, without specific diagnosis and history of spine injury that could, e.g., indicate spinal cord injury without radiographic abnormality (SCIWORA). Comparison between JIA and non-JIA groups is shown on Table 1.

All patients were referred for imaging by rheumatologists at a reference center with clinical suspicion of cervical spine arthritis (pain, limited motion, or torticollis). All patients had been previously diagnosed with JIA. The symptoms suggesting cervical spine involvement were not present at initial diagnosis. Severe neurological symptoms were not observed.

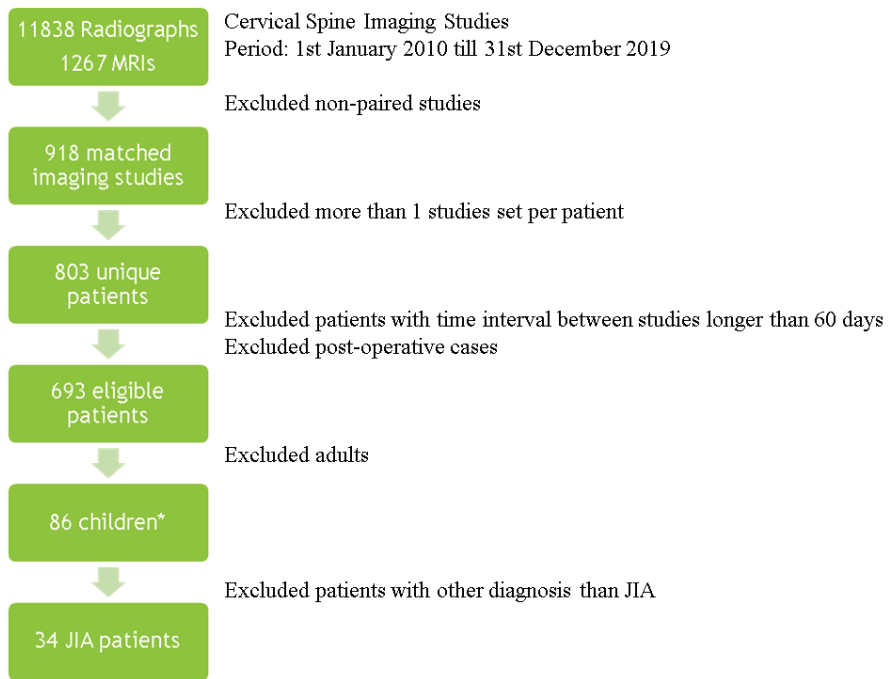


Figure 1. Summary of the inclusion process. *, 52 children with non-JIA diagnosis, after age and sex matching 38 patients, JIA—juvenile idiopathic arthritis, MRI- magnetic resonance imaging.

Table 1. Comparison between JIA and non-JIA patients.

	JIA Group	Non-JIA Group	<i>p</i>
Number	34	38	
Age (years) *	15.5 (13.0–17.0)	15.0 (13.0–16.0)	0.668
Sex (%)	Female: 25 (74%) Male: 9 (26%)	Female: 28 (74%) Male: 10 (26%)	1.000

JIA—juvenile idiopathic arthritis, * non-normally disturbed data: median and interquartile range were used.

All patients with JIA had both radiographs and MRI, whereas in the non-JIA group all patients had cervical spine radiographs and MRI was performed in 23 of them. The time interval between radiographs and MRI did not exceed 60 days. In the case that a patient had multiple cervical spine radiographs or MRI, the studies with the smallest time interval were included.

Plain radiography in lateral neutral projection was supplemented in some patients by flexion and extension views. All 3 projections were performed in the erect patient, with left side against the upright detector. Following the neutral projection, functional views were performed, with patient’s neck in the gentle extension (chin up) or flexion (chin down) positions. The following lesions were evaluated on radiography: Demineralization (osteopenia, osteoporosis), cysts and erosions of the odontoid process, and atlanto-axial subluxations (AAS-anterior, or vertical a.k.a. basilar invagination/settling or cranial settling). On the subaxial level, subaxial subluxations (SAS), apophyseal joint ankylosis, vertebral and/or disc hypoplasia, and longitudinal ligament calcifications were reported [9].

For the MRI examinations, a 1.5 T MRI scanner (Siemens Avanto) and the head/neck 8-channel coil were used. The protocol included coronal T2-weighted (w), axial T2w, sagittal T1w, T2w, T2w TIRM (turbo inversion recovery magnitude) sequences, and postcontrast T1w with fat saturation. Only one patient received intravenous contrast. At the atlanto-

axial level, bone marrow oedema (BME), effusion, pannus, subluxations, cysts and erosions were looked for (Figure 2). At the subaxial level, BME, apophyseal joint ankylosis, SAS, and vertebral or disc hypoplasia were searched for [10,11]. Anterior AAS was diagnosed when a distance between the posterior aspect of the anterior arch of the atlas and the anterior aspect of the dens exceeded 5 mm [12] (Figure 3).

Several methods were used to measure vertical subluxation; the most frequently used methods were McGregor's (cut off value: 4.5 mm) [13] or the Sakaguchi–Kauppi method. In the latter, vertical AAS is diagnosed when the superior facets of C2 crosses the line formed by the lower aspects of the anterior and posterior arches of C1 vertebra [14]. SAS was reported in patients with the displacement between the upper and lower endplates of adjacent vertebrae exceeding 2 mm (Figure 4) [15].

Since radiography and MRI are not fully compatible in terms of methodology, diagnosed lesions and tissues (functional radiographs in the standing position are superior for the diagnosis of anterior and SAS subluxations, and are more accurate than MRI for the diagnosis of calcifications and ankylosis, whereas MRI in the horizontal position usually does not confirm anterior AAS but it provides evaluation of active inflammation), inflammatory features on radiographs and MRI were assessed separately in a binary way 0: absent, 1 present. Lesions on radiographs were assessed according to study of Espada et al. [9] whereas on MRI they were evaluated on the basis of Hospach et al. and Ključevšek et al. reports [10,11]. Inter-reader reliability was assessed.

Each radiograph and MRI were evaluated in clinical blinded and randomized order. The data set were evaluated independently by a radiologist with 20 years of experience (ISS) and senior radiology resident (MK; 4 years of experience) both working in rheumatology center.

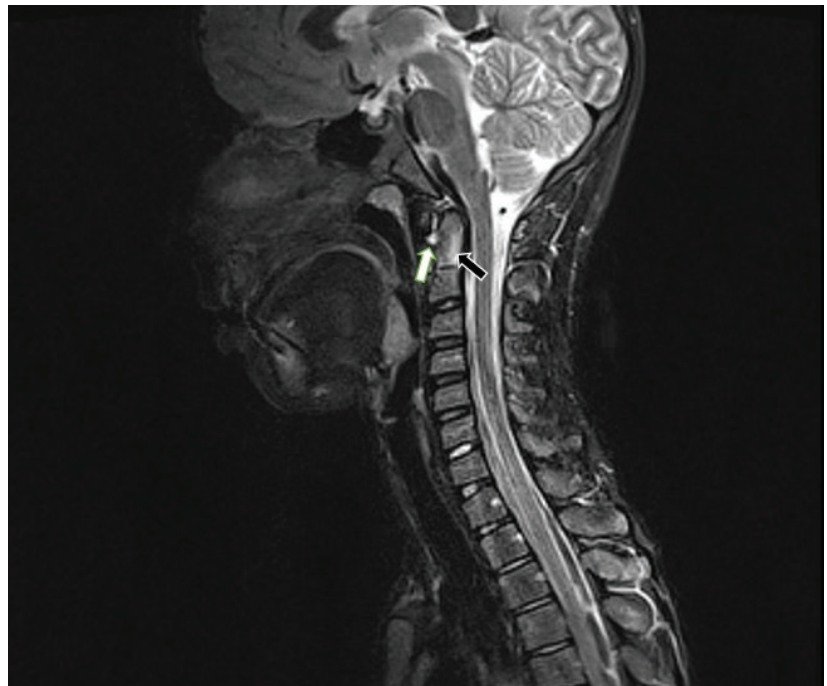


Figure 2. Sagittal MRI, TIRM T2w sequence in a 12-year-old boy diagnosed with enthesitis-related arthritis shows BME in the dens (black arrow) and atlantoaxial effusion (white arrow). MRI—magnetic resonance imaging, TIRM T2w—turbo inversion recovery magnitude T2 weighted, BME—bone marrow edema.



Figure 3. Lateral radiograph in neutral position in a 12-year-old boy (the same patient as in Figure 2) showing anterior atlantoaxial subluxation 6 mm (white line).

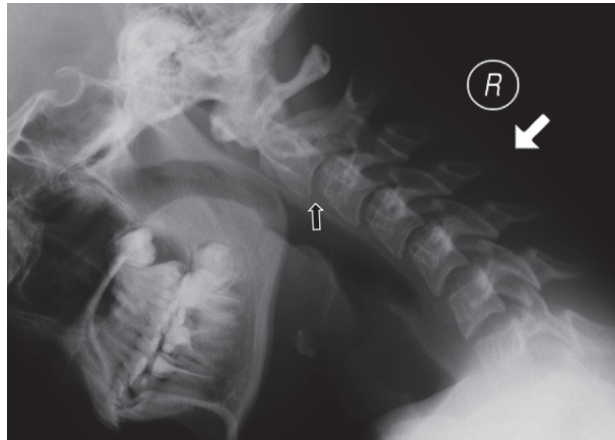


Figure 4. Lateral radiograph in flexion (indicated by white arrow) in a 13-year-old girl showing subaxial subluxation at C2/C3 level (black arrow).

In addition, clinical data such as age, sex, disease duration, and current treatment were collected. Laboratory data, including C-reactive protein (CRP; cut-off value 10 mg/L) and erythrocyte sedimentation rate level (ESR; cut-off value 15 mm/h) were extracted, as well as the presence of antinuclear antibodies (ANA; titre higher or equal to 1:160), anticyclic citrullinated peptide antibodies (anti-CPP; cut-off value 17 IU/mL), rheumatoid factor (RF; cut-off value 34 IU/mL), and human leukocyte antigen (HLA) B-27 antigen.

Statistical Analysis

The SPSS software package (SPSS Inc., Chicago, IL, USA) was used for the purposes of this study. The Shapiro–Wilk test was used to check the normal distribution of continuous variables. Normally distributed data were presented with mean and standard deviation (SD), while non-normally distributed data were presented with median and interquartile

range (IQR). Student's *t*-test was performed for normally distributed continuous data, and a Mann–Whitney U test was used for the analysis of non-normally distributed continuous data. A chi-squared test and Fischer exact test were performed to examine categorical data. *p*-values of less than 0.05 were interpreted as statistically significant. For inter-reader reliability kappa value was used and level of agreement was classified as almost perfect (kappa value above 0.90), strong (0.80–0.90), moderate (0.60–0.79), weak (0.40–0.59), minimal (0.21–0.39), none (0–0.20) [16].

3. Results

Thirty-four patients diagnosed with JIA were analyzed (median age 15.5 years; IQR 13.0–17.0 years), of which 25 were girls (74%). The mean age of diagnosis was 9.2 ± 4.5 years, and the mean disease duration was 4.6 ± 3.2 years. In seven children clinically suspected of subluxation dynamic lateral radiographs were performed, while in the remaining 27 patients only radiographs in a neutral position were obtained.

RF-negative polyarthritis was the most common form of JIA, and it was diagnosed in 13 patients; oligoarthritis was diagnosed in 10 cases, ERA in 5, systemic-onset arthritis in 2, undifferentiated arthritis in 2, and RF-positive polyarthritis and PsA were diagnosed in 1 patient each.

The cervical spine was affected in 35% (12 out of 34) of the included JIA patients (Table 2). SAS was the most common complication and was found in 8 out of 34 children with JIA (8/34, 24%) and in 2 subjects in non-JIA group (2/38, 5%, $p = 0.039$). All these cases were confirmed by radiography, while only two were seen in MRI. More cases diagnosed with radiography resulted from both the erect positioning of the patient and use of functional projections.

Three patients (9%) had abnormalities at the C1/C2 level. All had effusion (9%), anterior AAS was seen in 2 patients (6%), vertical AAS in 2 patients (6%), odontoid pannus in 2 patients (6%) (Figure 2), and BME of the dens in 1 patient (3%). One patient received intravenous contrast and at C1/C2 level enhancement was seen. C1/C2 soft tissue involvement and BME were seen on MRI only.

Anterior AAS was diagnosed in dynamic radiography (2 cases) but was not confirmed in MRI. Regarding abnormalities that are diagnosed by means of radiography and MRI (Table 3), SAS was seen more commonly on radiographs than MRI.

Three patients (9%) had apophyseal joint ankylosis: two at the C2/C3 level and one at the C3/C4 level, and this was diagnosed by both MRI and radiography in all cases (Table 3). No one developed cysts or erosions of the odontoid process, nor calcification of the anterior or posterior longitudinal ligaments. We did not see any pathology of the brain stem or spinal cord. Regarding subtypes of JIA, most lesions (40%) were seen in patients with ERA, followed by four patients (31%) with RF-negative polyarthritis and three patients (30%) with oligoarthritis. Basilar setting occurred in RF-negative polyarthritis patients only (two cases). Only one patient in the study group had PsA, and no abnormalities in his cervical spine were seen.

In the whole group, 89% of JIA patients received medical treatment; 18 of them were taking methotrexate, eight steroids, four biological treatments (adalimumab, infliximab, etanercept, or tocilizumab), five chloroquine, and three sulfasalazine. Nine patients were taking two or more drugs. Additionally, 14 patients had positive ANA titer, one had positive anti-CPP values, two had positive RF values, and four patients had the HLA-B27 antigen present. Table 4 shows the differences between patients with cervical spine involvement and those without involvement with regard to analyzed clinical and laboratory data. Cervical spine involvement was associated with a higher concentration of CRP (12.3 versus 6.6 mg/mL; $p = 0.014$) and ESR (24.2 versus 11.9 mm/h; $p = 0.012$). No association was found between cervical spine lesions and disease duration, age at diagnosis, treatment, or peripheral arthritis of the joints.

Table 2. Prevalence of different lesions in cervical spine in patients diagnosed with JIA.

Keyrpnx	RF Negative Polyarthritits (n = 13)	RF Positive Polyarthritits (n = 1)	Oligoarthritits (n = 10)	ERA (n = 5)	Systemic-onset Arthritits (n = 2)	uA (n = 2)	PsA (n = 1)	Total (n = 34)	Control Group (n = 38)	Interobserver Kappa Value
Prevalence in JIA	11–28%	2–7%	27–56%	3–11%	4–17%	11–21%	2–11%			
Study prevalence *	38%	3%	29%	15%	6%	6%	3%	1 (3%)	0 (0%)	1.0
BME	-	-	-	1	-	-	-	-	0 (0%)	1.0
Effusion	2	-	-	1	-	-	-	3 (9%)	0 (0%)	0.85
Pannus	1	-	-	1	-	-	-	2 (6%)	0 (0%)	1.0
Contrast enhancement **	-	-	-	1	-	-	-	1 (3%)	0 (0%)	1.0
Cl/C2 level										
Dens erosions	-	-	-	-	-	-	-	0 (0%)	0 (0%)	1.0
Anterior AAS	1	-	-	1	-	-	-	2 (6%)	0 (0%)	0.79
Vertical AAS	2	-	-	-	-	-	-	2 (6%)	0 (0%)	1.0
SAS	2	1	2	1	1	1	-	8 (24%)	2 (5%)	0.84
Ankylosis	1	1	1	-	-	-	-	3 (9%)	0 (0%)	0.79
hypoplasia of vertebral body or disc	1	-	-	-	-	-	-	1 (3%)	0 (0%)	1.0
Deminerlization	-	-	-	1	-	-	-	1 (3%)	0 (0%)	0.66
Total	4 (31%)	1 (100%)	3 (30%)	2 (40%)	1 (50%)	1 (50%)	0 (0%)	12 (35%)	2 (5%)	

JIA—juvenile idiopathic arthritits, ERA—enthesitis-related arthritits, PsA—psoriatic arthritits, uA—undifferentiated arthritits, RF—rheumatoid factor, BME—bone marrow edema, AAS—atlanto-axial subluxation, SAS—subaxial subluxation, * visualized by at least one technique, ** contrast was given in 1 case only.

Table 3. Number of patients with JIA (total $n = 34$) with lesions diagnosed on radiography and MRI.

Pathology	Radiography	MRI
Anterior AAS	2	0
Vertical AAS	2	2
SAS	8	2
Dens erosions	0	0
Ankylosis	3	3
Hypoplasia of vertebral body or disc	1	1

All differences were not statistically significant ($p > 0.05$). MRI—magnetic resonance imaging, AAS—atlanto-axial subluxation, SAS—subaxial subluxation.

Table 4. Comparison between JIA patients diagnosed with cervical spine involvement on imaging with JIA patients without confirmed cervical spine involvement.

Kerryprnx	Cervical Spine Involvement ($n = 12$)	No Cervical Spine Involvement ($n = 22$)	p	
Age (years) *	15.0 (13.0–16.8)	15.5 (12.3–17.0)	0.817	
Sex (female, %)	10 (83%)	15 (68%)	0.439	
Age at onset (years)	9.9 ± 4.1	8.5 ± 4.7	0.604	
Disease duration (years)	4.4 ± 2.8	4.7 ± 3.4	0.813	
CRP (mg/mL) *	8.0 (5.0–14.5)	4.0 (2.5–5.5)	0.014	
ESR (mm/h) *	29.5 (11.5–39.0)	9.0 (5.0–17.5)	0.012	
ANA positivity ($n, \%$)	8 (80%)	10 (59%)	0.406	
Treatment	Methotrexate ($n, \%$)	8 (80%)	10 (59%)	0.406
	Steroids ($n, \%$)	5 (50%)	3 (18%)	0.102
	Chloroquine	1 (10%)	4 (24%)	0.621
	Biological treatment ($n, \%$)	3 (30%)	1 (6%)	0.128

JIA—juvenile idiopathic arthritis, CRP—C-reactive protein, ESR—erythrocyte sedimentation rate, ANA—antinuclear antibodies, * non-normally disturbed data: median and interquartile range were used. The bold means significant.

Interestingly, the only pathology found in non-JIA group was SAS described in 2 children (2/38, 5%). SAS in this group most probably resulted from natural laxity of spine in children described by Lustrin et al. [17].

The overall inter-reader reliability was in most cases almost perfect (kappa value 1.00), despite SAS (0.84) and effusion (0.85), where level of agreement was strong. Regarding anterior AAS (0.79), ankylosis (0.79) and demineralization (0.66) the observed strength of agreement was moderate (Table 2).

4. Discussion

The current study found radiographic and MRI lesions in 35% of JIA patients with clinical suspicion of cervical spine arthritis, including 25% of them developed serious complications, such as atlanto-axial subluxations or ankylosis. Both techniques provided complementary information.

The most frequent abnormality was SAS. It was seen in eight out of all included patients with JIA (24%), all with 4.5 years history of JIA. All lesions were seen on radiographs, whereas only two were confirmed on MRI which results from the different position of a patient at each examination. In other studies, the prevalence of SAS was lower and affected 6–7% of JIA patients [6,8]. Most commonly, level C4/C5 was affected [8], which was also confirmed in the current study. The lower prevalence of SAS in the mentioned studies could result from the coexistence of apophyseal joint ankylosis, which hinders SAS. In this study, SAS was more frequently seen than in other studies with a similar low prevalence of ankylosis. However, this finding was interpreted with caution, bearing in mind that the SAS appearance may result from the natural flexibility of the pediatric cervical spine as seen in 5% of the current non-JIA group and was also described by other authors [17].

Ankylosis was seen in 9% of JIA patients. It was diagnosed in patients with late onset disease (mean 12 years of age) however 1.5 year after the diagnosis of JIA. This confirms that ankylosis might occur early in JIA. Espada et al. reported cervical spine ankylosis in 6.5% of patients with JIA during the first year after diagnosis, with 27% occurring during the first five years after diagnosis and the remaining 73% five years or more after the diagnosis. The mean time to develop vertebral fusion was 8.6 years [9]. Other researchers have shown a higher prevalence of cervical spine ankylosis compared with our or Espada et al.'s [3,9,10]. Laiho et al. reported apophyseal joint ankylosis in 41% of patients with JIA, and the mean age of JIA onset was 6.9 years, significantly earlier than in a group without ankylosis [8]. Usually, fusion begins at the C2/C3 level and affects patients with systemic-onset JIA, polyarthritis, or oligoarthritic disease [8,9]. In our group, it developed in two patients with polyarthritis JIA and one with oligoarthritic. In two cases, level C2/C3 was affected.

Data regarding the occurrence of osseous lesions, such as ankylosis, cysts, erosions, and spinal canal stenosis vary among researchers. Some showed an increased occurrence regardless of the clinical improvement and treatment [10], whereas Ključevšek et al. [11] did not. None of the patient in the current study had cysts or erosions. Only one patient out of 15 studied by Ključevšek et al. developed dens deformation, causing spinal canal compression, thickening of the transverse ligament, and persistent anterior AAS [11]. The lower prevalence of chronic changes could be explained by earlier diagnosis and aggressive treatment with anti-TNF alpha drugs [11]. Several studies have confirmed that successful treatment with biological agents and methotrexate decreases the intensity of inflammation (seen also on MRI as reduction of BME and synovitis) as well as the incidence of complications such as subluxations [10,11].

Some authors suggest that JIA may lead to myelopathy and progressive neurological dysfunction, as in RA; however, there is a lack of publications regarding this topic in JIA [18]. No one from the current study developed lesions in the spinal cord. However, discrete early biochemical changes could not be excluded. A recent study performed by Manczak et al. [19] on adult patients with RA revealed biochemical changes in the spinal cord in patients with anterior AAS diagnosed by apparent diffusion coefficient.

Among our JIA group, 9% had active inflammation at the C1/C2 level (including pannus formation, periodontoid effusions, BME, and postcontrast enhancement). They all occurred within three years from the disease onset. BME was seen in only one patient. In both adults and children, BME is a strong predictor of dens erosions [20]. In our study, nobody developed dens erosions, but in other publications, the prevalence of dens erosions in JIA varied from 13% to 19% [3,6,9]. Hospach et al. in a group of 13 JIA patients, found BME in 93% of the cases; 100% had synovitis and 15% had dens erosions. The high prevalence of all lesions in that study could result from the more common use of MRI in the early stages of the disease in patients with clinical symptoms suggesting cervical spine disease. After treatment with methotrexate and biological therapy, a decrease was noted, with BME seen in 77% and synovitis in 80%. However, despite treatment, the prevalence of dens erosions increased to 31% [10].

In the present study, anterior AAS was diagnosed in 6% of cases. Kjellberg et al. [3] reported similar results (5%); however, in young adults with JIA, anterior AAS was found in up to 33% of patients [6]. Basilar setting (vertical AAS) occurred in two of our patients (6%) after 8 years of JIA diagnosis, although in other studies the prevalence of this type of subluxation reaches 13%, and even 25% in young adults with JIA [3,8]. Basilar setting results from severe damage at the C1/C2 level and may lead to brain stem compression or even sudden death [21].

Bone demineralization (bone loss) was seen on radiographs in only one patient with ERA (3% of our group). Typically, it is observed in patients with polyarthritis and systemic-onset disease [22]. Excluding patients treated with steroids, Henderson et al. revealed that low total body bone mineral density is associated with active and severe forms of JIA [23].

Reduced bone mineral density and osteopenia affect young adults following JIA, even those in remission. Both conditions predispose to osteoporosis and bone fractures [24,25].

In the current study only one patient was diagnosed with hypoplasia of the posterior arch of C1 and C2/C3 disc. This is entirely different from data presented by other authors, where vertebral and disc hypoplasia are regarded as the second most common complication in JIA. They are observed in patients with earlier onset of JIA and are almost always seen at the level of ankylosis [9]. We can presume that the prevalence of vertebral hypoplasia and other chronic lesions is less common nowadays in the era of biological treatment. Vertebral and disc hypoplasia were also associated with a severe course and progression of JIA. Indeed, in the present study, the patient with vertebral hypoplasia of the C1 posterior arch and C2/C3 disc hypoplasia developed ankylosis, SAS, and vertical AAS. Most frequently, hypoplasia is seen at the C3–C6 level, and it is probably caused by inflammation or/and aggressive pharmacotherapy with steroids [26]. The fourth cervical vertebra is most severely affected by hypoplasia (up to 26% of cases), whereas the spinal canal diameter is almost the same as in the healthy population [6,8,26].

No cases of anterior or posterior longitudinal ligament calcification were observed in the present study. Espada et al. [9], in their study published in 1988, reported posterior longitudinal ligament calcification in 6.6% of the patients, and almost half of these developed anterior longitudinal ligament calcifications. The disease duration was approximately 13 years prior to the onset of calcification, and a slightly higher occurrence was noted in males and in individuals with earlier disease start (3.8 years). All patients with longitudinal ligament calcification had multilevel ankylosis, suggesting that chronic immobilization due to ankylosis could lead to ligament calcification [9]. This study again confirms the more successful treatment of JIA nowadays.

In the current study, cervical spine involvement was associated with elevated ESR ($p = 0.012$) and CRP ($p = 0.014$). According to the ACR, CRP and ESR are considered biomarkers of JIA activity [4], and their prolonged elevation is associated with poor prognosis in JIA [4] and with lack of remission [27]. Additionally, ESR seems to predict the development of uveitis in JIA [28]. Although CRP and ESR have low specificity and sensitivity, they were found useful in the diagnosis and follow-up of patients with JIA. ESR was also included in the Juvenile Arthritis Disease Activity Score (JADAS) [29].

Overall, although MRI may show early inflammatory lesions, the dynamic radiography is superior in the diagnosis of cervical spine instabilities (Table 3). Both severe AAS and SAS may cause cervical cord pathologies, even including sudden death. Thus, functional radiography should be still performed in the suspicion of cervical spine instabilities. The radiography is cheap and widely available, but the major disadvantages include radiation, superimposition of anatomical structures and limited use for soft tissues imaging. In comparison, MRI is superior in assessment of soft tissue pathologies, spinal cord and nerve roots, and may visualize BME. However, MRI is expensive and due to long time of acquisition young children or claustrophobic patients may require sedation.

The major limitation of the study is the retrospective study protocol. The small number of JIA group (34) and cervical spine lesions (12) does not allow making robust comments about the results of the study. Another limitation resulting from the nature of JIA underlined in literature is a lack of direct correspondence between cervical pain and presence of alterations on radiographs and MRI since silent cervical spine arthritis has also been reported [5]. The current study focused on patients previously diagnosed with JIA and clinical symptoms suggesting cervical spine arthritis. Only patients examined with two imaging methods were enrolled and no asymptomatic children with JIA were analyzed. It would have been better to extend the investigation including also JIA patients with no cervical symptoms in order to evaluate the eventual presence of silent alterations in this group. Whereas from an ethical point of view it is impossible for radiography, it is possible for MRI. Finally, the major strength and originality of our study was the presentation of both radiographic and MRI features of cervical spine involvement in JIA. Previous studies focused only on one method.

5. Conclusions

In conclusion, cervical spine lesions may affect up to 35% of JIA patients, and 25% of them develop serious complications, such as atlanto-axial subluxations and ankylosis. Despite clear advantages of MRI in terms of imaging of early inflammatory lesions in soft tissues and bone, radiography shows superiority in the diagnosis of AAS and SAS. The predominance of chronic features, such as SAS, AAS and ankylosis over early inflammatory abnormalities, including BME and synovitis along with the several years of history of JIA suggest that clinical manifestation of cervical spine involvement is discrete or even absent in the first years of the disease, which lets the cervical arthritis progress unrecognized until a more advanced stage.

Author Contributions: Conceptualization, P.G. and I.S.-S.; Data curation, M.K., P.G. and I.S.-S.; Formal analysis, M.K., M.P. and I.S.-S.; Investigation, M.K.; Methodology, M.K., P.G., M.P. and I.S.-S.; Supervision, I.S.-S.; Validation, M.K. and M.P.; Writing—original draft, M.K.; Writing—review and editing, M.K., P.G., M.P. and I.S.-S. All authors have read and agreed to the published version of the manuscript.

Funding: This research received no external funding.

Institutional Review Board Statement: The study was conducted according to the guidelines of the Declaration of Helsinki, and approved by the Institutional Review Board of National Institute of Geriatrics, Rheumatology and Rehabilitation (no. KBT-3/2/2018).

Informed Consent Statement: Not applicable.

Data Availability Statement: The study data may be available on request. The data presented in this study are available on request from the corresponding author. The data are not publicly available due to ethical concerns.

Conflicts of Interest: The authors declare no conflict of interest.

References

1. Ravelli, A.; Martini, A. Juvenile idiopathic arthritis. *Lancet* **2007**, *369*, 767–778. [CrossRef]
2. Hemke, R.; Herregods, N.; Jaremko, J.L.; Åström, G.; Avenarius, D.; Becce, F.; Bielecki, D.K.; Boesen, M.; Dalili, D.; Giraudo, C.; et al. Imaging assessment of children presenting with suspected or known juvenile idiopathic arthritis: ESSR-ESPR points to consider. *Eur. Radiol.* **2020**, *30*, 5237–5249. [CrossRef]
3. Kjellberg, H.; Pavlou, I. Changes in the cervical spine of children with juvenile idiopathic arthritis evaluated with lateral cephalometric radiographs: A case control study. *Angle Orthod.* **2011**, *81*, 447–452. [CrossRef] [PubMed]
4. Beukelman, T.; Patkar, N.M.; Saag, K.G.; Tolleson-Rinehart, S.; Cron, R.Q.; DeWitt, E.M.; Ilowite, N.T.; Kimura, Y.; Laxer, R.M.; Lovell, D.J.; et al. 2011 American College of Rheumatology Recommendations for the Treatment of Juvenile Idiopathic Arthritis: Initiation and Safety Monitoring of Therapeutic Agents for the Treatment of Arthritis and Systemic Features. *Arthritis Care Res.* **2011**, *63*, 465–482. [CrossRef]
5. Tzaribachev, N. High Prevalence of Cervical Spine and Temporomandibular Joint Involvement in Patients with Juvenile Idiopathic Arthritis [Internet]. *Arthritis Rheum* **2012**, *2026*. Available online: <https://acrabstracts.org/abstract/high-prevalence-of-cervical-spine-and-temporomandibular-joint-involvement-in-patients-with-juvenile-idiopathic-arthritis/> (accessed on 17 May 2020).
6. Elhai, M.; Wipff, J.; Bazeli, R.; Freire, V.; Feydy, A.; Drapé, J.L.; Quartier, P.; Kahan, A.; Job-Deslandre, C. Radiological cervical spine involvement in young adults with polyarticular juvenile idiopathic arthritis. *Rheumatol. Oxf. Engl.* **2013**, *52*, 267–275. [CrossRef] [PubMed]
7. Kotecki, M.; Sotniczuk, M.; Gietka, P.; Gasik, R.; Sudol-Szopińska, I. Imaging of cervical spine involvement in inflammatory arthropathies: A review. *Pol. J. Radiol.* **2021**, *86*, e620–e629. [CrossRef]
8. Laiho, K.; Hannula, S.; Savolainen, A.; Kautiainen, H.; Kauppi, M. Cervical spine in patients with juvenile chronic arthritis and amyloidosis. *Clin. Exp. Rheumatol.* **2001**, *19*, 345–348. [PubMed]
9. Espada, G.; Babini, J.C.; Maldonado-Cocco, J.A.; Garcia-Morteo, O. Radiologic review: The cervical spine in juvenile rheumatoid arthritis. *Semin. Arthritis Rheum.* **1988**, *17*, 185–195. [CrossRef]
10. Hospach, T.; Maier, J.; Müller-Abt, P.; Patel, A.; Horneff, G.; von Kalle, T. Cervical spine involvement in patients with juvenile idiopathic arthritis-MRI follow-up study. *Pediatr. Rheumatol. Online J.* **2014**, *12*, 9. [CrossRef]
11. Ključevšek, D.; Emeršič, N.; Toplak, N.; Avčič, T. Clinical and MRI outcome of cervical spine lesions in children with juvenile idiopathic arthritis treated with anti-TNF α drugs early in disease course. *Pediatr. Rheumatol. Online J.* **2017**, *15*, 38. [CrossRef]
12. Locke, G.R.; Gardner, J.I.; Van Epps, E.F. Atlas-dens interval (ADI) in children: A survey based on 200 normal cervical spines. *Am. J. Roentgenol. Radium Nucl. Med.* **1966**, *97*, 135–140. [CrossRef]

13. McGregor, M. The significance of certain measurements of the skull in the diagnosis of basilar impression. *Br. J. Radiol.* **1948**, *21*, 171–181. [CrossRef] [PubMed]
14. Kauppi, M.; Sakaguchi, M.; Konttinen, Y.T.; Hämäläinen, M. A new method of screening for vertical atlantoaxial dislocation. *J. Rheumatol.* **1990**, *17*, 167–172. [PubMed]
15. White, A.A.; Johnson, R.M.; Panjabi, M.M.; Southwick, W.O. Biomechanical analysis of clinical stability in the cervical spine. *Clin. Orthop.* **1975**, *109*, 85–96. [CrossRef]
16. McHugh, M.L. Interrater reliability: The kappa statistic. *Biochem. Med.* **2012**, *22*, 276–282. [CrossRef]
17. Lustrin, E.S.; Karakas, S.P.; Ortiz, A.O.; Cinnamon, J.; Castillo, M.; Vaheesan, K.; Brown, J.H.; Diamond, A.S.; Black, K.; Singh, S. Pediatric cervical spine: Normal anatomy, variants, and trauma. *Radiogr. Rev. Publ. Radiol. Soc. N. Am. Inc.* **2003**, *23*, 539–560. [CrossRef]
18. Sunahara, N.; Matsunaga, S.; Mori, T.; Ijiri, K.; Sakou, T. Clinical course of conservatively managed rheumatoid arthritis patients with myelopathy. *Spine* **1997**, *22*, 2603–2607. [CrossRef]
19. Mańczak, M.; Pracoń, G.; Sudoł-Szopińska, I.; Gasik, R. Apparent diffusion coefficient as an indicator of spinal cord compression due to anterior atlanto-axial subluxation in rheumatoid arthritis patients. *Soc. Eur. Sect. Cerv. Spine Res. Soc.* **2019**, *28*, 2352–2358. [CrossRef]
20. Udoł-Szopińska, I.; Grochowska, E.; Gietka, P.; Plaza, M.; Pracoń, G.; Saied, F.; Walentowska-Janowicz, M. Imaging of juvenile idiopathic arthritis. Part II: Ultrasonography and MRI. *J. Ultrason.* **2016**, *16*, 237–251.
21. Parish, D.C.; Clark, J.A.; Liebowitz, S.M.; Hicks, W.C. Sudden death in rheumatoid arthritis from vertical subluxation of the odontoid process. *J. Natl. Med. Assoc.* **1990**, *82*, 297–304.
22. Brabnikova Maresova, K. Secondary Osteoporosis in Patients with Juvenile Idiopathic Arthritis. *J. Osteoporos.* **2011**. Available online: <https://www.ncbi.nlm.nih.gov/pmc/articles/PMC3043287/> (accessed on 27 April 2020).
23. Henderson, C.J.; Specker, B.L.; Sierra, R.I.; Wilmott, R.W.; Lovell, D.J.; Cawkwell, G.D.; Campaigne, B.N. Predictors of total body bone mineral density in non-corticosteroid-treated prepubertal children with juvenile rheumatoid arthritis. *Arthritis Rheum.* **1997**, *40*, 1967–1975. [CrossRef]
24. Haugen, M.; Lien, G.; Flatø, B.; Kvammen, J.; Vinje, O.; Sørskaar, D.; Førre, Ø. Young adults with juvenile arthritis in remission attain normal peak bone mass at the lumbar spine and forearm. *Arthritis Rheum.* **2000**, *43*, 1504–1510. [CrossRef]
25. French, A.R.; Mason, T.; Nelson, A.M.; Crowson, C.S.; O’Fallon, W.M.; Khosla, S.; Gabriel, S.E. Osteopenia in adults with a history of juvenile rheumatoid arthritis. A population based study. *J. Rheumatol.* **2002**, *29*, 1065–1070. [PubMed]
26. Endén, K.; Laiho, K.; Kautiainen, H.; Arkela-Kautiainen, M.; Belt, E.; Kauppi, M. Subaxial cervical vertebrae in patients with juvenile idiopathic arthritis—something special? *Jt. Bone Spine* **2009**, *76*, 519–523. [CrossRef]
27. Alberdi-Saugstrup, M.; Zak, M.; Nielsen, S.; Herlin, T.; Nordal, E.; Berntson, L.; Anders, F.; Marite, R.; Klaus, M. High-sensitive CRP as a predictive marker of long-term outcome in juvenile idiopathic arthritis. *Rheumatol. Int.* **2017**, *37*, 695–703. [CrossRef] [PubMed]
28. Haasnoot, A.J.W.; van Tent-Hoeve, M.; Wulfraat, N.M.; Schalijs-Delfos, N.E.; Los, L.I.; Armbrust, W.; Zuihoff, N.P.; De Boer, J.H. Erythrocyte sedimentation rate as baseline predictor for the development of uveitis in children with juvenile idiopathic arthritis. *Am. J. Ophthalmol.* **2015**, *159*, 372–377. [CrossRef] [PubMed]
29. Zhu, S.; Xu, W.; Luo, Y.; Zhao, Y.; Liu, Y. Cervical spine involvement risk factors in rheumatoid arthritis: A meta-analysis. *Int. J. Rheum. Dis.* **2017**, *20*, 541–549. [CrossRef]



Article

MRI Findings in Hip in Juvenile Idiopathic Arthritis

Monika Ostrowska ¹, Piotr Gietka ², Małgorzata Mańczak ³, Emil Michalski ^{1,*} and Iwona Sudol-Szopińska ¹

- ¹ Department of Radiology, National Institute of Geriatrics, Rheumatology and Rehabilitation, 02-637 Warsaw, Poland; monique.ostrowska@gmail.com (M.O.); sudolszopinska@gmail.com (I.S.-S.)
² Clinic of Paediatric Rheumatology, National Institute of Geriatrics, Rheumatology and Rehabilitation, 02-637 Warsaw, Poland; malgieta1@gmail.com
³ Department of Gerontology, Public Health and Didactics, National Institute of Geriatrics, Rheumatology and Rehabilitation, 02-637 Warsaw, Poland; m.manczak@op.pl
* Correspondence: emil.michalski.md@gmail.com; Tel.: +48-22-67-09-192

Abstract: The aim of this study was to evaluate if magnetic resonance imaging allows hip arthritis in JIA to be differentiated from hip arthralgia of unknown etiology in juveniles clinically suspected for hip arthritis. This was a retrospective observational study which included 97 children with clinically suspected hip arthritis. Each hip was assessed and scored in MRI for signs of active and destructive inflammatory lesions and developmental lesions. MRI findings between JIA-confirmed patients and without final diagnosis of JIA were compared and the MRI summarized score was calculated, as the sum of scorings of all 24 hip lesions in an individual patient (i.e., effusion, synovitis, bone marrow edema, enthesitis). MRI showed at least one lesion in the majority of patients (95 patients; 98%). Effusion was the most common feature, followed by bone marrow oedema and synovitis. All lesions were more common in patients with a final diagnosis of JIA, especially synovitis and enthesitis ($p = 0.037$ and $p = 0.047$). The MRI summarized score was significantly higher in the JIA group than the non-JIA group: 3 (2–5) vs. 2 (2–2), respectively, $p = 0.002$. Using a cut-off score of 6, the MRI summarized score showed 25% sensitivity and 100% specificity indicating a good ability in discriminating hip arthritis during JIA from non-JIA patients. MRI allows hip arthritis in JIA to be differentiated from hip arthralgia of unknown etiology with good specificity, thus, may be helpful in confirming the diagnosis of JIA.

Citation: Ostrowska, M.; Gietka, P.; Mańczak, M.; Michalski, E.; Sudol-Szopińska, I. MRI Findings in Hip in Juvenile Idiopathic Arthritis. *J. Clin. Med.* **2021**, *10*, 5252. <https://doi.org/10.3390/jcm10225252>

Keywords: arthritis; juvenile; hip; arthralgia; magnetic resonance imaging

Received: 16 September 2021
Accepted: 6 November 2021
Published: 11 November 2021

Publisher's Note: MDPI stays neutral with regard to jurisdictional claims in published maps and institutional affiliations.



Copyright: © 2021 by the authors. Licensee MDPI, Basel, Switzerland. This article is an open access article distributed under the terms and conditions of the Creative Commons Attribution (CC BY) license (<https://creativecommons.org/licenses/by/4.0/>).

1. Introduction

Juvenile idiopathic arthritis (JIA) is a heterogeneous group of diseases with an onset before 16 years of age [1,2]. It typically lasts for more than six months, with arthritis present for at least six weeks [1,2] and is the most common form of childhood arthritis [3–7]. Joint involvement usually starts with synovitis and the formation of inflammatory tissue, called the pannus, which destroys hyaline cartilage, erodes the bone and leads to articular destruction and ankylosis [5,6]. As highly effective treatment is now available for treating JIA, there is increasing demand for novel imaging techniques to provide objective and accurate measures of inflammatory changes to monitor the disease and treatment response [8].

Hip arthritis develops in 20–63% of children with JIA, mainly in juveniles with the systemic subtype of the disease [1,4,5,9–11] and is often a predictor of severe disease and high-risk disability [1]. The clinical features are not specific for active hip inflammation and may occur due to previous joint damage [11] or other hip diseases, including malignancies. Furthermore, since it is not a superficial joint, hip involvement is particularly difficult to detect clinically, as inflamed synovium and effusions cannot be directly palpated [4,12].

Magnetic resonance imaging (MRI) is a sensitive and valuable technique in pediatric musculoskeletal pathologies and is considered to be the most suitable technique for detecting synovial hypertrophy and bone marrow oedema (BME) [13–18]. It allows the visualization of joints in several dimensions using a multiplanar technique [4]. The most common

pathologies in JIA are effusions and synovitis, which are most accurately diagnosed using gadolinium injection, following which the highly vascular pannus enhances brightly while joint effusion remains of low signal [19]. Recent studies have highlighted potential adverse effects of gadolinium [20,21]. Consequently, due to observed gadolinium depositions in the brain, the European Medicines Agency (EMA) has now banned several linear gadolinium-based contrast agents. Moreover, even though macrocyclic contrast agents have not been suspended, they should still be used with care and a strict indication [20]. The new term “effusion/synovial thickening” was used lately by Panwar et al. [22] defined as “an increased amount (greater than physiologic) of high signal intensity within the joint space distending the joint capsule on T2-weighted fat—saturated or STIR or fluid sensitive sequences”. “Effusion/synovial thickening” was considered altogether as a single item as it is often difficult to differentiate these two findings by MRI without intravenous administration of contrast [22]. In addition to synovitis and osteitis, other inflammatory lesions that may be seen in children with JIA include bursitis, enthesitis and myositis [23–26]. Inflammation may also involve the triradiate cartilage and growth plates. Destructive, irreversible lesions in the hip joint include cysts, erosions, joint space narrowing, chondromalacia and ankylosis. Such joint inflammation that interferes with bone growth may eventually lead to skeletal growth disturbances and developmental disorders, such as bone remodeling.

Several scoring systems for juvenile hip arthritis assessment on MRI have been proposed [4,5,11,27,28]; however, none of them includes all the above-mentioned items in JIA (i.e., active, destructive and developmental) and, to date, a validated MRI scoring system for assessing the hips in JIA has not been established [29]. An important methodological work on standardizing the whole-body-MRI scoring system, including the hip joint, for assessment of disease activity in JIA was published in 2021 by the MRI in JIA OMERACT working group [22].

Understanding limitations of clinical assessment of hip joint arthritis, the aim of this study was to investigate if MRI allows hip arthritis in JIA to be differentiated from hip arthralgia of unknown etiology.

2. Materials and Methods

2.1. Patients

This was a retrospective single center study which included 97 children aged 4–16 years with clinically suspected hip disease in JIA [30,31]. The study was based on the analysis of data available in the hospital database. All children meeting the inclusion criteria hospitalized in the period from 2016 and 2019 were included in the analysis.

Reported complaints included hip pain at rest or on movement, or restricted movement of the hip (or both hips) on clinical evaluation, persisting for more than six weeks [30,31]. All patients were referred by pediatric rheumatologists from the referential center for pediatric rheumatology. Children with diagnoses other than arthritis were excluded. None of the patients had an intraarticular corticosteroid injection.

Parents of all patients gave informed consent to take part in the study. The study was performed in accordance with the Declaration of Helsinki and was approved by the local ethics committee (KBT-3/5/2018).

Collected clinical data included age, sex, information on which hip was affected (unilaterally or bilaterally) and the final diagnosis.

2.2. MRI Protocol and Interpretation of Imaging Features

Non-contrast MRI examinations were performed on both hips on a 1,5 Tesla system (Siemens Avanto) in a dedicated pelvis coil. Patients were examined in a supine position. No sedation was used.

The following sequences were used: coronal T1-weighted (w) and T2 Turbo Inversion Recovery Magnitude (TIRM), axial T2w, T2 TIRM and Proton Density (PD) with fat saturation (FS), sagittal PD and axial oblique PD FS. Slice thickness was 3 mm, gap 0.6 mm.

The images were independently evaluated and scored by two radiologists (MO and IS), both with 15 years of experience in musculoskeletal imaging (10 years in rheumatological centre), blinded to clinical, laboratory data and final diagnoses. Cohen’s kappa coefficient describing inter-rater variability was calculated for each evaluated lesion. Kappa values below 0.20 were considered poor agreement, 0.21–0.40 fair, 0.41–0.60 moderate, 0.61–0.80 good and 0.81–1.00 very good [32]. In case of divergent opinions, the final diagnosis was established by consensus.

Hip MRIs were evaluated with the aim of identifying the number of active, destructive and developmental lesions that were all presented in Table 1. Definitions of lesions were adopted from the European Society of Musculoskeletal Radiology (ESSR) recommendation paper for the use of MRI in musculoskeletal rheumatic diseases [33]. Briefly, joint effusions are hyperintense on T2 and PDw images, hypointense on T1w images [33]. Synovial thickening in the active stage indicating active synovitis, shows high signal intensity on T2w, T2 FS, PD FS and T2 TIRM/STIR (Short Tau Inversion Recovery) sequences but lower than high signal from effusions in these sequences. BME in the course of the inflammation is seen as a hyperintense area on T2 and PDw images, best visualized by T2 FS or STIR/TIRM sequences, hypointense on T1w images [33]. Enthesis is hyperintense on T2 and PDw images, best visualized by T2 FS or STIR/TIRM sequences and is hypointense on T1w images. The bony part of an enthesitis may show BME [33]. Bone erosions are sharply marginated trabecular bone defects with disrupted cortical bone continuity, seen in at least two planes, with low signal intensity on T1-w images. Intraosseous cysts present as high signal intensity foci on T2-w images and low signal intensity on T1-w images and they are better delineated compared with ill-defined areas of BME [33].

Table 1. MRI scoring system.

	MRI Feature	Scoring
1	Effusion	0–3 0: no fluid; 1: trace of fluid and maximum thickness of ≤2 mm 2: continual effusion and thickness >2 mm and ≤5 mm 3: effusion with distension of capsule and thickness >5 mm
2	BME head	0–2 0: BME not seen 1: BME up to 50% of the head width 2: BME > 50% of the head width
3	BME neck	0–2 0: BME not seen 1: BME up to 50% of the neck width 2: BME > 50% of the neck width
4	BME acetabulum	0–2 0: BME not seen 1: BME up to 50% of the acetabular width 2: BME > 50% of the acetabular width
5	BME greater trochanter	0–1
6	Synovitis	0–1 0: synovium not visible 1: synovium visible regardless the thickness
7	Bursitis	0–1
8	Enthesitis	0–1

Table 1. *Cont.*

	MRI Feature	Scoring
9	Tendinitis	0–1
10	Myositis	0–1
11	Triradiate cartilage involvement	0–1
12	Physeal involvement	0–1
13	Cyst femoral head	0–1
14	Cyst acetabulum	0–1
15	Erosion femoral head	0–1
16	Erosion acetabulum	0–1
17	Chondromalacia	0–1
18	Joint space narrowing	0–1
19	Protrusio acetabuli	0–1
20	Ankylosis	0–1
21	Sclerotization	0–1
22	Osteophytes	0–1
23	Avascular necrosis	0–1
24	Bone remodeling	0–1

All active, destructive and developmental lesions were then scored and the MRI scoring system is presented in Table 1.

In addition, other inflammatory features in the pelvis were reported, within the field of view, such as sacroiliitis, pubitis and involvement of ischiopubic synchondrosis.

2.3. Statistical Analysis

To identify if MRI allows hip arthritis in JIA to be differentiated from hip arthralgia of unknown etiology firstly, the MRI lesions were presented as numbers and percentages. The chi-squared test (or a chi-squared test with Yates’ correction when the expected values were <5) was used for comparisons between groups. The receiver operating characteristic (ROC) curve analysis was used to verify the discriminant ability of the MRI summarized score. Sensitivity, specificity, positive predictive value (PPV) and negative predictive value (NPV) of the created diagnostic test were calculated. The statistical significance was established at $p < 0.05$. Statistical analyses were performed using Statistica v.13.1 (Dell Inc 2016, Tulsa, OK, USA).

3. Results

This retrospective observational study included 97 children with clinically suspected arthritis in whom non-contrast MRI of the hips was performed from 2016 to 2019. The median age of the patients was 14 years (range: 4–16 years) with a slight male predominance (52 male; 45 female).

Among the 97 included patients, JIA was confirmed in 73 (75%): 31 had oligoarthritis, 13 had the enthesitis-related arthritis subtype, 10 had polyarthritis, three had psoriatic arthritis, three had systemic JIA and 13 had undifferentiated JIA. In the remaining 24 (25%) patients, JIA was excluded and arthralgia of unknown etiology was diagnosed.

MRI showed at least one lesion in 95 patients (98%). Abnormalities in right hips were seen in five children, in left hips in six children and both hips were affected in the remaining 84 patients. Only two children were lesions free. Table 2 shows the MRI scoring results in the JIA group and the non-JIA group, divided into the left and right hips. Table 3 presents the frequency of MRI features in the compared groups.

Table 2. MRI scoring results for left and right hips.

	MRI Lesions and Scorings	JIA Confirmed Group <i>n</i> = 73		Non-JIA Group <i>n</i> = 24	
		Number of Lesions		Number of Lesions	
		Left Hip	Right Hip	Left Hip	Right Hip
1	Effusion				
	0	6	7	3	3
	1	59	54	20	20
	2	4	6	1	1
2	3	4	6	0	0
	BME head				
	0	62	66	24	23
	1	9	3	0	1
3	2	2	4	0	0
	BME neck				
	0	66	67	24	24
	1	4	4	0	0
4	2	3	2	0	0
	BME acetabulum				
	0	70	68	24	24
	1	3	3	0	0
5	2	0	2	0	0
	BME greater trochanter				
	0	66	69	24	24
	1	7	4	0	0
6	Synovitis				
	0	67	64	24	24
	1	6	9	0	0
	Bursitis				
7	0	68	72	23	24
	1	5	1	1	0
	Enthesitis				
	0	65	66	24	24
8	1	8	7	0	0
	Tendinitis				
	0	73	73	24	24
	1	0	0	0	0
9	Myositis				
	0	72	71	24	24
	1	1	2	0	0
	Triradiate cartilage involvement				
10	0	72	72	24	24
	1	1	1	0	0
	Physal involvement				
	0	73	73	24	24
11	1	0	0	0	0

Table 2. Cont.

	MRI Lesions and Scorings	JIA Confirmed Group <i>n</i> = 73		Non-JIA Group <i>n</i> = 24	
		Number of Lesions		Number of Lesions	
		Left Hip	Right Hip	Left Hip	Right Hip
13	Cyst femoral head	71	72	24	24
	1	2	1	0	0
14	Cyst acetabulum	72	72	24	24
	1	1	1	0	0
15	Erosion femoral head	73	71	24	24
	1	0	2	0	0
16	Erosion acetabulum	72	73	24	24
	1	1	0	0	0
17	Chondromalacia	68	71	24	24
	1	5	2	0	0
18	Joint space narrowing	71	70	24	24
	1	2	3	0	0
19	Protrusio acetabuli	73	73	24	24
	1	0	0	0	0
20	Ankylosis	73	73	24	24
	1	0	0	0	0
21	Sclerotization	73	73	24	24
	1	0	0	0	0
22	Osteophytes	73	73	24	24
	1	0	0	0	0
23	Avascular necrosis	71	72	24	23
	1	2	1	0	1
24	Bone remodeling	72	72	24	23
	1	1	1	0	1

Table 3. Frequency of MRI features in the compared groups.

	MRI Feature and Scoring at Least in One Hip	JIA Confirmed Group	Non-JIA Group	<i>p</i> *
1	Effusion			
	0	12 (16%)	5 (21%)	0.856
	1	66 (90%)	22 (92%)	0.825
	2	8 (11%)	1 (4%)	0.555
	3	10 (14%)	0 (0%)	0.127
	2 or 3	17 (23%)	1 (4%)	0.074
2	BME head			
	0	71 (97%)	24 (100%)	0.993
	1	11 (15%)	1 (4%)	0.294
	2	6 (8%)	0 (0%)	0.336
	1 or 2	16 (22%)	1 (4%)	0.094
3	BME neck			
	0	72 (99%)	24 (100%)	0.556
	1	8 (11%)	0 (0%)	0.206
	2	5 (7%)	0 (0%)	0.433
	1 or 2	12 (16%)	0 (0%)	0.078
4	BME acetabulum			
	0	72 (99%)	24 (100%)	0.556
	1	6 (8%)	0 (0%)	0.336
	2	2 (3%)	0 (0%)	0.993
	1 or 2	7 (10%)	0 (0%)	0.263
5	BME greater trochanter			
	0	70 (96%)	24 (100%)	0.742
	1	8 (11%)	0 (0%)	0.206
6	Synovitis			
	0	73 (100%)	24 (100%)	1
	1	15 (21%)	0 (0%)	0.037
7	Bursitis			
	0	72 (99%)	24 (100%)	0.556
	1	5 (7%)	1 (4%)	0.988
8	Enthesitis			
	0	72 (99%)	24 (100%)	0.556
	1	14 (19%)	0 (0%)	0.047
9	Tendinitis			
	0	73 (100%)	24 (100%)	1
	1	0 (0%)	0 (0%)	1
10	Myositis			
	0	73 (100%)	24 (100%)	1
	1	3 (4%)	0 (0%)	0.742
11	Triradiate cartilage involvement			
	0	73 (100%)	24 (100%)	1
	1	1 (1%)	0 (0%)	0.556
12	Physal involmment			
	0	73 (100%)	24 (100%)	1
	1	0 (0%)	0 (0%)	1
13	Cyst femoral head			
	0	73 (100%)	24 (100%)	1
	1	3 (4%)	0 (0%)	0.742

Table 3. Cont.

	MRI Feature and Scoring at Least in One Hip	JIA Confirmed Group	Non-JIA Group	<i>p</i> *
14	Cyst acetabulum			
	0	73 (100%)	24 (100%)	1
15	Erosion femoral head			
	0	73 (100%)	24 (100%)	1
16	Erosion acetabulum			
	0	73 (100%)	24 (100%)	1
17	Chondromalacia			
	0	73 (100%)	24 (100%)	1
18	Joint space narrowing			
	0	72 (99%)	24 (100%)	0.556
19	Protrusio acetabuli			
	0	73 (100%)	24 (100%)	1
20	Ankylosis			
	0	73 (100%)	24 (100%)	1
21	Sclerotization			
	0	73 (100%)	24 (100%)	1
22	Osteophytes			
	0	73 (100%)	24 (100%)	1
23	Avascular necrosis			
	0	73 (100%)	24 (100%)	1
24	Bone remodeling			
	0	72 (99%)	23 (96%)	0.556
	1	1 (1%)	1 (4%)	0.993

* The *p*-value refers to a comparison of the frequency of the score listed in the first column to the frequency of all other scores for that feature, for example (2 or 3) for effusion is the comparison of scores (2 or 3) vs. (1 or 0). Values of one feature do not add up to 100%, because the scores relate to assessment in at least one hip in each child (as noted in the column header).

Effusion was the most frequent abnormality (Figure 1). Almost all children had joint effusion of stage 1, 2, or 3 (*n* = 95, 98%). Stage 1 effusion was most frequently identified in all children, regardless of diagnosis (i.e., 90% vs. 92% in the JIA vs. non-JIA group, respectively); thus, it had no discriminatory value (*p* = 0.825). In contrast, the incidence of stage 2 and 3 effusion was higher in JIA patients than in the non-JIA group (25% vs. 4%, respectively), with stage 3 effusion only present in the JIA group. The next most common abnormalities were BME in the femoral head, synovitis, enthesitis and BME in the neck of the femur (Tables 2 and 3) (Figures 1 and 2).

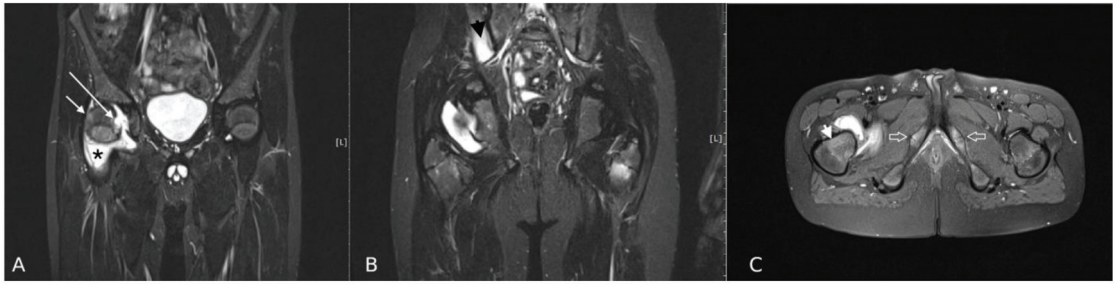


Figure 1. MRI of the hips in a 10-year-old boy with JIA: (A,B) Coronal T2 TIRM, (C) Axial T2 TIRM images. Right hip: joint effusion (stage 3), synovitis (stage 1) (asterisk), BME in femoral head (stage 1) (white short arrow), BME in the neck of femur (stage 2) (arrowhead on “C”), erosion in the femoral head (white long arrow). Left hip: BME in the femoral neck (stage 2). Right sided sacroiliitis (arrowhead on “B”). Involvement of ischiopubic synchondrosis bilaterally (empty arrows on “C”).

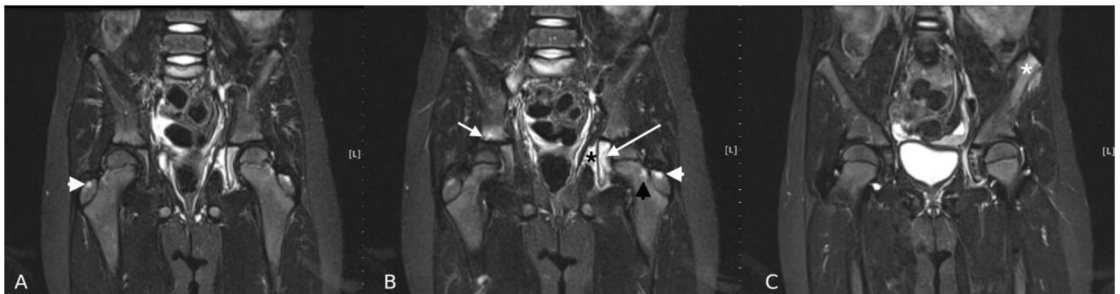


Figure 2. MRI of the hips in a 7-year-old girl with JIA. (A–C) Coronal T2 TIRM images. Right hip: BME in the greater trochanter (stage 1) (arrowhead) and in the acetabulum (stage 1) (white short arrow). Left hip: BME in the greater trochanter (stage 1) (white arrowhead), in the acetabulum (stage 2) and triradiate cartilage (stage 1) (white long arrow) and in the femoral neck (stage 1) (black arrowhead). Obturator internus myositis (stage 1) (black asterisk). Left anterior superior iliac spine (ASIS) enthesitis (white asterisk). Right sided sacroiliitis.

All lesions were more common in the JIA group than the non-JIA group; however, none of them was significantly more common in JIA vs. non-JIA group. Several lesions were approaching the level of significance $p < 0.05$: in JIA group effusion 2 or 3 were seen in 23% vs. 4% ($p = 0.074$), BME within femoral head in 22% vs. 4% ($p = 0.094$) and BME of the femoral neck in 16% vs. 0% ($p = 0.078$). BME within the neck, acetabulum and greater trochanter, stage 2 BME in the head of the femur, stage 3 effusion, as well as synovitis, myositis and triradiate cartilage involvement were exclusively seen in the JIA group (Tables 2 and 3). Destructive lesions were only diagnosed in JIA group and most frequent were: chondromalacia, followed by JSN, cysts and erosions (Tables 2 and 3). None of the 97 patients had protrusio acetabuli, ankylosis, physis involvement, or secondary osteoarthritis features, such as sclerotization and osteophytes. Single cases of AVN and bone remodeling (widening of the femoral neck) were seen in both groups (Tables 2 and 3).

Sacroiliitis was observed in four (5%) children with JIA and in one (4%) without a final diagnosis of JIA ($p = 0.780$) (Figures 1 and 2). Pubitis was present in two children with JIA (3%) and in none from the non-JIA group ($p = 0.993$).

There was a very good interobserver agreement for scoring all active and destructive lesions, except for six features: BME in the head of femur (two cases, kappa 0.94), BME in the neck of the femur (two cases, kappa 0.91), joint effusion (one case, kappa 0.99) and gluteus medius tendon enthesitis (one case, kappa 0.98). In all 6 cases of interobserver disagreements the border scores were provided, including: score 0 was given by one observer and score 1 by the second in case of discrete BME in the femoral head, score 1 and

2 when BME was around 50% of femoral head and score 0 and 1 in case of small joint fluid, that was interpreted as physiology by one observer and as a small effusion by the second.

Due to the fact that any single lesion was significantly more common in children with JIA compared to the non-JIA group, we decided to build a scoring. The MRI summarized score was the sum of scorings of all hip lesions in an individual patient. The score included all 24 lesions presented in Table 1. The frequencies of MRI scores in the whole group of patients are presented in Figure 3.

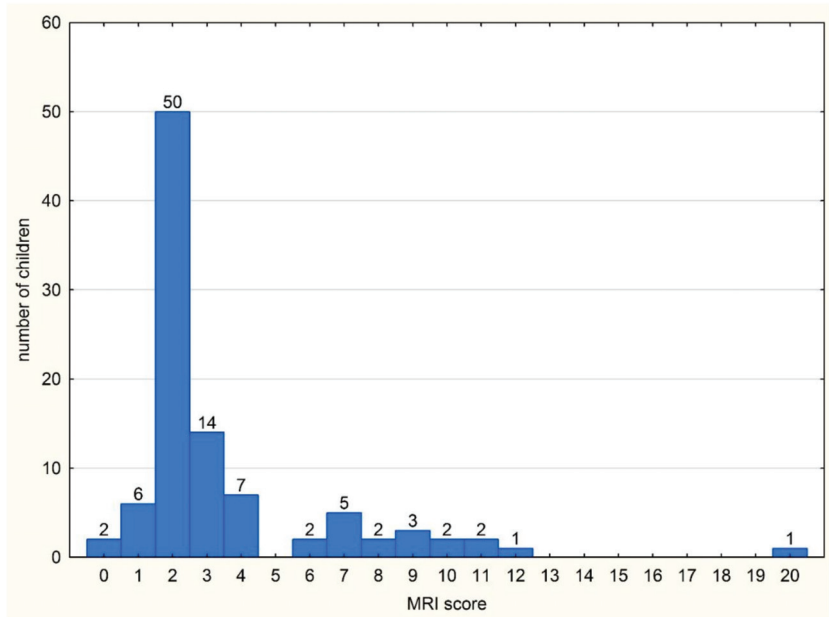


Figure 3. The frequency of individual MRI scores in the whole group of patients ($n = 97$).

The median interquartile range (IQR) of MRI summarized score was significantly higher in patients with a final diagnosis of JIA compared to the non-JIA group: median (IQR) 3 (2–5) vs. 2 (2–2), respectively, $p = 0.002$.

Table 4 shows the properties of diagnostic tests based on MRI summarized score values. At the cut-off point set at 3, the MRI summarized score has a sensitivity of 48% and a specificity of 83%. However, if a patient has an MRI summarized score of 6, the specificity of the method increases to 100%, but the sensitivity drops to 25%. The area under the curve (AUC) for this diagnostic test amounted to 0.704 (95% confidence interval (CI): 0.595–0.813), indicating good discriminative ability between JIA and non-JIA (Figure 4).

Table 4. Diagnostic value of the summarized MRI score as a predictor of JIA.

MRI Summarised Score	JIA	Non-JIA	True Pos.	False Pos.	False Neg.	True Neg.	Sens.	Spec.	PPV	NPV
20	1	0	1	0	72	24	0.014	1.000	1.000	0.250
12	1	0	2	0	71	24	0.027	1.000	1.000	0.253
11	2	0	4	0	69	24	0.055	1.000	1.000	0.258
10	2	0	6	0	67	24	0.082	1.000	1.000	0.264
9	3	0	9	0	64	24	0.123	1.000	1.000	0.273
8	2	0	11	0	62	24	0.151	1.000	1.000	0.279
7	5	0	16	0	57	24	0.219	1.000	1.000	0.296
6	2	0	18	0	55	24	0.247	1.000	1.000	0.304

Table 4. Cont.

MRI Summarised Score	JIA	Non-JIA	True Pos.	False Pos.	False Neg.	True Neg.	Sens.	Spec.	PPV	NPV
4	6	1	24	1	49	23	0.329	0.958	0.960	0.319
3	11	3	35	4	38	20	0.479	0.833	0.897	0.345
2	34	16	69	20	4	4	0.945	0.167	0.775	0.500
1	3	3	72	23	1	1	0.986	0.042	0.758	0.500
0	1	1	73	24	0	0	1.000	0.000	0.753	

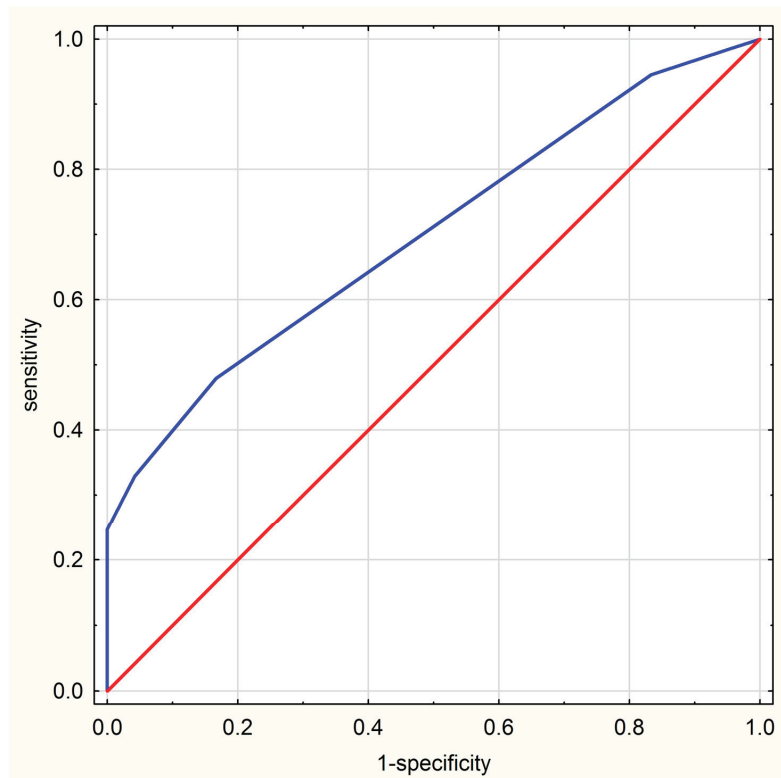


Figure 4. ROC curve of MRI score.

4. Discussion

MRI allows hip arthritis in JIA to be differentiated from hip arthralgia of unknown etiology with good specificity, thus, may be helpful in confirming the diagnosis of JIA. Despite limited sensitivity, the specificity of MRI is high and for the summarized score 6 it comes to 100%.

Over the last decade, there has been an increasing move towards earlier and more aggressive treatment of JIA with methotrexate and biological therapy in the hope of preventing joint damage [8,34]. However, in the context of coxitis, decisions to escalate treatment may be limited because of the difficulties in confirming arthritis by clinical examination [4,11,16,34–36].

Contrary to wrist and knee joints, only a few studies have examined the role of MRI in evaluating hip disease in JIA [5,6,8,11]. Our findings indicate that MRI is more useful in

confirming hip arthritis in JIA than clinical assessment. Likewise, a higher sensitivity of MRI over clinical diagnosis was reported by El-Azeem et al. [4] and Nistala et al. [11].

The most common abnormality was stage 1 effusion, in both JIA-confirmed and non-JIA groups (90% vs. 92%, respectively) and had no discriminatory value ($p = 0.825$). Stage 1 effusion, which was a trace of fluid (thickness ≤ 2 mm) was also used in other researchers' staging systems for hip joint [4,27,37]. At the same time, such small amounts of fluid in the hip were detected in healthy joints and was regarded as physiologic [22,37]. In a study performed on adult patients with normal and ischemic hips [37], stage 1 fluid was seen in the majority of asymptomatic hips (95%), whereas stage 2 fluid (surrounding the femoral neck) was present in only four hips (5%) and none had stage 3 effusion.

Synovitis, which is a hallmark of joint inflammation, was significantly more common in the JIA group than in the non-JIA group (15 vs. 0 patients; $p = 0.037$). We used a score of 1 if any visible synovium was observed in the hip on non-contrast MRI, regardless of its thickness. This classification is in contrast to most other MRI studies on different joints in JIA, where an abnormal synovium was defined as a thickness of ≥ 2 mm [2,4,8,27], or the thickness was not specified [5,6,11]. We chose to include any visible synovium as there is limited data on the normal values for synovium thickness. In healthy individuals, the synovium comprises an intimal layer, which is 20–40 μm thick in cross-section and an areolar subintima, which can be up to 5 mm in thickness [38]. Meanwhile, El-Azeem et al. [4] reported that the synovial thickness in clinically active juvenile hips was 3.56 ± 1.81 mm, indicating that a synovial thickness of less than 2 mm layer can be pathologic. Therefore, more studies are needed to define normal and pathologic values for the synovium on MRI.

We did not use an intravenous contrast agent in this study, as it not only prolongs the examination time, increases costs and patient discomfort and has an added (albeit rarely in MRI) risk of allergic reactions. The most important risks in pediatric JIA patients are those connected with the accumulation of the contrast agent in the kidneys and basal ganglia, even after a prolonged period [20,21]. As JIA often involves numerous joints and contrast agent must be injected for multiple examinations (i.e., for both diagnosis and monitoring), it can cause a significant burden. Hemke et al. [2] found unenhanced MRI of the knee joint of low sensitivity (0.62) than Gadolinium-enhanced MRI for the detection of synovial hypertrophy, but specificity remained high (0.97). On the other hand, Nusman et al. found enhancing synovium in 52% of the knees in healthy children [39]. The current study showed that non-contrast MRI of hip joints is satisfactory in discriminating between JIA and non-JIA patients and—with the use of the proposed MRI summarized score—may diagnose JIA with a specificity up to 100%. These results are promising; however, more studies focused on the hip joint are needed to confirm the findings.

Features of advanced hip damage (such as cysts, erosions, chondromalacia and JSN) were only observed in the JIA group in three patients. The disease duration in these patients was nine months in one patient and nine years in the other two. AVN was observed in four children: three in the JIA group and one in the non-JIA group. AVN is more common in older juveniles [1] and, indeed, our patients were 13 years (two patients) and 16 years (two patients). Only one patient was taking corticosteroids for three months before MRI. This is in agreement with observations that AVN in rheumatic patients is not exclusively related to steroid intake but may also result from the disease itself (i.e., the released cytokines or vasculopathy) [40].

As for now, the role of imaging is limited for the diagnosis of JIA, because it is based on the clinical findings and laboratory data. However, the recent classification criteria proposed by Pediatric Rheumatology International Trials Organization (PRINTO) already recommend the use of imaging to evaluate sacroiliitis [30,41]. For the hip joint, which is also difficult to assess by clinical examination, when radiographs and ultrasound findings are equivocal, an MRI could be performed to confirm the diagnosis and for narrowing the differential diagnoses [29]. The proposed scoring may have practical applicability in predicting JIA involvement. Based on results it can be concluded that a child who has the MRI summarized score of at least 6 has a high probability of suffering from JIA. In future

studies, these values may be modified and another cut-off value might be proposed based on the frequency of diagnosed lesions; some features might be deleted whereas others, e.g., those at the border of significance (effusion, BME) may become significant.

The main strength of this study is the inclusion of a large number of patients. All children were referred from a single pediatric rheumatology center, indicating the clinical examination was reliable. Another benefit of this study is a large number of MRI features (24 altogether) included in the scoring system, which improves statistical characteristics of proposed diagnostic test. Short time needed to fill the scoring sheet (c.a. 2 min) is also encouraging.

The main limitation of this study was omitting the contrast agent. This was a conscious decision reflecting the authors' everyday practice. Moreover, the study did not include a healthy control group and only hip joints in children without a final diagnosis of JIA served for comparison. While it is hard to get pediatric and adolescent control data, these would be absolutely required for future.

5. Conclusions

MRI is useful in confirming hip inflammatory features in children with clinically suspected arthritis. Patients with JIA develop more lesions and are more advanced than children with hip arthralgia of unknown origin. The MRI allows hip arthritis in JIA to be differentiated from hip arthralgia of unknown etiology with good specificity and, thus, may be helpful in confirming the diagnosis of JIA. Future studies are needed to validate this new scoring system and to further investigate for clinical practice.

Author Contributions: Conception or design of the work: M.O. and I.S.-S.; Data collection: M.O., I.S.-S., P.G. and E.M.; Data analysis and interpretation M.O., I.S.-S., M.M., P.G. and E.M.; Drafting the article: M.O., I.S.-S., P.G., E.M. and M.M.; Critical revision of the article: M.O., I.S.-S., M.M., P.G. and E.M.; Final approval of the version to be published M.O., I.S.-S., M.M., P.G. and E.M. All authors have read and agreed to the published version of the manuscript.

Funding: This research received no external funding.

Institutional Review Board Statement: The study was conducted according to the guidelines of the Declaration of Helsinki, and approved by the Institutional Ethics Committee of the National Institute of Geriatrics, Rheumatology and Rehabilitation in Warsaw (KBT-3/5/2018).

Informed Consent Statement: Informed consent was obtained from all subjects involved in the study.

Conflicts of Interest: The authors declare no conflict of interest.

References

1. Rostom, S.; Amine, B.; Bensabbah, R.; Abouqal, R.; Hajjaj-Hassouni, N. Hip involvement in juvenile idiopathic arthritis. *Clin. Rheumatol.* **2008**, *27*, 791–794. [[CrossRef](#)] [[PubMed](#)]
2. Hemke, R.; Kuijpers, T.W.; Berg, J.v.D.; Van Veenendaal, M.; Dolman, K.M.; Van Rossum, M.A.J.; Maas, M. The diagnostic accuracy of unenhanced MRI in the assessment of joint abnormalities in juvenile idiopathic arthritis. *Eur. Radiol.* **2013**, *23*, 1998–2004. [[CrossRef](#)] [[PubMed](#)]
3. Lovell, D.J. Juvenile idiopathic arthritis: Clinical features. In *Primer on the Rheumatic Diseases*; Klippel, J.H., Stone, J.H., Crofford, L.J., White, P.F., Eds.; Springer: New York, NY, USA, 2008; pp. 142–148.
4. El-Azeem, M.I.A.; Taha, H.A.; El-Sherif, A.M. Role of MRI in evaluation of hip joint involvement in juvenile idiopathic arthritis. *Egypt. Rheumatol.* **2012**, *34*, 75–82. [[CrossRef](#)]
5. I Argyropoulou, M.; Fanis, S.L.; Xenakis, T.; Efremidis, S.C.; Siamopoulou, A. The role of MRI in the evaluation of hip joint disease in clinical subtypes of juvenile idiopathic arthritis. *Br. J. Radiol.* **2002**, *75*, 229–233. [[CrossRef](#)] [[PubMed](#)]
6. Murray, J.G.; Ridley, N.T.; Mitchell, N.; Rooney, M. Juvenile chronic arthritis of the hip: Value of contrast-enhanced MR imaging. *Clin. Radiol.* **1996**, *51*, 99–102. [[CrossRef](#)]
7. Sudoł-Szopińska, I.; Jans, L.; Jurik, A.G.; Hemke, R.; Eshed, I.; Boutry, N. Imaging Features of the Juvenile Inflammatory Arthropathies. *Semin. Musculoskelet. Radiol.* **2018**, *22*, 147–165. [[CrossRef](#)]
8. Malattia, C.; Damasio, M.B.; Basso, C.; Verri, A.; Magnaguagno, F.; Viola, S.; Gattorno, M.; Ravelli, A.; Toma, P.; Martini, A. Dynamic contrast-enhanced magnetic resonance imaging in the assessment of disease activity in patients with juvenile idiopathic arthritis. *Rheumatology* **2009**, *49*, 178–185. [[CrossRef](#)] [[PubMed](#)]

9. Avenarius, D.F.M.; Nusman, C.; Malattia, C.; de Horatio, L.T.; Rosendahl, K.; Maas, M.; Müller, L.-S.O. Current status of wrist imaging in juvenile idiopathic arthritis. *Pediatr. Radiol.* **2018**, *48*, 801–810. [[CrossRef](#)]
10. Shelmerdine, S.C.; Di Paolo, P.L.; De Horatio, L.T.; Malattia, C.; Magni-Manzoni, S.; Rosendahl, K. Imaging of the hip in juvenile idiopathic arthritis. *Pediatr. Radiol.* **2018**, *48*, 811–817. [[CrossRef](#)]
11. Nistala, K.; Babar, J.; Johnson, K.; Campbell-Stokes, P.; Foster, K.; Ryder, C.; McDonagh, J. Clinical assessment and core outcome variables are poor predictors of hip arthritis diagnosed by MRI in juvenile idiopathic arthritis. *Rheumatology* **2006**, *46*, 699–702. [[CrossRef](#)]
12. Friedman, S.; A Gruber, M. Ultrasonography of the hip in the evaluation of children with seronegative juvenile rheumatoid arthritis. *J. Rheumatol.* **2002**, *29*, 629–632.
13. Packham, J.C.; Hall, M.A. Long-term follow-up of 246 adults with juvenile idiopathic arthritis: Functional outcome. *Rheumatology* **2002**, *41*, 1428–1435. [[CrossRef](#)]
14. Janet, M.; Greg, I.; Karl, J. MRI in juvenile idiopathic arthritis and juvenile dermatomyositis. *Ann. N. Y. Acad. Sci.* **2009**, *1154*, 52–83.
15. McKay, G.M.; A Cox, L.; Long, B.W. Imaging juvenile idiopathic arthritis: Assessing the modalities. *Radiol. Technol.* **2010**, *81*, 318–327. [[PubMed](#)]
16. Gylys-Morin, V.M.; Graham, T.B.; Blebea, J.S.; Dardzinski, B.J.; Laor, T.; Johnson, N.D.; Oestreich, A.E.; Passo, M.H. Knee in Early Juvenile Rheumatoid Arthritis: MR Imaging Findings. *Radiology* **2001**, *220*, 696–706. [[CrossRef](#)] [[PubMed](#)]
17. Sudoł-Szopińska, I.; Kontny, E.; Maśliński, W. The pathogenesis of rheumatoid arthritis in radiological studies. Part I: For-mation of inflammatory infiltrates within the synovial membrane. *J. Ultrason.* **2012**, *12*, 202–213. [[CrossRef](#)]
18. Ostrowska, M.; Maśliński, W.; Prochorec-Sobieszek, M.; Nieciecki, M.; Sudoł-Szopińska, I. Cartilage and bone damage in rheumatoid arthritis. *Reumatologia* **2018**, *56*, 111–120. [[CrossRef](#)] [[PubMed](#)]
19. McQueen, F.M. Magnetic resonance imaging in early inflammatory arthritis: What is its role? *Rheumatology* **2000**, *39*, 700–706. [[CrossRef](#)] [[PubMed](#)]
20. Gulani, V.; Calamante, F.; Shellock, F.G.; Kanal, E.; Reeder, S.B. International Society for Magnetic Resonance in Medicine. Gadolinium deposition in the brain: Summary of evidence and recommendations. *Lancet Neurol.* **2017**, *16*, 564–570. [[CrossRef](#)]
21. Ranga, A.; Agarwal, Y.; Garg, K.J. Gadolinium based contrast agents in current practice: Risks of accumulation and toxicity in patients with normal renal function. *Indian J. Radiol. Imaging* **2017**, *27*, 141–147. [[CrossRef](#)]
22. Panwar, J.; Tolend, M.; Redd, B.; Srinivasalu, H.; Colbert, R.A.; Akikusa, J.; Appenzeller, S.; Carrino, J.A.; Herregods, N.; Jans, L.; et al. Consensus-driven conceptual development of a standardized whole body-MRI scoring system for assessment of disease activity in juvenile idiopathic arthritis: MRI in JIA OMERACT working group. *Semin. Arthritis Rheum.* **2021**. [[CrossRef](#)] [[PubMed](#)]
23. Liu, S.W.; Velez, N.F.; Lam, C.E.; Femia, A.; Granter, S.R.; Townsend, H.B.; Vleugels, R.A. Dermatomyositis induced by anti-tumour necrosis factor in a patient with juvenile idio-pathic arthritis. *JAMA Dermatol.* **2013**, *149*, 1204–1208. [[CrossRef](#)]
24. Gietka, P.; Rutkowska-Sak, L.; Lisowska, B. Myositis in the course of the systemic form juvenile idiopathic arthritis. *Reumatologia/Rheumatology* **2014**, *2*, 142–145. [[CrossRef](#)]
25. Lindehammar, H.; Lindvall, B. Muscle involvement in juvenile idiopathic arthritis. *Rheumatology* **2004**, *43*, 1546–1554. [[CrossRef](#)] [[PubMed](#)]
26. Lindehammar, H.; Bäckman, E. Muscle function in juvenile chronic arthritis. *J. Rheumatol.* **1995**, *22*, 1159–1165. [[PubMed](#)]
27. Kirkhus, E.; Flatø, B.; Riise, O.; Reiseter, T.; Smith, H.-J. Differences in MRI findings between subgroups of recent-onset childhood arthritis. *Pediatr. Radiol.* **2010**, *41*, 432–440. [[CrossRef](#)] [[PubMed](#)]
28. Porter-Young, F.M.; Offiah, A.C.; Broadley, P.; Lang, I.; McMahon, A.-M.; Howsley, P.; Hawley, D.P. Inter- and intra-observer reliability of contrast-enhanced magnetic resonance imaging parameters in children with suspected juvenile idiopathic arthritis of the hip. *Pediatr. Radiol.* **2018**, *48*, 1891–1900. [[CrossRef](#)] [[PubMed](#)]
29. Hemke, R.; Herregods, N.; Jaremko, J.L.; Åström, G.; Avenarius, D.; Becce, F.; Bielecki, D.K.; Boesen, M.; Dalili, D.; Giraudo, C.; et al. Imaging assessment of children presenting with suspected or known juvenile idiopathic arthritis: ESSR-ESPR points to consider. *Eur. Radiol.* **2020**, *30*, 5237–5249. [[CrossRef](#)]
30. Martini, A.; Ravelli, A.; Avcin, T.; Beresford, M.W.; Burgos-Vargas, R.; Cuttica, R.; Ilowite, N.T.; Khubchandani, R.; Laxer, R.M.; Lovell, D.J.; et al. Toward New Classification Criteria for Juvenile Idiopathic Arthritis: First Steps, Pediatric Rheumatology International Trials Organization International Consensus. *J. Rheumatol.* **2018**, *46*, 190–197. [[CrossRef](#)] [[PubMed](#)]
31. Petty, R.E.; Southwood, T.R.; Manners, P.; Baum, J.; Glass, D.N.; Goldenberg, J.; He, X.; Maldonado-Cocco, J.; Orozco-Alcala, J.; Prieur, A.-M.; et al. International League of Associations for Rheumatology classification of juvenile idiopathic arthritis: Second revision, Edmonton, 2001. *J. Rheumatol.* **2004**, *31*, 390–392. [[PubMed](#)]
32. Landis, J.R.; Koch, G.G. The Measurement of Observer Agreement for Categorical Data. *Biometrics* **1977**, *33*, 159–174. [[CrossRef](#)] [[PubMed](#)]
33. Jurik, A.G.; Eshed, I.; Lennart, J.; Grainger, A.; Østergaard, M.; Klausner, A.; Cotten, A.; Wick, M.C.; Maas, M.; Miese, F.; et al. Recommendations of the ESSR Arthritis Subcommittee for the Use of Magnetic Resonance Imaging in Musculoskeletal Rheumatic Diseases. *Semin. Musculoskelet. Radiol.* **2015**, *19*, 396–411. [[CrossRef](#)] [[PubMed](#)]
34. Ramanan, A.V.; Whitworth, P.; Baildam, E.M. Use of methotrexate in juvenile idiopathic arthritis. *Arch. Dis. Child.* **2003**, *88*, 197–200. [[CrossRef](#)]

35. Mitchell, D.G.; Rao, V.; Dalinka, M.; E Spritzer, C.; Gefter, W.B.; Axel, L.; Steinberg, M.; Kressel, H.Y. MRI of joint fluid in the normal and ischemic hip. *Am. J. Roentgenol.* **1986**, *146*, 1215–1218. [[CrossRef](#)] [[PubMed](#)]
36. Koski, J.M. Ultrasonographic evidence of hip synovitis in patients with rheumatoid arthritis. *Scand. J. Rheumatol.* **1989**, *18*, 127–131. [[CrossRef](#)]
37. Rydholm, U.; Wingstrand, H.; Egund, N.; Elborg, R.; Forsberg, L.; Lidgren, L. Sonography, arthroscopy, and intracapsular pressure in juvenile chronic arthritis of the hip. *Acta Orthop. Scand.* **1986**, *57*, 295–298. [[CrossRef](#)] [[PubMed](#)]
38. Smith, M.D.; Wechalekar, M.D. The synovium. In *Rheumatology*, 6th ed.; Mosby: Philadelphia, PA, USA, 2015; pp. 27–32.
39. Nusman, C.M.; Hemke, R.; Benninga, M.A.; Schonenberg-Meinema, D.; Kindermann, A.; van Rossum, M.A.J.; van den Berg, J.M.; Maas, M.; Kuijpers, T.W. Contrast-enhanced MRI of the knee in children unaffected by clinical arthritis compared to clinically active juvenile idiopathic arthritis patients. *Eur. Radiol.* **2016**, *26*, 1141–1148. [[CrossRef](#)] [[PubMed](#)]
40. Horton, D.B.; Haynes, K.; Denburg, M.R.; Thacker, M.; Rose, C.D.; E Putt, M.; Leonard, M.B.; Strom, B.L. Oral glucocorticoid use and osteonecrosis in children and adults with chronic inflammatory diseases: A population-based cohort study. *BMJ Open* **2017**, *7*, e016788. [[CrossRef](#)] [[PubMed](#)]
41. Lambert, R.; Bakker, P.A.C.; Van Der Heijde, D.; Weber, U.; Rudwaleit, M.; Hermann, K.-G.; Sieper, J.; Baraliakos, X.; Bennett, A.; Braun, J.; et al. Defining active sacroiliitis on MRI for classification of axial spondyloarthritis: Update by the ASAS MRI working group. *Ann. Rheum. Dis.* **2016**, *75*, 1958–1963. [[CrossRef](#)]

Article

Radiological Evaluation of Cervical Spine Involvement in Rheumatoid Arthritis: A Cross-Sectional Retrospective Study

Mateusz Kotecki ^{1,*}, Robert Gasik ², Piotr Głuszko ³ and Iwona Sudół-Szopińska ¹

¹ Department of Radiology, National Institute of Geriatrics, Rheumatology and Rehabilitation, 02-637 Warsaw, Poland; sudolszopinska@gmail.com

² Department of Neuroorthopaedics and Neurology, National Institute of Geriatrics, Rheumatology and Rehabilitation, 02-637 Warsaw, Poland; robert.gasik@spartanska.pl

³ Department of Rheumatology, National Institute of Geriatrics, Rheumatology and Rehabilitation, 02-637 Warsaw, Poland; zruj@mp.pl

* Correspondence: mateuszjankotecki@gmail.com; Tel.: +48-694-976-677

Abstract: Background: Cervical spine lesions are a common manifestation of rheumatoid arthritis (RA). The purpose of this study was to conduct a retrospective analysis of radiological lesions in cervical spine in patients with RA and to correlate findings with clinical and laboratory parameters. Methods: Overall, 240 consecutive patients with RA were referred for imaging by clinicians based on symptoms suggesting cervical spine involvement and/or long disease duration. In each patient, lateral radiographs and MRI of the cervical spine were performed. The imaging data were correlated with clinical records and laboratory data. Results: The cervical spine was affected in 179 patients (75%). The most common lesions were anterior atlanto-axial subluxation (AAS; 58%), subaxial subluxation (58%), and demineralization (48%). Cervical spine involvement was linked to longer disease duration ($p = 0.007$), the presence of rheumatoid factor (RF; $p = 0.010$), elevated C-reactive protein (CRP) levels ($p = 0.016$), and accelerated erythrocyte sedimentation rate (ESR; $p = 0.025$). Longer disease duration was associated with anterior AAS ($p = 0.005$), subaxial subluxation ($p = 0.005$), and basilar settling ($p = 0.003$). Conclusions: As many as 75% of RA patients develop lesions that can be observed on radiographs and through MRI. The most frequent radiological findings include anterior AAS and subaxial subluxation. Long disease duration, RF seropositivity, and elevated inflammatory markers were risk factors for cervical spine involvement.

Keywords: cervical spine; rheumatoid arthritis; atlanto-axial subluxation; radiography; magnetic resonance imaging

Citation: Kotecki, M.; Gasik, R.; Głuszko, P.; Sudół-Szopińska, I. Radiological Evaluation of Cervical Spine Involvement in Rheumatoid Arthritis: A Cross-Sectional Retrospective Study. *J. Clin. Med.* **2021**, *10*, 4587. <https://doi.org/10.3390/jcm10194587>

Academic Editor: Santos Castañeda

Received: 26 August 2021

Accepted: 3 October 2021

Published: 5 October 2021

Publisher's Note: MDPI stays neutral with regard to jurisdictional claims in published maps and institutional affiliations.



Copyright: © 2021 by the authors. Licensee MDPI, Basel, Switzerland. This article is an open access article distributed under the terms and conditions of the Creative Commons Attribution (CC BY) license (<https://creativecommons.org/licenses/by/4.0/>).

1. Introduction

Rheumatoid arthritis (RA) is an immune-mediated inflammatory disease affecting numerous joints of the peripheral and axial skeleton. Cervical spine involvement is the third most common manifestation of RA after hands and feet and may develop in 17–88% of patients [1]. Atlanto-axial level is the most frequent cervical spine location of RA with possible life-threatening complications. Chronic inflammation at the C1/C2 joint may lead to the progressive destruction of bones and ligaments causing subluxations [1], with further cervical spine compression and even sudden death [2]. At the subaxial level, the most prevalent lesions are subluxations, but bony ankylosis or spinous process erosions may also occur [1]. The main risk factors for cervical spine involvement in RA include early onset of RA, advanced disease in peripheral joints, presence of rheumatoid factor (RF), and chronic use of corticosteroids [3,4].

Imaging plays an important role in the diagnosis of cervical spine pathologies, with classic radiography being a first-line approach. Magnetic resonance imaging (MRI) and computer tomography (CT) are used for more precise evaluation of bones and soft tissues. MRI has the possibility to show early inflammatory changes such as effusions, synovitis,

bone marrow edema (BME), and the relation of spinal lesions to brain stem, spinal cord, and nerve roots, whereas CT is the most precise technique for complex bone anatomy.

In the last two decades, biological agents have been introduced, and awareness of early RA diagnosis and treatment to prevent chronic complications has grown. Some studies suggest that early aggressive treatment with disease-modifying antirheumatic drugs (DMARDs) may prevent the development of new lesions but does not prevent the progression of existing ones [5]. Given the improved RA management over the past few decades, the aim of this study was to assess the prevalence of RA-specific lesions in cervical spine on radiographs and MRI and to correlate findings with clinical and laboratory parameters.

2. Materials and Methods

The study was approved by the Ethics Committee (no. KBT-3/2/2018). Conventional radiographs in three lateral views (maximum flexion, neutral (resting), and maximum extension) as well as MRI of the cervical spine of 240 consecutive patients with confirmed RA performed at our institution from 1 January 2010 to 28 February 2018 were retrospectively analyzed.

Patients were qualified for imaging by clinicians based on symptoms suggesting cervical spine involvement (e.g., neck pain, limited motion of the cervical spine, numbness of upper extremity) and/or long disease duration. Patients with osteoarthritis served as a control group. Exclusion criteria included past surgery on cervical spine and traumatic lesions. The maximal time interval between radiography and MRI did not exceed 60 days.

MRI was performed in a 1.5 T Siemens Avanto with the use of an 8-channel neck coil. The MRI protocol included sagittal T1-weighted (w), T2-w, T2-w TIRM, axial T2-w, and coronal T2-w sequences as well as postcontrast axial and sagittal T1-w with fat saturation (fs) sequences in some patients.

MRI and radiographic lesions were scored in a binary way: 0—absence of pathology, 1—presence of pathology. On radiographs, the following lesions were scored: (1) in the whole cervical spine: demineralization, cysts and erosions, bone ankylosis, and spinal stenosis; (2) at the C1/C2 level: dens erosions, anterior atlanto-axial subluxation (AAS), basilar settling (vertical AAS), posterior AAS; and (3) at the C2–C7 subaxial level: subluxations (SAS) (Table 1).

Table 1. Prevalence of pathologies in the study group. * MRI results are presented as a gold standard, # Radiography findings are presented as a gold standard as a study providing dynamic assessment of subluxations, contrary to static MRI, \$ Ankylosis is present, when detected by at least one method. AAS: atlanto-axial subluxation, BME: bone marrow edema, MRI: magnetic resonance imaging, ns: not significant (difference between rheumatoid arthritis and control group), SAS: subaxial subluxation.

	MRI Lesions	Radiographic Lesions	Percentage	Control n (%)	Interobserver Kappa Value
C1/C2 level					
BME	11	not applicable	11 (5%)	1 (0.5%)	0.91
Effusions	26	not applicable	26 (11%)	5 (2.5%)	0.89
Pannus	50	not applicable	50 (21%)	1 (0.5%)	0.93
Contrast enhancement	12	not applicable	12 (5%)	0 (0%)	0.83
Dens erosions	36	11	36 (15%) *	2 (1%)	0.89
Anterior AAS	78	140	140 (58%) #	7 (3.5%)	0.79
Posterior AAS	7	0	7 (3%)	0 (0%)	0.83
Lateral AAS	11	not applicable	11 (5%)	0 (0%)	0.84
Vertical AAS	25	27	25 (10%) *	2 (1%)	0.93
Brain stem compression	8	not applicable	8 (3%)	2 (1%) ns	0.95

Table 1. Cont.

	MRI Lesions	Radiographic Lesions	Percentage	Control n (%)	Interobserver Kappa Value
Subaxial C2-C7 level					
BME	11	not applicable	11 (5%)	6 (3%) ns	0.86
Effusions	1	not applicable	1 (0.4%)	0 (0%) ns	0.67
Pannus	1	not applicable	1 (0.4%)	0 (0%) ns	0.67
Contrast enhancement	2	not applicable	2 (1%)	2 (1%) ns	0.66
SAS	102	139	139 (58%) #	78 (39%)	0.83
Whole cervical spine C1-C7					
Ankylosis	14	19	23 (10%) \$	3 (1.5%)	0.87
Spinous process erosions	0	14	14 (6%)	0 (0%)	0.83
Deminerlization	not applicable	114	114 (48%)	35 (18%)	0.76
Myelopathy	14	not applicable	14 (6%)	7 (3.5%) ns	0.92
Cervical spine compression	72	not applicable	72 (30%)	59 (30%) ns	0.95
Spinal stenosis	93	64	93 (39%) *	72 (36%) ns	0.92
Total	138 (58%)	159 (66%)	179 (75%)	95 (48%)	

On MRI, bone marrow edema (BME) in the cervical spine, cysts, erosions, bone ankylosis, spinal stenosis, and the compression of brain stem or spinal cord and myelopathy were evaluated. In addition, at the C1/C2 level joint effusion, inflammatory pannus and lateral subluxation were reported, and at the C2–C7 level, the presence of SAS was reported (Table 1).

Anterior AAS was reported when the distance between the posterior surface of the anterior arch of the atlas and anterior margin of the dens exceeded 3 mm [1]. The anterior atlanto-dental interval was calculated in neutral position and if eligible in flexion. A posterior atlanto-dental interval (PADI) less than 14 mm required prompt neurosurgical consultation (potential cord compromise, compression) [1]. Lateral AAS was diagnosed when there was >2 mm displacement or an asymmetry of dens in relation to C1 body [6]. Basilar settling (i.e., vertical AAS, cranial settling) was considered when the apex of dens was located >4.5 mm above McGregor's line [7]. SAS was considered when there was >2 mm displacement between adjacent vertebrae [8].

For assessment of cervical spinal stenosis on radiography, the canal to body ratio (Torg-Pavlov ratio) was used. The ratio is calculated on sagittal planes dividing the diameter of the spinal canal by the diameter of the vertebral body. A ratio of below <0.8 is considered cervical spinal stenosis [9]. Spinal stenosis on MRI was diagnosed when the AP diameter of the spinal canal was lower than 10 mm [10]. Myelopathy was reported when there was a high signal of spinal cord in T2-w turbo inversion recovery magnitude (TIRM) images.

Every radiograph and MRI scan was assessed in a blinded and randomized manner by two independent radiologists—ISS (20 year of experience) and MK (senior radiology resident). Both readers work in a reference center. The obtained data were analyzed for inter-reader reliability.

In each case, the following demographic, clinical, and laboratory data were collected: age, gender, disease duration, current medical treatment, serum concentration of C-reactive protein (CRP, mg/L), erythrocyte sedimentation rate (ESR, m/h), antinuclear antibodies (ANA) titer, seropositivity for anti-cyclic citrullinated peptides (anti-CCP antibodies), and RF. For ANA titer, higher than or equal to 1:160 was considered as significant. A concentration of >17 IU/mL was considered as positive for anti-CCP antibodies, while >34 IU/mL was considered positive for RF.

Statistical Analysis

The statistical analysis was performed using SPSS software. The Shapiro–Wilk test was used to assess the distribution of continuous variables. Normally distributed data are expressed as mean \pm standard deviation. Non-normally distributed data are presented as median and interquartile range (IQR). Student's t-test and Mann–Whitney U-test were used to evaluate data when appropriate. Categorical Chi-squared test and Fisher's exact test were used to assess nominal data when appropriate. *p*-values < 0.05 were considered as significant. The sensitivity and specificity of radiography for basilar settling and dens erosions were calculated relative to the gold standard of MRI and for MRI for anterior AAS and SAS relative to the gold standard of dynamic radiography. The inter-reader reliability kappa value was calculated using McHugh's assumptions [11]. The level of agreement was classified as follows: almost perfect (kappa value above 0.90), strong (0.80–0.90), moderate (0.60–0.79), weak (0.40–0.59), minimal (0.21–0.39), none (0–0.20).

3. Results

Overall, 240 patients aged 23–86 years were enrolled (median age 62.0; IQR 53.0–69.0; 86% female), with a median duration of disease of 14.0 years; IQR 7.0–23.0. The mean age of RA onset was 42.7 ± 14.4 years.

Moreover, 198 patients with diagnosis of cervical spine osteoarthritis were recruited to serve as a control group. They were age and gender matched to the RA group (83% female, median age 62.0, IQR 54.0–70.0).

In the RA group, out of all 240 included patients, functional lateral radiographs were performed in 160 patients, while lateral neutral projection only was performed in 80 patients. Non-contrast MRI was performed in 168 patients and contrast-enhanced MRI was performed in the remaining 72 patients.

In the control group, functional radiographs were performed in 96 patients, and neutral projection only was performed in 102 patients. Twenty-one patients from the control group had post-contrast MRI of the cervical spine.

Out of 240 patients in the RA group, 179 (75%) had RA-related abnormalities of the cervical spine seen on radiographs and/or MRI. The most common lesions were anterior AAS (Figure 1) diagnosed in 140 patients (58%) with radiographs and in 78 (33%) with MRI, SAS seen in 139 patients (58%) on radiographs and in 102 patients (43%) with MRI, and demineralization diagnosed in 114 patients (48%) entirely with radiographs (Table 1).

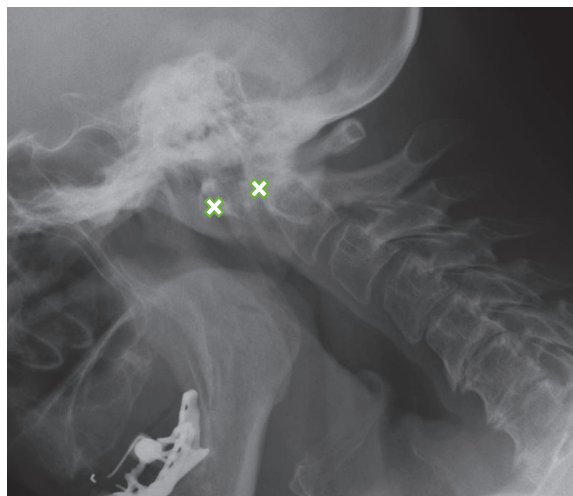


Figure 1. Lateral flexion view radiograph in a 63-year-old female with rheumatoid arthritis shows anterior AAS-8.8 mm (between crosses). AAS: atlanto-axial subluxation.

At the C1/C2 level, the most frequently diagnosed abnormalities (apart from anterior AAS) were (Table 1) vertical AAS (25 [10%] seen on MRI, 27 [11%] on radiography), posterior AAS (11 [5%]) and lateral AAS (7 [3%]); the latter two were observed only with MRI. Dens erosions were seen in 36 patients (15%; Figure 2) on MRI, while radiography showed dens erosions in 11 subjects. With MRI only, pannus was diagnosed in 50 patients (21%; Figure 3), periodontal effusion in 26 (11%), BME in 11 (5%), and contrast enhancement of bone (osteitis) and/or synovium in 12 (5%) patients. MRI showed brain stem compression in eight patients (3%).



Figure 2. Sagittal MRI, T2-w TIRM image in a 65-year-old female with rheumatoid arthritis shows dens erosions (arrowhead) and periodontal effusion and pannus (long arrow). MRI: magnetic resonance imaging, TIRM: turbo inversion recovery magnitude.



Figure 3. Sagittal postcontrast MRI, T1-w image in a 76-year-old female with rheumatoid arthritis with pannus formation in periodontal area (arrow). MRI: magnetic resonance imaging.

Among 140 cases of anterior AAS, 43 were seen on neutral lateral view and confirmed by functional radiography, while 69 of them were missed on neutral projections and diagnosed using additional views. Overall, 62% patients of anterior AAS were visible only on functional radiographs.

At the subaxial level, the most common lesion was SAS (139 (58%) seen on radiography, 102 (43%) on MRI).

The radiography sensitivity compared to MRI in detection of the basilar settling was 76%, while specificity was 96%, respectively. The sensitivity of radiography in the detection of dens erosions is 25%, while specificity was 99%. The sensitivity of functional radiography compared to static MRI in the diagnosis of anterior AAS was 50.7%, while specificity is 93%. In the case of SAS, the sensitivity of MRI was 54% and specificity was 73%.

At least one method discovered ankylosis in 23 patients (10%) (MRI in 14 patients, radiography in 19 patients). Spinal stenosis was seen with MRI in 93 patients (39%) and with radiography in 63 patients (26%). MRI showed cervical spine compression in 72 patients (30%) and cervical myelopathy in 14 patients (6%).

MRI revealed BME in 11 patients (5%), effusion in one patient, pannus formation in one patient, and contrast enhancement of bone (osteitis) and/or synovium in two patients. Spinous process erosions were seen in 14 patients (6%) and demineralization was seen in 114 (48%).

Most (90%) patients were taking at least one DMARD, two or more drugs were taken by 105 patients (71%), and 20 patients were on biological treatment.

Anti-CCP antibodies were present in 78 patients (78%), RF was present in 51 (51%), and ANA was present in 34 (34%). The median CRP value was 15 mg/L (IQR 7.0–30.3), while the median ESR value was 33 mm/h (IQR 16.3–56.8). Table 2 presents detailed clinical and laboratory data.

Table 2. Characteristics of RA group. ANA: antinuclear antibodies, CCP: cyclic citrullinated peptides, CRP: C-reactive protein, ERP: erythrocyte sedimentation rate, MRI: magnetic resonance imaging, RA: rheumatoid arthritis, RF: rheumatoid factor.

Rheumatoid Arthritis	Cervical Spine Lesions on Radiographs and/or MRI (n = 179)	No Abnormalities on Imaging (n = 61)	p
Age (years)	61.0 [52.0–68.0]	59.5 [50.5–66.8]	0.491
Sex (female; %)	154 (86%)	53 (87%)	0.868
Age at onset (years)	41.8 ± 13.6	45.3 ± 16.3	0.229
Disease duration (years)	15.0 [9.0–27.0]	9.0 [4.0–15.8]	0.007
CRP (mg/mL)	19.0 [7.0–32.0]	11.5 [6.3–19.8]	0.016
ESR (mm/h)	35.0 [19.0–58.0]	28.0 [13.3–48.8]	0.025
ANA positivity n (%)	20 (31%)	14 (39%)	0.408
RF positivity n (%)	39 (60%)	12 (35%)	0.010
Anti-CCP positivity n (%)	54 (83%)	24 (67%)	0.060

Cervical spine involvement was linked with longer duration of RA (15 years (range: 9.0–27.0) vs. 9 (4.0–16.0, $p = 0.007$), presence of RF (39 (60%) vs. 12 (35%); $p = 0.010$), elevated CRP (19.0 (7.0–32.0) vs. 11.5 (6.3–19.8); $p = 0.016$) and ESR (35.0 (19.0–58.0) vs. 28.0 (13.3–48.8); $p = 0.025$). The longer duration of RA was associated with the presence of subaxial subluxation (30 years (15.0–40.0) vs. 13 (6.0–21.0); $p = 0.005$), anterior AAS (15 years (10.0–27.0) vs. 9.5 (3.0–18.0); $p = 0.005$) and basilar settling (17 years (9.0–27.0) vs. 10 (5.0–16.0); $p = 0.003$). Basilar settling prevalence was lower in patients treated with methotrexate (6% vs. 17%; $p = 0.041$). Vertical AAS was also linked with the presence of demineralization (18% vs. 4%, $p = 0.001$). No other significant associations were found between detected abnormalities and treatment.

Comparing RA and the control group, the majority of lesions had statistically higher prevalence in RA (Table 1). For the spinal stenosis, myelopathy, cervical cord and brain stem compression, as well as subaxial lesions (BME, effusion, pannus, and contrast enhancement of bone (osteitis) and/or synovium), no statistically significant differences were found between the RA group and the control group.

The overall inter-reader reliability (for the reference method) was usually almost perfect (kappa value >0.90) or strong (0.80–0.90). For anterior AAS (0.79), demineralization (0.76), and subaxial lesions (effusion—0.66; pannus—0.66, and contrast enhancement—0.67), the agreement was moderate (Table 1).

4. Discussion

The current study confirmed the high prevalence of cervical spine pathologies in RA patients. Out of 240 included patients, 75% developed cervical spine abnormalities, with 71% on DMARDS therapy.

The most common lesions were anterior AAS (58%), followed by SAS (58%) and bone loss (48%). The cervical spine involvement was linked with long-standing RA, raised inflammatory markers, and RF seropositivity. Vertical AAS, anterior AAS, and subaxial subluxation developed late in the course of RA, while the remaining lesions including dens erosions may occur anytime.

The most serious complication of cervical spine arthritis is subluxations. Recent studies showed that anterior AAS was present in 18–32% of patients [8,12,13], whereas in our study, it was diagnosed in 58% of patients by radiographs, most likely because the study was conducted in a reference center for rheumatic diseases. Usually, AADI (anterior atlanto-dental interval) higher than 6 mm is considered for surgery [14]. In the current study, inter-reader agreement for anterior AAS was moderate (kappa—0.79). This usually resulted from suboptimal visualization/superimposition of anatomical structures due to destructive lesions of dens or border cases where the AADI was approximately 3 mm.

The second most commonly diagnosed abnormality was SAS, and it was again more common in our study (139 patients [58%]) than in those published by other authors (6–16%) [8,12]. SAS is caused by destructive changes in intervertebral, uncovertebral, and apophyseal joints as well as ligamental damage. In the current study, SAS developed in patients with a median of 30 years of history of RA. As other subluxations, SAS may also lead to myelopathy. The severity of subaxial myelopathy may be associated with vertebral or intervertebral disc destruction, the spinous process, or apophyseal joint erosions. Long-standing RA, younger age, and treatment with corticosteroids are risk factors for developing subaxial myelopathy [15].

Vertical AAS occurred in 10% of the RA patients, which is a similar prevalence to that observed in previous studies [8,12]. The assessment of vertical AAS is challenging on classic radiography due to the superimposition of anatomical structures and bone damage in the course of RA. Several methods are used to assess vertical AAS: Chamberlain, Clark, McRae, McGregor, Redlund-Johnell, Ranawat, Fischgold-Metzger, Wackenheim, and Kauppie-Sakaguchi [7,16–23]. In the current study, the McGregor method was used, and vertical AAS was considered when the apex of dens was located >4.5 mm above McGregor's line [7]. Riew et al. revealed that no method is ideal [24]. The authors suggest that combined measurements with Clark, Ranawat, and Redlund-Johnell methods are preferable. If any of these three methods is positive for the detection of vertical AAS, the sensitivity reaches 94% [24].

Care must be taken in patients with vertical subluxation, since in significant ligamental damage with the coexistence of anterior and vertical AAS, the anterior distance between the C1 arch and dens (AADI) may decrease and even normalize, causing pseudostabilization.

Other types of AAS, such as lateral or posterior, are rare. Only 5% of included patients developed lateral AAS, while 3% developed severe posterior AAS. The prevalence of these types of AAS is similar to previous studies [6]. Posterior AAS is usually caused by odontoid erosions or fracture, while lateral AAS is caused by rotatory deformations. Posterior AAS is

an indicator for surgery. PADI less than 14 mm requires prompt neurosurgical consultation due to high risk of spinal cord compressions and is a poor prognostic factor leading to neurological deficit [14,25].

Dens and spinous process erosions are a hallmark of RA. Dens erosions were seen in 15% of our patients, in line with published data by Olah et al. [12], which reported a prevalence of 16%. The prevalence of spinous process erosions in our study was 6%. Moreover, correlation between dens erosions and destruction in peripheral joints was found [12].

In the current study, at the C1/C2 level, pannus was seen in 21% of patients, showing postcontrast enhancement in 5% of the patients, periodontal effusion in 11%, and BME in 5%. Another study showed similar results; the prevalence of pannus formation was almost 25% [13]. Carotti et al. [26] found cervical spine arthritis in 24% of patients in early RA (less than a year from the diagnosis). The vast majority of lesions included BME, pannus, and dens erosions [26]. However, in our study, no link between BME, pannus formation or effusion, and duration of disease was confirmed.

Deminerlization was found on radiographs in almost half of the patients. Han et al. suggested that patients with low bone mineral density (BMD) and lower body mass index (BMI) have a higher risk of AAS [27]. Rossini et al. suggested that osteoporosis may be an independent risk factor for bone erosions in RA [28]. In the current study, bone deminerlization was positively linked to vertical AAS only ($p = 0.001$). Although the major adverse effect of steroid treatment is reduced BMD, the recent metanalysis revealed that patients with early RA after 24 months of corticosteroid therapy have no changes in BMD [29]. For deminerlization, the interobserver kappa value was moderate (0.76). However, radiography is the only axillary method, while the gold standard for assessment of BMD is dual-energy X-ray absorptiometry.

Apophyseal bony ankylosis is not a specific feature of RA, but it can be observed with long duration of disease. In the current study, cervical spine ankylosis was diagnosed in 10% of the patients. Iizuka et al. [30] found cervical ankylosis in 24% of RA patients, and it most commonly affected the atlanto-occipital joint. At the subaxial level, ankylosis may be the risk factor for instability and stenosis and may even lead to myelopathy. At the upper cervical level, patients with ankylosis had neurological impairment [30].

Lesions of spinal cord and brainstem were assessed on MRI and included spinal stenosis (39%), cervical cord compression (30%), cervical myelopathy (6%), and brainstem compression (3%). It is speculated that the incidence of spinal compression is underestimated in clinical practice, which is mainly due to nonspecific symptoms or a lack of symptoms, and therefore, it may lead to a sudden death [31]. If not operated, myelopathy deteriorates in 76% of patients. Within 3 years, all patients become bedridden, and the cumulative survival rate after 7 years was 0% [32]. When operated, 71% of patients with paralysis improved neurologically [25]. Neva et al. reported that 2% of patients with RA died due to cervical spine compression, resulting in sudden death, postoperative complications, and paraparesis or quadriplegia [2]. Cervical myelopathy is usually caused by mechanical compression or vascular ischemia [33]. With MRI, it manifests as a focal area of increased signal in fluid-sensitive images; however, very early changes might remain undetected. Recently, apparent diffusion coefficient (ADC) allows the early identification of cervical cord pathologies in patients with anterior AAS and normal MRI. This parameter may be useful for spinal surgery qualification [34]. Compared to a control group of patients with osteoarthritis, there were no statistically significant differences in prevalence of spinal stenosis, cervical cord compression, cervical myelopathy, and brain stem compression between patients with RA and osteoarthritis. In RA, these lesions are caused mainly by subluxations, while in osteoarthritis, they are caused by degenerative changes such as osteophytes or disc protrusion/extrusion.

The current study confirmed that a long duration of RA, elevated CRP concentration, and elevated ESR level as well as the presence of RF are associated with cervical spine arthritis. Other studies also showed that female sex, long treatment with steroids, extensive

peripheral joint involvement, and the presence of anti-CCP antibodies may be risk factors for cervical spine arthritis [4,12]. Although raised CRP and ESR are seen in RA and correspond with disease activity, both markers are nonspecific and may be elevated in other inflammatory conditions or RA complications. Furthermore, a recent study found histological features of inflammation in the synovium of the knee in RA patients with normal CRP. Thus, relying exclusively on inflammatory markers for disease severity score may not be ideal [35].

The first-line treatment for RA is methotrexate. One-third of patients on methotrexate did not show radiological progression, and this positive effect is even greater in combination with other drugs [36]. The current study showed a lower prevalence of vertical AAS in patients treated with methotrexate. The intensive use of a combination of three DMARDs (methotrexate, sulfasalazine, hydroxychloroquine) with prednisolone limited the development of anterior AAS [37]. Regarding biological treatment, Saliı et al. reported that infliximab therapy reduced periodontal pannus area and spinal cord edema [38]. Sandstrom et al. [39] focused on the prevalence of cervical spine involvement after 10 years of follow-up during triple DMARD therapy with prednisolone in patients who also received infliximab as part of a double-blind randomized study. The incidence of cervical spine involvement was as low as 4.7% regardless of infliximab use [39]. Biological agents prevented the development of new cervical spine lesions but did not inhibit the progression of preexisting involvement. Thus, the progressive nature of RA may still be uncontrollable [5]. Other authors reported lower prevalence of cervical spine involvement in the era of biological treatment, but their study failed to determine the role of biological agents [40]. In addition, metalloproteinase-3 levels predicted bone damage in treated patients [41,42]. Therefore, patients diagnosed with cervical spine instability tend to have progressive disease even under appropriate medical treatment, whereas patients without cervical involvement may benefit from the treatment [40–42].

Radiography and MRI are complementary methods. Radiographs remain a first-line method in imaging of the cervical spine. Neutral view in a standing position, supplemented by dynamic projections are superior to standard MRI (without flexion and extension) in the diagnosis of anterior and posterior AAS and SAS. However, MRI with no superimposition of anatomical structures allows better visualization of vertical AAS and dens erosions. The current study showed that functional projections detected 62% of all anterior AAS, which were not seen in the neutral position. This is similar to previous observations [43]. The sensitivity of dynamic radiography compared to static MRI in the supine position in diagnosis of anterior AAS was 51% and specificity was 93%. For SAS, the sensitivity of MRI was 54% and specificity was 73% compared to radiography. In the case of anterior AAS, Hung et al. list a number of features that are seen on MRI and may suggest anterior AAS, namely: dens erosions, anterior atlantoaxial joint titling (situation where the anterior tubercle of C1 and the anterior cortex of the odontoid process are not parallel), effusion, lateral facet arthropathy, abnormalities of spinolaminar line, and cervical myelopathy [44]. Otherwise, MRI is used to assess the activity of inflammation and complications, including other directions of subluxation (lateral, vertical, rotatory, mixed) and is the method of choice to visualize spinal cord and brainstem lesions such as compression or myelopathy [45]. Our study showed the superiority of MRI in the diagnosis of dens erosions and vertical AAS. Radiography showed 25% sensitivity and 99% specificity as a diagnostic modality for dens erosions and 76% sensitivity and 96% specificity for the detection of vertical AAS. The major limitation of radiography is the superimposition of anatomical structures used as reference points for measurements, which obscures anatomical landmarks.

The major advantage of the current study was the large, single-center cohort of 240 patients diagnosed with RA. In the study, both MRI and radiographic methods were analyzed, and the pros and cons of each modality were shown. The main limitation was the retrospective nature of the analysis.

5. Conclusions

The current study showed that RA-related lesions occur in most RA patients (75%), and they most frequently include anterior AAS (58%) and SAS (58%) followed by bone loss (48%). Dynamic radiographs and MRI are complementary and should both be performed for optimal diagnosis. Long disease duration, elevated inflammatory markers, and RF seropositivity were positively linked with abnormalities. In this cohort, the prevalence of vertical AAS was reduced in patients taking methotrexate, whereas no effect on remaining subluxations or RA features was noted.

Author Contributions: Conceptualization, R.G., P.G. and I.S.-S.; Data curation, M.K., R.G., P.G. and I.S.-S.; Formal analysis, M.K. and I.S.-S.; Investigation, M.K.; Methodology, M.K., R.G., P.G. and I.S.-S.; Supervision, I.S.-S.; Validation, M.K.; Writing—original draft, M.K.; Writing—review and editing, M.K., R.G., P.G. and I.S.-S. All authors have read and agreed to the published version of the manuscript.

Funding: This research received no external funding.

Institutional Review Board Statement: The study was conducted according to the guidelines of the Declaration of Helsinki, and approved by the Institutional Review Board of National Institute of Geriatrics, Rheumatology and Rehabilitation (no. KBT-3/2/2018).

Informed Consent Statement: Not applicable.

Data Availability Statement: The study data may be available on request.

Conflicts of Interest: The authors declare no conflict of interest.

References

1. Wasserman, B.R.; Moskovich, R.; Razi, A.E. Rheumatoid arthritis of the cervical spine—clinical considerations. *Bull. NYU Hosp. Jt. Dis.* **2011**, *69*, 136–148. [[PubMed](#)]
2. Neva, M.H.; Myllykangas-Luosujärvi, R.; Kautiainen, H.; Kauppi, M. Mortality associated with cervical spine disorders: A population-based study of 1666 patients with rheumatoid arthritis who died in Finland in 1989. *Rheumatology* **2001**, *40*, 123–127. [[CrossRef](#)] [[PubMed](#)]
3. Ahn, J.K.; Hwang, J.-W.; Oh, J.-M.; Lee, J.; Lee, Y.S.; Jeon, C.H.; Cha, H.-S.; Koh, E.-M. Risk factors for development and progression of atlantoaxial subluxation in Korean patients with rheumatoid arthritis. *Rheumatol. Int.* **2011**, *31*, 1363–1368. [[CrossRef](#)] [[PubMed](#)]
4. Zhu, S.; Xu, W.; Luo, Y.; Zhao, Y.; Liu, Y. Cervical spine involvement risk factors in rheumatoid arthritis: A meta-analysis. *Int. J. Rheum. Dis.* **2017**, *20*, 541–549. [[CrossRef](#)] [[PubMed](#)]
5. Zhang, T.; Pope, J. Cervical spine involvement in rheumatoid arthritis over time: Results from a meta-analysis. *Arthritis Res. Ther.* **2015**, *17*, 1–9. [[CrossRef](#)] [[PubMed](#)]
6. Younes, M.; Belghali, S.; Kriâa, S.; Zrour, S.; Bejia, I.; Touzi, M.; Bergaoui, N. Compared imaging of the rheumatoid cervical spine: Prevalence study and associated factors. *Jt. Bone Spine* **2009**, *76*, 361–368. [[CrossRef](#)] [[PubMed](#)]
7. McGregor, M. The Significance of Certain Measurements of the Skull in the Diagnosis of Basilar Impression. *Br. J. Radiol.* **1948**, *21*, 171–181. [[CrossRef](#)]
8. Yurube, T.; Sumi, M.; Nishida, K.; Miyamoto, H.; Kohyama, K.; Matsubara, T.; Doita, M. Incidence and aggravation of cervical spine instabilities in rheumatoid arthritis: A prospective minimum 5-year follow-up study of patients initially without cervical involvement. *Spine* **2012**, *37*, 2136–2144. [[CrossRef](#)]
9. Pavlov, H.; Torg, J.S.; Robie, B.; Jahre, C. Cervical spinal stenosis: Determination with vertebral body ratio method. *Radiology* **1987**, *164*, 771–775. [[CrossRef](#)]
10. Ulbrich, E.J.; Schraner, C.; Boesch, C.; Hodler, J.; Busato, A.; Anderson, S.E.; Eigenheer, S.; Zimmermann, H.; Sturzenegger, M. Normative MR Cervical Spinal Canal Dimensions. *Radiology* **2014**, *271*, 172–182. [[CrossRef](#)]
11. McHugh, M.L. Interrater reliability: The kappa statistic. *Biochem. Med.* **2012**, *22*, 276–282. [[CrossRef](#)]
12. Baek, I.-W.; Bin Joo, Y.; Park, K.-S.; Kim, K.-J. Risk factors for cervical spine instability in patients with rheumatoid arthritis. *Clin. Rheumatol.* **2021**, *40*, 547–555. [[CrossRef](#)]
13. Oláh, C.; Kardos, Z.; Kostyál, L.; Hodosi, K.; Tamási, L.; Bereczki, D.; Szekanez, Z. Assessment of cervical spine involvement in rheumatoid arthritis patients in the era of biologics: A real-life, cross-sectional MRI study. *Rheumatol. Int.* **2020**, *40*, 915–921. [[CrossRef](#)]
14. Gillick, J.; Wainwright, J.; Das, K. Rheumatoid Arthritis and the Cervical Spine: A Review on the Role of Surgery. *Int. J. Rheumatol.* **2015**, *2015*, 1–12. [[CrossRef](#)]
15. Yonezawa, T.; Tsuji, H.; Matsui, H.; Hirano, N. Subaxial lesions in rheumatoid arthritis. Radiographic factors suggestive of lower cervical myelopathy. *Spine* **1995**, *20*, 208–215. [[CrossRef](#)]

16. Chamberlain, W.E. Basilar Impression (Platybasia): A Bizarre Developmental Anomaly of the Occipital Bone and Upper Cervical Spine with Striking and Misleading Neurologic Manifestations. *Yale J. Biol. Med.* **1939**, *11*, 487.
17. Clark, C.R.; Goetz, D.D.; Menezes, A.H. Arthrodesis of the cervical spine in rheumatoid arthritis. *J. Bone Jt. Surg. Am. Vol.* **1989**, *71*, 381–392. [[CrossRef](#)]
18. McRae, D.L.; Barnum, A.S. Occipitalization of the atlas. *Am. J. Roentgenol. Radium Ther. Nucl. Med.* **1953**, *70*, 23–46.
19. Redlund-Johnell, I.; Pettersson, H. Radiographic measurements of the cranio-vertebral region. Designed for evaluation of abnormalities in rheumatoid arthritis. *Acta Radiol. Diagn.* **1984**, *25*, 23–28. [[CrossRef](#)]
20. Ranawat, C.S.; O’Leary, P.; Pellicci, P.; Tsairis, P.; Marchisello, P.; Dorr, L. Cervical spine fusion in rheumatoid arthritis. *J. Bone Jt. Surg. Am.* **1979**, *61*, 1003–1010. [[CrossRef](#)]
21. Fischgold, H.; Metzger, J. Radio-tomography of the impression fractures of the cranial basis. *Rev. Du Rhum. Et Des Mal. Osteo-artic.* **1952**, *19*, 261–264.
22. Wackenheim, A. *Roentgen Diagnosis of the Craniovertebral Region*; Springer: New York, NY, USA, 1974.
23. Kauppi, M.; Sakaguchi, M.; Kontinen, Y.T.; Hämäläinen, M. A new method of screening for vertical atlantoaxial dislocation. *J. Rheumatol.* **1990**, *17*, 167–172. [[PubMed](#)]
24. Riew, K.D.; Hilibrand, A.S.; Palumbo, M.A.; Sethi, N.; Bohlman, H.H. Diagnosing Basilar Invagination in the Rheumatoid Patient. *J. Bone Jt. Surg. Am. Vol.* **2001**, *83*, 194–200. [[CrossRef](#)] [[PubMed](#)]
25. Boden, S.D.; Dodge, L.D.; Bohlman, H.H.; Rechten, G.R. Rheumatoid arthritis of the cervical spine. A long-term analysis with predictors of paralysis and recovery. *J. Bone Jt. Surg. Am.* **1993**, *75*, 1282–1297. [[CrossRef](#)]
26. Carotti, M.; Salaffi, F.; Di Carlo, M.; Sessa, F.; Giovagnoni, A. Magnetic resonance imaging of the craniovertebral junction in early rheumatoid arthritis. *Skelet. Radiol.* **2019**, *48*, 553–561. [[CrossRef](#)]
27. Han, M.H.; Ryu, J.I.; Kim, C.H.; Cheong, J.H.; Bak, K.H.; Chun, H.J. Influence of systemic bone mineral density on atlantoaxial subluxation in patients with rheumatoid arthritis. *Osteoporos. Int.* **2017**, *37*, 1938–2136. [[CrossRef](#)]
28. Rossini, M.; Adami, G.; Viapiana, O.; Idolazzi, L.; Orsolini, G.; Fassio, A.; Giollo, A.; Gatti, D. Osteoporosis: An Independent Determinant of Bone Erosions in Rheumatoid Arthritis? *J. Bone Miner. Res.* **2017**, *32*, 2142–2143. [[CrossRef](#)]
29. Blavnsfeldt, A.-B.G.; de Thurah, A.; Thomsen, M.D.; Tarp, S.; Langdahl, B.; Hauge, E.-M. The effect of glucocorticoids on bone mineral density in patients with rheumatoid arthritis: A systematic review and meta-analysis of randomized, controlled trials. *Bone* **2018**, *114*, 172–180. [[CrossRef](#)]
30. Iizuka, H.; Nishinome, M.; Sorimachi, Y.; Ara, T.; Nakajima, T.; Iizuka, Y.; Takagishi, K. The characteristics of bony ankylosis of the facet joint of the upper cervical spine in rheumatoid arthritis patients. *Eur. Spine J.* **2009**, *18*, 1130–1134. [[CrossRef](#)]
31. Parish, D.C.; Clark, J.A.; Liebowitz, S.M.; Hicks, W.C. Sudden death in rheumatoid arthritis from vertical subluxation of the odontoid process. *J. Natl. Med. Assoc.* **1990**, *82*, 297–304.
32. Sunahara, N.; Matsunaga, S.; Mori, T.; Ijiri, K.; Sakou, T. Clinical Course of Conservatively Managed Rheumatoid Arthritis Patients With Myelopathy. *Spine* **1997**, *22*, 2603–2607, discussion 2608. [[CrossRef](#)]
33. Delamarter, R.B.; Bohlman, H.H. Postmortem Osseous and Neuropathologic Analysis of the Rheumatoid Cervical Spine. *Spine* **1994**, *19*, 2267–2274. [[CrossRef](#)]
34. Mańczak, M.; Pracoń, G.; Sudoł-Szopińska, I.; Gasik, R. Apparent diffusion coefficient as an indicator of spinal cord compression due to anterior atlanto-axial subluxation in rheumatoid arthritis patients. *Eur. Spine J.* **2019**, *28*, 2352–2358. [[CrossRef](#)]
35. Orr, C.K.; Najm, A.; Young, F.; McGarry, T.; Biniecka, M.; Fearon, U.; Veale, D. The Utility and Limitations of CRP, ESR and DAS28-CRP in Appraising Disease Activity in Rheumatoid Arthritis. *Front. Med.* **2018**, *5*, 185. [[CrossRef](#)]
36. Weinblatt, M.E. Methotrexate in Rheumatoid Arthritis: A Quarter Century of Development. *Trans. Am. Clin. Clim. Assoc.* **2013**, *124*, 16–25.
37. Kauppi, M.J.; Neva, M.H.; Laiho, K.; Kautiainen, H.; Luukkainen, R.; Karjalainen, A.; Hannonen, P.J.; Leirisalo-Repo, M.; Korpela, M.; Ilva, K.; et al. Rheumatoid Atlantoaxial Subluxation Can Be Prevented by Intensive Use of Traditional Disease Modifying Antirheumatic Drugs. *J. Rheumatol.* **2009**, *36*, 273–278. [[CrossRef](#)]
38. Salli, A.; Sahin, N.; Paksoy, Y.; Kucuksarac, S.; Ugurlu, H. Treatment of Periodontoid Pannus With Infliximab in a Patient With Rheumatoid Arthritis. *JCR: J. Clin. Rheumatol.* **2009**, *15*, 250–251. [[CrossRef](#)]
39. Sandström, T.; Rantalaiho, V.; Yli-Kerttula, T.; Kautiainen, H.; Malmi, T.; Karjalainen, A. Cervical Spine Involvement is very rare in Patients with Rheumatoid Arthritis Treated actively with Treat to Target Strategy. Ten-Year Results of the NEORACo Study. *J. Rheumatol.* **2019**, 19013. [[CrossRef](#)]
40. Takahashi, S.; Suzuki, A.; Koike, T.; Yamada, K.; Yasuda, H.; Tada, M.; Sugioka, Y.; Okano, T.; Nakamura, H. Current prevalence and characteristics of cervical spine instability in patients with rheumatoid arthritis in the era of biologics. *Mod. Rheumatol.* **2014**, *24*, 904–909. [[CrossRef](#)]
41. Kaito, T.; Hosono, N.; Ohshima, S.; Ohwaki, H.; Takenaka, S.; Fujiwara, H.; Makino, T.; Yonenobu, K. Effect of Biological Agents on Cervical Spine Lesions in Rheumatoid Arthritis. *Spine* **2012**, *37*, 1742–1746. [[CrossRef](#)]
42. Kaito, T.; Ohshima, S.; Fujiwara, H.; Makino, T.; Yonenobu, K. Predictors for the progression of cervical lesion in rheumatoid arthritis under the treatment of biological agents. *Spine* **2013**, *38*, 2258–2263. [[CrossRef](#)]
43. Kauppi, M.; Neva, M.H. Sensitivity of lateral view cervical spine radiographs taken in the neutral position in atlantoaxial subluxation in rheumatic diseases. *Clin. Rheumatol.* **1998**, *17*, 511–514. [[CrossRef](#)]

44. Hung, S.-C.; Wu, H.-M.; Guo, W.-Y. Revisiting Anterior Atlantoaxial Subluxation with Overlooked Information on MR Images. *Am. J. Neuroradiol.* **2009**, *31*, 838–843. [[CrossRef](#)]
45. Sudol-Szopińska, I.; Jans, L.; Teh, J. Rheumatoid arthritis: What do MRI and ultrasound show. *J. Ultrason.* **2017**, *17*, 5–16. [[CrossRef](#)]

Article

Reliability of the Preliminary OMERACT Juvenile Idiopathic Arthritis MRI Score (OMERACT JAMRIS-SIJ)

Tarimobo M. Otobo ^{1,*}, Nele Herregods ², Jacob L. Jaremko ³, Iwona Sudol-Szopinska ⁴,
Walter P. Maksymowych ⁵, Arthur B. Meyers ⁶, Pamela Weiss ⁷, Shirley Tse ⁸, Joel Paschke ⁹, Rahim Moineddin ¹⁰,
Nigil Haroon ¹¹, Nikolay Tzaribachev ¹², Simone Appenzeller ¹³, Olympia Papakonstantinou ¹⁴, Eva Kirkhus ¹⁵,
Marion A. J. van Rossum ¹⁶, John Carrino ¹⁷, Philip G. Conaghan ¹⁸, Mirkamal Tolend ¹, Jennifer Stimec ¹,
Lennart Jans ², Robert G. Lambert ³, Dax Rumsey ⁵ and Andrea S. Doria ^{1,*}

- ¹ Department of Diagnostic Radiology, Hospital for SickKids, Toronto, ON M5G 1X8, Canada; mirkamal.tolend@sickkids.ca (M.T.); jennifer.stimec@sickkids.ca (J.S.)
- ² Division of Pediatric of Radiology, Universitair Ziekenhuis Ghent, 9000 Ghent, Belgium; nele_herregods@telenet.be (N.H.); lennart.jans@ugent.be (L.J.)
- ³ Department of Radiology and Diagnostic Imaging, University of Alberta, Edmonton, AB T6G 2R3, Canada; jjaremko@ualberta.ca (J.L.J.); rlambert@ualberta.ca (R.G.L.)
- ⁴ Department of Radiology, National Institute of Geriatrics Rheumatology and Rehabilitation, 02-637 Warsaw, Poland; sudolszopinska@gmail.com
- ⁵ Department of Rheumatology, University of Alberta, Edmonton, AB T6G 2R3, Canada; walter.maksymowych@ualberta.ca (W.P.M.); dax.rumsey@albertahealthservices.ca (D.R.)
- ⁶ Department of Radiology, Cincinnati Children's Hospital Medical Center, Cincinnati, OH 45229, USA; arthurbmeyers@yahoo.com
- ⁷ Department of Rheumatology, Children Hospital of Philadelphia, Philadelphia, PA 19104, USA; weisspa@email.chop.edu
- ⁸ Department of Rheumatology, Hospital for SickKids, Toronto, ON M5G 1X8, Canada; shirley.tse@sickkids.ca
- ⁹ Care Arthritis Ltd., Edmonton, AB T6W 2Z8, Canada; joel.paschke@carearthritis.com
- ¹⁰ Department of Family Medicine, University of Toronto, Toronto, ON M5G 1V7, Canada; rahim.moineddin@utoronto.ca
- ¹¹ Department of Rheumatology, Toronto Western Hospital, Toronto, ON M5T 2S8, Canada; nigil.haroon@uhn.ca
- ¹² Department of Pediatric Rheumatology, Medical Center Bad Bramstedt, 24576 Bramstedt, Germany; tzaribachev@pri-research.com
- ¹³ Department of Orthopedics, Rheumatology and Traumatology, University of Campinas, Campinas 13083-970, Brazil; appenzellersimone@yahoo.com
- ¹⁴ Department of Radiology, National and Kapodistrian University of Athens, 157-72 Athens, Greece; sogofianol@gmail.com
- ¹⁵ Department of Radiology, Oslo University Hospital, 0372 Oslo, Norway; ekirkhus@ous-hf.no
- ¹⁶ Amsterdam Rheumatology and Immunology Center | Reade and Emma Children's Hospital Amsterdam University Medical Centers, 1105 Amsterdam, The Netherlands; m.a.vanrossum@amsterdamumc.nl
- ¹⁷ Department of Radiology and Imaging, Hospital for Special Surgery, New York, NY 10021, USA; carrinoj@hss.edu
- ¹⁸ Leeds Institute of Rheumatic and Musculoskeletal Medicine, University of Leeds and NIHR Leeds Biomedical Research Center, Leeds LS7 4SA, UK; p.conaghan@leeds.ac.uk
- * Correspondence: tarimobo.otobo@sickkids.ca (T.M.O.); andrea.doria@sickkids.ca (A.S.D.)

Citation: Otobo, T.M.; Herregods, N.; Jaremko, J.L.; Sudol-Szopinska, I.; Maksymowych, W.P.; Meyers, A.B.; Weiss, P.; Tse, S.; Paschke, J.; Moineddin, R.; et al. Reliability of the Preliminary OMERACT Juvenile Idiopathic Arthritis MRI Score (OMERACT JAMRIS-SIJ). *J. Clin. Med.* **2021**, *10*, 4564. <https://doi.org/10.3390/jcm10194564>

Academic Editor: Mitsuhiro Takeno

Received: 28 August 2021

Accepted: 26 September 2021

Published: 30 September 2021

Publisher's Note: MDPI stays neutral with regard to jurisdictional claims in published maps and institutional affiliations.



Copyright: © 2021 by the authors. Licensee MDPI, Basel, Switzerland. This article is an open access article distributed under the terms and conditions of the Creative Commons Attribution (CC BY) license (<https://creativecommons.org/licenses/by/4.0/>).

Abstract: This study reports the reliability of the juvenile idiopathic arthritis magnetic resonance imaging scoring system (JAMRIS-SIJ). The study comprised of eight raters—two rheumatologists and six radiologists—and 30 coronal T1 and Short-Tau Inversion Recovery (STIR) MRI scans of patients with enthesitis-related juvenile spondylarthritis. The median age of patients was 15 years with a mean disease duration of 5 years and 22 (73.3%) of the sample were boys. The inter-rater agreement of scores for each of the JAMRIS-SIJ items was calculated using a two-way random effect, absolute agreement, and single rater intraclass correlation coefficient (ICC 2.1). The ICC was interpreted together with kurtosis, since the ICC is also affected by the distribution of scores in the sample. The eight-rater, single measure inter-rater ICC (and kurtosis) values for JAMRIS-SIJ inflammation and damage components were the following: bone marrow edema (BME), 0.76 (1.2); joint space inflammation, 0.60 (1.8); capsulitis, 0.58 (9.2); enthesitis, 0.20 (0.1); ankylosis, 0.89 (35); sclerosis,

0.53 (4.6); erosion, 0.50 (6.5); fat lesion, 0.40 (21); backfill, 0.38 (38). The inter-rater reliability for BME and ankylosis scores was good and met the a priori set ICC threshold, whereas for the other items it was variable and below the selected threshold. Future directives should focus on refinement of the scores, definitions, and methods of interpretation prior to validation of the JAMRIS-SIJ through the assessment of its measurement properties.

Keywords: OMERACT; JIA; measurement instrument; outcome measure; MRI; SIJ; reliability

1. Introduction

Juvenile idiopathic arthritis (JIA) is a chronic inflammatory disease of childhood that affects peripheral and axial joints with onset in a child less than 16 years of age. It is characterized by persistent arthritis for at least 6 weeks and the exclusion of other known conditions. Uncontrolled disease activity has the potential to cause joint damage and growth abnormalities [1–3]. Children within the JIA categories including those with enthesitis-related arthritis, arthritis and psoriatic arthritis, and undifferentiated arthritis (often referred to as juvenile spondyloarthritis in case of axial involvement) or juvenile spondyloarthritis (ERA/JSpA) have frequent involvement of their entheses and joints, including the sacroiliac joint (SIJ) [3]. Several JIA disease activity measures exist [4–6]; however, their reliability is variable [7], and they often do not represent or include arthritis in axial joints. Clinical examination of the SIJ is a commonly used measure of SIJ disease activity in JIA and is often defined as pain with palpation of the SIJ. However, the validity of clinical assessment is limited by the anatomy and deep location of the SIJ and is not useful in truly differentiating true arthritis from a normal joint in many cases [8,9].

Magnetic resonance imaging (MRI) is considered a valuable non-invasive tool for assessing SIJ inflammation and damage, and for monitoring treatment effectiveness and disease activity in JIA [9–11]. Radiography is a frequently used diagnostic imaging technique for SIJ, but its utility is limited because it cannot directly detect early features of disease activity such as bone marrow inflammation [12]. MRI is the most sensitive modality available to assess inflammation in the SIJ [12–14]. Reliable and valid MRI imaging instruments have been developed to assess SIJ inflammation and damage in adults [15,16], with special regards to the application of adult joint imaging instruments for the wrist and SIJ in children [1,17–20]. The need for an imaging outcome measure that was cognizant of the nuances of pediatric bone marrow MRI signal and dynamic bone growth underpinned the development of the preliminary OMERACT juvenile idiopathic arthritis MRI-SIJ score (JAMRIS-SIJ). This score is a standardized, objective, semi-quantitative, MRI-based outcome measurement instrument developed by a multi-disciplinary international group of experts for the evaluation of SIJ inflammation and structural changes in children with JIA [21]. We aim to assess the inter-rater reliability of this preliminary score in a cohort of children with ERA/JSpA.

2. Patients and Methods

Magnetic resonance imaging of boys and girls ≤ 18 years with confirmed imaging and clinical diagnosis of ERA/JSpA who had a SIJ MRI study performed at The Hospital for Sick Children (Toronto, ON, Canada), the Children's Hospital of Philadelphia (Philadelphia, PA, USA), or Ghent University Hospital (Ghent, Belgium) comprised the study sample. The MRI examinations were acquired between January 2017 and December 2018. All MR images were anonymized, and patient information was extracted from electronic clinical charts before scoring. All available cases contained at a minimum semicoronal T1-weighted (T1W), T2-weighted (T2W) fat-suppressed, or Short Tau Inversion Recovery (STIR) sequences. Details of sequence protocol are reported in Appendix A. Cases with history of comorbidities such as primary or metastatic bone cancer, SIJ fractures, and not containing the minimum imaging protocol for this study were excluded. The study MRI

cases were reviewed for the presence of SIJ pathologies by two pediatric radiologists (JLJ and NH) who were blinded to the clinical history and other imaging findings. The final 30 cases included in the study were randomly selected following a sample size estimation using the Donner and Eliasziw sample size estimation formula for reliability study [22]. They were scored by using the JAMRIS-SIJ scoring methods (Table 1, Figure 1A–C) by 8 raters—2 rheumatologists (one adult and one pediatric rheumatologist) and 6 radiologists (5 pediatric and 1 adult radiologist)—who had between 5 and 33 years of experience assessing pediatric MRIs, (interquartile range (IQR): 10–20, median 14 years).

Table 1. Features and definitions of inflammation and structural components of an MRI scoring system for sacroiliac joints.

Features	Definitions	Scores
Inflammation MRI Components		Score range/slide
BME	An ill-defined area of high bone marrow signal intensity † within the subchondral bone in the ilium or sacrum on fluid-sensitive images	Score 4 quadrant/SIJ 0/1, range 0–8
BME Intensity	Hyperintensity of the marrow edema using the presacral veins as reference	Score each SIJ 0/1, 0–2
BME Depth	Continues to increase the signal of depth ≥ 5 mm/ ≥ 1 cm from the articular surface	Score each SIJ 0/1, 0–2
Capsulitis	High signal on fluid-sensitive and/or post-contrast enhancement involving the SIJ capsule	Score halves / SIJ 0/1, 0–4
JSI	Increased signal on fluid-sensitive or contrast-enhanced T1-weighted images within the joint space of the cartilaginous portion of the SIJ	Score halves/ SIJ 0/1, 0–4
Enthesitis	High signal in bone marrow and/or soft tissue on a fluid-sensitive sequences or a contrast-enhanced T1-weighted sequence at sites where ligaments and tendons attach to a bone	Score each case 0/1, 0–1
Structural MRI Components		
Sclerosis	A substantially wider than normal area of low subarticular bone signal on T1-weighted and fluid-sensitive images (of ≥ 5 mm in adolescents)	Score 4 quadrants/SIJ 0/1, 0–8
Erosion	Bony defect (or irregularity with associated bone marrow edema, sclerosis, or fatty lesion) at the osteochondral interface involving both contour and signal on both T1-weighted and fluid-sensitive images	Score 4 quadrants/SIJ 0/1, 0–8
Fat Lesion	Increased homogenous signal intensity on T1-weighted non-FS image in subchondral bone with a distinct border	Score 4 quadrants /SIJ 0/1, 0–8
Backfill	A bright signal on a T1-weighted sequence in a typical location for an erosion, with signal intensity greater than normal bone marrow, and meeting the following requirements. 1. It is associated with complete loss of the dark appearance of the subchondral cortex at its expected location. 2. It is clearly demarcated from adjacent bone marrow by an irregular band dark signal reflecting sclerosis at the border of the original erosion	Score halves/SIJ 0/1, 0–4
Ankylosis	Presence of signal equivalent to regional bone marrow continuously bridging a portion of the joint space between the iliac and sacral bones	Score halves/0/1, 0–4

Statement of overarching consideration for all definitions—“[. . .] in comparison to physiological changes normally seen in MRIs of age and sex matched children, and visible in two planes where available”. † Caveat for bone marrow edema—“[. . .] compared to the signal intensity of the iliac crest, edges of the vertebrae, and triradiate cartilage where available”. JAMRIS-SIJ: juvenile arthritis magnetic resonance image sacroiliac joint scoring system; MRI: magnetic resonance imaging; BME: bone marrow edema; SIJ: sacroiliac joint; FS: fat suppressed.

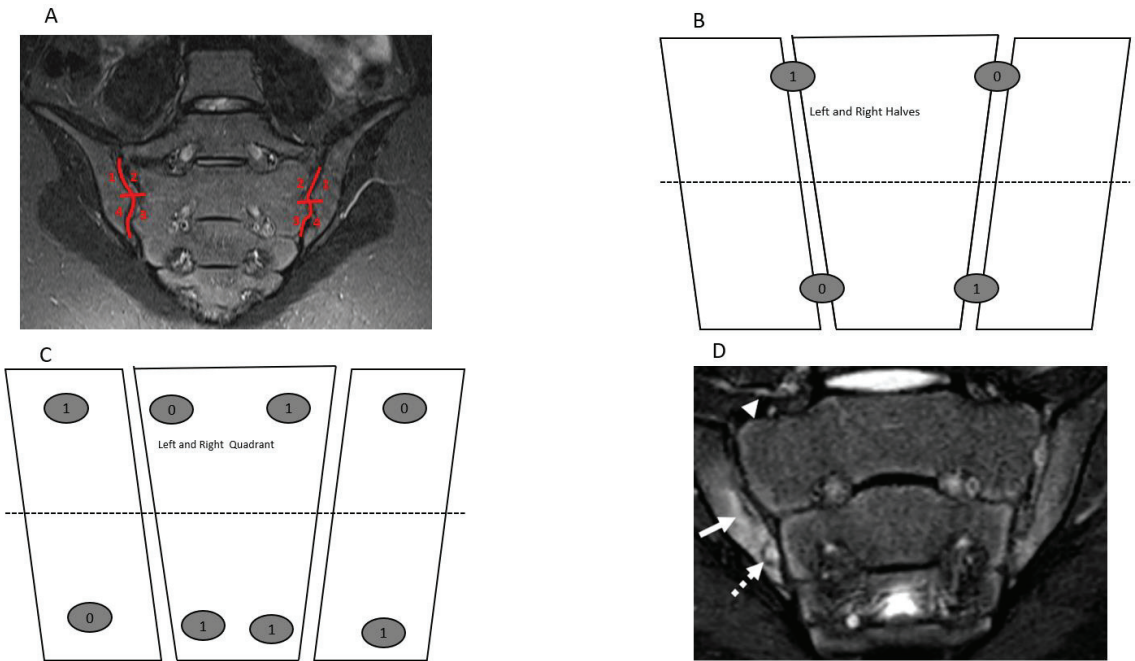


Figure 1. Semicoronal T2 Short Tau Inversion Recovery (STIR) MR images (A,D) and sketches (B,C) through the sacroiliac joint (SIJ) illustrate the measurement and method and component of the JAMRIS-SIJ. (A) SIJ in a 14-year-old boy shows a normal SIJ divided into quadrants by a vertical line through the joint space and a horizontal line that intersects at the mid portion of the joint (red lines) into superior iliac, sacral, inferior sacral and iliac quadrants in clockwise direction on the right and direction on the left side. (B,C) Corresponding schema of the SIJ, with (B) showing the division of the SIJ into halves and (C) showing the division into quadrants with a corresponding example of the scoring JAMRIS-SIJ components. (D) SIJ in a 12-year-old boy with enthesitis-related arthritis/juvenile spondylarthritis (ERA/JSPpA) demonstrates bone marrow edema (BME) involving the inferior aspect of the right ilium (A—solid arrow). The intensity of the BME signal (arrow) is equal to the signal of the presacral veins. There is a bony defect in the inferior aspect of the right iliac bone seen on both T2-weighted (A) and T1-weighted (Figure 2D) images (dashed arrow) with associated BME, consistent with an erosion.

The JAMRIS-SIJ is a dichotomous item-based instrument that assesses the presence or absence of SIJ inflammation and structural lesions on successive semicoronal T1W, T2W fat-suppressed, and/or STIR sequences through the cartilaginous portion of the SIJ (Table 1). The scores for each item of the JAMRIS-SIJ scale were based on the compilation of information from consecutive semicoronal slices that included the cartilaginous portion of the joint. The definition and scoring methods for the features of the JAMRIS-SIJ scale are described in Table 1 and illustrated in Figure 1A–C. Visualizing a minimum of 1 cm vertical height of the cartilaginous portion of the SIJ is required to meet scoring eligibility. To standardize bone marrow signal for scoring of bone marrow edema (BME), the iliac crest, triradiate cartilage, sacral interforaminal area, and ischiopubic synchondrosis were selected as internal reference comparators for normal pediatric bone marrow signal intensity, and the presacral vein was used as reference for depth.

The inter-rater reliability was calculated by using the two-way random effects model, absolute agreement, and single rater intraclass class correlation coefficient (ICC 2.1) [23]. The reliability estimates assume that both raters and subjects (cases) were randomly selected and represent the population of raters and subjects (cases) from which they were drawn.

Therefore, results can be generalized to other raters and subjects with comparable attributes. The ICCs are reported as absolute agreement for all raters, rheumatologists and radiologists. An a priori determined that an ICC > 0.7 represented an inter-rater reliability estimate, for $\alpha = 0.05$ and $\beta = 0.20$. ICC values were regarded as < 0.5 (poor), 0.5 to 0.75 (moderate), 0.75 to 0.9 (good), and > 0.9 (excellent) reliability [23]. ICC estimates were interpreted together with kurtosis, since the ICC is also affected by the distribution of scores in the sample. Kurtosis is a measure of probability of the tails of a distribution compared to a normal reference kurtosis of 3 (mesokurtic) representing a normal distribution. Kurtosis > 3 (leptokurtic) indicates more distribution of the data in the tail, whereas kurtosis < 3 (platykurtic) refers to a data distribution with a wide bell and less data distribution in the tail.

All raters received initial online training session from an expert developer (NH), comprising examples of SIJ pathologies and how the JAMRIS-SIJ scoring system would be used for the cases, as well as common pitfalls. After the training session, a cognitive debriefing was conducted through email correspondence to clarify any questions or concerns about the scoring method. Lesions were recorded directly on a custom-designed web-based interface (CARE Arthritis) [24] depicting schematics of the SIJ according to SIJ quadrants or halves. Raters were blinded to all patient information except age.

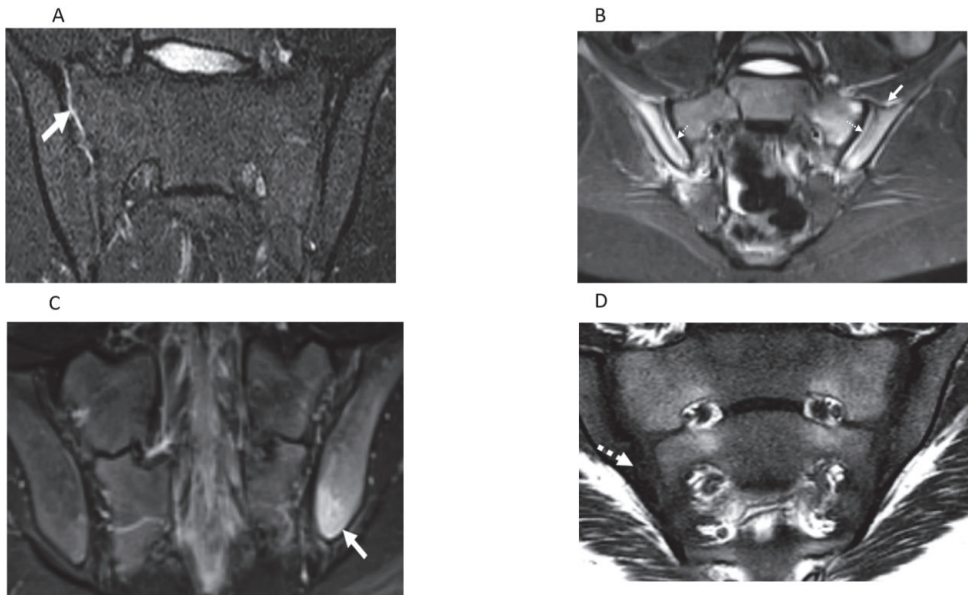


Figure 2. Semicoronal T2 Short Tau Inversion Recovery (STIR) MR images (A–C) and T1-weighted MR image (D) through the sacroiliac joint (SIJ) illustrate measurement components of the JAMRIS-SIJ. (A) SIJ in a 17-year-old boy with ERA/JSpA shows joint space inflammation (JSI) as an increased signal intensity within the superior portion of the right SIJ (arrow) compared to the normal signal in the left SIJ. (B) SIJ in a 15-year-old boy with ERA/JSpA demonstrates capsulitis as a high signal intensity (arrow) at the superior aspect of the SIJ and JSI (dashed arrow), which is the most pronounced on the right side. (C) SIJ in a 17-year-old boy shows edema in the left iliac bone (arrow) inferior and posterior, consistent with enthesitis. (D) SIJ in a 12-year-old boy with enthesitis-related arthritis/juvenile spondylarthritis (ERA/JSpA) demonstrates erosion involving the inferior aspect of the right ilium (dashed solid arrow). The bony defect at the osteochondral interface in the inferior aspect of the right iliac bone corresponds to the location of bone marrow edema (dashed arrow) seen on the T2-weighted sequence of the image (Figure 1D), consistent with an erosion.

3. Results

Out of the 30 patients who had MRI examinations selected for the study 22 (73.3%) were males. The median age of the patients was 14 years (12.3–15.7, range 6–18 years). The degree of disease activity at the time of imaging ranged from minimally active, moderately active, and severe, as 16 (53.3%) cases showed negligible disease burden as reported by the median count of active joints and tender enthesitis of 1, and the remainder of cases showed moderate to severe self-reported pain and a physician global assessment of 5 and 6, respectively. The incidence of JAMRIS-SIJ pathologies among the study MRI examinations were 17 (56%) erosions, 16 (53%) BME; 11 (36.6%) sclerosis, 10 (33.3%) joint space inflammation (JSI), 7 (23.3%) fat lesions; 5 (16.6%) capsulitis, 4 (13.3%) enthesitis, 2 (6.6%) backfill and 1 (3.3%) ankylosis. Seven (23.3%) of the MRI examinations were normal for the patient's age, exhibiting varying normal growth and age-related variants of the bone marrow signal in the SI region. Descriptive statistics and ICCs for the JAMRIS-SIJ items are reported in Tables 2–4. The mean slice count was 8 ± 2 (IQR 7–10), with a minimum of 1 and maximum of 14. Further details on slice counts and mean JAMRIS-SIJ item score among radiologist and rheumatologist are reported in Appendix B and Tables 3 and 4.

The inter-rater reliability ICCs (and kurtosis) of JAMRIS-SIJ for the inflammation and damage domains were 0.77 (1.0) and 0.60 (6.1), respectively. Among radiologists, the inter-rater reliability estimates were 0.76 (0.48) for the inflammation domain and 0.60 (5.1) for the damage domain, and for the rheumatologists, it was 0.73 (0.84) for the inflammation domain and 0.85 (1.58) for the damage domain.

Table 2. JAMRIS-SIJ inflammation and damage component descriptive statistic and intraclass correlation coefficients (ICCs) for both radiologists and rheumatologists.

	Bone Marrow Edema	Joint Space Inflammation	Capsulitis	Enthesitis	Inflammation Domain	Sclerosis	Erosion	Fat Lesion	Ankylosis	Backfill	Damage Domain
Mean	17.36	5.48	1.42	0.21	24.26	1.89	6.33	2.49	0.31	0.68	11.70
Median	3	0	0	0	5	0	3	0	0	0	5
SD	24.94	8.30	3.74	0.41	34.26	3.74	9.03	6.31	1.75	3.14	15.54
Kurtosis	1.23	1.75	9.18	0.13	1.06	4.65	6.48	21.11	35.27	38.08	6.14
Skewness	1.48	1.52	3.00	1.46	1.44	2.27	2.19	3.98	5.92	5.93	2.15
Range	99	42	22	1	141	19	60	53	14	27	99
Minimum	0	0	0	0	0	0	0	0	0	0	0
Maximum	99	42	22	1	141	19	60	53	14	27	99
Confidence Level (95.0%)	3.17	1.06	0.48	0.06	4.36	0.48	1.15	0.80	0.22	0.40	1.98
ICC	0.76	0.61	0.58	0.20	0.77	0.54	0.51	0.40	0.90	0.38	0.60

IQR—interquartile range; ICC—intraclass correlation coefficient; SDD—standard deviation.

Table 3. JAMRIS-SIJ inflammation components’ descriptive statistic and intraclass correlation coefficients (ICCs) for six radiologists and two rheumatologists.

Radiologist	Bone Marrow Edema	Joint Space Inflammation	Capsulitis	Enthesitis	Inflammation Domain	Rheumatologist	Bone Marrow Edema	Joint Space Inflammation	Capsulitis	Enthesitis	Inflammation Domain
Mean	19.87	5.84	1.64	0.21	27.35	Mean	9.85	4.38	0.75	0.08	14.98
Median	4	0	0	0	7	Median	1	0	0	0	1
SD	26.98	8.59	4.09	0.40	36.79	SD	15.28	7.30	2.27	0.28	23.03
Kurtosis	0.52	1.78	7.48	0.04	0.49	Kurtosis	1.16	0.76	9.74	7.83	0.84
Skewness	1.28	1.51	2.77	1.43	1.29	Skewness	1.54	1.478	3.23	3.09	1.48
Range	99	42	22	1	141	Range	56	24	11	1	80
Confidence level (95.0%)	3.97	1.26	0.60	0.06	5.41	Confidence Level (95.0%)	3.95	1.89	0.59	0.07	5.95
IQR	0–35	0–11	0–0	0–0	0–50	IQR	0–14	0–6	0–0	0–0	0–21
ICC	0.82	0.61	0.60	0.16	0.81	ICC	0.76	0.50	0.80	0.09	0.73

IQR—interquartile range; ICC—intraclass correlation coefficient; SDD—standard deviation.

Table 4. JAMRIS-SIJ damage components' descriptive statistic and intraclass correlation coefficients (ICCs) for six radiologists and two rheumatologists.

Radiologist	Sclerosis	Erosion	Fatty Lesion	Ankylosis	Backfill	Damage Domain	Rheumatologist	Sclerosis	Erosion	Fatty Lesion	Ankylosis	Backfill	Damage Domain
Mean	1.93	6.66	3.19	0.28	0.72	12.77	Mean	1.75	5.37	0.38	0.40	0.57	8.47
Median	0	3	0	0	0	6	Median	0	2.5	0	0	0	4.5
SD	3.88	9.58	7.10	1.57	3.23	16.87	SD	3.30	7.09	1.53	2.20	2.87	10.04
Kurtosis	4.72	6.47	15.77	34.49	36.95	5.16	Kurtosis	3.55	0.20	22.47	30.85	45.25	1.58
Skewness	2.30	2.24	3.44	5.88	5.81	2.04	Skewness	2.05	1.22	4.66	5.57	6.49	1.34
Range	19	60	53	11	27	99	Range	14	24	9	14	21	44
Confidence level (95.0%)	0.57	1.41	1.04	0.23	0.48	2.48	Confidence Level (95.0%)	0.85	1.83	0.40	0.57	0.74	2.59
IQR	0–2	0–10	0–4	0–0	0–0	0–20	IQR	0–2	0–9	0–0	0–0	0–0	0–15
ICC	0.61	0.44	0.52	0.90	0.29	0.62	ICC	0.17	0.17	0.02	0.95	0.53	0.86

IQR—interquartile range; ICC—intraclass correlation coefficient; SDD—standard deviation.

4. Discussion

The reliability of a measurement instrument is a prerequisite for the assessment of its longitudinal and discriminative validity. The final purpose of developing the OMERACT JAMRIS-SIJ was to detect longitudinal change of the SIJ as a post intervention outcome in order to assess treatment efficacy in clinical trials and to quantify axial disease severity in JIA at a given timepoint. Thus, detection of true change is contingent on the optimal reliability of the instrument. This study is the first in the series of validation steps towards evaluating the measurement properties of the JAMRIS-SIJ. Domain-wise inter-rater reliability of the JAMRIS-SIJ achieved the pre-specified threshold for reliability in the study ($ICC \geq 0.7$) for inflammation (Table 2, Figures 1D and 2A–C), but not for damage (Table 2, Figures 1D, 2D and 3A–D). Within the inflammation domain, the inter-rater reliability for BME achieved the pre-specified threshold for reliability: however, JSI, capsulitis, and enthesitis did not (Table 2). Within the damage domain, except for ankylosis that reached an $ICC \geq 0.7$, the ICCs for sclerosis, erosions, fat lesion and backfill were all < 0.7 . The low reliability of the JAMRIS-SIJ structural domain scores (SDS) is consistent with that of other studies [16,19]. Defining an SDS component requires that raters interpret findings based on the assessment of multiple MRI sequences: nevertheless core and optimal protocols for data interpretation have not been agreed upon. This is especially important in children as many patients are small, and the ability to detect subtle findings, such as erosion, may be influenced more by the optimization of the MRI imaging than any disagreement surrounding the definition. At the inception of the JAMRIS-SIJ score, the definitions of structural domain components (SDC) were ambitious. Although consensus was achieved during the development of the SDC definitions, these definitions had minority dissent among the experts. This may have contributed to the low ICC among raters. Of particular importance is the reliability of scoring erosions, since MRI evidence of erosions, BME, and inflammation constitute criteria for the use of biologics in children with JIA [25].

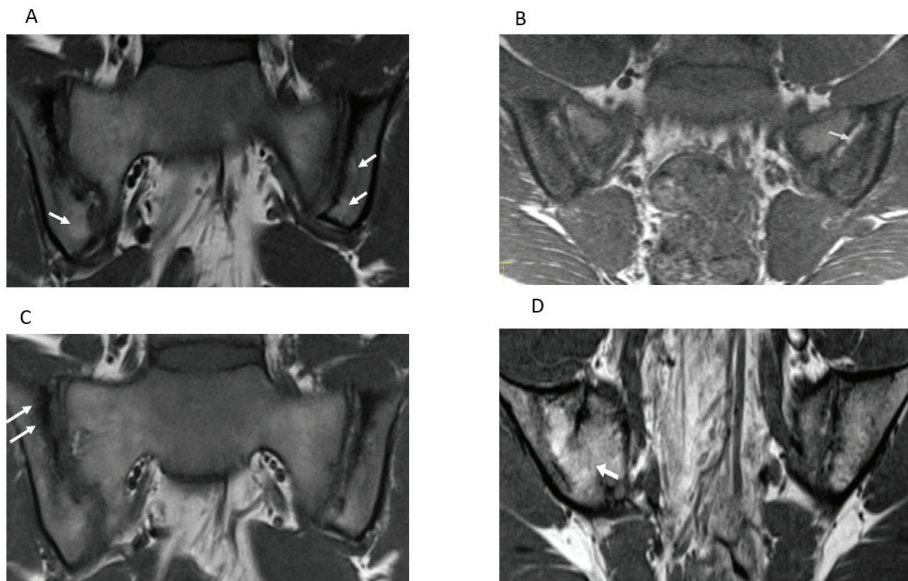


Figure 3. Semicoronal T1-weighted MR images (A–D) through the sacroiliac joint (SIJ) illustrate measurement components the JAMRIS-SIJ. (A) SIJ in a 16-year-old girl with ERA/JSpA. (A) shows fat lesions as a homogenous increased T1 signal intensity within the inferior iliac subchondral bone (arrows), which is the more prominent on the left. (B) SIJ in a 15-year-old boy with ERA/JSpA, shows an area of backfill in the mid to superior subchondral cortex of the left iliac bone. There is increased signal (arrow) that is clearly demarcated from the adjacent normal marrow by irregular dark signal. (C) SIJ in a 16-year-old boy with ERA/JSpA shows sclerosis as a low subarticular signal on the superior iliac subchondral bone (arrows). (D) SIJ in a 13-year-old boy shows the bone marrow signal extending across the right SIJ (arrow), consistent with ankylosis.

There was a slight difference in ICCs obtained for radiologists and rheumatologists (Tables 3 and 4), and depending on the JAMRIS-SIJ component, the difference in ICC was either high or low between the specialties (Tables 3 and 4). Since the scoring method was equally available to all raters, the differences in ICCs may represent different levels of experience of the raters in interpreting musculoskeletal findings in pediatric SIJ MRI [26].

BME is an abnormality that appears in most MRI scoring systems [14]. Its definition had excellent consensus during the development of JAMRIS-SIJ. In this study, inter-rater reliability of BME was consistent, and the good reliability estimates of BME scores may partly be due to the fact that a detailed definition was previously available for scoring of adult and similar description of BME lesions in pediatric SIJs [1,15]. In addition, some of the raters in this study were already familiar with the definition and scoring process of BME. Furthermore, the spectrum of BME abnormalities available in this study may have been limited, which facilitated the decision making of raters during the exercise. Note should be made, however, that the normal spectrum of SIJ signals varies according to the degree of skeletal maturation of children and adolescents [27,28]. As a result, atlases should be developed to address physiologic variation of bone marrow signals across age groups of children and adolescents in future exercises that involve bone marrow scoring in growing joints.

The ICC statistic reflects the proportion of the total variance that is due to variability between subjects in the frequency and extent of the lesion. Consequently, ICC levels will tend to be lower for structural lesions than for BME and applying the same ICC cut-off for what constitutes an acceptable level of reliability may not be appropriate [29]. Notwithstanding the extensive subject content experience and training of most of our study raters, the low ICC performance of some JAMRIS-SIJ items could also be due to the distribution of pathology among cases. There are pragmatic issues with subject selection towards providing a comparable distribution of lesion components represented in each JAMRIS-SIJ domain in opportunity samples such is the case in this study. Noteworthy is the infrequent presence of SIJ ankylosis (an extreme manifestation of JIA) in our study sample. These inherent challenges in the JAMRIS-SIJ measurement component distribution may have adversely affected both subject and component heterogeneity, which, in turn, would have impacted the study inter-rater reliability estimates.

To investigate the non-uniform distribution of our study subjects and components of the JAMRIS-SIJ, the kurtosis of the JAMRIS-SIJ scores was calculated and reported in addition to ICCs. Most JAMRIS-SIJ components were leptokurtic (kurtosis > 3), indicating a substantial deviation of the scores from a uniform distribution. The positive kurtosis alters the subject variance, thereby reducing the reliability estimate. ICC is sensitive to different subject distributions, with optimal ICCs achieved in uniform distributions when rater variability is constant. The values of ICC in our study had a tendency towards under uniformity of distribution as the magnitude of non-uniformity decreased. The overt reliance of ICCs on subject distribution alters the interpretation of ICC as an estimate of agreement in determining the quality of the measurement instrument when the uniformity of the sample subjects and instruments components cannot be guaranteed [29]. These characteristics of the reliability estimates may have contributed to the low reliability in some JAMRIS-SIJ components.

By summing up the component scores of the JAMRIS-SIJ to report the inflammation domain score and structural domain score, equal weight is assumed for each component. However, this may not exactly represent the relative importance of the components in measuring JIA disease activity in the JAMRIS-SIJ inflammation and damage (structural) domains. Furthermore, there may have been overrepresentation of individual components within the domain scores. For instance, within the IDC, the BME item encompasses a significant part of the inflammation domain score (IDS) and consists of three parts: the presence of BME, BME intensity, and BME depth. While BME is a relevant component of the JAMRIS-SIJ, as it signals the beginning of osteochondral inflammation, the appropriate weighting of BME and other components of JAMRIS-SIJ were not considered in this study.

Our study has limitations. Chief among them is the non-uniform case distribution, as noted through the wide variability of score ranges among items of the scale (Tables 2–4). Since it was a retrospective study design and the cases were non-randomly selected, we were limited by the availability of cases, making it difficult to achieve a uniform distribution of JAMRI-SIJ pathological lesion. Consequently, uncommon abnormalities such as ankylosis were underrepresented in the study sample, and common abnormalities such as erosions and BME were overrepresented. The significant deviation from uniformity of the case distribution across JAMRIS-SIJ components may have influenced the reliability estimates. Application of sampling methods that reduce the effect of subject distribution on ICC should be adopted in future studies. Further, since this was the first data-driven assessment for inter-rater reliability of the JAMRIS-SIJ item definitions, it was not uncommon for raters to experience challenges to apply the definitions into the scoring methods.

Future directions of research in our study include the utilization of a calibration module for raters and the development of an annotated reference atlas of the JAMRIS-SIJ item abnormalities as a companion measurement aid prior to the next scoring exercise. Moreover, refining the definitions of the JAMRIS-SIJ items based on the challenges encountered in this reliability scoring exercise is critical. Lessons learned from this study will inform steps towards such refinement of the JAMRIS-SIJ items.

5. Conclusions

The development of a measurement instrument is an iterative process that follows several steps, comprising of construct definition, selection, definition of measurement items, optimization of scoring methods, conduct of pilot studies, and field testing. This reliability study was a preliminary field testing of the JAMRIS-SIJ, as part of a series of validation processes towards establishing its measurement properties. In this study, we reported the results of the initial inter-rater reliability exercise of the JAMRIS-SIJ in children and adolescents with ERA/JSpA. The JAMRIS-SIJ was originally developed to detect change after treatment intervention (multi-timepoint) and disease severity at a single timepoint in JIA, with special consideration for the unique MRI characteristics of the anatomy of growing SIJs. The JAMRIS-SIJ demonstrated good reliability for the inflammation domain across radiologist and rheumatologist raters. Future steps should aim at the following: further defining the parameters of scoring such as the number of slices scored per reader, improving item-wise scores, item weighting, and item definition refinement; developing a measurement atlas that aligns with the proposed scale; and developing an objective rater calibration and training to improve the JAMRIS-SIJ reliability before proceeding to test its reliability and responsiveness.

Author Contributions: Conceptualization, T.M.O., A.S.D., J.L.J. and N.H. (Nele Herregods); methodology, T.M.O., A.S.D., W.P.M., R.G.L., J.L.J., L.J. and N.H. (Nele Herregods); software, J.P., W.P.M., T.M.O. and M.T.; validation, N.H. (Nele Herregods) and J.L.J.; formal analysis, T.M.O.; investigation, T.M.O., A.S.D., J.L.J., N.H. (Nele Herregods), W.P.M., R.G.L., A.B.M., I.S.-S., P.W., S.T., R.M., N.H. (Nigil Haroon), L.J., N.T., S.A., O.P., E.K., M.A.J.v.R., D.R., J.S., J.C. and P.G.C.; resources, T.M.O., A.S.D., I.S.-S., P.W., J.L.J., N.H. (Nele Herregods), and W.P.M.; data curation, T.M.O., M.T., P.W., N.H. (Nele Herregods); J.L.J., A.B.M., A.S.D., J.P. and W.P.M.; writing—original draft preparation, T.M.O.; writing—review and editing, T.M.O., A.S.D., J.L.J., N.H. (Nele Herregods), W.P.M., R.G.L., A.B.M., P.W., S.T., R.M., N.H. (Nigil Haroon), L.J., N.T., S.A., J.P., O.P., M.T., E.K., M.A.J.v.R., D.R., J.S., I.S.-S., J.C. and P.G.C.; visualization, T.M.O. and M.T.; supervision, A.S.D., N.H. (Nigil Haroon), W.P.M., N.H. (Nele Herregods) and R.M.; project administration, T.M.O.; funding acquisition, T.M.O. All authors have read and agreed to the published version of the manuscript.

Funding: This research received no external funding.

Institutional Review Board Statement: This study was conducted according to the guidelines of the Declaration of Helsinki and approved by the research ethics board of The Hospital for Sick Children, Toronto, ON, Canada, protocol number 1000059077).

Informed Consent Statement: Expert imagers and clinicians were informed of study rationale and procedures in writing, and that their voluntary completion and submission of image score data constituted their implied consent to participate. Study image data were acquired retrospectively and anonymized; therefore, the written consent requirement was waived.

Data Availability Statement: Data presented in this study are available on request from the corresponding author.

Acknowledgments: The authors would like to acknowledge the funding provided by the Hospital for SickKids Restracom graduate trainee award and the Queen Elizabeth II/Dunlop Foundation Graduate Student Award in Science and Technology towards salary to T.M.O. PGC is funded in part through the NIHR Leeds Biomedical Research Centre, Leeds UK. The views expressed are those of the authors and not necessarily those of the United Kingdom NHS, the NIHR, or the Department of Health.

Conflicts of Interest: The authors declare no conflict of interest.

Appendix A

MRI protocols for data acquisition of sacroiliac joints cases in the study sample.

The Hospital for Sick Children (Toronto, Canada) Protocol.

All examinations were performed on a 1.5 Tesla MR scanner (Magnetom Avanto, Siemens), including semicoronal (parallel to the long axis of the sacrum) and axial (through the sacroiliac joints) imaging planes. Semicoronal oblique Short Tau Inversion Recovery (STIR) (repetition time (TR)/echo time (TE): 4500/81 ms, matrix (Ma) 256 × 192, slice thickness (SL) 4 mm, and gap 4.5 mm), semicoronal T1-weighted turbo spin echo (TR/TE 560/12, Ma 256 × 192, SL 4 mm and gap 4.5 mm), axial T2 (TR/TE: 5680/111, Ma: 256 × 135, SL: 5 mm and gap: 6), axial T1 (TR/TE: 518/14, Ma: 512 × 180, SL: 5 mm and gap: 6), and if required, post-contrast sequences, was used Post-contrast images were semicoronal fat-saturated T1 (TR/TE: 380/12, Ma: 256 × 192, SL: 4 mm and gap: 4.5), coronal (through the sacroiliac joints) fat-saturated T1 (TR/TE: 520/14, Ma: 320 × 199, SL: 5 mm and gap: 6.0), and axial (through the sacroiliac joints) fat saturated T1 (TR/TE: 456/14, Ma: 288, SL: 5 mm and gap: 6.0. A large field of view (FOV) adjustable to the patient's biotype was used for semicoronal images.

Ghent University Hospital (Ghent, Belgium) MRI Protocol.

MR images were acquired with a body flexed array coil in a 1.5 T MRI unit (Aera/Avanto, Siemens Medical, Erlangen, Germany). The sequence protocol included the following: semicoronal (along the long axis of the sacral bone perpendicular to the second sacral (S2) vertebral body) T1-weighted (T1) turbo spin echo (TSE) (slice thickness (ST): 3 mm; repetition time/echo time (TR/TE): 368/20 ms; field of view (FOV): 320; matrix: 512 × 384; averages: 2; turbo factor (TF): 3), semicoronal Short Tau Inversion Recovery sequence (STIR) (ST: 3 mm; TR/TE/Inversion Time (TI): 5030/67/150 ms; FOV: 320; matrix: 320 × 320; averages 2; TF: 7), and axial STIR (ST: 5 mm; TR/TE/TI: 7540/67/150 ms; FOV: 400 mm; matrix: 320 × 320; averages: 1; TF: 7).

Children's Hospital of Philadelphia (Philadelphia, PA, USA) Protocol.

MR images were acquired on a 3.0 Tesla MR scanner (Siemens Medical Systems, Erlangen, Germany) and included the semicoronal (parallel to the long axis of the sacrum) and axial (through the sacroiliac joints) imaging planes. Short Tau Inversion Recovery (STIR) (repetition time (TR)/echo time (TE): 4000/52 ms, matrix (Ma) 320 × 240, slice thickness (SL) 3 mm, and gap 0.3 mm), T1-weighted turbo spin echo (TR/TE 650/9, Ma 320 × 240, SL 3 mm and gap 0.3 mm), and 3D Dual-Echo Steady State (DESS) (TR/TE 15.3/4.4, Ma 320 × 240, SL 0.7 mm, and gap 0 mm) were collected on the semicoronal plane along with T2-weighted turbo spin echo with fat saturation (fs) (TR/TE 5300/90, Ma 320 × 240, SL 3 mm, and gap 0.3 mm). Large field of view (FOV) coronal sequences were also collected for visualization of both hips (TR/TE 5800/90, Ma 320 × 294, SL 3 mm, and gap 0.3 mm).

Appendix B

Table A1. Slice count for JAMRIS-SJJ components.

	Bone Marrow Edema	Joint Space Inflammation	Capsulitis	Sclerosis	Erosion	Fat Lesion	Ankylosis	Backfill
Right upper ilium	8.09	8.09	8.09	8.41	8.41	8.41	8.41	8.41
Right upper sacrum	8.09			8.41				
Right lower ilium	8.06	8.09	8.09	8.41	8.41	8.41	8.41	8.41
Right lower sacrum	8.09			8.41	8.41	8.41		
Right depth	8.09							
Right intensity	8.09							
Left Upper Ilium	8.09	8.09	8.09	8.41	8.41	8.41	8.41	8.41
Left Upper Sacrum	8.09			8.41	8.41	8.41		
Left Lower Ilium	8.09	8.09	8.09	8.41	8.41	8.41	8.41	8.41
Left Lower Sacrum	8.09			8.41	8.41	8.41		
Left Depth	8.09							
Left Intensity	8.09							
R+L Upper Ilium	8.09 (7-9, 8)	8.09 (7-9, 8)	8.09 (7-9, 8)	8.41 (7-10, 8)	8.41 (7-10, 8)	8.41 (7-10, 8)	8.41 (7-10, 8)	8.41 (7-10, 8)
R+L Upper Sacrum	7.95 (7-9, 8)			8.41 (7-10, 8)	8.41 (7-10, 8)	8.41 (7-10, 8)		
R+L Lower Ilium	8.07 (7-9, 8)	8.09 (7-9, 8)	8.09 (7-9, 8)	8.41 (7-10, 8)	8.41 (7-10, 8)	8.41 (7-10, 8)	8.41 (7-10, 8)	8.41 (7-10, 8)
R+L Lower Sacrum	8.09 (7-7, 8)			8.41 (7-10, 8)	8.41 (7-10, 8)	8.41 (7-10, 8)		
R+L Depth	8.09 (7-7, 8)							
R+L Intensity	8.09 (7-9, 8)							

IQR—interquartile range.

Appendix C

Table A2. SIJ location-wise intraclass correlation coefficients (ICC) for JAMRIS-SIJ MRI.

	Bone Marrow Edema	Joint Space Inflammation	Capsulitis	Erosion	Fat Lesion	Ankylosis	Backfill
Right upper ilium	0.17	0.18	0.06	0.14	0.06	0.03	0.02
Right upper sacrum	0.15			0.05	0.05		
Right lower ilium	0.17	0.16	0.03	0.10	0.05	0.01	0.02
Right lower sacrum	0.13			0.04	0.03		
Right depth	0.23						
Right intensity	0.11						
Left Upper Ilium	0.20	0.18	0.05	0.18	0.06	0.00	0.02
Left Upper Sacrum	0.16			0.06	0.03		
Left Lower Ilium	0.29	0.16	0.04	0.17	0.03	0.00	0.01
Left Lower Sacrum	0.15			0.03	0.01		
Left Depth	0.30						
Left Intensity	0.14						
R+L Upper Ilium	0.19	0.18	0.05	0.16	0.06	0.01	0.02
R+L Upper Sacrum	0.16			0.05	0.04		
R+L Lower Ilium	0.23	0.16	0.03	0.13	0.04	0.00	0.03
R+L Lower Sacrum	0.14			0.04	0.02		
R+L Depth	0.26						
R+L Intensity	0.12						

ICC—intraclass correlation coefficient, SIJ—sacroiliac joint, MRI—magnetic resonance imaging.

References

1. Weiss, P.F.; Maksymowych, W.P.; Lambert, R.G.; Jaremko, J.L.; Biko, D.M.; Paschke, J.; Brandon, T.G.; Xiao, R.; Chauvin, N.A. Feasibility and reliability of the Spondyloarthritis Research Consortium of Canada sacroiliac joint inflammation score in children. *Arthritis Res. Ther.* **2018**, *20*, 56. [[CrossRef](#)] [[PubMed](#)]
2. Petty, R.E.; Southwood, T.R.; Manners, P.; Baum, J.; Glass, D.N.; Goldenberg, J.; He, X.; Maldonado-Cocco, J.; Orozco-Alcala, J.; Prieur, A.-M.; et al. International League of Associations for Rheumatology classification of juvenile idiopathic arthritis: Second revision, Edmonton, 2001. *J. Rheumatol.* **2004**, *31*, 390–392. [[PubMed](#)]
3. Martini, A.; Ravelli, A.; Avcin, T.; Beresford, M.W.; Burgos-Vargas, R.; Cuttica, R.; Ilowite, N.T.; Khubchandani, R.; Laxer, R.M.; Lovell, D.J.; et al. Toward New Classification Criteria for Juvenile Idiopathic Arthritis: First Steps, Pediatric Rheumatology International Trials Organization International Consensus. *J. Rheumatol.* **2019**, *46*, 190–197. [[CrossRef](#)] [[PubMed](#)]
4. Consolaro, A.; Ruperto, N.; Bazso, A.; Pistorio, A.; Magni-Manzoni, S.; Filocamo, G.; Malattia, C.; Viola, S.; Martini, A.; Ravelli, A. Development and validation of a composite disease activity score for juvenile idiopathic arthritis. *Arthritis Care Res. Off. J. Am. Coll. Rheumatol.* **2009**, *61*, 658–666. [[CrossRef](#)]
5. Consolaro, A.; Negro, G.; Gallo, M.C.; Bracciolini, G.; Ferrari, C.; Schiappapietra, B.; Pistorio, A.; Bovis, F.; Ruperto, N.; Martini, A.; et al. Defining criteria for disease activity states in nonsystemic juvenile idiopathic arthritis based on a three-variable juvenile arthritis disease activity score. *Arthritis Care Res.* **2014**, *66*, 1703–1709. [[CrossRef](#)] [[PubMed](#)]
6. Fox, R.S.; Malcarne, V.L.; Roesch, S.C.; Sadler, G.R. The Cultural Health Attributions Questionnaire (CHAQ): Reliability, validity, and refinement. *Cult. Divers. Ethn. Minor. Psychol.* **2014**, *20*, 283–292. [[CrossRef](#)] [[PubMed](#)]
7. Ringold, S.; Angeles-Han, S.T.; Beukelman, T.; Lovell, D.; Cuello, C.A.; Becker, M.L.; Colbert, R.A.; Feldman, B.M.; Ferguson, P.J.; Gewanter, H.; et al. 2019 American College of Rheumatology/Arthritis Foundation Guideline for the Treatment of Juvenile Idiopathic Arthritis: Therapeutic Approaches for Non-Systemic Polyarthritis, Sacroiliitis, and Enthesitis. *Arthritis Care Res.* **2019**, *71*, 717–734. [[CrossRef](#)]
8. Vleeming, A.; Schuenke, M.D.; Masi, A.T.; Carreiro, J.E.; Willard, F.H. The sacroiliac joint: An overview of its anatomy, function and potential clinical implications. *J. Anat.* **2012**, *221*, 537–567. [[CrossRef](#)]
9. Colebatch-Bourn, A.N.; Edwards, C.J.; Collado, P.; D’Agostino, M.-A.; Hemke, R.; Jousse-Joulin, S.; Maas, M.; Martini, A.; Naredo, E.; Østergaard, M.; et al. EULAR-PreS points to consider for the use of imaging in the diagnosis and management of juvenile idiopathic arthritis in clinical practice. *Ann. Rheum. Dis.* **2015**, *74*, 1946–1957. [[CrossRef](#)]
10. Cellucci, T.; Guzman, J.; Petty, R.E.; Bathish, M.; Benseler, S.M.; Ellsworth, J.E.; Houghton, K.M.; Leblanc, C.M.A.; Huber, A.M.; Luca, N.; et al. Management of Juvenile Idiopathic Arthritis 2015: A position statement from the pediatric Committee of the Canadian Rheumatology Association. *J. Rheumatol.* **2016**, *43*, 1773–1776. [[CrossRef](#)]
11. Restrepo, R.; Lee, E.Y.; Babyn, P.S. Juvenile idiopathic arthritis: Current practical imaging assessment with emphasis on magnetic resonance imaging. *Radiol. Clin. N. Am.* **2013**, *51*, 703–719. [[CrossRef](#)]
12. Herregods, N.; Dehoorne, J.; Joos, R.; Jaremko, J.L.; Baraliakos, X.; Leus, A.; Van den Bosch, F.; Verstraete, K.; Jans, L. Diagnostic value of MRI features of sacroiliitis in juvenile spondyloarthritis. *Clin. Radiol.* **2015**, *70*, 1428–1438. [[CrossRef](#)] [[PubMed](#)]
13. Lambert, R.G.; Bakker, P.A.C.; van der Heijde, D.; Weber, U.; Rudwaleit, M.; Hermann, K.-G.A.; Sieper, J.; Baraliakos, X.; Bennett, A.; Braun, J.; et al. Defining active sacroiliitis on MRI for classification of axial spondyloarthritis: Update by the ASAS MRI working group. *Ann. Rheum. Dis.* **2016**, *75*, 1958–1963. [[CrossRef](#)]
14. Maksymowych, W.P.; Weber, U. Diagnostic utility of MRI in early spondyloarthritis. *Curr. Rheumatol. Rep.* **2011**, *13*, 402–408. [[CrossRef](#)]
15. Maksymowych, W.P.; Inman, R.D.; Salonen, D.; Dhillon, S.S.; Williams, M.; Stone, M.; Conner-spady, B.; Palsat, J.; Lambert, R.G.W. Spondyloarthritis research Consortium of Canada magnetic resonance imaging index for assessment of sacroiliac joint inflammation in ankylosing spondylitis. *Arthritis Rheum.* **2005**, *53*, 703–709. [[CrossRef](#)] [[PubMed](#)]
16. Maksymowych, W.P.; Wichuk, S.; Chiowchanwisawakit, P.; Lambert, R.G.; Pedersen, S.J. Development and preliminary validation of the spondyloarthritis research consortium of Canada magnetic resonance imaging sacroiliac joint structural score. *J. Rheumatol.* **2015**, *42*, 79–86. [[CrossRef](#)]
17. Malattia, C.; Damasio, M.B.; Pistorio, A.; Ioseliani, M.; Vilca, I.; Valle, M.; Ruperto, N.; Viola, S.; Buoncompagni, A.; Magnano, G.M.; et al. Development and preliminary validation of a paediatric-targeted MRI scoring system for the assessment of disease activity and damage in juvenile idiopathic arthritis. *Ann. Rheum. Dis.* **2011**, *70*, 440–446. [[CrossRef](#)]
18. Althoff, C.E.; Sieper, J.; Song, I.-H.; Haibel, H.; Weiß, A.; Diekhoff, T.; Rudwaleit, M.; Freundlich, B.; Hamm, B.; Hermann, K.-G.A. Active inflammation and structural change in early active axial spondyloarthritis as detected by whole-body MRI. *Ann. Rheum. Dis.* **2013**, *72*, 967–973. [[CrossRef](#)]
19. Weiss, P.F.; Maksymowych, W.P.; Lambert, R.G.; Jaremko, J.L.; Biko, D.M.; Paschke, J.; Brandon, T.G.; Xiao, R.; Chauvin, N.A. Feasibility and Reliability of the Spondyloarthritis Research Consortium of Canada Sacroiliac Joint Structural Score in Children. *J. Rheumatol.* **2018**, *45*, 1411–1417. [[CrossRef](#)] [[PubMed](#)]
20. Panwar, J.; Tse, S.M.L.; Lim, L.; Tolend, M.A.; Radhakrishnan, S.; Salman, M.; Moineddin, R.; Doria, A.S.; Stimec, J. Spondyloarthritis Research Consortium of Canada Scoring System for Sacroiliitis in Juvenile Spondyloarthritis/Enthesitis-related Arthritis: A Reliability, Validity, and Responsiveness Study. *J. Rheumatol.* **2019**, *46*, 636–644. [[CrossRef](#)]

21. Otopo, T.M.; Conaghan, P.G.; Maksymowych, W.P.; van der Heijde, D.; Weiss, P.; Sudol-Szopinska, I.; Herregods, N.; Jaremko, J.L.; Meyers, A.B.; Rumsey, D.; et al. Preliminary Definitions for Sacroiliac Joint Pathologies in the OMERACT Juvenile Idiopathic Arthritis MRI Score (OMERACT JAMRIS-SIJ). *J. Rheumatol.* **2019**, *46*, 1192–1197. [[CrossRef](#)]
22. Walter, S.D.; Eliasziw, M.; Donner, A. Sample size and optimal designs for reliability studies. *Stat. Med.* **1998**, *17*, 101–110. [[CrossRef](#)]
23. Koo, T.K.; Li, M.Y. A Guideline of Selecting and Reporting Intraclass Correlation Coefficients for Reliability Research. *J. Chiropr. Med.* **2016**, *15*, 155–163. [[CrossRef](#)] [[PubMed](#)]
24. Maksymowych, W.P.; Krabbe, S.; Biko, D.; Weiss, P.; Maksymowych, M.P.; Cheah, J.; Kröber, G.; Weber, U.; Danebod, K.; Bird, P.; et al. FRI0597 Validation of web-based calibration modules for imaging scoring systems based on principles of artificial intelligence: The sparcc mri sacroiliac joint inflammation score. *Ann. Rheum. Dis.* **2018**, *77*, 822. [[CrossRef](#)]
25. Leblanc, C.M.A.; Lang, B.; Bencivenga, A.; Chetaille, A.-L.; Dancey, P.; Dent, P.; Miettunen, P.; Oen, K.; Rosenberg, A.; Roth, J.; et al. Access to Biologic Therapies in Canada for Children with Juvenile Idiopathic Arthritis. *J. Rheumatol.* **2012**, *39*, 1875–1879. [[CrossRef](#)] [[PubMed](#)]
26. Clemente, E.J.L.; Tolend, M.; Junhasavasdikul, T.; Stimec, J.; Tzaribachev, N.; Koos, B.; Spiegel, L.; Moineddin, R.; Doria, A.S. Qualitative and semi-quantitative assessment of temporomandibular joint MRI protocols for juvenile idiopathic arthritis at 1.5 and 3.0 T. *Eur. J. Radiol.* **2018**, *98*, 90–99. [[CrossRef](#)]
27. Chauvin, N.A.; Xiao, R.; Brandon, T.G.; Biko, D.M.; Francavilla, M.; Khrichenko, D.; Weiss, P.F. MRI of the Sacroiliac Joint in Healthy Children. *Am. J. Roentgenol.* **2019**, *212*, 1–7. [[CrossRef](#)]
28. Herregods, N.; Jans, L.B.O.; Chen, M.; Paschke, J.; De Buyser, S.L.; Renson, T.; Dehoorne, J.; Joos, R.; Lambert, R.G.W.; Jaremko, J.L. Normal subchondral high T2 signal on MRI mimicking sacroiliitis in children: Frequency, age distribution, and relationship to skeletal maturity. *Eur. Radiol.* **2021**, *31*, 3498–3507. [[CrossRef](#)]
29. Mehta, S.; Bastero-Caballero, R.F.; Sun, Y.; Zhu, R.; Murphy, D.K.; Hardas, B.; Koch, G. Performance of intraclass correlation coefficient (ICC) as a reliability index under various distributions in scale reliability studies. *Stat. Med.* **2018**, *37*, 2734–2752. [[CrossRef](#)]



Article

Assessing the Reliability of the OMERACT Juvenile Idiopathic Arthritis Magnetic Resonance Scoring System for Temporomandibular Joints (JAMRIS-TMJ)

Mirkamal Tolend ¹, Andrea S. Doria ^{1,2,*}, Arthur B. Meyers ³, Tore A. Larheim ⁴, Shelly Abramowicz ^{5,6}, Julien Aguet ², Simone Appenzeller ⁷, Linda Z. Arvidsson ⁴, Lauren W. Averill ⁸, Brian M. Feldman ^{1,9}, Saurabh Guleria ¹⁰, Emilio J. Inarejos Clemente ¹¹, Jacob L. Jaremko ¹², Thitiporn Junhasavasdikul ¹³, Thelma von Kalle ¹⁴, Eva Kirkhus ¹⁵, Bernd Koos ¹⁶, Elka Miller ¹⁷, Rahim Moineddin ¹⁸, Jyoti Panwar ¹⁹, Zachary S. Peacock ²⁰, Cory M. Resnick ²¹, Marion A. van Rossum ^{22,23}, Jennifer Stimec ², George Tomlinson ²⁴, Nikolay Tzaribachev ²⁵ and Christian J. Kellenberger ²⁶

- ¹ Institute of Medical Science, University of Toronto, Toronto, ON M5S 1A8, Canada; m.tolend@mail.utoronto.ca (M.T.); brian.feldman@sickkids.ca (B.M.F.)
- ² Department of Diagnostic Imaging, The Hospital for Sick Children, Toronto, ON M5G 1X8, Canada; Julien.Aguet@sickkids.ca (J.A.); jennifer.stimec@sickkids.ca (J.S.)
- ³ Department of Radiology, Cincinnati Children’s Hospital Medical Center, Cincinnati, OH 45229, USA; arthur.meyers@cchmc.org
- ⁴ Department of Maxillofacial Radiology, Institute of Clinical Dentistry, University of Oslo, 0317 Oslo, Norway; t.a.larheim@odont.uio.no (T.A.L.); l.z.arvidsson@odont.uio.no (L.Z.A.)
- ⁵ Division of Oral and Maxillofacial Surgery, Departments of Surgery and Pediatrics, Emory University School of Medicine, Atlanta, GA 30322, USA; sabram5@emory.edu
- ⁶ Oral and Maxillofacial Surgery, Children’s Healthcare of Atlanta, Atlanta, GA 30322, USA
- ⁷ Department of Orthopedics, Rheumatology and Traumatology, School of Medical Science, University of Campinas, Campinas 13083-970, Brazil; appenzellersimone@yahoo.com
- ⁸ Department of Medical Imaging, Nemours Children’s Health System, Alfred I. duPont Hospital for Children, Wilmington, DE 19803, USA; lauren.averill@nemours.org
- ⁹ Division of Rheumatology, The Hospital for Sick Children, Toronto, ON M5G 1X8, Canada
- ¹⁰ Austin Radiological Association, Austin, TX 78731, USA; saurabhguleria@gmail.com
- ¹¹ Department of Diagnostic Imaging, Hospital Sant Joan de Deu, 08950 Barcelona, Spain; einarejos@sjdhospitalbarcelona.org
- ¹² Department of Radiology & Diagnostic Imaging, University of Alberta, Edmonton, AB T6G 2B7, Canada; jjaremko@ualberta.ca
- ¹³ Faculty of Medicine Ramathibodi Hospital, Mahidol University, Bangkok 10400, Thailand; maprangpo@hotmail.com
- ¹⁴ Department of Pediatric Radiology, Radiologisches Institut, Olgahospital Klinikum Stuttgart, 70174 Stuttgart, Germany; t.vonkalle@klinikum-stuttgart.de
- ¹⁵ Department of Radiology, Oslo University Hospital, 0424 Oslo, Norway; eva.kirkhus@ous-hf.no
- ¹⁶ Department of Orthodontics, University Hospital Tübingen, 72076 Tübingen, Germany; Bernd.Koos@med.uni-tuebingen.de
- ¹⁷ Department of Medical Imaging, Children’s Hospital of Eastern Ontario, University of Ottawa, Ottawa, ON K1H 8L1, Canada; EMiller@cheo.on.ca
- ¹⁸ Department of Family & Community Medicine, University of Toronto, Toronto, ON M5G 1V7, Canada; rahim.moineddin@utoronto.ca
- ¹⁹ Department of Radiology, Christian Medical College and Hospital, Vellore 632004, Tamil Nadu, India; drjyoticmch@gmail.com
- ²⁰ Department of Oral and Maxillofacial Surgery, Massachusetts General Hospital, Boston, MA 02114, USA; zpeacock@partners.org
- ²¹ Department of Plastic and Oral Surgery, Boston Children’s Hospital, Boston, MA 02115, USA; Cory.Resnick@childrens.harvard.edu
- ²² Department of Pediatrics, Emma Children’s Hospital, Amsterdam University Medical Center, 1105 AZ Amsterdam, The Netherlands; m.a.vanrossum@amsterdamumc.nl
- ²³ Amsterdam Rheumatology and Immunology Center, Reade, 1007 MB Amsterdam, The Netherlands
- ²⁴ Department of Medicine, University Health Network, Toronto, ON M5G 2C4, Canada; george.tomlinson@utoronto.ca
- ²⁵ Pediatric Rheumatology Research Institute, 24576 Bad Bramstedt, Germany; tzaribachev@pri-research.com
- ²⁶ Department of Diagnostic Imaging, University Children’s Hospital Zürich, 8032 Zürich, Switzerland; Christian.Kellenberger@kispj.uzh.ch

Citation: Tolend, M.; Doria, A.S.; Meyers, A.B.; Larheim, T.A.; Abramowicz, S.; Aguet, J.; Appenzeller, S.; Arvidsson, L.Z.; Averill, L.W.; Feldman, B.M.; et al. Assessing the Reliability of the OMERACT Juvenile Idiopathic Arthritis Magnetic Resonance Scoring System for Temporomandibular Joints (JAMRIS-TMJ). *J. Clin. Med.* **2021**, *10*, 4047. <https://doi.org/10.3390/jcm10184047>

Academic Editors:
Iwona Sudol-Szopińska and
Mihra Taljanovic

Received: 23 July 2021
Accepted: 27 August 2021
Published: 7 September 2021

Publisher’s Note: MDPI stays neutral with regard to jurisdictional claims in published maps and institutional affiliations.



Copyright: © 2021 by the authors. Licensee MDPI, Basel, Switzerland. This article is an open access article distributed under the terms and conditions of the Creative Commons Attribution (CC BY) license (<https://creativecommons.org/licenses/by/4.0/>).

* Correspondence: Andrea.Doria@sickkids.ca; Tel.: +1-416-813-6079

Abstract: Contrast-enhanced magnetic resonance imaging (MRI) remains the most comprehensive modality to assess juvenile idiopathic arthritis (JIA)-related inflammation and osteochondral damage in the temporomandibular joints (TMJ). This study tested the reliability of a new JIA MRI scoring system for TMJ (JAMRIS-TMJ) and the impact of variations in calibration and reader specialty. Thirty-one MRI exams of bilateral TMJs were scored independently using the JAMRIS-TMJ by 20 readers consisting of radiologists and non-radiologist clinicians in three reading groups, with or without a calibrating atlas and/or tutorial. The inter-reader reliability in the multidisciplinary cohort assessed by the generalizability coefficient was 0.61–0.67 for the inflammatory and 0.66–0.74 for the damage domain. The atlas and tutorial did not improve agreement within radiologists, but improved the agreement between radiologist and non-radiologist groups. Agreements between different calibration levels were 0.02 to 0.08 lower by the generalizability coefficient compared to agreement within calibration levels; agreement between specialty groups was 0.04 to 0.10 lower than within specialty groups. Averaging two radiologists raised the reliability above 0.8 for both domains. Therefore, the reliability of JAMRIS-TMJ was moderate-to-good depending on the presence of specialty and calibration differences. The atlas and tutorial are necessary to improve reliability when the reader cohort consists of multiple specialties.

Keywords: juvenile idiopathic arthritis; magnetic resonance imaging; temporomandibular joints; outcome measure; reliability; generalizability theory

1. Introduction

There is an increasing need to standardize the imaging assessment of temporomandibular joints (TMJ) in children with juvenile idiopathic arthritis (JIA). The involvement of the TMJ in JIA is frequent yet often difficult to detect clinically at early stages. The reported frequency of TMJ involvement in large series varies between 40 and 70% [1–4]. These changes often develop without clinical findings, yet may lead to irreversible facial changes and functional impairments in severe cases [5–8]. The effective use of TMJ imaging is therefore important for enabling earlier disease detection and the start of medical, orthodontic, orthopedic, and physiotherapeutic management to prevent or minimize severe functional outcomes. Contrast enhanced magnetic resonance imaging (MRI) is currently the most informative imaging modality, as it allows visualization of both the active inflammatory disease as well as the extent of structural damage in the TMJ. Other imaging modalities cannot comprehensively assess both domains of disease burden [1,3,9–15]. However, there remains great variability in the acquisition and interpretation of TMJ MRI.

An international, multidisciplinary expert group was formed within the Outcome Measures in Rheumatology (OMERACT) network to develop MRI scoring systems for JIA (JAMRI working group), with a dedicated subgroup for developing the TMJ-specific scoring system (JAMRIS-TMJ). A consensus scoring system was drafted based on the testing of existing TMJ MRI scoring systems and subsequent formal consensus techniques, including Delphi surveys, nominal group technique, and consensus voting [16]. Relative importance weights of the items and grades were determined through a discrete choice experiment method and were shown to possess face validity and construct validity in an image-based vignette ranking exercise [17]. The present study was undertaken as the next step in testing the required clinimetric properties of the weighted JAMRIS-TMJ, specifically its reliability, in line with the instrument appraisal framework of OMERACT [18].

In this study, we examined the reliability of the semiquantitative JAMRIS-TMJ scoring system with a large multicenter, multidisciplinary group of readers. We tested the impact of multiple sources of variance on the JAMRIS-TMJ score, estimating not only the impact of differences in readers, but also the differences in levels of reader calibration (i.e., imaging atlas [19], with or without tutorial), reader specialty, and patient-level correlation. Specif-

ically, our primary aim was to compare the scoring system's inter-reader reliability by subgroups, at different levels of calibration and by radiologist and non-radiologist clinician groups. Secondary aims included the assessment of reliability in less controlled scenarios, where multiple sources of variability coexist in the scoring method. These sources included within-reader variations, between readers with different levels of calibration, between radiologist and non-radiologist clinician groups, as well as the score correlation between the right and left TMJ within the same patient. The analysis was based on generalizability (G) theory [20,21], as it is able to produce comparable reliability coefficients that can integrate these additional sources of variance (for more background information, please see Appendix A). By comparing the reliability coefficients and the relative impact of these variances on the overall measurement error, we proposed recommendations on the reading conditions to improve reliability.

2. Materials and Methods

2.1. Scoring Materials and TMJ MRI Exams

The scoring system tested in this study is developed to evaluate the MRI-observable changes in the TMJs in children with JIA (named JAMRIS-TMJ) [16]. It consists of 8 weighted items grouped into inflammatory and osteochondral damage domains. The items are graded in two or three levels, and include bone marrow edema, bone marrow enhancement, joint effusion, synovial thickening, and joint enhancement in the inflammatory domain, and condylar flattening, erosion, and disk abnormalities in the damage domain. The definitions of items and grades of the JAMRIS-TMJ appear in Appendix . The two TMJs visualized in the same MRI exam are scored independently of the contralateral side.

The TMJ MRI exams used for the reading were performed on a 1.5 Tesla system with dual ring coils in 25 patients and larger multichannel surface coil in 6 patients. The imaging sequences contained T1-weighted, proton density-weighted, and fat suppressed T2-weighted precontrast sequences in the sagittal oblique plane, and T1-weighted fat suppressed Gadolinium-enhanced sequences in the sagittal oblique and coronal planes (Appendix C). A TMJ MRI atlas for JIA that supplements the JAMRIS-TMJ was used in some of the reading groups to study the difference in reader calibration. The atlas included ideal representations and descriptions of each of the scored items and grades in relevant imaging sequences, as well as key image interpretation pitfalls [19]. The reading order of the exams was randomized for each reader and scoring scenario.

Sample size was estimated using reference tables based on the intraclass correlation coefficient (ICC). Assuming 5 readers, using 32 cases would achieve a 95% confidence interval width of 0.2 around an expected ICC of 0.8, or 0.3 around 0.6 [22,23]. In total, bilateral joints from 31 patients were used, with the 62 total joints analyzed in a hierarchically nested model. Scans were chosen nonrandomly from previously imaged patients with known or suspected JIA to represent the full range of TMJ pathology in this condition, from normal appearances to severe inflammation and deformity.

2.2. Reading Exercise and Data Structure

A schematic summary of the study design is shown in Figure 1. Bilateral TMJ MR studies from 31 patients were read by a total of 20 readers (15 radiologists, 2 surgeons, 2 rheumatologists and 1 orthodontist) in three groups blinded to clinical information:

- Group 1 included five radiologists, one oral-maxillofacial surgeon, and one rheumatologist. These seven readers first scored the 31 cases with just the provided scoring system (dataset 1A), then scored the same cases again after 1–2 months, using the imaging atlas (dataset 1B).
- Group 2 included five radiologists and one oral-maxillofacial surgeon. These six readers first scored the same 31 cases using the scoring system and the atlas (dataset 2A), then scored the same cases again after 1–2 months, following a group calibration tutorial session (dataset 2B).

- Group 3 consisted of seven readers including 5 pediatric radiologists, 1 pediatric rheumatologist, and 1 orthodontist who also scored the same cases, but only once, after the group calibration session that was held together with the group 2 readers (dataset 3).

The 13 readers in groups 1 and 2 were randomly assigned to their respective groups. The group 3 readers were analyzed separately, since they had previously participated in a reliability exercise using 21 of these 31 cases and three existing TMJ MRI scoring systems from which this new scoring system was developed [16].

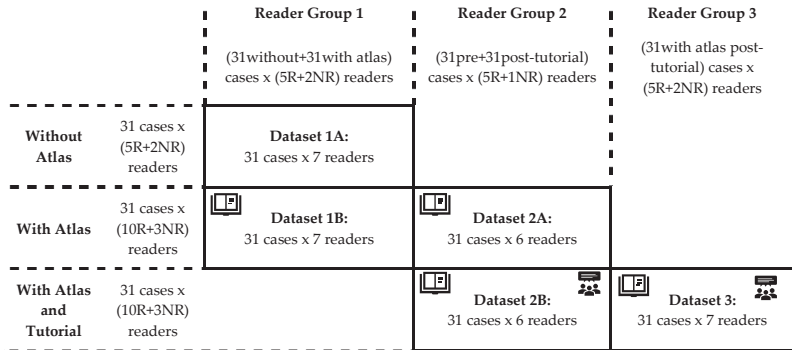


Figure 1. Schematic representation of the composition and methods of the different reader groups. All reader groups in this study used the same set of 31 bilateral temporomandibular joint (TMJ) examinations from patients with diagnosed or suspected juvenile idiopathic arthritis (JIA, clinical characteristics shown on Table 1). Pooling datasets 1B with 2A, and 2B with 3 enables the calculation of inter-reader reliability in larger reader groups and within and between reader specialty groups (results shown on Table 2). Pooling datasets 1A with 1B, and 2A with 2B enables the calculation of intrareader reliability between levels of calibration and inter-reader reliability between and within levels of calibration (results shown on Table 3). Abbreviations: R, radiologist; NR, non-radiologist clinician.

2.3. Data Analysis

Reliability of score on a single joint was assessed using G coefficients, which are extensions of the intraclass correlation coefficient (Appendix A). Two- or three-facet G coefficients were calculated based on whether a third variable level for each observation was stratified or pooled, respectively (Figure 1), as described below.

The two-facet G coefficients contain the “Reader” and “Patient” facets and are presented by stratifying the “Aid” variable in three groups (i.e., baseline, atlas, atlas + tutorial levels), and also the “Specialty” variable in three groups (radiologists, non-radiologist clinicians, and total), yielding 3 × 3 matrix of two-facet G coefficients for each domain.

For the three-facet G coefficients, in addition to the “Rater” and “Patient” facets, a third facet, either the “Aid” or “Specialty”, is included in the calculation. The five datasets are pooled according to the third facet variable by:

1. Combining the different calibration levels while keeping radiologist and non-radiologist groups separate, i.e., dataset 1A with 1B for +/–atlas, and 2A and 2B for +/–tutorial (vertical pooling on Figure 1).
2. Combining the radiologist and non-radiologist data while keeping the calibration level separate, i.e., dataset 1B with 2A, and 2B with 3 (horizontal pooling on Figure 1).

2.4. Statistical Methods

Multiway ANOVA was performed using the VARCOMP procedure with the restricted maximum likelihood method in SAS 9.4 (Cary, NC, USA) to determine the variance components corresponding to the main effect and interactions of the clustering variables in this study, which are the joint (J), patient (P), reader (R), the presence or absence of aid

(A), and whether the reader was a radiologist or non-radiologist clinician (S, for specialty). Using these variance components, G coefficients corresponding to various types of measurement scenarios were calculated by the formulae in Appendix D, which were derived from references on G theory analysis [20,21].

3. Results

The clinical characteristics of the patient sample are listed in Table 1. There was a high prevalence of females (84%) and the oligoarticular subtype of JIA (55%). On MRI, by median of 13 tutorial-calibrated readers, 71% of joints showed nonzero grade for the JAMRIS-TMJ inflammation domain (range 55–95%, IQR 68–79%), and 69% for the damage domain (range 47–81%, IQR 58–74%). Unilateral inflammatory findings, i.e., non-zero inflammation domain score only on one side, was seen in 19% of patients (range 10–32%, IQR 13–23%); unilateral osteochondral damage was also seen in 19% of patients (range 6–35%, IQR 13–26%).

Table 1. Clinical characteristics of the cohort of 31 patients whose MRI examinations of temporomandibular joints (TMJs) were used for the reliability exercise. Laboratory and physical examination test values are those available at the closest date within three months in relation to the study MRI date. Abbreviations: JIA (juvenile idiopathic arthritis), SD (standard deviation), HLA-B27 (human leukocyte antigen B27), ANA (antinuclear antibody), RF (rheumatoid factor), DMARD (disease modifying antirheumatic drug), anti-TNF (tumor necrosis factor inhibitor).

Clinical Characteristics of Patient Sample	
Age at diagnosis (years)	8.0 (SD 4.5, range 0.5–15.3)
Age at MRI (years)	11.6 (SD 3.0, range 6.2–16.9)
Disease duration (years)	3.6 (SD 4.4, range 6.8–15.7)
Sex	5 male, 26 female
JIA subtype	
Oligoarticular	12
Oligoarticular extended	5
Polyarticular	9 (all RF–)
Enthesitis related	1
Psoriatic arthritis	1
Undifferentiated	1
No JIA diagnosis	2
HLA-B27+ (<i>n</i> tested, % of tested)	1 (19, 5%)
ANA+	18 (58%)
RF+ (<i>n</i> tested, % of tested)	1 (30, 3%)
Uveitis	7 (23%)
Facial changes (including asymmetry, decreased condylar translation, retrognathia)	19 (61%)
Crepitation	4 (13%)
Decreased mouth opening (<10th percentile)	10 (32%)
TMJ pain	7 (23%)
Active treatment (including NSAIDs, DMARDs, anti-TNF, etc.)	20 (65%)
History of DMARD use (past and/or current)	15 (48%)

3.1. Two-Facet G Coefficients: Reliability by Subgroups of Measurement Aid and Reader Specialty

Table 2 lists the results of reliability in each of the reader subgroups. The inter-reader reliability coefficients in the typical research setting, where multiple radiologists score the images with the aid of the atlas and after an interactive calibration tutorial, were 0.73 for the inflammatory and 0.77 for the damage domain (Table 2). These correspond to a 95% measurement error of +/− 25 percentage points each on the respective JAMRIS-TMJ domains.

Table 2. Two-facet generalizability coefficients. Agreement on the TMJ score with two sources of variance—patient and reader. The 95% confidence interval of measurement reflects the measurement error interval around a given score, in the units of the respective JAMRIS domain.

Inter-Reader Absolute Agreement Reliability	Generalizability Coefficient			95% CI of Score (+/− Percentage Points)		
	Baseline	Atlas	Atlas + Tutorial	Baseline	Atlas	Atlas + Tutorial
Inflammatory domain						
Radiologists (n = 5, 10, 10)	0.71	0.73	0.73	27	26	25
Non-radiologist clinicians (n = 2, 3, 3)	0.49	0.53	0.45	35	30	37
All readers (n = 7, 13, 13)	0.61	0.66	0.67	32	28	28
Damage domain						
Radiologists (n = 5, 10, 10)	0.76	0.77	0.77	24	25	25
Non-radiologist clinicians (n = 2, 3, 3)	0.44	0.46	0.70	42	42	28
All readers (n = 7, 13, 13)	0.68	0.66	0.74	29	31	27

When the radiologist and non-radiologist clinician groups were pooled together, the atlas (13 readers) and the atlas + tutorial (13 readers) cohorts showed increasing inter-reader reliability compared to the baseline cohort (7 readers). For the radiologist subgroups, the inter-reader reliability did not change with the use of the atlas and with the addition of a tutorial for both the inflammatory and damage domains. For the non-radiologist clinician subgroups, the inter-reader reliability for both domains were lower than those of radiologists.

3.2. Multiway ANOVA: Contextual Impact of Calibration Level and Reader Specialty

The variance components obtained through multiway ANOVA (Appendix E) showed that the score given to a TMJ was modified non-trivially by the reader rating the images, their specialty group, as well as the level of reading aid used (calibration level). The main aid-related variance component by itself was small and insignificant. However, the three-way interaction terms involving the aid, reader, and patient variables showed statistical significance ($p < 0.0001$) for the radiologist readers, suggesting that the atlas and tutorial caused context-specific changes to the TMJ score in some reader-patient combinations. The equivalent interaction effect in the non-radiologist clinical group did not reach statistical significance after Bonferroni correction, despite showing higher variance components to the radiologists' data (18 vs. 13% of the total variance for the inflammation score, and 7 vs. 6% for the damage score), likely owing to the lower number of non-radiologist participants. Furthermore, for the damage domain, the aid*reader interaction was significant, suggesting that some readers rated all cases higher in general after the tutorial.

When pooling across different reader specialty groups (i.e., $n = 7, 13,$ or 13 readers across the three calibration levels), there was a significant systematic difference associated with the readers for both domains and all calibration levels, meaning some readers systematically gave higher grades across all patients. However, this was not correlated with whether the reader was a radiologist or non-radiologist, since the specialty main effect and patient*specialty interaction were not significant. The interaction terms with reader and patient were significant, suggesting that some readers scored the two joints of the same patient more similarly than other readers.

3.3. Three-Facet G coefficients: Reliability When Variations in Calibration or Specialties Exist in the Dataset

Table 3 describes the reliability when some measurement characteristics are not controlled, such as when not all the readers have attained the same calibration level or that readers from different specialties are participating in the reader cohort. Agreement between radiologists belonging to the same calibration level ranged from 0.69–0.81 for the two domains and two calibration gradients (Table 3, data row 1). The opposite scenario, which is the agreement within the same reader between the use and disuse of a calibration aid, was higher, ranging from 0.77–0.88 for the two domains and two calibration gradients (row 2). The combination of these sources of error, i.e., when comparing different readers who also differ in their level of calibration, the agreement ranged from 0.68–0.78 (row 3). When keeping the calibration level variable constant to estimate the impact of reader specialty, the agreement between radiologists and non-radiologist clinicians ranged between 0.56–0.70 (row 9). Agreement among readers of the same specialty was higher, ranging between 0.67–0.76 (row 10). In terms of measurement error, the presence of heterogeneity in the level of calibration and reader specialty widen the measurement error by up to 4% and 7%, respectively (row 1 vs. 3, and 9 vs. 10).

Agreement on the domain score between the right and left joint of the same patient was generally low but not absent. In the most reliable measurement scenario, i.e., when assessed by the same reader within the same level of calibration (rating both joints in the same sitting), the right–left correlation ranged from 0.30–0.49, or approximately within 45–51% domain score points in 95% of cases (Table 3 rows 8 and 12). In the least reliable scenario, i.e., when both the reader and the level of calibration or specialty differed, the agreement still ranged between 0.12–0.39 (contralateral TMJ score within 53–65% points in 95% of cases, rows 7 and 11). In general, the right–left joint correlation was higher for the damage domain.

Table 3. Three-facet generalizability coefficients. Agreement on TMJ score with three sources of variance—patient, reader and aid or reader specialty. The 95% confidence interval of measurement reflects the measurement error interval around a measured score, in the units of the respective JAMRIS-TMJ domain. Abbreviations: A, aid; J, temporomandibular joint; Non-Rad, non-radiologist clinician reader; P, patient; R, reader; Rad, radiologist reader; S, specialty (binary, radiologist or non-radiologist clinician).

Measurement Scenario (Main Effects Definitions)	95% CI of Measurement (+/- Percentage Points)																	
	Generalizability Coefficient				Inflammatory Domain				Damage Domain									
	Inflammatory Domain		Atlas +/- Tutorial Rad		+/- Atlas		Atlas +/- Tutorial Rad		+/- Atlas		Atlas +/- Tutorial Rad							
Between readers of the same calibration (R random, P and A fixed)	0.49	0.69	0.81	0.39	0.78	0.80	0.80	28	21	35	28	47	24	23				
Same reader with vs. without aid (A random, P and R fixed)	0.65	0.86	0.83	0.59	0.77	0.88	0.88	17	20	29	17	33	24	18				
Between readers with different calibration (A and R random, P fixed)	0.41	0.67	0.75	0.37	0.76	0.78	0.78	29	25	37	29	48	25	25				
Between readers with different calibration, averaging two readings per reader (A and R random, P fixed, A/2)	0.50	0.73	0.83	0.43	0.86	0.84	0.84	31	26	31	26	42	18	20				
Between readers with different calibration, averaging two readers at a time (A and R random, P fixed, R/2)	0.56	0.81	0.84	0.53	0.86	0.88	0.88	28	19	28	21	35	18	17				
Between readers of the same calibration, averaging two readers at a time (R random, P and A fixed, R/2)	0.65	0.82	0.90	0.56	0.87	0.89	0.89	25	15	25	20	34	17	16				
Between right and left joints when scored by different readers with different calibration (J, A and R random)	0.12	0.20	0.27	0.23	0.39	0.34	0.34	54	55	54	56	65	54	56				
Between right and left joints when scored by the same reader with the same calibration (J random, A and R fixed)	0.30	0.39	0.43	0.39	0.47	0.44	0.44	48	47	48	47	51	50	50				
Pooling the Readings from Same Calibration																		
Measurement Scenario (Main Effects Definitions)	Generalizability Coefficient				Inflammatory Domain				95% CI of Measurement				Damage Domain					
	Inflammatory Domain		Atlas +/- Tutorial Rad		Baseline		Atlas		Tutorial		Baseline		Atlas		Tutorial			
	Baseline	Atlas	Tutorial	Rad	Baseline	Atlas	Tutorial	Rad	Baseline	Atlas	Tutorial	Rad	Baseline	Atlas	Tutorial	Rad	Atlas	Rad
Between radiologists and non-radiologists (R and S random, P fixed)	0.56	0.59	0.63	0.64	0.61	0.70	0.70	36	31	29	29	30	33	28				
Between readers of the same specialty (R random, S and P fixed)	0.67	0.69	0.67	0.68	0.70	0.76	0.76	29	27	28	28	29	29	26				
Between right and left joints when scored by a radiologist and a clinician (J, R and S random)	0.12	0.25	0.26	0.35	0.32	0.30	0.30	60	53	60	53	56	55	56				
Between right and left joints when scored by the same reader (J random, R and S fixed)	0.34	0.43	0.40	0.49	0.41	0.42	0.42	48	46	48	45	49	50	50				

3.4. Variation of Reliability by Study Design Differences

For assessing the impact of sources of variabilities in different study designs, as well as to calculate the sample size needed to detect a hypothesized level of difference, the potential level of measurement error of JAMRIS-TMJ can be estimated using the G coefficient formulas in Appendix D and variance component estimates specific to the model, such as in Appendix E. Between-reader variance was a much greater source of measurement variability when compared to within-reader changes due to calibration aid. The latter consists of both the random intrareader variations over time in addition to any systematic change in score caused by the atlas or the tutorial. In study designs where measurements are taken in replicate to reduce measurement error, it will thus be more beneficial to average scores across different readers, rather than averaging multiple scores given by the same reader (provided at different states of calibration). For example, considering the use case where the reliability of readers with different levels of calibration is 0.78 for the damage domain (95% CI of measurement at ± 25 percentage points), averaging two different readers achieves 0.88 ($\pm 19\%$), whereas averaging two readings of the same reader achieves 0.84 ($\pm 20\%$).

4. Discussion

Our study assessed the reliability of a tool for the semiquantitative grading of TMJ arthritis, JAMRIS-TMJ, as well as the relative impact of various potential sources of measurement error in its application. In the most controlled and typical use case, i.e., a group of radiologists grading with the atlas and after a calibration tutorial, the true score is expected to be within ± 25 percentage points of any given score 95% of the time (Table 2). The atlas and tutorial caused significant contextual changes in the reader's assessment of the joints as per the ANOVA results. However, the variable presence of this effect did not further improve the group-level clustering of scores among radiologists. Instead, the impact of calibration aids was limited to improving the agreement between radiologist and non-radiologist clinician readers. It is important to note that calibration is nevertheless required to improve the accuracy of scores irrespective of its effect on improving reliability, since the two are independent characteristics of measurement error.

The reliability results observed in this study are comparable to the moderate-to-good range of results seen with other TMJ MRI scoring systems published in the literature [16,24,25]. Compared to larger joints such as the knees and hips, grading change in the TMJ on MRI may be less reliable due to the limitations in image resolution and the TMJ's anatomical complexity. The small size of the TMJ reduces the score range in which the TMJ can be graded, by limiting both the number of definable disease features as well as the range of their grading. This quantitative limitation in turn reduces the between-patient variance relative to other variances in measurement, leading to reduced measurement reliability coefficients. Furthermore, despite best efforts to specify the definitions and representation in the JAMRIS-TMJ, it remains challenging to identify, differentiate, and grade the features. Some specific issues that introduce subjectivity in scoring the inflammatory changes include the physiological age-related conversion of hematopoietic bone marrow, the nonuniformity of signal across the surface coil (Figure 2), and differentiating the inflamed synovium from the joint fluid. The structural changes also remain challenging to score, as the patient-referenced normal joint shape is often unavailable and would need to be assumed and imagined by the reader to serve as reference for grading flattening and erosions.

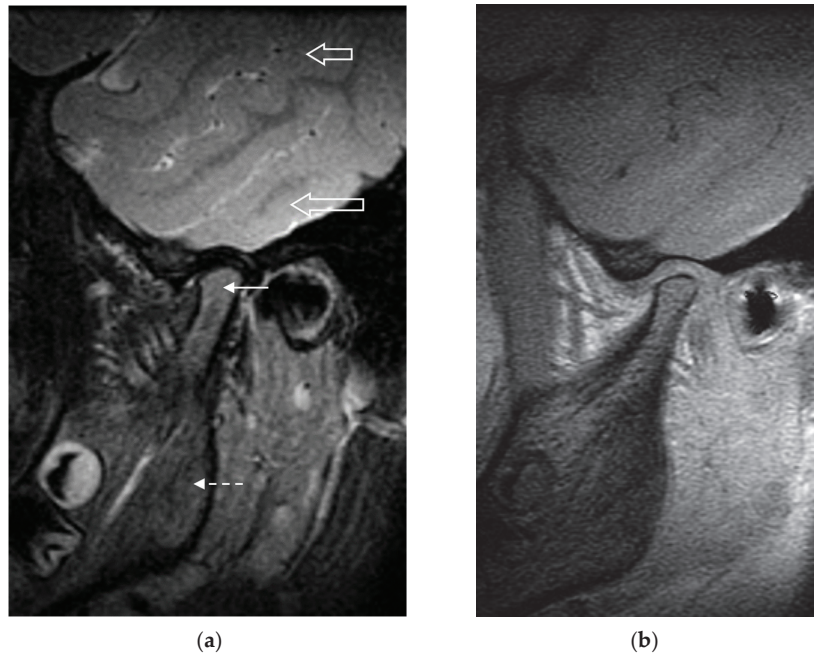


Figure 2. (a) Sagittal T2-weighted fat suppressed MR image of the left temporomandibular joint in a 9-year-old girl. The signal intensity of the bone marrow in the mandibular condyle (solid arrow) is increased compared to the signal intensity of that in the mandibular ramus (dashed arrow). Following the exact definition of bone marrow edema in the scoring system would cause this to be scored as grade 1 (present) bone marrow edema. However, this increased signal intensity is likely secondary to the generally higher signal in structures at the center of the field of view versus those at the periphery: notice the higher signal intensity of brain parenchyma nearer the center of the image (lower open arrow) versus that at the periphery of the image (upper open arrow). If this were true marrow edema, the signal intensity on the corresponding precontrast T1-weighted image (b) would be expected to be decreased, which was not the case.

A further step in investigating the reliability of JAMRIS-TMJ is to also quantify the patient- and imaging-related changes over time. Changes in the TMJ score between repeat imaging of the same state of disease may be significant when the imaging parameters are not standardized, or the imaging interval is long enough to introduce physiological changes. Quantitative methods for scoring the degree of inflammation have demonstrated a high degree of discriminatory validity [26,27] but are also affected by temporal variations [28]. In a semiquantitative scoring system such as the JAMRIS-TMJ, these errors may be relatively low compared to the between-reader variance but should still be accounted for when using the scoring system in longitudinal evaluation. Another type of variance that may be important to identify is the impact of comparing to the contralateral TMJ on the score. The patient variance component in this study does not differentiate how much patient-wise correlation is due to the pathophysiological factors that cause the two sides to be correlated, and how much is due to the reader intentionally adjusting the joint score by comparing to the contralateral side. A more sophisticated study design utilizing artificially paired right and left TMJ exams would be able to identify the magnitude of this effect, which may be helpful for improving the grading of items that require a within-patient comparator.

Our study conclusions should be interpreted in the context of several potential limitations. One limitation is that methods for calculating confidence intervals for these more complex types of G coefficients are not yet available and currently limited to the simplest

one-facet crossed design [21]. The point estimates of various G coefficients presented in this paper should be used for identifying trends in the relative impact of quality controls in the measurement and on the estimation of sample size. Secondly, although the group 1 and 2 readers read the same cases twice, there was a change in the aid they used, which makes the coefficient a “within-reader, between-aid” agreement, rather than the traditional intrareader reliability where there are no external changes to the measurement scenario. However, it is reasonable to assume that the intrareader reliability will be at least as high as the within-reader, between-aid reliability since the latter is additionally lowered by any systematic variations attributable to the use and disuse of the aid.

5. Conclusions

In summary, this study demonstrates that semiquantitative MRI scoring of TMJ arthritis using the JAMRIS-TMJ is reliable in the calibrated setting, particularly when performed as a double-read by two radiologists, forming the foundation for its potential use in the clinically important assessment of change over time and with therapy. The use of atlas and tutorial calibration is recommended when multiple specialty groups are participating in reading.

Author Contributions: Conceptualization, M.T., A.S.D. and C.J.K.; data curation, M.T.; formal analysis, M.T.; investigation, M.T., A.S.D., A.B.M., T.A.L., S.A. (Shelly Abramowicz), J.A., S.A. (Simone Appenzeller), L.Z.A., L.W.A., S.G., E.J.I.C., J.L.J., T.J., T.v.K., E.K., B.K., E.M., J.P., Z.S.P., C.M.R., J.S., N.T. and C.J.K.; methodology, M.T., A.S.D., B.M.F. and C.J.K.; Project administration, M.T. and A.S.D.; Resources, A.S.D. and C.J.K.; supervision, A.S.D., T.A.L., B.M.F., R.M., M.A.v.R., G.T. and C.J.K.; visualization, M.T., A.B.M., J.A. and C.J.K.; writing—original draft, M.T.; writing—review and editing, M.T., A.S.D., A.B.M., T.A.L., S.A. (Shelly Abramowicz), J.A., S.A. (Simone Appenzeller), L.Z.A., L.W.A., B.M.F., S.G., E.J.I.C., J.L.J., T.J., T.v.K., E.K., B.K., E.M., R.M., J.P., Z.S.P., C.M.R., M.A.v.R., J.S., G.T., N.T. and C.J.K. All authors have read and agreed to the published version of the manuscript.

Funding: Mirkamal Tolend was supported by research scholarship awards from Queen Elizabeth II/Edward Dunlop foundation, Peterborough K. M. Hunter Charitable Foundation, The Hospital for Sick Children ResTraComp, Ontario Graduate Scholarship and Mergelas Family foundation for this study.

Institutional Review Board Statement: This study was conducted according to the guidelines of the Declaration of Helsinki and approved by the research ethics board at The Hospital for Sick Children (Toronto, ON, Canada, Study #1000042164).

Informed Consent Statement: Participants in the reading exercise were informed of the study rationale and procedures in writing, and that their voluntary completion and submission of image score data constituted their implied consent to participate. Based on the anonymized and retrospective nature of the imaging exams used for the study, written consent requirement was waived.

Data Availability Statement: Data presented in this study are available on request from the corresponding author.

Conflicts of Interest: The authors declare no conflict of interest.

Appendix A. Background Information on Generalizability Theory as Applied to Imaging

Reliability studies have often used the intraclass correlation coefficient (ICC) deriving from classical test theory, which models measurements by two components—the true score and error. This approach is limited to the analysis of a single source of measurement error. In the typical inter-reader reliability study where multiple readers score the same set of images, one- or two-way analysis of variance (ANOVA) is used to determine how much of the variance in the study data is associated with the image variable (the true score component), and how much is associated with the reader variable (part of the error component). However, there are often more than one source of variance that may be important to analyze in an instrument's typical use case. For example, assessment of systemic treatments in arthritis may require the scoring of multiple joints from each patient, especially for the bilateral joints, such as the TMJs. The existence of any patient-level correlation in the score variance introduces a source of clustering in the data which must be analyzed as a fixed effect under the assumptions regarding the independence of data for common statistical tests. Other sources of variance may exist in the study sample, including differences in the imaging protocols and equipment used to acquire the exams, training background and experience of the readers, as well as the measurement aids or calibration tutorials used for the scoring. If using the traditional ICC, the study sample would need to be stratified at each level of these variations to study these other sources of variance, or assume such variances do not exist.

A more comprehensive approach called the generalizability theory allows the estimation of an overall ICC that is generalized over multiple sources of variability [20,21]. The generalizability study (G-Study) extends upon the CTT definition of ICC by using multiway ANOVA, which allows the quantification of more than two sources of variance (called facets) and their interactions. When these are known, it is possible to calculate additional reliability coefficients that may be important in order to understand the measurement variability across common variations in measurement methods. The design of such a G-Study will require measuring the same data under different conditions and pooling the dataset across the levels of the generalizing variables. For example, in an inter-reader study where each reader also read the same MRI exam twice, a G-study can calculate both the inter-reader and intrareader reliability coefficient using the complete set of data, without the need to create different subgroups for the two coefficients, hence maintaining study power and improving external validity. Furthermore, the results of the multiway ANOVA identify the relative impact of the sources of variance to the overall measurement error, which allows for the optimization of study designs by simulating the measurement conditions (at an analysis step called the design study, or D-Study). For example, it will be possible to compare the expected reliability between averaging different readers' score for each joint versus averaging multiple readings done by the same readers, allowing the researchers to choose a design that best minimizes the number of measurements needed to meet a priori study power and effect size thresholds.

Appendix B. JAMRIS-TMJ Scoring System

Table A1. The scoring system tested in the exercise is referred to as the Juvenile Idiopathic Arthritis Magnetic Resonance Scoring System for Temporomandibular Joints (JAMRIS-TMJ). The semiquantitative grades are weighted per domain to yield domain scores which are scaled from 0–100% [17]. The two temporomandibular joints are graded separately.

INFLAMMATORY DOMAIN					
	Bone Marrow Edema	Bone Marrow Enhancement	Effusion	Synovial Thickening	Joint Enhancement
Definition	Compared to the mandibular ramus, hyperintense marrow signaling within the condyle on T2w FS or STIR images, and/or hypointense signaling on pre-contrast T1w images without FS.	Compared to the mandibular ramus, hyperintense marrow signaling within the condyle on post-contrast T1w FS images.	Increased joint fluid with isointense signaling of joint space compared to that of cerebrospinal fluid on T2w FS or STIR images.	Thickened synovial lining of the TMJ with intermediate signal on T2w images.	Signal intensity of the synovium, capsule, and joint fluid higher than that of muscle on post-contrast T1w FS images.
Grading	Absent Present	Absent Present	Normal: ≤1mm fluid in joint recess Small: >1 and ≤2mm fluid in recess or involving entire joint compartment Large: >2mm fluid in recess or involving entire joint compartment	Absent: No synovium visible (joint space ≤1 mm width) Mild: >1 and ≤2mm thickness at the point of maximum synovial thickening Moderate/Severe: >2mm thickness at the point of maximum synovial thickening	Normal: High signal intensity confined to signal perimeter of normal amount of joint fluid on corresponding fluid-sensitive image Mild: High signal intensity focally exceeding signal perimeter of physiologic amount of joint fluid on corresponding fluid-sensitive image Moderate/Severe: High signal intensity diffusely involving one or both joint compartments
DAMAGE DOMAIN					
Definition	Condylar Flattening Loss of the round or slightly rectangular shape of the condylar head, viewed in the sagittal-oblique plane. Normal round/slightly rectangular shape	Erosions Any irregularity or breaks of the bony joint surfaces leading to the loss of the smooth continuous surface of the bone, seen in both sagittal and coronal planes No irregularities or deep breaks	Disk Abnormalities Any abnormality of the articular disk, including flattening, displacement, or destruction. Absent		
Grading	Mild: Extent of flattening involves part of the surface of the condyle Moderate/Severe: Extent of flattening involves the entire surface of the condyle, or loss of height in the condyle.	Mild: Presence of irregularities involving only part of the articular surface of the condyle Moderate/Severe: Presence of deep breaks in the subchondral bone seen in two planes, or irregularities involving the entire articular surface of the condyle	Present		

C. Imaging Protocol

Table 2. Representative MRI protocol for the TMJ exams used in the reliability exercise. Abbreviations: FOV, field-of-view; FS, fat suppression sequence; FSE, fast spin echo; FSPGR, fast spoiled gradient recalled echo; + Gd, post gadolinium injection; mm, millimeter; ms, milliseconds; PD, proton density-weighted sequence; SE, spin echo.

	Imaging Sequence (in Order of Acquisition from Left to Right)					
	T1 FSPGR	PD FSE	T2 FSE FS	T1 FSE FS + Gd	T1 SE FS + Gd	3D FSPGR + Gd
Plane	Sagittal oblique	Sagittal oblique	Sagittal oblique	Sagittal oblique	Coronal	Sagittal oblique
Echo time (ms)	4.2	25	86	11	19	10.4
Repetition time (ms)	325	2660	2840	600	600	4.2
Flip angle	80	90	90	90	90	20
FOV (mm × mm)	120	120	120	120	160	100
Acquisition Matrix	384 × 224	256 × 224	256 × 224	256 × 224	256 × 192	256 × 192
Slice thickness (mm)	2	2	2	2	2	2
Slice spacing (mm)	2	2	2	2	2	1
Echo train length	-	8	16	3	-	-

D. Generalizability Coefficient Formulae

Table 3. Formulae used to calculate the G and Φ generalizability coefficients in Table 3, derived from references [20,21]. Abbreviations: A, aid or calibration level; J, temporomandibular joint; P, patient; R, reader; S, specialty (binary, radiologist or non-radiologist clinician); colon (:), nested relation, (e.g., J:P means joint is nested within the patient variable); cross (x), crossed relation (e.g., RxA means each Reader provides data at all levels of the aid variable).

Coefficient Meaning	Formula
J:P × R × A Design—Pooling Across Use or Disuse of Aid, Separately for Radiologist and Non-Radiologist Readers	
Between readers of the same calibration (R random, P and A fixed)	$G(R) = \frac{J:P+A;J:P}{J:P+A;J:P+R+R;J:P+AR;J:P}$
Same reader with vs. without aid (A random, P and R fixed)	$G(A) = \frac{J:P+R;J:P}{J:P+R;J:P+A+AJ:P+AR;J:P}$
Between readers with different calibration (A and R random, P fixed)	$G(R, A) = \frac{J:P}{J:P+A+R+AR+AJ:P+R;J:P+AR;J:P}$
Between readers with different calibration, averaging 2 readings per reader (A and R random, P fixed, A/2)	$G(R, A) = \frac{J:P}{J:P+\frac{A}{2}+R+\frac{AR}{2}+\frac{AJ:P}{2}+R;J:P+\frac{AR;J:P}{2}}$
Between readers with different calibration, averaging 2 readers at a time (A and R random, P fixed, R/2)	$G(R, A) = \frac{J:P}{J:P+A+\frac{R}{2}+\frac{AR}{2}+AJ:P+\frac{R;J:P}{2}+\frac{AR;J:P}{2}}$
Between readers of the same calibration, averaging two readers at a time (R random, P and A fixed, R/2)	$G(R) = \frac{J:P+A;J:P}{J:P+A;J:P+\frac{R}{2}+\frac{R;J:P}{2}+\frac{AR;J:P}{2}}$
Right-left joint agreement when scored by different readers with different calibration (J, A and R random)	$\Phi(J, R, A) = \frac{P}{P+J:P+R+A+PA+PR+AR+PAR+AJ:P+R;J:P+AR;J:P}$
Right-left joint agreement when scored by the same reader with the same calibration (J random, A and R fixed)	$G(J) = \frac{P+PA+PR+PAR}{P+PA+PR+PAR+J:P+AJ:P+R;J:P+AR;J:P}$
J:P × R:S Design—Pooling Across Radiologist and Non-Radiologist Readers, Separately for Each Aid	
Between radiologists and non-radiologists (R and S random, P fixed)	$G(R, S) = \frac{J:P}{J:P+R;S+S+J:P;PS+R;PS}$
Between readers of the same specialty (R random, S and P fixed)	$G(R) = \frac{J:P+J;PS}{J:P+J;PS+R;S+J;R;PS}$
Right-left joint agreement when scored by radiologist and non-radiologist (J, S and R random)	$\Phi(J, R, S) = \frac{P}{P+J:P+R;S+S+PS+PR;S+J;PS+J;R;PS}$
Right-left joint agreement when scored by the same reader (J random, R and S fixed)	$G(J) = \frac{P+PS+PR;S}{P+PS+PR;S+J;P+J;PS+J;R;PS}$

E. Multiway ANOVA Results

Table 4. Analysis of the JAMRIS-TMJ scores by multiway ANOVA, where all effects are modeled as random. In the J:P × R × A design (top half), the effects of three factors, patient, aid, and reader on the joint score are analyzed by combining the 1A and 1B datasets under the atlas column, and the 2A and 2B datasets under the tutorial column from the radiologists. In the J:P × R:S design, the effect of patient, reader and specialty are analyzed by combining the 1B and 2A datasets for the atlas row, and 2B and 3 datasets for the tutorial row, with 1A as baseline. Bolded *p* values are those which remained significant after applying Bonferroni correction for multiple testing.

Variance Component	J:P × R × A Design						Inflammatory Domain						Damage Domain						
	Atlas Radiologists		Atlas Non-Radiologists		Tutorial Radiologists		Atlas Non-Radiologists		Atlas Radiologists		Tutorial Radiologists		Atlas Non-Radiologists		Atlas Radiologists		Tutorial Radiologists		
	Var Comp	<i>p</i>	Var Comp	<i>p</i>	Var Comp	<i>p</i>	Var Comp	<i>p</i>	Var Comp	<i>p</i>	Var Comp	<i>p</i>	Var Comp	<i>p</i>	Var Comp	<i>p</i>	Var Comp	<i>p</i>	
Joint (patient)	44%	<0.0001	27%	0.00	46%	<0.0001	40%	<0.0001	24%	0.00	46%	<0.0001	24%	0.00	46%	<0.0001	24%	0.00	46%
Patient	20%	0.05	14%	0.11	27%	0.02	38%	0.00	23%	0.01	34%	0.01	23%	0.01	34%	0.01	23%	0.01	34%
Reader	8%	0.03	0%	0.30	3%	0.06	0%	0.91	19%	0.00	4%	0.05	19%	0.00	4%	0.05	19%	0.00	4%
Aid	0%	0.41	2%	0.40	3%	0.04	1%	0.19	1%	0.14	0%	0.44	1%	0.14	0%	0.44	1%	0.14	0%
Reader*joint (patient)	4%	<0.0001	16%	0.00	1%	0.16	0%	0.66	4%	0.29	0%	0.32	4%	0.29	0%	0.32	4%	0.29	0%
Aid*joint (patient)	0%	0.75	5%	0.09	0%	0.34	0%	0.86	2%	0.86	0%	0.93	2%	0.86	0%	0.93	2%	0.86	0%
Reader*Patient	2%	0.13	1%	0.45	5%	0.00	0%	0.43	3%	0.25	3%	0.00	3%	0.25	3%	0.00	3%	0.25	3%
Aid*patient	0%	0.63	0%	0.91	0%	0.34	1%	0.19	0%	0.74	0%	0.33	0%	0.74	0%	0.33	0%	0.74	0%
Aid*reader	2%	0.00	0%	0.34	1%	0.00	1%	0.00	0%	0.98	2%	0.00	0%	0.98	2%	0.00	0%	0.98	2%
Aid*reader*patient	13%	<0.0001	18%	0.00	8%	<0.0001	6%	<0.0001	7%	0.06	4%	<0.0001	7%	0.06	4%	<0.0001	7%	0.06	4%
Residual	8%		17%		7%		12%		18%		7%		18%		7%		18%		7%
J:P × R:S Design																			
Variance Component		Baseline		Atlas		Atlas+Tutorial		Baseline		Atlas		Atlas+Tutorial		Baseline		Atlas		Atlas+Tutorial	
		Var Comp	<i>p</i>	Var Comp	<i>p</i>	Var Comp	<i>p</i>	Var Comp	<i>p</i>	Var Comp	<i>p</i>	Var Comp	<i>p</i>	Var Comp	<i>p</i>	Var Comp	<i>p</i>	Var Comp	<i>p</i>
Joint (patient)		38%	<0.0001	35%	<0.0001	38%	<0.0001	34%	<0.0001	36%	<0.0001	43%	<0.0001	36%	<0.0001	43%	<0.0001	36%	<0.0001
Patient		11%	0.13	24%	0.01	27%	0.01	35%	0.00	32%	0.01	29%	0.01	32%	0.01	29%	0.01	32%	0.01
Reader (specialty)		5%	<0.0001	7%	<0.0001	6%	<0.0001	5%	<0.0001	5%	<0.0001	4%	<0.0001	5%	<0.0001	4%	<0.0001	5%	<0.0001
Specialty		9%	0.07	1%	0.21	0%	0.84	0%	0.79	0%	0.33	1%	0.19	0%	0.33	1%	0.19	0%	0.33
Patient*specialty		0%	0.88	0%	0.53	1%	0.31	3%	0.08	0%	0.84	1%	0.15	0%	0.84	1%	0.15	0%	0.84
Patient*reader (specialty)		19%	<0.0001	15%	<0.0001	11%	<0.0001	9%	<0.0001	7%	<0.0001	8%	<0.0001	7%	<0.0001	8%	<0.0001	7%	<0.0001
Specialty*joint (patient)		2%	0.07	5%	<0.0001	3%	0.01	2%	0.05	2%	<0.0001	2%	0.00	2%	<0.0001	2%	0.00	2%	<0.0001
Residual		16%		13%		15%		12%		14%		11%		14%		11%		14%	

References

1. Larheim, T.A.; Doria, A.S.; Kirkhus, E.; Parra, D.A.; Kellenberger, C.J.; Arvidsson, L.Z. TMJ Imaging in JIA Patients—An Overview. *Semin. Orthod.* **2015**, *21*, 102–110. [\[CrossRef\]](#)
2. Billiau, A.D.; Hu, Y.; Verdonck, A.; Carels, C.; Wouters, C. Temporomandibular Joint Arthritis in Juvenile Idiopathic Arthritis: Prevalence, Clinical and Radiological Signs, and Relation to Dentofacial Morphology. *J. Rheumatol.* **2007**, *34*, 1925–1933.
3. Weiss, P.F.; Arabshahi, B.; Johnson, A.; Bilaniuk, L.T.; Zarnow, D.; Cahill, A.M.; Feudtner, C.; Cron, R.Q. High Prevalence of Temporomandibular Joint Arthritis at Disease Onset in Children with Juvenile Idiopathic Arthritis, as Detected by Magnetic Resonance Imaging but Not by Ultrasound. *Arthritis Rheum.* **2008**, *58*, 1189–1196. [\[CrossRef\]](#) [\[PubMed\]](#)
4. Cannizzaro, E.; Schroeder, S.; Müller, L.M.; Kellenberger, C.J.; Saurenmann, R.K. Temporomandibular Joint Involvement in Children with Juvenile Idiopathic Arthritis. *J. Rheumatol.* **2011**, *38*, 510–515. [\[CrossRef\]](#)
5. Larheim, T.A.; Hoyeraal, H.M.; Stabrun, A.E.; Haanaes, H.R. The Temporomandibular Joint in Juvenile Rheumatoid Arthritis. Radiographic Changes Related to Clinical and Laboratory Parameters in 100 Children. *Scand. J. Rheumatol.* **1982**, *11*, 5–12. [\[CrossRef\]](#)
6. Karhulahti, T.; Rönning, O.; Jämsä, T. Mandibular Condyle Lesions, Jaw Movements, and Occlusal Status in 15-Year-Old Children with Juvenile Rheumatoid Arthritis. *Scand. J. Dent. Res.* **1990**, *98*, 17–26. [\[CrossRef\]](#)
7. Svensson, B.; Adell, R.; Kopp, S. Temporomandibular Disorders in Juvenile Chronic Arthritis Patients. A Clinical Study. *Swed Dent. J.* **2000**, *24*, 83–92. [\[PubMed\]](#)
8. Twilt, M.; Mober, S.M.L.M.; Arends, L.R.; ten Cate, R.; Suijlekom-Smit, L. van Temporomandibular Involvement in Juvenile Idiopathic Arthritis. *J. Rheumatol.* **2004**, *31*, 1418–1422. [\[PubMed\]](#)
9. Schanberg, L.E.; Anthony, K.K.; Gil, K.M.; Maurin, E.C. Daily Pain and Symptoms in Children with Polyarticular Arthritis. *Arthritis Rheum.* **2003**, *48*, 1390–1397. [\[CrossRef\]](#) [\[PubMed\]](#)
10. Goldmuntz, E.A.; White, P.H. Juvenile Idiopathic Arthritis: A Review for the Pediatrician. *Pediatr. Rev.* **2006**, *27*, e24–e32. [\[CrossRef\]](#)
11. Muller, L.; Kellenberger, C.J.; Cannizzaro, E.; Ettl, D.; Schraner, T.; Bolt, I.B.; Peltomaki, T.; Saurenmann, R.K. Early Diagnosis of Temporomandibular Joint Involvement in Juvenile Idiopathic Arthritis: A Pilot Study Comparing Clinical Examination and Ultrasound to Magnetic Resonance Imaging. *Rheumatology* **2009**, *48*, 680–685. [\[CrossRef\]](#)
12. Zwir, L.F.; Terreri, M.T.; do Amaral e Castro, A.; Rodrigues, W.D.R.; Fernandes, A.R.C. Is Power Doppler Ultrasound Useful to Evaluate Temporomandibular Joint Inflammatory Activity in Juvenile Idiopathic Arthritis? *Clin. Rheumatol.* **2020**, *39*, 1237–1240. [\[CrossRef\]](#)
13. Rongo, R.; Alstergren, P.; Ammendola, L.; Bucci, R.; Alessio, M.; D’Antò, V.; Michelotti, A. Temporomandibular Joint Damage in Juvenile Idiopathic Arthritis: Diagnostic Validity of Diagnostic Criteria for Temporomandibular Disorders. *J. Oral Rehabil.* **2019**, *46*, 450–459. [\[CrossRef\]](#) [\[PubMed\]](#)
14. Bernini, J.M.; Kellenberger, C.J.; Eichenberger, M.; Eliades, T.; Papageorgiou, S.N.; Patcas, R. Quantitative Analysis of Facial Asymmetry Based on Three-Dimensional Photography: A Valuable Indicator for Asymmetrical Temporomandibular Joint Affection in Juvenile Idiopathic Arthritis Patients? *Pediatr. Rheumatol. Online J.* **2020**, *18*, 1–8. [\[CrossRef\]](#)
15. Bollhalder, A.; Patcas, R.; Eichenberger, M.; Müller, L.; Schroeder-Kohler, S.; Saurenmann, R.K.; Kellenberger, C.J. Magnetic Resonance Imaging Followup of Temporomandibular Joint Inflammation, Deformation, and Mandibular Growth in Juvenile Idiopathic Arthritis Patients Receiving Systemic Treatment. *J. Rheumatol.* **2020**, *47*, 909–916. [\[CrossRef\]](#) [\[PubMed\]](#)
16. Tolend, M.A.; Twilt, M.; Cron, R.Q.; Tzaribachev, N.; Guleria, S.; von Kalle, T.; Koos, B.; Miller, E.; Stimec, J.; Vaid, Y.; et al. Toward Establishing a Standardized Magnetic Resonance Imaging Scoring System for Temporomandibular Joints in Juvenile Idiopathic Arthritis. *Arthritis Care Res.* **2018**, *70*, 758–767. [\[CrossRef\]](#) [\[PubMed\]](#)
17. Tolend, M.; Junhasavasdikul, T.; Cron, R.Q.; Clemente, E.J.I.; von Kalle, T.; Kellenberger, C.J.; Koos, B.; Miller, E.; van Rossum, M.A.; Saurenmann, R.K.; et al. Discrete Choice Experiment on a Magnetic Resonance Imaging Scoring System for Temporomandibular Joints in Juvenile Idiopathic Arthritis. *Arthritis Care Res.* **2021**. [\[CrossRef\]](#) [\[PubMed\]](#)
18. Beaton, D.E.; Maxwell, L.J.; Shea, B.J.; Wells, G.A.; Boers, M.; Grosskleg, S.; Bingham, C.O.; Conaghan, P.G.; D’Agostino, M.A.; de Wit, M.P.; et al. Instrument Selection Using the OMERACT Filter 2.1: The OMERACT Methodology. *J. Rheumatol.* **2019**, *46*, 1028–1035. [\[CrossRef\]](#) [\[PubMed\]](#)
19. Kellenberger, C.J.; Junhasavasdikul, T.; Tolend, M.; Doria, A.S. Temporomandibular Joint Atlas for Detection and Grading of Juvenile Idiopathic Arthritis Involvement by Magnetic Resonance Imaging. *Pediatr. Radiol.* **2018**, *48*, 411–426. [\[CrossRef\]](#)
20. Bloch, R.; Norman, G. Generalizability Theory for the Perplexed: A Practical Introduction and Guide: AMEE Guide No. 68. *Med. Teach.* **2012**, *34*, 960–992. [\[CrossRef\]](#)
21. Brennan, R.L. *Generalizability Theory; Statistics for Social and Behavioral Sciences*; Springer: New York, NY, USA, 2001; ISBN 978-0-387-95282-6.
22. Doros, G.; Lew, R. Design Based on Intra-Class Correlation Coefficients. *Am. J. Biostat.* **2010**, *1*, 1–8.
23. Girardeau, B.; Mary, J.Y. Planning a Reproducibility Study: How Many Subjects and How Many Replicates per Subject for an Expected Width of the 95 per Cent Confidence Interval of the Intraclass Correlation Coefficient. *Stat. Med.* **2001**, *20*, 3205–3214. [\[CrossRef\]](#)

24. Vaid, Y.N.; Dunnavant, F.D.; Royal, S.A.; Beukelman, T.; Stoll, M.L.; Cron, R.Q. Imaging of the Temporomandibular Joint in Juvenile Idiopathic Arthritis. *Arthritis Care Res.* **2014**, *66*, 47–54. [[CrossRef](#)]
25. Koos, B.; Tzaribachev, N.; Bott, S.; Ciesielski, R.; Godt, A. Classification of Temporomandibular Joint Erosion, Arthritis, and Inflammation in Patients with Juvenile Idiopathic Arthritis. *J. Orofac. Orthop.* **2013**, *74*, 506–519. [[CrossRef](#)]
26. Peacock, Z.S.; Vakilian, P.; Caruso, P.; Resnick, C.M.; Vangel, M.; Kaban, L.B. Quantifying Synovial Enhancement of the Pediatric Temporomandibular Joint. *J. Oral Maxillofac. Surg.* **2016**, *74*, 1937–1945. [[CrossRef](#)]
27. Resnick, C.M.; Vakilian, P.M.; Kaban, L.B.; Peacock, Z.S. Quantifying the Effect of Temporomandibular Joint Intra-Articular Steroid Injection on Synovial Enhancement in Juvenile Idiopathic Arthritis. *J. Oral Maxillofac. Surg.* **2016**, *74*, 2363–2369. [[CrossRef](#)] [[PubMed](#)]
28. Caruso, P.; Buch, K.; Rincon, S.; Hakimelahi, R.; Peacock, Z.S.; Resnick, C.M.; Foster, C.; Guidoboni, L.; Donahue, T.; Macdonald, R.; et al. Optimization of Quantitative Dynamic Postgadolinium MRI Technique Using Normalized Ratios for the Evaluation of Temporomandibular Joint Synovitis in Patients with Juvenile Idiopathic Arthritis. *Am. J. Neuroradiol.* **2017**, *38*, 2344–2350. [[CrossRef](#)]

Article

MR Imaging Biomarkers for Clinical Impairment and Disease Progression in Patients with Shoulder Adhesive Capsulitis: A Prospective Study

Romain Gillet ^{1,*}, François Zhu ¹, Pierre Padoin ¹, Aymeric Rauch ¹, Gabriela Hossu ²,
Pedro Augusto Gondim Teixeira ¹ and Alain Blum ¹

¹ Guilloz Imaging Department, Central Hospital, University Hospital Center of Nancy, 54000 Nancy, France; f.zhu@chru-nancy.fr (F.Z.); pierre.padoin@gmail.com (P.P.); aym.rauch@gmail.com (A.R.); p.teixeira@chru-nancy.fr (P.A.G.T.); a.blum@chru-nancy.fr (A.B.)

² CIC-IT, CHRU Nancy, Université de Lorraine, 54000 Nancy, France; g.hossu@chru-nancy.fr

* Correspondence: r.gillet@chru-nancy.fr; Tel.: +33-3-83-85-21-61; Fax: +33-3-83-85-97-25

Abstract: Background: MRI diagnostic criteria of shoulder adhesive capsulitis (AC) are nowadays widely used, but there is little information available on the association between MRI findings and clinical impairment. Purpose: To determine the correlation of MRI findings with the Constant–Murley Score (CMS), pain duration and symptoms at the one-year follow-up in AC patients. Materials and methods: This monocentric prospective study included 132 patients with a clinical diagnosis of shoulder AC who underwent shoulder MRI. Mean patient age was 54.1 ± 9.3 years, and there were 55 men and 77 women. A radiologist examined all patients and completed the CMS just prior to MRI. Pain duration was assessed along with the signal intensity and measured the maximal thickness of the inferior glenohumeral ligament (IGHL) by two radiologists. Medical record analysis was performed in a sub-group of 49 patients to assess prognosis approximately one year after the MRI examination. Linear regression analysis with the Pearson test and the Fisher exact test were used to determine the association between MRI findings and clinical impairment. Results: There was a significant difference in mean pain duration score (3.8 ± 1.2 versus 3.2 ± 0.9 and 3.8 ± 1.2 versus 3.2 ± 0.9 , respectively, for readers 1 and 2) and in mean mobility scores (15.7 ± 8 points versus 19.6 ± 10.1 points and 15.8 ± 8.2 points versus 19.4 ± 10 points, respectively, for readers 1 and 2) in patients with a high IGHL signal compared to those with a low IGHL signal ($p < 0.05$). IGHL was thicker in patients with clinical improvement at one-year follow-up compared to those presenting clinical stability or worsening ($p < 0.05$). Conclusions: In patients with shoulder AC, the degree of signal intensity at the IGHL was inversely related to shoulder pain duration and range of motion, and a thickened IGHL indicated a favorable outcome at one-year follow-up.

Keywords: adhesive capsulitis; MRI; shoulder; constant-murley score; inferior gleno-humeral ligament

Citation: Gillet, R.; Zhu, F.; Padoin, P.; Rauch, A.; Hossu, G.; Teixeira, P.A.G.; Blum, A. MR Imaging Biomarkers for Clinical Impairment and Disease Progression in Patients with Shoulder Adhesive Capsulitis: A Prospective Study. *J. Clin. Med.* **2021**, *10*, 3882. <https://doi.org/10.3390/jcm10173882>

Academic Editors: Mihra Taljanovic and Iwona Sudol-Szopińska

Received: 3 August 2021

Accepted: 27 August 2021

Published: 29 August 2021

Publisher's Note: MDPI stays neutral with regard to jurisdictional claims in published maps and institutional affiliations.



Copyright: © 2021 by the authors. Licensee MDPI, Basel, Switzerland. This article is an open access article distributed under the terms and conditions of the Creative Commons Attribution (CC BY) license (<https://creativecommons.org/licenses/by/4.0/>).

1. Introduction

Adhesive capsulitis (AC) of the shoulder is a common condition with an incidence in the general population varying considerably from 2 to 5.3% for primary and from 4.3 to 38% for secondary AC (e.g., AC preceded by a clinical or surgical event) [1]. Although spontaneous resolution is the rule, years can ensue (mean 18–30 months) before joint mobility returns to normal [2]. Various treatment options exist for AC (e.g., oral anti-inflammatory drugs, intraarticular corticoid injection, physiotherapy, percutaneous capsular distention, surgical release, etc.) depending on the level of clinical impairment, and on an accurate diagnosis. Thus, disease staging and identification of inflammatory changes could have an impact on patient management [3].

AC is classically diagnosed based on clinical presentation, medical history, and physical examination. Diagnosing this condition, however, can be challenging as AC may occur

in various clinical scenarios and has multiple potential differential diagnoses (e.g., rotator cuff tears, calcifying tendonitis, osteoarthritis, inflammatory tumors . . .) [2]. Imaging plays an ever-growing role in the evaluation of patients with suspected AC, ruling out pathologic conditions that can clinically mimic AC [4], and in diagnostic confirmation when clinical findings are equivocal [5–14]. AC-suggestive MRI findings are well recognized and primarily involve inferior glenohumeral ligament (IGHL) (hypersignal and thickening) and rotator interval (RI) scarring and inflammation [7,9,10,12,15–17].

Patients with AC typically complain of a gradual and progressive onset of pain, sleep-disturbing night pain, and active and passive limitation at various degrees of ranges of motion (ROM), both in elevation and rotation, for at least 1 month [18]. The Constant–Murley Score (CMS) is often used to evaluate the impact of AC in shoulder function, with potential implications in patient management [19]. Although the correlation of MRI findings with clinical staging was demonstrated in 2008 by Sofka et al. [20], there is little information available on the association between MRI findings and clinical impairment, which could be important for therapeutic decision making [21–27]. We hypothesize MR imaging signs, particularly the IGHL signal and thicknesses, could serve as biomarkers for shoulder function impairment and AC progression over time. The aim of our study was to evaluate the correlation between MRI findings in AC patients, CMS, and symptoms at the one-year follow-up.

2. Material and Methods

2.1. Study Group

Our institutional review board approved this study, and all patients gave written informed consent. From 10 October 2013 to 16 October 2017, 170 patients over 18 years of age were enrolled prospectively and consecutively. These patients had been referred by orthopedic surgeons or rheumatologists due to the clinical diagnosis of shoulder AC and underwent shoulder radiographs and MRI.

Patients with MRI contraindications, prior shoulder surgery, severe rotator cuff damage with at least a full-thickness tear of one tendon, shoulder osteoarthritis (osteophytes on radiographs), calcific tendinosis, shoulder bursitis, biceps tendinosis, and fractures on MRI were excluded. One patient withdrew from the study; four were excluded because of missing clinical data, and 33 because of extensive rotator cuff damage. Thus, the final study population consisted of 132 patients with a mean age of 54.1 ± 9.3 (22–78) years. There were 55 men (mean age 53.5 ± 8.8 (22–70) years) and 77 women (mean age 54.4 ± 10.8 (22–78) years) with a M/F sex ratio of 0.63. Two patients were suspected of having bilateral AC, yielding 134 shoulder MRI studies.

2.2. Shoulder Function Assessment

A modified CMS was applied to all patients by a senior radiologist just prior to the MRI examination [19]. Two subjective variables for a maximum score of 35 were evaluated: daily living pain (varying from 0—severe pain to 15 points—no pain) and daily living activity limitation (varying from 0—maximal limitation to 20 points—no limitation). The patients answered a questionnaire assessing the degree of pain (no pain, slight, moderate, or severe pain), activity level (pain during work, sports and recreation, sleep) and arm range of motion (ROM) (arm elevation up to the waist, xiphoid process, neck, top of the head, above the head). The examiner received prior training on performing the CMS. ROM was also quantitatively assessed with a goniometer in a seated position, in external and internal rotation, forward and lateral elevation, and scored in each position by the examiner (varying $0-30^\circ = 0$ to $151-180^\circ = 10$ points for each movement). Thus, the ROM score varied from 0—minimal mobility to 40—maximal mobility). The final CMS, therefore, ranged from 0, indicating a highly impaired shoulder function to 75 points, indicating a normal shoulder function (Table S1). Shoulder strength, which was part of the original CMS, was not evaluated in this study, because no reliable measurement device was available in our department.

In addition to the modified CMS score, the pain duration was graded as follows:

- 1 = less than 6 weeks
- 2 = between 6 weeks and 3 months
- 3 = between 3 and 6 months
- 4 = between 6 months and 1 year
- 5 = over 1 year

The presence of diurnal pain, nocturnal pain, and nocturnal pain predominance were also evaluated.

2.3. Clinical Follow-Up

A clinical follow-up was available in a sub-group of 49 patients with a mean age of 54 ± 8.8 (37–74) years treated by physical therapy. Other patients were lost to follow-up or were treated in other institutions. There were 17 men (mean age 50.9 ± 6.6 (38–61) years) and 32 women (mean age 55.7 ± 9.6 (37–74) years) with a M/F sex ratio of 0.53. Based on medical record data (pain, activities, and ROM), and the symptoms at 9 to 13 months after the MRI examination were classified as improved, stable, or worsened. None of these patients had been treated by intra-articular corticosteroid injection.

2.4. Mri Examination

MRI examinations were performed with either a 1.5 T (105 patients) or a 3.0 T (27 patients) scanner (Signa HDxt, GE Healthcare, Milwaukee, WI, USA) using a dedicated eight-channel shoulder coil and similar protocols.

All MRI examinations consisted of an axial and oblique sagittal fast spin-echo (FSE) T1-weighted acquisitions (at 1.5 T: TR/TE, 500/10; echo-train length (ETL), 2; matrix, 352×320 ; NEX, 0.5; FOV, 160 mm; gap, 5 mm; slice thickness, 4 mm; at 3.0 T: TR/TE, 740/minimum full; ETL, 2; matrix, 352×256 ; NEX, 1; FOV, 150 mm; gap, 1 mm; slice thickness, 3 mm); axial, oblique sagittal and oblique coronal FSE T2-weighted fat-saturated images (at 1.5 T: TR/TE, 3500/50; ETL, 12; matrix, 384×320 ; NEX, 1.5; FOV, 160 mm; gap, 3.9 mm; slice thickness, 3.5 mm; at 3.0 T: TR/TE, 3040/45; ETL, 11; matrix, 352×256 ; NEX, 2; FOV, 150 mm; gap, 0.3 mm; slice thickness, 3 mm).

2.5. Image Analysis

The images were retrospectively reviewed by two musculoskeletal radiologists with three (FZ) and seven years (PP) of clinical experience with MRI using a PACS station (Synapse[®], v4.1.600, Fujifilm, Montigny, France). A third radiologist (P.A.G.T.) with 11 years of clinical experience with MRI performed a training session with the two readers with 20 MRI studies of patients with AC, not included in the study population prior to the readouts. The readers were blinded to clinical and demographic data.

The signal intensity of the IGHL on oblique coronal T2-weighted fat-saturated images was graded as follows (Figure 1):

- 1: normal homogenous low signal intensity
- 2: partial or foci of signal hyperintensity
- 3: global signal hyperintensity
- 4: linear hyperintensity of the peri-articular soft tissues

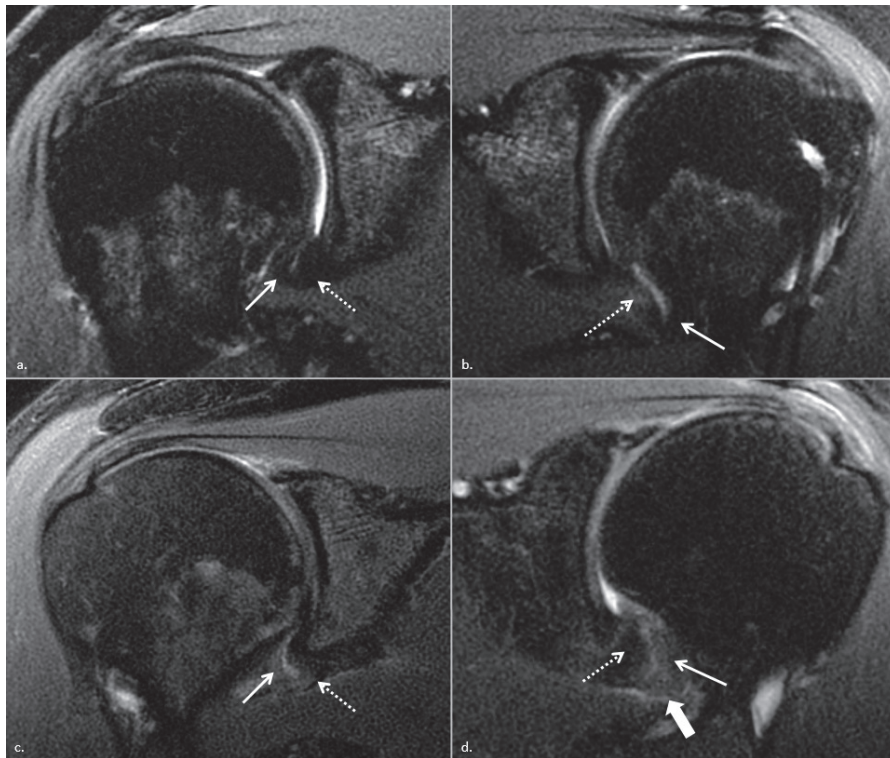


Figure 1. (a–d) Frontal oblique non-contrast fat-suppressed T2-weighted fast spin-echo MRI shows method used to grade glenohumeral inferior ligament signal on its glenoidal (white arrow) and humeral (dotted arrow) insertions, without signal abnormality in the right shoulder of a 55-year-old woman with adhesive capsulitis graded 1 in (a), a discontinuous glenoidal side IGHL hypersignal graded 2 in the left shoulder of the same woman with contralateral adhesive capsulitis in (b), a global both side IGHL hypersignal graded 3 in the left shoulder of a 43-year-old man with adhesive capsulitis in (c) and an overflow of the hypersignal in adjacent soft tissues (thick white arrow) graded 4 in the right shoulder of a 46 years old man with adhesive capsulitis in (d).

The whole ligamentous complex was considered in the analysis: the anterior band, posterior band, and hammock portion. The patients with IGHL scores of 1 and 2 were considered to have a low IGHL signal intensity, and those with grades 3 and 4 were considered to have high IGHL signal intensity. The thickness of the IGHL was measured at the glenoidal and humeral insertions on oblique coronal T2-weighted fat-saturated images, according to Mengiardi et al. [9] and classified as <4 mm, between 4 and <6 mm and ≥ 6 mm (Figure 2) [28]. The thickest portion of the coracohumeral ligament (CHL) was measured on the sagittal T2-weighted fat-saturated images, according to Mengiardi et al. [9] (Figure 3). The size of the axillary recess and superior glenohumeral ligament thickness were not assessed as MR arthrograms were not available.

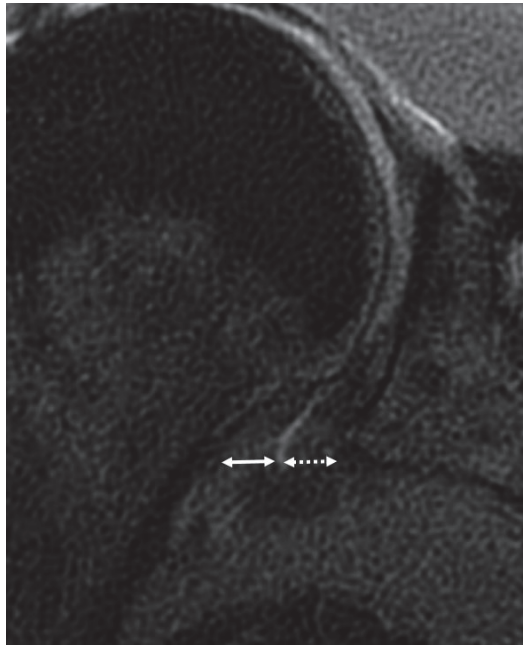


Figure 2. Coronal oblique non-contrast fat-suppressed T2-weighted fast spin-echo MRI of the right shoulder in a 44-year-old woman with adhesive capsulitis shows method used to measure inferior glenohumeral ligament thickness at its glenoidal (dotted double arrow) (4 mm) and humeral insertion (double arrow) (4.5 mm).

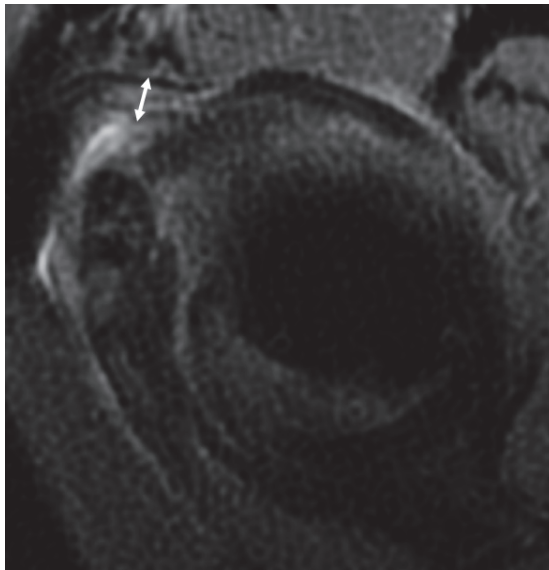


Figure 3. Sagittal oblique non-contrast fat-suppressed T2-weighted fast spin-echo MRI of the left shoulder in a 55-year-old man with adhesive capsulitis shows method used to measure coracohumeral ligament thickness (double white arrow) (4 mm). Additionally, note its high signal intensity.

2.6. Statistical Analysis

The R Development Core Team software (version 3.0.12013, R Foundation for Statistical Computing, Vienna, Austria) was used to perform statistical analysis. Statistical significance for all tests was defined as $p < 0.05$. Quantitative data are presented as mean \pm standard deviation (range).

Linear regression analysis with the Pearson test was used to evaluate the correlation between the signs of AC studied on MRI and pain, mobility, activity scores, and pain duration. The association between MRI findings, global modified CMS score, diurnal pain, night pain, and predominance of night pain was assessed with the Fisher exact test. The association between MRI findings and clinical follow-up was assessed with the Wilcoxon test. For each MRI measurement, intraclass correlation coefficients (ICC) were calculated to assess interobserver variability. ICC values below 0.5 were considered poor, between 0.5 and 0.75 moderate, between 0.75 and 0.90 good, and above 0.9 excellent [29].

3. Results

Table 1 shows demographic characteristics and modified CMS in the study population. The mean global modified CMS was 31.3 ± 14.2 (2–69) points, and the mean pain duration grade was 3.5 ± 1.1 (1–5). Clinical pain characteristics are shown in Table 2. Night pain was frequent and predominant in about half of the concerned patients. Table 3 shows the pain duration grade in each grade of IGHL signal intensity. IGHL signal intensity was low in 70 shoulders (52.2%) and high in 64 (47.8%) for reader 1. These figures were 72 (53.7%) and 62 (46.3%), respectively, for reader 2. Table 4 shows the MRI findings in the shoulders evaluated.

Table 1. Summary of patients’ ages and clinical impairment items.

Parameter	Minimum	Maximum	Mean	Standard Deviation
Patient Age				
All patients ($n = 132$)	22	78	54.1	9.3
Men ($n = 55$)	22	70	53.5	8.8
Women ($n = 77$)	22	78	54.4	10.8
Modified Constant-Murray score	2	69	31.3	14.2
Pain Intensity Score	0	15	4	3.8
Activity Score	0	20	9.8	4.5
Mobility Score	0	40	17.7	9.3
Pain Duration Grade	1	5	3.5	1.1

Table 2. Summary of patients’ pain characteristics.

Parameter	Effective
Pain Duration Grade	$n = 112$ *
1	4.5% ($n = 5$)
2	13.4% ($n = 15$)
3	32.1% ($n = 36$)
4	24.1% ($n = 27$)
5	25.9% ($n = 29$)
Diurnal Pain	94.7% ($n = 127$)
Night Pain	87.3% ($n = 117$)
Predominance of Night Pain	46.2% ($n = 62$)

* 22 data were missing because patients were not able to determine it.

Table 3. Pain duration grade according to inferior glenohumeral ligament signal intensity grade.

IGHL Signal Intensity				Pain Duration Grade	
Reader 1		Reader 2		Reader 1	Reader 2
1	(n = 34)	1	(n = 34)	3.9 ± 1.1	3.8 ± 1.2
2	(n = 24)	2	(n = 25)	3.6 ± 1.3	3.7 ± 1.1
3	(n = 21)	3	(n = 34)	3.3 ± 0.9	3.2 ± 0.9
4	(n = 33)	4	(n = 19)	3.1 ± 1	3.1 ± 1

IGHL: inferior glenohumeral ligament, results of pain duration score are presented as mean ± standard deviation. Range of all sub-groups of pain duration grade was 1–5.

Table 4. Summary of patients’ MRI measurements.

Parameter	Minimum		Maximum		Mean		Standard Deviation	
	R1	R2	R1	R2	R1	R2	R1	R2
IGHL thickness (glenoidal side)	2	2	10	8	4.3	4.5	1.3	1.2
IGHL thickness (humeral side)	2	2	8	7	3.8	3.7	1.3	1.2
CHL thickness	1.5	1	5	4	2.5	2.2	0.6	0.6

Values are given in millimeters. IGHL: inferior glenohumeral ligament, CHL: coracohumeral ligament. R1: Reader 1, R2: Reader 2.

ICC was excellent in grading IGHL signal as low or high (0.96), and moderate when taking in account all the four grades (0.67). ICC values were moderate for IGHL thickness (glenoidal insertion: 0.72, humeral insertion: 0.61) and poor for CHL thickness (0.09).

Mobility scores were significantly different in patients with high IGHL signal intensity compared to those with low intensity for both readers ($p = 0.04$ and 0.02 for readers 1 and 2). The mean mobility scores between shoulders with low and high IGHL signal intensity grades were 19.6 ± 10.1 (2–40) points versus 15.7 ± 8 (0–38) points for readers 1 and 19.4 ± 10 (0–40) points versus 15.8 ± 8.2 (0–38) points for reader 2. The variation of mobility scores with respect to IGHL signal intensity grade is shown in Figure 4.

For both readers, pain duration was significantly shorter in patients with high IGHL signal intensity compared to those with a low signal IGHL ($p = 0.03$ and 0.04 for readers 1 and 2). The pain duration grades in patients with low and high IGHL signal intensity were 3.8 ± 1.2 (1–5) versus 3.2 ± 0.9 (1–5) for reader 1 and 3.8 ± 1.2 (1–5) versus 3.2 ± 0.9 (1–5) for reader 2. Similarly, as the IGHL signal intensity grade increased, there was also a decrease in mean pain duration for both readers (Table 3 and Figure 5). The presence of high IGHL signal intensity was also significantly associated with nocturnal pain predominance for both readers ($p = 0.003$ and 0.003).

The glenoidal IGHL thickness was significantly correlated with activity limitation scores for reader 1 ($p = 0.005$). Patients with IGHL measuring < 4 mm, between 4 and < 6 mm, and ≥ 6 mm presented a progressive increase in activity limitation scores of 8.9 ± 5 (0–20) points, 9.7 ± 4.5 (0–20) points, and 11.5 ± 3.8 (4–20) points, respectively for reader 1. For reader 2, these figures were 8.4 ± 3.9 (0–20) points, 10.5 ± 4.7 (2–20) points, and 9.9 ± 4.6 (0–20) points, respectively, which suggest a similar tendency for values < 6 mm, but this variation was not statistically significant ($p = 0.09$). The IGHL thickness at the humeral insertion was significantly associated with pain duration for both readers ($p = 0.04$ and 0.02). For reader 1, with an increasing humeral IGHL thickness, the pain duration decreased (pain duration grades of 3.6 ± 1.1 (1–5), 3.3 ± 1.1 (1–5) and 3.3 ± 1.2 (1–5) points for patients with IGHL thicknesses of < 4 mm, between 4 and < 6 mm and ≥ 6 mm, respectively). For reader 2, the same tendency was found for patients with IGHL of < 6 mm in thickness; however, for patients with ligaments ≥ 6 mm, the pain duration was longer (3.6 ± 0.8 [3–5] points).

CHL measurements are shown in Table 4. This ligament could not be measured confidently in five patients for reader 1 and 20 patients for reader 2. There was no association between CHL thickness and clinical impairment.

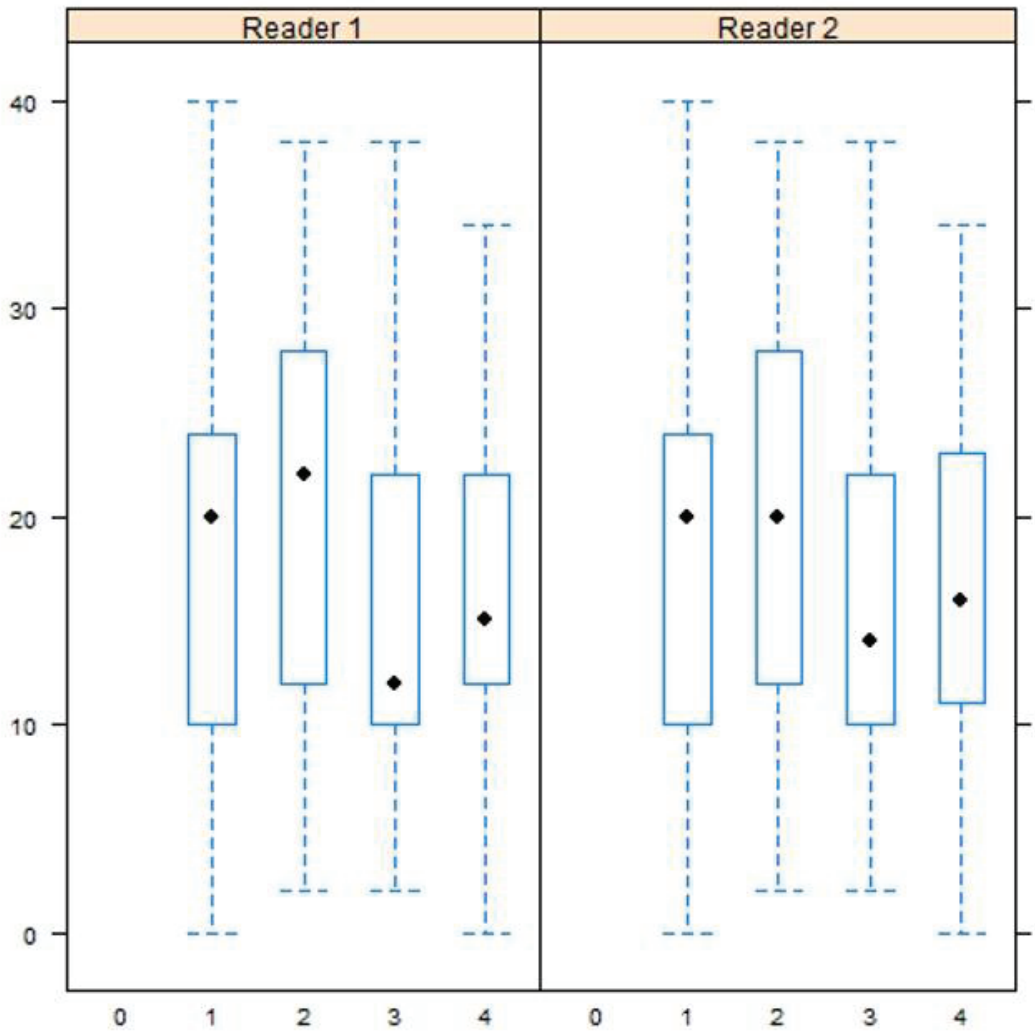


Figure 4. Box-plot showing mean mobility score (y -axis) according to inferior glenohumeral ligament intensity grade (x -axis) for reader 1 and reader 2.

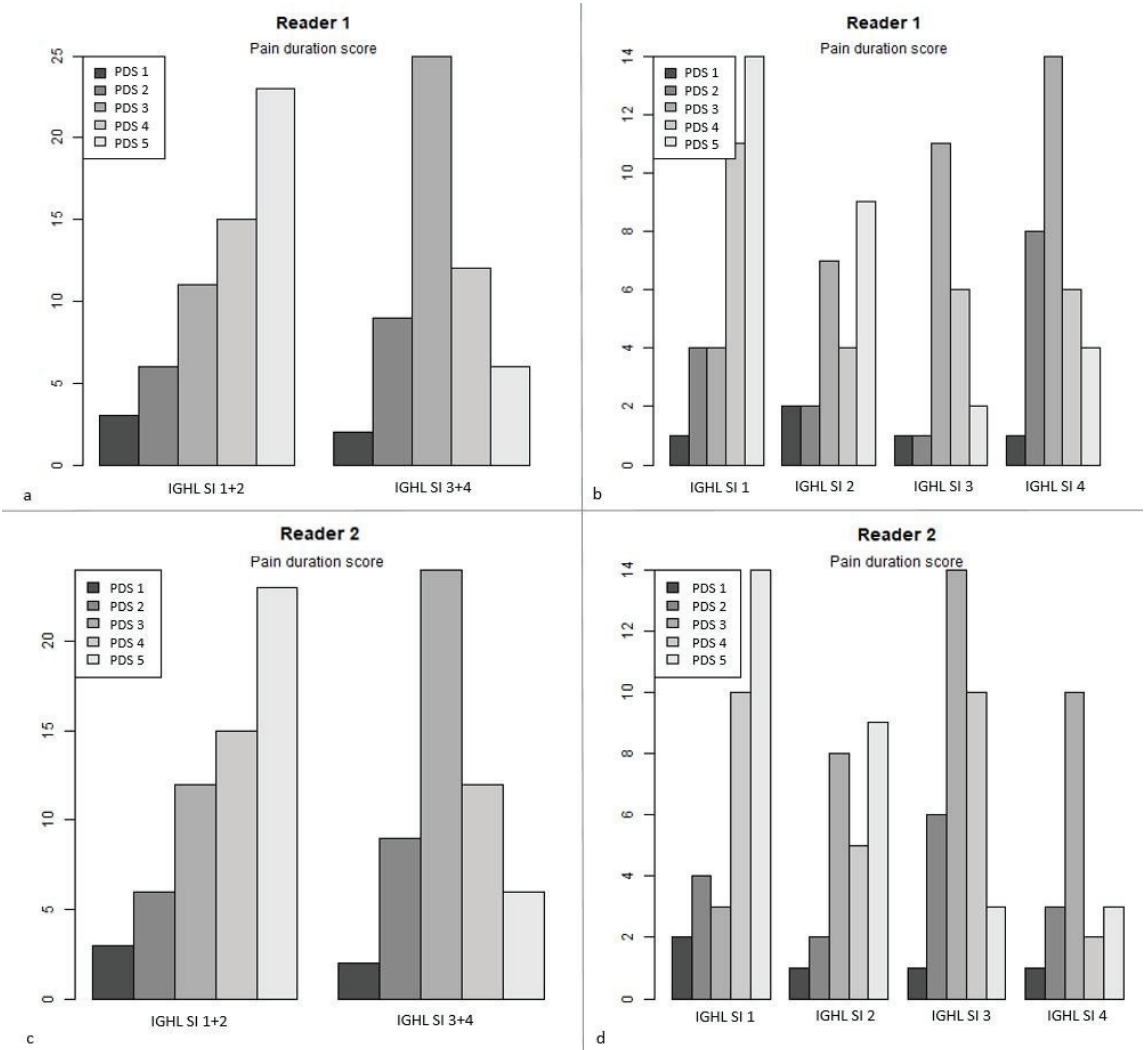


Figure 5. Bar plot representing pain score duration (PDS) (number of patients on y-axis) according to inferior glenohumeral ligament signal intensity (IGHL SI) (x-axis), shown for reader 1 for grade 1 + 2 and 3 + 4 in (a), for each grade (1, 2, 3, 4) in (b), and for reader 2 for grade 1 + 2 and 3 + 4 in (c), for each grade in (d).

Concerning disease progression, 31 patients (13 men, 18 women, mean age 55 ± 9.1 (38–74) years) showed improvement, 11 patients (2 men, 9 women, mean age 55 ± 10.1 (37–67) years) stability, and 7 worsening (2 men, 5 women, mean age 54 ± 6 (49–67) years). IGHL thickness was significantly correlated with clinical outcomes on the humeral side for both readers ($p = 0.005$ and 0.04 for readers 1 and 2) and on the glenoidal side for reader 1 ($p = 0.002$ and 0.05 for readers 1 and 2). Patients with clinical improvement had thicker IGHL on its humeral side (4 ± 1.5 (2–8) mm and 4 ± 1.3 (2–7) mm for readers 1 and 2) than those with worsening (2.2 ± 0.4 (2,3) mm and 2.7 ± 0.7 (2–4) mm for readers 1 and 2). For reader 1, patients with a stable clinical outcome also had a thicker IGHL than those with worsening, on both sides (glenoidal side: $p = 0.02$, humeral side $p = 0.005$). The same tendency was observed for reader 2, but these differences were not statistically significant

($p = 0.2$). For both readers, the presence of high IGHL signal intensity was not significantly correlated with disease progression ($p > 0.05$). In patients with worsening, IGHL was found to be ≤ 3 mm in 66 to 83% for reader 1, and 83% to 100% for reader 2. IGHL thickness distribution according to clinical outcomes is shown in Figure 6.

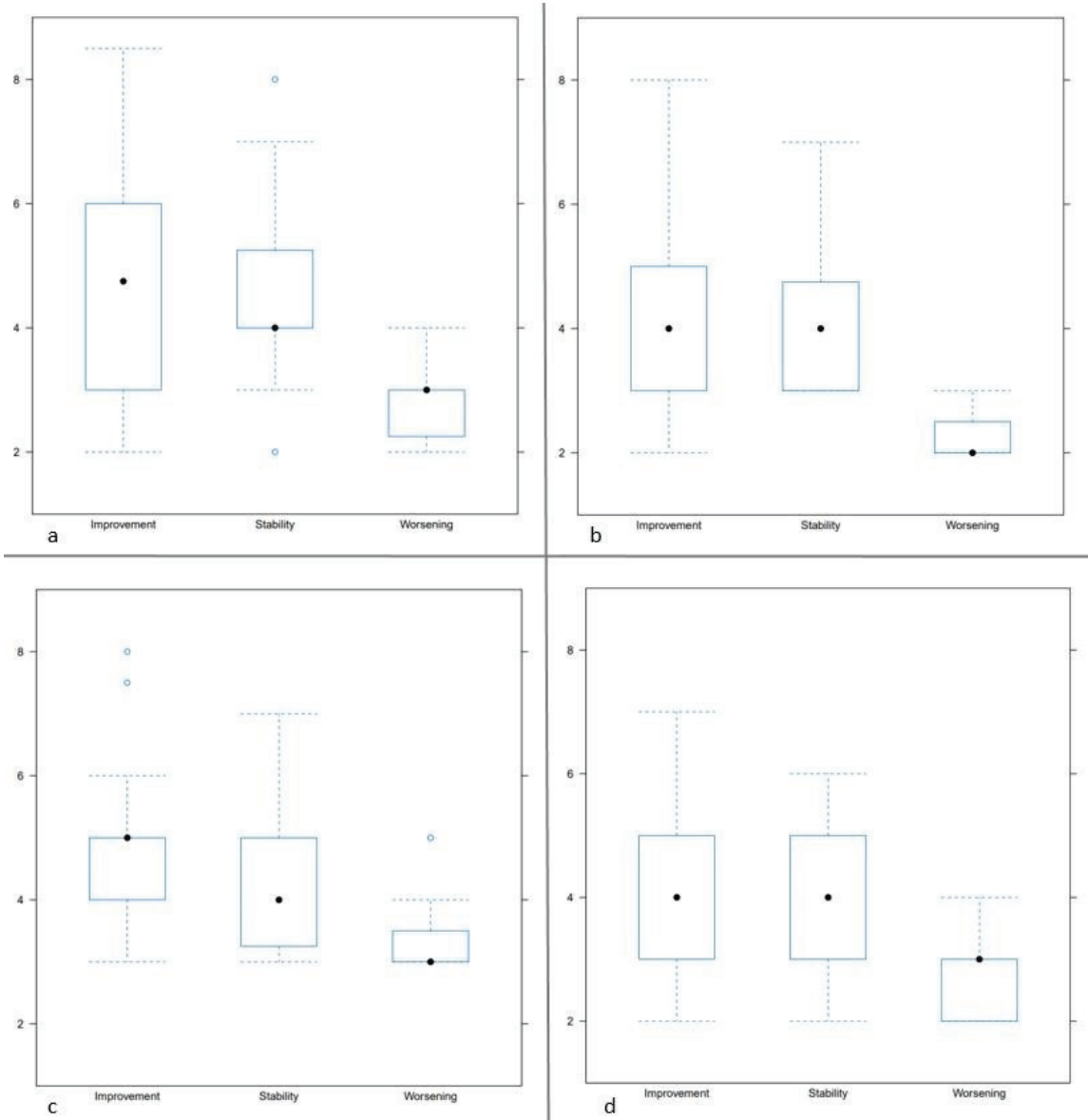


Figure 6. Box plot representing inferior glenohumeral ligament thickness (y -axis) according to clinical outcomes for reader 1 on the glenoidal (a) and humeral side (b), and for reader 2 on the glenoidal (c) and humeral side (d).

For both readers, there was no association between CMS modified global score, pain intensity grade, diurnal pain, and MRI findings.

4. Discussion

Our study showed a significant correlation between high IGHL signal intensity and the pain duration in patients with AC, with a clear high signal predominance in the patients presenting with pain from three to six months. Additionally, the reproducibility for the differentiation between low- and high-signal IGHL was considered excellent. Those results are in agreement with Sofka et al. [20], who stated that capsular high signal intensity in the axillary pouch was most closely associated with pain from three to nine months. High IGHL signal was also associated with night pain, which may have a negative impact on sleep quality and mental health [30,31]. Another important finding was the significant decrease in mobility scores in patients with high IGHL signal hyperintensity, which was not previously reported. Prior reports have also indicated that capsular edema and rotator interval signal abnormalities, were independent predictors of a better outcome for pain relief after glenohumeral corticosteroid injections, confirming the inflammatory nature of these MR findings [32]. In light of these results, increased IGHL signal intensity in patients with AC can be considered as a maker for an early inflammatory disease stage, and is associated with inflammatory-type pain and limited ROM. Thus, the treatment of patients with such finding should be aimed at reducing (e.g., intra-articular corticosteroid injection, cryotherapy) or limiting (e.g., gentle physiotherapy) the capsular inflammatory process [33–37]. Previous studies demonstrated that MRI could not predict AC prognosis [21] or the outcome after capsular distension [38]. Our results, however, indicate that patients with a thick IGHL (4 mm or higher, particularly on the humeral side) were very likely to have a favorable outcome at follow-up (performed approximately one year after imaging). Conversely, thin IGHL (3 mm or lower) was associated with clinical worsening. This could be related to collagen accumulation in the joint capsule in late disease phases [39,40]. As AC is a disease with a self-limited course, a thicker IGHL could be an indicator of a late disease phase and hence be associated with a favorable outcome. Similar to signal changes, the IGHL thickness may have implications in the therapeutic decision-making of AC patients. Although further studies are necessary, these patients might be more suitable for therapeutic options aiming at decreasing capsular stiffness (e.g., hydrodilatation, physiotherapy with active-assisted ROM exercises, stretching, and muscle strengthening) [41–43].

Unlike Anh et al. [26], we did not find any correlation between MRI findings and the degree of pain, but we did not rate IGHL enhancement, as its signal on T2-weighted fat-saturated FSE images has been shown to be reliable without improvement after gadolinium injection [6]. Additionally, systematic gadolinium injection is not currently recommended for the evaluation of patients with AC and should be reserved for patients with equivocal findings on conventional sequences [44,45]. None of the MRI findings evaluated was correlated with global CMS results, in agreement with Park et al. [23]. Capsule thickness in the axillary recess has been described as a reliable diagnostic tool of AC when >4 mm [28,46], but in our study, less than 30% of patients fulfilled this criterion at the humeral insertion. Contrary to the presented results, some authors indicated that capsular thickness on ultrasound and MRI was associated with shoulder function impairment [23,46]. We hypothesize that these differences are related to patient selection bias, and that IGHL thickness could be a more reliable diagnostic tool in patients' later AC phases, whereas in earlier disease phases the implications of this finding could be less clear.

This study has limitations. Most importantly, AC diagnosis was confirmed neither by arthroscopy nor histologically. However, clinical findings remain the basis for the diagnosis of AC, and the diagnostic performance of MRI diagnostic criteria has been previously evaluated [6–8,10–12,17,46,47]. As the estimation of pain duration provided by patients may be imprecise, a pain score system with time intervals was used to limit this potential bias. Since the correlation between MRI findings and the range of motion in each direction is still debated [23–25,46], we preferred to analyze global motion scores only, which could be responsible for some of the differences between the presented results and prior reports. There was no control group and no systematic clinical or MRI follow-up of the patients included. We did not rate intra-observer agreement. The study population is relatively

heterogeneous with various disease stages and clinical impairment levels; however, the study population is one of the largest reported so far and is representative of routine clinical practice. Finally, the AC etiology (e.g., idiopathic versus secondary) could have an impact on the natural disease course and was not considered in this study.

In conclusion, two potentially useful MR biomarkers in patients with AC could be identified. First, the increased T2 signal intensity at the IGHL, which is an indicator of an early inflammatory phase AC and is associated with recent pain (3–6 months), nocturnal pain, and decreased ROM. Secondly, the thickness of the IGHL was significantly related to the clinical outcome (>4 mm is associated with a favorable outcome, whereas <3 mm with a worse prognosis). These findings should be considered in the MRI evaluation of patients with AC, with likely therapeutic implications.

Supplementary Materials: The following are available online at <https://www.mdpi.com/article/10.3390/jcm10173882/s1>, Table S1: Modified Constant-Murley Score.

Author Contributions: Conceptualization, R.G. and P.A.G.T.; methodology, P.A.G.T.; software, G.H.; validation, R.G., A.B. and P.A.G.T. formal analysis, A.B.; investigation, A.R.; resources, F.Z. and P.P.; data curation, F.Z. and P.P.; writing—original draft preparation, R.G.; writing—review and editing, R.G.; visualization, P.A.G.T.; supervision, A.B.; project administration, P.A.G.T. All authors have read and agreed to the published version of the manuscript.

Funding: This research received no external funding.

Institutional Review Board Statement: The study was conducted according to the guidelines of the Declaration of Helsinki and approved by the Institutional Review Board of the University Hospital of Nancy (1685709v0).

Informed Consent Statement: Written informed consent was obtained from all subjects involved in the study.

Conflicts of Interest: The authors declare no conflict of interest.

Abbreviations

AC	adhesive capsulitis
CHL	coracohumeral ligament
CMS	Constant-Murley Score
ETL	echo-train length
FOV	field of view
FSE	fast spin-echo
IGHL	inferior glenohumeral ligament
NEX	number of excitations -ROM: range of motion

References

1. Kelley, M.J.; Shaffer, M.A.; Kuhn, J.E.; Michener, L.A.; Seitz, A.L.; Uhl, T.L.; Godges, J.J.; McClure, P. Shoulder Pain and Mobility Deficits: Adhesive Capsulitis: Clinical Practice Guidelines Linked to the International Classification of Functioning, Disability, and Health From the Orthopaedic Section of the American Physical Therapy Association. *J. Orthop. Sports Phys. Ther.* **2013**, *43*, A1–A31. [\[CrossRef\]](#)
2. Brue, S.; Valentin, A.; Forssblad, M.; Werner, S.; Mikkelsen, C.; Cerulli, G. Idiopathic adhesive capsulitis of the shoulder: A review. *Knee Surg. Sports Traumatol. Arthrosc.* **2007**, *15*, 1048–1054. [\[CrossRef\]](#)
3. D’Orsi, G.M.; Via, A.G.; Frizziero, A.; Oliva, F. Treatment of adhesive capsulitis: A review. *Muscles Ligaments Tendons J.* **2012**, *2*, 70–78.
4. Sano, H.; Hatori, M.; Mineta, M.; Hosaka, M.; Itoi, E. Tumors masked as frozen shoulders: A retrospective analysis. *J. Shoulder Elbow Surg.* **2010**, *19*, 262–266. [\[CrossRef\]](#)
5. Zappia, M.; Di Pietto, F.; Aliprandi, A.; Pozza, S.; De Petro, P.; Muda, A.; Sconfienza, L.M. Multi-modal imaging of adhesive capsulitis of the shoulder. *Insights Imaging* **2016**, *7*, 365–371. [\[CrossRef\]](#) [\[PubMed\]](#)
6. Teixeira, P.A.G.; Balaj, C.; Chanson, A.; Lecocq, S.; Louis, M.; Blum, A. Adhesive Capsulitis of the Shoulder: Value of Inferior Glenohumeral Ligament Signal Changes on T2-Weighted Fat-Saturated Images. *Am. J. Roentgenol.* **2012**, *198*, W589–W596. [\[CrossRef\]](#)

7. Suh, C.H.; Yun, S.J.; Jin, W.; Lee, S.H.; Park, S.Y.; Park, J.S.; Ryu, K.N. Systematic review and meta-analysis of magnetic resonance imaging features for diagnosis of adhesive capsulitis of the shoulder. *Eur. Radiol.* **2019**, *29*, 566–577. [[CrossRef](#)] [[PubMed](#)]
8. Song, K.D.; Kwon, J.W.; Yoon, Y.C.; Choi, S.-H. Indirect MR Arthrographic Findings of Adhesive Capsulitis. *Am. J. Roentgenol.* **2011**, *197*, W1105–W1109. [[CrossRef](#)]
9. Mengiardi, B.; Pfirrmann, C.W.A.; Gerber, C.; Hodler, J.; Zanetti, M. Frozen Shoulder: MR Arthrographic Findings. *Radiology* **2004**, *233*, 486–492. [[CrossRef](#)] [[PubMed](#)]
10. Lefevre-Colau, M.-M.; Drapé, J.-L.; Fayad, F.; Rannou, F.; Diche, T.; Minvielle, F.; Demaille-Wlodyka, S.; Mayoux-Benhamou, M.-A.; Fermanian, J.; Poiraudou, S.; et al. Magnetic resonance imaging of shoulders with idiopathic adhesive capsulitis: Reliability of measures. *Eur. Radiol.* **2005**, *15*, 2415–2422. [[CrossRef](#)] [[PubMed](#)]
11. Harris, G.; Bou-Haidar, P.; Harris, C. Adhesive capsulitis: Review of imaging and treatment: Adhesive capsulitis: Review of imaging and treatment. *J. Med. Imaging Radiat. Oncol.* **2013**, *57*, 633–643. [[CrossRef](#)]
12. Jung, J.-Y.; Jee, W.-H.; Chun, H.J.; Kim, Y.-S.; Chung, Y.G.; Kim, J.-M. Adhesive capsulitis of the shoulder: Evaluation with MR arthrography. *Eur. Radiol.* **2006**, *16*, 791–796. [[CrossRef](#)] [[PubMed](#)]
13. Chi, A.S.; Kim, J.; Long, S.S.; Morrison, W.B.; Zoga, A.C. Non-contrast MRI diagnosis of adhesive capsulitis of the shoulder. *Clin. Imaging* **2017**, *44*, 46–50. [[CrossRef](#)]
14. Ahn, K.-S.; Kang, C.H.; Kim, Y.; Jeong, W.-K. Diagnosis of adhesive capsulitis: Comparison of contrast-enhanced MRI with noncontrast-enhanced MRI. *Clin. Imaging* **2015**, *39*, 1061–1067. [[CrossRef](#)] [[PubMed](#)]
15. Lee, K.H.; Park, H.J.; Lee, S.Y.; Youn, I.Y.; Kim, E.; Park, J.H.; Park, S.J. Adhesive Capsulitis of the Shoulder Joint: Value of Glenohumeral Distance on Magnetic Resonance Arthrography. *J. Comput. Assist. Tomogr.* **2017**, *41*, 116–120. [[CrossRef](#)]
16. Kim, K.C.; Rhee, K.J.; Shin, H.D. Adhesive capsulitis of the shoulder: Dimensions of the rotator interval measured with magnetic resonance arthrography. *J. Shoulder Elb. Surg.* **2009**, *18*, 437–442. [[CrossRef](#)] [[PubMed](#)]
17. Connell, D.; Padmanabhan, R.; Buchbinder, R. Adhesive capsulitis: Role of MR imaging in differential diagnosis. *Eur. Radiol.* **2002**, *12*, 2100–2106. [[CrossRef](#)]
18. Binder, A.I.; Bulgen, D.Y.; Hazleman, B.L.; Roberts, S. Frozen shoulder: A long-term prospective study. *Ann. Rheum. Dis.* **1984**, *43*, 361–364. [[CrossRef](#)]
19. Constant, C.R.; Murley, A.H. A clinical method of functional assessment of the shoulder. *Clin. Orthop. Relat. Res.* **1987**, 160–164. [[CrossRef](#)]
20. Sofka, C.M.; Ciavarrá, G.A.; Hannafin, J.A.; Cordasco, F.A.; Potter, H.G. Magnetic Resonance Imaging of Adhesive Capsulitis: Correlation with Clinical Staging. *HSS J.* **2008**, *4*, 164–169. [[CrossRef](#)]
21. Yoon, J.P.; Chung, S.W.; Lee, B.J.; Kim, H.S.; Yi, J.H.; Lee, H.-J.; Jeong, W.-J.; Moon, S.G.; Oh, K.-S.; Yoon, S.T. Correlations of magnetic resonance imaging findings with clinical symptom severity and prognosis of frozen shoulder. *Knee Surg. Sports Traumatol. Arthrosc.* **2017**, *25*, 3242–3250. [[CrossRef](#)] [[PubMed](#)]
22. Park, S.; Lee, D.-H.; Yoon, S.-H.; Lee, H.Y.; Kwack, K.-S. Evaluation of Adhesive Capsulitis of the Shoulder With Fat-Suppressed T2-Weighted MRI: Association Between Clinical Features and MRI Findings. *Am. J. Roentgenol.* **2016**, *207*, 135–141. [[CrossRef](#)] [[PubMed](#)]
23. Park, G.-Y.; Park, J.H.; Kwon, D.R.; Kwon, D.G.; Park, J. Do the Findings of Magnetic Resonance Imaging, Arthrography, and Ultrasonography Reflect Clinical Impairment in Patients With Idiopathic Adhesive Capsulitis of the Shoulder? *Arch. Phys. Med. Rehabil.* **2017**, *98*, 1995–2001. [[CrossRef](#)] [[PubMed](#)]
24. Lee, Y.-T.; Chun, K.-S.; Yoon, K.J.; Park, H.-J.; Lee, S.-Y.; Kim, E.; Park, Y.S.; Seo, K.-H. Correlation of Joint Volume and Passive Range of Motion With Capsulo-Synovial Thickness Measured by Contrast-Enhanced Magnetic Resonance Imaging in Adhesive Capsulitis. *PM&R* **2018**, *10*, 137–145. [[CrossRef](#)]
25. Lee, S.-Y.; Park, J.; Song, S.-W. Correlation of MR Arthrographic Findings and Range of Shoulder Motions in Patients With Frozen Shoulder. *Am. J. Roentgenol.* **2012**, *198*, 173–179. [[CrossRef](#)]
26. Ahn, K.-S.; Kang, C.H.; Oh, Y.-W.; Jeong, W.-K. Correlation between magnetic resonance imaging and clinical impairment in patients with adhesive capsulitis. *Skelet. Radiol.* **2012**, *41*, 1301–1308. [[CrossRef](#)]
27. Kim, D.H.; Cho, C.-H.; Sung, D.H. Ultrasound measurements of axillary recess capsule thickness in unilateral frozen shoulder: Study of correlation with MRI measurements. *Skelet. Radiol.* **2018**, *47*, 1491–1497. [[CrossRef](#)]
28. Emig, E.W.; Schweitzer, M.E.; Karasick, D.; Lubowitz, J. Adhesive capsulitis of the shoulder: MR diagnosis. *Am. J. Roentgenol.* **1995**, *164*, 1457–1459. [[CrossRef](#)]
29. Koo, T.K.; Li, M.Y. A Guideline of Selecting and Reporting Intraclass Correlation Coefficients for Reliability Research. *J. Chiropr. Med.* **2016**, *15*, 155–163. [[CrossRef](#)]
30. Fine, P.G. Long-term consequences of chronic pain: Mounting evidence for pain as a neurological disease and parallels with other chronic disease states. *Pain Med.* **2011**, *12*, 996–1004. [[CrossRef](#)]
31. Haack, M.; Simpson, N.; Sethna, N.; Kaur, S.; Mullington, J. Sleep deficiency and chronic pain: Potential underlying mechanisms and clinical implications. *Neuropsychopharmacology* **2020**, *45*, 205–216. [[CrossRef](#)]
32. Fritz, B.; Del Grande, F.; Sutter, R.; Beeler, S.; Peterson, C.K.; Pfirrmann, C.W.A. Value of MR arthrography findings for pain relief after glenohumeral corticosteroid injections in the short term. *Eur. Radiol.* **2019**, *29*, 6416–6424. [[CrossRef](#)]
33. Wang, W.; Shi, M.; Zhou, C.; Shi, Z.; Cai, X.; Lin, T.; Yan, S. Effectiveness of corticosteroid injections in adhesive capsulitis of shoulder: A meta-analysis. *Medicine* **2017**, *96*, e7529. [[CrossRef](#)]

34. Sun, Y.; Lu, S.; Zhang, P.; Wang, Z.; Chen, J. Steroid Injection Versus Physiotherapy for Patients With Adhesive Capsulitis of the Shoulder: A PRIMSA Systematic Review and Meta-Analysis of Randomized Controlled Trials. *Medicine* **2016**, *95*, e3469. [[CrossRef](#)]
35. Swenson, C.; Swärd, L.; Karlsson, J. Cryotherapy in sports medicine. *Scand. J. Med. Sci. Sports* **1996**, *6*, 193–200. [[CrossRef](#)]
36. Gooch, J.L.; Geiringer, S.R.; Akau, C.K. Sports medicine. 3. Lower extremity injuries. *Arch. Phys. Med. Rehabil.* **1993**, *74*, S438–S442. [[PubMed](#)]
37. Anjum, R.; Aggarwal, J.; Gautam, R.; Pathak, S.; Sharma, A. Evaluating the Outcome of Two Different Regimes in Adhesive Capsulitis: A Prospective Clinical Study. *Med. Princ. Pract.* **2020**, *29*, 225–230. [[CrossRef](#)] [[PubMed](#)]
38. Park, Y.H.; Park, Y.S.; Chang, H.J.; Kim, Y. Correlations between MRI findings and outcome of capsular distension in adhesive capsulitis of the shoulder. *J. Phys. Ther. Sci.* **2016**, *28*, 2798–2802. [[CrossRef](#)] [[PubMed](#)]
39. Bunker, T.D.; Anthony, P.P. The pathology of frozen shoulder. A Dupuytren-like disease. *J. Bone Joint Surg. Br.* **1995**, *77*, 677–683. [[CrossRef](#)] [[PubMed](#)]
40. Kraal, T.; Lübbers, J.; van den Bekerom, M.P.J.; Alessie, J.; van Kooyk, Y.; Eygendaal, D.; Koorevaar, R.C.T. The puzzling pathophysiology of frozen shoulders—A scoping review. *J. Exp. Orthop.* **2020**, *7*, 91. [[CrossRef](#)]
41. Pandey, V.; Madi, S. Clinical Guidelines in the Management of Frozen Shoulder: An Update! *Indian J. Orthop.* **2021**, *55*, 299–309. [[CrossRef](#)]
42. Favejee, M.M.; Huisstede, B.M.A.; Koes, B.W. Frozen shoulder: The effectiveness of conservative and surgical interventions—Systematic review. *Br. J. Sports Med.* **2011**, *45*, 49–56. [[CrossRef](#)]
43. Griggs, S.M.; Ahn, A.; Green, A. Idiopathic adhesive capsulitis. A prospective functional outcome study of nonoperative treatment. *J. Bone Joint Surg Am.* **2000**, *82*, 1398–1407. [[CrossRef](#)] [[PubMed](#)]
44. Small, K.M.; Adler, R.S.; Shah, S.H.; Roberts, C.C.; Bencardino, J.T.; Appel, M.; Gyftopoulos, S.; Metter, D.F.; Mintz, D.N.; Morrison, W.B.; et al. ACR Appropriateness Criteria® Shoulder Pain-Atraumatic. *J. Am. Coll. Radiol.* **2018**, *15*, S388–S402. [[CrossRef](#)] [[PubMed](#)]
45. Pessis, E.; Mihoubi, F.; Feydy, A.; Campagna, R.; Guerini, H.; Roren, A.; Rannou, F.; Drapé, J.-L.; Lefèvre-Colau, M.-M. Usefulness of intravenous contrast-enhanced MRI for diagnosis of adhesive capsulitis. *Eur. Radiol.* **2020**, *30*, 5981–5991. [[CrossRef](#)] [[PubMed](#)]
46. Jung, J.H.; Kim, D.H.; Yi, J.; Kim, D.-H.; Cho, C.-H. Determination of magnetic resonance imaging criteria for diagnosis of adhesive capsulitis. *Rheumatol. Int.* **2019**, *39*, 453–460. [[CrossRef](#)] [[PubMed](#)]
47. Gokalp, G.; Algin, O.; Yildirim, N.; Yazici, Z. Adhesive capsulitis: Contrast-enhanced shoulder MRI findings: Adhesive capsulitis: MRI. *J. Med Imaging Radiat. Oncol.* **2011**, *55*, 119–125. [[CrossRef](#)]

Article

Shear Wave Elastography of the Plantar Fascia: Comparison between Patients with Plantar Fasciitis and Healthy Control Subjects

Daniel Baur ¹, Christoph Schwabl ^{1,*}, Christian Kremser ¹, Mihra S. Taljanovic ², Gerlig Widmann ¹, Luca Maria Sconfienza ^{3,4}, Judith Sztankay ⁵, Gudrun Feuchtner ¹ and Andrea S. Klauser ¹

¹ Radiology Department, Medical University Innsbruck, Anichstrasse 35, 6020 Innsbruck, Austria; daniel.baur@i-med.ac.at (D.B.); christian.kremser@i-med.ac.at (C.K.); gerlig.widmann@tirol-kliniken.at (G.W.); gudrun.feuchtner@i-med.ac.at (G.F.); andrea.klauser@i-med.ac.at (A.S.K.)

² Banner University Medical Center, Department of Medical Imaging, College of Medicine, The University of Arizona, Tucson, AZ 85724, USA; mihrat@radiology.arizona.edu

³ Unit of Diagnostic and Interventional Radiology, I.R.C.C.S. Istituto Ortopedico Galeazzi, 20097 Milano, Italy; luca.sconfienza@unimi.it

⁴ Dipartimento di Scienze Biomediche per la Salute, Università degli Studi di Milano, 20133 Milano, Italy

⁵ Department of Radiotherapy, Medical University of Innsbruck, 6020 Innsbruck, Austria; judith.sztankay@tirol-kliniken.at

* Correspondence: christoph.schwabl@i-med.ac.at

Citation: Baur, D.; Schwabl, C.; Kremser, C.; Taljanovic, M.S.; Widmann, G.; Sconfienza, L.M.; Sztankay, J.; Feuchtner, G.; Klauser, A.S. Shear Wave Elastography of the Plantar Fascia: Comparison between Patients with Plantar Fasciitis and Healthy Control Subjects. *J. Clin. Med.* **2021**, *10*, 2351. <https://doi.org/10.3390/jcm10112351>

Academic Editor:
Carifallia Sakellariou

Received: 11 May 2021
Accepted: 26 May 2021
Published: 27 May 2021

Publisher's Note: MDPI stays neutral with regard to jurisdictional claims in published maps and institutional affiliations.



Copyright: © 2021 by the authors. Licensee MDPI, Basel, Switzerland. This article is an open access article distributed under the terms and conditions of the Creative Commons Attribution (CC BY) license (<https://creativecommons.org/licenses/by/4.0/>).

Abstract: Background: The purpose of this study was to evaluate plantar fasciae of healthy subjects and patients with plantar fasciitis by shear wave velocity (SWV) and stiffness with correlation to B-Mode and color Doppler ultrasonography (CDUS) and to establish cut-off values. Methods: This observational study was conducted with the approval of the Institutional Review Boards (IRBs) of our institution. 108 unilateral plantar fasciae were evaluated by including 87 consecutive patients (mean age 51.7; range: 29–82) (66 women and 21 men) with plantar fasciitis and 21 asymptomatic age matched healthy volunteers (mean age 47.3; range: 32–58) (15 women and 6 men). All patients were prospectively imaged between July 2018 and March 2019. B-mode US was used to measure thickness and CDUS to grade vascularity. SWE measurements were repeated 3 times and mean was used for statistical analysis. Results: Mean SWV value in healthy subjects was 6.94 m/s and in patients 4.98 m/s with a mean stiffness value of 152.88 kPa and 93.54 kPa respectively ($p < 0.001$). For SWV a cut-off value of 6.16 m/s had a specificity of 80.95% and sensitivity of 79.31%. For stiffness a cut-off value of 125.57 kPa had a specificity of 80.95% and sensitivity of 80.46%. No correlation to CDUS was found. The mean thickness of healthy fascias was 3.3 mm (range 2.4–3.9) compared to 6.1 mm (range 2.0–22.0) in plantar fasciitis ($p < 0.001$) with no correlation to SWV or to stiffness ($r^2 = 0.02$, $p = 0.06$). Conclusion: SWE allows quantitative assessment of plantar fascia stiffness, which decreases in patients with plantar fasciitis. No correlation to the thickness of the plantar fascia was found, therefore it represents an independent factor for the diagnosis of plantar fasciitis and could be helpful in addition to thickness measurement in unclear cases.

Keywords: color doppler ultrasonography; elastography; plantar fasciitis; plantar fascia; shear wave

1. Introduction

Plantar fasciitis is the most common cause of heel pain in adults [1]. The lifetime prevalence may reach 10% of the general population worldwide. It has substantial impact on patients' quality of life, which is shown by a study from Palomo-López et al., where the significance of health-related quality of life for foot pain, foot function, footwear, and general foot health, especially in women, was demonstrated [2,3]. Although the etiology of plantar fasciitis is multifactorial, mechanical overload and degeneration have been

regarded as the main factors [4]. The plantar fascia seems to be affected even by foot deformities like hallus valgus deformity [5]. Therefore the importance of the plantar fascia as a main factor for foot health is evident. A prior systematic review revealed that increased age was also one of the factors associated with chronic plantar heel pain [6]. Age-related changes in tendons, as well as specific changes to the elastic modulus with degeneration, have been reported in prior studies [7–9] and may also occur in the plantar fascia [10].

Sonoelastography (SEL) is an ultrasound (US) imaging technique that allows for a noninvasive estimation of tissue stiffness [11]. It is based on the fact that softer tissue has greater tissue displacement than hard tissue when externally compressed. SEL allows calculation and comparison of tissue displacement before and after tissue compression with conventional US equipment but modified software and is used in MSK application [12,13].

Ultrasound-based shear wave elastography (SWE) allows for quantitative assessment of tissue stiffness [14,15]. Although it is well established in imaging of other regions, e.g., breast-imaging, the use in MSK imaging is still on the rise [16,17]. In the past 2 decades, sonoelastography has been progressively used as a tool to help evaluate soft-tissue elasticity and add information obtained with conventional gray-scale and Doppler ultrasonographic techniques. Recently introduced, SWE is considered to be more objective, quantitative, and reproducible than compression sonoelastography with increasing applications to the musculoskeletal system [13]. SWE uses an acoustic radiation force pulse sequence to generate shear waves, which propagate perpendicular to the ultrasound beam, causing transient displacements. SWE has a promising role in determining the severity of disease of various musculoskeletal tissues including tendons, muscles, nerves, and ligaments [12–15,18].

SEL has been applied to assess the stiffness of various tissues. It has been used to detect tendinopathy in the common extensor tendon of the elbow and the Achilles tendon [19–21]. Thus, SEL may add information about the mechanical properties of plantar fascia in addition to B-mode morphology.

SEL has been used previously in plantar fascia showing a softening in patients with plantar fasciitis [22,23]. SWE results for plantar fascia in healthy volunteers were reported by Chino et al. [24] and Wu et al. [22,25] however, to our knowledge there are only a few publications for SWE in plantar fasciitis, e.g., only preliminary results of Gatz et al. in 39 patients with plantar fasciitis [18]. The purpose of our study was to compare SWE of the plantar fascia between healthy subjects and patients with plantar fasciitis by shear wave velocity and stiffness with findings obtained by B-Mode and CDUS and to evaluate objective SWE parameters originating from the US system immanent calculation in a larger population, to gain new forms of information about the changes of the plantar fascia in plantar fasciitis, which could help in the diagnosis of unclear cases.

2. Materials and Methods

2.1. Ethical Consideration

All subjects gave their informed consent for inclusion before they participated in the study. The study was conducted in accordance with the Declaration of Helsinki, and the protocol was approved by the Institutional Review Boards (IRBs) of our institution (ethical approval code: 353/4.3).

2.2. Design and Sampling

The study is designed as an observational study with random sampling. The sampling size was sufficient. When considering 10% of the worldwide population we reached a CI of 95% with a margin of error of 6%. Healthy volunteers and patients were recruited from the trauma surgery department of the Medical University Innsbruck. Diagnosis of plantar fasciitis was based on the patient's history and on results of the physical examination. Patients presented with inferior heel pain on weight bearing, pain persisting for ≥ 6 months with discomfort improving after further ambulation and worsening with continued activity, exacerbating pain when walking barefoot, on toes, or upstairs [26]. The participants had no treatment so far. Alternative diagnosis have been ruled out by trauma surgery specialists.

If both feet were symptomatic, the more painful one was included in the evaluation. For healthy volunteers a random assessment of left or right heel was performed. The sonographer was blinded to clinical diagnosis and patients' symptoms. US was used as the first-line imaging examination.

2.3. Study Population

108 unilateral plantar fasciae (81 women and 27 men) with normal physical activity were evaluated by including 87 consecutive patients (mean age 51.7, range: 29.0–82.0) (66 women and 21 men) with plantar fasciitis and 21 asymptomatic healthy volunteers recruited from our hospital staff (mean age 47.3, range: 32–58) (15 women and 6 men). All patients were prospectively imaged between July 2018 and March 2019.

Inclusion criteria comprised the presence of unilateral heel pain at the origin of the plantar fascia on the medial tubercle of the calcaneus lasting for more than 6 month.

Exclusion criteria included affected patients because of Morbus Ledderhosen ($n = 1$), Achilles tendinosis ($n = 1$), any treatment for plantar fasciitis ($n = 1$) or any previous surgery of the examined foot ($n = 2$), stress fracture or tumors.

2.4. Data Recollection

US examination: All US studies were performed by a single radiologist with three years of experience in SWE. The experiments were carried out in the Department of Rheumatology- and Sports Imaging, Medical University Hospital Innsbruck. Each US examination was performed using a SuperLinear™ SL12-7 MHz transducer with a bandwidth of 7–12 MHz (SuperSonic Imagine's Aixplorer®, SuperSonic Imagine, 510 rue René Descartes, Les jardins de la Duranne Bât. F, 13857, Aix-en-Provence, France). Each examination was performed according to a standardized protocol with patients placed in a prone position, legs extended with their feet on a positioning role. Feet were kept relaxed during all measurements, hanging free over the examination bed in a 90 degree angle.

2.4.1. B-Mode US Examination

Maximum thickness (in mm, craniocaudal dimension) of each plantar fascia was measured in the longitudinal plane (i.e., perpendicular to the direction of the fibers) at the insertion of the plantar fascia at the calcaneus. (Figure 1).

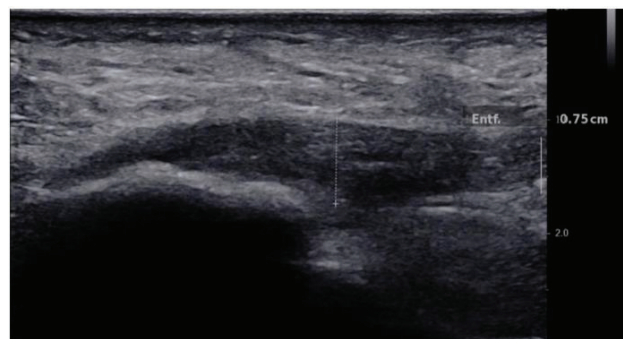


Figure 1. Longitudinal B-mode ultrasound image of a 50-year-old patient with plantar fascia shows hypoechoogenicity and thickening of the plantar fascia of 7 mm.

2.4.2. CDUS Examination

Accompanied hypervascularity modified according to Fenwick et al. was graded as per a semi-quantitative grading system consisting of 4 grades: Grade 0 = no vascularity (=normal), Grade 1 = 1/3 hypervascularity in the fascia, Grade 2 = 2/3 hypervascularity in the fascia, Grade 3 = 3/3 hypervascularity in the fascia [27]. CDUS was performed with standardized machine settings by using a frequency of 7 MHz with a pulse repetition

frequency of 750 to 1000 kHz, a low wall filter, and medium persistence. The window (colour box) was restricted to the plantar fascia. After visualization of colour-flow signals, pulsed wave spectral Doppler imaging was performed using the lowest filter setting and the smallest scale available that would display the Doppler waveforms as large as possible without aliasing. A spectral Doppler tracing was obtained to confirm that the CDUS signals represented true arterial or venous flow

2.4.3. SWE Examination

For stiffness and shear wave velocity three SWE measures were obtained at the same session in the longitudinal plane by manual tracking of a ROI which was repeated 3 times after unfreezing and freezing the SWE result. B-mode was used to longitudinally align the transducer with the plantar fascia. The transducer was kept stationary with light pressure on top of a generous amount of coupling gel for 4–5 s during the acquisition of each SWE sonogram. For each SWE sonogram, the ROI was tracked manually centered on the plantar fascia, ensuring that the diameter of the ROI was within the thickest part of the plantar fascia. For further analysis, the mean of the three measurements was used. The stiffness and SWE values were given in kPa and m/s, respectively, and tabulated. (Figures 2 and 3)

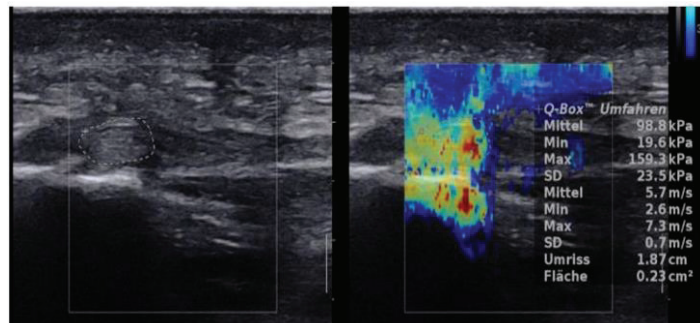


Figure 2. Longitudinal SWE image and B-mode ultrasound image of a 50-year-old patient with normal plantar fascia demonstrates stiffness of 98.8 kPa and SWV value of 5.7 m/s.

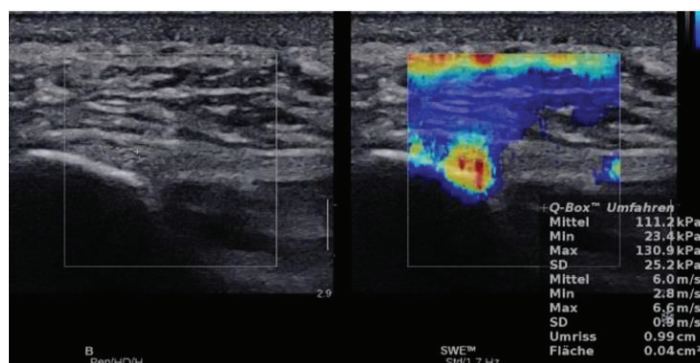


Figure 3. Longitudinal SWE image and B-mode ultrasound image of a 30 years old healthy volunteer with normal plantar fascia demonstrates stiffness of 111.2 kPa and SWV value of 6.0 m/s.

2.5. Statistical Analysis

Statistical analysis was performed using R Project for Statistical Computing 3.4.1. Core Team, written by Robert Gentleman and Ross Ihaka of the Statistics Department of the University of Auckland. For the three repeated SWE measurements, intra-rater variability was determined by calculating the intra-class correlation coefficient using the

irr package for R (Various Coefficients of Interrater Reliability and Agreement. R package version 0.84, by Matthias Gamer). The Shapiro-Wilk normality test was used to check for normal distribution. As patient data turned out to be normally distributed but not data for healthy subjects a Wilcoxon signed rank was used for group comparisons. To obtain cut-off values to distinguish between healthy and patient group receiver operating characteristic (ROC) analysis was applied using the pROC package for R (Robin X, Turck N, Hainard A, et al. (2011) pROC: an open-source package for R and S+ to analyze and compare ROC curves. BMC Bioinformatics (12:77). For analyzing correlation between SWE data and thickness values as determined by B-mode US a linear model was fitted to the data and the coefficient of determination (r^2) calculated. A coefficient (r) of <0.3 showed no correlation, 0.3 – 0.5 a weak correlation, 0.5 – 0.7 a moderate correlation and 0.7 – 1 a high correlation. p -values of <0.05 were considered statistically significant.

3. Results

We found a mean thickness in healthy plantar fasciae of 3.28 mm (SD: 0.41, range: 2.4–3.9) compared to 6.07 mm (SD: 2.37, range: 2.0–22.0) in plantar fasciitis ($p < 0.001$) (Figures 1 and 4). There was no correlation between SWV and plantar fascial thickness ($r^2 = 0.02$, $p = 0.06$) or between stiffness and plantar fascial thickness ($r^2 = 0.02$, $p = 0.06$) (Figure 5).

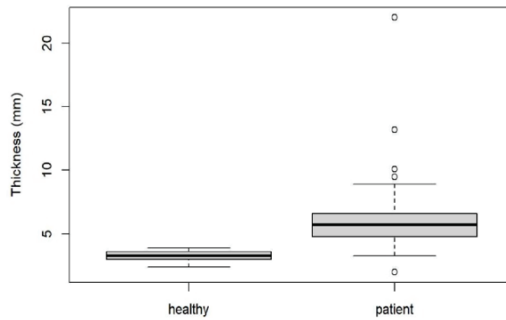


Figure 4. Box blot diagram showing plantar fascial thickness in healthy volunteers compared to patients with plantar fasciitis.

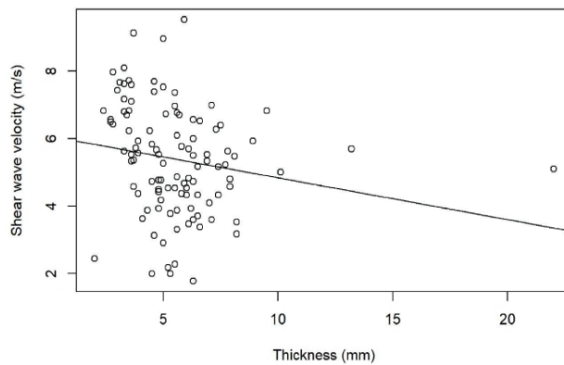


Figure 5. SWV and thickness for Patients with plantar fasciitis and Healthy volunteers, showing no correlation.

For thickness the obtained cut-off upper normal limit was 4.0 mm (AUC: 0.97, 95% CI: 0.94–0.99) with a specificity of 100% (95% CI: 100–100%) and a sensitivity of 90.8% (95% CI: 83.91–96.55%). No concomitant plantar fascia tears were found by B- mode US.

CDUS showed no correlation to stiffness and SWV ($r^2 < 0.007$, $p = 0.4$) and there was no significant difference for stiffness or SWV values between e.g., CDUS grade 0 and grade 3 ($p = 0.2$).

Mean SWE and stiffness values for healthy plantar fascia and plantar fasciitis are shown in Figures 6 and 7, and Figures 2 and 3 with an intra class correlation of 0.43–0.64 for SWE and 0.42–0.63 for SWV.

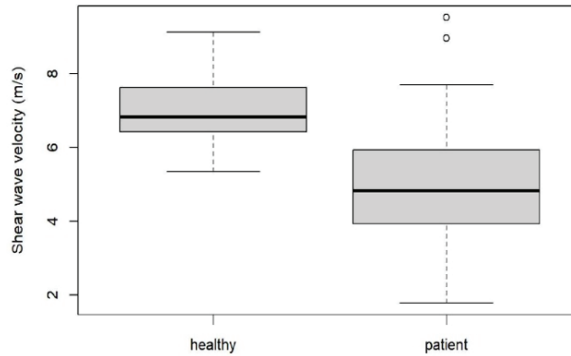


Figure 6. Box blot diagram showing SWV in healthy volunteers compared to patients.

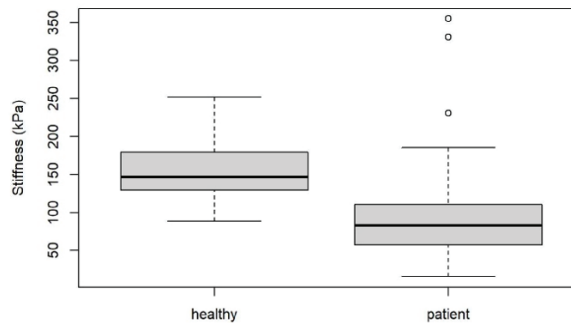


Figure 7. Box blot diagram showing Stiffness in healthy volunteers compared to patients.

There was a statistically significant difference in SWV and plantar fascial stiffness between healthy subjects and patients with plantar fasciitis ($p < 0.001$).

For SWV, ROC analysis resulted in a cut-off value of 6.16 m/s (AUC: 0.87, 95% CI: 0.80–0.94), giving a specificity of 80.95% (95% CI: 61.9–95.24%) and a sensitivity of 79.31% (95% CI: 70.11–87.36%). For stiffness a cut-off value of 125.57 kPa (AUC: 0.85, 95% CI: 0.77–0.92) was found with a specificity of 80.95% (95% CI: 61.9–95.24%) and a sensitivity of 80.46% (95% CI: 72.39–88.51%)

4. Discussion

Our results by using SWE confirmed softening of the plantar fascia in the patient group when compared to healthy volunteers, which already has been demonstrated by using SEL in recent studies [22,23,25].

Sconfienza et al. [23] demonstrated that the use of real-time SEL increases the diagnostic performance of B-mode US and may also be helpful in some cases in which the results of B-mode US are inconclusive. Their study confirmed that B-mode US can demonstrate specific signs of plantar fasciitis. Of those, fascia thickening and hypoechoic echotexture were more typical in plantar fasciitis than blurring of the fascial borders, which seems to be a less reproducible finding.

Our study confirms that B-mode US is still the most reliable diagnostic tool for plantar fasciitis diagnosis. Our thickness measurement results are in line with the literature, where a plantar fascial thickness greater than 4 mm has been postulated to be consistent with plantar fasciitis. A lack of standardization of the measurement process for plantar fascia thickness might limit the measurements. In particular, there are no universal guidelines existing on the positioning of the metatarsophalangeal (MTP) joints during the procedure and the literature also has inconsistent protocols [28]. We used the relaxed feet positioning, which is comfortable for the patient and examiner on the one site and minimizes errors through muscle tension on the other site [24].

Wu et al. showed that SEL was helpful in the diagnosis of plantar fasciitis in patients presenting with normal B-mode US thickness measurements [22,25]. In our study we found no correlation between SWE and plantar fascial thickness ($r^2 = 0.02$, $p = 0.06$) or between stiffness and plantar fascial thickness ($r^2 = 0.02$, $p = 0.06$). This is in line with the results of Wu et al.

CDUS has already been found with poor sensitivity in plantar fasciitis patients, which is in line with our results [29].

Putz et al. 2017 found that contrast enhanced US (CEUS) improved detection of hyperemia in 75% of patients and advocated CEUS as well as SWE as new diagnostic tools in the assessment of plantar fasciitis proving helpful for quantitative parameters and monitoring therapy [30].

Gatz et al. 2019 showed that SWE can improve the diagnostic accuracy in patients with plantar fasciitis compared to B-mode US. He found in healthies with a thickness of 3 mm and in patients, where the plantar fascia was thicker than 4.2 mm a cut off of 51.5 kPa and 4.14 m/s. He also showed lower values for plantar fasciitis of 31.9 kPa and 3.26 m/s and statistical significant higher values in asymptomatic of 93.3 kPa and 5.58 m/s with a sensitivity of 85% and specificity of 83% for SWE and a B-mode US sensitivity of 61% specificity of 95% [18].

One limitation of the study by Gatz et al. is that healthy volunteers were statistically significant different in age compared to the 39 fasciitis patients, therefore an age dependency might explain the difference to our results, which has already been demonstrated by Wu et al. showing that plantar fascia softens with age and in subjects with fasciitis [25]. Gatz also stated, that he worked with a relatively small sample group. Therefore our study adds valuable data. Our study had several limitations:

SWE values obtained on an Aixplorer system may not be equivalent to the SWE values obtained on other systems.

A small area analyzed on the color histogram does not represent the entire insertion of the plantar fascia. This would have been covered by axial transducer placement.

However, the thickest part of the plantar fascia was evaluated by SWE as detected by B-mode in longitudinal plane which is usually the proximal central band. Furthermore, because of the not parallel course of the fascia in that area, we adjusted the position and the tilting angle of the transducer to avoid anisotropy on B-mode sonogram and to obtain SWE measurements. Furthermore, no histologic testing was performed in this study. Further histopathologic and biomechanical examinations is required confirm our results. Our study has demonstrated SWE to be a reliable, in vivo noninvasive technique for examining the stiffness of the plantar fascia.

We did not have any other imaging as a reference. No measurements of the contralateral plantar fascia as an intern standard have been performed. We did not calculate a ratio. Finally, the healthy volunteers were referred from Hospital staff without any symptoms at the feet, what might have been a bias in the sampling.

5. Conclusions

SWE proved to be a valuable tool in the detection of plantar fasciitis and may be helpful in addition to B-mode US thickness measurement in unclear cases.

Author Contributions: Conceptualization, D.B., C.S., G.W., G.F. and A.S.K.; Data curation, D.B., J.S. and A.S.K.; Formal analysis, D.B., C.S., C.K., G.F. and A.S.K.; Investigation, D.B., C.S., J.S. and A.S.K.; Methodology, C.S., C.K. and A.S.K.; Project administration, C.S. and A.S.K.; Resources, J.S. and A.S.K.; Software, C.K.; Supervision, C.S., M.S.T., L.M.S., G.F. and A.S.K.; Validation, C.S., M.S.T., G.W., L.M.S. and A.S.K.; Visualization, C.S.; Writing—original draft, D.B. and C.S.; Writing—review & editing, D.B., C.S., M.S.T., G.W., L.M.S. and A.S.K. All authors have read and agreed to the published version of the manuscript.

Funding: This research received no external funding.

Institutional Review Board Statement: The study was conducted according to the guidelines of the Declaration of Helsinki, and approved by the Institutional Review Board (or Ethics Committee) of Medical University Innsbruck (protocol code 353/4.3).

Informed Consent Statement: Informed consent was obtained from all subjects involved in the study.

Conflicts of Interest: The authors declare no conflict of interest.

References

1. Rompe, J.D. Plantar fasciopathy. *Sports Med. Arthrosc. Rev.* **2009**, *17*, 100–104. [\[CrossRef\]](#)
2. Irving, D.B.; Cook, J.L.; Young, M.A.; Menz, H.B. Impact of chronic plantar heel pain on health-related quality of life. *J. Am. Podiatr. Med. Assoc.* **2008**, *98*, 283–289. [\[CrossRef\]](#) [\[PubMed\]](#)
3. López, P.P.; Vallejo, R.B.D.B.; Losa-Iglesias, M.E.; Rodríguez-Sanz, D.; Lobo, C.C.; López, D.L. Impact of plantar fasciitis on the quality of life of male and female patients according to the foot health status questionnaire. *J. Pain Res.* **2018**, *11*, 875–880. [\[CrossRef\]](#)
4. Wearing, S.C.; Smeathers, J.E.; Urry, S.R.; Hennig, E.M.; Hills, A.P. The pathomechanics of plantar fasciitis. *Sports Med.* **2006**, *36*, 585–611. [\[CrossRef\]](#)
5. Lobo, C.C.; Marín, A.G.; Sanz, D.R.; López, D.L.; López, P.P.; Morales, C.R.; Corbalán, I.S. Ultrasound evaluation of intrinsic plantar muscles and fascia in hallux valgus: A case-control study. *Medicine* **2016**, *95*, e5243. [\[CrossRef\]](#) [\[PubMed\]](#)
6. Irving, D.; Cook, J.; Menz, H. Factors associated with chronic plantar heel pain: A systematic review. *J. Sci. Med. Sport* **2006**, *9*, 11–22. [\[CrossRef\]](#) [\[PubMed\]](#)
7. Johnson, G.A.; Tramaglino, D.M.; Levine, R.E.; Ohno, K.; Choi, N.-Y.; Woo, S.L.-Y. Tensile and viscoelastic properties of human patellar tendon. *J. Orthop. Res.* **1994**, *12*, 796–803. [\[CrossRef\]](#)
8. Lewis, G.; Shaw, K.M. Tensile properties of human tendo achillis: Effect of donor age and strain rate. *J. Foot Ankle Surg.* **1997**, *36*, 435–445. [\[CrossRef\]](#)
9. Lee, T.Q.; Dettling, J.; Sandusky, M.D.; McMahon, P.J. Age related biomechanical properties of the glenoid–anterior band of the inferior glenohumeral ligament-humerus complex. *Clin. Biomech.* **1999**, *14*, 471–476. [\[CrossRef\]](#)
10. Wright, D.G.; Rennels, D.C. A study of the elastic properties of plantar fascia. *J. Bone Jt. Surg.* **1964**, *46*, 482–492. [\[CrossRef\]](#)
11. Hall, T.J. AAPM/RSNA physics tutorial for residents: Topics in US: Beyond the basics: Elasticity imaging with US. *Radiographics* **2003**, *23*, 1657–1671. [\[CrossRef\]](#)
12. Garra, B.S. Imaging and estimation of tissue elasticity by ultrasound. *Ultrasound Q.* **2007**, *23*, 255–268. [\[CrossRef\]](#) [\[PubMed\]](#)
13. Klauser, A.S.; Miyamoto, H.; Bellmann-Weiler, R.; Feuchtner, G.M.; Wick, M.C.; Jaschke, W.R. Sonoelastography: Musculoskeletal applications. *Radiology* **2014**, *272*, 622–633. [\[CrossRef\]](#) [\[PubMed\]](#)
14. Sandrin, L.; Tanter, M.; Gennisson, J.L.; Catheline, S.; Fink, M. Shear elasticity probe for soft tissues with 1-D transient elastography. *IEEE Trans. Ultrason. Ferroelectr. Freq. Control.* **2002**, *49*, 436–446. [\[CrossRef\]](#) [\[PubMed\]](#)
15. Taljanovic, M.S.; Gimber, L.H.; Becker, G.W.; Latt, L.D.; Klauser, A.; Melville, D.M.; Gao, L.; Witte, R.S. Shear-wave elastography: Basic physics and musculoskeletal applications. *Radiographics* **2017**, *37*, 855–870. [\[CrossRef\]](#)
16. Kim, S.J.; Park, H.J.; Lee, S.Y. Usefulness of strain elastography of the musculoskeletal system. *Ultrasonography* **2016**, *35*, 104–109. [\[CrossRef\]](#)
17. Davis, L.C.; Baumer, T.G.; Bey, M.J.; Van Holsbeeck, M.T. Clinical utilization of shear wave elastography in the musculoskeletal system. *Ultrasonography* **2019**, *38*, 2–12. [\[CrossRef\]](#)
18. Gatz, M.; Bejder, L.; Quack, V.; Schrading, S.; Dirrichs, T.; Tingart, M.; Kuhl, C.; Betsch, M. Shear wave elastography (SWE) for the evaluation of patients with plantar fasciitis. *Acad. Radiol.* **2020**, *27*, 363–370. [\[CrossRef\]](#)
19. De Zordo, T.; Lill, S.R.; Fink, C.; Feuchtner, G.M.; Jaschke, W.; Bellmann-Weiler, R.; Klauser, A.S. Real-time sonoelastography of lateral epi-condylitis: Comparison of findings between patients and healthy volunteers. *Am. J. Roentgenol.* **2009**, *193*, 180–185. [\[CrossRef\]](#)
20. De Zordo, T.; Fink, C.; Feuchtner, G.M.; Smekal, V.; Reindl, M.; Klauser, A.S. Real-time sonoelastography findings in healthy Achilles tendons. *Am. J. Roentgenol.* **2009**, *193*, W134–W138. [\[CrossRef\]](#)
21. Drakonaki, E.; Allen, G.; Wilson, D. Real-time ultrasound elastography of the normal Achilles tendon: Reproducibility and pattern description. *Clin. Radiol.* **2009**, *64*, 1196–1202. [\[CrossRef\]](#) [\[PubMed\]](#)

22. Wu, C.-H.; Chen, W.-S.; Wang, T.-G. Plantar fascia softening in plantar fasciitis with normal B-mode sonography. *Skelet. Radiol.* **2015**, *44*, 1603–1607. [[CrossRef](#)] [[PubMed](#)]
23. Sconfienza, L.M.; Silvestri, E.; Orlandi, D.; Fabbro, E.; Ferrero, G.; Martini, C.; Sardanelli, F.; Cimmino, M.A. Real-time sonoelastography of the plantar fascia: Comparison between patients with plantar fasciitis and healthy control subjects. *Radiology* **2013**, *267*, 195–200. [[CrossRef](#)]
24. Chino, K.; Lacourpaille, L.; Sasahara, J.; Suzuki, Y.; Hug, F. Effect of toe dorsiflexion on the regional distribution of plantar fascia shear wave velocity. *Clin. Biomech.* **2019**, *61*, 11–15. [[CrossRef](#)] [[PubMed](#)]
25. Wu, C.-H.; Chang, K.-V.; Mio, S.; Chen, W.-S.; Wang, T.-G. Sonoelastography of the plantar fascia. *Radiology* **2011**, *259*, 502–507. [[CrossRef](#)] [[PubMed](#)]
26. Thomas, J.L.; Christensen, J.C.; Kravitz, S.R.; Mendicino, R.W.; Schuberth, J.M.; Vanore, J.V.; Weil, L.S., Sr.; Zlotoff, H.J.; Bouché, R.; Baker, J. The diagnosis and treatment of heel pain: A clinical practice guideline-revision 2010. *J. Foot Ankle Surg.* **2010**, *49* (Suppl. S3), S1–S19. [[CrossRef](#)] [[PubMed](#)]
27. Fenwick, A.S.; Hazleman, B.L.; Riley, G.P. The vasculature and its role in the damaged and healing tendon. *Arthritis Res.* **2002**, *4*, 252–260. [[CrossRef](#)] [[PubMed](#)]
28. Granado, M.J.; Lohman, E.B.; Daher, N.S., III; Gordon, K.E. Effect of gender, toe extension position, and plantar fasciitis on plantar fascia thickness. *Foot Ankle Int.* **2019**, *40*, 439–446. [[CrossRef](#)]
29. McMillan, A.M.; Landorf, K.B.; Gregg, J.M.; De Luca, J.; Cotchett, M.P.; Menz, H.B. Hyperemia in plantar fasciitis determined by power doppler ultrasound. *J. Orthop. Sports Phys. Ther.* **2013**, *43*, 875–880. [[CrossRef](#)]
30. Putz, F.J.; Hautmann, M.G.; Banas, M.C.; Jung, E.M. Investigation of the acute plantar fasciitis with contrast-enhanced ultrasound and shear wave elastography—First results. *Clin. Hemorheol. Microcirc.* **2017**, *67*, 415–423. [[CrossRef](#)]



Review

Imaging in Hip Arthroplasty Management—Part 1: Templating: Past, Present and Future

Edouard Germain, Charles Lombard, Fatma Boubaker, Mathias Louis, Alain Blum, Pedro Augusto Gondim-Teixeira and Romain Gillet *

Guilloz Imaging Department, Central Hospital, University Hospital Center of Nancy, 29 Avenue du Maréchal de Lattre de Tassigny, 54035 Nancy, France

* Correspondence: r.gillet@chru-nancy.fr; Tel.: +33-3-8385-2161; Fax: +33-3-8385-9725

Abstract: Hip arthroplasty is a frequently used procedure with high success rates. Its main indications are primary or secondary advanced osteoarthritis, due to acute fracture, osteonecrosis of the femoral head, and hip dysplasia. The goals of HA are to reduce pain and restore normal hip biomechanics, allowing a return to the patient's normal activities. To reach those goals, the size of implants must suit, and their positioning must meet, quality criteria, which can be determined by preoperative imaging. Moreover, mechanical complications can be influenced by implant size and position, and could be avoided by precise preoperative templating. Templating used to rely on standard radiographs, but recently the use of EOS[®] imaging and CT has been growing, given the 3D approach provided by these methods. However, there is no consensus on the optimal imaging work-up, which may have an impact on the outcomes of the procedure. This article reviews the current principles of templating, the various imaging techniques used for it, as well as their advantages and drawbacks, and their expected results.

Keywords: hip; arthroplasty; CT; radiographs; 3D parameters

Citation: Germain, E.; Lombard, C.; Boubaker, F.; Louis, M.; Blum, A.; Gondim-Teixeira, P.A.; Gillet, R. Imaging in Hip Arthroplasty Management—Part 1: Templating: Past, Present and Future. *J. Clin. Med.* **2022**, *11*, 5465. <https://doi.org/10.3390/jcm11185465>

Academic Editors:
Iwona Sudol-Szopińska and
Mihra Taljanovic

Received: 20 July 2022
Accepted: 15 September 2022
Published: 16 September 2022

Publisher's Note: MDPI stays neutral with regard to jurisdictional claims in published maps and institutional affiliations.



Copyright: © 2022 by the authors. Licensee MDPI, Basel, Switzerland. This article is an open access article distributed under the terms and conditions of the Creative Commons Attribution (CC BY) license (<https://creativecommons.org/licenses/by/4.0/>).

1. Introduction

Hip arthroplasty (HA) is a frequently used procedure with high success rates. Its main indications are primary or secondary advanced osteoarthritis [1]. The goals of HA are to reduce pain and restore normal hip biomechanics, allowing a return to the patient's normal activities [2]. To reach those goals, the size of implants must suit, and their positioning must meet, quality criteria, such as maintenance of leg length and femoral offset (FO), anteversion and inclination of the cup, and antetorsion of the femoral stem [2]. Those factors can be determined by preoperative imaging, and when they are not respected, patient dissatisfaction and mechanical complications can occur. Moreover, accurate pre-operative implant sizing could reduce surgical time and inventory needs [2]. HA preoperative planning used to rely on standard radiographs, suffering from magnification factor-induced errors, but recently the use of EOS[®] imaging and CT is growing, given the 3D approach provided by these methods [2–10]. Especially, 3D printing offers an improvement in understanding patient-specific anatomy, thus enhancing patient outcomes (operation time, intra-operative blood loss, X-ray frequency, post-operative drainage), particularly in complex cases and for less experienced surgeons [11–13].

We present a narrative review of preoperative templating in HA, focusing on its classical aspects and emerging techniques, with their own advantages and drawbacks, driven by the hypothesis that those techniques have the potential to reinforce radiographic templating, but not yet to replace it.

2. Preoperative Planning

2.1. Background

Digital preoperative planning enables the surgeon to determine which prosthesis size to use and where to place it within the bone, aiming at optimal postsurgical functional restoration [14]. As oversized prostheses can increase the risk of periprosthetic fractures, and undersized prostheses can lead to dislocation, instability, and loosening, reliable prosthetic sizing and positioning is mandatory [5]. Thus, the aim of templating is to restore normal anatomy, especially the hip rotation center, femoral lateralization, and inferior limb length. Inadequate restoration of hip biomechanics is known to be a frequent cause of patient dissatisfaction. For example, 15–30% of patients complain of limb length discrepancy and up to 60% of THAs result in inadequate femoral offset (FO) [15]. Templating was classically performed on conventional radiographs, which are 2D and have a magnification factor that needs to be compensated. In this context, EOS[®] and CT imaging represent valid alternatives with good reproducibility [16].

2.2. Hip Deformities

2.2.1. Measurements and Their Implications

According to some authors and until recent years, surgery goals were to deepen the acetabular socket by reducing the AO, making room for the acetabular component, and increasing the FO to keep the GO constant [9,16]. Currently, the literature is not conclusive that the cup should be medialized and the femoral offset increased in compensation. In practice, cup placement should rather be anatomical [17]. A fully medialized reconstruction cannot be justified for now, especially in young patients who need to conserve their bone stock in case of revision surgery, as only small biomechanics gains were noted in a whole-body simulation of a gait cycle by De Pieri et al. [18]. Moreover, the acetabular offset should not be reduced, as it requires the use of stems with greater offsets than the natural femoral one, which induces a risk of impingement [17]. When severe hip joint deformity is present, the contralateral hip can be used for templating [19], but no clear recommendations exist in the case of bilateral severe deformity. Amongst preoperative measurements, some can also be used to evaluate postoperative outcomes in HA, among which are lower limb length, global offset (GO) (sum of acetabular (AO) and FO), and femoral neck antetorsion (FNA). These parameters can be measured on pelvic AP radiographs or EOS[®] imaging, and on coronal CT-reformatted images in the plane created by the femoral neck axis and the femoral mid-shaft axis [15]. Femoral offset measurement is more precise using 3D CT-scan reconstruction as it does not depend on test conditions, because the frame is placed within the femoral axis and is not influenced by position inconsistencies or hip pathologies [20].

AO corresponds to the distance between the femoral head center and the acetabular floor or the midline, FO to the distance between the femoral head center and the femoral mid-shaft axis. The cervico-diaphyseal angle (CDA) should also be reported (Figure 1).

FNA measurements have traditionally been done on radiographs but are not sufficiently precise for templating. EOS[®] imaging or CT-based measurements are therefore recommended (Figure 2) [16].

Hip function depends on the proper orientation of the muscles about the center of rotation of the joint (i.e., limb length imbalance and offset correction) [16]. An imbalance in GO may lead to limping due to abductor dysfunction. Reduced FO can lead to acetabular-polyethylene wear, dislocation, and loosening [15], whereas an increase can lead to residual pain and limping by exacerbation of muscle and soft-tissue tension. However, it is still unclear which of these parameters (GO, FO, or AO) should be taken into account for offset correction. FNA below 10° is supposed to be deleterious to the long-term outcome for cemented stems [16].

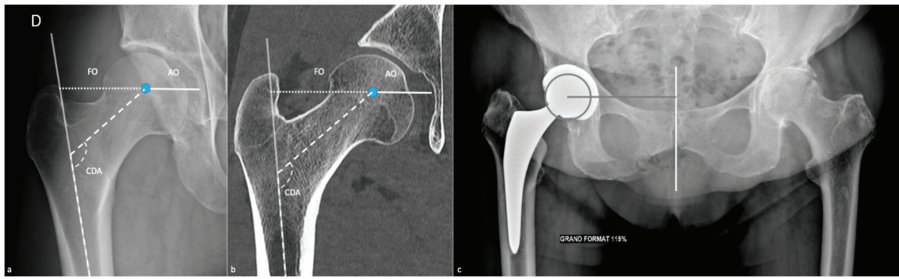


Figure 1. Preoperative measurements. Those values can be measured on (a) an anteroposterior pelvic radiograph and on (b) a coronal CT image, in the plane established by the femoral neck axis and the femoral midshaft. AO corresponds to the acetabular offset (white line: distance between the femoral head center (blue circle) and the acetabular floor), FO to the femoral offset (little-dotted line: distance between the femoral head center and the femoral midshaft axis (mild transparent white line)), CDA to the cervico-diaphyseal angle (large-dotted white line). A measurement of AO from the pelvic midline is shown on (c) an AP pelvic view [21], as it is more suitable in case of hip prosthesis, especially in case of cup protrusion.

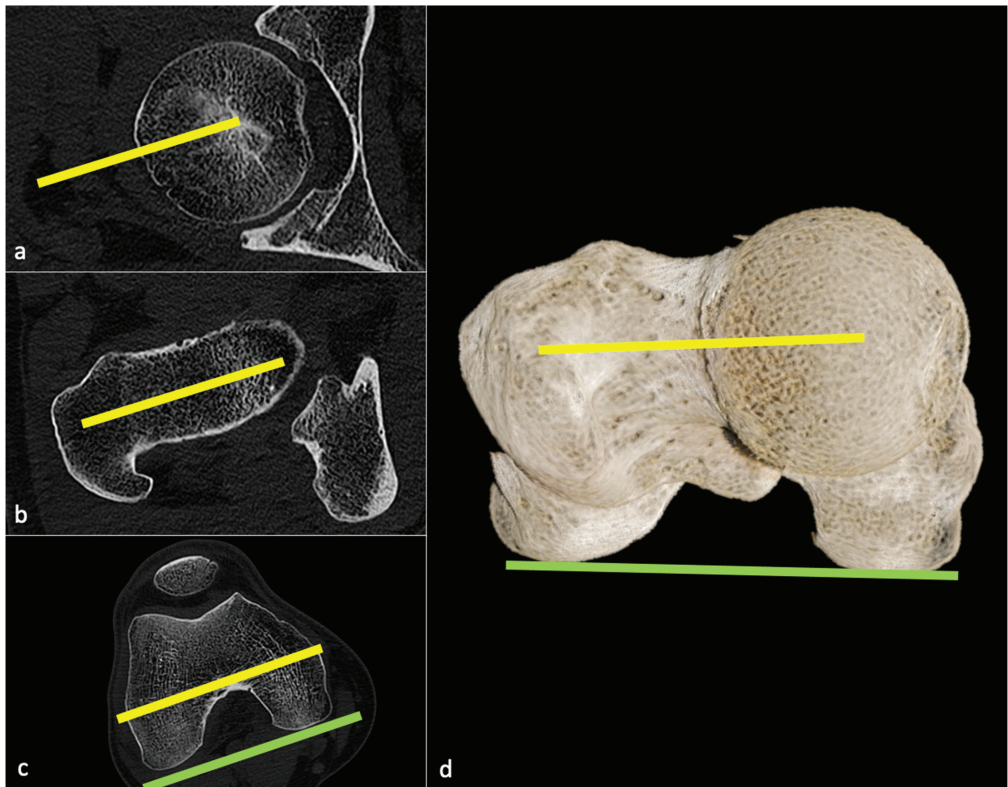


Figure 2. Femoral neck antetorsion measurement. Three axial CT slices must be selected: one shown in (a) at the femoral head center, one in (b) at the femoral neck to measure the femoral neck axis (yellow line), then one in (c) at the level of the roman arch to determine the intercondylar axis (green line). In (d), a global illumination reformat is shown to illustrate the 3D rendering of this measure, corresponding to the angle between the yellow and green lines.

Much less attention has been given to the sagittal orientation of the stem. With the recently increased use of the anterior surgical approach, and the rise in popularity of the femoral short stems, the femoral component might get implanted in a flexed position. Yoshitani et al. did not find significant differences concerning radiological and clinical follow-up at approximately 5 years between flexion and neutral alignment, but long-term studies are required [22]. This measurement is difficult to assess precisely on lateral radiographs [22]. As for FNA, CT represents a valuable tool (Figure 3). EOS[®] must be evaluated in this setting. An anterior acetabular offset can be measured (distance between the center of the femoral head and the retrocondylar axis in the axial plane), but its usefulness remains to be determined.

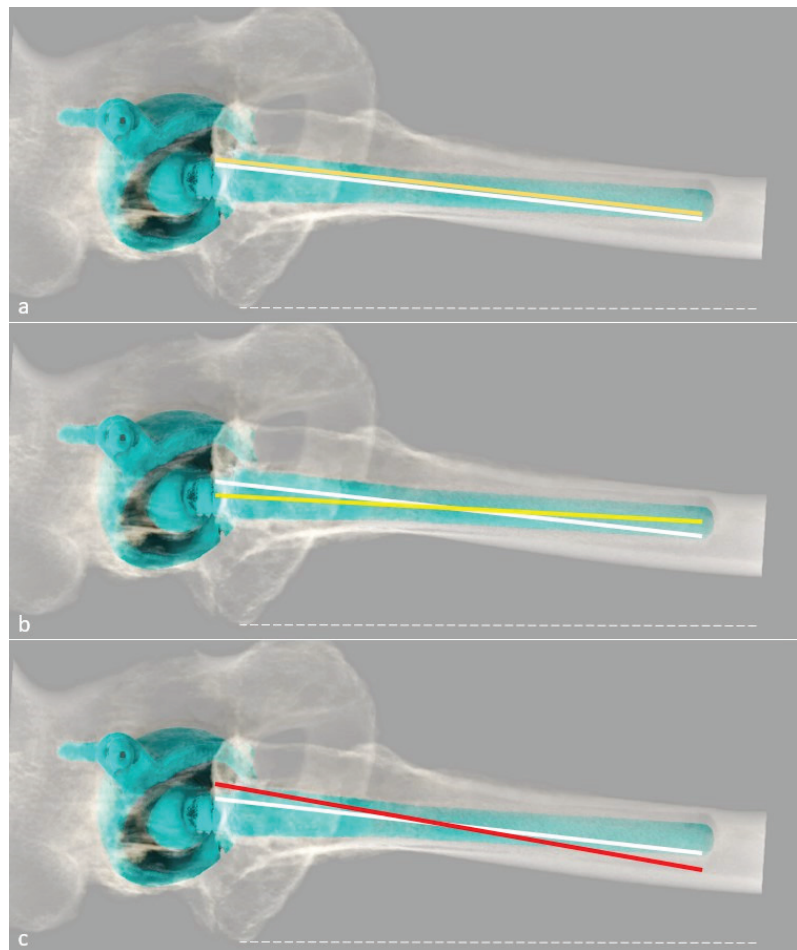


Figure 3. Representation of the flexion/extension of the femoral stem, using 3D CT-scan reformat, adapted from Abe et al. [23]. The dotted white line represents the retrocondylar axis, the white line the sagittal femoral tilt, and the colored line the stem axis. A theoretical neutral position is shown in (a) with the orange line; a negative value superior to -3° between the femoral tilt and the sagittal stem tilt is defined as flexion in (b) with the yellow line, which is the actual axis of this prosthesis; and a positive value superior to 3° is defined as an extension in (c) with the red line.

2.2.2. Types of Architectural Deformities and Their Implications

A recent classification has been proposed by Kase et al. to distinguish different types of architectural hip deformities and their associated abnormalities, according to femoral head-translation patterns, using the distance between the femoral head center and the acetabular center [15]. In this study, femoral heads were centered in 61% of the patients studied. In 26% of patients, hips were lateralized and often presented femoro-acetabular osteophytes. There were only 4% of medialized hips (often accompanied by acetabular protrusion), 3% of proximally displaced hips (flattening of the femoral head or acetabular deformation), and 6% of proximo-lateral displacement (femoral head and acetabular superolateral deformity) (Figure 4).

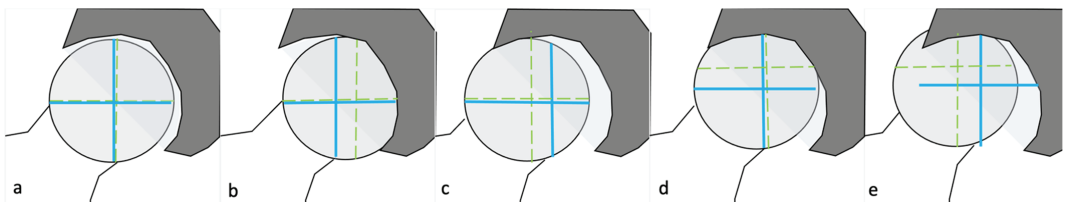


Figure 4. Hip deformities. Five types of hip deformities are shown, adapted from Kase et al. [11]. On each scheme, the femoral head is colored in grey, the acetabulum in dark grey, and the acetabular cavity in transparent grey. The blue lines correspond to the acetabular center and the green dotted line to the vertical and horizontal axis of the femoral head. In (a), a centered hip is shown as both axes are superimposed; in (b), a medialized (medialization of the vertical axis of the femoral head with respect to the acetabular one); in (c) a lateralized (lateralization of the vertical axis of the femoral head with respect to the acetabular one); in (d) a proximalized (cephalic displacement of the horizontal axis of the femoral head with respect to the acetabular one); and in (e) a proximo-lateralized (cephalic displacement of the horizontal axis of the femoral head with respect to the acetabular one, and lateral displacement of the vertical axis of the femoral head with respect to the acetabular one). An arbitrary cut-off of 3 mm was used by the authors to consider a displacement in each plane.

Proximal and proximo-lateralized displacement induced considerable limb shortening. Femoral head translation on radiographs or CT has to be taken into account to correct limb shortening and/or pathologic offset [15], as it allows surgeons to restore preoperative anatomy. More precisely, in centered hips, AO was similar to healthy hips [24], and reproducing native anatomy could restore the hip rotation center [15]. On the other hand, in medialized hips, one should consider rotation center lateralization to avoid impingement and FO reduction to avoid excessive soft-tissue tension with a potential clinical impact [15].

2.3. Principles and Methods

2.3.1. Radiographs Technical Aspects

Templating has conventionally been made by applying tracing papers on radiographs but has become impractical with the implantation of digital radiographs, which presents a similar reproducibility [25]. The different measurements necessary for hip templating are summarized in Table 1.

In the authors' institution, radiographs include an anteroposterior pelvic view, from the iliac crest to the femoral proximal third, to visualize the femoral stem destination. The patient should be standing with 15° of internal hip rotation if he can, whereas, in case of fracture, he might be lying down on his back. The X-ray beam is centered 2 cm under the pubic symphysis and its source at 1.50 m, which corresponds to a magnification factor of 1.15, like the tracing papers supplied by the manufacturers. The magnification factor might be variable amongst the distance X-ray source/detector, and femoro-acetabular joint/detector; therefore, it is dependent on the patient body habitus and position variations induced by pain, potentially leading to limitations in radiographic templating [26].

Table 1. Measurement to be made on preoperative radiographs for hip arthroplasty templating.

Parameter	Utility
Magnification	Measurement adaptation
Pelvic axis (teardrop sign)	Limb length discrepancy
	Frontal inclination of the acetabular component
Femoro-acetabular joint rotation center	Acetabular component positioning and size determination
Width of the endosteal diaphyseal and metaphyseal canal diaphysis	Size of the femoral component
	Femoral offset determination
	Matching of femoral head and joint centers
Femoral neck resection length	Positioning of the femoral component
Cervico-diaphyseal angle	Positioning of the femoral component
Height and diameter of the femoral head	

While standing radiographs are obtained without difficulties in most ambulatory patients, it might be impossible in emergency situations or in case of advanced disease. This issue is largely compensated by the fact that it is reasonable to consider the pelvic position in the supine position, as the acetabular component had an optimal orientation in 90% of the cases in the study by Nishihara et al. [27]. Those results were recently confirmed by Uemura et al., since the pelvic sagittal inclination changes from supine to standing were smaller than 10° in approximately 80% of the cases in their study [28], and pelvic positions in supine and standing postures were reproducible in a second recent study by the same team [29]. The pelvic position in the supine position at 10 years of follow-up was shown to be a good functional reference by Tamura et al., as it did not show variation over time, unlike the standing pelvic sagittal inclination [30]. On the other hand, in some patients with developmental dysplasia of the hip, the acetabular version differed between the supine and standing positions, so that Tani et al. recommended the use of the values obtained in the standing position for preoperative planning [31], and Tachibana et al. [32] and Bhanushali et al. [33] recommended assessing postural changes (radiographs in both standing and supine positions) in the sagittal pelvic tilt in case of dysplasia and called for other studies to determine how those postural changes affect the biomechanical environment of the acetabulum. Therefore, in the authors' opinion, even though radiographs have tended in the last years to be realized in the standing position to reproduce functional position, supine radiographs can be obtained in any patient with good confidence in pelvic position, especially in the emergency setting. However, both standing and supine radiographs should be obtained, if possible, in patients with hip dysplasia.

With radiographs, the first step is to determine the magnification factor by using an existing body implant or a radiographic marker of known dimensions [14].

Then, the pelvic axis must be determined, most commonly by drawing a line between the iliopubic branch contours on anteroposterior pelvic radiographs (e.g., teardrop sign) (Figure 5). On radiographs, limb length discrepancy can be calculated by drawing a line perpendicular from the inter-teardrop axis to the top of the lesser trochanter. One should consider 5 mm as a cut-off, as symptoms are infrequent beyond this value [34–36].

If available, an EOS® acquisition can be performed and the inter-teardrop axis will also be used to calculate the appropriate inclination angle of the acetabular component [14].

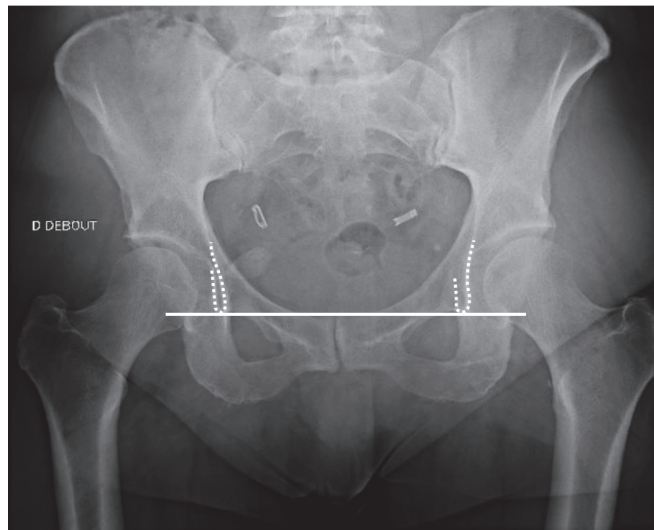


Figure 5. Inter-teardrop axis. The inter-teardrop axis shown on an anteroposterior pelvic radiograph (white line), the teardrops being represented by the dotted lines.

Acetabular Cup Templating

The femoro-acetabular joint rotation center can be determined by placing a digital acetabular template at an angle of approximately 40–45° to the pelvic axis [14], or by applying different tracing papers to match acetabular morphology, so that the acetabular component can be positioned with an inclination of 40–50° and an anteversion of 20–30° to avoid bony impingement [37]. Concerning hip stability, the “acetabular safe zone” initially described by Lewinneck et al.—of 40 ± 10 degrees and 15 ± 10 degrees, respectively [38]—has been refuted and is more likely to be multifactorial and patient-specific, so that new unique values have not yet been clearly defined [39,40] and the hypothesis of a static safe zone is simplistic [41]. More precisely, the optimal positioning of the acetabular cup is thought to depend on sagittal pelvic mobility. Some authors, therefore, call for the development of standardized algorithms for the placement of kinematically aligned acetabular components [42].

However, important variations between operative and radiographic angles have been reported [17]. Cup inclination can be visualized on an AP pelvic view or with an EOS® imaging system. Cup anteversion measurement is more variable. CT with multi-planar reformation has been shown to be more accurate than intraoperative measurements or radiographs [43]. EOS® imaging can also be used. Several methods exist using radiographs. The most common method used to be the one proposed by Woo and Morrey [44], corresponding to the angle formed by a line drawn tangential to the face of the acetabulum, and a line perpendicular to the horizontal plane, as seen on a lateral view of the pelvis. However, recently Lee et al. demonstrated that using AP radiographs (pelvic or hip), the methods by Pradhan et al. [45], Liaw et al. [46], and Lewinnek et al. [38] might provide accurate anteversion measurements with high reliability, regardless of the type of radiographs (hip or pelvis) [47]. All those imaging data do not seem sufficient, as Grammatopoulos recommended implanting the cup in 5° less inclination and 8° more anteversion than planned to achieve the target radiographic position [48]. To guide angular positioning, a jig or a protractor placed on the inserter handle can be used. Presently, patient-specific measurements are being developed, and classical approaches are clearly called into question.

Femoral Stem Templating

The size of the femoral component is determined by measuring the width of the endosteal canal distally within the femoral diaphysis and metaphysis; its position is chosen by placing it within the femur in a position to reproduce limb length or correct any discrepancy, obtain an appropriate FO, and match the center of the femoral head with the center of rotation of the joint. This positioning must consider the length of femoral neck resection (measured proximal to the lesser trochanter or distal to the greater trochanter), which can vary to achieve postoperative goals, as the prosthetic neck length, cervico-diaphyseal angle in the case of a modular implant, and height and diameter of the femoral head can be adjusted if needed. Osteointegration depends on several factors, including bone quality. The Dorr classification [49] aims to guide indications for the type of femoral component fixation (e.g., cemented or uncemented) and evaluates the risk of perioperative fracture of the proximal femur. It is based on the cortical index, corresponding to the ratio of the canal diameter, 10 cm distal to the midportion of the lesser trochanter divided by the inner canal diameter at the midportion of the lesser trochanter (Figure 6), and the femoral cortical aspects on radiographs (AP and lateral views) [50,51].



Figure 6. Cortical index calculation. Cortical index is calculated by measuring the ratio between the diaphyseal diameter between the cortices at the level (orange double-headed arrow) and the inner canal diaphyseal diameter 10 cm below the lesser trochanter (yellow double-headed arrow).

The Singh index analyzes the trabecular pattern of the proximal femur, classifies osteoporosis into six grades (grade 6 represents normal bone density and grade 1 reflects severe osteoporosis), and is available for routine use and mass screening [52]. It has

been shown that Dorr types were correlated with occult osteoporosis in postmenopausal women with osteoarthritis, and these radiographic features have been postulated to be determinants of fracture risk and prosthesis longevity [53]. However, a clearly defined role of the Singh classification has not yet been described for HA templating.

2.4. Perspectives

2.4.1. CT-Scan

Background

Even though radiographic templating is a well-known process in HA planning, it is also admitted that surgeons need better methods due to the magnification factor and patients' position differences using standard radiographs [54]. CT has gradually gained interest and will probably complement radiographs in templating as it is more accurate in planning implant size, component alignment, and postoperative leg length than radiographs. Additionally, with recent advances in CT technology and image reconstruction algorithms—including deep-learning reconstruction—radiation dose exposure can be potentially reduced to values similar to radiographs [55]. CT can also provide 3D information and assist surgeons intraoperatively [7–9,16,55,56]. Furthermore, it allows a precise evaluation of bone stock and of the osteophytes that should be resected. Inoue et al. stated that CT-based 3D templating made it possible to achieve reproducible stem antetorsion (between pre- and postoperative CT scans) and choose accurate stem and cup sizes in the case of developmental dysplasia of the hip [6]. Madadi et al. underscore that if inclination and anteversion were crucial for acetabular cup placement, which can be performed considering four directions (e.g., inward, outward, upward, and downward), osteophytes might displace the femoral head and acetabular fossa. These latter were well depicted on CT (e.g., central osteophytes and hypertrophic OA) and their preoperative depiction was deemed crucial for planning [57]. For the diagnosis of acetabular bone loss in revision surgery, an expert panel stated that an AP pelvis radiograph is sufficient only in the case of minimal bone loss. CT should be considered in more severe cases, especially in case of fracture, concomitant rotation of the hemipelvis, extensive osteolysis, and medial migration of the acetabular component [58].

Finally, one should be aware that CT for preoperative planning rather than radiographs might lead to the discovery of incidental findings (e.g., acute diverticulitis, masses, osseous tumors, aneurysms, or abdominal wall hernias), which lead to delay or cancelation of arthroplasty in 5% [59].

CT could therefore be systematically performed preoperatively for standard measurements, especially in the case of the presence of osteophytes and for revision surgery, and if specific low-dose reconstruction algorithms are available. CT-based navigation systems and 3D-printed templates still need more studies to be systematically recommended as they might be costly and time-consuming.

Technical Aspect

CT scan measurements have been defined in Figures 1 and 2.

In practice:

- (1) the hip can be classified as mentioned above (e.g., centered, medialized, lateralized, proximalized, or proximo-lateralized);
- (2) the pre-arthritic centers of the femoral head and acetabulum must be determined (potentially using the contralateral hip if healthy), and the optimal diameter of the acetabular cup measured on a transverse CT slice, so that its template can be positioned at the level of the true acetabular floor medially and of the subchondral bone proximally, slightly superior and medial to the center of the native acetabulum to simulate reaming;
- (3) the stem size and model can be determined, such that the templated head center can match the templated cup center craniocaudally, with the native mediolateral center

maintained original even if pathologic, except in case of medialized head, which has to match templated cup center in both axis [60].

CT-based preoperative planning usually relies on 3D templating software, but Chinzei et al. demonstrated that templating using CT multiplanar reconstructions alone is more available and may be useful as a complementary tool without additional costs [4]. Practically speaking, a multiplanar reconstruction can be constructed without additive software, as most picture archiving & communication systems (PACS) include 3D reformat options. First, the femoral shaft axis has to be determined in the frontal and sagittal planes, then this image is reproduced on the plane passing through both the axis and the center of the femoral head [4]. This technique also allowed the authors to measure femoral head cup diameter, stem size, length of the modular neck, and distance from the neck osteotomy. Then, transparent template sheets were applied to the screen and the image externally rotated until the lesser trochanter was displayed, to finally determine the neck osteotomy level [4]. However, this procedure was time-consuming and does not seem practical, in our opinion. Moreover, its inter- and intraobserver correlation were not assessed.

Geijer et al., using a 3D templating software and low-dose CT with an acquisition from hip to knee, showed near-perfect inter- and intraobserver agreement in measuring AO, FO, and FNA. These authors stated that using 3D datasets practically eliminated the need for exact patient positioning, in pre- and postoperative CT scans [16]. One must keep in mind that there are various methods for FNA measurement described in the literature hampering the comparison of different studies [16]. Regardless, CT scan measurements of femoral antetorsion remain the gold standard, as shown in Figure 2 [61]. Automated measurement algorithms might be available in the near future, as Veilleux et al. showed an effective automated technique for determining pelvic and acetabular orientation, using 3D images from CT scans, as an aid in preoperative planning, which is therefore less time-consuming than manual calculation [62].

CT-based templating has improved imaging measurements and postoperative results in terms of component placement. Nishihara et al. stated that the use of a CT-based navigation system improved cup positioning compared to freehand cup placement, even in the supine position with a direct anterior approach, though it is thought to be as reliable as CT-based navigation [8]. Scheerlinck et al. even declared that based on CT-3D templating in non-deformed femora, the non-modular femoral stem could restore the anatomical hip rotation center so that failure to restore anatomy might be due to surgical inaccuracy rather than lack of implants matching the patient's native anatomy [9]. More than classical imaging measurements and standardized values, 3D data obtained from CT have been shown effectively in intraoperative simulations using 3D-printed materials [7,56]. Those advantages are also advocated in revision surgery in the case of acetabular bone loss, as CT allows a 360° assessment of bone loss with a pelvic 3D rotation, a better assessment of osteolysis, a segmentation to evaluate the pelvis with the implant subtracted, and the generation of 3D-printed materials which can help in implant choice and design [58].

Three-dimensional printing technology, also called rapid prototyping, allows to create 3D scale models of physical objects quickly, using imaging data and thermoadhesive materials such as thermoplastic or liquid metals. It is supposed to improve osteointegration in acetabular implants, developmental dysplasia of the hip, and generally help the surgeon in their operative planning, but it is not yet available for soft tissue preoperative imaging [63,64].

Main Strengths

In our opinion, the main strengths of CT are its ability to provide precise measurements and its 3D capacities, allowing the use of software and reducing the need for optimal patient positioning, which could improve patient workflow and reduce image post-treatment additional work time.

Limitations

3D CT templating remains complex, costly, and not widely available [60]. Its indication also remains controversial, as to whether it should be limited to special issues such as hip dysplasia or advanced degenerative changes, or recommended for all HA procedures [60]. Direct costs of a preoperative CT were reported to range from 53 to 116 euros in a German study, and thus considered low [65], but remained more expensive than radiographs. The radiation dose used to be of concern, but is nowadays decreasing, and tends to approach that of radiographs [16,60,66]. Kobayashi et al. combined the reliability of CT with the simplicity of acetate templating, by applying templates on real printed CT images in adjusted coronal and axial planes (parallel to the neck axis and to the femoral shaft axis), including the lesser trochanter in the frontal plane and the femoral head maximal diameter in the axial plane. Even though they recognized CT advantages, they could not demonstrate the superiority of CT scans over radiographs. Therefore, they stated that high-quality radiographs are sufficient for now until reliable surgical tools and post-operative image acquisition become available and affordable in the surgeon's routine using CT but mentioned that they would continue CT-based templating as it remains more accurate in their opinion [60].

2.4.2. EOS® Imaging Background

It has recently been shown that planning software, based on radiographs obtained with the EOS® imaging system (EOS® imaging, Paris, France), could also be useful in templating, as it was more accurate than 2D radiographs and equal to CT [2]. It corresponds to a low dose biplanar digital radiographic imaging system involving gaseous photon detectors, used in over 400 medical centers worldwide. It takes approximately 20 s for an adult full-body scan [67], therefore a little bit longer than CT, and quite shorter than radiographs, as several views are acquired one at a time. Contrary to CT and radiographs, the EOS® imaging system allows the simultaneous acquisition of two orthogonal radiographic images without magnification factor, and considers lower limb deformities, with a patient in a functional standing or sitting position inside the system [68], allowing to study the variation of the sagittal acetabular version. This system then creates a 3D reconstruction for parameter calculation [68], so that it is used as a gold standard in limb length discrepancy compared to radiographs [69]. The same study can provide femoral length, tibial length, and hip, pelvic, and spine parameters (beyond the scope of this paper) (Figures 7 and 8). Mayr et al. showed a strong overall correlation between the EOS® imaging system and CT scan measurements, and high inter- and intrareader reliability in measuring the femoral antetorsion angle, but in case of torsional malalignment, EOS® did not correlate with CT, and presented an advantage as it does not depend on legs' positioning [61]. It is also proposed to be used in the postoperative follow-up, as measurements are relatively quickly realized [67], coupled with the low-dose advantage [2,26] and the absence of metallic artifacts from implants [70]. Some authors have even proposed to replace standard radiographs with the EOS® imaging system [2], in the pre- and postoperative setting, but this attitude requires more studies to be sustained, for as another study points out, difficulties exist in defining reference points on the 3D images provided by EOS® imaging after THA [71]. Of note, this technique can also be used in limb length discrepancy measurement in children, knee architectural disorders, and spine disorders analysis. It has recently been used to show altered hip functional outcomes postoperatively when femoral malrotation occurred after femoral shaft intramedullary nailing in patients with fractures [72].

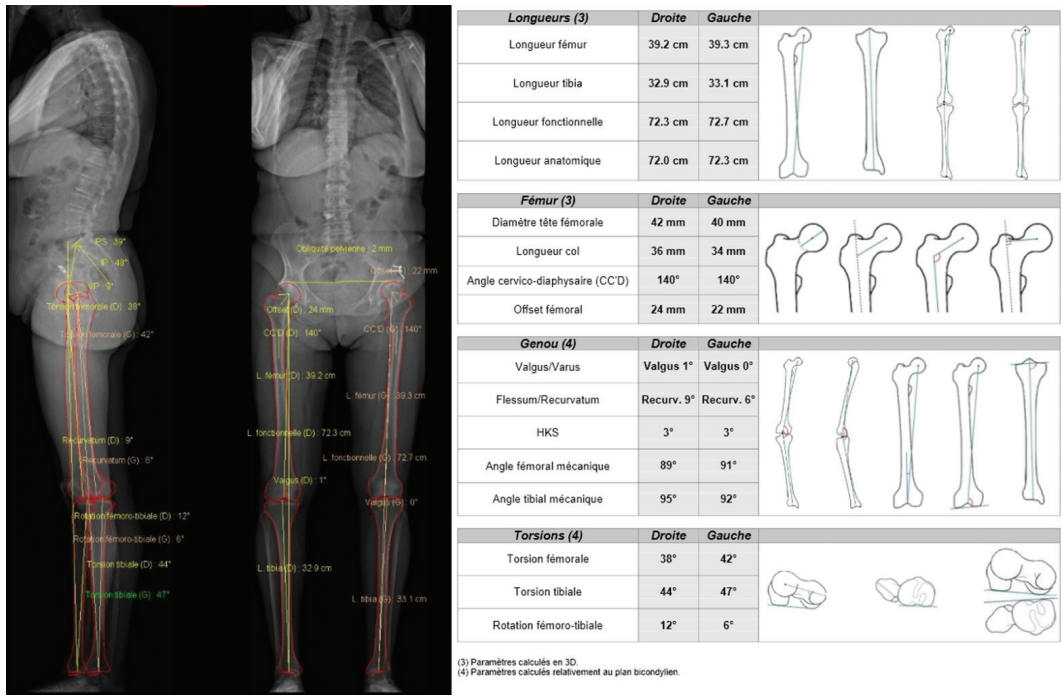


Figure 7. EOS® imaging example showing pelvic and lower limbs measurements. In this example, pelvic parameters are shown (PS: sacral slope, IP: pelvic incidence, VP: pelvic version), and multiple lower limbs measurements are available (femoral and tibial length, femoral head diameter, femoral neck length, cervico-diaphyseal angle, femoral offset, femoral and tibial version/torsion, knee valgus/varus, hip-knee shaft angle, femoral flessum/recurvatum).

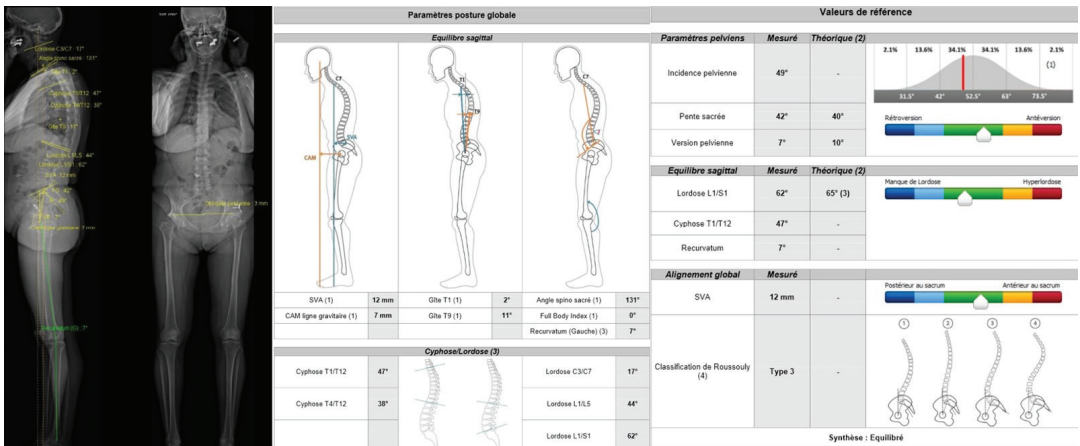


Figure 8. EOS® imaging example showing spine parameters and their relationship with pelvic parameters. Spinal kyphosis and lordosis angles are provided along with the sagittal vertical axis measurement, as well as pelvic parameters, to provide a global appreciation of the spinopelvic complex, considered well balanced in this example.

Concerning radiation dose, it is 4–30 times lower than that of CT [73] and 6–9 times lower than that of radiographs [74]. In the United States, its cost is about $\frac{1}{4}$ to $\frac{1}{6}$ relative to CT [68].

In our opinion, this technique could be performed in conjunction with hip radiographs or CT to study the spinopelvic complex, the spine, and the lower limbs, and to consider the hip in its whole environment, especially in the case of lower back pain or prior surgery.

Practical Aspect

Practically speaking, preoperative images are modeled in 3D using sterEOS[®] software, in which different points are manually positioned to obtain automatic data-sets [61], and the hipEOS[®] planning software (EOS[®] imaging, Paris, France) integrates the manufacturers' 3D component templates into the modeled bones [2]. Using this software, surgical planning can be performed by the surgeon, with the determination of the size of the femoral stem and of the acetabular cup, the change in leg length, and FO [2]. For primary THA, Knafo et al. showed that, in conjunction with a navigation system, the EOS[®]-based planned acetabular and femoral component size corresponded with that implanted ± 1 size in 100% and 94% of the cases, respectively. They also found a postoperative leg length of 1.9 ± 5.9 mm compared to the planned value, and an agreement between the postoperative and the planned FO value of 0.3 mm (SD ± 5.6), which was also acceptable and inferior to that of CT [2,66].

Huang et al. also described better performances of EOS[®] preoperative planning compared to radiographs, using a digital-templating system without any software [5].

Main Strengths

In our opinion, this technique should be increasingly used as it provides 3D information based on 2D acquisition, also to be used with software, at a price lower than that of CT and similar to that of radiographs, with a dramatically decreased radiation dose. It also allows a potential whole-body acquisition on a single occasion, highlighting a combined approach of lower limbs, hips, and spinopelvic complex, which may be key in acetabular cup templating in the near future, especially with the possibility of combined imaging in the standing and sitting position.

Limitations

The soft-tissue analysis is impossible with an EOS[®] imaging system. EOS[®]-based templating has not yet been investigated in the case of hip dysplasia, previous acetabular surgery, and revision surgeries. Its use is limited in the case of previous hip or knee prosthesis, as the sterEOS[®] software cannot be used in the presence of implants [2]. It also features limitations in patients who cannot stand and is susceptible to movement artifacts [61]. In those cases, CT remains a valuable alternative.

Rationale for Preoperative Planning

Even though surgeons are responsible for implant choice and preoperative templating, radiologists must be aware of the different measurements required and not solely rely on the manufacturer's software's automatic measurement. Radiologists are guarantors of the quality and reliability of imaging studies, which must provide adequate support for templating without increasing radiation dose. Even though radiographic templating remains the reference, its limits are well-known and can be reduced with the use of CT and EOS[®] imaging, which are both thought to be more precise without increasing radiation dose [2,5,61,67–73,75]. Strengths and limitations of 2D and 3D techniques are summarized in Table 2. Therefore, to improve functional results and avoid HA complications, radiologists must be aware of the advantages and limitations of the measurement methods of each imaging technique, keeping in mind that even using CT, which is thought to be the most reliable, templating should still be used as a guide rather than an absolute model [60]. For example, the preoperatively measured and planned stem orientation was never achieved

in Belzunce’s study with CT (discrepancy of -1.4 ± 8.2 degrees with a 95% confidence interval of $[-16.9, 13.8]$) [76], and the preoperatively determined femoral stem and acetabular component are reliable in almost all cases, but within one size with EOS imaging, for example [2]. Moreover, Cech et al. stated that implanting components of different sizes than planned did not compromise THA outcomes, whereas medialized hips had worse outcomes, therefore underscoring the need of considering the hip in its whole geometry rather than in terms of strict quantitative measurements [3]. Concerning shoulder arthroplasty, CT-based templating has become a standard procedure and is now well-known to improve patients’ outcomes [77–80]. Tridimensional data have even been shown to be more effective than 2D datasets [79,80]. In the same way, knee arthroplasty templating using 3D data is becoming more and more popular, derived from 2D radiographs [81] or CT [82], sometimes with printed templates [83] and even machine-learning contributions in implant choice [84]. In this context, it seems reasonable to believe that technological advances in imaging will also improve patients’ care and the technical aspects of HA. Regardless of the other methods used for templating (CT and/or EOS®), radiographs remain fundamental for HA preoperative templating for comparison purposes with a postoperative radiographic follow-up. In our opinion, for straightforward situations such as non-deformed centered hips without limb length discrepancy or lumbar spine pathology, conventional radiographs are generally sufficient, as this strategy might be cost-effective. Hip structural deformities require CT, including the femoral condyles in the acquisition to assess acetabular morphology and FNA [12,56], even though it remains costly, as EOS® imaging has not yet been investigated in this context, and post-operative complications might induce many more additional costs than an optimal preoperative imaging work-up. 3D CT-based templating seems to be the most promising technique in implant choice, while standard CT is essentially useful in depicting hip anatomy and degenerative changes. If a CT-based navigation system is available, it might be considered for acetabular cup placement. In both scenarios, EOS® imaging should be performed, if available, to acquire weight-bearing information concerning both the lower limbs and spinopelvic complex, and 3D templating using software must likewise be considered [2,5,68,70,73,75,85]. If EOS® is not available, one must keep in mind that CT-based measurements tend to limit positional variations. Finally, in our opinion, to clearly define if those techniques should replace radiographs or not, their use for the postoperative follow-up should be investigated and compared to radiographs.

Table 2. Strengths and limitations of 2D and 3D templating imaging techniques.

	Radiographs (2D)	CT and EOS Imaging (3D)
Advantages/Strengths	- Reference technique	EOS imaging:
	- Commonly and widely used	- Considers spinopelvic complex mobility
	- Still considered essential for follow-up	- More precise and reproductive than radiographic measurements (lower limb length+++)
	- Used for Dorr classification	- Semi-automated
	- No metal artifact	- No metal artifact
		- Lowest radiation dose
		CT:
		- Osteophyte depiction (acetabulum)
		- Bone stock analysis, reconstruction with subtraction of the implants, vascular analysis, for revision surgery +++
		- More precise implants design and positioning
	- More precise for sagittal inclination of the stem, femoral offset and femoral neck antetorsion measurement	
	- 3D printing: patient-specific design, effective intraoperative simulation	
	- Not depending on patients’ position	
	- Preoperative soft tissue (muscle and tendons) partial analysis	

Table 2. Cont.

	Radiographs (2D)	CT and EOS Imaging (3D)
Drawbacks	<ul style="list-style-type: none"> - Magnification factor - Variation between operative and radiographic measurements - Femoral and limb length measurements depending on patient’s position and lower limb rotation - No soft tissue analysis 	EOS imaging: <ul style="list-style-type: none"> - Less reproducible in the postoperative setting - No soft tissue analysis
		CT: <ul style="list-style-type: none"> - No acquisition in standing position - Radiation dose exposure (without low dose reconstruction algorithms) - Cost - Time consuming post-treatment - Metal artifacts

3. Conclusions

The HA preoperative imaging work-up classically relies on pelvic and hip radiographs, but two main evolutions seem to delineate, potentially improving postsurgical functional outcomes: the EOS[®] imaging system, which evaluates the whole physiological environment of the hip, including the spinopelvic complex and lower limbs, and seems to replace radiographs in lower limb discrepancy; and CT, allowing optimal assessment of acetabular morphology, FNA, and femoral flexion/extension, and supporting dedicated software to propose patient-specific implant designs, especially with the recent development of 3D-printing, which has been shown to be helpful in complex cases and developmental dysplasia of the hip and to increase postoperative outcomes. To date, those procedures might not yet replace radiographs but should be considered as complementary imaging technique, to improve patients’ outcomes. Even though preoperative templating remains a guide and should not be considered ideal in any case, we believe that for non-deformed centered hips without excessive degenerative changes, lower limb, or lumbar spine pathology, conventional radiographs might remain sufficient, whereas deformed and frankly degenerative hips, revision surgery, cases with concomitant lumbar spine, or lower limb discrepancy should be more widely explored (CT and/or EOS[®] imaging), as preventable complications might occur in case of insufficient imaging procedures in the preoperative work-up.

Author Contributions: Conceptualization, R.G., E.G. and C.L.; methodology, R.G.; software, P.A.G.-T.; validation, A.B. and P.A.G.-T.; formal analysis, F.B.; investigation, M.L.; resources, A.B.; data curation, R.G.; writing—original draft preparation, E.G., C.L. and R.G.; writing—review & editing, P.A.G.-T.; visualization, A.B.; supervision, A.B. and P.A.G.-T.; project administration, F.B. All authors have read and agreed to the published version of the manuscript.

Funding: This research received no external funding.

Institutional Review Board Statement: Not applicable.

Informed Consent Statement: Not applicable.

Data Availability Statement: Not applicable.

Conflicts of Interest: The authors declare no conflict of interest.

Abbreviations

AO	acetabular offset
AP	anteroposterior
CDA	cervico-diaphyseal angle
CT	computed tomography
FNA	femoral neck antetorsion
FO	femoral offset

GO	global offset
HA	hip arthroplasty
PE	polyethylene
THA	total hip arthroplasty

References

- Gillet, R.; Teixeira, P.; Bonarelli, C.; Coudane, H.; Sirveaux, F.; Louis, M.; Blum, A. Comparison of Radiographs, Tomosynthesis and CT with Metal Artifact Reduction for the Detection of Hip Prosthetic Loosening. *Eur. Radiol.* **2019**, *29*, 1258–1266. [[CrossRef](#)] [[PubMed](#)]
- Knafo, Y.; Houfani, F.; Zaharia, B.; Egrise, F.; Clerc-Urmès, I.; Mainard, D. Value of 3D Preoperative Planning for Primary Total Hip Arthroplasty Based on Biplanar Weightbearing Radiographs. *BioMed Res. Int.* **2019**, *2019*, 1932191. [[CrossRef](#)] [[PubMed](#)]
- Cech, A.; Kase, M.; Kobayashi, H.; Pagenstert, G.; Carrillon, Y.; O’Loughlin, P.F.; Ait-Si-Selmi, T.; Bothorel, H.; Bonnin, M.P. Pre-Operative Planning in THA. Part III: Do Implant Size Prediction and Offset Restoration Influence Functional Outcomes after THA? *Arch. Orthop. Trauma Surg.* **2020**, *140*, 563–573. [[CrossRef](#)] [[PubMed](#)]
- Chinzei, N.; Noda, M.; Nashiki, H.; Matsushita, T.; Inui, A.; Hayashi, S. Conventional Computed Tomography Software Can Be Used for Accurate Pre-Operative Templating in Bipolar Hip Arthroplasty: A Preliminary Report. *J. Clin. Orthop. Trauma* **2021**, *13*, 1–8. [[CrossRef](#)] [[PubMed](#)]
- Huang, J.; Zhu, Y.; Ma, W.; Zhang, Z.; Shi, W.; Lin, J. A Novel Method for Accurate Preoperative Templating for Total Hip Arthroplasty Using a Biplanar Digital Radiographic (EOS) System. *JBJS Open Access* **2020**, *5*, e20.00078. [[CrossRef](#)] [[PubMed](#)]
- Inoue, D.; Kabata, T.; Maeda, T.; Kajino, Y.; Fujita, K.; Hasegawa, K.; Yamamoto, T.; Tsuchiya, H. Value of Computed Tomography-Based Three-Dimensional Surgical Preoperative Planning Software in Total Hip Arthroplasty with Developmental Dysplasia of the Hip. *J. Orthop. Sci.* **2015**, *20*, 340–346. [[CrossRef](#)] [[PubMed](#)]
- Mishra, A.; Verma, T.; Rajkumar; Agarwal, G.; Sharma, A.; Maini, L. 3D Printed Patient-Specific Acetabular Jig for Cup Placement in Total Hip Arthroplasty. *JOJO* **2020**, *54*, 174–180. [[CrossRef](#)]
- Nishihara, S.; Hayashida, K. Comparison between Freehand Technique and Computed Tomography-Based Navigation in Acetabular Cup Placement through Direct Anterior Approach for Total Hip Arthroplasty. *Arch. Orthop. Trauma Surg.* **2021**, *142*, 323–329. [[CrossRef](#)] [[PubMed](#)]
- Scheerlinck, T.; De Winter, E.; Sas, A.; Kolk, S.; Van Gompel, G.; Vandemeulebroucke, J. Hip Implants Can Restore Anatomical and Medialized Rotation Centres in Most Cases: A 3D Templating Study Comparing Four Implantation Strategies. *Bone Jt. Open* **2021**, *2*, 476–485. [[CrossRef](#)] [[PubMed](#)]
- Thurston, D.; El-Ashry, S.; Gella, S.; Theivendran, K. Digital Templating in Hip Hemiarthroplasty: Is It Possible to Accurately Predict Femoral Head Size from Magnification Alone? *J. Clin. Orthop. Trauma* **2022**, *32*, 101952. [[CrossRef](#)]
- Ma, S.; Xiao, L.; Guo, D.; Shi, Q.; Shen, R.; Li, X. Application of 3D-Printed Osteotomy Guides in Periacetabular Osteotomy: A Short-Term Clinical Study. *Int. J. Artif Organs* **2022**, 3913988221120026. [[CrossRef](#)] [[PubMed](#)]
- Morgan, S.; Barriga, J.; Dadia, S.; Merose, O.; Sternheim, A.; Snir, N. Three Dimensional Printing as an Aid for Pre-Operative Planning in Complex Cases of Total Joint Arthroplasty: A Case Series. *J. Orthop.* **2022**, *34*, 142–146. [[CrossRef](#)] [[PubMed](#)]
- Liu, F.; Tang, K.; Zheng, P.-F.; Zhang, Z.-Q.; Ling, G.; Lou, Y. Performance of Tönnis Triple Osteotomy in Older Children with Developmental Dysplasia of the Hip (DDH) Assisted by a 3D Printing Navigation Template. *BMC Musculoskelet. Disord.* **2022**, *23*, 712. [[CrossRef](#)] [[PubMed](#)]
- Bono, J.V. Digital Templating in Total Hip Arthroplasty. *J. Bone Jt. Surg. Am.* **2004**, *86-A* (Suppl. S2), 118–122. [[CrossRef](#)] [[PubMed](#)]
- Kase, M.; O’Loughlin, P.F.; Ait-Si-Selmi, T.; Pagenstert, G.; Langlois, J.; Bothorel, H.; Bonnin, M.P. Pre-Operative Templating in THA. Part I: A Classification of Architectural Hip Deformities. *Arch. Orthop. Trauma Surg.* **2020**, *140*, 129–137. [[CrossRef](#)] [[PubMed](#)]
- Geijer, M.; Kiernan, S.; Sundberg, M.; Flivik, G. Pre- and Postoperative Offset and Femoral Neck Version Measurements and Validation Using 3D Computed Tomography in Total Hip Arthroplasty. *Acta Radiol. Open* **2020**, *9*, 205846012096491. [[CrossRef](#)] [[PubMed](#)]
- Bhaskar, D.; Rajpura, A.; Board, T. Current Concepts in Acetabular Positioning in Total Hip Arthroplasty. *Indian J. Orthop.* **2017**, *51*, 386–396. [[CrossRef](#)] [[PubMed](#)]
- De Pieri, E.; Atzori, F.; Ferguson, S.J.; Dendorfer, S.; Leunig, M.; Aepli, M. Contact Force Path in Total Hip Arthroplasty: Effect of Cup Medialisation in a Whole-Body Simulation. *HIP Int.* **2021**, *31*, 624–631. [[CrossRef](#)] [[PubMed](#)]
- Zhao, R.; Cai, H.; Tian, H.; Zhang, K. Morphological Consistency of Bilateral Hip Joints in Adults Based on the X-Ray and CT Data. *Surg. Radiol. Anat.* **2021**, *43*, 1107–1115. [[CrossRef](#)]
- Pasquier, G.; Ducharne, G.; Sari Ali, E.; Giraud, F.; Mouttet, A.; Durante, E. Total Hip Arthroplasty Offset Measurement: Is C T Scan the Most Accurate Option? *Orthop. Traumatol. Surg. Res.* **2010**, *96*, 367–375. [[CrossRef](#)] [[PubMed](#)]
- Bjarnason, J.A.; Reikeras, O. Changes of Center of Rotation and Femoral Offset in Total Hip Arthroplasty. *Ann. Transl. Med.* **2015**, *3*, 355. [[CrossRef](#)] [[PubMed](#)]
- Yoshitani, J.; Kabata, T.; Kajino, Y.; Takagi, T.; Ohmori, T.; Ueno, T.; Ueoka, K.; Tsuchiya, H. The Effect of Flexion Alignment in Total Hip Arthroplasty with a Cementless Tapered-Wedge Femoral Stem. *Eur. J. Orthop. Surg. Traumatol.* **2018**, *28*, 1625–1632. [[CrossRef](#)]

23. Abe, H.; Sakai, T.; Takao, M.; Nishii, T.; Nakamura, N.; Sugano, N. Difference in Stem Alignment Between the Direct Anterior Approach and the Posterolateral Approach in Total Hip Arthroplasty. *J. Arthroplast.* **2015**, *30*, 1761–1766. [[CrossRef](#)] [[PubMed](#)]
24. Bonnin, M.P.; Archbold, P.H.A.; Basigliani, L.; Fessy, M.H.; Beverland, D.E. Do We Medialise the Hip Centre of Rotation in Total Hip Arthroplasty? Influence of Acetabular Offset and Surgical Technique. *HIP Int.* **2012**, *22*, 371–378. [[CrossRef](#)]
25. Kosashvili, Y.; Shasha, N.; Olschewski, E.; Safir, O.; White, L.; Gross, A.; Backstein, D. Digital versus Conventional Templating Techniques in Preoperative Planning for Total Hip Arthroplasty. *Can. J. Surg.* **2009**, *52*, 6. [[PubMed](#)]
26. Mainard, D. Planification Pré-Opératoire: Pourquoi, Quand et Comment Planifier? In *La Hanche*; SIMS; Sauramps: Montpellier, France, 2019; Volume 46, pp. 177–187.
27. Nishihara, S.; Sugano, N.; Nishii, T.; Ohzono, K.; Yoshikawa, H. Measurements of Pelvic Flexion Angle Using Three-Dimensional Computed Tomography. *Clin. Orthop. Relat. Res.* **2003**, *411*, 140–151. [[CrossRef](#)] [[PubMed](#)]
28. Uemura, K.; Takao, M.; Otake, Y.; Koyama, K.; Yokota, F.; Hamada, H.; Sakai, T.; Sato, Y.; Sugano, N. Change in Pelvic Sagittal Inclination from Supine to Standing Position Before Hip Arthroplasty. *J. Arthroplast.* **2017**, *32*, 2568–2573. [[CrossRef](#)] [[PubMed](#)]
29. Uemura, K.; Takao, M.; Otake, Y.; Koyama, K.; Yokota, F.; Hamada, H.; Sakai, T.; Sato, Y.; Sugano, N. Reproducibility of Pelvic Sagittal Inclination While Acquiring Radiographs in Supine and Standing Postures. *J. Orthop. Surg.* **2019**, *27*, 2309499019828515. [[CrossRef](#)]
30. Tamura, S.; Nishihara, S.; Takao, M.; Sakai, T.; Miki, H.; Sugano, N. Does Pelvic Sagittal Inclination in the Supine and Standing Positions Change Over 10 Years of Follow-Up After Total Hip Arthroplasty? *J. Arthroplast.* **2017**, *32*, 877–882. [[CrossRef](#)] [[PubMed](#)]
31. Tani, T.; Takao, M.; Uemura, K.; Otake, Y.; Hamada, H.; Ando, W.; Sato, Y.; Sugano, N. Posterior Pelvic Tilt from Supine to Standing in Patients With Symptomatic Developmental Dysplasia of the Hip. *J. Orthop. Res.* **2020**, *38*, 578–587. [[CrossRef](#)]
32. Tachibana, T.; Fujii, M.; Kitamura, K.; Nakamura, T.; Nakashima, Y. Does Acetabular Coverage Vary Between the Supine and Standing Positions in Patients with Hip Dysplasia? *Clin. Orthop. Relat. Res.* **2019**, *477*, 2455–2466. [[CrossRef](#)] [[PubMed](#)]
33. Bhanushali, A.; Chimutengwende-Gordon, M.; Beck, M.; Callary, S.A.; Costi, K.; Howie, D.W.; Solomon, L.B. The Variation in Hip Stability Measurements between Supine and Standing Radiographs of Dysplastic Hips. *Bone Jt. J.* **2021**, *103-B*, 1662–1668. [[CrossRef](#)] [[PubMed](#)]
34. Tsang, H.; Bouz, T.; Kwan, K.; French, M. The Intraoperative Pelvic Radiograph During Total Hip Arthroplasty: Is It Reliable to Estimate Leg Length? *Arthroplast. Today* **2022**, *16*, 9–14. [[CrossRef](#)] [[PubMed](#)]
35. O'Brien, S.; Kernohan, G.; Fitzpatrick, C.; Hill, J.; Beverland, D. Perception of Imposed Leg Length Inequality in Normal Subjects. *HIP Int.* **2010**, *20*, 505–511. [[CrossRef](#)]
36. Renkawitz, T.; Weber, T.; Dullien, S.; Woerner, M.; Dendorfer, S.; Grifka, J.; Weber, M. Leg Length and Offset Differences above 5mm after Total Hip Arthroplasty Are Associated with Altered Gait Kinematics. *Gait Posture* **2016**, *49*, 196–201. [[CrossRef](#)]
37. Weber, M.; von Kunow, F.; Inmann, M.; Meyer, M.; Thieme, M.; Jerabek, S.; Renkawitz, T. Which Safe Zone Is Safe in Total Hip Arthroplasty? The Effect of Bony Impingement. *JPM* **2022**, *12*, 812. [[CrossRef](#)]
38. Lewinnek, G.E.; Lewis, J.L.; Tarr, R.; Compere, C.L.; Zimmerman, J.R. Dislocations after Total Hip-Replacement Arthroplasties. *J. Bone Jt. Surg. Am.* **1978**, *60*, 217–220. [[CrossRef](#)]
39. Meneghini, R.M. Investigation of the Unstable Total Hip Arthroplasty. *J. Arthroplast.* **2018**, *33*, 1325–1327. [[CrossRef](#)]
40. Pour, A.E.; Schwarzkopf, R.; Patel, K.P.; Anjaria, M.; Lazennec, J.Y.; Dorr, L.D. Is Combined Anteversion Equally Affected by Acetabular Cup and Femoral Stem Anteversion? *J. Arthroplast.* **2021**, *36*, 2393–2401. [[CrossRef](#)]
41. McCarthy, T.F.; Alipit, V.; Nevelos, J.; Elmallah, R.K.; Mont, M.A. Acetabular Cup Anteversion and Inclination in Hip Range of Motion to Impingement. *J. Arthroplast.* **2016**, *31*, 264–268. [[CrossRef](#)]
42. Niemeier, T.E.; Wills, B.W.; Theiss, S.M.; Strom, S.F. Sagittal Pelvic Kinematics in Hip Arthroplasty. *Curr. Rev. Musculoskelet. Med.* **2020**, *13*, 240–246. [[CrossRef](#)] [[PubMed](#)]
43. Loftus, M.; Ma, Y.; Ghelman, B. Acetabular Version Measurement in Total Hip Arthroplasty: The Impact of Inclination and the Value of Multi-Planar CT Reformation. *HSS J.* **2015**, *11*, 65–70. [[CrossRef](#)] [[PubMed](#)]
44. Woo, R.Y.; Morrey, B.F. Dislocations after Total Hip Arthroplasty. *J. Bone Jt. Surg. Am.* **1982**, *64*, 1295–1306. [[CrossRef](#)]
45. Pradhan, R. Planar Anteversion of the Acetabular Cup as Determined from Plain Anteroposterior Radiographs. *J. Bone Jt. Surg. Br.* **1999**, *81*, 431–435. [[CrossRef](#)]
46. Liaw, C.-K.; Hou, S.-M.; Yang, R.-S.; Wu, T.-Y.; Fuh, C.-S. A New Tool for Measuring Cup Orientation in Total Hip Arthroplasties from Plain Radiographs. *Clin. Orthop. Relat. Res.* **2006**, *451*, 134–139. [[CrossRef](#)]
47. Lee, G.C.; Lee, S.H.; Kang, S.W.; Park, H.S.; Jo, S. Accuracy of Planar Anteversion Measurements Using Anteroposterior Radiographs. *BMC Musculoskelet. Disord.* **2019**, *20*, 586. [[CrossRef](#)]
48. Grammatopoulos, G.; Pandit, H.G.; da Assunção, R.; Taylor, A.; McLardy-Smith, P.; De Smet, K.A.; Murray, D.W.; Gill, H.S. Pelvic Position and Movement during Hip Replacement. *Bone Jt. J.* **2014**, *96-B*, 876–883. [[CrossRef](#)]
49. Dorr, L.D.; Faugere, M.C.; Mackel, A.M.; Gruen, T.A.; Bogner, B.; Malluche, H.H. Structural and Cellular Assessment of Bone Quality of Proximal Femur. *Bone* **1993**, *14*, 231–242. [[CrossRef](#)]
50. Blum, A. Prothèse Douloureuse: L'interface Osseuse. In *La Hanche*; SIMS; Sauramps: Montpellier, France, 2019; Volume 46, pp. 215–231.
51. Wilkerson, J.; Fernando, N.D. Classifications in Brief: The Dorr Classification of Femoral Bone. *Clin. Orthop. Relat. Res.* **2020**, *478*, 1939–1944. [[CrossRef](#)]

52. Singh, M.; Nagrath, A.R.; Maini, P.S. Changes in Trabecular Pattern of the Upper End of the Femur as an Index of Osteoporosis. *JBS* **1970**, *52*, 457–467. [[CrossRef](#)]
53. Sah, A.P.; Thornhill, T.S.; LeBoff, M.S.; Glowacki, J. Correlation of Plain Radiographic Indices of the Hip with Quantitative Bone Mineral Density. *Osteoporos. Int.* **2007**, *18*, 1119–1126. [[CrossRef](#)] [[PubMed](#)]
54. Knight, J.L.; Atwater, R.D. Preoperative Planning for Total Hip Arthroplasty. Quantitating Its Utility and Precision. *J. Arthroplast.* **1992**, *7* (Suppl. S1), 403–409. [[CrossRef](#)]
55. Salem, H.S.; Marchand, K.B.; Ehiorobo, J.O.; Tarazi, J.M.; Matzko, C.N.; Sodhi, N.; Hepinstall, M.S.; Mont, M.A. Benefits of CT Scanning for the Management of Hip Arthritis and Arthroplasty. *Surg. Technol. Int.* **2020**, *36*, 364–370. [[PubMed](#)]
56. Liang, J.; Zhao, Y.; Gao, X.; Fang, X.; Xu, Y.; Lu, S. Design of Custom-Made Navigational Template of Femoral Head and Pilot Research in Total Hip Resurfacing Arthroplasty. *BMC Surg.* **2020**, *20*, 144. [[CrossRef](#)] [[PubMed](#)]
57. Madadi, F.; Yazdanshenas, H.; Madadi, F.; Bazargan-Hejazi, S. Double Acetabular Wall—A Misleading Point for Hip Arthroplasty: An Anatomical, Radiological, Clinical Study. *Int. Orthop.* **2013**, *37*, 1007–1011. [[CrossRef](#)] [[PubMed](#)]
58. Sculco, P.K.; Wright, T.; Malahias, M.-A.; Gu, A.; Bostrom, M.; Haddad, F.; Jerabek, S.; Bolognesi, M.; Fehring, T.; Gonzalez DellaValle, A.; et al. The Diagnosis and Treatment of Acetabular Bone Loss in Revision Hip Arthroplasty: An International Consensus Symposium. *HSS J.* **2022**, *18*, 8–41. [[CrossRef](#)]
59. Tran, G.; Khalil, L.S.; Wrubel, A.; Klochko, C.L.; Davis, J.J.; Soliman, S.B. Incidental Findings Detected on Preoperative CT Imaging Obtained for Robotic-Assisted Joint Replacements: Clinical Importance and the Effect on the Scheduled Arthroplasty. *Skelet. Radiol.* **2020**, *50*, 1151–1161. [[CrossRef](#)]
60. Kobayashi, H.; Cech, A.; Kase, M.; Pagenstart, G.; Carrillon, Y.; O’Loughlin, P.F.; Bothorel, H.; Ait-Si-Selmi, T.; Bonnin, M.P. Pre-Operative Templating in THA. Part II: A CT-Based Strategy to Correct Architectural Hip Deformities. *Arch. Orthop. Trauma Surg.* **2020**, *140*, 551–562. [[CrossRef](#)]
61. Mayr, H.O.; Schmidt, J.-P.; Haasters, F.; Bernstein, A.; Schmal, H.; Prall, W.C. Anteversion Angle Measurement in Suspected Torsional Malalignment of the Femur in 3-Dimensional EOS vs Computed Tomography—A Validation Study. *J. Arthroplast.* **2021**, *36*, 379–386. [[CrossRef](#)]
62. Veilleux, N.J.; Kalore, N.V.; Vossen, J.A.; Wayne, J.S. Automatic Characterization of Pelvic and Sacral Measures from 200 Subjects. *J. Bone Jt. Surg. Am.* **2020**, *102*, e130. [[CrossRef](#)]
63. Liang, S.; Xie, J.; Wang, F.; Jing, J.; Li, J. Application of Three-Dimensional Printing Technology in Peripheral Hip Diseases. *Bioengineered* **2021**, *12*, 5883–5891. [[CrossRef](#)] [[PubMed](#)]
64. Yan, L.; Wang, P.; Zhou, H.-B. Application of 3D printing guide plate in total hip arthroplasty for developmental dysplasia of the hip. *Zhongguo Gu Shang* **2020**, *33*, 1001–1005. [[CrossRef](#)] [[PubMed](#)]
65. Huppertz, A.; Radmer, S.; Asbach, P.; Juran, R.; Schwenke, C.; Diederichs, G.; Hamm, B.; Sparmann, M. Computed Tomography for Preoperative Planning in Minimal-Invasive Total Hip Arthroplasty: Radiation Exposure and Cost Analysis. *Eur. J. Radiol.* **2011**, *78*, 406–413. [[CrossRef](#)] [[PubMed](#)]
66. Sariali, E.; Mauprivez, R.; Khiami, F.; Pascal-Mousselard, H.; Catonné, Y. Accuracy of the Preoperative Planning for Cementless Total Hip Arthroplasty. A Randomised Comparison between Three-Dimensional Computerised Planning and Conventional Templating. *Orthop. Traumatol. Surg. Res.* **2012**, *98*, 151–158. [[CrossRef](#)]
67. Wade, R.; Yang, H.; McKenna, C.; Faria, R.; Gummerson, N.; Woolacott, N. A Systematic Review of the Clinical Effectiveness of EOS 2D/3D X-Ray Imaging System. *Eur. Spine J.* **2013**, *22*, 296–304. [[CrossRef](#)]
68. Bendaya, S.; Anglin, C.; Lazennec, J.-Y.; Allena, R.; Thoumie, P.; Skalli, W. Good vs Poor Results After Total Hip Arthroplasty: An Analysis Method Using Implant and Anatomic Parameters with the EOS Imaging System. *J. Arthroplast.* **2016**, *31*, 2043–2052. [[CrossRef](#)]
69. Park, K.-R.; Lee, J.-H.; Kim, D.-S.; Ryu, H.; Kim, J.; Yon, C.-J.; Lee, S.-W. The Comparison of Lower Extremity Length and Angle between Computed Radiography-Based Teleoroentgenogram and EOS® Imaging System. *Diagnostics* **2022**, *12*, 1052. [[CrossRef](#)]
70. Lazennec, J.-Y.; Rousseau, M.-A.; Brusson, A.; Folinis, D.; Amel, M.; Clarke, I.; Pour, A.E. Total Hip Prostheses in Standing, Sitting and Squatting Positions: An Overview of Our 8 Years Practice Using the EOS Imaging Technology. *TOORTHJ.* **2015**, *9*, 26–44. [[CrossRef](#)]
71. Tokunaga, K.; Okamoto, M.; Watanabe, K. Implant Orientation Measurement After THA Using the EOS X-Ray Image Acquisition System. *Adv. Exp. Med. Biol.* **2018**, *1093*, 335–343. [[CrossRef](#)]
72. Boscher, J.; Alain, A.; Vergnenegre, G.; Hummel, V.; Charissoux, J.-L.; Marcheix, P.-S. Femoral Shaft Fractures Treated by Antegrade Locked Intramedullary Nailing: EOS Stereoradiographic Imaging Evaluation of Rotational Malalignment Having a Functional Impact. *Orthop. Traumatol. Surg. Res.* **2022**, *108*, 103235. [[CrossRef](#)]
73. Delin, C.; Silvera, S.; Bassinet, C.; Thelen, P.; Rehel, J.-L.; Legmann, P.; Folinis, D. Ionizing Radiation Doses during Lower Limb Torsion and Anteversion Measurements by EOS Stereoradiography and Computed Tomography. *Eur. J. Radiol.* **2014**, *83*, 371–377. [[CrossRef](#)] [[PubMed](#)]
74. Deschênes, S.; Charron, G.; Beaudoin, G.; Labelle, H.; Dubois, J.; Miron, M.-C.; Parent, S. Diagnostic Imaging of Spinal Deformities: Reducing Patients Radiation Dose with a New Slot-Scanning X-Ray Imager. *Spine* **2010**, *35*, 989–994. [[CrossRef](#)]
75. Lazennec, J.Y.; Rousseau, M.A.; Rangel, A.; Gorin, M.; Belicourt, C.; Brusson, A.; Catonné, Y. Pelvis and Total Hip Arthroplasty Acetabular Component Orientations in Sitting and Standing Positions: Measurements Reproducibility with EOS Imaging System versus Conventional Radiographies. *Orthop. Traumatol. Surg. Res.* **2011**, *97*, 373–380. [[CrossRef](#)] [[PubMed](#)]

76. Belzunce, M.A.; Henckel, J.; Di Laura, A.; Hart, A. Uncemented Femoral Stem Orientation and Position in Total Hip Arthroplasty: A CT Study. *J. Orthop. Res.* **2020**, *38*, 1486–1496. [[CrossRef](#)] [[PubMed](#)]
77. Olaiya, O.R.; Nadeem, I.; Horner, N.S.; Bedi, A.; Leroux, T.; Alolabi, B.; Khan, M. Templating in Shoulder Arthroplasty—A Comparison of 2D CT to 3D CT Planning Software: A Systematic Review. *Shoulder Elb.* **2020**, *12*, 303–314. [[CrossRef](#)] [[PubMed](#)]
78. Freehill, M.T.; Weick, J.W.; Ponce, B.A.; Bedi, A.; Haas, D.; Ruffino, B.; Robbins, C.; Prete, A.M.; Costouros, J.G.; Warner, J.J. Anatomic Total Shoulder Arthroplasty: Component Size Prediction with 3-Dimensional Pre-Operative Digital Planning. *J. Shoulder Elb. Arthroplast.* **2022**, *6*, 24715492221098816. [[CrossRef](#)] [[PubMed](#)]
79. Blakeney, W.G.; Urvoy, M.; Chaoui, J.; Raiss, P.; Athwal, G.S.; Walch, G. Development and Assessment of 3-Dimensional Computed Tomography Measures of Proximal Humeral Bone Density: A Comparison to Established 2-Dimensional Measures and Intraoperative Findings in Patients Undergoing Shoulder Arthroplasty. *JSES Int.* **2021**, *5*, 1008–1013. [[CrossRef](#)] [[PubMed](#)]
80. Werner, B.C.; Denard, P.J.; Tokish, J.M.; Bedi, A.; Donegan, R.P.; Metcalfe, N.; Dines, J.S. The Addition of Preoperative Three-Dimensional Analysis Alters Implant Choice in Shoulder Arthroplasty. *Shoulder Elb.* **2022**, *14*, 378–384. [[CrossRef](#)] [[PubMed](#)]
81. Klag, E.A.; Lizzio, V.A.; Charters, M.A.; Ayoola, A.S.; Wesemann, L.; Banka, T.R.; North, W.T. Increased Accuracy in Templating for Total Knee Arthroplasty Using 3D Models Generated from Radiographs. *J. Knee Surg.* **2022**. [[CrossRef](#)]
82. Tiefenboeck, S.; Sesselmann, S.; Taylor, D.; Forst, R.; Seehaus, F. Preoperative Planning of Total Knee Arthroplasty: Reliability of Axial Alignment Using a Three-Dimensional Planning Approach. *Acta Radiol.* **2022**, *63*, 1051–1061. [[CrossRef](#)]
83. Gu, F.; Li, L.; Zhang, H.; Li, X.; Ling, C.; Wang, L.; Yao, Q. Three-Dimensional-Printed Guiding Template for Unicompartmental Knee Arthroplasty. *BioMed Res. Int.* **2020**, *2020*, 7019794. [[CrossRef](#)] [[PubMed](#)]
84. Kunze, K.N.; Polce, E.M.; Patel, A.; Courtney, P.M.; Sporer, S.M.; Levine, B.R. Machine Learning Algorithms Predict within One Size of the Final Implant Ultimately Used in Total Knee Arthroplasty with Good-to-Excellent Accuracy. *Knee Surg. Sports Traumatol. Arthrosc.* **2022**, *30*, 2565–2572. [[CrossRef](#)] [[PubMed](#)]
85. Lazennec, J.-Y.; Brusson, A.; Rousseau, M.-A. Hip-Spine Relations and Sagittal Balance Clinical Consequences. *Eur. Spine J.* **2011**, *20* (Suppl. S5), 686–698. [[CrossRef](#)] [[PubMed](#)]



Review

Update on Current Imaging of Systemic Lupus Erythematosus in Adults and Juveniles

Iwona Sudoł-Szopińska ^{1,*}, Ewa Żelnio ¹, Marzena Olesińska ², Piotr Gietka ³, Sylwia Ornowska ², Deborah Jane Power ⁴ and Mihra S. Taljanovic ^{5,6}

¹ Department of Radiology, National Institute of Geriatrics, Rheumatology and Rehabilitation, 02-637 Warsaw, Poland

² Connective Tissue Disease Department, Institute of Geriatrics, Rheumatology and Rehabilitation, 02-637 Warsaw, Poland

³ Clinic of Paediatric Rheumatology, National Institute of Geriatrics, Rheumatology and Rehabilitation, 02-637 Warsaw, Poland

⁴ Catalina Pointe Arthritis & Rheumatology Specialists, P.C. 7520 North Oracle Road, Suite 100, Tucson, AZ 85704, USA

⁵ Departments of Medical Imaging and Orthopaedic Surgery, University of Arizona, Tucson, AZ 85719, USA

⁶ Department of Radiology, University of New Mexico, Albuquerque, NM 87131, USA

* Correspondence: sudolszopinska@gmail.com; Tel.: +48-22-67-09-192

Abstract: Systemic lupus erythematosus (SLE) is an autoimmune disease involving multiple organs and organ systems. Musculoskeletal (MSK) involvement is one of the most frequent and the earliest locations of disease. This disease affects joints and periarticular soft tissues, tendon sheaths and tendons, bones, and muscles. Multimodality imaging, including radiography, ultrasound (US), and magnetic resonance imaging (MRI), plays a significant role in the initial evaluation and treatment follow up of MSK manifestations of the SLE. In this paper, we illustrate MSK imaging features in three clinical forms of SLE, including nondeforming nonerosive arthritis, deforming nonerosive arthropathy, and erosive arthropathy, as well as the other complications and features of SLE within the MSK system in adults and juveniles. Advances in imaging are included. Conventional radiography primarily shows late skeletal lesions, whereas the US and MRI are valuable in the diagnosis of the early inflammatory changes of the soft tissues and bone marrow, as well as late skeletal manifestations. In nondeforming nonerosive arthritis, US and MRI show effusions, synovial and/or tenosynovial hypertrophy, and vascularity, whereas radiographs are normal. Deforming arthritis clinically resembles that observed in rheumatoid arthritis, but it is reversible, and US and MRI show features of inflammation of periarticular soft tissues (capsule, ligaments, and tendons) without the pannus and destruction classically observed in RA. Erosions are rarely seen, and this form of disease is called rhus syndrome.

Keywords: lupus arthritis; systemic lupus erythematosus; juvenile lupus erythematosus; lupus hand; rhus; imaging; radiography; ultrasonography; magnetic resonance imaging

Citation: Sudoł-Szopińska, I.; Żelnio, E.; Olesińska, M.; Gietka, P.; Ornowska, S.; Power, D.J.; Taljanovic, M.S. Update on Current Imaging of Systemic Lupus Erythematosus in Adults and Juveniles. *J. Clin. Med.* **2022**, *11*, 5212. <https://doi.org/10.3390/jcm11175212>

Academic Editor: Gerard Espinosa

Received: 13 July 2022

Accepted: 1 September 2022

Published: 3 September 2022

Publisher's Note: MDPI stays neutral with regard to jurisdictional claims in published maps and institutional affiliations.



Copyright: © 2022 by the authors. Licensee MDPI, Basel, Switzerland. This article is an open access article distributed under the terms and conditions of the Creative Commons Attribution (CC BY) license (<https://creativecommons.org/licenses/by/4.0/>).

1. Introduction

Systemic lupus erythematosus (SLE) is a chronic, autoimmune, multisystem inflammatory disease which affects multiple organs and organ systems. The pathogenesis of this disease is only partially understood [1–4]. Antinuclear antibodies (ANA) are present in all patients [5], and almost one third of patients have antiphospholipid antibodies, which may cause thromboembolic complications [6]. SLE mainly affects women of reproductive age, and is characterized by heterogeneous degrees of severity as well as unpredictable flares and remissions [7].

Involvement of the skin and the MSK system are the most common manifestation of SLE, occurring in up to the 94% of patients [1,4,7]. Involvement of the MSK system is

also often (in c.a. 50% of patients) the earliest manifestation of SLE [1,4,7,8]. Any joint may be affected, however, like in rheumatoid arthritis (RA), but most commonly, there is symmetric polyarthritis or oligoarthritis involving the hands, wrists, knees, and less frequently, the feet, ankle, shoulder, and elbow joints [2,6,9]. A hallmark of this disorder are articular deformities without fixed contractures [5].

The three main clinical manifestations of MSK SLE imaging features include: non-deforming and nonerosive arthritis (NDNE), deforming nonerosive arthropathy, called Jaccoud's arthropathy (JA), and erosive arthropathy, called rhupeus.

1.1. Nondeforming and Nonerosive Arthritis (NDNE)

The incidence of arthritis in patients with SLE of different races ranges from 69% to 95% [2]. About 78% of patients with lupus have arthritis at the initial diagnosis, and about 58% of patients with SLE relapses have active arthritis [2]. The typical manifestation of SLE arthritis is symmetrical, classically described as nonerosive, migratory, and reversible polyarticular inflammation. Most commonly, metacarpophalangeal (MCP), proximal interphalangeal (PIP), distal interphalangeal (DIP) joints, as well as knees and shoulders, are involved (2, 1). Only Iagnocco et al. [7] found that foot joints were the most frequently involved. Clinically, symptoms of arthritis can last from several hours to several months.

Ultrasound (US) and MRI show effusions and synovial and/or tenosynovial hypertrophy. Power and color doppler US, including newer microvascular techniques and contrast-enhanced MRI, show active synovial inflammation [2] (Figure 1). Compared with RA, the swelling caused by effusion and synovial hyperplasia and vascularity in SLE arthritis is relatively light [2]. Pathology reveals widespread vasculitis affecting capillaries, arterioles, and venules, and—unlike pannus in RA—villous hypertrophy of the synovium covered by fibrin and low-grade lymphoplasmacytic inflammatory cell infiltrates in the subintima [5].

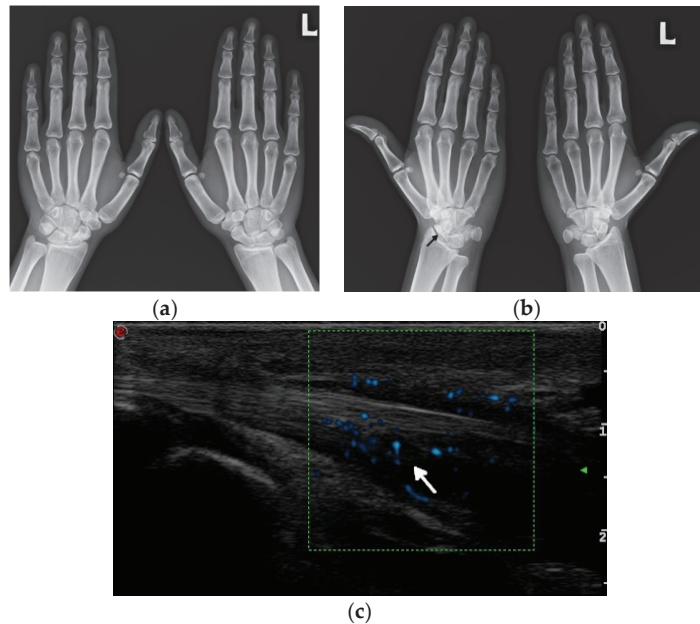


Figure 1. Cont.

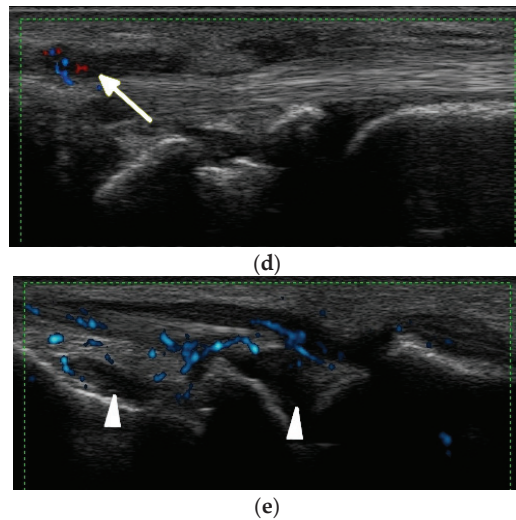


Figure 1. A 34-year-old female with systemic lupus erythematosus. (a) Posterior–anterior and oblique (b) radiographs of the bilateral hands show a non-united fracture of the right scaphoid waist, with increased sclerosis of the proximal pole and proximal waist consistent with osteonecrosis (arrow), possibly steroid-induced, and with no additional deformities. (c) Long-axis power Doppler ultrasound images at the volar aspect of the ring finger, (d) dorsal ulnar aspect of the wrist, and (e) volar aspect of the wrist show increased synovial vascularity involving the ring finger in (c) and the 6th extensor compartment tendon sheath in (d), consistent with tenosynovitis (arrows). Synovitis at the volar aspect of the radiocarpal and midcarpal joints without erosive bone changes is seen in (e) (arrowheads).

1.2. Deforming Nonerosive Arthropathy/Jaccoud’s Arthropathy (JA)/Lupus Hand

This deforming arthritis without erosions, called Jaccoud’s arthropathy (JA), is pathognomonic for SLE [5]. As recently as the early 2000s, it was observed in up to 35% of patients [6], and now, as a result of more effective treatment, JA occurs far less frequently. This form of deforming arthritis resembles that observed in RA, but it is reversible [1,6]. This means that unlike in RA, where malalignments result mainly from intraarticular inflammation with destructive synovitis leading to articular bone damage, in SLE, the deformities occur secondary to a loss of support from the ligamentous and capsular structures around the joint, ligamentous laxity, and muscle contractures, and at least in the early stage of disease, they are completely reducible [5]. This reversible finding may be missed if only PA radiographs of hands are obtained (Figure 2). However, when hands are freed, different deviations become evident (thus the name reversible). They all result from inflammation followed by fibrosis of the periarticular soft tissues, including joint capsule, ligaments, and tendons without the pannus, which is classically observed in RA [1,10]. Deformities in the “lupus hand” include contractures in the MCP and interphalangeals joints, subluxation of MCP joints (aka ulnar deviation/ulnarization—the earliest pathology), swan-neck and boutonniere deformities, hitchhiker’s thumb, known as the “Z” deformity of the thumb, scapholunate dissociation, and ulnar translocation of the carpals [6,9]. Carpal instability as recently as the 1990s was found in 15% of SLE patients [11] and current data are not known. In feet, the deformities include contractures, the lateral deviation of metatarsophalangeal joints, hallux valgus and hammer toes [6,9]. Deformities may involve any other joint, such as the knees and shoulders [1].

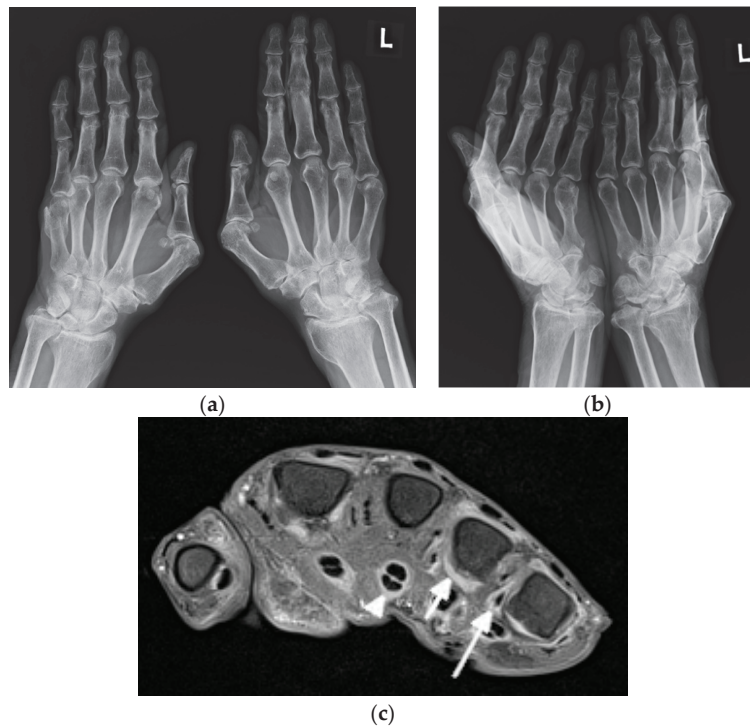


Figure 2. A 63-year-old male with systemic lupus erythematosus and Jaccoud’s deformities on clinical examination. (a) Posterior–anterior and (b) oblique radiographs of the bilateral hands show ulnar deviation of the lesser finger phalanges of the right hand, with malalignment of the 3rd–5th digits proximal interphalangeal (PIP) joints that are more apparent in (b). They also show contracture at the 3rd PIP joint of the left hand, osteoarthritis of the bilateral wrists and scattering of the metacarpophalangeal (MCP) joints, bilateral positive ulnar variance, and posttraumatic deformities of the bilateral distal radial metaphysis and of the distal right 5th metacarpal. (c) Axial postcontrast T1-weighted magnetic resonance image with fat saturation of the right hand shows MCP joints 2, 4, and 5 synovitis (short arrow pointing to MCP 4), MCP 2, 4, and 5 capsular enhancement (long arrow pointing to MCP 5), and 2–5 flexor tendons tenosynovitis (arrowhead pointing to middle finger flexor tendon sheath).

Spronk et al. developed criteria to describe the severity of Jaccoud deformities [6], primarily based on the metacarpal axis deviation, and whether they are reversible or not based on the so-called Jaccoud’s index [12] (Table 1). Three different forms of deforming arthropathy in this disease were later proposed as follows: Jaccoud’s arthropathy (JA), mild deforming arthropathy (with less deformities), and the erosive form of SLE, called rhupus (Figure 3) [1].

1.3. Erosive Arthropathy, Called Rhupus

Rhupus syndrome (rhupus disease) is a rare form of SLE with malalignments and erosions, representing a type of SLE resembling RA [6] or an overlap syndrome, when RA coexists with SLE [1] (Figure 4). According to publications from the 1980s and 1990s, it accounts for c.a. 1–25% of SLE patients [6], and current data are lacking. Rhupus is indistinguishable from RA or RA patterns of psoriatic arthritis on imaging [10]. In all, articular erosions, tenosynovitis, tendon tears, and bone marrow edema (BME) are seen [9,10]. In SLE, Bywaters described hook deformities at the MCP joints [6], and Reilly

et al. found ulnar styloid erosions [6]—in both locations, postulated due to adjacent tenosynovitis/tendinitis—so called compressive erosions [6].

Table 1. Diagnostic criteria according to Spronk. Jaccoud’s arthropathy is considered present if the scoring (Jaccoud’s index; JI) achieved is >5 [6].

Jaccoud’s Arthropathy Index (JI)	Number of Affected Fingers	Score
Ulnar deviation	1–4	2
	5–8	3
‘Swan-neck’ deformity	1–4	2
	5–8	3
Boutonniere deformity	1–4	2
	5–8	3
‘Z’ deformity of thumb	1	2
	2	3

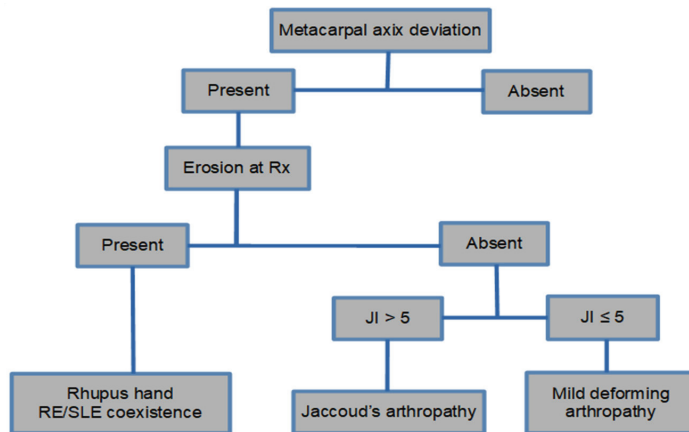


Figure 3. Algorithm with the forms of classification of joint involvement in SLE [13].

The imaging features of three types of SLE described above are summarized in Table 2.

Table 2. Imaging findings in three types of systemic lupus erythematosus on radiographs, ultrasound, and magnetic resonance imaging.

Magnetic Resonance Imaging	Ultrasonography	Radiography	
Effusions	Joint effusions	Periarticular bone demineralization	
Synovial thickening	Synovial thickening Hyperemia	Soft tissue swelling	Nondeforming and nonerosive arthritis
Postcontrast enhancement			
Periarticular BME			
Capsular inflammation (synovitis) Inflammation of the ligaments, tendon sheaths, tendons (tenosynovitis, tendinitis)	Capsular inflammation (synovitis) Inflammation of the ligaments, tendon sheaths and tendons (tenosynovitis, tendinitis)	Reversible malalignments	Deforming non erosive arthropathy/JA
Periarticular BME			
Erosions, synovitis and tenosynovitis, tendinitis, Periarticular BME	Erosions, synovitis, tenosynovitis, tendinitis	Erosions and malalignments	Erosive arthropathy/rhusus



Figure 4. A 64-year-old female with SLE diagnosed in 1980 with Jaccoud’s arthropathy for hands and feet. (a) Posterior–anterior and (b) oblique radiographs of the hands show bone demineralization; soft tissue swelling at the wrists; periarticular calcifications; malalignment at the distal radioulnar, radiocarpal, and midcarpal joints; dislocation of the 1st carpometacarpal and subluxation of the 1st metacarpophalangeal joints; and joint space narrowing with cyst-like and erosive/destructive changes consistent with rhus syndrome. Note the reversible contractures at the proximal interphalangeal joints, apparent in (b) and resolved or less apparent in (a). (c) Anterior–posterior standing radiograph of the bilateral feet and (d) lateral standing radiograph of the left foot show bone demineralization, bilateral hallux valgus deformities, and bilateral 2nd and 3rd hammer toes, as well as a right foot with moderate lateral subluxation.

2. Update on Imaging of SLE on Radiography, Ultrasonography, and MRI

2.1. Arthritis

2.1.1. Radiography

Arthritis in SLE is usually non-erosive in radiography, even in the 5–15% of patients with a long-standing disease who develop hand and foot deformities as hallmarks of Jaccoud’s arthropathy [14]. Radiographs are usually the first method in the imaging work-up. Bilateral radiographs are performed to evaluate the location and spectrum of imaging features and to differentiate between SLE and other rheumatic diseases [10]. SLE, like RA, involves the hand and wrist in a bilateral manner, whereas unilateral involvement is typical for Still’s disease [10].

In the case of hand and wrist involvement, the posterior–anterior (PA) view is supplemented with oblique radiographs in supination or the Nørgaard view (the ball-catcher view) [10]. This is especially appreciated in SLE, where, in addition to detecting more erosions in an additional view, reversible malalignment may not be apparent on a PA radiograph, corrected by the pressure of the hand against the radiographic cassette [5,9].

Radiographic features in SLE typically include [5,6,9]:

- Periarticular bone demineralization
- Periarticular soft tissue swelling
- Symmetrical polyarthritis, most commonly involving hands, wrists, knees, feet, and shoulders
- Preserved joint spaces
- Deforming, non-erosive arthropathy (Jaccoud’s arthropathy)
- Occasionally erosive arthropathy (rhumus)
- Acral sclerosis, acroosteolysis in some patients;
- Frequent osteonecrosis, most commonly of the femoral head, as the result of vasculitis and steroid therapy;
- Insufficiency fractures, possible due to disuse demineralization or osteopenia;
- Bacterial and fungal joint infections due to steroid administration and renal disease;
- Myositis, in a small number of patients, sometimes with the presence of calcifications;
- Uncommon spine manifestations, with atlanto-axial subluxation.

2.1.2. Ultrasound and Magnetic Resonance Imaging

The imaging findings in US and MRI are nonspecific for many rheumatic diseases because synovitis, tenosynovitis, and BME can be seen in many of them, such as RA, juvenile idiopathic arthritis (JIA), PsA, and SLE [10]. In SLE, however, US and MRI improve understanding of the erosive disease and joint pathology [2] (Figures 2 and 5). These advanced imaging methods identify articular and periarticular abnormalities in the early disease phase with high sensitivity, allowing for a more appropriate and accurate management and follow-up [3].

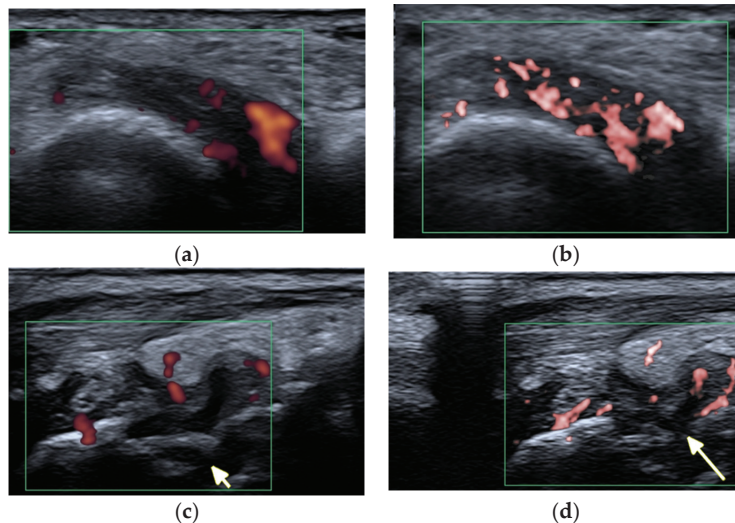


Figure 5. A 57-year-old patient with systemic lupus erythematosus. (a) Short-axis power Doppler and (b) superb micro-vascular imaging (SMI) ultrasound (US) images of the distal radioulnar joint. (c) Long-axis power Doppler and (d) SMI US images at the dorsal aspect of the radiocarpal and midcarpal joints show joint effusions and hyperemia consistent with synovitis with more vessels seen with SMI (b,d). Note an intra-osseous cyst-like change (short arrow) and cortical erosion (long arrow in (d)) in the carpal bone related to rhumus syndrome.

A literature search conducted by Ceccarelli et al. [3] in a number of databases on SLE imaging [3] found reported synovitis in almost 60% of patients with SLE, and the presence of erosions with a frequency ranging from 2% to 87% [3]. As expected, 87% of rhumus

patients showed US-detected erosions. Patients with rhus not only had a greater number of erosions, but also larger erosions than those with JA or NDNE arthritis, with prevalent involvement of the MCP joints [14]. US appeared more sensitive than conventional radiography in detecting bone erosions in SLE, although, comparing it with CT, the overall reliability of US in detecting bone erosions was moderate for rhus syndrome (0.55) and JA (0.58) and poor for NDNE arthritis (0.10) [14].

Iagnocco et al., in a prospective study on 62 consecutive SLE patients, reported that the MTP joints were the most commonly affected site, with joint effusions, synovial hypertrophy, or synovitis (72.6 %) compared with the wrist, MCP, and PIP joints [7,15]. Synovitis was most commonly detected in MTP 2 and 4 [7,15]. The MTP synovial hypertrophy was present in 80% of the SLE cases, but with power Doppler signals seen in only 10% of cases, which was attributed to mechanical tissue irritation [7]. In the same study [7], at least a single US abnormality was detected in the majority of patients (87.1%), supporting the concept of a high prevalence of joint involvement in SLE [7]. However, only 40% of patients presented as having clinical features of joint involvement [7]. This dissociation between clinical and US imaging findings suggests a condition of subclinical inflammation.

The prevalence of subclinical synovitis in heterogenous studies, including—in most of them—consecutive, both symptomatic and asymptomatic, patients with lupus, ranges between 10% and 95% [8]. Honghu et al. [2], in a retrospective study, aimed to compare the role of hand and wrist US in diagnosing subclinical synovitis in SLE patients. Out of 41 included patients, 95.1% had joint abnormality. The most common US finding was synovitis (with a frequency of 19.7%), followed by tenosynovitis (7.1%), joint effusion (5.7%), and bone erosions (0.6%). Among the MCP joints, the most commonly affected joint was the MCP 3, followed by the MCP 4, MCP 2, MCP 1, and MCP 5 joints. Almost 32% of patients had wrist joint involvement, 4.8% had interphalangeal joint involvement of the thumb, 24.4% had PIP 2 involvement, 41.5% had PIP 3 involvement, 29.3% had PIP 4 involvement, and 7.3% had PIP 4 involvement. Twelve patients (29.3%) demonstrated knee joint involvement. Guillen et al. [8], in a multicenter cross-sectional study, found US features of arthritis in hands in about one-third of asymptomatic SLE patients with synovial thickening on gray scale images, while synovial hyperemia on power Doppler US was seen in one-fifth of the patients. The global prevalence of subclinical synovitis in the group with arthralgias was 38.2%. In the group without joint symptoms, that prevalence was 30%. No erosions or tendon ruptures were found in any patient [8]. Subclinical synovitis was reported in one study in 58.3% of SLE patients without joint involvement, through the US of the wrist and second and third MCP joints [8], and in 77% of SLE asymptomatic patients, with synovial hyperemia in 23% [8]. In another study identified in this cross-sectional study, 25% of patients with arthralgia of the hands had synovial effusion or hypertrophy. Iagnocco et al. [7] studied prospectively the foot and wrist of 62 consecutive SLE patients who were mostly asymptomatic during the US, demonstrating synovitis in about 20–32% of MCP and 8–11% of PIP joints.

The advantage of MRI is an ability to visualize BME and the additional location of inflammation, as well as the ability to detect more erosions with the benefit of multiplanar imaging and access to all bone surfaces. In SLE patients, BME at the wrist level, as found in Ceccarelli et al. from a literature search quoted earlier [3], ranges from 13% to 35% of the cases [3]. Ostendorf et al. [6] found that MRI of the hands of 14 SLE patients showed periarticular capsular swelling in all cases, joint effusion in 7, and mild synovial hypertrophy in 10 cases.

Recent application of US and MRI have probable influenced revision of the current Systemic Lupus International Collaborating Clinics (SLICC) criteria introduced in 2012 [3]. According to these criteria, patients with no swelling but positive US synovitis may benefit from escalating immunosuppressive therapy [16]. Conversely, a negative US may indicate that it is safe to taper corticosteroids, which is important given the toxicity of long-term corticosteroids [16]. Mahmoud et al. [16], in their longitudinal multicenter study involving

133 SLE patients, showed that 20% of patients with swollen joints upon clinical assessment do not have active synovitis.

Despite the clear advantages of US and MRI, SLE-specific quantification of inflammation is lacking. In 2003, early investigations with MRI noted the different features of SLE arthritis compared with RA, particularly the presence of edematous tenosynovitis and capsular swelling. Since that time, a few new evaluations of lupus arthritis using MRI have been reported [4]. One study [4] assessed the utility of Rheumatoid Arthritis Magnetic Resonance Imaging Score (RAMRIS) in the quantification of lupus arthritis scoring, as well as identified features of lupus arthritis that are incompletely captured by the RAMRIS. The authors compared patients who had objective findings of swelling upon clinical examination and low RAMRIS component scores, and found joint effusions that would not be scored as there was no enhancement with a gadolinium-based contrast and no synovial proliferation. They also noted tenosynovitis throughout the hand and fingers seen in these patients with SLE, even when tenosynovitis was minimal in the wrist. It is worth recalling that RAMRIS is the Rheumatoid Arthritis MRI Scoring system, and perhaps there is a need for an SLE MRI scoring system.

2.2. Tendons

Spontaneous tendon ruptures are a rare complication of SLE. US is the foremost imaging modality for tendon pathologies, since it is more sensitive than clinical examinations and MRI for detecting pathological structural changes within tendons [17]. The degree of tendon inflammation in rheumatologic diseases, namely tenosynovitis, paratenonitis, or tendinitis, as well as the extent of tendon damage, can be evaluated [17]. In such cases, US is able to depict tenosynovial effusion, tenosynovial thickening, and hyperemia, as well as tendon tears (partial, full-thickness, incomplete, or complete) [7,10]. In a literature search by Ceccarelli et al. [3], the prevalence of tenosynovitis ranged between 4% to 57%. Ostendorf et al. [6] in the MRI of the hands of 14 patients with SLE, found tendon sheath effusion (“edematous tenosynovitis”) in 42%.

Typical for SLE are spontaneous tendon ruptures (Figures 6–8), most commonly of the patellar and Achilles tendons. In SLE, inflammatory changes as well as tears may be observed not only on the background of tenosynovitis, but also involving the tendon in the absence of tenosynovitis, even along the intramuscular segment [10] (Figure 8).

Contrary to RA, where tendon ruptures occur almost always in the hands as a result of tendinitis secondary to tenosynovitis and/or tendon tears against the eroded bone, in SLE, tears are most frequently seen in the lower limbs, affecting the patellar, Achilles, and quadriceps tendons, frequently associated with corticosteroid therapy with a superimposed mechanical component [1,10]. Tendon tears result mainly from corticosteroid’s antimycotic effect and fibroblasts’ inhibition of collagenase stimulus and consequential structural fiber disorganization [1]. Less frequently, tears are secondary to tenosynovitis, like in RA [1]. A systematic review using the MEDLINE, Scielo, and LILACS databases (1966 to 2009) demonstrated that almost one-third of the SLE patients with tendon ruptures also have JA; thus, this arthropathy may be recognized as a risk marker for tendon ruptures [18].

2.3. Myositis

In 5% to 10% of SLE patients, inflammatory myopathy is diagnosed based on laboratory findings, and muscular disease may be present in up to 50% of cases [1]. The main presenting symptoms are muscle weakness and myopathy detected by electromyography and muscle functional tests (i.e., MMT8—the Manual Muscle Test 8—diminished). Inflammatory myositis may be caused by the disease itself, but more commonly, SLE patients suffer from non-inflammatory myositis associated with the use of corticosteroids, chloroquine, or hydroxychloroquine [1]. The diagnosis is confirmed by muscular biopsy.

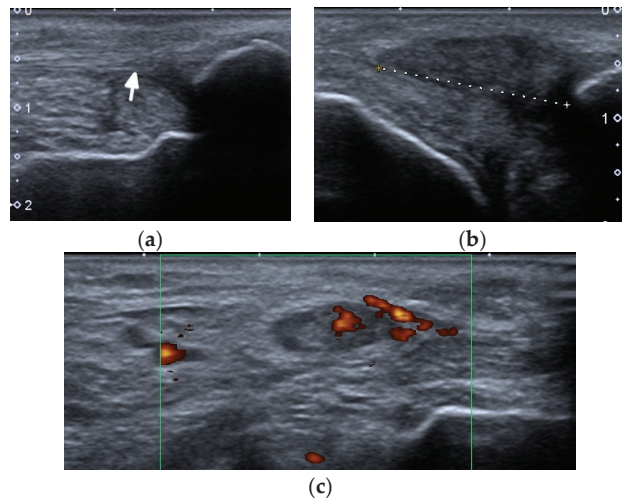


Figure 6. A complete spontaneous tear of the right posterior tibialis tendon (PTT) 2 cm above the medial malleolus in a 46-year-old female with systemic lupus erythematosus. (a,b) short-axis gray-scale ultrasound (US) images of the medial aspect of the bilateral ankles show the normal echogenic fibrillar appearance of the healthy left PTT (a, arrow) compared to an enlarged, torn right hypoechoic PTT in the same region between calipers in (b). (c) Short-axis power Doppler US image of the affected right side shows hyperemia in the PTT tendon stump, with additional hyperemia in the tendon sheath consistent with tendinopathy and tenosynovitis. Two tiny red dots at the periphery of green Doppler box represent normal vessels.

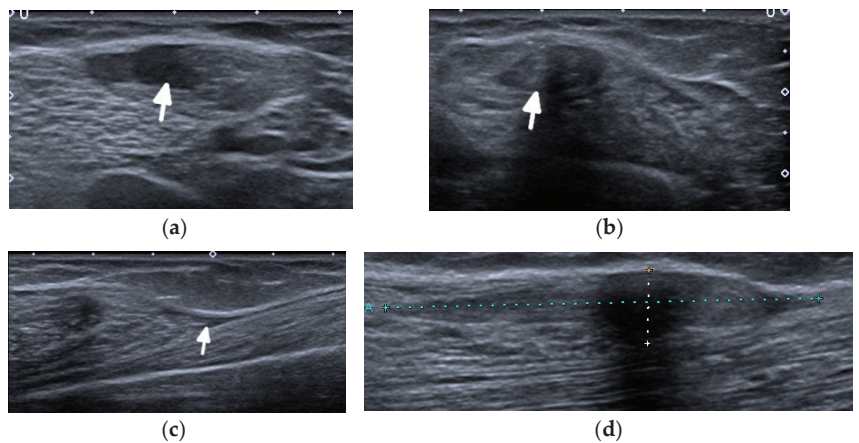


Figure 7. A complete tear of the proximal part of the bare tendon of the distal biceps brachii bilaterally in the same patient as in Figure 6. Short-axis (a,b) and long-axis (c,d) gray-scale ultrasound images of the bilateral elbow/distal arms show rupturing of the bilateral distal biceps tendons at the level of the myotendinous junction with hypoechoic proximal stumps consistent with tendinopathy (arrows). In (c,d), note the retracted bilateral biceps muscles.

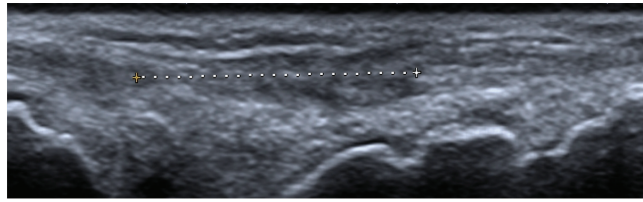


Figure 8. A long-axis gray-scale ultrasound image shows a complete tear of an extensor digitorum tendon of the middle finger at the level of the wrist (between calipers) in the same patient as in Figures 6 and 7.

MRI is the most appropriate modality for the evaluation of muscle involvement, despite its low specificity, and US plays a complementary role [1,19] (Figure 9). MRI is used in the differential diagnosis and as a follow-up to a therapeutic response, and is useful to define the biopsy site [1,19]. Fat-saturated, fluid-sensitive MR sequences with long time until echo recovery are the most sensitive for identifying acute inflammation, manifesting as areas of high signals within the muscle [19]. Inflamed muscles also demonstrate contrast enhancement (Figure 9). In the chronic phase, involved muscles may undergo fatty infiltration with or without a loss of muscle bulk. These are seen on MRIs on T1-weighted sequences as areas of high signal intensity, replacing the normal intermediate signal of muscle fibers [19].

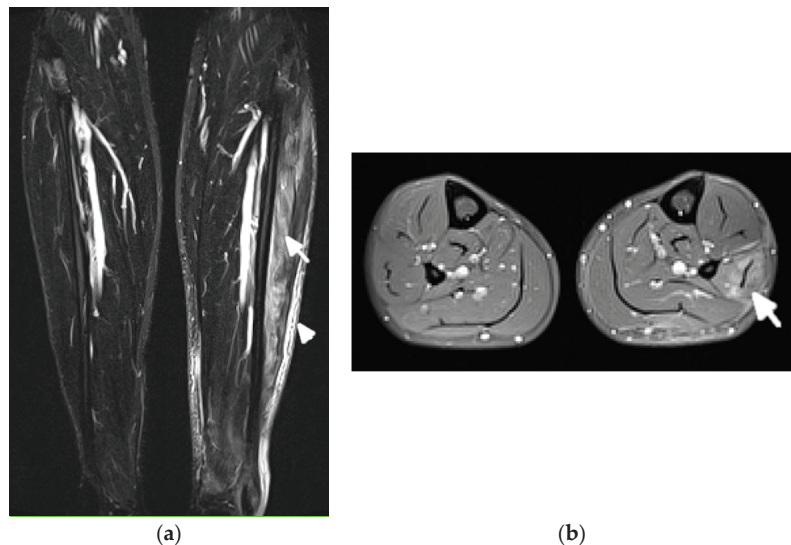


Figure 9. Magnetic resonance (MR) imaging of lower legs of a 34-year-old male with systemic lupus erythematosus with myositis. (a) Coronal T2 turbo inversion recovery magnitude and (b) axial postcontrast T1-weighted MR images with fat saturation show increased signals in the muscles of the lower left leg (arrows), especially peroneus brevis and the lateral head of gastrocnemius, and to a lesser extent, soleus musculature, with heterogeneous enhancement in (b) after the administration of a gadolinium base contrast agent. In (a), note the subcutaneous edema around the left lower leg (arrowhead).

US may assist with the diagnosis and characterization of disease activity in inflammatory myopathies, with reported 82.9% sensitivity for detecting histologically proven myositis [17]. Inflammation and edema cause patchy or diffusely increased echogenicity of muscles, which may also appear swollen [17,19]. Increased vascularity on power Doppler

may be seen [19]. In chronic diseases, the muscles appear atrophic with reduced volume and further increased echogenicity due to the progressive infiltration of fatty tissue [1,17,19]. In addition, by shear-wave elastography (SWE), US is able to evaluate muscle stiffness [20]. Di Matteo et al. [20] performed SWE on the quadriceps muscles in 30 SLE patients (without previous/current myositis or neuromuscular disorders) as well as 15 healthy subjects that matched the patients in age, sex, and BMI. SWE was significantly lower in SLE patients compared with the healthy subjects (1.5 m/s vs. 1.6 m/s respectively, $p = 0.01$).

2.4. Adipose Tissue and Lupus Panniculitis

Lupus panniculitis (LP), also referred to as lupus erythematosus profundus (LEP), is a chronic recurrent inflammation of the subcutaneous fat. It occurs in 1% to 3% of patients with SLE [21].

LP affects the deep dermis and subcutaneous adipose layer, and mainly involves the proximal extremities (lateral aspects of the arms and shoulders), thighs, buttocks, trunk, face, and scalp [21]. Patients usually present with persistent, often tender and painful skin lesions, or subcutaneous nodules, that range from 1 to 5 cm in diameter.

The imaging features of facial LP are extremely scarce in the literature (Figure 10).

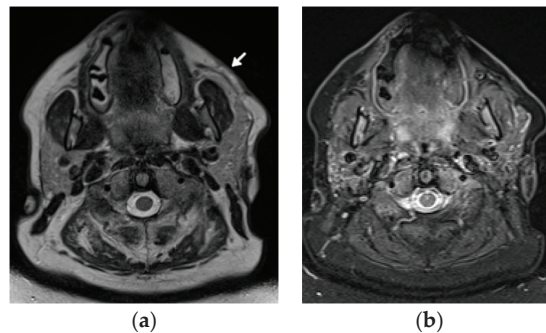


Figure 10. A 48-year-old female patient with systemic lupus erythematosus and a long history of lupus panniculitis and post-inflammatory atrophy of the subcutaneous tissues of the left cheek without active inflammation (arrow), seen in (a) the axial T2-weighted time spin echo and (b) T2 turbo inversion recovery magnitude MR images.

US will likely show inflammatory changes and hyperemia along the involved and surrounding subcutaneous adipose layer. However, the main role of US is to exclude an underlying abscess, drainable fluid collection, or mass.

If US is unrevealing, MRI is the imaging modality of choice. The hallmark of LP on MRI is the loss of the normal T1 bright signal within the subcutaneous adipose layer. In active stages, a high signal intensity is seen on the fluid-sensitive sequences with bright, hazy enhancement on the post contrast T1-weighted images with fat saturation. It is important to distinguish LP from lymphoma, which unlike LP, does not track along the fatty tissue planes.

2.5. Bones

2.5.1. Osteonecrosis

The prevalence of osteonecrosis (ON, avascular necrosis) in SLE according to the different authors ranges from 2% to 50% [1,11]. High-dose corticosteroid therapy (>20 mg/day) is undoubtedly the main determining factor, and AVN can develop within the first months of the initiation of treatment [1,6]. In SLE patients, ON occurs more frequently than in patients with other diseases that are treated alike [11]. Only 5–10% of patients are symptomatic [6]. The hips (femoral head accounts for >70%), knees, and shoulders are most commonly affected, but the ON of small bones can also occur [1,6].

Conventional radiography typically does not show any distinct pathology in the early phase of the disease, whereas the presence of subchondral sclerosis already infers irreversible osseous damage [1] (Figure 1). Abnormal findings in ON include a ‘crescent sign’, representing subchondral collapse; cyst-like or sclerotic changes; an abnormal contour; and the collapse of the femoral head with subsequent secondary degenerative changes [22]. MRI is the most sensitive modality in the diagnosis and quantification of the extent of ON [2,11,22]. Classic findings of medullary bone edema are observed on the fluid-sensitive sequences with fat saturation, with linear areas of low signal intensity inside representing the separation of normal and necrotic bones and the outer increased linear signal related to the vascularity of granulation tissue [11,22]. Whole-body MRIs may detect multifocal ON. Bone scans are less specific for the diagnosis of ON. Other limitations include the radiation dose, poor spatial resolution, and inability to quantify the lesion for prognostic purposes [22].

2.5.2. Osteoporosis and Insufficiency Fractures

Many factors, such as renal failure, amenorrhea, early menopause, chronic inflammatory cytokines, and mainly, the chronic use of corticosteroids and anticoagulants, are involved in the genesis of osteoporosis in SLE [1]. Particularly in patients with SLE, the latter is a determining factor in the development of insufficiency fractures of the spine and other sites (particularly lower limbs). The prevalence of upper osteoporotic vertebral fractures in a study of Bultink et al. on 107 SLE patients was >20% [23].

Imaging modalities used in the assessment of osteoporosis include conventional radiography, conventional computer tomography (CT), dual-energy X-ray absorptiometry (DXA), quantitative CT, quantitative US, and MRI [24]. Today, radiography and DXA are the techniques of choice for vertebral fracture identification, whereas CT and MRI are used for characterization (dating and differential diagnosis) [25] (Figure 11).

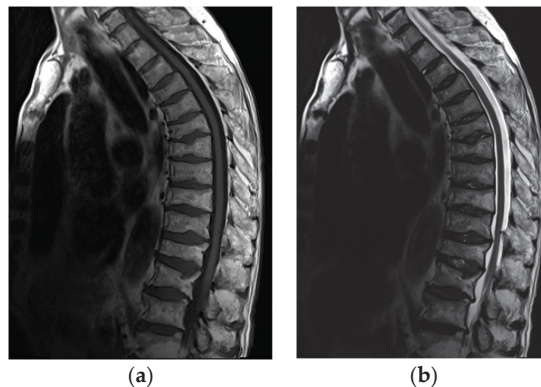


Figure 11. MRI of the spine in a 61-year-old patient with systemic lupus erythematosus with multiple compression fractures. (a) Sagittal T1-weighted and (b) T2-weighted Time Spin Echo MR images of the thoracic spine show a loss of height in nearly all thoracic and L1 and L2 vertebral bodies without significant bone marrow edema in (b). This is consistent with chronic compression fractures with associated disc dehydration and marginal endplate osteophytes, but without significant retropulsion.

2.5.3. Calcifications and Acro-Osteolysis

Two types of periarticular calcifications occasionally occur in patients with SLE [6] (Figure 5). The first is dystrophic, like in dermatomyositis (DM), polymyositis (PM), systemic sclerosis, and mixed connective tissue disease (MCTD). The second is skin calcifications, like in calcinosis cutis [6].

Acro-osteolysis/acral resorption of distal phalanges and acral sclerosis may occur and are nonspecific for SLE. The acro-osteolysis is more frequently seen in scleroderma,

hyperparathyroidism, and psoriatic arthritis (PsA) [6]. Acral sclerosis is seen in 10–12% of SLE patients, as found on radiographs by Braunstein et al. [26], but also may occur in RA, scleroderma, DM, sarcoidosis, and normal individuals [6].

3. Special Features of Juvenile Systemic Lupus Erythematosus

Childhood/juvenile systemic lupus erythematosus (jSLE, juvenile-onset SLE) has its onset before 18 years of age and accounts for up to 20% of SLE patients [11,27]. In contrast to the adult form, the adolescent onset of lupus is more aggressive and has worse outcomes, as found by a matched, multi-ethnic case–control study by Tucker et al. [28]. MSK symptoms were present in 60–90% of jSLE patients, depending on the study type, as analyzed by Levy et al. [24]. They include—like in adults—SLE-specific features (arthritis, tenosynovitis, myositis, osteitis, calcifications), disease-associated complications (osteoporosis and ON with insufficiency fractures), and infections [29].

3.1. Articular and Periarticular Abnormalities

The most common, and usually the first, sign of arthritis is transient joint inflammation, most often involving the knees, ankles, hands, wrists, and less often, the elbow joints [11]. The arthritis is almost always nonerosive and nondeforming, migratory, and reversible [11,29].

Out of the three forms of deforming arthropathy concerning the hand, including mildly deforming arthropathy, Jaccoud’s arthropathy (JA), and rhyphus hand, the last is not observed in children [11]. Moreover, JA is extremely rare, and epidemiology for the pediatric population is not available [11].

The imaging approach, like in adults, is based on radiography and US. Reversible deformities may be seen on PA and on the oblique views. US findings are similar to those seen in adults [11]. The prevalence of wrist synovitis found in a prospective study on 30 juveniles with SLE is 10.3%, as compared to 80% in adults [30].

Over time, ligamentous laxity and the instability of supporting structures may become fixed, resulting in contractures and muscle atrophy [11]. Dynamic US has the ability to differentiate contractures from tendons tears, although the latter is very rarely seen in children.

3.2. Myositis

Inflammatory myopathy is more common in children than adults. It is unclear if myositis is secondary to SLE, or is primary and only coexists with SLE [11]. MRI is the imaging method of choice with a supplementary application of US, including an assessment of vascularity and tissue elasticity with SWE.

3.3. Osteonecrosis and Insufficiency Fracture

In jSLE, ON is also observed, but less frequently than in adults [31]. Low bone mineral density related to corticosteroid use is frequent, and it is associated with an increased fracture risk, with a higher prevalence of upper spine vertebral fractures as well as at other sites, particularly the lower limbs [11]. However, risk factors for jSLE-related bone impairment are poorly understood [32]. Dual-energy X-ray absorptiometry (DXA) is the most widely used clinical tool for the assessment of bone density in children [33].

Diagnosis of ON and fractures is based on MRI in early stages (Figure 12) and radiography in advanced stages, like in adults.



Figure 12. Magnetic resonance (MR) imaging of the femoral head osteonecrosis (ON) in a 14-year-old female with juvenile systemic lupus erythematosus. (a) Coronal and (b) axial proton density-weighted with fat saturation (right) MR images of the pelvis and right hip show a geographic serpiginous lesion in the right femoral head, with a bone marrow edema irregular contour and demarcation line consistent with ON (arrow).

4. Conclusions

Conventional radiography, US, and MRI have their specific applications in imaging of the MSK system's involvement in SLE. Radiography is an important modality for differential diagnosis and treatment monitoring, including post-operative evaluation [3]. US is helpful in the case of an early disease or clinically evident synovitis. Both radiography and US are important tools in the differentiation between JA and RA, clinically presenting the same malalignments. MRI is useful in the assessment of soft tissue inflammation, BME, and erosive bone changes, and it is the imaging modality of choice in the early diagnosis of some complications such as ON, insufficiency fractures, or osteomyelitis.

Despite the clear advantages of US and MRI, an improved description and quantification of lupus arthritis is needed to move lupus treatment into an era of precision medicine [4]. In 2003, early investigations with MRI noted the different features of SLE arthritis compared with RA, particularly the presence of edematous tenosynovitis and capsular swelling. Since that time, a few new evaluations of lupus arthritis using MRI have been reported [4]. Still, contrary to RA, there is no scoring to measure the intensity of the inflammation of SLE on imaging. Further research is therefore needed to address specific imaging characteristics of SLE, in order both to increase the awareness of such findings among the radiological community and to be able to better serve clinicians in early diagnosis and treatment follow-ups.

Author Contributions: Resources, M.O., P.G. and S.O.; Supervision, I.S.-S.; Visualization, E.Ž.; Writing—original draft, I.S.-S.; Writing—review & editing, E.Ž., M.O., P.G., D.J.P. and M.S.T. All authors have read and agreed to the published version of the manuscript.

Funding: This review received no external funding.

Institutional Review Board Statement: Not applicable.

Informed Consent Statement: Not applicable.

Conflicts of Interest: The authors declare no conflict of interest.

References

1. Ribeiro, D.S.; de Araújo Neto, C.; D'Almeida, F. Imaging findings of musculoskeletal disorders associated with systemic lupus erythematosus. *Radiol. Bras.* **2011**, *44*, 52–58. [[CrossRef](#)]
2. Honghu, T.; Yi, L.; Hua, Z. Comparison of Role of Hand and Wrist Ultrasound in Diagnosis of Subclinical Synovitis in Patients with Systemic Lupus Erythematosus and Rheumatoid Arthritis: A Retrospective, Single-Center Study. *Med. Sci. Monit.* **2020**, *26*, e926436. [[CrossRef](#)]
3. Ceccarelli, F.; Perricone, C.; Cipriano, E.; Massaro, L.; Natalucci, F.; Capalbo, G.; Leccese, I.; Bogdanos, D.; Spinelli, F.R.; Alessandri, C.; et al. Joint involvement in systemic lupus erythematosus: From pathogenesis to clinical assessment. *Semin. Arthritis Rheum.* **2017**, *47*, 53–64. [[CrossRef](#)]

4. Zollars, E.S.; Hyer, M.; Wolf, B.; Chapin, R. Measuring lupus arthritis activity using contrasted high-field MRI. Associations with clinical measures of disease activity and novel patterns of disease. *Lupus Sci. Med.* **2018**, *5*, e000264. [[CrossRef](#)] [[PubMed](#)]
5. Greenspan, A. Connective tissue arthropathies. Systemic lupus erythematosus. In *Imaging in Rheumatology*; Greenspan, A., Gershwin, A.E., Eds.; Wolters Kluwer: Philadelphia, PA, USA, 2018; pp. 310–313.
6. Weissman, M.D.; Barbara, N. Systemic lupus erythematosus and related conditions and vasculitis syndrome. In *Imaging of Arthritis and Metabolic Bone Disease*; Weisman, B.N., Ed.; Elsevier: Philadelphia, PA, USA, 2009; pp. 376–382.
7. Iagnocco, A.; Ceccarelli, F.; Rizzo, C.; Truglia, S.; Massaro, L.; Spinelli, F.R.; Vavala, C.; Valesini, G.; Conti, F. Ultrasound evaluation of hand, wrist and foot joint synovitis in systemic lupus erythematosus. *Rheumatology* **2013**, *53*, 465–472. [[CrossRef](#)] [[PubMed](#)]
8. A Guillén-Astete, C.; Revenga-Martinez, M.; Zea-Mendoza, A.; Brito-Brito, E. Prevalence of subclinical synovitis of the hand in patients with systemic lupus erythematosus. *Lupus* **2020**, *29*, 1423–1429. [[CrossRef](#)] [[PubMed](#)]
9. Sudoł-Szopińska, I.; Matuszewska, G.; Pracoń, G. *Radiographic Atlas of Inflammatory Rheumatic Diseases*; Medisfera: Otwock, Poland, 2022.
10. Sudoł-Szopińska, I.; Teh, J.; Cotten, A. Rheumatoid Hand and Other Hand-deforming Rheumatic Conditions. *Semin. Musculoskelet. Radiol.* **2021**, *25*, 232–245. [[CrossRef](#)]
11. Pracoń, G.; Gómez, M.P.A.; Simoni, P.; Gietka, P.; Sudoł-Szopińska, I. Conventional Radiography and Ultrasound Imaging of Rheumatic Diseases Affecting the Pediatric Population. *Semin. Musculoskelet. Radiol.* **2021**, *25*, 68–81. [[CrossRef](#)]
12. Bywaters, E.G.L. The relation between heart and joint disease including “rheumatoid heart disease” and chronic post-rheumatic arthritis (type Jaccoud). *Br. Heart J.* **1950**, *12*, 101–131. [[CrossRef](#)]
13. Van Vugt, R.M.; Derksen, R.H.W.M.; Kater, L.; Bijlsma, J.W.J. Deforming arthropathy or lupus and rhuypus hands in systemic lupus erythematosus. *Ann. Rheum. Dis.* **1998**, *57*, 540–544. [[CrossRef](#)]
14. Piga, M.; Saba, L.; Gabba, A.; Congia, M.; Balestrieri, A.; Mathieu, A.; Cauli, A. Ultrasonographic assessment of bone erosions in the different subtypes of systemic lupus erythematosus arthritis: Comparison with computed tomography. *Arthritis Res. Ther.* **2016**, *18*, 222. [[CrossRef](#)] [[PubMed](#)]
15. Naredo, E.; Rodriguez-Garcia, S.C.; Terslev, L.; Martinoli, C.; Klauser, A.; Hartung, W.; Hammer, H.B.; Cantisani, V.; Zaottini, F.; Vlad, V.; et al. The EFSUMB Guidelines and Recommendations for Musculoskeletal Ultrasound—Part II: Joint Pathologies, Pediatric Applications, and Guided Procedures. *Ultraschall Med. Eur. J. Ultrasound* **2021**, *43*, 252–273. [[CrossRef](#)]
16. Mahmoud, K.; Zayat, A.S.; Yusof, Y.; Dutton, K.; Teh, L.S.; Yee, C.-S.; D’Cruz, D.; Ng, N.; Isenberg, D.; Ciurtin, C.; et al. Ultrasound to identify systemic lupus erythematosus patients with musculoskeletal symptoms who respond best to therapy: The US Evaluation For mUculoskeletal Lupus longitudinal multicentre study. *Rheumatology* **2021**, *60*, 5194–5204. [[CrossRef](#)]
17. Bamber, J.; Cosgrove, D.; Dietrich, C.F.; Fromageau, J.; Bojunga, J.; Calliada, F.; Cantisani, V.; Correias, J.-M.; D’Onofrio, M.; Drakonaki, E.E.; et al. EFSUMB Guidelines and Recommendations on the Clinical Use of Ultrasound Elastography. Part 1: Basic Principles and Technology. *Ultraschall Med.* **2013**, *34*, 169–184. [[CrossRef](#)] [[PubMed](#)]
18. Alves, E.M.; Macieira, J.C.; Borba, E.; Chiuchetta, F.A.; Santiago, M.B. Spontaneous tendon rupture in systemic lupus erythematosus: Association with Jaccoud’s arthropathy. *Lupus* **2010**, *19*, 247–254. [[CrossRef](#)] [[PubMed](#)]
19. Endo, Y.; Miller, T.T. Myositis and fasciitis: Role of imaging. *Semin. Musculoskelet. Radiol.* **2018**, *22*, 286–298.
20. Di Matteo, A.; Smerilli, G.; Cipolletta, E.; Wakefield, R.J.; De Angelis, R.; Risa, A.M.; Salaffi, F.; Farah, S.; Villota-Eraso, C.; Maccarrone, V.; et al. Muscle involvement in systemic lupus erythematosus: Multimodal ultrasound assessment and relationship with physical performance. *Rheumatology* **2022**, keac196. [[CrossRef](#)]
21. Kimball, H.; Kimball, D.; Siroy, A.; Tuna, I.; Boyce, B.J.; Albayram, M.S. Novel diagnostic imaging features of facial lupus panniculitis: Ultrasound, CT, and MR imaging with histopathology correlate. *Clin. Imaging* **2019**, *58*, 177–181. [[CrossRef](#)]
22. Chan, K.L.; Mok, C.C. Glucocorticoid-Induced Avascular Bone Necrosis: Diagnosis and Management. *Open Orthop. J.* **2012**, *6*, 449–457. [[CrossRef](#)]
23. Bultink, I.E.; Lems, W.F.; Kostense, P.J.; Dijkmans, B.A.C.; Voskuyl, A.E. Prevalence of and risk factors for low bone mineral density and vertebral fractures in patients with systemic lupus erythematosus. *Arthritis Rheum.* **2005**, *52*, 2044–2050. [[CrossRef](#)]
24. Fan, Y.L.; Peh, W.C.G. Radiology of Osteoporosis: Old and New Findings. *Semin. Musculoskelet. Radiol.* **2016**, *20*, 235–245. [[CrossRef](#)] [[PubMed](#)]
25. Bazzocchi, A.; Guglielmi, G. Vertebral Fracture Identification. *Semin. Musculoskelet. Radiol.* **2016**, *20*, 317–329. [[PubMed](#)]
26. Braunstein, E.M.; Weissman, B.N.; Sosman, J.L.; Schur, P.H. Radiologic findings in late-onset systemic lupus erythematosus. *Am. J. Roentgenol.* **1983**, *140*, 587–589. [[CrossRef](#)]
27. O’Leary, D.; O’Connor, C.; Nertney, L.; MacDermott, E.J.; Mullane, D.; Franklin, O.; Killeen, O.G. Juvenile systemic lupus erythematosus presenting as pancarditis. *Pediatr. Rheumatol.* **2019**, *17*, 71. [[CrossRef](#)] [[PubMed](#)]
28. Tucker, L.; Uribe, A.; Fernández, M.; Vilá, L.; McGwin, G.; Apte, M.; Fessler, B.; Bastian, H.; Reveille, J.; Alarcón, G. Adolescent onset of lupus results in more aggressive disease and worse outcomes: Results of a nested matched case-control study within LUMINA, a multiethnic US cohort (LUMINA LVII). *Lupus* **2008**, *17*, 314–322. [[CrossRef](#)]
29. Levy, D.M.; Kamphuis, S. Systemic Lupus Erythematosus in Children and Adolescents. *Pediatr. Clin. N. Am.* **2012**, *59*, 345–364. [[CrossRef](#)]
30. Demirkaya, E.; Özçakar, L.; Türker, T.; Haghari, S.; Ayaz, N.A.; Bakkaloğlu, A.; Özen, S. Musculoskeletal sonography in juvenile systemic lupus erythematosus. *Arthritis Care Res.* **2009**, *61*, 58–60. [[CrossRef](#)]

31. Gurion, R.; for the Atherosclerosis Prevention in Pediatric Lupus Erythematosus Investigators; Tangpricha, V.; Yow, E.; Schanberg, L.E.; McComsey, G.A.; Robinson, A.B. Avascular necrosis in pediatric systemic lupus erythematosus: A brief report and review of the literature. *Pediatr. Rheumatol.* **2015**, *13*, 13. [[CrossRef](#)]
32. de Sousa, L.F.A.; Paupitz, J.A.; Aikawa, N.E.; Takayama, L.; Caparbo, V.F.; Pereira, R.M.R. Risk factors for bone loss in juvenile-onset systemic lupus erythematosus: A prospective study. *Lupus* **2019**, *28*, 1224–1232. [[CrossRef](#)]
33. Adams, J.E. Bone Densitometry in Children. *Semin. Musculoskelet. Radiol.* **2016**, *20*, 254–268. [[CrossRef](#)]



Review

Imaging in Hip Arthroplasty Management Part 2: Postoperative Diagnostic Imaging Strategy

Charles Lombard ¹, Pierre Gillet ^{2,3}, Edouard Germain ¹, Fatma Boubaker ¹, Alain Blum ^{1,2},
Pedro Augusto Gondim Teixeira ^{1,2} and Romain Gillet ^{1,2,*}

¹ Guilloz Imaging Department, Central Hospital, University Hospital Center of Nancy, 29 Avenue du Maréchal de Lattre de Tassigny, F-54000 Nancy, France; c.lombard@chru-nancy.fr (C.L.); e.germain@chru-nancy.fr (E.G.); f.boubaker@chru-nancy.fr (F.B.); alain.blum@gmail.com (A.B.); ped_gt@hotmail.com (P.A.G.T.)

² Université de Lorraine, CNRS, IMoPA, F-54000 Nancy, France; pierre.gillet@univ-lorraine.fr

³ Laboratoire de Pharmacologie-Toxicologie, Pharmacovigilance & CEIPA, Bâtiment de Biologie Médicale et de Biopathologie, CHRU de Nancy-Brabois, 5 Rue du Morvan, F-54500 Vandœuvre-Lès-Nancy, France

* Correspondence: r.gillet@chru-nancy.fr; Tel.: +33-3-83-85-21-61; Fax: +33-3-83-85-97-25

Abstract: Hip arthroplasty (HA) is a frequently used procedure with high success rates, but 7% to 27% of the patients complain of persistent postsurgical pain 1 to 4 years post-operation. HA complications depend on the post-operative delay, the type of material used, the patient's characteristics, and the surgical approach. Radiographs are still the first imaging modality used for routine follow-up, in asymptomatic and painful cases. CT and MRI used to suffer from metallic artifacts but are nowadays central in HA complications diagnosis, both having their advantages and drawbacks. Additionally, there is no consensus on the optimal imaging workup for HA complication diagnosis, which may have an impact on patient management. After a brief reminder about the different types of prostheses, this article reviews their normal and pathologic appearance, according to each imaging modality, keeping in mind that few abnormalities might be present, not anyone requiring treatment, depending on the clinical scenario. A diagnostic imaging workup is also discussed, to aid the therapist in his imaging studies prescription and the radiologist in their practical aspects.

Keywords: hip; arthroplasty; CT; MRI; loosening

Citation: Lombard, C.; Gillet, P.; Germain, E.; Boubaker, F.; Blum, A.; Gondim Teixeira, P.A.; Gillet, R. Imaging in Hip Arthroplasty Management Part 2: Postoperative Diagnostic Imaging Strategy. *J. Clin. Med.* **2022**, *11*, 4416. <https://doi.org/10.3390/jcm11154416>

Academic Editors: Iwona Sudol-Szopińska and Mihra Taljanovic

Received: 22 May 2022

Accepted: 24 July 2022

Published: 29 July 2022

Publisher's Note: MDPI stays neutral with regard to jurisdictional claims in published maps and institutional affiliations.



Copyright: © 2022 by the authors. Licensee MDPI, Basel, Switzerland. This article is an open access article distributed under the terms and conditions of the Creative Commons Attribution (CC BY) license (<https://creativecommons.org/licenses/by/4.0/>).

1. Introduction

Hip arthroplasty (HA) is a frequently used procedure with high success rates, its main indications being osteoarthritis, acute fracture, osteonecrosis of the femoral head, and hip dysplasia. Despite its good clinical outcomes, 7% to 27% of patients complain of persistent postsurgical pain 1 to 4 years post-operation, with approximately 12% of the patients describing it as a significant issue [1–4]. Follow-up surgery is necessary for about 1.3% of all total hip arthroplasty (THA) cases per year, including all types of complications [2]. HA complications depend on the post-operative delay, the type of material used, the surgical approach, and the patient's comorbidities and activities [5,6]. Imaging in THA patients has several purposes: normal follow-up (to detect complications without clinical symptoms), patients' complaints (to determine or help to determine the cause of the patients' symptoms), biopsy or fluid collection guidance, and planning for the treatment of complications (i.e., implants positioning, bone stock evaluation). Therefore, clinicians must be aware of these factors to comprehensively evaluate patients with HA [7] and order prompt imaging workup for an optimal diagnosis. Radiographs are the first imaging modality used for routine follow-up in asymptomatic and painful cases [7]. CT and MRI used to suffer from metallic artifacts, but are nowadays central in HA complications diagnosis [8–39]. Nuclear medicine studies are helpful when CT and MRI are inconclusive when a complication is

suspected [40] but are beyond the scope of this paper. Ultrasonography is often limited to evaluating periprosthetic soft tissues and image-guided procedures, especially joint fluid aspiration [13]. All imaging modalities should be considered complementary in terms of a diagnostic strategy. In this review, after a brief reminder about the different types of HA implants, we will focus on HA post-operative normal appearance and complications, via an imaging approach, according to each imaging modality. Each imaging technique's place and technical aspect will also be discussed.

2. Types of HA

2.1. Type of Prosthesis and Implants

Acknowledging the prosthesis type is an essential prerequisite to its imaging analysis, concerning its anticipated appearance and potential complications. If not present in the medical file, this information can be reached by a systematic study of the implant's appearance.

A hip replacement can be either a hemi-prosthesis or a total prosthesis (THA), depending on which part of the joint is replaced [37], with different designs of implants, components, bearing surfaces, fixations, and surgical approaches (posterior, direct-lateral, anterolateral, and anterior [8]).

THA can be conventional or resurfacing types and replaces both the femoral and acetabular sides of the hip. The component's analysis must include the acetabular cup, the femoral head, and the femoral stem. Acetabular and femoral components may themselves be modular (neck-head and/or neck-stem junctions) or nonmodular (one piece), the latter being currently uncommon [13]. Therefore, the femoral component might be composed of one, two, or three parts (stem, collar, head) and the acetabular component of one or two (metal-back and insert) pieces. Dual mobility works by containing a three-component system: a socket, a free polyethylene (PE) liner, and a head, allowing mobility between the femoral head and the liner and between the liner and the acetabular cup [41]. "Sandwich" liner refers to a PE insert outlined in its inner face by a ceramic or metallic layer to combine PE elasticity and metal or ceramic resistance, and in its outer surface by an acetabular metal back so that the PE finds itself in a "sandwich" position between two "hard" layers [42]. A resurfacing prosthesis only replaces the proximal femoral head, leaving the native femoral neck and a part of the femoral head intact. This kind of prosthesis is mostly used in younger patients as it preserves bone stock and allows for easier revision than conventional THA [14,32] (Figure 1).

A hemi-prosthesis only replaces the femoral head and can be unipolar (femoral component articulating with the native acetabulum) or bipolar (femoral component articulating with a non-fixated acetabular cup) (Figure 2). Distinguishing a hemi-prosthesis from THA is crucial and can be completed by analyzing acetabular native cartilage and subchondral plate, both preserved in hemiarthroplasty. One must keep in mind that the acetabular cartilage might wear down, leading to a protrusion of the acetabular modular piece, which might be confused with an acetabular THA component. Additionally, a bipolar femoral head has a slightly greater than hemispheric shape, lacks screw holes, and has a smooth outer surface rather than a textured one in case of THA [37].

According to Gulow et al., THA femoral components can be classified as: (1) resurfacing endoprostheses anchoring on the epiphysis, (2) collum endoprostheses solely anchoring on the metaphysis, (3) short collum preserving stems anchoring on the metaphysis with short anchorage on the diaphysis, and (4) conventional stems anchoring on the metaphysis with a long diaphyseal anchorage [43].

Conventional stems can be associated with peri-prosthetic fractures, thigh pain, and proximal stress shielding and expose to the loss of bone stock in case of revision surgery. Therefore, short stems (length inferior to 120 mm) have been developed, as they are thought to induce less stress shielding, preserve bone stock, restrict proximo-distal mismatch, and reduce pain. Even though no long-term data are available, clinical and radiological outcomes are promising [44].

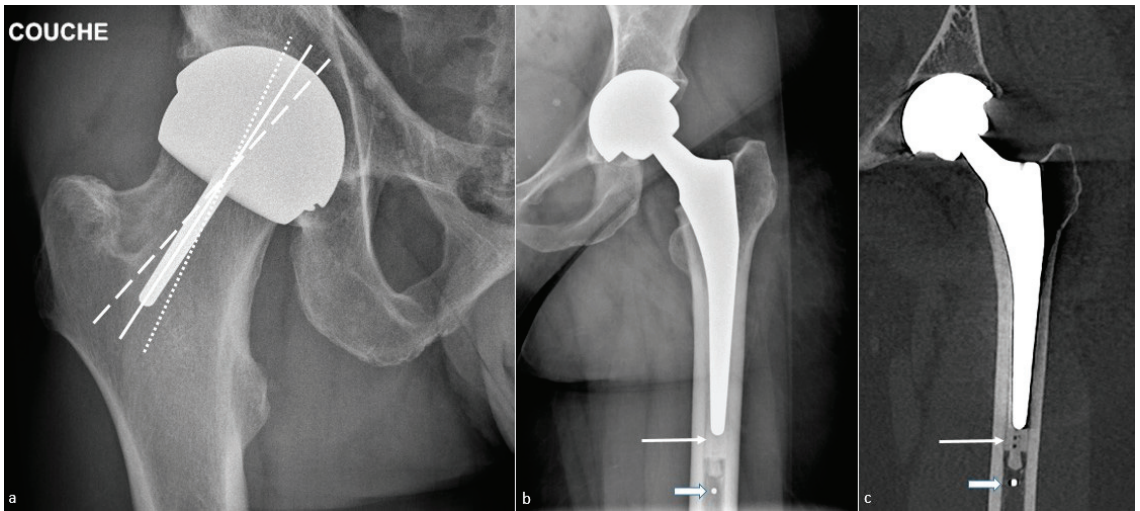


Figure 1. Total hip arthroplasties. A resurfacing arthroplasty is shown on (a) an antero-posterior hip radiograph and a conventional arthroplasty on (b) an antero-posterior hip radiograph and (c) a frontal CT-scan reformat. On (a), note the neutral position of the stem of the femoral component (white line). One should consider that slight valgus can be tolerated (little-dotted white line) and that varus positioning should not occur (large-dotted white line). On (b,c), also note the cement (thin arrow) and a metallic marker at the distal part of a cement restrictor (thick arrow).

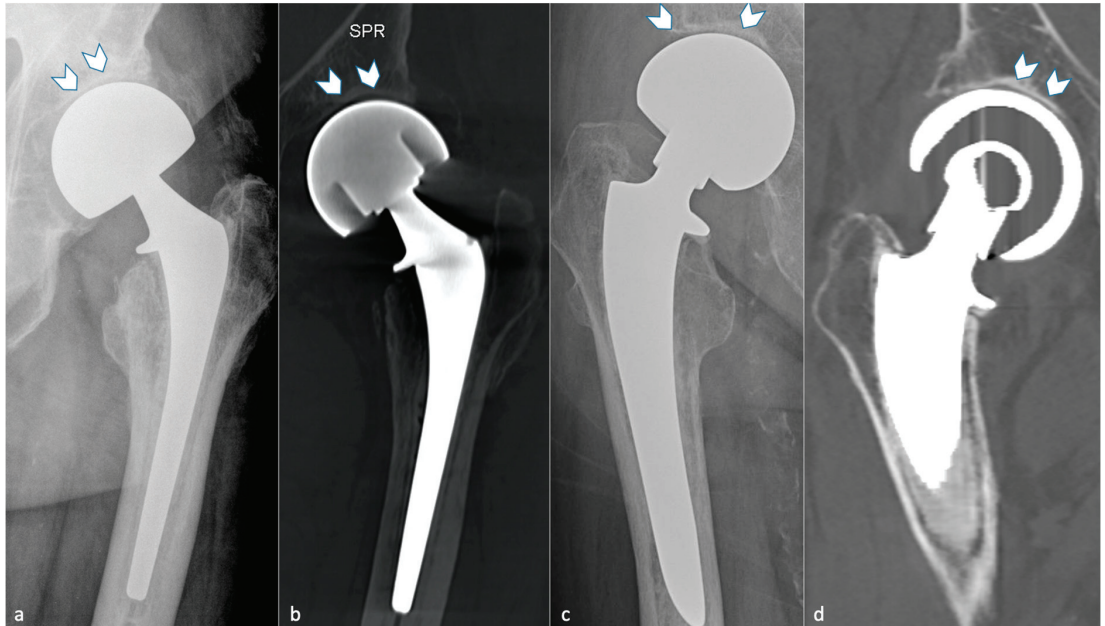


Figure 2. Hip hemi-arthroplasties. A unipolar arthroplasty is shown on (a) an antero-posterior hip radiograph and (b) a coronal slice of CT-MAR. A bipolar arthroplasty is shown on (c) an antero-posterior hip radiograph and on (d) a coronal slice of CT-MAR. Note that the native acetabulum can be seen on all imaging modalities in both cases (white arrowhead).

2.2. Type of Fixation

HA components can be fixed with or without cement, the latter being predominant. Hybrid THA refers to a cemented femoral stem and a cementless acetabular piece, and reverse hybrid THA to the contrary [45].

In cemented femoral components, intramedullary plugs are commonly used and are available in a wide variety of materials and shapes, both biodegradable and non-resorbable. Osteolytic changes around biodegradable models have even been described [46]. Some types of restrictors have a metallic marker that can appear at the tip of the stem (Figure 1). Additionally, a proximal and/or distal centralizer can be used to obtain a uniform cement mantle and neutral alignment of the femoral stem [47]. It is composed of polymethylmethacrylate [48] and can appear as a radiolucent zone not to be mistaken for osteolysis (Figure 3).

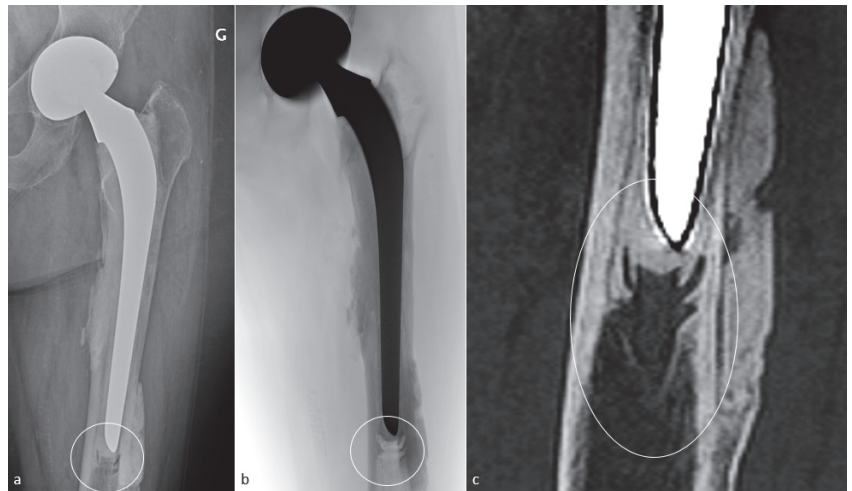


Figure 3. Distal centralizer in a cemented femoral stem. A centralizer is shown on an anteroposterior radiograph (a), a tomosynthesis (b), and a CT-scan reformat (c) (white circle). Note its radiolucent and hypodense aspect.

In cementless fixation, components stimulate osseous incorporation by their geometry or surface texture and coating. They are impacted for primary fixation, then screws can be added for additional security.

It has recently been shown that stem design and cementation impacted post-operative femoral ante-torsion, the cemented ones showing the less variability and lowest rates of retro-torsion [49]. On the other hand, acetabular fixation failure was not encountered in cementless implants in Coden's study, revision being essentially secondary to dislocation [50]. In case of femoral neck fracture in elderly patients, cemented prostheses have better functional outcomes (higher Harris Hip score) and lower rates of revision, fracture, and dislocation than uncemented implants, even though no difference exists in terms of visual analog pain scale, loosening rate, and heterotopic ossification [51].

2.3. Bearing Surfaces

Multiple combinations are possible depending on the joint side. Polyethylene (PE), metal, and ceramic might be used on the acetabular side, whereas, on the femoral side, only ceramic and metal can be. Combinations including PE and ceramic or metal are called "hard-on-soft" (most commonly used) and those without PE "hard-on-hard". The bearing surface is a significant factor in determining the longevity of THA, as worldwide concerns

regarding expanding burden for revision procedures are emerging, secondary to loosening and osteolysis, depending on the type of bearing couples [52].

The four couples used are metal–PE (MoP), ceramic–PE (CoP), metal–metal (MoM), and ceramic–ceramic (CoC) (Figure 4). However, the optimal bearing surfaces are still under debate. PE liners are often used on the acetabular side, regardless of the artificial head [52]. MoM THA with large femoral head diameters have led to a high rate of adverse reactions to metal debris and pseudo-tumors, leading to an almost worldwide cessation of their use and reinforced surveillance [53]. MoP bearing was known to lead to particles disease secondary to contact pressure-induced wear, but recent data showed that the use of an acetabular ultra-high molecular weight PE cup in association with a titanium alloy femoral head could reduce the wear rate compared to cobalt chromium molybdenum and stainless steel so that it can extend the life of THA, in developing countries, especially for Indonesian and, more widely, Asian people [6]. Additionally, to decrease the amount of PE wear debris, alumina ceramics can be used with newer PE, with good long-term functional and radiologic outcomes, so that CoP is thought to be an excellent bearing couple and accounts for more than half of THA in the USA [52]. CoC bearings have been widely used in Korea for economic purposes but can lead to ceramic fractures and squeaking. Those specific complications rate might be dramatically decreased by the use of CoP bearing surfaces [52].

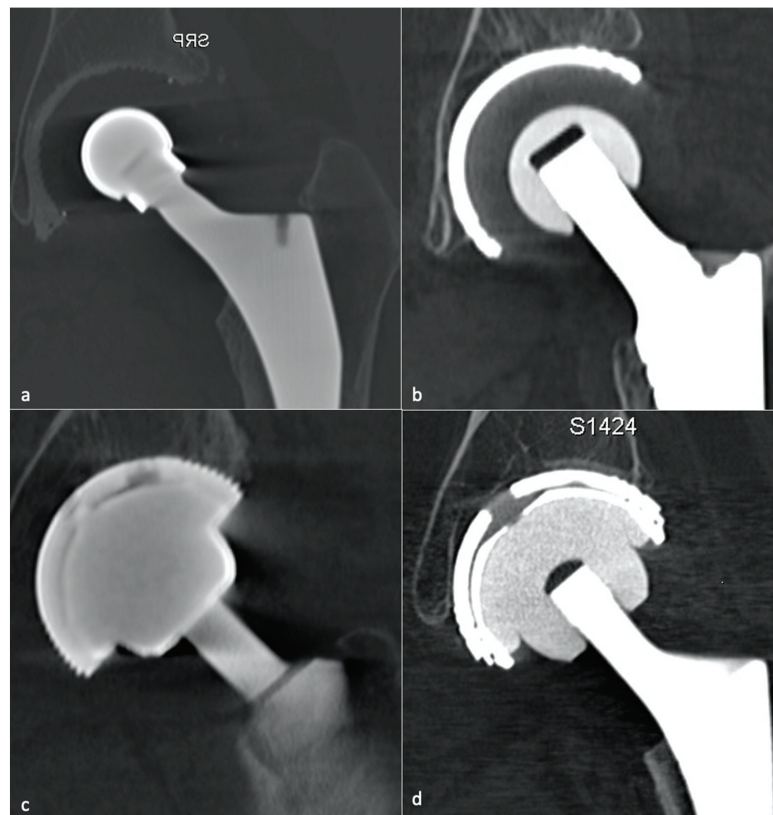


Figure 4. Bearing surfaces. Coronal slices of CT-scan showing on (a) a metal–polyethylene couple, (b) a ceramic–polyethylene couple, on (c) a metal–metal couple, and on (d) a ceramic–ceramic couple. The material can be recognized by its density with a «visual» scale as polyethylene is less dense than ceramic which is itself less dense than metal.

3. Imaging Follow-Up of HA

3.1. Initial Imaging Assessment

As for preoperative planning, radiographic follow-up includes an anteroposterior pelvic view, ideally standing, and an anteroposterior and profile (urethral, surgical, or Lequesne) hip view, ideally in the supine position, covering the whole material. The Lequesne view offers the possibility to measure cup inclination. Radiographs are performed for the standard follow-up and in case of complications, which may require further imaging techniques. CT is indicated in case of normal or equivocal radiographic findings in case of painful hip, for the assessment of osteolysis when revision is considered, for the evaluation of periarticular masses, fluid collections, and soft-tissue ossifications, and to measure component placement [37]. MRI is mainly used in case of complications, especially for imaging soft tissues around the prosthesis, but its place is not clearly defined yet [37].

3.2. Technical Aspects

3.2.1. Computed Tomography

CT acquisition should extend from a few centimeters above the acetabulum to at least 1 cm distal to the tip of the femoral stem (or to the femoral condyles if implant positioning must be checked) with the lowest thickness slice possible and a FOV of approximately 32 cm, concerning the hip. The patient should be placed with a lower limb extended, without pelvic version or rotation, without hip flexion, and foot neutrally rotated [54]. Multiplanar reconstructions must be provided in soft tissue, prosthetic, and bone kernels, with and without metal artifact reduction (MAR) techniques [55]. MAR and native images should both be analyzed as algorithms might change bone and metal appearance (Figure 5). In case of bilateral prostheses, one hip can be elevated during the acquisition to minimize artifacts [54]. Narrower collimation, low pitch (inferior to 1), higher kilovolt peak, and milliamperes seconds value improve image quality [37]. At the author's institution, a single volume is acquired starting 3 cm proximal to the acetabular roof, with the parameters acquisition determined by the patient's body mass index: tube rotation time 0.75–1 s, 120–135 kVp, 100–450 mAs, slice thickness 0.5 mm, FOV 32 cm, and matrix 512 × 512. In case of infection or pseudo-tumor suspicion, iodinated IV contrast media is used for a second acquisition approximately 2 min after injection, allowing a subtraction reconstruction to assess better contrast uptake (subtraction of the non-contrast-enhanced (CE) images from the CE images). Arterial and/or venous-angio-CT (subtracted CT angiography if available) can also be practiced in case of suspicion of vascular pathology [56].

3.2.2. Magnetic Resonance Imaging

MRI used to suffer from metal artifacts but has become a part of the routine workup for patients with THA in many institutions. A pelvic acquisition with a large FOV can be acquired with a body coil or a multichannel surface body coil system. Then, a hip acquisition with a small FOV can be obtained with a multi-channel surface coil, a two-part shoulder coil, or a wrapped coil, extending from the anterior to the posterior skin surface, transversally from the pubic symphysis to the skin surface, and craniocaudally from above the acetabulum to the distal end of the prosthesis [57]. To minimize metal artifacts, the amplitude of the gradient must be increased. Therefore, one should prefer a 1.5 T scanner to a 3 T one (as susceptibility artifacts are proportional to the magnetic field strength) and fast spin-echo (FSE) to echo-gradient (EG) sequences, using high receiver bandwidth and thick sections [57]. Adjusting the direction of the frequency-encoding gradient along the axis of the prosthesis can also diminish artifacts [11]. Slice encoding metal artifact correction (SEMAC) (Siemens Healthcare, Erlangen, Germany) and multi-acquisition variable resonance image combination (MAVRIC) (GE Healthcare, Waukesha, WI, USA) have been shown to reduce metal artifacts and improve the depiction of the synovium and bony interfaces with the implant. Notably, isotropic MAVRIC sequences improve the signal-to-noise ratio, conspicuity of lesions, synovium, and periprosthetic bone depiction with less blurring than conventional MAVRIC sequences, at the price of

a slightly longer acquisition time [39]. A MAVRIC-SEMAC fusion sequence, MAVRIC SL, can acquire proton density, T1 weighted, and STIR images [58]. To improve image quality, an intermediate echo time should be used to obtain fluid-sensitive images, so are a large matrix in the frequency direction (e.g., 512), a high number of excitations, and an inversion-recovery fat suppression (e.g., STIR) [57].

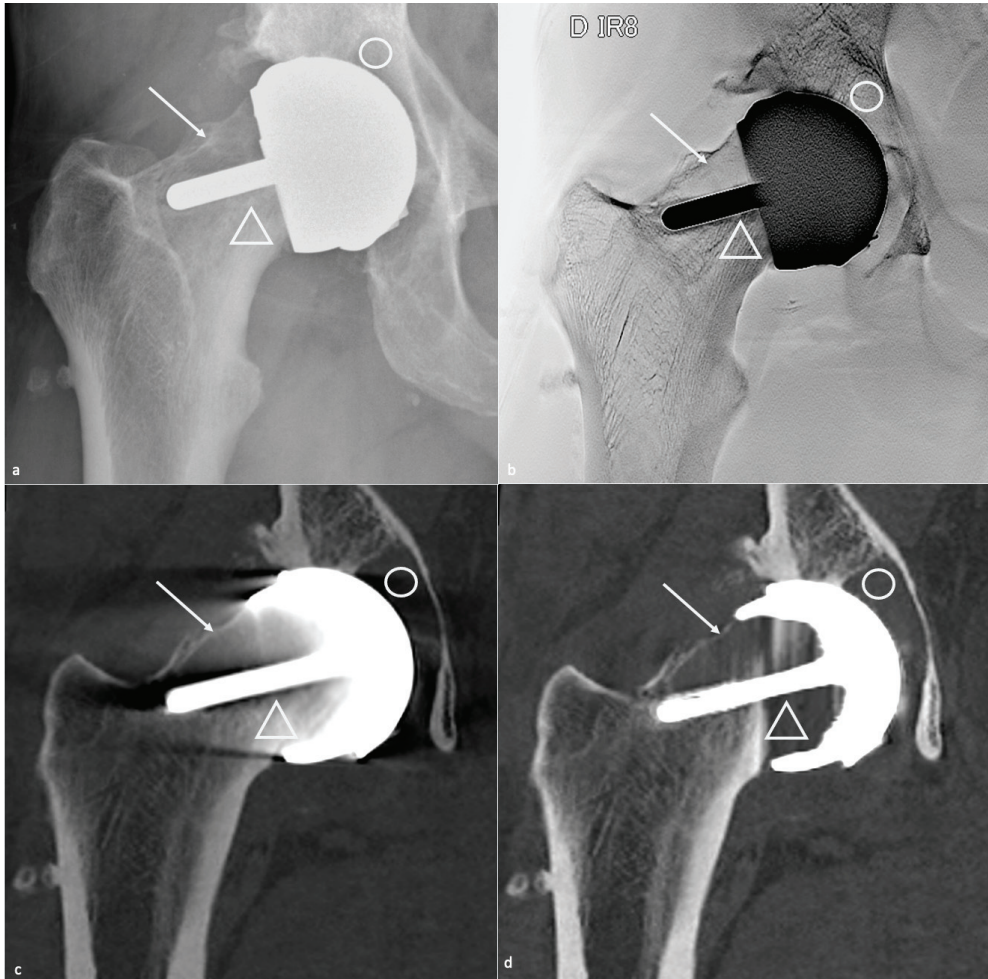


Figure 5. Peri-prosthetic osteolysis. Radiolucent zones are shown on (a) an anteroposterior hip radiograph, (b) an anteroposterior tomosynthesis view, (c) a coronal CT image, and (d) a coronal metal-artifact reduction CT image. All imaging modalities depict true osteolysis in the superomedial acetabulum (grey circle). Superior femoral neck osteolysis (grey arrow) is doubtful on (a,d) but is depicted on tomosynthesis (b) and CT with metal-artifact reduction (d). On the other hand, artefactual osteolysis is seen in (d) (grey triangle), underscoring the need for a combined interpretation of all imaging modalities.

Practically speaking, according to the Radiological Society of North America, intermediate-weighted FSE sequences with a high spatial resolution (periprosthetic bone and soft tissues analysis) and STIR or fat-saturated heavily T2-weighted sequences (fluid and bone marrow edema depiction) should be used [13,57]. T1-weighted and CE sequences

are not always recommended. European teams usually perform T1-weighted sequences, and so does the author’s team. The French Society of Musculo-Skeletal Imaging (SIMS) proposes a 3D-T1-weighted MAVRIC sequence (FOV 40 cm, matrix 352 × 352, slice thickness 1.4 mm) or axial and coronal T1-weighted images (MAVRIC or SEMAC), then axial and coronal ± sagittal STIR images (FOV 46 cm, matrix 3384 × 362, slice thickness 3 mm), for a total acquisition time of approximately 19 min [59], without systematic CE sequences, which should be discussed case by case.

3.3. Implants Positioning and Their Implications

The initial placement of prosthetic components must be checked. A good implant position is mandatory from a functional point of view, but mispositioning can also lead to complications, such as dislocation, impingement, and peri-prosthetic fractures. Therefore, radiologists must assess leg length, acetabular inclination and anteversion, the acetabular center of rotation position, femoral offset (FO), femoral neck anteversion (FNA), and femoral stem position (i.e., varus, valgus, or femoral stem position centered, no displacement over time) (Table 1) [14,31–33,37,60–62].

Table 1. Prosthetic implant positioning and their implications.

Measurement	Normal Value	Consequences of Mispositioning
Leg Length	<0.5–1 cm of differences between both sides	Increased discrepancy: gluteal and iliopsoas muscles affection
Acetabular side		
Frontal acetabular inclination	40 ± 15°	- Decreased: hip abduction limitation - Increased: dislocation risk
Sagittal acetabular inclination	35–40 ± 10° in standing position 52 ± 11° in sitting position	- Increased: posterior impingement, anterior dislocation - Decreased: anterior impingement between the cup and the neck, posterior dislocation
Acetabular anteversion	5–25°	- Lack of anteversion or retroversion: posterior dislocation, iliopsoas impingement - Excessive anteversion: anterior dislocation
Acetabular center of rotation position	Similar to the contralateral hip	Lateralized: dislocation risk
Femoral Offset	41–44 mm (or similar to contralateral hip)	- Decreased: limping, mobility limitation, and dislocation by gluteal muscles weakness - Increased: gluteal muscles pain and polyethylene wear
Femoral side		
Femoral Stem position	Neutral or slight valgus	Periprosthetic fracture and stress reaction in case of varus
Femoral Neck Anteversion	10–15°	- Increased: anterior dislocation and ischio-femoral impingement - Decreased: posterior dislocation
Femoral Head	Centered or slightly inferiorly located	- Particle disease if located upwards (wear)

Leg length discrepancies should not be superior to 0.5–1 cm, as an excessive difference can affect gluteal and iliopsoas muscles [63–65]. In this setting, an EOS-imaging should be performed if available [66].

It has recently been proposed (1) to consider the spine and hip relationship (beyond the scope of this review) and (2) to realize a profile radiographic acquisition in the standing and sitting positions on an EOS system, if available, in the preoperative setting in case of lumbar degenerative pathology, and in case of painful or unstable prosthesis before revision [67].

3.3.1. Acetabular Side

The acetabular vertical center of rotation corresponds to the vertical distance between the center of the femoral head and the trans-ischial tuberosity line, and the horizontal center of rotation to the distance between the center of the femoral head and the teardrop shadow (Figure 6). Those values should be similar to the contralateral hip [32], as a lateralized horizontal center might favor dislocation.

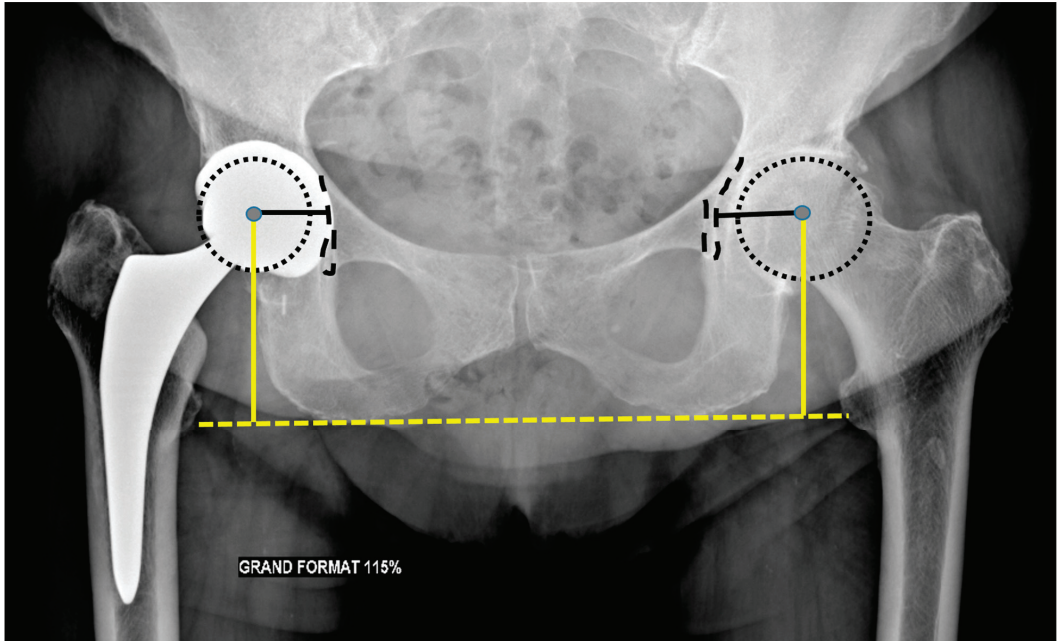


Figure 6. Acetabular centers of rotation. Pelvic anteroposterior radiograph. The horizontal center (black line) corresponds to the distance between the femoral head (dotted circle) center (grey point) and the teardrop (large black dotted curve) shadow, the vertical one (yellow line) to the distance between the center of the femoral head and the transischial line (dotted yellow line).

The frontal acetabular inclination is the angle between the lateral edge of the cup and a transischial tuberosity line in the frontal plane and should be of $40 \pm 15^\circ$, as a lesser angulation would limit hip abduction, whereas a greater one would increase the risk of dislocation [32] and premature wear. The inferomedial border of the acetabular component should be aligned with the bottom of the teardrop on an AP pelvic view (Figure 7).

Acetabular anteversion is the angle between the acetabular axis and the coronal plane. It is usually measured on a profile radiograph and corresponds to the angle between the edge of the acetabulum and a perpendicular line to the horizontal plane [32]. It also can be measured on a CT-scan, at the level of the center of the femoral head, on an axial oblique plane perpendicular to the pelvic axis (defined by the middle of the superior plate of S1 and the center of the femoral heads), regarding the transischial line [68]. Its value should be $5\text{--}25^\circ$, as lack of anteversion or retroversion can lead to posterior dislocation or iliopsoas impingement and excessive anteversion to anterior dislocation (Figure 8).

Sagittal acetabulum inclination corresponds to the angle between the edges of the cup and the horizontal axis in the sagittal plane. Its value should be $35\text{--}40 \pm 10^\circ$ (Figure 8) and $52 \pm 11^\circ$, respectively, in the standing and sitting positions. In the sitting position, a low inclination leads to an anterior impingement between the cup and the neck and a compensative augmentation of hip flexion at risk of posterior dislocation, also favored by a

femoral retroversion. Inversely, in the standing position, an excessive inclination might lead to a posterior impingement and a risk of anterior dislocation [67].

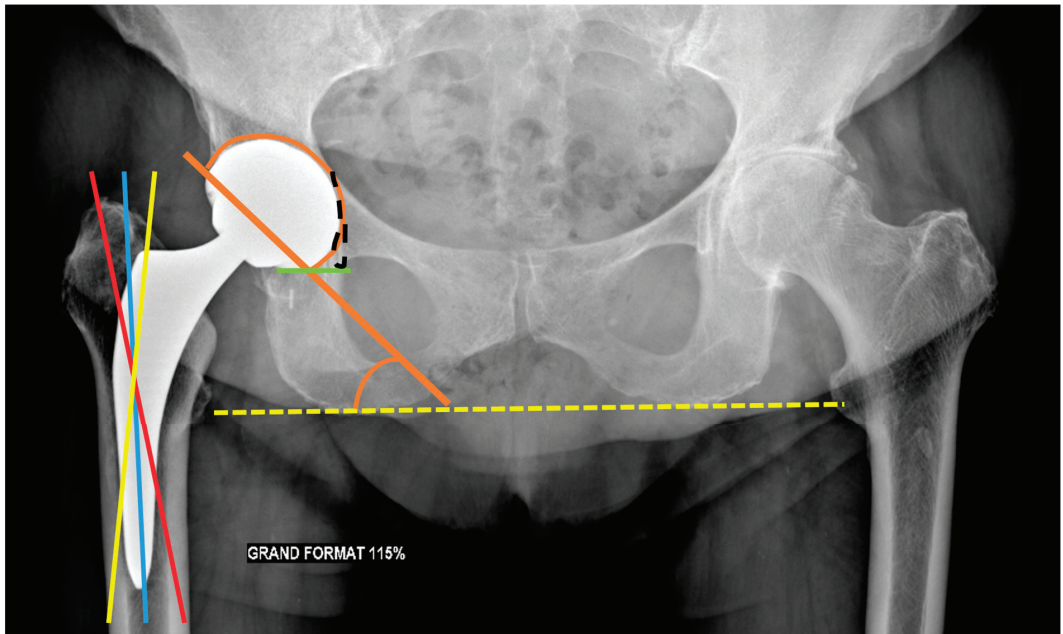


Figure 7. Acetabular frontal inclination and femoral stem position. Pelvic anteroposterior radiograph. The acetabular inclination corresponds to the orange angle between the acetabular piece contour (orange circle) and the transischiatric line (dotted yellow line). Additionally, note that the acetabular piece is aligned (green line) with the bottom of teardrop shadow (dotted black curve). The femoral stem should be placed in a neutral position (blue line). A slight valgus (red line) can be tolerated, but varus (yellow line) should not occur.

Bendaya investigated anatomical pelvic (beyond the scope of this paper) and implant positioning measurements in patients with good versus poor THA outcomes. The only significantly different parameter was acetabular implant position, essentially with lower frontal inclination in the poor prognosis patients' group. Femoral implant and pelvic parameters did not significantly differ between the two groups, but the poor patient's group showed a higher number of parameters deriving from typical values in the standing position only. Those data underscore the need for a global patient analysis better than correcting single parameters to improve planning for both primary and revision surgery [69]. From a functional point of view, a retroversion of the pelvis occurs from standing to sitting position, which also affects the anteversion and inclination of the acetabular implant (6–10° increase for each parameter) [69]. It has been shown that patients who underwent THA without spine disorder had more changes in acetabular implant orientation due to greater adaptability of the spinopelvic junction than patients who had spine fusion, who might be at risk of posterior dislocation because of less femoral head coverage and less acetabular anteversion. Additionally, the more fused levels, the more acetabular anteversion and inclination decrease (about 1° for each fused group for each value) [70]. Therefore, it has been proposed by Lazennec et al. to evaluate lumbosacral junction using standing and sitting EOS imaging or radiographs in patients with spine fusion in THA planning and follow-up [71–73], but this attitude is not yet officially recommended.

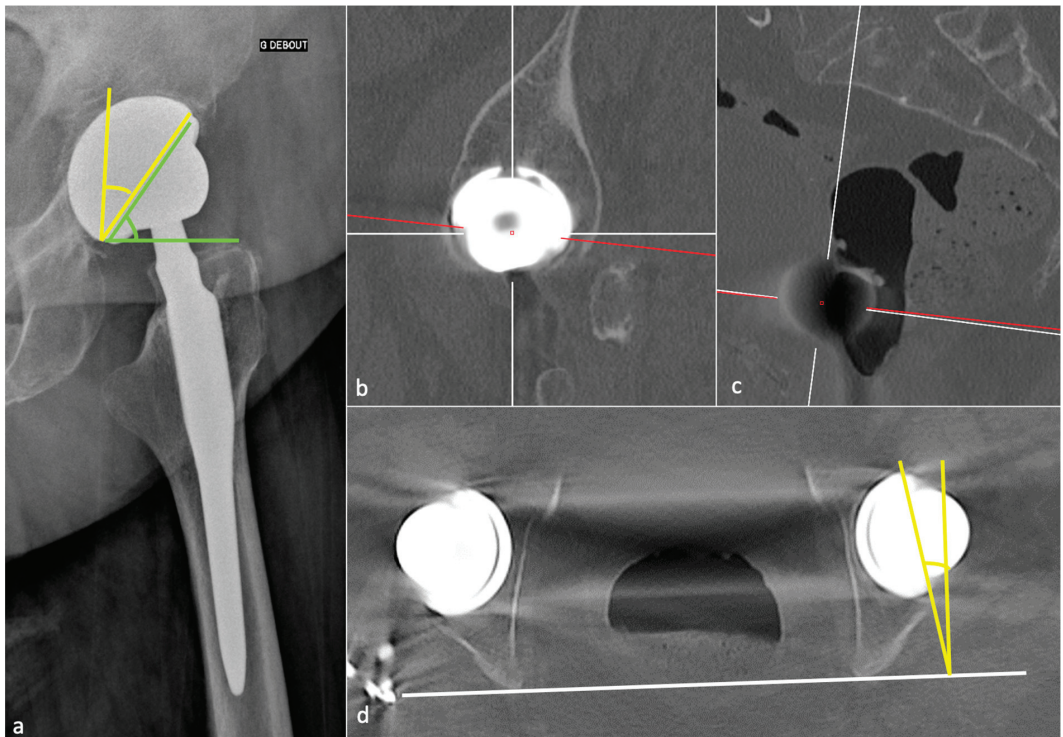


Figure 8. Acetabular cup anteversion and sagittal inclination. The radiographic angle of anteversion is shown on (a) a hip profile radiograph and corresponds to the angle between the vertical axis and the acetabular piece edges (yellow angle). The sagittal acetabular inclination is shown in (a) and corresponds to the angle between the horizontal axis and the acetabular piece edges (green angle). A CT method is then proposed to calculate anteversion: on (b) a sagittal CT slice, one should restore the femoral head center, then align it within the middle of S1 superior plate as shown on (c) in the sagittal plane. The anteversion can be measured in the so-created plane (red lines) on (d), as the yellow angle between the cup edges and the perpendicular line to the transischial line (white line).

3.3.2. Femoral Side

The femoral stem position must be analyzed on a pelvic anteroposterior view and a profile hip view. It should be aligned within the femoral shaft with its tip well centered. Varus mispositioning is associated with pejorative outcomes and can lead to lateral pain with a femoral lateral cortical thickening. Valgus positioning can be tolerated [54] (Figure 7).

The FO should be like the contralateral hip and measure 41–44 mm. This value must be measured on an anteroposterior hip view in neutral rotation, as rotation might induce significant measure variation. It can also be obtained with the EOS system or CT-scan (a method proposed in Figure 9) [54]. A low FO can lead to limping, mobility limitation, and dislocation by gluteal muscles weakness. A loss of FO negatively influences patients' satisfaction after THA [74]. A too high FO might induce gluteal muscle pain because of exacerbated tension and PE wear.

FNA should be 10 to 15° to allow a good hip flexion and can be measured on EOS imaging or CT-scan [75] (by applying the method proposed in part 1 of this paper). An excessive FNA increases the risk of anterior dislocation and ischio-femoral impingement [76]. An insufficient one, or a retroversion, increases the risk of posterior dislocation. It has recently been shown that surgeons should be cautious with the expectation of achieving the femoral stem version of an uncemented prosthesis from the preoperative 3D-CT planning, as the

preoperatively measured and planned stem orientation was never achieved in Belzunce's study (discrepancy of -1.4 ± 8.2 degrees with a 95% confidence interval of $(-16.9, 13.8)$), also with a 2 mm larger FO than the planned one. The latter, however, remained in a normal range [10].

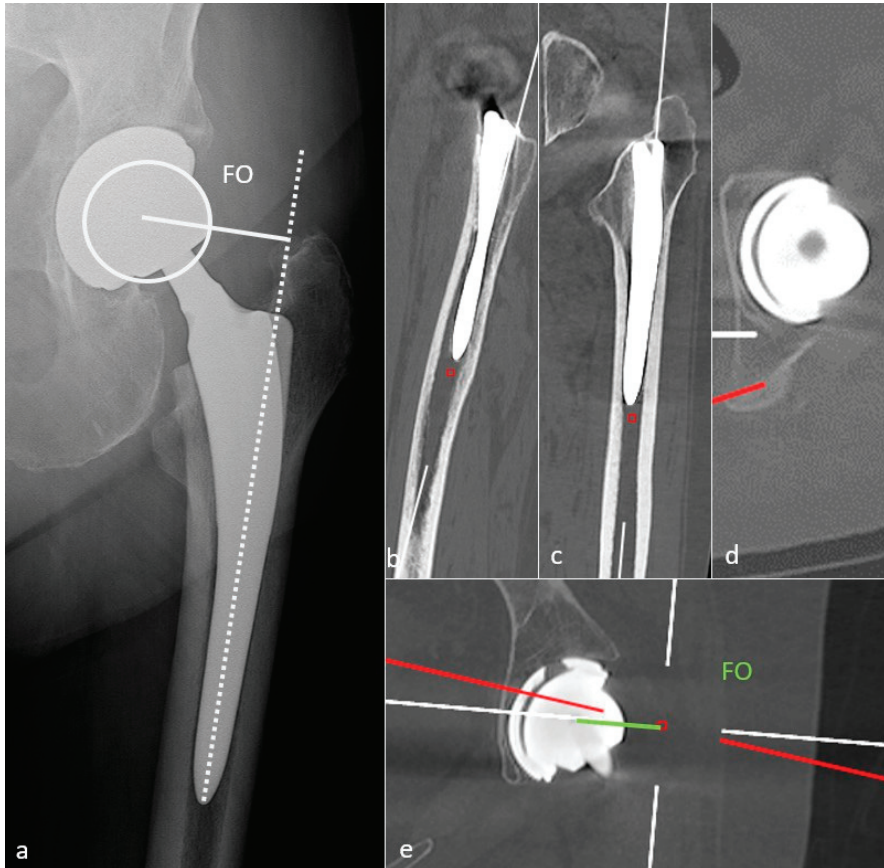


Figure 9. Femoral offset (FO). The radiographic method is shown on (a) an anteroposterior hip view and corresponds to the perpendicular distance (white line) between the femoral head (white circle) and the femoral axis (dotted white line). A CT method is also proposed. First, on (b), in the sagittal plane, the femoral inclination is considered, then on (c) in the frontal plane, and the level of the center of the femoral head is repaired in (d). Finally, in (e), the FO can be measured (green line) as the perpendicular distance between the resulting femoral axis (white vertical line) and the center of the femoral head.

Resurfacing arthroplasty responds to specific issues. Even though the acetabular component position does not differ from other types of prosthesis (lateral inclination of $30\text{--}50^\circ$ and anteversion of $5\text{--}25^\circ$), the femoral component must be placed in a relative valgus position of $5\text{--}10^\circ$ to avoid notching the neck (in case of excessive valgus) and to adequately cover the femoral neck [32] (Figure 1).

The prosthetic femoral head should be centered within the acetabular cup or slightly inferiorly located as the PE liner has a thicker superior rim. In case of PE liner, wear of 0.1 mm/year is considered normal [54]. Therefore, if it is located upwards, it indicates PE wear and should raise suspicion for granulomatous osseous resorption (Figure 10).

Components should not displace over time, and components, screws, or cement should not become fractured. Ensuring the absence of material displacement requires a careful comparison of all available radiographs, including the early post-operative ones. One should know that some types of the prosthetic stem can subside from 1–2 mm, especially superolaterally, but no longer than two years or greater than 1 cm [77].

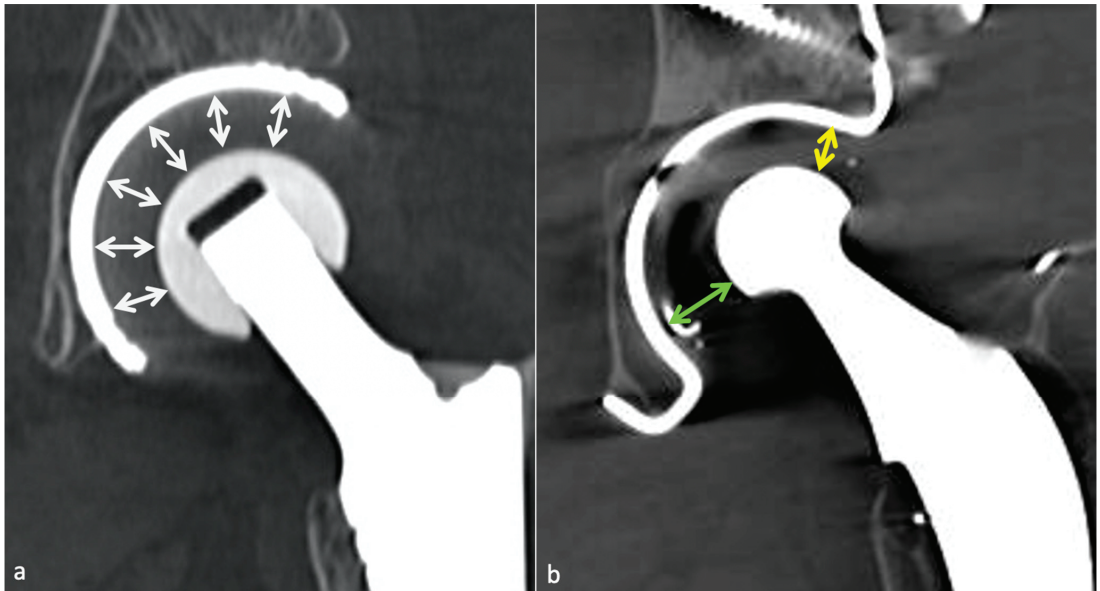


Figure 10. Polyethylene wear. Normal polyethylene appearance is shown in (a) a frontal CT-scan slice, with a regular thickness as all double arrows are equal, whereas wear is shown in (b) a similar frontal CT-scan slice, with asymmetric thickness as the superior yellow double arrow is smaller than the inferior green one.

3.4. Normal Imaging Findings

3.4.1. Radiolucent Zones (Radiographs, Tomosynthesis and CT)

With radiographs or CT, the presence of periprosthetic radiolucent zones (RLZ) might be a normal finding if it meets strict criteria. Pathologic or regular, they should be described according to the classification of De Lee and Charnley for the acetabular component and with the Gruen zones for the femoral component (Figure 11). Concerning resurfacing arthroplasty, three zones are described around the peg [78] (Figure 11). RLZ around the metaphyseal stem of a resurfacing prosthesis are often asymptomatic, and a neck narrowing can be found without clinical significance [79].

A thin linear RLZ in femoral zone 1 is a frequent finding at the component–cement interface; it results from a lack of contact between these structures during surgery and is thought to be expected if stable over time [32]. An irregular interface between cement and cancellous bone, especially in the greater trochanteric region, and a thin radiolucent line outlined by a sclerotic line parallel to the stem along with the bone–cement interface or around the surface of a cementless component (corresponding to a fibrous membrane) are also considered normal, if non-evolutive [32]. Thin RLZ inferior to or equal to 2 mm are considered normal, but one should know that RLZ superior to 2 mm might be acceptable if stable over time, and RLZ inferior to 2 mm might indicate loosening if they appear during follow-up [37]. Air bubbles into the cement are acceptable and should not raise suspicion of infection if isolated [37].

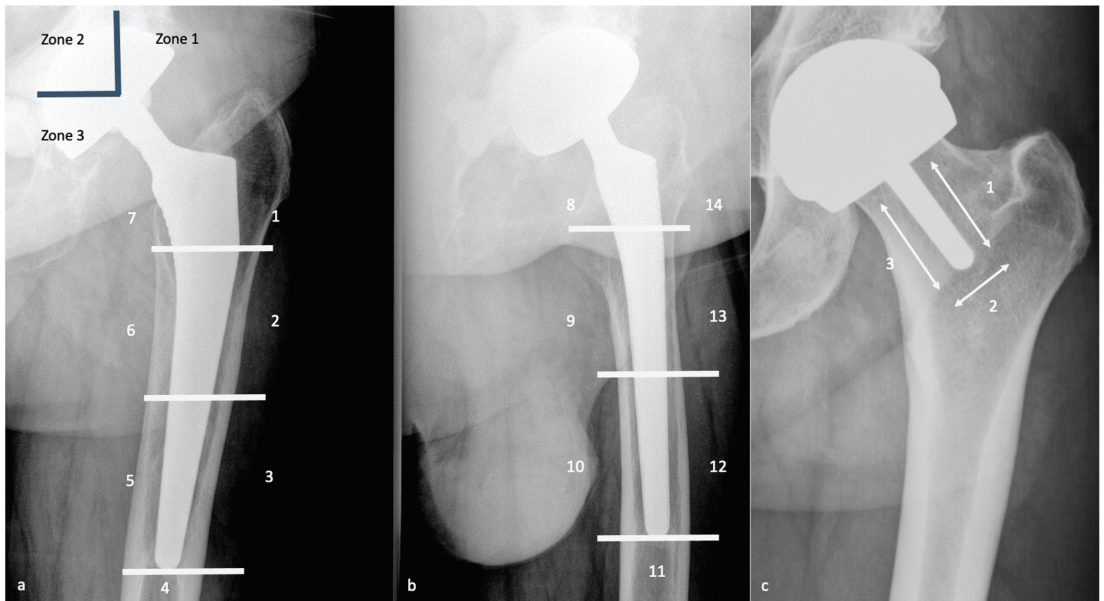


Figure 11. Acetabular and Femoral Zones to be described for osteolysis. The De Lee and Charnley acetabular zones and Gruen 1–7 femoral zones are shown on (a) an anteroposterior hip view, the Gruen 8–14 femoral zones on (b) a profile hip radiograph. The three zones to consider for femoral stem in resurfacing arthroplasties are shown on (c) an anteroposterior hip radiograph.

3.4.2. Adaptative Changes (Radiographs, Tomosynthesis and CT)

Mechanical loading of the hip is assumed by the femoral component in case of HA and transferred distally to the host bone. This results in proximal femoral bone demineralization. Adaptative atrophy also occurs with cementless components in the superomedial acetabulum and in the proximal medial femur within the first two post-operative years and must remain stable. For the same reason, cortical thickening and periosteal reaction at the distal point of the stem reflect successful fixation and appear to be homogeneous and circumstantial in typical cases (Figure 12). Below the tip of the stem, a bone pedestal can occur as a sclerotic transverse line in zone 4, bridging the medullary canal, and can be associated with loosening if it appears or disappears throughout follow-up. Such bone density changes, called “stress shielding”, are secondary to a non-optimal osteointegration and might be asymptomatic or painful (Figure 13). Therefore, follow-up radiographs are mandatory to ensure they do not move into an authentic loosening. In case of uncemented implants, spot welds refer to bone formation from the endosteal surface reaching the prosthesis and indicate stability (Figure 12) [37].

3.4.3. MRI

MRI interpretation is challenging because of an overlap between asymptomatic patients’ imaging findings and clinically relevant ones. The standard post-operative appearance depends not only on the type of implant but also on the post-operative delay. Synovitis, extensive edema or fluid in the implant area, and tracking along soft tissue planes may be encountered in the immediate post-operative time. Over months, soft tissue anomalies tend to regress but may persist along with the surgical incision site or transform into seromas without signs of infection [13]. Signal perturbation related to metal susceptibility often occurs at the superior aspect of the acetabular component and at the femoral stem [13].

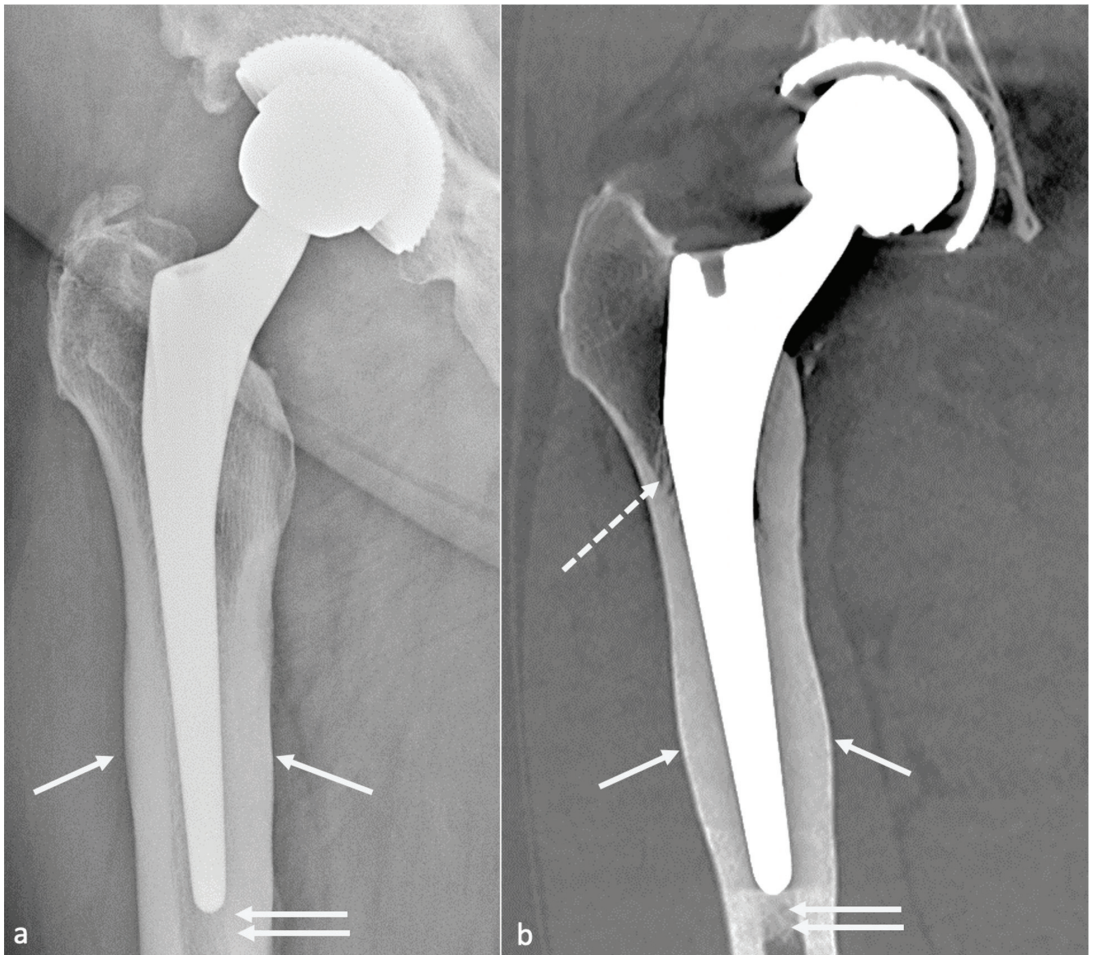


Figure 12. Successful fixation of an uncemented total hip arthroplasty. Regular and circumferential cortical thickening (white arrow) and bony pedestal (double white arrow) are seen on (a) an anteroposterior hip view and (b) a coronal CT-scan slice. Additionally, note spot welds (white dotted arrow) better depicted on CT-scan, and the slight valgus position of the femoral stem, better depicted on the radiograph.

The intact periprosthetic cortex and periosteum appear hypointense on STIR and intermediate-weighted fast SE sequences [57]. Complete osseous integration corresponds to direct contact between a sharply demarcated implant or cement and the surrounding bone without separation [57]. A fibrous membrane at the prosthetic interface can be present and manifest as a hyperintense layer of 1–2 mm thickness, suggesting closer surveillance as its effect on implant fixation is poorly known, to make sure it does not move to loosening (Figure 14) [57]. The normal pseudo-capsule should be thin, of low signal intensity, and closely applied to the neck of the implant. Still, a small amount of post-operative fluid without synovitis is standard [57]. In the author's experience, the pseudo-capsule is not always seen because of artifacts and its interpretation should remain cautious.

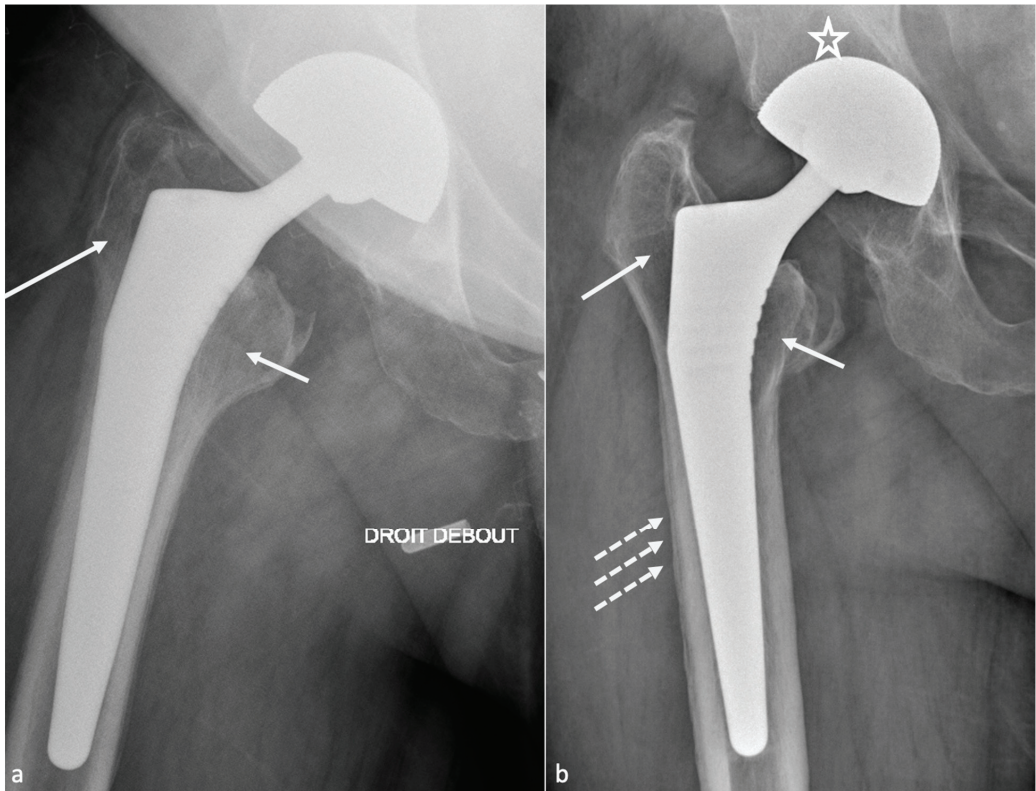


Figure 13. Stress shielding. Post-operative (a) and one-year follow-up (b) radiographs show proximal femoral (white arrows) and superomedial (white star) acetabular demineralization. Additionally, note the subtle lateral unilamellar periosteal reaction (dotted white arrows) on (b), which might be favored by the slight varus position of the stem.

Germann et al. investigated normal MRI findings after uncemented THA for two years and found that:

- Bone marrow edema was frequent all over the femoral stem and in the central acetabular zone at 3 and 6 months after surgery, decreased during follow-up, and sometimes persisted in Gruen zones 1 and 7 overtime, but often in only one area;
- Inferomedial edema in the acetabulum was infrequent and should raise suspicion for pathology;
- Periprosthetic bone resorption was frequent during the second post-operative year in Gruen zones 1 and 8 but never thicker than 2 mm;
- Periosteal edema was shared on the femoral side with a decrease over time, rarely present at two years, and only in non-adjacent Gruen zones, without acetabular side attempt;
- In the first six months, soft-tissue edema was a constant feature in the surgical access route but never occurred in the second year;
- Joint effusion was decreasing over time but could be present in the lateral aspect of the joint capsule at two years [19].

On the other hand, one should know that bone marrow edema in the proximal aspect of the stem is frequent in asymptomatic and symptomatic patients, that osteolysis is thought to be more frequent in symptomatic patients in Gruen zone 7, and periosteal reaction is more frequent in symptomatic patients in Gruen zones 5 and 6 [16].

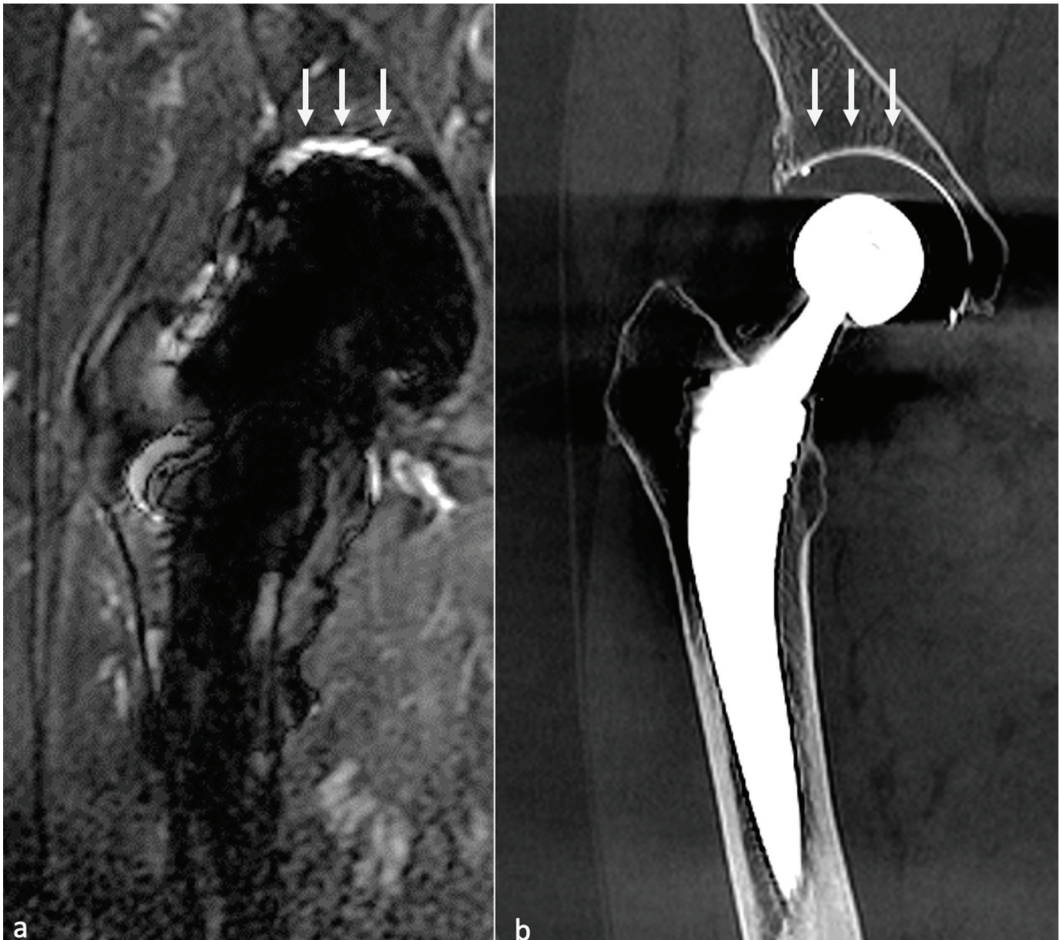


Figure 14. Acetabular fibrous membrane. A thin STIR hyperintense layer (white arrows) is shown close to the acetabular piece on (a) a frontal STIR image, without osteolysis in the corresponding zone on (b) a coronal CT-scan slice.

4. Complications

HA revision mainly concerns instability (dislocation), loosening, and infection. Other complications include periprosthetic fractures, hardware failure, adverse local tissue reactions, component wear-induced synovitis, tendino-muscular pathologies, heterotopic ossification, and neuropathy.

Complications can be classified as common to all kinds of arthroplasties (loosening, dislocation, peri-prosthetic fractures, psoas impingement, heterotopic ossification, implant failure, neurovascular and muscle pathology), and specific to bearing surfaces (MoP: wear and osteolysis; MoM: metallosis, pseudo-tumor, and trunnionosis; CoC: squeaking and prosthetic fracture; CoP: ceramic fracture and wear). Resurfacing arthroplasty complications are developed in a separate section. An imaging-based algorithm is proposed in Figure 15 [80,81].

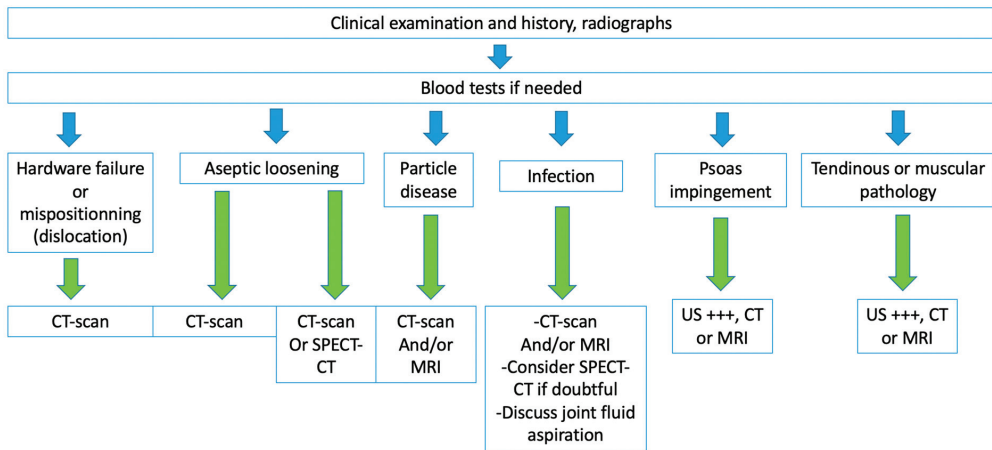


Figure 15. Imaging diagnostic algorithm proposition, adapted from Blum et al. [80,81].

4.1. Dislocation

4.1.1. Background

Dislocation can be early (within three months), of good prognostic with a low rate of recurrence, or late (above three months), with high recurrence risk.

Early dislocations, diagnosed on radiographs, might be secondary to post-operative gluteal muscle weakness and/or articular capsule laxity, non-compliance with post-operative restrictions, trauma, and implant mispositioning [19]. They are also favored by a posterior or anterior approach (respectively, posterior and anterior dislocation) [33]. In patients with femoral neck fractures, the use of the posterior approach increases the risk of dislocation, while a non-significant risk is present in cases of dual mobility cup implantation via the lateral approach [82]. In case of single-event dislocation, radiographs are sufficient. It may be treated with “hip precautions” (exercises and positions to avoid) if components are well-positioned on radiographs and proper hip biomechanics are restored. If no trauma or abnormal movement is declared prior to dislocation, muscular weakness can be suspected. On the other hand, if two or more episodes happen, a CT-scan should be performed to determine implant positioning. However, surgery will be required in about one-third of the patients, with a remaining risk of 21–30% of dislocation after revision [83]. Surgical procedures commonly used include increasing femoral head size, correction of implant mispositioning, use of a dual mobility implant, constrained liner, and soft tissue repair, with various efficacies and proper complications (for instance, increased PE wear for larger femoral head) [83].

Late dislocations are often multifactorial. The main causes are PE wear, loosening of implants, trauma, non-compliance with post-operative restrictions, trochanteric pseudarthrosis, or amyotrophy. After five years post-operative, soft tissue progressive laxity is also incremented [33]. Primary implant mispositioning is not probable if no dislocation occurred in the post-operative period, but it can be secondary to loosening, which makes implants move into a wrong position, prone to dislocation. The first episode can also be treated with “hip precautions” if trauma or abnormal movements are found in the medical history prior to dislocation and if radiographs are normal, as muscular weakness can also be suspected. In case of recurrent dislocation, even if muscular weakness is possible, a CT-scan is necessary to search for radiographic occult loosening, to evaluate implant positioning and to plan an eventual revision procedure. MRI can also be prescribed to evaluate gluteal muscle and tendons.

Concerning dual mobility cup, dislocation can be of two types: a loss of contact between the PE insert covering the head and the acetabular piece (classical) or an intra-

prosthetic PE dislocation [84], defined as a loss of contact between the head and the PE. The latter can occur during the reduction of a classical dislocation in the early setting and lately secondary to wear [85] (Figure 16).

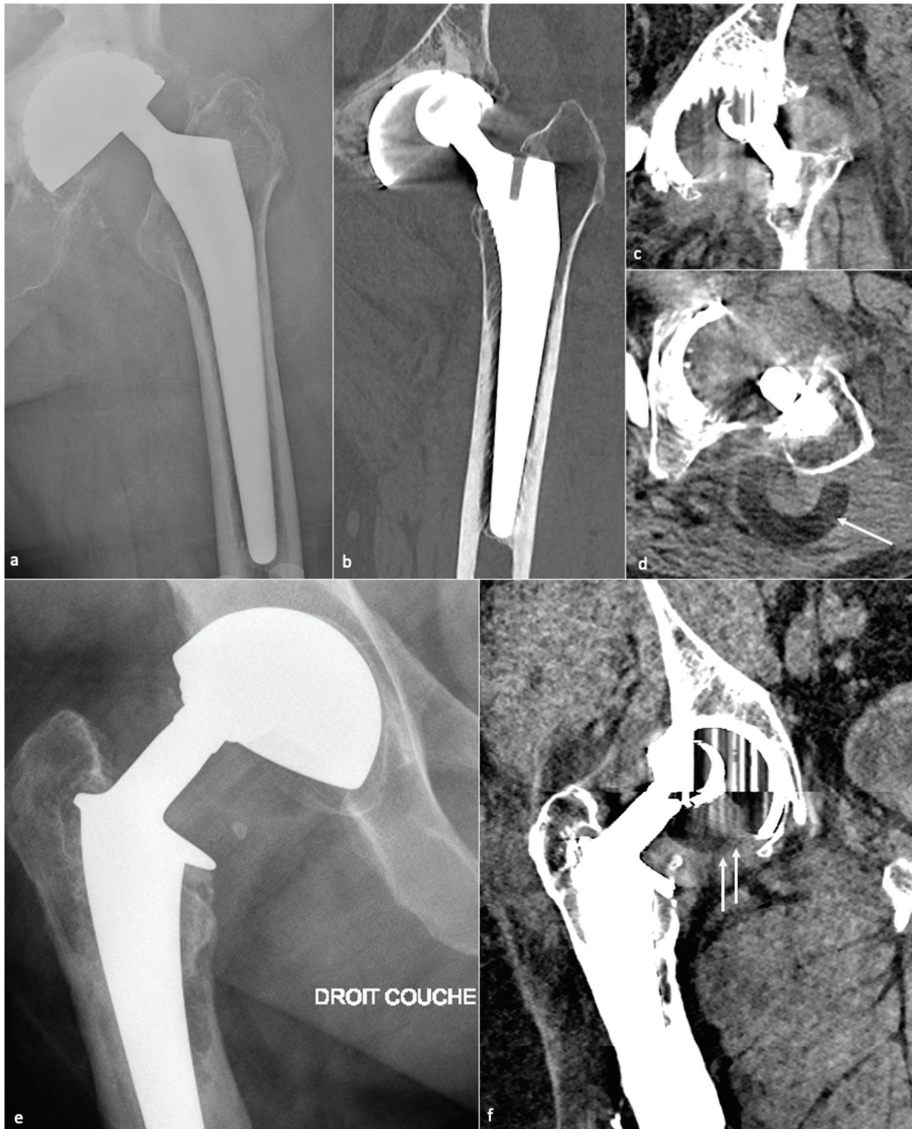


Figure 16. Polyethylene dislocations. An intra-prosthetic dislocation is shown on (a) an anteroposterior radiograph and (b) a coronal CT-scan with bone kernel where out-of-round of the femoral head is seen. Using soft tissue kernel in (c) frontal and (d) axial CT-scan slices, no polyethylene is seen in its usual position in (c) but is depicted behind the great trochanter in (d) (white arrow). In another patient, an intra-prosthetic dislocation is shown on (e) an anteroposterior hip radiograph where exentration of the femoral head is seen, and on (f) a frontal CT-scan slice where the polyethylene (double white arrow) is located downwards.

Dislocation is thought to be related to impingement between bone, implants, or soft tissues, as a dynamic process driven by multiple factors, including hip offset, implant design, component position, and bony geometry [83]. Therefore, evaluating all those factors is mandatory to treat this condition properly.

Posterior dislocations might be secondary to posterior capsule dehiscence, short external rotator dysfunction, and anterior dislocation to excessive acetabular cup anteversion and anterior capsule lesion [57].

4.1.2. Imaging

Therefore, radiographs and/or CT-scan can be realized to assess implant position, especially looking for an excessive acetabular frontal inclination and an inadequate anteversion, an incorrect FO and/or FNA, or a lower limb length discrepancy. CT also allows for studying gluteal muscle trophicity. MRI is better for studying periprosthetic soft tissues, especially the posterior joint capsule and the short external rotator muscles. An intact posterior capsule is in contact with the greater trochanter but is rarely clearly seen in the author's experience. A fluid gap indicates failed repair of the posterior capsule and/or muscles, and scar tissue can be seen with high or intermediate signal intensity. Muscle atrophy and fatty infiltration might indicate a nonfunctioning tendon unit [57]. The anterior joint capsule can undergo plastic deformation due to instability and appear thickened, hyperintense, and scarred. CT and MRI may also indicate additional findings after dislocation as component fractures, displacement of the acetabular liner, and persistent dislocation [57]. In the author's opinion, radiographs and CT are sufficient, and MRI should be realized only in selected cases.

4.1.3. Imaging Perspectives

As dislocation is mostly posterior and occurs during rising from a chair or bending over, frontal and lateral radiographs (EOS imaging or standard) from the spine to the ankles might be performed to assess pelvic alignment and implant position in different functional situations [73,83]. Additionally, Sutphen et al. have proposed an algorithm for recurrent posterior dislocation treatment based on 3D models from CT-scan allowing to simulate of hip kinematics during dislocation (i.e., flexion, adduction, internal rotation) using dynamic modeling software. This procedure allowed to identify bone-on-bone or material-bone impingement in half of the patients, and allowed to properly plan reorientation of the acetabular component, revision of the femoral head to increase hip offset, reorientation of the femoral stem, increasing femoral neck length, and removing impinging bone (i.e., anterior inferior iliac spine and anterior aspect of the proximal femur) to increase hip range of motion. In the other half of their patients, no impingement or limited range of motion were found, suggesting a soft tissue cause [83]. Those data seem to encourage the realization of EOS images or radiographs in different positions and 3D CT-based templating but additional studies are required before recommending their systematic use, in our opinion.

4.2. Ergonomics

4.2.1. Background

Prosthetic mispositioning and spinopelvic mobility troubles might lead to femoro-acetabular impingement, pain, wear, and instability. In the majority of revision procedures for unstable prosthesis, Marchetti et al. found macroscopic signs of impingement [86]. Additionally, spinopelvic unbalance can destabilize a hip prosthesis and vice versa, causing a "spine-hip syndrome" or a "hip-spine syndrome" [87]. In the sitting position, an insufficient cup anteversion can lead to an anterior impingement between the cup and the femoral neck with a compensatory hyperflexion of the hip, at risk of posterior dislocation. Contrarily, in the standing position, an excessive anteversion of the cup can lead to a posterior impingement, at risk of anterior dislocation. In case of rigid spinopelvic junction, the cup might be positioned with more inclination and anteversion, but in case of

spinopelvic hypermobility, it should be placed with less inclination and anteversion [67]. Some authors recommend anteversion and inclination values in function of the sagittal spinal deformity [88].

Even if THA implantation does not narrow the ischio-femoral space, ischio-femoral impingement can occur. It has been recently shown to be associated with a high femoral ante-torsion (approximately of 20°, compared to 15° in a control group). Of note, patients often present non-specific hip pain, so that imaging signs should help radiologists to raise suspicion of ischio-femoral impingement rather than affirm its diagnosis on imaging alone [89].

4.2.2. Imaging

Some mispositionings are obvious on standard radiographs or CT-scans, such as a frankly vertical or horizontal cup, a medialized femoral pivot, or a limb length discrepancy. In other cases, anterior and lateral pelvic and hip radiographs should be realized in the standing and sitting positions (if available with an EOS system imaging), taking into account all the pelvic parameters, prosthesis positioning, and limb length. A CT-scan can also be performed, as it allows to depict an anterior or posterior offset of the cup and to rule out another complication [67].

In the case of ischio-femoral impingement syndrome, CT can be realized to measure femoral ante-torsion, and ischio-femoral and quadratus femoris space. MRI is the best imaging modality, as it can achieve the above-mentioned measurements (respectively, positive if inferior to 15 and 10 mm) and identify edema and fatty infiltration of the quadratus femoris muscle. Abductors’ tears might also be ruled out as they could play a role in this setting [89].

4.3. Osteolysis and Loosening

4.3.1. Background

Even though complete osseous integration leads to the highest probability of implant fixation, limited osseous integration might be sufficient to achieve solid fixation without an amount clearly defined [57].

Most of the failures occurring at five years or later result from osteolysis, leading to aseptic loosening and peri-prosthetic fractures. Loosening corresponds to the loss of fixation of a cemented prosthesis or the absence or loss of osteointegration of an uncemented one. In imaging studies, loosening, therefore, corresponds to implant mobilization over time, raising the need to visualize previous radiographs, even the post-operative in the best-case scenario. Infection must be ruled out by puncture in case of doubt. Loosening can be “mechanical” (implant mispositioning or miss-dimensioning, poor primary fixation) or “biological”, secondary to almost all kinds of particles released (bone, cement, PE, metal, ceramic) by mechanical wear leading to granulation tissue formation in the osteolytic zones (Figure 17).

Those osteolytic zones have the appearance of RLZ around the prosthesis at the bone-cement or bone-prosthesis interface, may appear or increase during follow-up, and should be described as mentioned above. In case of cemented prosthesis, the Barrack classification appreciates the quality of the femoral stem cementation [90] (Table 2).

Table 2. Barrack classification.

Stage	Radiological Aspect
A	Complete filling of the medullary canal
B	RLZ inferior to 50% of the cement-bone interface
C	RLZ of 50–99% of the cement-bone interface
D	Complete RLZ at the cement-bone interface

RLZ: radiolucent zone.

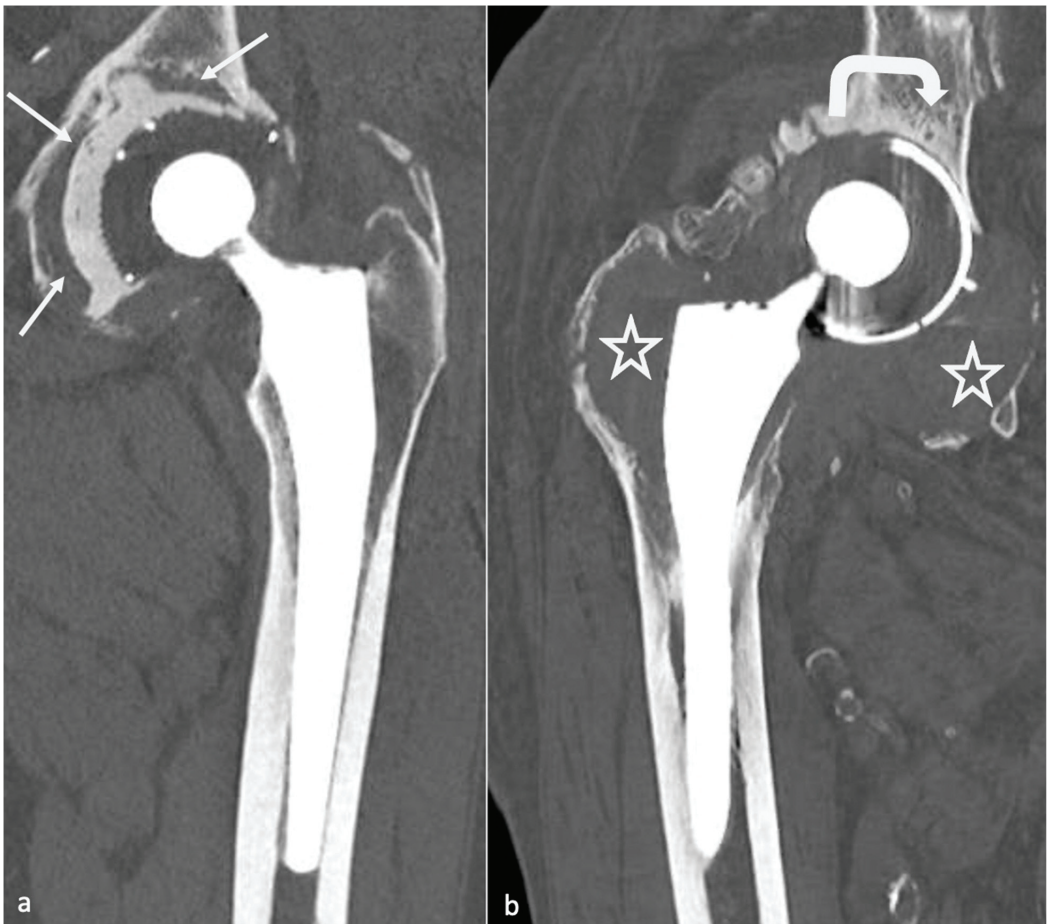


Figure 17. Mechanical and granulomatous loosening. An acetabular mechanical loosening is shown on (a) a frontal CT-scan slice with regular acetabular osteolysis (white arrows). A granulomatous loosening is shown on (b) a frontal CT-scan slice and consists of bulky osteolysis (white stars) both on the femoral and acetabular sides, with a displacement of the acetabular metal-back (white curved arrow).

4.3.2. Imaging

Even though radiographs have been described sufficient for loosening diagnosis, tomosynthesis might increase its diagnostic value and is superior to CT without MAR [55,91]. CT-scan with state-of-the-art MAR better depicts peri-prosthetic osteolysis, especially on the acetabular side [55], and implants complications. CT-angiography of the pelvis should be performed before revision surgery in acetabular piece pelvic protrusion to study the iliofemoral vascular pedicle [54].

4.3.3. Radiographs, Tomosynthesis, and CT

On the acetabular side, the loosening risk becomes higher when the number of RLZ increases (71% in case of 2 zones and 94% in case of 3 zones) [92], and the presence of an RLZ in zone 1 should raise suspicion for loosening and call for close surveillance [80]. In the case of uncemented prosthesis on the femoral side, the apparition of an RLZ of more than 2 mm is always pathologic, except in zone 1 and 7 [80].

Component displacement (i.e., cranial for the acetabular side, distal and varus inclination for the femoral side), pedestal regression, and cement or component fractures are also indicators of loosening, but the only finding indicating definite loosening is excessive component movement, the others being associated with loosening but remaining nonspecific [37]. For those reasons, composite scores have been developed to assess prosthesis stability and fixation [93–95] but are beyond the scope of this paper.

Concerning treatment, in cases of acetabular bone defects, the Paprosky classification should be used (Table 3), as it is composed of imaging and surgical findings, and includes treatment recommendations [40]. Before revision surgery, the radiologist must check for acetabular loosening and the amount and type of bone stock loss, the amount and direction of component migration, and liner wear [40]. A 3D-CT reformats whit removal of the femoral head can improve acetabular visualization, in the author’s opinion. Cavitory defects at the acetabular roof and walls, segmental defects of the acetabular rim, lysis of the medial or posterior ischial wall (with or without pelvic discontinuity), and an estimated percentage of host bone in contact with the acetabular cup might be described, as both hip center of rotation and bone stock must be restored. Of note, bone stock loss areas are usually located away from the acetabular rim and are large. In contrast, pre-existing degenerative cysts are smaller and often found at the acetabular roof [40]. Bone grafts or additional acetabular hardware (acetabular cups, rings and cages, metallic acetabular augments) can be used. Revision surgery complications include neuro-vascular damages, infection, fractures, dislocation, bone graft failure, and dislocation of the prosthetic liner [40].

Table 3. Paprosky classification.

Type	Imaging and Operative Findings
I	Acetabular rim and columns intact
	Almost complete host bone support of the component
II	Superior migration inferior to 3 cm
	Distorted acetabular rim without columns attempt Host bone support superior to 50%
IIA	Superior and medial cavitation. Intact rim
IIB	Segmental supero-lateral defect (less than 1/3 of circumference)
IIC	Medial wall lysis with acetabular protrusion
III	Migration superior to 3 cm
	Missing bone in the 10 AM-2 PM positions, teardrop lysis
IIIA	Walls compromised
	Columns nonsupportive Superior migration
IIIB	Missing bone in the 9 AM-5 PM positions, teardrop lysis
	Walls compromised Columns nonsupportive Superior or medial migration
Pelvic Discontinuity	Fracture line through columns
	Obturator foramen asymetry on AP pelvis radiograph
	Superior and inferior hemipelvis separation

4.3.4. MRI

MRI has gained more and more attention with the amelioration of the sequences previously mentioned. The axial plane would be the most useful for evaluating the bone-

implant interface [57]. A hyperintense layer between the host bone and the implant or cement indicates fibrous membrane formation when inferior to 2 mm thickness (Figure 14) or periprosthetic bone resorption when superior to 2 mm and irregular [57]. One must keep in mind that the evaluation of acetabular component fixation is complex because of the convex surface of the implant, exaggerating artifacts [57]. For uncemented prosthesis, STIR hyperintense margin at the metal–bone interface (i.e., osteolysis) indicates loosening (>1.5 mm for the acetabular side and >3.5 mm for the femoral side). Additional contrast enhancement at the metal–bone interface and STIR signal hyperintensity are indicators of prosthetic joint infection (PJI). The magnitude of bone resorption is also an essential factor, as circumferential bone resorption may suggest loosening [57]. Mechanical loosening may be inferred if blood tests for infection and imaging findings for wear-induced synovitis are negative and circumferential osseous resorption is present, as wear-induced synovitis rather induces bulky osteolysis, particularly in case of implant displacement [57]. Therefore, serial MR scans may be necessary to prove loosening [57].

Periprosthetic soft tissue edema can be found in aseptic loosening or PJI. Still, soft tissue anomalies (including edema, abscess, and enlarged lymph nodes of more than 17 mm) and the involvement of both sides of the joint are more frequent in infectious cases. Schwaiger et al. proposed a two-stage approach [38]. First, radiologists should evaluate the presence of signal changes at the periosteum: any signal changes on the acetabular side and the diameter of the signal anomalies adjacent to the metal–bone interface using the cut-offs mentioned above are indicators of PJI or aseptic loosening. Then, soft-tissue abnormalities must be evaluated: enlarged regional lymph nodes and/or both joint sides' affection might be in favor of PJI. The IV contrast media administration is still debated and might not be indispensable if such findings can be seen on non-CE images.

When conventional imaging techniques are nondiagnostic, bone SPECT-CT can be used as a second-line imaging modality, mainly due to its high negative predictive value, allowing the stopping of investigations in cases of regular exams [96].

The occurrence of primary bone or soft-tissue neoplasms at the site of HA is rare. Still, one must keep in mind that soft tissue tumors are more frequent than osseous and that a mass arising from the bone with bony destruction and extension in the soft tissue or a soft-tissue mass invading the bone is more likely to be a tumor than a “simple” osteolysis from loosening [57]. Differential diagnosis might be challenging when the mass is adjacent to the synovium.

4.4. Infection

4.4.1. Background

There are four types of PJI: positive intraoperative cultures, early post-operative infection, late chronic infection, or acute hematogenous infection [89]. No test offers great sensibility or specificity for diagnosing PJI. The diagnosis of PJI is based on a combination of clinical findings, laboratory evaluation of blood and synovial fluid, and intraoperative findings [97]. The gold standard remains articular fluid aspiration and culture. A recent study showed that almost 30% of PJI were culture-negative after intra-operative sampling. In those cases, next-generation sequencing showed infection in 66% of the cases, which was polymicrobial in 91% [97]. Blood tests are often negative and should not be mistaken for aseptic loosening before articular fluid analysis [97].

Significantly, imaging findings might range from standard to frank bone destruction, mimicking loosening or particle disease [33]. Several definitions of PJI exist, but imaging techniques are lacking in most scoring systems. For example, the Musculoskeletal Infection Society has established a scoring system, not considering imaging techniques, that requires at least two positive cultures of the same organism (even in case of commensal micro-organism) or sinus tract with evidence of communication to the joint or visualization of the prosthesis to diagnose PJI, or composite scores with pre- and peri-operative items [98].

Nuclear medicine techniques (beyond the scope of this paper) and MRI are more specifically concerned with the imaging workup of this condition [36], but in the authors' experience, a CT-scan is often required in the first place by the referring physician.

4.4.2. Septic versus Aseptic Loosening Imaging Signs

Nonetheless, septic loosening is faster than aseptic using previous radiographs and can be associated with femoral periosteal reaction and soft tissue collections [33]. In the author's institution, when a joint-fluid aspiration is required, a CT-arthrogram is realized at the same time to depict better sinus tracts and loosening zones, often opacified by contrast media.

MRI signs have been described above and mainly concern synovitis (more precisely lamellation of a thickened hyperintense synovium), extracapsular tissue and bone edema and enhancement, extracapsular collections and sinus tracts, osteolysis, and lymphadenopathy [57]. According to Guerini, the association of a triple hypersignal (i.e., intra-osseous at the contact of the prosthesis, cortical, and peri-osseous in the soft tissues) is of great significance for infection [59] (Figure 18). Galley et al. compared patients with PJI and controls who underwent MRI at least six weeks after THA and found that periosteal reaction, capsular edema, and intramuscular edema were more frequent in PJI [18]. In addition to conventional MRI features, Albano et al. stated that lymph nodes indices, especially concerning their number, compared between the affected and the unaffected side, might be biomarkers of THA infection [99].

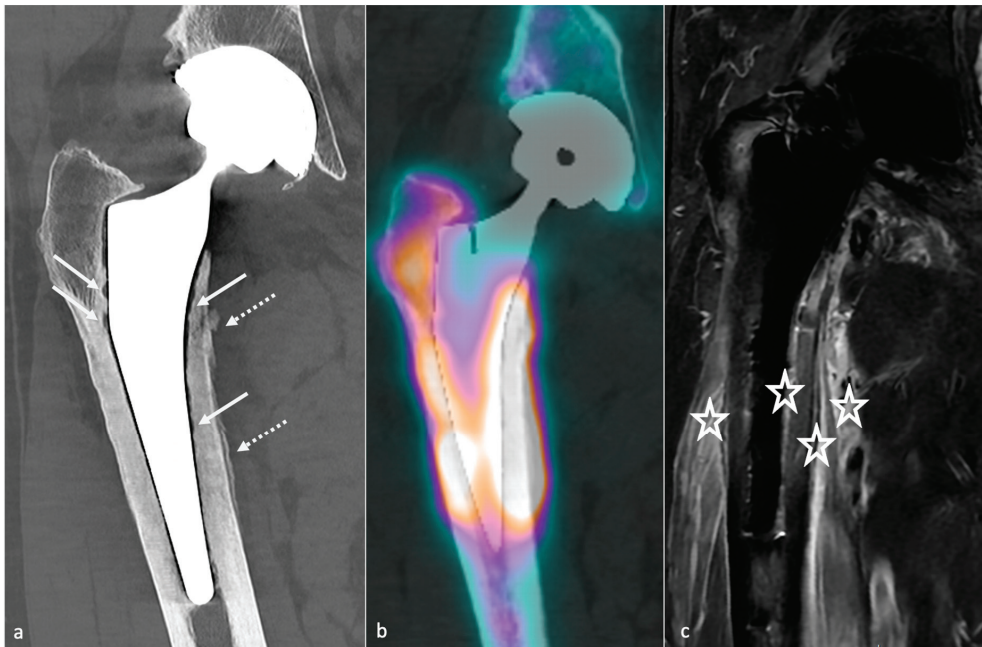


Figure 18. Infectious loosening (staphylococcus lugdunensis). An infectious loosening is shown on (a) a frontal CT-scan slice with irregular femoral endosteal osteolysis (white arrows) and periosteal reaction (dotted arrows), (b) a frontal SPECT-CT slice with diffuse hyperfixation, (c) a frontal T2 STIR image with a peri-prosthetic, cortical, and soft tissue hypersignal (white stars).

One should be aware of the aspect of temporary cement spacer, impregnated with antibiotics, temporarily used when revision surgery is performed to allow functional hip movement while locally treating an infection (Figure 19). Dislocation, periprosthetic fractures, and secondary infection can occur [100].

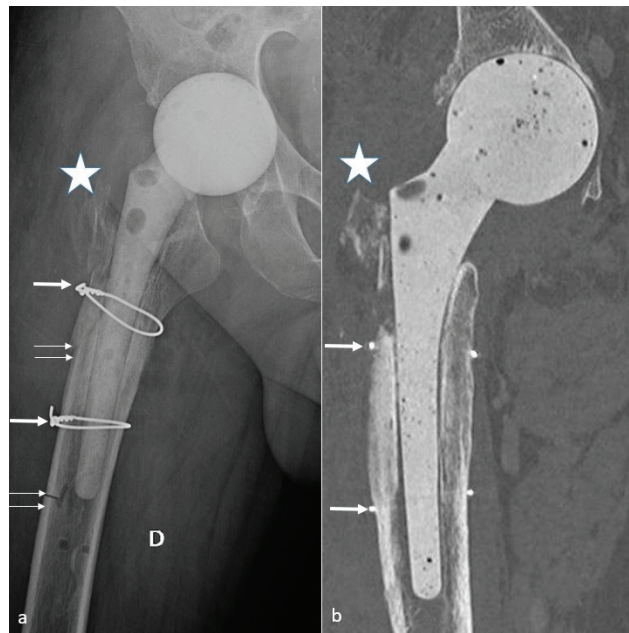


Figure 19. Spacer appearance. A spacer is shown on an AP radiograph (a) and a coronal CT-scan slice (b). Note the cerclage wires (thick arrows), the trochanteric lysis (white star), and the femorotomy sequelae (thin double arrows). NB: “D” in (a) means “droite” and is referred to the right side.

4.5. Synovitis

4.5.1. Background

Joint fluid can be seen either on MRI or CT with metal-artifact reduction, but MRI is more useful in detecting, characterizing, and defining synovitis [57].

4.5.2. Classification and Contribution of Imaging Methods

Nonspecific synovitis appears as a simple joint fluid of uniform fluid signal intensity with a thickened synovial wall lining, but its clinical importance in the absence of symptoms is unknown [57]. In capsular disruption, fluid might extend into the greater trochanteric or iliopsoas bursae.

PE wear-induced synovitis is secondary to contact pressure between the PE and the femoral head, leading to its wear and intra-articular particle release [6]. On imaging, it manifests as the expansion of the hip pseudocapsule by thick and particulate-appearing synovitis of low to intermediate signal intensity, often isointense to muscles, that might communicate and extend into other bursae. Extra-articular deposits from capsular decompression might result in pseudo-tumors formation, resembling those associated with adverse local tissue reactions of metal debris. Bulky osteolysis is often present, with particulate debris in periprosthetic trabecular bone [57]. CT allows a good depiction of osteolysis and osseous granuloma formation, but MRI is superior in soft tissue involvement analysis. MRI should also be interesting before revision surgery in case of frank PE wear for “soft tissue mapping” or if a stable or tiny granuloma depicted on other imaging techniques does not seem sufficient to explicate the patient’s symptoms [59].

When a histologic diagnosis is available, adverse local tissue reaction (also called pseudo-tumors or aseptic lymphocytic vasculitis-associated lesions) corresponds to arthroplasty-related metal products, including metallosis caused by metal debris, reactive tissue inflammation to metal ions, and corrosion products, or a combination of those. MRI plays a key role in diagnosing this condition, which must be precocious because of the

aggressiveness of soft-tissue destruction. Implant wear contributes to metallic products in joint fluid and periprosthetic soft tissues in well and mispositioned implants (abrasion and corrosion, edge loading secondary to mispositioning, neck-on-cup impingement). Although metal ion levels alone should not be relied on as the sole parameter to determine revision surgery, serum cobalt level of >1 ng/mL and a Cobalt/Chromium ratio > 2 thresholds are thought to be associated with adverse local tissue reaction in MoP THA [101]. Those values were, respectively, 2.8 and 3.8 for dual modular taper THA in Kwon's study [102].

- Metallosis* results from the shedding of metallic debris (secondary to a MoM prosthesis with corrosion, a conflict between a metallic acetabular cup and the prosthetic neck, or a contact between a metallic head and an acetabular metal back in case of PE wear or dislocation) that induces synovitis and an indolent pattern of osteolysis, potentially leading to loosening (i.e., potentially looking similar to osteolysis and PE wear). Synovitis may contain low-signal intensity or metallic density debris, causing MRI artifacts and bone erosion, best depicted on CT-MAR (Figure 20). Such debris might also be located in periprosthetic soft tissue and lymph nodes [54,57]. Metallic debris presence might also accentuate PE wear (i.e., third fragment wear) [54]. Of note, high serum metal-ion levels can be found in symptomatic and asymptomatic patients and would be associated with pseudo-tumors, so that such a biological finding should lead to the prescription of an MRI to rule out a pseudo-tumor even in asymptomatic patients [6,103].

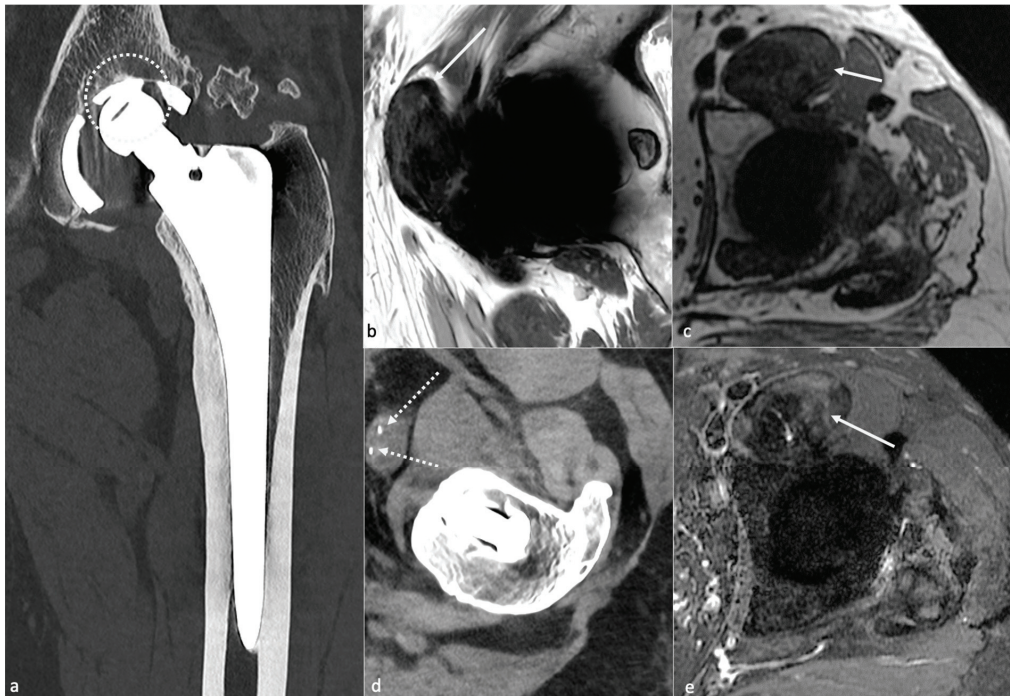


Figure 20. Metallosis. Contact between the acetabular metal-back and the femoral head (dotted white circle) is shown on (a) a frontal CT-scan slice, secondary to polyethylene wear. A pseudo-tumor extending into the iliopsoas bursae is shown on (b) a sagittal T2-weighted image, (c) an axial T1 MAVRIC and STIR (e) images as hypointense. Additionally, note on (d) an axial CT-scan slice the presence of metallic debris (dotted white arrows) into the pseudo-tumor.

- Additionally, referred to as *trunnionosis*, trunnion corrosion corresponds to a soft-tissue reaction to metal debris released from micromotion and mechanical wear at the head–neck or neck–stem junction of modular MoP HA. On MRI, it manifests as an adverse local reaction associated with medial calcar resorption [11,104].

4.5.3. MRI Focus

MRI is the best imaging technique for monitoring adverse reactions to metal debris [12,105]. Its findings range from expansion of the pseudo-capsule with homogenous joint fluid to amounts of synovial proliferation, potentially extended into bursae, and debris causing pseudo-tumors. Peri-synovial soft tissue edema and nodal pathology can also be present and call to rule out infection [57]. A synovial thickness superior to 7 mm and a mixed solid–cystic synovial pattern is thought to be the best predictors of moderate or severe adverse local tissue reaction [106]. MRI findings of metallosis and local adverse tissue reaction may coexist [57]. Three pseudo-tumor grading systems have been described by Anderson [107], Matthies [108], and Hauptfleisch [109], but using MRI with MAR techniques, all showed limited interobserver reliability [110]. In the author’s country, the Hauptfleisch classification is the most used: type I (cystic lesion with a thin wall), type II (cystic lesion with a wall thicker than 3 mm), and type III (predominantly solid lesion containing necrosis and metallic debris) [109], the severity of the symptoms and the revision rate becoming higher from type I to III. Cystic lesions might be challenging to differentiate from infectious lesions, especially in the Anderson classification [85,107].

4.6. Psoas Impingement

4.6.1. Background

In the early post-operative months, during the physical activity recovery, pain secondary to impingement between psoas muscle-tendon unit and the uncovered acetabular can occur. This impingement leads to tendinous lesions and can be accompanied by local bursitis, inconstant and nonspecific. Blood tests are negative, and no infectious symptoms are present. As the psoas bursae and the joint capsule might communicate [111,112], care must be taken not to overlook an articular pathology, especially in cases of PJI.

4.6.2. Imaging

Imaging purposes are to rule out loosening in the first place, then to confirm the diagnosis, and to look for anatomic predisposition.

Radiographs can show an oversized acetabular or femoral head component, a lack of acetabular anteversion, a screw in the projection of the iliopsoas tendon, an anterior acetabular offset, or an insufficient acetabular covering on a profile view.

A CT-scan is considered the reference exam. It can easily depict anterior acetabular offset, considered pathologic when superior to 12 mm in the axial plane and usually well seen in the sagittal plane [54]. This offset can be due to a lack of acetabular anteversion or retroversion. Impingement might also result from a screw or a cement leak. One should know that the extension of screws beyond cortical margins can be asymptomatic and, therefore, be cautious when mentioning this finding in the imaging report [57].

Ultrasounds can show the anterior offset and the musculotendinous abnormalities, reproduce the pain, and especially guide a local test injection.

Concerning MRI, the iliopsoas muscle and tendon are best depicted in the axial plane, but the tendon can be obscured by metallic artifacts and, therefore, better seen in the coronal and sagittal planes. In tendinosis, a partial or full-thickness tendon tear can be seen, and atrophy and fatty infiltration can be indirect signs of tendon dysfunction or prior release [57].

4.7. Squeaking

Although its origin is still debated, this phenomenon, occurring in CoC (in 1–21% of the cases) or MoM THA, might be favored by implant mispositioning (i.e., a too vertical-

ized acetabular component, excessive or insufficient acetabular cup anteversion) [113]. A component fracture must be ruled out.

4.8. Muscle Pathology

4.8.1. Background

Concerning most of the gluteus medius and minimus, tendinopathy can be favored by a trans-gluteal approach, a too early reeducation, a lower limb length discrepancy, or an excessive FO. Those tendons' pathologies can cause lateral hip pain, abductor insufficiency, limpness, and anterior dislocation [57]. In the preoperative setting, asymptomatic gluteus medius and minimus pathology diagnosed on MRI has been shown to correlate with inferior 2-year post-operative outcomes [114], so they should be described even in the post-operative setting in the author's opinion. Additionally, isolated open repair or THA and concomitant repair of gluteal tendon tear have been shown to be safe procedures with high levels of satisfaction at short- to mid-term follow-up (visual analog scale of pain and satisfaction), even though the presence of a full thickness tear was a predictor of worst outcomes in Requicha's study [115].

The rectus femoris tendon analysis must be careful, especially in the case of the anterior surgical approach.

4.8.2. Imaging

MRI and US are usually performed, can confirm the diagnosis, study bursae, and quantify amyotrophy or fatty degeneration. Imaging findings must be strictly correlated to symptoms, typically occurring in hip abduction with limping, as an abnormal aspect of those tendons is frequent with age. Gluteus medius tendon tears are the more clinically relevant, and the gluteus minimus tendon may be released at the time of surgery and/or denervated, diminishing its attempt clinical relevance [57]. On MRI, in the acute setting, peritendinous edema can be found [57] and help to promote tendon pathology to explain patients' symptoms, as partial tears are frequently encountered in clinical practice in symptomatic and asymptomatic patients.

MRI can depict a surgical approach, and Agten et al. showed that anterior and direct lateral approaches resulted in less muscle and tendon damage than the posterior and direct lateral approaches [116]. The anterior approach results in less muscular atrophy than the others [117], even though the posterior approach seems to be the most frequently used [118], and some authors do not find differences in clinical outcome scores at one year between the different methods [117]. Wang et al. showed, using 3D MRI images, that the posterior approach seriously damages external rotator muscle and function and that effective muscle repair is beneficial to the muscular morphological insufficiency, therefore calling for an effective valuable repair of the external rotators to improve early post-operative recovery [118]. Via the posterior approach, the piriformis might lose half of its volume, and the root of the internal obturator be damaged, the latter being involved in pelvic organ support and urinary incontinence [118].

4.9. Neurovascular Complications

The superior gluteal nerve innervates the gluteus minimus and medius and the tensor fascia lata muscles. Postsurgical damage of this nerve should be suspected in case of atrophy of those abductor's muscles, especially in limps. In contrast, fatty atrophy of the anterior gluteus minimus fibers with an intact tendon is often found in asymptomatic patients due to selective denervation without clinical relevance. On the other hand, fatty atrophy of the posterior fibers of the gluteus minimus and medius should raise suspicion of a tendon tear [119].

In the immediate post-operative period, edema might involve the sciatic nerve and irritate it but typically resolves over time. An unexpected evolution should raise suspicion for an impingement related to hardware malposition or collection. Deep vein thrombosis related to hardware may also occur [13].

In the chronic setting, neurovascular complications are often related to synovial expansions, and periprosthetic neuroma may be detected by MRI [13].

4.10. Peri-Prosthetic Fractures and Stress Reactions

4.10.1. Background

With an overall incidence of 18%, they occur during component implantation or after surgery and are favored by periprosthetic bone resorption, osteolysis, implant loosening, osteoporosis, femoral stem varus positioning, and trauma [57].

Mainly concerning the femoral side, fractures are classified according to the Vancouver classification, based on the location of the fracture, the amount of available proximal bone stock, and the stability of the stem. Type A fractures are peri-trochanteric fractures (subtypes: AL = lesser trochanter and AG = greater trochanter). Type B fractures occur around or just below the tip of the stem (subtypes: B1 = well-fixed stem, B2 = not-well-fixed stem, B3 = poor bone stock in the proximal femur and not-well-fixed stem). Type C fractures occur below the femoral stem. These fractures can be peri-operative during femoral stem placement (especially for uncemented prosthesis), secondary to minor trauma, or varus positioning. They need to be detected as they can require further treatment.

Acetabular fractures are rare and usually result from trauma or osteolysis. Radiographically occult acetabular fractures can occur during cup fixation, especially at the superolateral wall, but do not require further treatment if secure fixation has been confirmed during surgery [120]. Acetabular, femoral, or pelvic stress fractures are rare, difficult to diagnose on radiographs, and justify a CT and/or MRI pelvic acquisition whenever they are suspected [54,57].

Trochanteric pseudarthrosis can result from revision procedures or technical difficulties, is favored by gluteal muscle tension, and lead to a risk of dislocation. On imaging, they might appear as metallic wires rupture, fracture, and trochanteric ascension and fragmentation [54]. Femoral neck fractures only occur in resurfacing arthroplasty [33].

4.10.2. Imaging

The above-mentioned findings are variably depicted with radiographs but are clearly visible with CT-scan in the author's experience, which is often required for pre-operative planning.

On MRI, stress reactions are localized signal hyperintensity of the marrow cavity and endosteum, thickening and hyperintensity of the cortex and periosteum without fracture, and adjacent soft-tissue edema (Figure 21). Marrow signal hyperintensity can be a normal finding after several months, secondary to implantation of surgical technique. In this setting, the lack of periosteal reaction and the typical appearance of soft tissues help to make it commonplace [57].

4.11. Heterotopic Ossification

In up to half of the patients during post-operative weeks, they correspond to the formation of new lamellar bone within periprosthetic soft tissues. During the osseous maturation phase, local pain and swelling with body temperature may occur and be difficult to differentiate from infection. On MRI, immature bone manifests as heterogeneous processes with mass effect on the surrounding tissue, but CT easily depicts mineralization [57]. On radiographs, the Brooker classification ranges from stage 1 (small ossifications) to stage 4 (bony ankylosis); CT and MRI are helpful for precise anatomical relationships with soft tissues and vascular structures [54].

4.12. Implant Failure

The femoral stem can break, its modular component dissociate, and its sintered beads shear off (opaque micro-fragments separated from the porous-coated femoral stem) [33]. Additionally, the acetabular liner can wear, break, or dissociate.

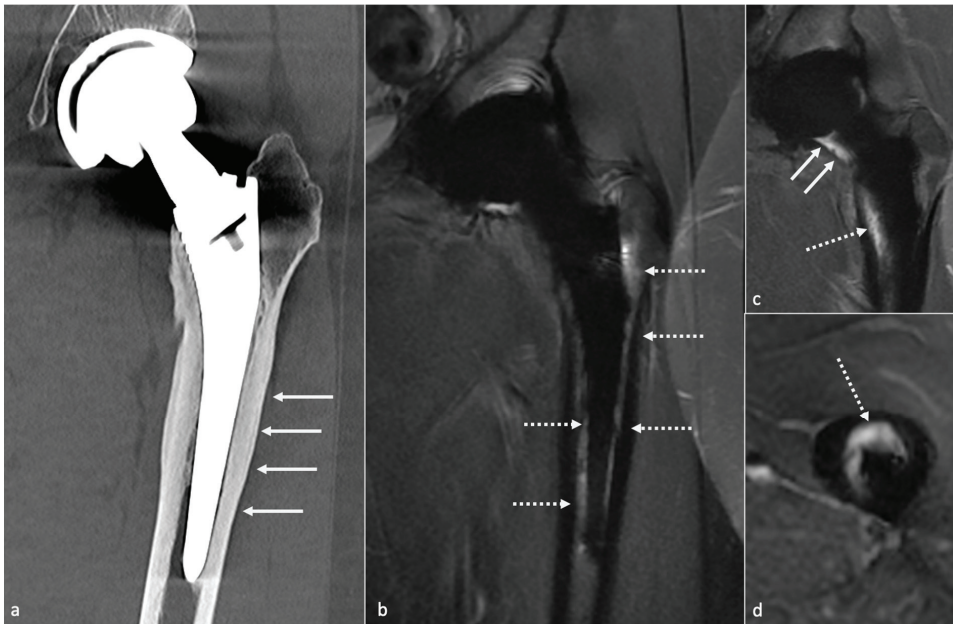


Figure 21. Stress reaction. A stress reaction is shown on (a) a coronal CT-scan slice with a varus stem position and asymmetric periosteal reaction (arrows). Periprosthetic bone marrow edema (dotted arrows) is doubtful on (b) a coronal STIR image but is depicted on another (c) coronal and (d) axial STIR image. Additionally, note the small amount of joint fluid (double arrow) on (c), considered nonspecific.

Prosthetic fractures are rare, secondary to misleading conception or trauma, essentially concern CoC HA (head or acetabular insert), and require careful analysis of the components and of their environment as they can lead to particles reactive synovitis [54].

Still concerning CoC prosthesis, femoral head fracture is secondary to trauma or hyperactivity [85] and leads to functional impairment, whereas acetabular fractures are rare, non-secondary to trauma, and might become symptomatic only in case of displacement [13,113,121]. Acetabular fractures may be favored by excessive anteversion and poor implantation of the insert in the metal back [85]. Ceramic debris might lead to osteolysis and need to be carefully overlooked as it must be resected in case of revision before a new prosthesis becomes implanted (Figure 22).

As acetabular bone loss is a significant challenge in HA revision surgery, all the components used to reconstruct an acetabular socket might be carefully analyzed, as local constraints might favor their breaking and displacement. In the author's opinion, CT offers the best depiction of implant integrity.

4.13. Resurfacing Arthroplasties

Those prostheses, usually composed of cobalt/chrome components, can be considered apart. Complications are rare and mainly related to suboptimal surgical procedures leading to impingement or femoral neck fracture [3]. Uncomplicated components should have an abduction of about 40° and an anteversion of about 20° on the acetabular side, and a neutral or slightly valgus position on the femoral side. No notch should be seen at the neck. Minor RLZ around the femoral stem is normal. Femoral neck thinning adjacent to the femoral prosthesis is frequent, and about 70% of patients show narrowing without clearly defined significance [3].

A femoral neck fracture is an early complication. Infection and loosening rates are poorly known but thought to be rare. Dislocation is very rare. Mispositioning can lead to

impingement and pain on the acetabular side. An excessive femoral piece valgus position exposes to the risk of notching, and an excessive varus to the risk of fracture (Figure 1). Pseudo-tumors occur in approximately 1% of patients [3].

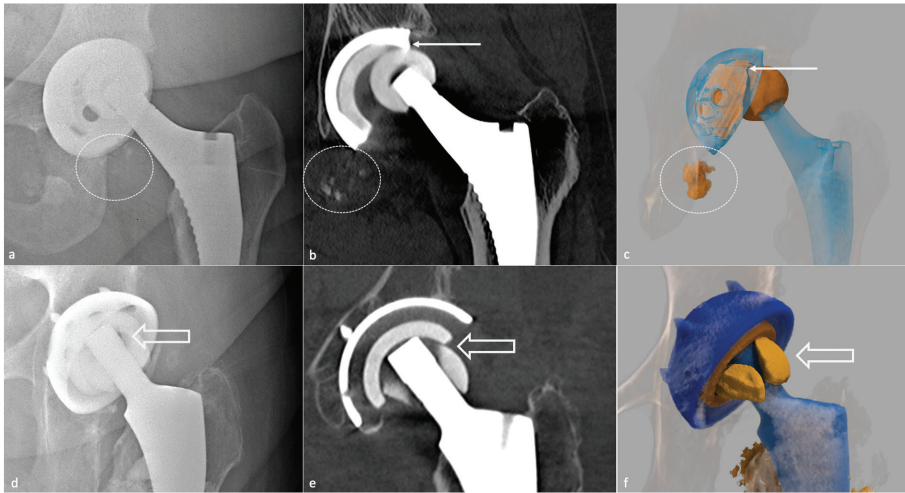


Figure 22. Ceramic fractures. An acetabular liner fracture is shown on (a) an anteroposterior hip radiograph, (b) a coronal CT-scan slice, and (c) a global illumination reformat with femoral head exenteration. The fracture is better depicted in (b,c) (white arrow), and ceramic debris can be seen on (a–c) (dotted circle). A femoral head fracture in a case of sandwich ceramic liner is shown on (d) an anteroposterior hip radiograph, (e) a coronal CT-scan slice (thick white arrow), and (f) a global illumination reformat. Note the interposition of a radiolucent space between the metal back and the ceramic liner due to the presence of PE, best seen on the CT-scan image.

5. Limitations

This paper brings a comprehensive and extensive literature review concerning THA imaging workup, concerning all imaging studies and implants design. However, to date, no consensus exists concerning the optimal imaging diagnostic strategy, and we are not able to bring clear evidence-based recommendations. After radiographs, imaging studies are often prescribed depending on the availability of each imaging technique in each institution and depending on the referring physician’s habits. Concerning asymptomatic patients’ follow-up, it is impossible to state that EOS imaging (if available) could replace radiographs. Nor can we recommend systematical standing and sitting radiographs in case of asymptomatic or symptomatic prosthesis. The use of MRI is growing, especially with MAR sequences, and for soft tissue analysis, but it is still considered a procedure that “may be useful to evaluate hip arthroplasties with suspected soft-tissue or periprosthetic abnormalities” by the American College of Radiology, which does not recommend MRI as a first intention procedure [122]. CT is readily available and has good diagnostic performances. In our experience, it is the best imaging technique to assess mechanical complications when considering implant integrity and osteolysis, but still exposes patients to ionizing radiations and IV contrast media, the latter being less frequent with MRI. However, depending on the local technical conditions, the clinical suspicion, and the patients’ comorbidities, different imaging strategies might still be applied. In this context, one should be aware of each technique’s advantages and drawbacks, to improve patient care.

6. Conclusions

HA follow-up requires systematic and standardized radiographic follow-up, even in asymptomatic patients, to assess bone stock and implant positioning. First, the type of HA,

its bearing surfaces, and fixation method must be recognized. Then, its position and the bone–prosthesis interface must be compared to previous radiographs if available to detect silent complications in case of systematic follow-up. Normal imaging findings, including radiographs, CT-scans, and MRI, might not be mistaken for complications and should be interpreted with caution and correlated to the clinical context. In cases of complication, a CT-scan used to be the standard reference, but MRI has gained more and more prevalence and technical improvement and might be part of the routine imaging workup in such patients, especially when it comes to soft tissue depiction and infectious loosening. Concerning implant mispositioning, even though CT-scan remains a valuable alternative, standing and sitting position radiographs seem to delineate as a useful tool to assess the patient-specific safe zone and include spine and lower limbs in the referring physician’s reflection when evaluating a painful hip prosthesis, especially in cases of instability. Proper imaging workup and diagnosis relies on acknowledging the type of prosthesis, the post-operative delay, the clinical history, and eventual blood tests. All these elements should be put together, leading to a robust and systematic analysis. Further studies comparing CT and MRI, both with MAR, in case of complications, and radiographs and EOS-imaging for standard follow-up should be realized. Additionally, “CT-like” MRI sequences could be evaluated in HA imaging.

Author Contributions: Conceptualization, R.G., P.G. and C.L.; Methodology, R.G.; Software, P.A.G.T. and P.G.; Validation, A.B. and P.A.G.T.; Formal Analysis, F.B. and E.G.; Investigation, R.G. and E.G.; Resources, A.B.; Data Curation, R.G.; Writing—Original Draft Preparation, C.L., P.G. and R.G.; Writing—Review and Editing, P.G.; Visualization, A.B.; Supervision, A.B. and P.A.G.T.; Project Administration, F.B. and E.G. All authors have read and agreed to the published version of the manuscript.

Funding: This research received no external funding.

Institutional Review Board Statement: Ethical review and approval were waived for this study due to its review type.

Informed Consent Statement: Not applicable.

Data Availability Statement: Not applicable.

Conflicts of Interest: The authors declare no conflict of interest.

Abbreviations

AO	Acetabular offset
CE	Contrast-enhanced
CoC	Ceramic-on-ceramic
CoP	Ceramic-on-polyethylene
CT	Computed tomography
FNA	Femoral neck anteversion
FO	Femoral offset
FOV	Field of view
FSE	Fast-spin echo
HA	Hip arthroplasty
MAR	Metal artifact reduction
MoM	Metal-on-metal
MoP	Metal-on-polyethylene
PE	Polyethylene
PJI	Prosthetic joint infection
RLZ	Radiolucent zone
SE	Spin echo
SPECT-CT	Single-photon emission computed tomography
STIR	Short TI inversion recovery
THA	Total hip arthroplasty

References

1. Wylde, V.; Hewlett, S.; Learmonth, I.D.; Dieppe, P. Persistent Pain after Joint Replacement: Prevalence, Sensory Qualities, and Postoperative Determinants. *Pain* **2011**, *152*, 566–572. [[CrossRef](#)]
2. Labek, G.; Thaler, M.; Janda, W.; Agreiter, M.; Stöckl, B. Revision Rates after Total Joint Replacement: Cumulative Results from Worldwide Joint Register Datasets. *J. Bone Jt. Surg. Br.* **2011**, *93*, 293–297. [[CrossRef](#)] [[PubMed](#)]
3. Nikolajsen, L.; Brandsborg, B.; Lucht, U.; Jensen, T.S.; Kehlet, H. Chronic Pain Following Total Hip Arthroplasty: A Nationwide Questionnaire Study. *Acta Anaesthesiol. Scand.* **2006**, *50*, 495–500. [[CrossRef](#)] [[PubMed](#)]
4. Beswick, A.D.; Wylde, V.; Gooberman-Hill, R.; Blom, A.; Dieppe, P. What Proportion of Patients Report Long-Term Pain after Total Hip or Knee Replacement for Osteoarthritis? A Systematic Review of Prospective Studies in Unselected Patients. *BMJ Open* **2012**, *2*, e000435. [[CrossRef](#)]
5. Pincus, D.; Jenkinson, R.; Paterson, M.; Leroux, T.; Ravi, B. Association Between Surgical Approach and Major Surgical Complications in Patients Undergoing Total Hip Arthroplasty. *JAMA* **2020**, *323*, 1070–1076. [[CrossRef](#)] [[PubMed](#)]
6. Jamari, J.; Ammarullah, M.I.; Santoso, G.; Sugiharto, S.; Supriyono, T.; Prakoso, A.T.; Basri, H.; van der Heide, E. Computational Contact Pressure Prediction of CoCrMo, SS 316L and Ti6Al4V Femoral Head against UHMWPE Acetabular Cup under Gait Cycle. *J. Funct. Biomater.* **2022**, *13*, 64. [[CrossRef](#)]
7. Department of Orthopaedics and Traumatology, Princess Margaret Hospital, Laichikok, Hong Kong; Lam, Y.; Chan, P.; Fu, H.; Yan, C.; Chiu, K. A Review of the Clinical Approach to Persistent Pain Following Total Hip Replacement. *Hong Kong Med. J.* **2016**, *22*, 600–608. [[CrossRef](#)] [[PubMed](#)]
8. Agten, C.A.; Sutter, R.; Dora, C.; Pfirrmann, C.W.A. MR Imaging of Soft Tissue Alterations after Total Hip Arthroplasty: Comparison of Classic Surgical Approaches. *Eur. Radiol.* **2017**, *27*, 1312–1321. [[CrossRef](#)]
9. Bäcker, H.C.; Steurer-Dober, I.; Beck, M.; Agten, C.A.; Decking, J.; Herzog, R.F.; Geller, J.A.; Bhure, U.; Roos, J.E.; Strobel, K. Magnetic Resonance Imaging (MRI) versus Single Photon Emission Computed Tomography (SPECT/CT) in Painful Total Hip Arthroplasty: A Comparative Multi-Institutional Analysis. *BJR* **2020**, *93*, 20190738. [[CrossRef](#)] [[PubMed](#)]
10. Belzunce, M.A.; Henckel, J.; Di Laura, A.; Hart, A. Uncemented Femoral Stem Orientation and Position in Total Hip Arthroplasty: A CT Study. *J. Orthop. Res.* **2020**, *38*, 1486–1496. [[CrossRef](#)]
11. Berkowitz, J.L.; Potter, H.G. Advanced MRI Techniques for the Hip Joint: Focus on the Postoperative Hip. *Am. J. Roentgenol.* **2017**, *23*, 534. [[CrossRef](#)] [[PubMed](#)]
12. Bozza, N.; Guindani, N.; Pezzotta, G.; Alberto, F.; Castelli, C.C. 15-Year follow-up of MoM 36-Mm THA: Clinical, Laboratory, and Radiological (CT and MRI) Prospective Assessment. *HIP Int.* **2020**, *30*, 42–51. [[CrossRef](#)]
13. Burge, A. Total Hip Arthroplasty: MR Imaging of Complications Unrelated to Metal Wear. *Semin. Musculoskelet. Radiol.* **2015**, *19*, 31–39. [[CrossRef](#)]
14. Deshmukh, S.; Omar, I.M. Imaging of Hip Arthroplasties: Normal Findings and Hardware Complications. *Semin. Musculoskelet. Radiol.* **2019**, *23*, 162–176. [[CrossRef](#)] [[PubMed](#)]
15. Docking, S.I.; Cook, J.; Chen, S.; Scarvell, J.; Cormick, W.; Smith, P.; Fearon, A. Identification and Differentiation of Gluteus Medius Tendon Pathology Using Ultrasound and Magnetic Resonance Imaging. *Musculoskelet. Sci. Pract.* **2019**, *41*, 1–5. [[CrossRef](#)] [[PubMed](#)]
16. Filli, L.; Jungmann, P.M.; Zingg, P.O.; Rüdiger, H.A.; Galley, J.; Sutter, R.; Pfirrmann, C.W.A. MRI with State-of-the-Art Metal Artifact Reduction after Total Hip Arthroplasty: Periprosthetic Findings in Asymptomatic and Symptomatic Patients. *Eur. Radiol.* **2020**, *30*, 2241–2252. [[CrossRef](#)] [[PubMed](#)]
17. Galea, V.P.; Laaksonen, I.; Connelly, J.W.; Matuszak, S.J.; Nortje, M.; Madanat, R.; Muratoglu, O.; Malchau, H. What Is the Clinical Presentation of Adverse Local Tissue Reaction in Metal-on-Metal Hip Arthroplasty? An MRI Study. *Clin. Orthop. Relat. Res.* **2019**, *477*, 353–360. [[CrossRef](#)] [[PubMed](#)]
18. Galley, J.; Sutter, R.; Stern, C.; Filli, L.; Rahm, S.; Pfirrmann, C.W.A. Diagnosis of Periprosthetic Hip Joint Infection Using MRI with Metal Artifact Reduction at 1.5 T. *Radiology* **2020**, *296*, 98–108. [[CrossRef](#)] [[PubMed](#)]
19. Germann, C.; Filli, L.; Jungmann, P.M.; Graf, D.N.; Fritz, J.; Pfirrmann, C.W.A.; Sutter, R. Prospective and Longitudinal Evolution of Postoperative Periprosthetic Findings on Metal Artifact-Reduced MR Imaging in Asymptomatic Patients after Uncemented Total Hip Arthroplasty. *Skelet. Radiol.* **2020**, *50*, 1177–1188. [[CrossRef](#)] [[PubMed](#)]
20. Giori, N.J. CORR Insights®: MRI of THA Correlates with Implant Wear and Tissue Reactions: A Cross-Sectional Study. *Clin. Orthop. Relat. Res.* **2019**, *477*, 175–176. [[CrossRef](#)] [[PubMed](#)]
21. Hargunani, R.; Madani, H.; Khoo, M.; Fotiadou, A.; Pressney, L.; Calleja, M.; O'Donnell, P. Imaging of the Painful Hip Arthroplasty. *Can. Assoc. Radiol. J.* **2016**, *67*, 345–355. [[CrossRef](#)] [[PubMed](#)]
22. Jennings, J.M.; Czuczman, G.J.; Johnson, R.M.; Dennis, D.A. Metal Artifact Reduction Sequence Magnetic Resonance Imaging Abnormalities in Asymptomatic Patients with a Ceramic-on-Ceramic Total Hip Replacement. *J. Arthroplast.* **2021**, *36*, 612–615. [[CrossRef](#)] [[PubMed](#)]
23. Jungmann, P.M.; Bensler, S.; Zingg, P.; Fritz, B.; Pfirrmann, C.W.; Sutter, R. Improved Visualization of Juxtaprosthetic Tissue Using Metal Artifact Reduction Magnetic Resonance Imaging: Experimental and Clinical Optimization of Compressed Sensing SEMAC. *Investig. Radiol.* **2019**, *54*, 23–31. [[CrossRef](#)] [[PubMed](#)]
24. Khodarahmi, I.; Fritz, J. Advanced MR Imaging after Total Hip Arthroplasty: The Clinical Impact. *Semin. Musculoskelet. Radiol.* **2017**, *21*, 616–629. [[CrossRef](#)] [[PubMed](#)]

25. Khodarahmi, I.; Nittka, M.; Fritz, J. Leaps in Technology: Advanced MR Imaging after Total Hip Arthroplasty. *Semin. Musculoskelet. Radiol.* **2017**, *21*, 604–615. [[CrossRef](#)] [[PubMed](#)]
26. Khodarahmi, I.; Rajan, S.; Sterling, R.; Koch, K.; Kirsch, J.; Fritz, J. Heating of Hip Arthroplasty Implants During Metal Artifact Reduction MRI at 1.5- and 3.0-T Field Strengths. *Investig. Radiol.* **2020**, *56*, 232–243. [[CrossRef](#)]
27. Klemt, C.; Simeone, F.J.; Melnic, C.M.; Tirumala, V.; Xiong, L.; Kwon, Y.-M. MARS MRI Assessment of Fatty Degeneration of the Gluteal Muscles in Patients with THA: Reliability and Accuracy of Commonly Used Classification Systems. *Skelet. Radiol.* **2020**, *50*, 665–672. [[CrossRef](#)]
28. Koff, M.F.; Esposito, C.; Shah, P.; Mfa, M.M.; Bs, E.B.; Fields, K.; Bauer, T.; Padgett, D.E.; Wright, T.; Potter, H.G. MRI of THA Correlates with Implant Wear and Tissue Reactions: A Cross-Sectional Study. *Clin. Orthop. Relat. Res.* **2018**, *477*, 16. [[CrossRef](#)] [[PubMed](#)]
29. Kovalak, E.; Özdemir, H.; Ermutlu, C.; Obut, A. Assessment of Hip Abductors by MRI after Total Hip Arthroplasty and Effect of Fatty Atrophy on Functional Outcome. *Acta Orthop. Traumatol. Turc.* **2018**, *52*, 196–200. [[CrossRef](#)]
30. Mahajan, J.; Bonner, B.; Oganessian, R.; Yeo, I.; Klemt, C.; Kwon, Y.-M. MARS MRI Characteristics of Adverse Local Tissue Reactions in Taper Corrosion of Metal-On-Polyethylene THA Differ from Metal-On-Metal THA. *J. Arthroplast.* **2020**, *35*, 3338–3342. [[CrossRef](#)]
31. Marchica, D.; Gallazzi, E.; Materazzi, G.; Battaglia, G.A.; Zagra, L. MRI Findings, Metal Ion Levels and Clinical Outcome of a Complete Series of Large Metal on Metal THA: What's Really Going on? *HIP Int.* **2018**, *28*, 48–53. [[CrossRef](#)] [[PubMed](#)]
32. Mulcahy, H.; Chew, F.S. Current Concepts of Hip Arthroplasty for Radiologists: Part 1, Features and Radiographic Assessment. *Am. J. Roentgenol.* **2012**, *199*, 559–569. [[CrossRef](#)]
33. Mulcahy, H.; Chew, F.S. Current Concepts of Hip Arthroplasty for Radiologists: Part 2, Revisions and Complications. *Am. J. Roentgenol.* **2012**, *199*, 570–580. [[CrossRef](#)] [[PubMed](#)]
34. Müller, G.M.; Månsson, S.; Müller, M.F.; von Schewelov, T.; Nittka, M.; Ekberg, O.; Lundin, B. MR Imaging with Metal Artifact-Reducing Sequences and Gadolinium Contrast Agent in a Case-Control Study of Periprosthetic Abnormalities in Patients with Metal-on-Metal Hip Prostheses. *Skelet. Radiol.* **2014**, *43*, 1101–1112. [[CrossRef](#)] [[PubMed](#)]
35. Nam, D.; Barrack, R.L.; Potter, H.G. What Are the Advantages and Disadvantages of Imaging Modalities to Diagnose Wear-Related Corrosion Problems? *Clin. Orthop. Relat. Res.* **2014**, *472*, 9. [[CrossRef](#)] [[PubMed](#)]
36. Romanò, C.L.; Petrosillo, N.; Argento, G.; Sconfienza, L.M.; Treglia, G.; Alavi, A. The Role of Imaging Techniques to Define a Peri-Prosthetic Hip and Knee Joint Infection: Multidisciplinary Consensus Statements. *J. Clin. Med.* **2020**, *9*, 2548. [[CrossRef](#)] [[PubMed](#)]
37. Roth, T.D.; Maertz, N.A.; Parr, J.A.; Buckwalter, K.A.; Choplin, R.H. CT of the Hip Prosthesis: Appearance of Components, Fixation, and Complications. *RadioGraphics* **2012**, *32*, 1089–1107. [[CrossRef](#)]
38. Schwaiger, B.J.; Gassert, F.T.; Suren, C.; Gersing, A.S.; Haller, B.; Pfeiffer, D.; Dangelmaier-Dawirs, J.; Roski, F.; von Eisenhart-Rothe, R.; Prodinger, P.M.; et al. Diagnostic Accuracy of MRI with Metal Artifact Reduction for the Detection of Periprosthetic Joint Infection and Aseptic Loosening of Total Hip Arthroplasty. *Eur. J. Radiol.* **2020**, *131*, 109253. [[CrossRef](#)] [[PubMed](#)]
39. Zochowski, K.C.; Miranda, M.A.; Cheung, J.; Argentieri, E.C.; Lin, B.; Kaushik, S.S.; Burge, A.J.; Potter, H.G.; Koff, M.F. MRI of Hip Arthroplasties: Comparison of Isotropic Multiacquisition Variable-Resonance Image Combination Selective (MAVRIC SL) Acquisitions with a Conventional MAVRIC SL Acquisition. *Am. J. Roentgenol.* **2019**, *213*, W277–W286. [[CrossRef](#)] [[PubMed](#)]
40. Choplin, R.H.; Henley, C.N.; Edds, E.M.; Capello, W.; Rankin, J.L.; Buckwalter, K.A. Total Hip Arthroplasty in Patients with Bone Deficiency of the Acetabulum. *RadioGraphics* **2008**, *28*, 771–786. [[CrossRef](#)] [[PubMed](#)]
41. Chughtai, M.; Mistry, J.B.; Diedrich, A.M.; Jauregui, J.J.; Elmallah, R.K.; Bonutti, P.M.; Harwin, S.F.; Malkani, A.L.; Kolisek, F.R.; Mont, M.A. Low Frequency of Early Complications with Dual-Mobility Acetabular Cups in Cementless Primary THA. *Clin. Orthop. Relat. Res.* **2016**, *474*, 2181–2187. [[CrossRef](#)] [[PubMed](#)]
42. Szymanski, C.; Guériot, S.; Boniface, O.; Deladerrière, J.-Y.; Luneau, S.; Maynou, C. Taux de fracture des inserts de céramique « sandwich » dans un cotyle ATLAS IIITM: Étude de 144 prothèses totales de hanche de première intention à 74 mois de recul. *Rev. Chir. Orthop. Traumatol.* **2011**, *97*, 485–492. [[CrossRef](#)]
43. Gulow, J.; Scholz, R.; Freiherr von Salis-Soglio, G. Short-stemmed endoprostheses in total hip arthroplasty. *Orthopade* **2007**, *36*, 353–359. [[CrossRef](#)]
44. Tottas, S.; Ververidis, A.; Kougioumtzis, I.; Tilkeridis, K.; Tsigalou, C.; Karaglani, M.; Drosos, G. MINIMA Short Stem versus Standard Profemur (TL) Stem in Primary Total Hip Replacement: A Comparative Study. *Cureus* **2022**, *14*, e23771. [[CrossRef](#)] [[PubMed](#)]
45. Pluot, E.; Davis, E.T.; Revell, M.; Davies, A.M.; James, S.L.J. Hip Arthroplasty. Part 1: Prosthesis Terminology and Classification. *Clin. Radiol.* **2009**, *64*, 954–960. [[CrossRef](#)] [[PubMed](#)]
46. Erschbamer, M.; Zdravkovic, V.; Erhardt, J.; Öhlschlegel, C.; Grob, K. Osteolytic Changes around Biodegradable Cement Restrictors in Hip Surgery. *Acta Orthop.* **2016**, *87*, 239–244. [[CrossRef](#)] [[PubMed](#)]
47. Kusserow, A.; Ficklscherer, A.; Kreuz, P.C.; Finze, S.; Mittelmeier, W.; Jansson, V.; Milz, S.; Wegener, B. Importance of a Distal Centralizer in Experimental Malpositioning of Cemented Stems. A Biomechanical Study on Human Femora. *Arch. Med. Sci.* **2015**, *11*, 1324–1329. [[CrossRef](#)] [[PubMed](#)]

48. Weber, E.; Olsson, C.; Kesteris, U.; Flivik, G. Is a Hollow Centralizer Necessary When Using a Polished, Tapered, Cemented Femoral Stem? *Acta Orthop.* **2017**, *88*, 377–382. [[CrossRef](#)]
49. Fischer, T. Impact of Stem Design and Cementation on Postoperative Femoral Antetorsion in 227 Patients with Total Hip Arthroplasty (THA). *Skelet. Radiol.* **2020**, *9*, 2001–2009. [[CrossRef](#)] [[PubMed](#)]
50. Coden, G.; Matzko, C.; Hushmehdy, S.; Macaulay, W.; Hepinstall, M. Impact of Acetabular Implant Design on Aseptic Failure in Total Hip Arthroplasty. *Arthroplast. Today* **2021**, *7*, 60–68. [[CrossRef](#)] [[PubMed](#)]
51. Raja, B.S.; Gowda, A.K.S.; Singh, S.; Ansari, S.; Kalia, R.B.; Paul, S. Comparison of Functional Outcomes and Complications of Cemented vs. Uncemented Total Hip Arthroplasty in the Elderly Neck of Femur Fracture Patients: A Systematic Review and Meta-Analysis. *J. Clin. Orthop. Trauma* **2022**, *29*, 101876. [[CrossRef](#)] [[PubMed](#)]
52. Shim, B.-J.; Park, S.-J.; Park, C.H. The Wear Rate and Survivorship in Total Hip Arthroplasty Using a Third-Generation Ceramic Head on a Conventional Polyethylene Liner: A Minimum of 15-Year Follow-Up. *Hip Pelvis* **2022**, *34*, 115–121. [[CrossRef](#)] [[PubMed](#)]
53. Matharu, G.S.; Judge, A.; Eskelinen, A.; Murray, D.W.; Pandit, H.G. What Is Appropriate Surveillance for Metal-on-Metal Hip Arthroplasty Patients?: A Clinical Update. *Acta Orthop.* **2018**, *89*, 29–39. [[CrossRef](#)] [[PubMed](#)]
54. Fantino, O.; Tayot, O.; Sans, N.; Cyteval, C. Imaging of total hip arthroplasty: Normal and pathological imaging features, role of ultrasound, CT and MRI. *J. Radiol.* **2011**, *92*, 594–620. [[CrossRef](#)] [[PubMed](#)]
55. Gillet, R.; Teixeira, P.; Bonarelli, C.; Coudane, H.; Sirveaux, F.; Louis, M.; Blum, A. Comparison of Radiographs, Tomosynthesis and CT with Metal Artifact Reduction for the Detection of Hip Prosthetic Loosening. *Eur. Radiol.* **2019**, *29*, 1258–1266. [[CrossRef](#)]
56. Blum, A.; Gillet, R.; Rauch, A.; Urbaneja, A.; Biouchi, H.; Dodin, G.; Germain, E.; Lombard, C.; Jaquet, P.; Louis, M.; et al. 3D Reconstructions, 4D Imaging and Postprocessing with CT in Musculoskeletal Disorders: Past, Present and Future. *Diagn. Interv. Imaging* **2020**, *101*, S2211568420302254. [[CrossRef](#)]
57. Fritz, J.; Lurie, B.; Miller, T.T.; Potter, H.G. MR Imaging of Hip Arthroplasty Implants. *RadioGraphics* **2014**, *34*, E106–E132. [[CrossRef](#)]
58. Koff, M.F.; Burge, A.; Koch, K.M.; Potter, H.G. Magnetic Resonance Imaging Near Orthopaedic Hardware. *J. Magn. Reson. Imaging* **2017**, *46*, 24–39. [[CrossRef](#)]
59. Guerini, H. IRM Des Ptohéses de Hanche. In *La Hanche*; SIMS; Sauramps: Montpellier, France, 2019; Volume 46, pp. 233–247.
60. Lecerf, G.; Fessy, M.H.; Philippot, R.; Massin, P.; Giraud, F.; Flecher, X.; Girard, J.; Mertl, P.; Marchetti, E.; Stindel, E. Femoral Offset: Anatomical Concept, Definition, Assessment, Implications for Preoperative Templating and Hip Arthroplasty. *Orthop. Traumatol. Surg. Res.* **2009**, *95*, 210–219. [[CrossRef](#)]
61. Meneghini, R.M. Investigation of the Unstable Total Hip Arthroplasty. *J. Arthroplast.* **2018**, *33*, 1325–1327. [[CrossRef](#)]
62. Gejjer, M.; Kiernan, S.; Sundberg, M.; Flivik, G. Pre- and Postoperative Offset and Femoral Neck Version Measurements and Validation Using 3D Computed Tomography in Total Hip Arthroplasty. *Acta Radiol. Open* **2020**, *9*, 2058460120964911. [[CrossRef](#)] [[PubMed](#)]
63. Tsang, H.; Bouz, T.; Kwan, K.; French, M. The Intraoperative Pelvic Radiograph during Total Hip Arthroplasty: Is It Reliable to Estimate Leg Length? *Arthroplast. Today* **2022**, *16*, 9–14. [[CrossRef](#)] [[PubMed](#)]
64. O'Brien, S.; Kernohan, G.; Fitzpatrick, C.; Hill, J.; Beverland, D. Perception of Imposed Leg Length Inequality in Normal Subjects. *HIP Int.* **2010**, *20*, 505–511. [[CrossRef](#)] [[PubMed](#)]
65. Renkawitz, T.; Weber, T.; Dullien, S.; Woerner, M.; Dendorfer, S.; Grifka, J.; Weber, M. Leg Length and Offset Differences above 5mm after Total Hip Arthroplasty Are Associated with Altered Gait Kinematics. *Gait Posture* **2016**, *49*, 196–201. [[CrossRef](#)] [[PubMed](#)]
66. Park, K.-R.; Lee, J.-H.; Kim, D.-S.; Ryu, H.; Kim, J.; Yon, C.-J.; Lee, S.-W. The Comparison of Lower Extremity Length and Angle between Computed Radiography-Based Teleoroentgenogram and EOS® Imaging System. *Diagnostics* **2022**, *12*, 1052. [[CrossRef](#)] [[PubMed](#)]
67. Ponsot, A. Analyse Du Positionnement Des Pièces Prothétiques et Complications Précoces. In *La Hanche*; SIMS; Sauramps: Montpellier, France, 2019; Volume 46, pp. 187–205.
68. Fouque, O. Prothèse Totale de Hanche: Quelles Mesures Essentielles Le Radiologue Doit-Il Connaître? In *Savoir Faire en Radiologie Ostéo-Articulaire: Hanche et Ceinture Pelvienne*; Sauramps: Montpellier, France, 2018; Volume 20, pp. 211–223.
69. Bendaya, S.; Anglin, C.; Lazennec, J.-Y.; Allena, R.; Thoumie, P.; Skalli, W. Good vs. Poor Results after Total Hip Arthroplasty: An Analysis Method Using Implant and Anatomic Parameters with the EOS Imaging System. *J. Arthroplast.* **2016**, *31*, 2043–2052. [[CrossRef](#)]
70. Pour, A.E.; Schwarzkopf, R.; Patel, K.P.K.; Anjaria, M.P.; Lazennec, J.Y.; Dorr, L.D. How Much Change in Pelvic Sagittal Tilt Can Result in Hip Dislocation Due to Prosthetic Impingement? A Computer Simulation Study. *J. Orthop. Res.* **2021**, *39*, 2604–2614. [[CrossRef](#)]
71. Lazennec, J.Y.; Clark, I.C.; Folinais, D.; Tahar, I.N.; Pour, A.E. What Is the Impact of a Spinal Fusion on Acetabular Implant Orientation in Functional Standing and Sitting Positions? *J. Arthroplast.* **2017**, *32*, 3184–3190. [[CrossRef](#)]
72. Lazennec, J.Y.; Kim, Y.; Folinais, D.; Pour, A.E. Sagittal Spinopelvic Translation Is Combined with Pelvic Tilt During the Standing to Sitting Position: Pelvic Incidence Is a Key Factor in Patients Who Underwent THA. *Arthroplast. Today* **2020**, *6*, 672–681. [[CrossRef](#)]
73. Lazennec, J.-Y.; Rousseau, M.-A.; Brusson, A.; Folinais, D.; Amel, M.; Clarke, I.; Pour, A.E. Total Hip Prostheses in Standing, Sitting and Squatting Positions: An Overview of Our 8 Years Practice Using the EOS Imaging Technology. *Open Orthop. J.* **2015**, *9*, 26–44. [[CrossRef](#)]

74. Perronne, L.; Haehnel, O.; Chevret, S.; Wybier, M.; Hannouche, D.; Nizard, R.; Bousson, V. How Is Quality of Life after Total Hip Replacement Related to the Reconstructed Anatomy? A Study with Low-Dose Stereoradiography. *Diagn. Interv. Imaging* **2021**, *102*, 101–107. [[CrossRef](#)] [[PubMed](#)]
75. Fackler, C.D.; Poss, R. Dislocation in Total Hip Arthroplasties. *Clin. Orthop. Relat. Res.* **1980**, 169–178. [[CrossRef](#)]
76. Fischer, T.; Stern, C.; Fritz, B.; Zingg, P.O.; Pfirrmann, C.W.; Sutter, R. MRI Findings of Ischiofemoral Impingement after Total Hip Arthroplasty Are Associated with Increased Femoral Antetorsion. *Acta Radiol.* **2021**, *63*, 2841851211021044. [[CrossRef](#)]
77. Pluot, E.; Davis, E.T.; Revell, M.; Davies, A.M.; James, S.L.J. Hip Arthroplasty. Part 2: Normal and Abnormal Radiographic Findings. *Clin. Radiol.* **2009**, *64*, 961–971. [[CrossRef](#)] [[PubMed](#)]
78. Amstutz, H.C.; Beaulé, P.E.; Dorey, F.J.; Le Duff, M.J.; Campbell, P.A.; Gruen, T.A. Metal-on-Metal Hybrid Surface Arthroplasty: Two to Six-Year Follow-up Study. *J. Bone Jt. Surg. Am.* **2004**, *86*, 28–39. [[CrossRef](#)]
79. Amstutz, C.; Duff, M.J.L.; Campbell, P.A.; Gruen, T.A.; Wisk, L.E. Clinical and Radiographic Results of Metal-on-Metal Hip Resurfacing with a Minimum Ten-Year Follow-Up. *J. Bone Jt. Surg. Am.* **2010**, *92*, 2663–2671. [[CrossRef](#)] [[PubMed](#)]
80. Blum, A. Prothèse Douleureuse: L'interface Osseuse. In *La Hanche*; SIMS; Sauramps: Montpellier, France, 2019; Volume 46, pp. 215–231.
81. Blum, A.; Gondim-Teixeira, P.; Gabiache, E.; Roche, O.; Sirveaux, F.; Olivier, P.; Coudane, H.; Raymond, A.; Louis, M.; Grandhay, M.; et al. Developments in Imaging Methods Used in Hip Arthroplasty: A Diagnostic Algorithm. *Diagn. Interv. Imaging* **2016**, *97*, 735–747. [[CrossRef](#)] [[PubMed](#)]
82. Rogmark, C.; Nätman, J.; Jobory, A.; Hailer, N.P.; Cnudde, P. The Association of Surgical Approach and Bearing Size and Type with Dislocation in Total Hip Arthroplasty for Acute Hip Fracture. *Bone Jt. J.* **2022**, *104-B*, 844–851. [[CrossRef](#)] [[PubMed](#)]
83. Pelissou, C.; Miquel, A.; Phan, C.; Paycha, F.; Sautet, A.; Arrivé, L. L'imagerie des prothèses de hanche: Complications communes et spécifiques des différents couples de frottements. *J. D'imagerie Diagn. Interv.* **2020**, *3*, 47–66. [[CrossRef](#)]
84. Sutphen, S.A.; Lipman, J.D.; Jerabek, S.A.; Mayman, D.J.; Esposito, C.I. Treatment of Recurrent Dislocation after Total Hip Arthroplasty Using Advanced Imaging and Three-Dimensional Modeling Techniques: A Case Series. *HSS J.* **2020**, *16*, 245–255. [[CrossRef](#)]
85. De Martino, I.; D'Apolito, R.; Waddell, B.S.; McLawhorn, A.S.; Sculco, P.K.; Sculco, T.P. Early Intraprosthetic Dislocation in Dual-Mobility Implants: A Systematic Review. *Arthroplast. Today* **2017**, *3*, 197–202. [[CrossRef](#)] [[PubMed](#)]
86. Marchetti, E.; Krantz, N.; Berton, C.; Bocquet, D.; Fouilleron, N.; Migaud, H.; Girard, J. Component Impingement in Total Hip Arthroplasty: Frequency and Risk Factors. A Continuous Retrieval Analysis Series of 416 Cup. *Orthop. Traumatol. Surg. Res.* **2011**, *97*, 127–133. [[CrossRef](#)] [[PubMed](#)]
87. Lazennec, J.Y.; Brusson, A.; Rousseau, M.A. Lumbar-Pelvic-Femoral Balance on Sitting and Standing Lateral Radiographs. *Orthop. Traumatol. Surg. Res.* **2013**, *99*, S87–S103. [[CrossRef](#)] [[PubMed](#)]
88. Phan, D.; Bederman, S.S.; Schwarzkopf, R. The Influence of Sagittal Spinal Deformity on Anteversion of the Acetabular Component in Total Hip Arthroplasty. *Bone Jt. J.* **2015**, *97-B*, 1017–1023. [[CrossRef](#)] [[PubMed](#)]
89. Tsukayama, D.T.; Estrada, R.; Gustilo, R.B. Infection after Total Hip Arthroplasty. A Study of the Treatment of One Hundred and Three Infections. *J. Bone Jt. Surg. Am.* **1996**, *78*, 512–523. [[CrossRef](#)]
90. Barrack, R.L.; Mulroy, R.D.; Harris, W.H. Improved Cementing Techniques and Femoral Component Loosening in Young Patients with Hip Arthroplasty: A 12-Year Radiographic Review. *J. Bone Jt. Surg. Br.* **1992**, *74*, 385–389. [[CrossRef](#)] [[PubMed](#)]
91. Tang, H.; Huang, X.; Cheng, X.; Yang, D.; Huang, Y.; Zhou, Y. Evaluation of Peri-Prosthetic Radiolucent Lines Surrounding the Cementless Femoral Stem Using Digital Tomosynthesis with Metal Artifact Reduction: A Cadaveric Study in Comparison with Radiography and Computed Tomography. *Quant. Imaging Med. Surg.* **2020**, *10*, 1786–1800. [[CrossRef](#)]
92. Hodgkinson, J.P.; Shelley, P.; Wroblewski, B.M. The Correlation between the Roentgenographic Appearance and Operative Findings at the Bone-Cement Junction of the Socket in Charnley Low Friction Arthroplasties. *Clin. Orthop. Relat. Res.* **1988**, *228*, 105–109. [[CrossRef](#)]
93. Engh, C.A.; Massin, P.; Suthers, K.E. Roentgenographic Assessment of the Biologic Fixation of Porous-Surfaced Femoral Components. *Clin. Orthop. Relat. Res.* **1990**, *257*, 107–128. [[CrossRef](#)]
94. Roche, O.; Girard, J.; Canovas, F.; Migaud, H.; Bonnomet, F.; Goldschild, M.; Le Béguet, P. Assessment of Fixation in Cementless Femoral Revision of Total Hip Arthroplasty: Comparison of the Engh Score versus Radiolucent Line Measurement. *Int. Orthop.* **2016**, *40*, 907–912. [[CrossRef](#)] [[PubMed](#)]
95. Canovas, F.; Putman, S.; Girard, J.; Roche, O.; Bonnomet, F.; Le Béguet, P. Global Radiological Score for Femoral Cementless Revision Stem. *Int. Orthop.* **2018**, *42*, 1007–1013. [[CrossRef](#)]
96. Van den Wyngaert, T.; Paycha, F.; Strobel, K.; Kampen, W.U.; Kuwert, T.; van der Bruggen, W.; Gnanasegaran, G. SPECT/CT in Postoperative Painful Hip Arthroplasty. *Semin. Nucl. Med.* **2018**, *48*, 425–438. [[CrossRef](#)]
97. Goswami, K.; Clarkson, S.; Phillips, C.D.; Dennis, D.A.; Klatt, B.A.; O'Malley, M.J.; Smith, E.L.; Gililand, J.M.; Pelt, C.E.; Peters, C.L.; et al. An Enhanced Understanding of Culture-Negative Periprosthetic Joint Infection with Next-Generation Sequencing: A Multicenter Study. *J. Bone Jt. Surg. Am.* **2022**. [[CrossRef](#)]
98. Parvizi, J.; Tan, T.L.; Goswami, K.; Higuera, C.; Della Valle, C.; Chen, A.F.; Shohat, N. The 2018 Definition of Periprosthetic Hip and Knee Infection: An Evidence-Based and Validated Criteria. *J. Arthroplast.* **2018**, *33*, 1309–1314.e2. [[CrossRef](#)]

99. Albano, D.; Messina, C.; Zagra, L.; Andreatta, M.; De Vecchi, E.; Gitto, S.; Sconfienza, L.M. Failed Total Hip Arthroplasty: Diagnostic Performance of Conventional MRI Features and Locoregional Lymphadenopathy to Identify Infected Implants. *J. Magn. Reson. Imaging* **2021**, *53*, 201–210. [[CrossRef](#)]
100. Scharfenberger, A.; Clark, M.; Lavoie, G.; O'Connor, G.; Masson, E.; Beaupre, L.A. Treatment of an Infected Total Hip Replacement with the PROSTALAC System. Part 1: Infection Resolution. *Can. J. Surg.* **2007**, *50*, 24–28.
101. Kwon, Y.-M.; MacAuliffe, J.; Arauz, P.G.; Peng, Y. Sensitivity and Specificity of Metal Ion Level in Predicting Adverse Local Tissue Reactions due to Head-Neck Taper Corrosion in Primary Metal-on-Polyethylene Total Hip Arthroplasty. *J. Arthroplast.* **2018**, *33*, 3025–3029. [[CrossRef](#)]
102. Kwon, Y.-M.; Tsai, T.-Y.; Leone, W.A.; Liow, M.H.L. Sensitivity and Specificity of Metal Ion Levels in Predicting “Pseudotumors” due to Taper Corrosion in Patients with Dual Taper Modular Total Hip Arthroplasty. *J. Arthroplast.* **2017**, *32*, 996–1000. [[CrossRef](#)]
103. Kwon, Y.-M.; Khormae, S.; Liow, M.H.L.; Tsai, T.-Y.; Freiberg, A.A.; Rubash, H.E. Asymptomatic Pseudotumors in Patients with Taper Corrosion of a Dual-Taper Modular Femoral Stem: MARS-MRI and Metal Ion Study. *J. Bone Jt. Surg. Am.* **2016**, *98*, 1735–1740. [[CrossRef](#)]
104. Mistry, J.B.; Chughtai, M.; Elmallah, R.K.; Diedrich, A.; Le, S.; Thomas, M.; Mont, M.A. Trunnionosis in Total Hip Arthroplasty: A Review. *J. Orthop. Traumatol.* **2016**, *17*, 1–6. [[CrossRef](#)]
105. Petscavage-Thomas, J.M.; Ha, A. Best Practices: Best Imaging Modality for Surveillance of Metal-on-Metal Hip Arthroplasty. *AJR Am. J. Roentgenol.* **2021**, *216*, 311–317. [[CrossRef](#)]
106. Nawabi, D.H.; Gold, S.; Lyman, S.; Fields, K.; Padgett, D.E.; Potter, H.G. MRI Predicts ALVAL and Tissue Damage in Metal-on-Metal Hip Arthroplasty. *Clin. Orthop. Relat. Res.* **2014**, *472*, 471–481. [[CrossRef](#)]
107. Anderson, H.; Toms, A.P.; Cahir, J.G.; Goodwin, R.W.; Wimbhurst, J.; Nolan, J.F. Grading the Severity of Soft Tissue Changes Associated with Metal-on-Metal Hip Replacements: Reliability of an MR Grading System. *Skelet. Radiol.* **2011**, *40*, 303–307. [[CrossRef](#)] [[PubMed](#)]
108. Matthies, A.K.; Skinner, J.A.; Osmani, H.; Henckel, J.; Hart, A.J. Pseudotumors Are Common in Well-Positioned Low-Wearing Metal-on-Metal Hips. *Clin. Orthop. Relat. Res.* **2012**, *470*, 1895–1906. [[CrossRef](#)]
109. Hauptfleisch, J.; Pandit, H.; Grammatopoulos, G.; Gill, H.S.; Murray, D.W.; Ostlere, S. A MRI Classification of Periprosthetic Soft Tissue Masses (Pseudotumours) Associated with Metal-on-Metal Resurfacing Hip Arthroplasty. *Skelet. Radiol.* **2012**, *41*, 149–155. [[CrossRef](#)]
110. Smeekes, C. Pseudotumor in Metal-on-Metal Hip Arthroplasty: A Comparison Study of Three Grading Systems with MRI. *Skelet. Radiol.* **2018**, *47*, 1099–1109. [[CrossRef](#)] [[PubMed](#)]
111. Avasarala, S.K.; Ahsan, S.T. Bilateral Lower-Extremity Edema Caused by Iliopsoas Bursal Distention after Hip Arthroplasty. *Tex. Heart Inst. J.* **2016**, *43*, 550–551. [[CrossRef](#)] [[PubMed](#)]
112. Czuczman, G.J.; Mandell, J.C.; Khurana, B. Iliopsoas Bursal Extension of Lipohearthrosis: A Novel Imaging Finding Associated with Hip Fracture. *Skelet. Radiol.* **2017**, *46*, 253–257. [[CrossRef](#)]
113. El-Desouky, I.I.; Helal, A.H.; Mansour, A.M.R. Ten-Year Survival of Ceramic-on-Ceramic Total Hip Arthroplasty in Patients Younger than 60 Years: A Systematic Review and Meta-Analysis. *J. Orthop. Surg. Res.* **2021**, *16*, 679. [[CrossRef](#)]
114. Rosinsky, P.J.; Bheem, R.; Meghpara, M.B.; Haden, M.; Shapira, J.; Maldonado, D.R.; Lall, A.C.; Domb, B.G. Asymptomatic Gluteal Tendinopathies Negatively Impact Outcomes of Total Hip Arthroplasty: A Propensity Score-Matched Study. *J. Arthroplast.* **2021**, *36*, 242–249. [[CrossRef](#)]
115. Requicha, F.; Edwards, S.M.; Rickman, M.S.; Comley, A.S. Outcomes Analysis of Anterior and Lateral Approach for Open Repair of Hip Abductor Tendons. *HIP Int.* **2022**, 11207000221103440. [[CrossRef](#)] [[PubMed](#)]
116. Vasarhelyi, E.M.; Williams, H.A.; Howard, J.L.; Petis, S.; Barfett, J.; Lanting, B.A. The Effect of Total Hip Arthroplasty Surgical Technique on Postoperative Muscle Atrophy. *Orthopedics* **2020**, *43*, 361–366. [[CrossRef](#)]
117. Wang, T.; Shao, L.; Xu, W.; Li, F.; Huang, W. Surgical Injury and Repair of Hip External Rotators in THA via Posterior Approach: A Three-Dimensional MRI-Evident Quantitative Prospective Study. *BMC Musculoskelet. Disord.* **2019**, *20*, 22. [[CrossRef](#)]
118. Pfirrmann, C.W.A.; Notzli, H.P.; Dora, C.; Hodler, J.; Zanetti, M. Abductor Tendons and Muscles Assessed at MR Imaging after Total Hip Arthroplasty in Asymptomatic and Symptomatic Patients. *Radiology* **2005**, *235*, 969–976. [[CrossRef](#)]
119. Hasegawa, K.; Kabata, T.; Kajino, Y.; Inoue, D.; Tsuchiya, H. Periprosthetic Occult Fractures of the Acetabulum Occur Frequently During Primary THA. *Clin. Orthop. Relat. Res.* **2017**, *475*, 484–494. [[CrossRef](#)] [[PubMed](#)]
120. Chen, Z.; Pandit, H.; Taylor, A.; Gill, H.; Murray, D.; Ostlere, S. Metal-on-Metal Hip Resurfacings—A Radiological Perspective. *Eur. Radiol.* **2011**, *21*, 485–491. [[CrossRef](#)]
121. He, B.; Li, X.; Dong, R.; Tong, P.; Sun, J. A Multi-Center Retrospective Comparative Study of Third Generation Ceramic-on-Ceramic Total Hip Arthroplasty in Patients Younger than 45 Years with or without the Sandwich Liner: A Ten-Year Minimum. *J. Orthop. Surg.* **2022**, *30*, 10225536221109960. [[CrossRef](#)]
122. ACR. ACR-SPR-SSR Practice Parameter for the Performance and Interpretation of Magnetic Resonance Imaging (MRI) of the Hip and Pelvis for Musculoskeletal Disorders. Practice Parameters and Technical Standards. Available online: <https://www.acr.org/-/media/ACR/Files/Practice-Parameters/mr-hip-pelvis.pdf> (accessed on 10 January 2021).



Review

Gouty Arthropathy: Review of Clinical Manifestations and Treatment, with Emphasis on Imaging

Jennifer S. Weaver ^{1,*}, Ernest R. Vina ², Peter L. Munk ^{3,4}, Andrea S. Klauser ⁵, Jamie M. Elifritz ^{6,7}
and Mihra S. Taljanovic ^{1,8}

¹ Department of Radiology, University of New Mexico, Albuquerque, NM 87131, USA; mihrat@radiology.arizona.edu

² Department of Medicine, University of Arizona Arthritis Center, Tucson, AZ 85724, USA; evina@arizona.edu

³ Department of Radiology, University of British Columbia, Vancouver, BC V6T 1Z4, Canada; peter.munk@vch.ca

⁴ Department of Radiology, Vancouver General Hospital, Vancouver, BC V5Z 1M9, Canada

⁵ Radiology Department, Medical University Innsbruck, Anichstrasse 35, 6020 Innsbruck, Austria; andrea.klauser@i-med.ac.at

⁶ Departments of Radiology and Pathology, University of New Mexico, Albuquerque, NM 87131, USA; jelifritz@salud.unm.edu

⁷ New Mexico Office of the Medical Investigator, Albuquerque, NM 87131, USA

⁸ Departments of Medical Imaging and Orthopaedic Surgery, University of Arizona, Tucson, AZ 85721, USA

* Correspondence: jswaver@salud.unm.edu

Citation: Weaver, J.S.; Vina, E.R.; Munk, P.L.; Klauser, A.S.; Elifritz, J.M.; Taljanovic, M.S. Gouty Arthropathy: Review of Clinical Manifestations and Treatment, with Emphasis on Imaging. *J. Clin. Med.* **2022**, *11*, 166. <https://doi.org/10.3390/jcm11010166>

Academic Editors:
Chrong-Reen Wang,
Fabio Cacciapaglia and
Mitsuhiro Takeno

Received: 21 November 2021

Accepted: 26 December 2021

Published: 29 December 2021

Publisher's Note: MDPI stays neutral with regard to jurisdictional claims in published maps and institutional affiliations.



Copyright: © 2021 by the authors. Licensee MDPI, Basel, Switzerland. This article is an open access article distributed under the terms and conditions of the Creative Commons Attribution (CC BY) license (<https://creativecommons.org/licenses/by/4.0/>).

Abstract: Gout, a crystalline arthropathy caused by the deposition of monosodium urate crystals in the articular and periarticular soft tissues, is a frequent cause of painful arthropathy. Imaging has an important role in the initial evaluation as well as the treatment and follow up of gouty arthropathy. The imaging findings of gouty arthropathy on radiography, ultrasonography, computed tomography, dual energy computed tomography, and magnetic resonance imaging are described to include findings of the early, acute and chronic phases of gout. These findings include early monosodium urate deposits, osseous erosions, and tophi, which may involve periarticular tissues, tendons, and bursae. Treatment of gout includes non-steroidal anti-inflammatories, colchicine, glucocorticoids, interleukin-1 inhibitors, xanthine oxidase inhibitors, uricosuric drugs, and recombinant uricase. Imaging is critical in monitoring response to therapy; clinical management can be modulated based on imaging findings. This review article describes the current standard of care in imaging and treatment of gouty arthropathy.

Keywords: gout; monosodium urate crystals; crystalline arthropathy; imaging; magnetic resonance imaging; sonography; radiography; CT; dual energy CT; treatment

1. Introduction

Gout is the most common cause of inflammatory arthritis in adults [1–13]. It affects approximately 1–2% of the population of industrialized countries and is more common in older males [1,6,13–21]. Gouty arthropathy occurs secondary to abnormal purine metabolism, the end product of which is uric acid, combined with underexcretion or overproduction of uric acid, resulting in sustained hyperuricemia. Hyperuricemia, above the local solubility, can lead to monosodium urate (MSU) crystal deposition (Figure 1) in joints, on the surface of the hyaline cartilage and within periarticular soft tissues such as tendons, ligaments, retinacula, and bursae, with resulting inflammatory response [7,13,14,16,17,19,22–32]. Gout predominantly affects the peripheral joints, but the axial skeleton may also be affected [33].

Imaging has an important role in the initial evaluation, differential diagnosis, and the treatment follow-up of gouty arthropathy. Imaging is also essential when the presentation is atypical or involves deep structures such as the spine, hip, or sacroiliac joint [15]. The imaging findings of gouty arthropathy on radiography, ultrasonography (US), computed

tomography (CT) (both conventional and dual energy computed tomography (DECT)), and magnetic resonance imaging (MRI) (Figures 2–14) are described, to include findings of the early, acute and chronic phases of gout. These findings include early MSU crystal deposits as well as later osseous erosions and tophi, which may involve periarticular tissues, tendons, and bursae.

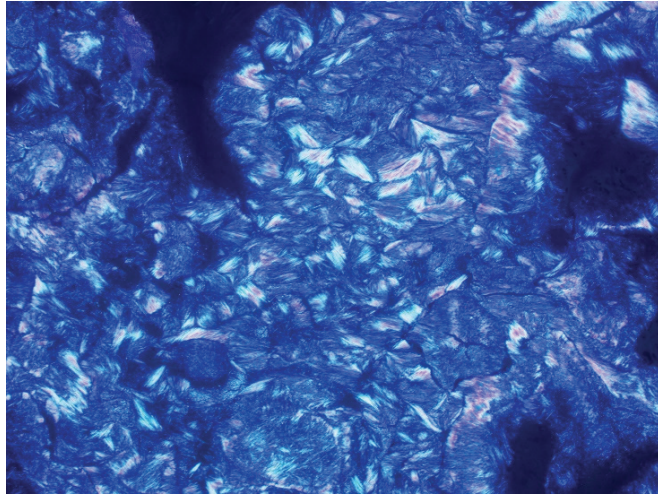


Figure 1. Image from polarizing microscopy 100× shows phagocytosed needle-shaped monosodium urate (MSU) crystals with strong negative birefringence. Image courtesy of Nadja Falk MD; Albuquerque, NM, USA.



Figure 2. A 74-year-old man with gouty arthropathy involving bilateral hands. PA radiograph of the right hand shows erosive and cyst-like changes about multiple joints of the hand and ulnar styloid with adjacent dense soft-tissue nodules (arrows) consistent with gouty arthropathy. Several erosions have overhanging edges, most notable at the radial aspect of the index finger proximal interphalangeal joint. Note faint calcifications within the nodular thickening adjacent to the ulnar styloid erosion.



Figure 3. Tophaceous gout of the posterior elbow in 3 different patients. (a) Initial lateral radiograph of the left elbow in a 57-year-old man shows cortical erosion of the posterior olecranon (black arrow) with marked distension and somewhat increased density of the overlying olecranon bursa (white arrow). Note increased density of the distal triceps tendon (dashed black arrow). (b) Lateral radiograph of the left elbow of the same patient obtained after surgical debridement redemonstrated cortical erosion at the posterior olecranon (black arrow) and increased density of the distal triceps tendon (dashed black arrow) with interval marked improvement of posterior soft-tissue thickening. (c) Lateral radiograph of the right elbow in a 62-year-old man shows a soft-tissue mass involving the olecranon bursa with associated calcifications (arrow). (d) Sagittal T2-weighted with fat saturation MR image in a 60-year-old man shows a large bone erosion involving the posterior olecranon (white arrow) with associated mild bone marrow edema subjacent to a markedly thickened and irregular distal triceps tendon of heterogeneous increased signal intensity (black arrow). Note mildly distended irregular shaped, heterogeneous, predominantly high-signal-intensity olecranon bursa extending into the distal triceps tendon (white arrow) and additional high-signal-intensity subcutaneous edema at the posterior aspect of the elbow.

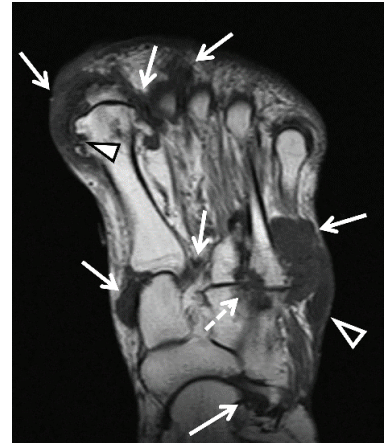


Figure 4. Cont.

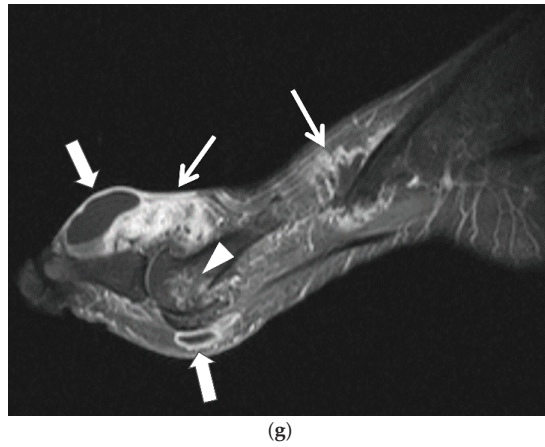


Figure 4. 60-year-old man with tophaceous gout of the right foot. (a) AP radiograph of the right foot shows dense nodular soft-tissue thickening at the medial aspect of the first metatarsophalangeal and first tarsometatarsal joints and at the lateral aspect of the fifth tarsometatarsal joint (arrows). (b) Axial and (c) sagittal STIR and (d) axial and (e) sagittal T1-weighted MR images show multiple areas of intermediate-to-low signal intensity in the periarticular regions of the forefoot and midfoot related to MSU deposits and tophaceous gout (white arrows), cortical erosion at the medial aspect of the first metatarsal head (white arrowheads) and cortical erosions between the third and fourth tarsometatarsal joints (dashed white arrows) which show heterogeneous enhancement on the (f) axial and (g) sagittal T1-weighted with fat saturation post-contrast MR images. In (b) note high-signal-intensity lobulated adventitial bursal collection at the lateral aspect of the proximal fifth metatarsal bone (open white arrowheads) which shows intermediate-to-low signal in (d) and rim enhancement in (f). Additional adventitial bursae (white block arrows) are seen at the dorsal and plantar aspect of the first metatarsophalangeal joint, which show high signal in (c), intermediate-to-low signal in (e) and rim enhancement in (g).

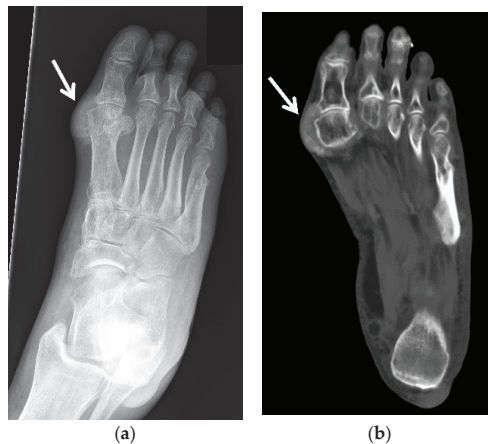


Figure 5. A 60-year-old man with gouty arthropathy of the right first metatarsophalangeal joint, also known as podagra. (a) Oblique radiograph and (b) axial CT image of the right foot shows erosive bone changes at the medial aspect of the great toe metatarsal head and proximal phalangeal base with overlying mass-like dense soft-tissue nodularity with faint calcifications consistent with MSU crystal deposition (arrows). Similar less pronounced findings are seen at the lateral aspect of the first metatarsophalangeal joint.

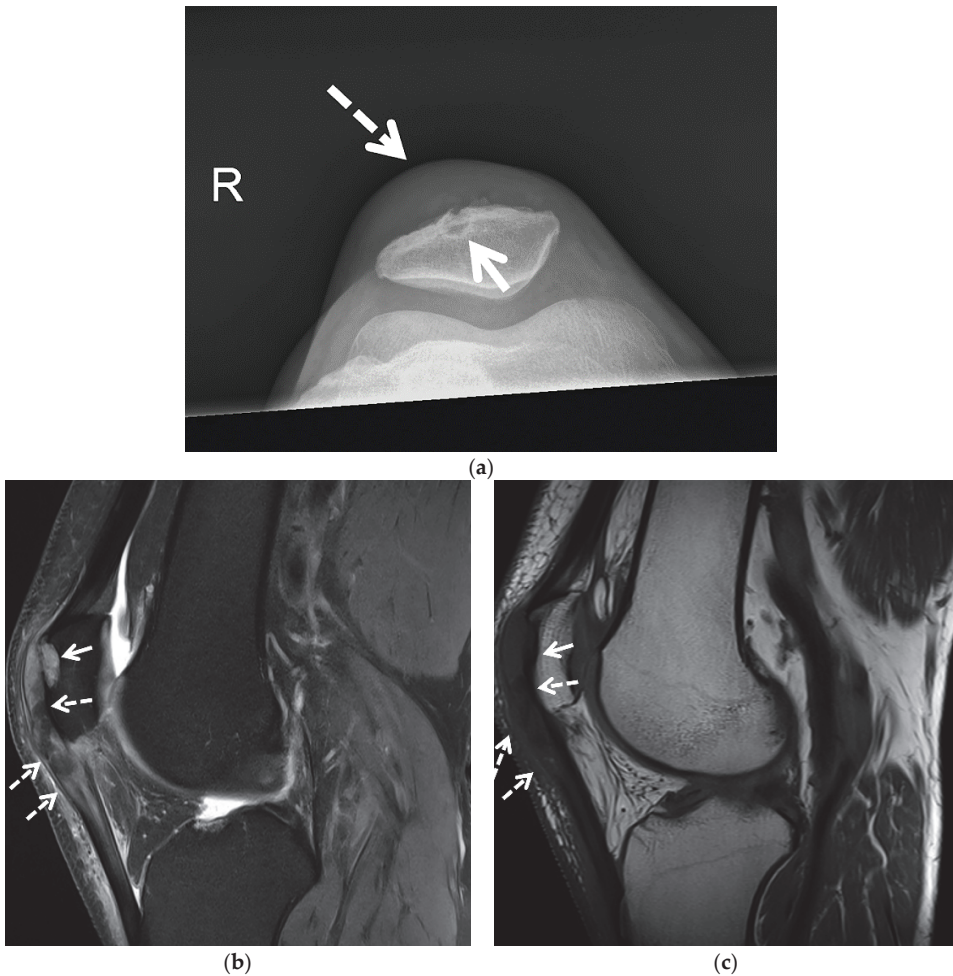
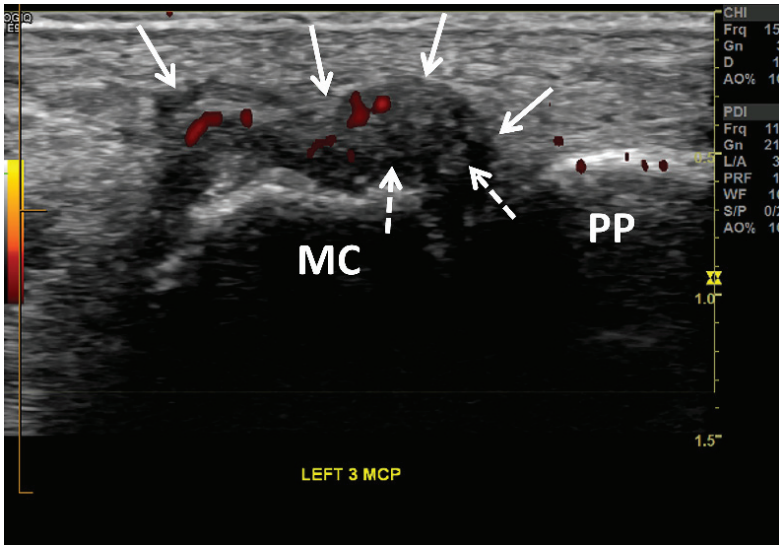
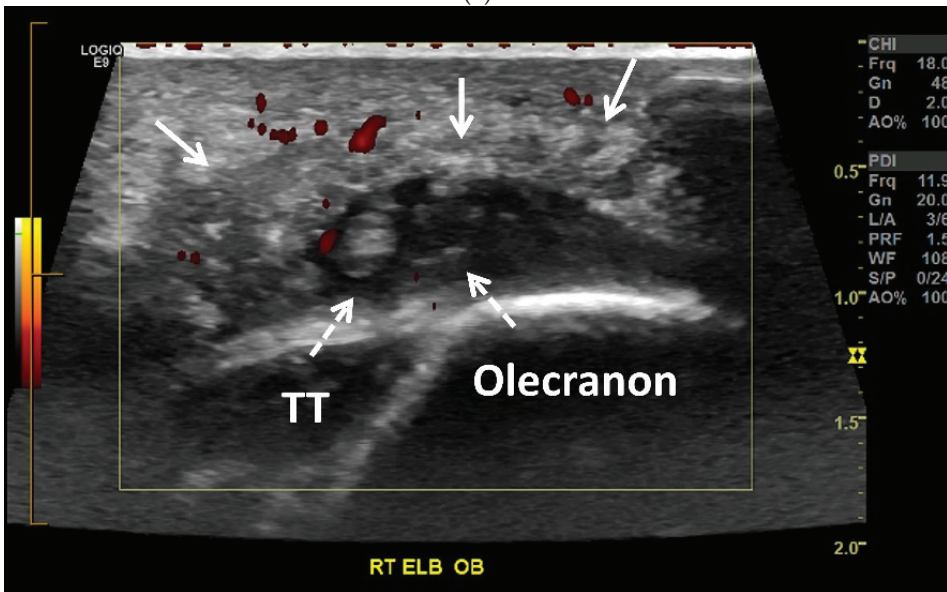


Figure 6. A 54-year-old man with tophaceous gout of the right knee. (a) Patellofemoral radiograph shows a well-marginated osseous erosion at the anterior aspect of the patella (arrow) with overlying soft-tissue edema (dashed arrow). Sagittal (b) proton density-weighted with fat saturation and (c) T1-weighted MR images show osseous erosion with soft-tissue deposit at the anterior surface of the patella (arrows) subjacent to the thickened heterogeneous quadriceps continuation in continuity with the heterogeneous thickened patellar tendon (dashed arrows). The affected extensor mechanism and the soft-tissue deposit at the anterior patellar osseous erosion site show heterogeneous increased signal in (b) and heterogeneous decreased signal in (c) consistent with MSU crystal deposition.

Gout can be successfully treated with urate-lowering therapy, which involves often inexpensive, well-tolerated medications focusing on either reducing serum uric acid formation or increasing the renal excretion of uric acid [22,34]. Early diagnosis and treatment are essential to prevent the long-term sequelae of joint damage and tophus formation, and to prevent other comorbidities such as renal failure and cardiovascular disease [9,10,12,24,27,35,36]. Imaging is critical in monitoring response to therapy; drug therapy can be modulated based on imaging findings to optimize patient outcomes. This review article describes the current standard of care in imaging and treatment of gouty arthropathy.



(a)



(b)

Figure 7. Gouty arthropathy in a 66-year-old woman. (a) Long-axis power Doppler US image along the dorsal aspect of the third metacarpophalangeal joint shows a moderate distension of the joint capsule (arrows) with numerous small echogenic foci related to MSU crystals (dashed arrows), creating “snowstorm” appearance. Note associated mild-to-moderate hyperemia (red). MC = metacarpal head. PP = proximal phalanx. (b) Obliquely oriented power Doppler US image along the posterior aspect of the right olecranon shows a heterogenous moderately distended olecranon bursa (arrows) with numerous small echogenic foci related to MSU crystals (dashed arrows). Note associated mild hyperemia (red). The distal triceps tendon (TT) is hypoechoic with scattered tiny hyperechoic foci consistent with tendinopathy and MSU crystal deposition.

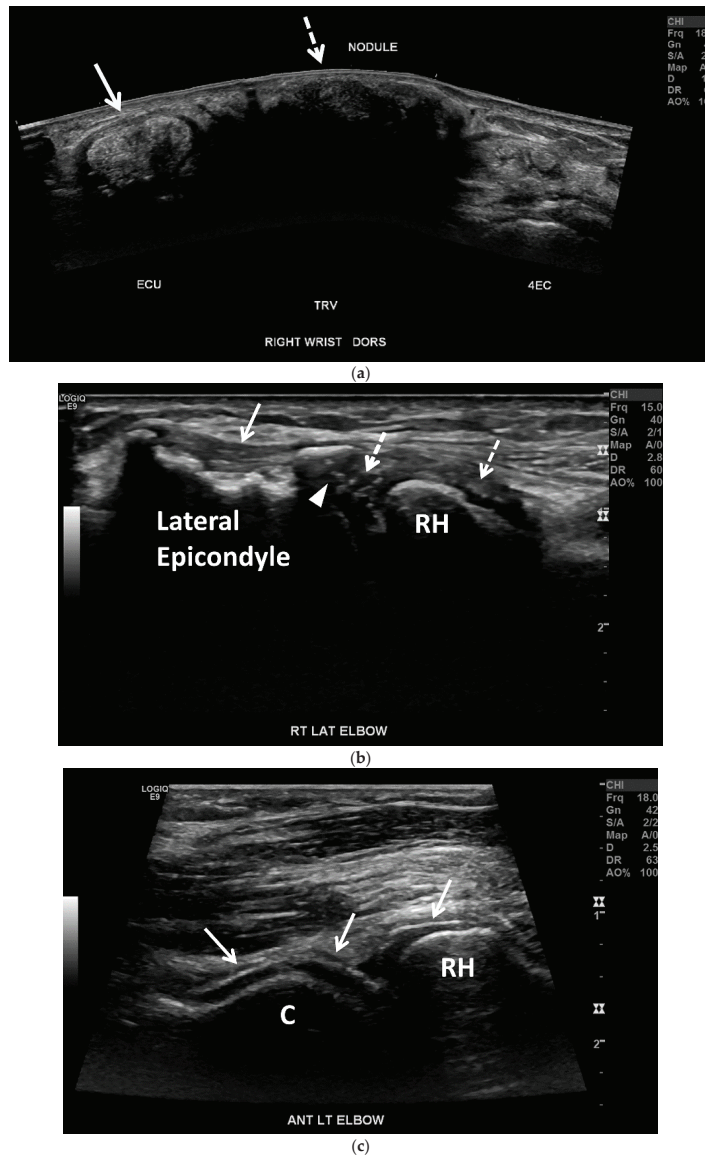


Figure 8. Tophaceous gout in a 73-year-old woman. (a) Panoramic transverse/short-axis gray-scale US image along the dorsal aspect of the right wrist shows markedly thickening and heterogeneous hyperechoic extensor carpi ulnaris tendon (ECU) related to tendinopathy with associated MSU crystal deposition (arrow). Note a large echogenic mass with posterior acoustic shadowing between the ECU and the fourth extensor compartment (4EC) related to a hard tophus (dashed arrow). (b) Long-axis gray-scale US image along the lateral aspect of the right elbow shows multiple small intra-articular echogenic foci related to MSU crystals (dashed arrows), undersurface erosion at the periphery of the capitellum (arrowhead) and cortical irregularity of the lateral humeral epicondyle subjacent to the heterogeneous common extensor tendon suggestive of chronic tendinopathy (arrow). C = capitellum. RH = radial head. (c) Long-axis gray-scale US image along the anterolateral aspect of the right elbow shows “double contour sign” along the radial head and capitellum articular cartilage related to MSU crystal deposition (arrows).

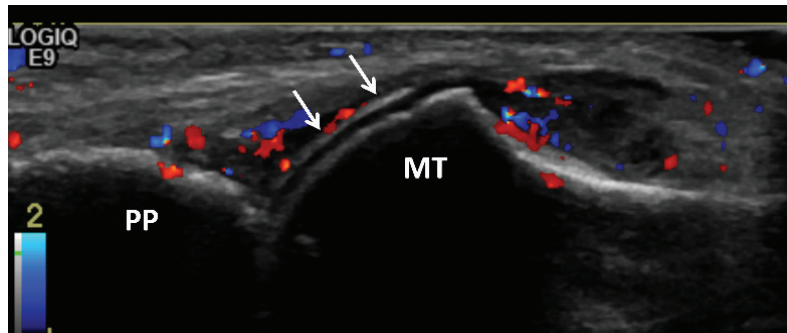
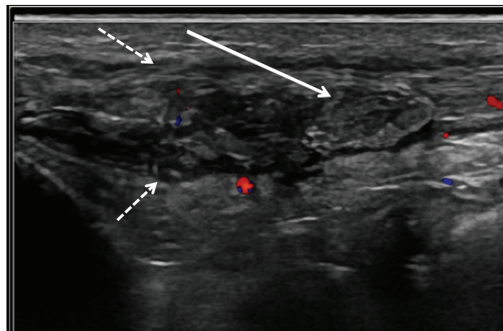


Figure 9. Gouty arthritis of the 1st metatarsophalangeal joint of 45-year-old male. Long-axis color Doppler US image along the dorsal aspect of the first metatarsophalangeal joint shows moderate distension of the joint capsule with moderate hyperemia consistent with synovitis. Note hyperechoic line that parallels the hyperechoic line of the subchondral bone, separated by anechoic cartilage along the metacarpal head (arrow) producing a “double contour” sign related to MSU crystal deposition. MT = metatarsal head. PP = proximal phalanx.



(a)

Figure 10. Cont.

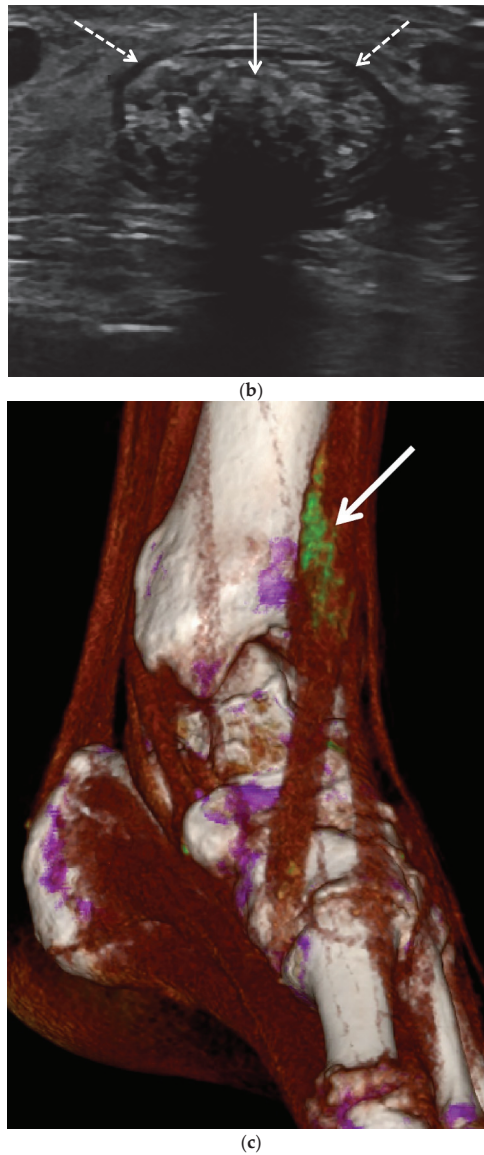
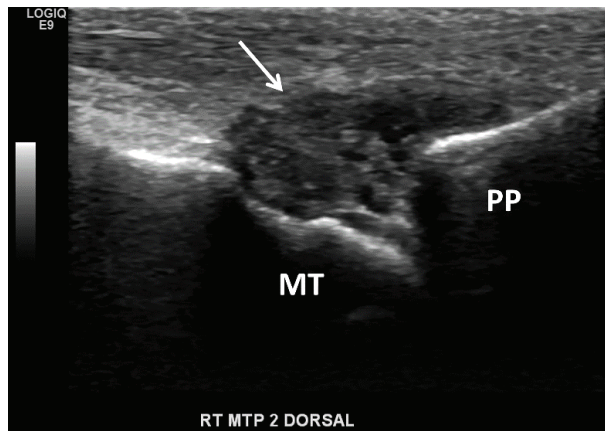
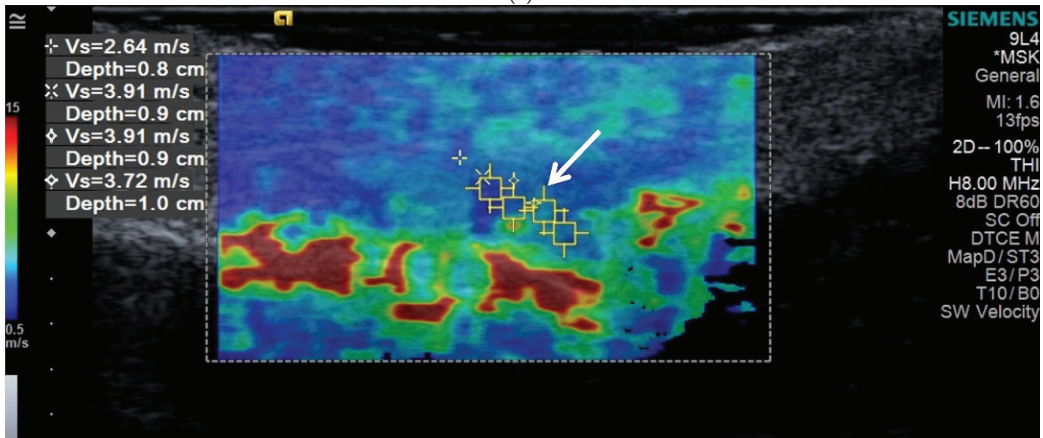


Figure 10. Gout of the tibialis anterior tendon. (a) Long-axis color Doppler US image along the dorsal aspect of the ankle and (b) short-axis gray scale US image of the tibialis anterior tendon in the same region show marked thickening and heterogeneous echogenicity of the tibialis anterior tendon consistent with severe tendinopathy and MSU crystal deposition (dashed arrows) with a more discrete echogenic focus of tophaceous gout (arrows) with posterior shadowing in (b). (c) A 3D reformatted dual energy CT (DECT) image of the ankle shows green encoded foci in the tibialis anterior tendon-related MSU crystal deposition concordant with US findings. DECT image acquired at 0.8–1.5 mm on a dual energy Siemens Somatom Force helical CT scanner using Syngovia post-processing software to demonstrate MSU crystals encoded in green.



(a)



(b)

Figure 11. Tophaceous gout at the right second metatarsophalangeal joint in a 49-year-old man. (a) Long-axis gray-scale US image along the dorsal aspect of the second right metatarsophalangeal joint shows heterogeneous intra-articular gouty tophus (arrow) abutting the metatarsal head (MT). PP = proximal phalanx. (b) Color elastogram of the same region shows low shear-wave velocity (arrow) (mean, 3.54 m/s) consistent with a soft gouty tophus. SWE data were collected using an Acuson S3000 US scanner with an L9-4-MHz linear transducer.

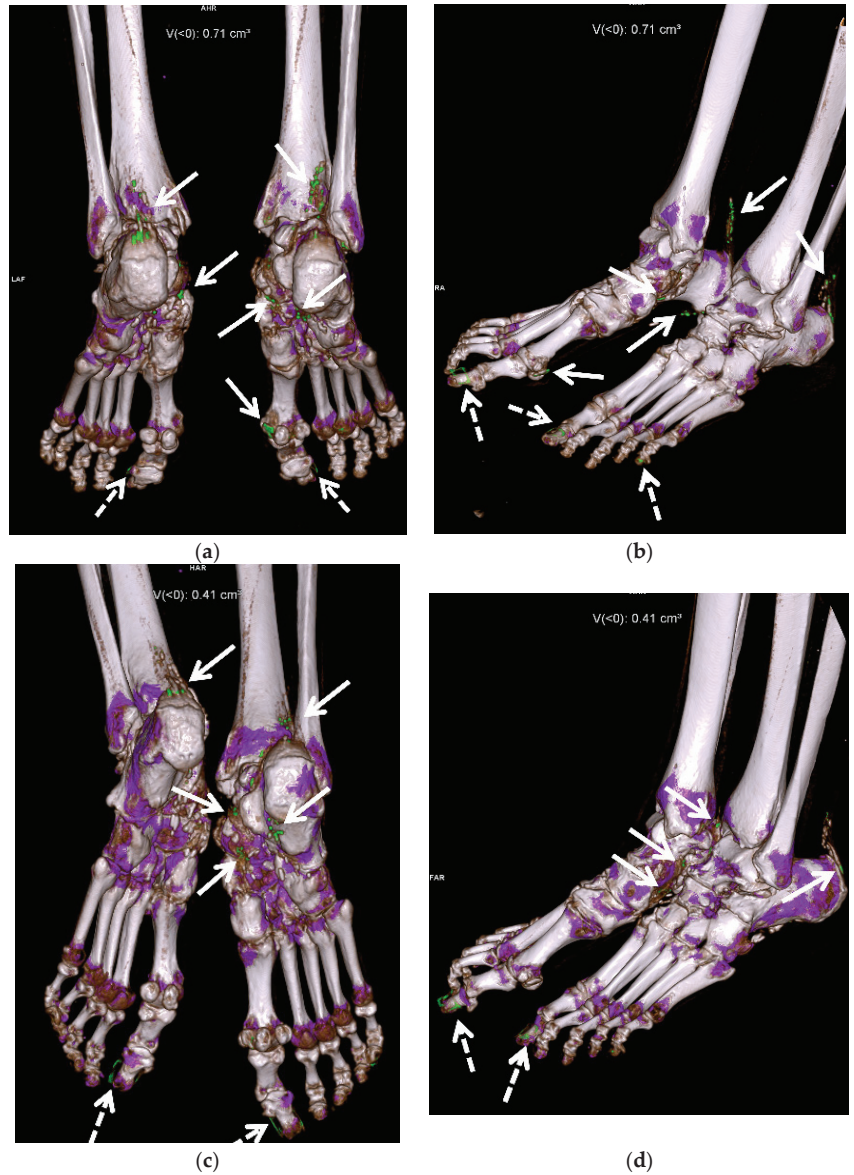


Figure 12. A 58-year-old female with extensive gouty arthropathy of the bilateral ankles and feet and decreased burden of MSU crystal deposition on the post-treatment 13-month follow-up DECT study. Pre-treatment (a,b) 3D reformatted DECT images of the bilateral ankles and feet show multiple green encoded foci of periarticular and articular MSU crystal deposition in both feet and distal Achilles tendons (arrows). Note green encoded foci about the great and little toenails related to imaging artifact (dashed arrows). (c,d) Three-dimensional reformatted DECT images of the bilateral ankles and feet obtained 13 months after initiation of treatment show interval decreased burden of periarticular and articular MSU crystal deposition in the same regions (arrows). Note green encoded foci about the great toenails related to imaging artifact (dashed arrows). All images acquired at 0.8–1.5 mm on a dual energy Siemens Somatom Force helical CT scanner using Syngovia post-processing software to demonstrate MSU crystals encoded in green.

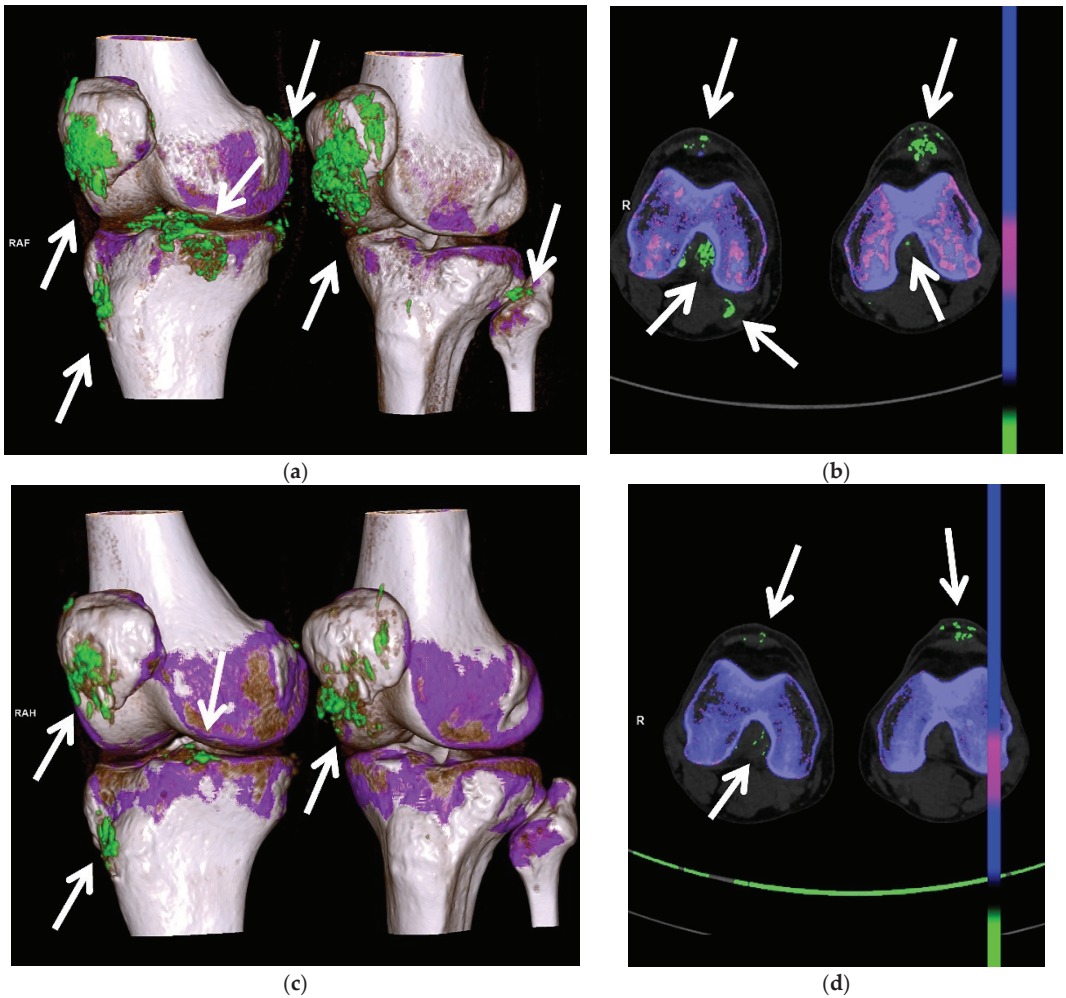


Figure 13. A 67-year-old male with extensive gouty arthropathy of both knees with decreased burden of MSU crystal deposition on the post-treatment 2-year follow-up DECT study. Pre-treatment (a) 3D and (b) 2D axial reformatted DECT images of the bilateral knees show multiple green encoded foci of extensive periarticular and articular MSU crystal deposition (arrows); (c) 3D and (d) 2D axial reformatted DECT images of the bilateral knees obtained 2 years after initiation of treatment show interval decreased burden of periarticular and articular MSU crystal deposition of both knees (arrows). All images acquired at 0.8–1.5 mm on a dual energy Siemens Somatom Force helical CT scanner using Syngovia post-processing software to demonstrate MSU crystals encoded in green.

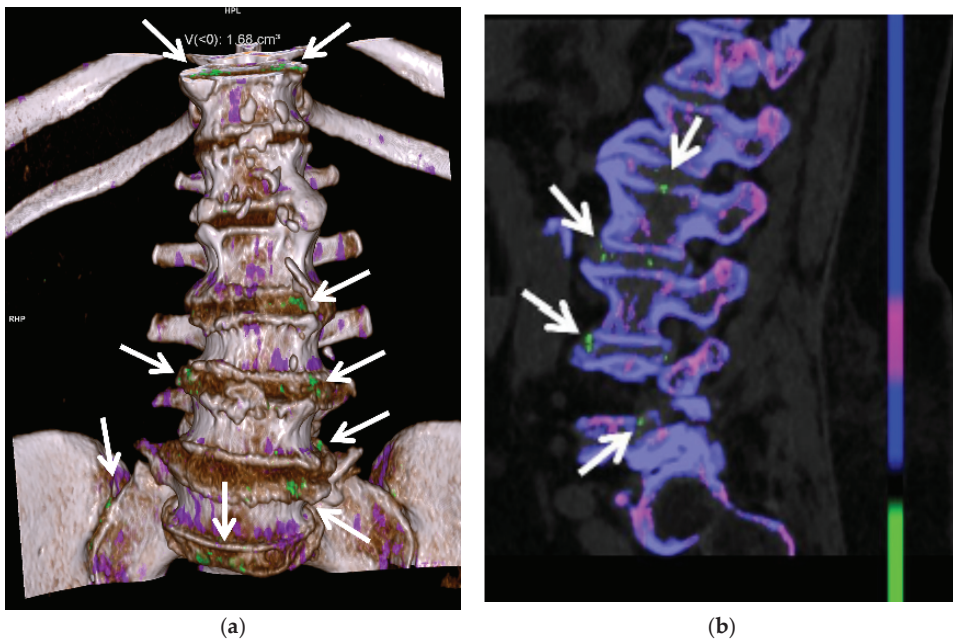


Figure 14. A 65-year-old female with spinal gout. (a) Three-dimensional and (b) two-dimensional sagittal reformatted DECT images of the lumbar spine show numerous green encoded foci of MSU crystal deposition along the lumbar and visualized lower thoracic spine, sacrum and sacroiliac joints. All images acquired at 0.8–1.5 mm on a dual energy Siemens Somatom Force helical CT scanner using Syngovia post-processing software to demonstrate MSU crystals encoded in green.

2. Clinical

Risk factors for gout include hyperuricemia, diet, alcohol consumption, fructose consumption, medications, age, sex, genetics, acute illness, and several chronic diseases [1,7,16,23,24,35,36]. Diets high in purines, which are found in red meat and seafood, can exacerbate gout [7,35]. Consumption of alcohol, especially beer and hard liquor, less so wine, is associated with gout, including recurrent gout attacks [2,7,35,37]. Several medications, including certain diuretics, β -blockers, angiotensin-converting enzyme inhibitors, non-losartan angiotensin II antagonists, cyclosporine, tacrolimus, and low-dose aspirin have been linked to gout [1,24]. The incidence of gout is 2–6 times higher in men than in women [1,18]. Menopause is associated with an increased risk of gout, particularly in surgical menopause and early-onset natural menopause [38]. The risk of gout is increased in postmenopausal women who are not treated with hormone replacement therapy [1,38]. Additionally, while higher levels of serum uric acid levels increase the risk of gout among women in a graded manner, women have a lower risk of gout than men at the same uric acid level [39]. Approximately 80 percent of patients with gout have a positive family history of gout or hyperuricemia [6,7,15]. MSU crystal deposition can result in end-organ damage in the kidneys and heart [40]. Gout has been associated with diabetes, obesity, hyperlipidemia, metabolic syndrome, insulin resistance, hypertension, renal disease, stroke, neurodegenerative diseases, and cardiac disease, and can lead to premature death [1,7,13,17,22,23,35,39,41–46]. Gout is not associated with an increased risk of fractures [47].

There are four phases of gout: asymptomatic hyperuricemia, and acute, intercritical, and chronic gout. Acute gouty arthropathy is typically monoarticular and most commonly involves the lower limb, particularly the first metatarsophalangeal (MTP) joint, known as podagra, which is seen in greater than 50 percent of patients [4,13,14,16–19,22,23,36,48–51].

The hands, tarsal joints, knees, elbows, ankles, and bursae are other common sites of involvement [16,17,22,23]. MSU crystals also frequently deposited in and about the tendons and at the entheses [13,52].

In acute gout, patients present with rapid onset of severe pain, swelling, and erythema of the affected joint, tendon or bursa. An acute gout attack may mimic infection, but is self-limited, usually resolving within a few days or 1–2 weeks [1,23,48]. Serum uric acid may be normal during an acute attack of gout, whereas inflammatory blood parameters may be elevated [22]. Intercritical gout is the asymptomatic interval between episodes of acute gouty attacks.

Repetitive attacks of acute gout eventually lead to chronic arthropathy, with chronic synovitis, tophus formation and deposition, and finally, erosions and joint destruction [1,14–16,23,48]. If left untreated, about a third of patients will develop tophaceous gout within 5 years [17,53]. Tophi are non-tender soft-tissue masses found in the subcutaneous soft tissues, intra-articular or periarticular soft tissues, tendons, ligaments, retinacula, and bursae, secondary to chronic granulomatous reaction to MSU crystals [15,19,22,36,53–55]. They have a fibrovascular matrix with a center of MSU crystals surrounded by granulation tissue [36,56]. Tophaceous gout often occurs in the hands and wrists and along the extensor surface of the knees and elbows and may eventually result in osseous erosions [14,16,17,22]. Tophi tend to occur in areas of mechanical stress, such as adjacent to the first MTP joint, the Achilles and patellar tendons, and the olecranon and prepatellar bursae [36,56]. The cruciate ligaments, peroneal tendons, popliteus tendon, and infrapatellar fat pad are common sites of MSU deposition [6,7,21,52,55]. Tophi can also occur in the auricular appendages and the tip of the nose [21]. They result in cosmetic deformity and can cause impaired joint mobility [53,54].

Gout is often a clinical diagnosis. Patients with gout may have normal serum urate levels and hyperuricemia can be present in patients without gout. Aspiration of the affected joint or bursa is the gold standard for diagnosis. Joint aspirate is evaluated for crystals, as well as white blood cells to exclude infection. Macroscopically, MSU crystals are white in color [48]. They are needle shaped and have negative birefringence on polarized microscopy (Figure 1) [7,17,22,23,46,48,49,57]. The American College of Rheumatology (ACR) and European League Against Rheumatism (EULAR) created the 2015 Gout Classification Criteria, a useful diagnostic and classification algorithm for gout [3,58]. This algorithm utilizes clinical, laboratory, and imaging findings. In 2018, the EULAR provided updated evidence-based recommendations for the diagnosis of gout, recommending joint aspiration or tophus biopsy in every patient with suspected gout, and imaging in patients with atypical presentations when aspiration is not possible [8]. The differential diagnosis includes septic arthritis, acute calcium pyrophosphate arthropathy, reactive arthritis, and psoriatic arthritis. Chronic tophaceous gout may mimic rheumatoid arthritis, or rarely, tumor or other tumor like lesions [21]. Clinical history and laboratory evaluation are helpful to differentiate gouty arthropathy from infectious or other inflammatory arthropathies. Arthrocentesis and fluid evaluation remain the gold standard for the diagnosis of both gouty arthritis and septic arthritis. US has been shown to have a high specificity (greater than 90%) for the diagnosis of gout in patients with a symptomatic joint when compared to joint aspiration [59]. It should be remembered that septic arthritis and acute crystal arthritis can occur simultaneously. The presence of tophi on imaging suggests gouty arthropathy rather than an infectious or inflammatory arthropathy. Imaging, particularly DECT, can help differentiate acute calcium pyrophosphate arthropathy from gouty arthropathy, although a recent study showed that DECT may have a lower sensitivity for acute gout flares than previously described, and that DECT sensitivity for acute calcium pyrophosphate crystal arthritis is lower than that of US [60].

Although joint aspiration is the gold standard of diagnosis, aspiration is a mildly invasive procedure with complication risk, which may not be readily available and may be inaccurate in the setting of small volume joint effusion [5,9,24,46,50,57].

3. Imaging

3.1. Radiographs

Radiographs (Figures 2, 3a–c, 4a, 5a and 6a) are often the initial imaging modality in a patient suspected of having gout, as they are readily accessible and inexpensive. However, in early gout, radiographs are often normal or show only soft-tissue swelling. Erosions may not be apparent until 5–10 years after the initial acute gout attack [5,22,23,28,61,62]. The classic radiographic findings of longstanding gout include marginal and juxta-articular erosions (Figures 2, 3a,b, 5a and 6a) with overhanging edges and sclerotic margins. Erosions may also be intra-articular. In chronic gout, tophi are seen as dense soft-tissue nodules (Figures 2, 3a–c, 4a, 5a and 6a) in the periarticular soft tissues or within the bursae with or without amorphous calcifications. Tophi may be radiographically occult if less than 5–10 mm [18,36]. Juxta-articular erosions are usually seen adjacent to tophi, as they frequently represent intraosseous extension of tophi [18]. Joint spaces and periarticular bone density are maintained until late disease. Radiography has a reported sensitivity of 31% and specificity of 93% in the diagnosis of gout [19,28].

3.2. Ultrasound (US)

Diagnostic US (Figures 7, 8, 9, 10a,b and 11), utilizing high frequency linear transducers (12 MHz and higher) is useful in the evaluation of gout. US can provide a diagnosis of gout, can be used to guide joint aspiration or soft-tissue biopsy, and can be used to monitor response to therapy. US has high spatial resolution and is multiplanar, uses no ionizing radiation, is a dynamic examination, is widely available, is relatively low cost, and is portable. However, US is operator-dependent, with a steep learning curve, and is limited to more superficial joints. US findings include joint effusion, synovitis, MSU crystal deposition, tophi and erosions [7,17]. A meta-analysis by Lee et al. in 2018 showed that US has an overall specificity of 89% and sensitivity of 65.1% for the diagnosis of gout [57].

The Outcome Measures in Rheumatology Clinical Trials (OMERACT) task force subgroup created consensus-based definitions on the US elementary gout lesions of double contour, aggregates, tophi, and erosions [63]. OMERACT defined aggregates as “heterogeneous hyperechoic foci that maintain their high degree of reflectivity even when the gain setting is minimized or the insonation angle is changed and which occasionally may generate posterior acoustic shadow” [63]. A new consensus definition was created in 2021, defining aggregates as “bright hyperechoic, isolated spots too small to fulfil the tophus definition and characterized by maintaining their high degree of reflectivity when the insonation angle is changed” [64].

Joint effusions in gout may range from simple, anechoic fluid to heterogeneous hyperechoic collection with synovitis (Figures 7a, 8b, 9, 10a,b and 11a) [17,28,65]. MSU crystal aggregates/microtophi can be seen in the joint as floating echogenic foci, known as the “snowstorm appearance” (Figure 7a) [7,9,13,15,17,18,28,29,31,36,59,65–67]. These echogenic foci could represent joint bodies, and US cannot differentiate MSU crystals from calcifications; DECT can be utilized for this [13]. Synovitis occurring in gout is usually heterogeneously hyperechoic due to MSU crystal deposition [7,15,18]. Intrinsic hyperechoic streaks and a hypoechoic peripheral rim with increased vascularity are also often present within the synovium in gout [7,28]. Synovial hyperemia, visualized on color or power Doppler imaging, may be secondary to active inflammation or may be due to the fibrovascular matrix of tophi, and may also be present in subclinical disease (Figures 7 and 9) [18,36].

MSU crystals also precipitate on the superficial layer of the hyaline cartilage, producing an irregular hyperechoic line over the anechoic cartilage. This hyperechoic line parallels the hyperechoic line of the subchondral bone, separated by anechoic cartilage, producing the “double contour sign” (Figures 8c and 9) [7,9,13,15,17,18,29,31,36,46,57,59,65–67]. OMERACT defined the double contour sign as “abnormal hyperechoic band over the superficial margin of the articular hyaline cartilage, independent of the angle of insonation and which may be either irregular or regular, continuous or intermittent and can be distinguished from the cartilage interface sign” [63]. The sensitivity of the double contour sign in patients with

gout ranges from 25–95% [7,17,25,66–69]. The double contour sign should not be confused with hyperechoic foci within the cartilage, as in calcium pyrophosphate deposition, or with the normal cartilage interface sign [7,13,15,29,65,66].

In chronic gout, erosions (Figure 8b) can be visible on US [7,9,13,17,18,31,70]. OMERACT defined erosions as “an intra- and/or extraarticular discontinuity of the bone surface (visible in 2 perpendicular planes)” [63]. Post-traumatic changes, degenerative changes, and normal variants can mimic erosions. Adjacent tophi, synovitis, and hyperemia with color Doppler imaging suggest active erosions [7]. US has been shown to detect erosions in gout earlier and at smaller size than radiography [15,17,25,26,66]. However, US can underestimate the extent of erosions compared to MRI [15,71].

OMERACT defined tophi as “a circumscribed, inhomogeneous, hyperechoic and/or hypoechoic aggregation (that may or may not generate posterior acoustic shadow) which may be surrounded by a small anechoic rim” [63]. On US, tophaceous deposits (Figures 8a and 10a,b) in chronic gout have a hyperechoic center, representing the MSU crystals, with an anechoic rim, representing the granulation tissue, and may have either a nodular or an infiltrative appearance (“soft tophi” (Figure 11)), or posterior acoustic shadowing (“hard tophi” (Figures 8a and 10b)) [7,15,17,18,21,29,36,65–67]. Tophaceous deposits within tendons are usually hypoechoic with scattered hyperechoic foci (Figure 7b), resulting in disruption of the normal fibrillar tendon echotexture; if chronic, hyperechoic bands with posterior shadowing are often present (Figures 8a and 10a,b) [17,65].

Shear wave elastography (SWE) (Figure 11b) uses ultrasound to obtain quantitative measurements of tissue elasticity to assess intrinsic tissue stiffness [72]. Forced acoustic radiation force from a linear US array generate shear waves which propagate perpendicularly to the primary US wave to produce local tissue displacement. Displacement and velocity are tracked as the shear waves propagate, and the tissue displacements are used to calculate shear wave velocity and shear modulus [72]. Quantitative shear modulus maps are produced to show shear wave velocities (meters per second) and tissue elasticity (kilopascals) [72]. SWE has been shown to be able to quantitatively differentiate gouty arthropathy from non-gouty arthropathy in patients without acute gout [73]. Wang et al. showed that the stiffness of the synovium is higher in the intercritical phase of gout than in the acute phase, and thus increases diagnostic performance in differentiating acute from intercritical gout in comparison with conventional US [74]. In gouty tophi, shear wave velocities are dependent on consistency, with harder tophi having higher velocities than soft tophi [72].

3.3. Computed Tomography (CT): Conventional and Dual Energy (DECT)

Both conventional CT (Figure 5b) and DECT (Figures 10c, 12, 13 and 14) are useful in the evaluation of gout. CT has high spatial resolution, is multi-planar and can visualize deep structures. This imaging modality is limited by cost, use of ionizing radiation, and lack of portability. Conventional CT is more widely available than DECT.

Conventional CT can be used to detect erosions and tophi in chronic gout [15]. Tophaceous nodules have a density of approximately 170 Hounsfield units [15]. Hyperdense deposits can be seen in the joints in acute gout (Figure 5b) [51].

DECT utilizes the photon-energy-dependent attenuation of different materials to identify MSU crystals. It uses two different energies (80 and 140 kVp) to determine the composition of materials using the properties of differing atomic number and mass density, which can be color coded during post-processing, to differentiate urate acid crystals/tophi from other calcifications [7,10–15,18,31,36,46,49,62,75,76]. DECT directly images MSU crystal deposition, and thus is independent of the current serum urate level [14]. DECT is a part of the 2015 and 2018 ACR/EULAR classification criteria for gout [3,8,76]. Quantitative measurement of tophi can be obtained with DECT [10,12,13,18,31,36,46,49,75]. Peripheral limbs may be scanned to create urate maps (Figures 12 and 13) [12,50,75]. Subclinical disease can also be detected with DECT, often within the joints and tendons, without tophi [14,36,46,77].

DECT is both sensitive (78–100%) and specific (89–100%) in identifying MSU deposition [5,10–12,14,31,50,75]. The sensitivity of DECT is lower for acute gout than for chronic gout [76,77]. In early gout, false-negative imaging can result if the MSU volume is low or the tophi are very small (less than 2 mm) [7,18,31,62]. Lee et al. showed that sensitivity of DECT for early gout can be increased when combined with conventional CT [51]. In this study, conventional CT was used to evaluate for the presence of hyperdense deposits in patients with suspected early gout. These deposits are nonspecific, and could represent MSU crystals or other crystal arthropathies such as calcium pyrophosphate deposition disease, which can be differentiated by DECT.

DECT is useful in patients with atypical clinical presentations and unusual site of involvement [14,49,78]. Gout in the axial skeleton (Figure 14) can be a challenging diagnosis due to rarity of presentation and difficulty of obtaining tissue sampling, and DECT can guide diagnosis when gout is suspected [24,79]. Zhu et al. showed that DECT is more accurate in the diagnosis of gout than US in the joints of the upper limb, thought to be due to the complex anatomy and smaller size of the upper-limb joints compared to the lower-limb joints [40]. Klauser et al. also showed that the percentage of gouty deposits detected by US was significantly lower than that by DECT, particularly within the extra-articular spaces [30]. DECT may be very useful when joint aspiration is either non-feasible or non-diagnostic.

Artifacts are prevalent in DECT [7]. These artifacts include green pixels in the skin particularly the heels, and in the nails and nail beds (Figure 12), due to keratin in callous and thickened nails, and artifactual pixilation from motion and metal [7,10,18,24,36,46,76]. False-positive imaging can occur in areas of apposed skin [75]. It is uncertain if urate-like pixilation uptake in vasculature represents true MSU crystal deposition or artifact, and it is under further investigation for the cardiovascular system [24,45,76]. DECT has lower specificity for gout in osteoarthritic knees [11,18,31].

A recent study shows promising results in the use of DECT to detect cardiovascular MSU deposits in the coronary arteries and the aorta of gout patients compared to controls [45]. MSU crystal detection on DECT has been shown to be predictive of developing new cardiometabolic disease and for increased mortality [80].

3.4. Magnetic Resonance Imaging (MRI)

MRI (Figures 3d and 4b–g) has high-contrast and spatial resolution, permitting detailed evaluation of the bone marrow, periarticular soft tissues, and articular cartilage, without the use of ionizing radiation. Limitations of MRI include long examination times, high cost, limited availability, lack of portability, claustrophobia, and restrictions by some implanted medical devices.

MRI is useful in evaluating gout in the spine and other deep areas not amenable to clinical or US evaluation [15]. In early gout, MRI can show bone-marrow and soft-tissue edema as well as simple or complex joint effusions and synovitis [18]. MSU crystal deposition on the surfaces of the hyaline cartilage is not visible by MRI [15].

On MRI, erosions (Figures 3d and 4b–g) have cortical disruption with overhanging edges with associated intra-articular and extra-articular soft-tissue tophi that may calcify. Acute erosions will have irregular margins with adjacent enhancing active synovitis while chronic erosions will appear more well-marginated with cortication, often without adjacent active synovitis [17]. Minimal bone marrow edema is present around erosions until late disease, and cartilage surfaces are spared from erosive changes until late disease [18,36,81]. The presence of tophi predicts eventual erosions, but the presence of bone marrow edema and synovitis do not [18,82].

MRI can demonstrate the extent of tophi, including within the bursae and tendons (Figures 3d and 4b–g) [15]. Tophi show intermediate-to-low signal on T1-weighted (T1W) MR images and heterogeneously high-to-intermediate signal on fluid-sensitive images, with heterogenous enhancement following intravenous administration of gadolinium-based

contrast (Figures 3d and 4b–g) [7,15,18,31,36,55]. Areas of low signal and non-enhancement suggest the presence of calcifications, especially if small can be missed on MR images.

3.5. Nuclear Medicine

Nuclear medicine imaging studies are not the preferred modalities for evaluation of gouty arthropathy. However, as gouty arthropathy is common, it may be encountered on these studies. On bone scintigraphy, gout can manifest as articular, periarticular, and soft-tissue radiotracer uptake [83,84]. Gouty tophus has been shown to be moderately hypermetabolic on fluorodeoxyglucose positron emission tomography CT (FDG PET CT) [85–87]. Tophaceous gout in the spine will show uptake on Gallium-67 imaging [88].

4. Laboratory Evaluation

Blood tests may show elevation of the erythrocyte sedimentation rate (ESR) or C-reactive protein (CRP) during a gout flare. These markers of inflammation can be elevated due to other diseases that can cause inflammatory arthritis, however. Serum urate levels may be elevated but can also be low or normal during a flare [89]. An elevated serum urate level may suggest gout but is not enough to make a diagnosis.

Analyzing an aspirated synovial fluid, on the other hand, can confirm a gout diagnosis. The synovial fluid in gout is typically inflammatory in nature, with a white blood cell count of at least 2000 per mm³. A flare is characterized by the presence of MSU crystals in synovial fluid found by examination of the fluid using compensated polarized light microscopy. MSU crystals are negatively birefringent and are needle shaped. Sensitivity of laboratory crystal analysis for MSU crystals ranges from 63–78%, and specificity ranges from 93–100% [90].

5. Medical Management of Acute Gouty Arthritis

The primary goal during an acute gout flare is quick and safe termination of pain. While a gout flare may resolve untreated within days or weeks, symptoms may resolve more quickly with the use of various different treatments.

5.1. Glucocorticoids

Oral glucocorticoids are often used in patients with a typical gout flare who are able to take oral medications but have contraindications to the use of nonsteroidal anti-inflammatory drugs (NSAIDs). A typical regimen would be prednisone initiated at 30–40 mg per day. This is then tapered over 7–10 days, but duration of the taper may be needed for up to 21 days. Glucocorticoids are similar (or even better) in efficacy and have no greater risk of adverse effects compared to other agents used to treat acute gout [91–93]. However, other treatment options may be preferred among those with suspected infection, prior glucocorticoid intolerance, or uncontrolled diabetes mellitus. Common adverse effects of glucocorticoid use include mood changes, hyperglycemia, hypertension, and fluid retention.

Intra-articular glucocorticoid injection may be an indication among those who are unable to take oral medications and with one or two active inflamed joints. Typically, triamcinolone acetonide (up to 40 mg for a large joint and 20 mg for medium joint) or methylprednisolone acetate is used. While the evidence for its use in the treatment of gout flares is limited, it can be a relatively safe and efficacious treatment [94]. In addition, parenteral glucocorticoids may be indicated among those who cannot take medications orally and are not candidates for intra-articular therapy (e.g., with >2 active inflamed joints) [95]. Intravenous methylprednisolone (20 mg) may be helpful among those with polyarticular involvement, with an intravenous access, and with no contraindication to glucocorticoids. Intramuscular triamcinolone acetate treatment (40–60 mg) may be an alternative treatment for patients with similar conditions.

5.2. Nonsteroidal Anti-Inflammatory Drugs (NSAIDs)

NSAIDs are very good alternatives to oral glucocorticoids in the treatment of acute gout [96–99]. They are particularly appropriate among younger patients who do not have renal, cardiovascular, or active gastrointestinal disease. Naproxen (500 mg twice daily) or indomethacin (50 mg three times a day) are traditionally used. However, other NSAIDs such as ibuprofen (800 mg three times daily), diclofenac (50 mg two–three times daily), celecoxib (100 mg twice daily), and meloxicam (15 mg daily) are probably as efficacious [96–98]. NSAIDs work best when initiated within 48 h of symptom onset and can be discontinued two to three days after clinical symptoms have resolved. There are contraindications to NSAID use, however, including: chronic kidney disease (typically creatinine clearance < 60 mL/min), active gastrointestinal ulcer, cardiovascular disease (especially heart failure), or concomitant treatment with anticoagulants. Adverse effects from short-term use of NSAIDs are rare but include gastrointestinal disturbances and worsening renal function.

5.3. Colchicine

Low-dose oral colchicine can be used for acute gouty flare, especially among patients with intolerance or contraindications to glucocorticoid and NSAID use. A typical dosage is a total of 1.8 mg during the first day of therapy, and treatment is indicated for the duration of the flare at 0.6 mg once or twice daily [100]. It works best when taken at the initial onset of gout symptoms. Common adverse effects include diarrhea and abdominal cramping, especially with high dose therapy. Colchicine would be contraindicated among those with significant renal or hepatic insufficiency, and among those taking medications that may inhibit the cytochrome P450 system component CYP3A4 (e.g., HIV protease inhibitors, azole antifungals) or medications that inhibit the P-gp efflux pump (e.g., macrolide antibiotics, tacrolimus, cyclosporine) [100,101]. Severe side effects, including blood cytopenias, myopathy, and peripheral neuropathy, are relatively rare.

5.4. Interleukin-1 (IL-1) Inhibitors

While IL-1 inhibitors may benefit certain patients with an acute gouty attack, they are typically reserved for those for whom other available treatments have failed or who have contraindications to them [91,102,103]. Anakinra (100 mg daily) is the preferred IL-1 inhibitor treatment for acute gout due to its short half-life and its relatively modest cost compared to other IL-inhibitors. It is given subcutaneously daily until symptoms of the gout flare improve, and can be useful among hospitalized patients with an active infection or who are in the perioperative setting [102]. Recurrent flares are not uncommon among anakinra-treated patients, however.

5.5. Urate-Lowering Therapies

Lifestyle modifications that may decrease patient urate levels include weight reduction, cessation of excessive alcohol consumptions, and moderation in the consumption of purine-rich food. However, lifestyle modifications may not be adequate, and pharmacologic therapies may be indicated in patients with chronic gout. Specific indications for the initiation of pharmacologic urate-lowering therapies in gout are as follows: (1) frequent (≥ 2 annually) gout flares; (2) evidence of radiographic damage due to gout; and (3) presence of ≥ 1 subcutaneous tophi [104]. Upon initiation of urate-lowering therapy, patients also receive prophylactic treatment to decrease and prevent recurrent gout flares. Prophylactic treatment options include colchicine, a NSAID, or a low-dose glucocorticoid [104,105]. Achieving a serum urate level of <6 mg/dL is the recommended goal according to the 2020 ACR Guideline for the Management of Gout [104].

5.6. Allopurinol

Allopurinol, a xanthine oxidase inhibitor, is the first-line urate-lowering therapy for most patients [104]. The starting dose is typically ≤ 100 mg/day with dose increase by

100 mg every two to four weeks to reach and maintain the target serum urate level. Patients of Southeast Asian descent (e.g., Chinese, Korean, Thai) and African-Americans should be tested for the HLA-B*5801 allele; HLA-B*5801 positive individuals have a much higher risk of developing severe cutaneous adverse reactions (SCARs) [106]. For a similar reason, patients with moderate-to-severe chronic kidney disease (stage ≥ 3) can be started on a lower dose. Doses up to 300 mg/day and even higher are often used. Mild adverse effects include rash, leukopenia or thrombocytopenia, and diarrhea. Severe reactions, which are rare, include DRESS (drug reaction with eosinophilia and systemic symptoms) syndrome and SCARs.

5.7. Febuxostat

Febuxostat is an alternative xanthine oxidase inhibitor that can also be used for treatment of hyperuricemia. A daily dosage (40 mg or 80 mg) produces a reduction that is equivalent or better than that seen in patients treated with allopurinol 300 mg once daily [107,108]. It can be given safely to those with renal insufficiency, but the cost of treatment tends to be higher compared to allopurinol. Potential adverse effects include transaminitis, nausea, arthralgia, and rash. Of particular concern, febuxostat, compared to allopurinol, is associated with higher risk of cardiovascular mortality and all-cause mortality. The medication currently carries a boxed warning for increased risk of death [109].

5.8. Probenecid

Probenecid is the only uricosuric medication that has been approved by the United States Food and Drug Administration for the purpose of promoting renal uric acid clearance. It is used uncommonly in the United States, however, as it is only appropriate for gout patients with relative renal underexcretion of uric acid. Multiple daily dosing (250–1000 mg) is also required, and the medication is not effective among those with moderate-to-severe kidney disease [110]. Potential side effects include gastrointestinal intolerance, rash, and kidney stones. A combination xanthine oxidase inhibitor and probenecid, however, can be effective when monotherapy with an oral urate-lowering drug fails [110].

5.9. Pegloticase

A recombinant form of the enzyme uricase, pegloticase can cause a rapid reduction of serum urate level. However, due to its cost and potential adverse effects, the ACR recommends against its use as first-line therapy for gout [104]. It is administered intravenously every two weeks (8 mg), and is associated with more rapid reduction of gout signs and symptoms compared to other urate-lowering therapies [111]. However, its efficacy and safety are influenced by the development of antidrug antibodies, which are associated with a rise in serum urate levels and the appearance of infusion reactions [112]. Hence, the medication is often reserved for patients with advanced gout and when other urate-lowering therapies are ineffective or contraindicated.

6. Surgical Management of Chronic Gouty Arthritis

Despite medical treatment, some patients may eventually need surgical intervention. Common indications for surgical intervention include restoration of function, treatment of symptoms such as pain and infection, and restoration of cosmesis, particularly of the hand and wrist [113]. Dissection and curettage can be used for infiltrative lesions of tendons [113]. In advanced disease, resection of the affected tendon with either primary repair or tendon transfer may be necessary [113]. Other surgical interventions include tenosynovectomy, tophectomy, hydrosurgery, and arthrodesis [113]. In the MTP joints, several surgical options are available, including both joint-sparing and joint-destructive procedures [114]. Surgical interventions in patients with advanced disease have high morbidity. These patients are at high risk of delayed postoperative wound healing due to poor circulation to the overlying skin and potential leakage of inadequately removed urate deposits through the

skin [113]. Some surgeons endorse earlier debulking surgery to decrease involvement of vital structures, decrease risk of infected or ulcerated tophi, and thus decrease morbidity and increase the ability to restore function [113].

7. New Horizons in the Treatment of Gouty Arthritis

Recent research on the anti-inflammatory effect of electromagnetic fields (currently used to promote bone healing) to decrease chronic inflammation and synovitis and thus prevent the progression of joint destruction appears promising [115–117].

8. Imaging of Treatment Response

The OMERACT working group established guidelines in 2015 for research on the role of imaging in gout therapy to include MSU deposition, joint inflammation, and bone erosion [32,118]. OMERACT endorses the following chronic gout domains: serum urate, tophus, pain, flares, and patient global assessment in assessing remission [119,120].

Radiographs can be used to monitor tophus size as an indicator for response to therapy [19,61].

US may be used to monitor therapy. With successful therapy, the double-contour cartilage sign can resolve, and tophi can reduce in size [7,9,20,26,27,31,32,67,118,121,122].

US can show resolution of urate deposits in patients on urate-lowering therapy with greater decrease of US tophus size and resolution of double-contour cartilage sign occurring in patients with lower serum urate levels than in those patients with higher serum urate levels [123]. It has been shown that the MSU crystal burden on US can predict fulfilling remission criteria for gout: the lower the baseline MSU burden estimated by US, the higher the chance to fulfil the remission criteria at 12 months, with the double-contour cartilage sign being the most useful measure [124]. Christiansen et al. showed that US can detect decreases in urate crystal deposition (double contour sign, tophi, aggregates and erosions) in patients on successful urate-lowering therapy [125]. Hammer et al. showed that patients treated with urate-lowering therapy to attain target serum urate levels (treat-to-target) had reduction of crystal deposition, with decreased double contour sign, decreased tophi, and decreased MSU aggregates on US [126]. Ebstein et al. found that a high reduction in US tophus size is associated with lower probability of relapse following the cessation of gout prophylaxis therapy [127].

DECT provides accurate and reproducible quantification of MSU crystal deposits and can be used to evaluate change in size and burden of tophi in response to therapy and provide quantitative measurement of response to therapy (Figures 10c, 12, 13 and 14) [7,14,31,32,54,62,118]. Greater number and volume of MSU crystal depositions on DECT correlate with greater disease severity, but even patients with controlled gout (target serum uric acid levels and no palpable tophi) can have crystal deposition on DECT, suggesting the need for increased urate-lowering therapy [128]. Dalbeth et al. showed that in patients with gout treated with allopurinol, remission as defined by these criteria (with the exception of flares and pain) is associated with less DECT urate crystal deposition [119]. The Gout in Norway study (NOR-Gout) showed that patients with gout treated to target with urate-lowering therapy had sustained reductions in urate deposition on DECT [129]. Dalbeth et al. also showed that treating to target led to decreased erosion scores and decreased urate deposition on DECT [130].

MRI can detect change in size of tophi as well as resolution of bone marrow edema [15,31]. US and MRI can detect resolving joint effusions and synovitis [15].

9. Conclusions

Imaging shows both the soft-tissue and osseous changes that occur in gout secondary to inflammatory changes from the deposition of MSU crystals. Current EULAR recommendations state that US is helpful in establishing a diagnosis of gout by detection of either a double contour sign on cartilage surfaces or non-clinically evident tophi [8]. DECT can help differentiate MSU crystal deposition from other calcifications. US and DECT may

provide an alternative to joint aspiration or soft-tissue biopsy in the diagnosis of certain cases of suspected gout, when joint aspiration or soft-tissue biopsy are not available. Goals of management include: (1) treatment and prophylaxis of acute attacks and (2) lowering of serum urate levels with the intent of avoiding flares and suppressing progression of joint damage. Advanced imaging such as US, DECT, and MRI are useful in the assessment of disease burden and response to treatment.

Author Contributions: Conceptualization, J.S.W. and M.S.T.; Writing—original draft preparation, J.S.W., J.M.E., E.R.V. and M.S.T.; Writing—review and editing, J.S.W., J.M.E., P.L.M., A.S.K., E.R.V. and M.S.T.; Supervision, M.S.T.; Funding acquisition, none. All authors have read and agreed to the published version of the manuscript.

Funding: This research received no external funding.

Institutional Review Board Statement: Not applicable.

Informed Consent Statement: Not applicable.

Conflicts of Interest: The authors declare no conflict of interest.

References

1. Kuo, C.F.; Grainge, M.J.; Zhang, W.; Doherty, M. Global epidemiology of gout: Prevalence, incidence and risk factors. *Nat. Rev. Rheumatol.* **2015**, *11*, 649–662. [[CrossRef](#)]
2. Neogi, T.; Chen, C.; Niu, J.; Chaisson, C.; Hunter, D.J.; Zhang, Y. Alcohol quantity and type on risk of recurrent gout attacks: An internet-based case-crossover study. *Am. J. Med.* **2014**, *127*, 311–318. [[CrossRef](#)] [[PubMed](#)]
3. Neogi, T.; Jansen, T.L.; Dalbeth, N.; Fransen, J.; Schumacher, H.R.; Berendsen, D.; Brown, M.; Choi, H.; Edwards, N.L.; Janssens, H.J.; et al. 2015 Gout Classification Criteria: An American College of Rheumatology/European League Against Rheumatism collaborative initiative. *Arthritis Rheumatol.* **2015**, *67*, 2557–2568. [[CrossRef](#)] [[PubMed](#)]
4. Taylor, W.J.; Fransen, J.; Jansen, T.L.; Dalbeth, N.; Schumacher, H.R.; Brown, M.; Louthrenoo, W.; Vazquez-Mellado, J.; Eliseev, M.; McCarthy, G.; et al. Study for Updated Gout Classification Criteria: Identification of Features to Classify Gout. *Arthritis Care Res. (Hoboken)* **2015**, *67*, 1304–1315. [[CrossRef](#)] [[PubMed](#)]
5. Low, E.; Ouellette, H.; Munk, P.L. Tophaceous Gout. *Ann. Acad. Med. Singap.* **2020**, *49*, 931–933. [[CrossRef](#)] [[PubMed](#)]
6. Monu, J.U.; Pope, T.L., Jr. Gout: A clinical and radiologic review. *Radiol. Clin. N. Am.* **2004**, *42*, 169–184. [[CrossRef](#)]
7. Girish, G.; Glazebrook, K.N.; Jacobson, J.A. Advanced imaging in gout. *AJR Am. J. Roentgenol.* **2013**, *201*, 515–525. [[CrossRef](#)] [[PubMed](#)]
8. Richette, P.; Doherty, M.; Pascual, E.; Barskova, V.; Becce, F.; Castaneda, J.; Coyfish, M.; Guillo, S.; Jansen, T.; Janssens, H.; et al. 2018 updated European League Against Rheumatism evidence-based recommendations for the diagnosis of gout. *Ann. Rheum. Dis.* **2020**, *79*, 31–38. [[CrossRef](#)]
9. Christiansen, S.N.; Østergaard, M.; Terslev, L. Ultrasonography in gout: Utility in diagnosis and monitoring. *Clin. Exp. Rheumatol.* **2018**, *36* (Suppl. 114), 61–67. [[PubMed](#)]
10. Glazebrook, K.N.; Guimarães, L.S.; Murthy, N.S.; Black, D.F.; Bongartz, T.; Manek, N.J.; Leng, S.; Fletcher, J.G.; McCollough, C.H. Identification of intraarticular and periarticular uric acid crystals with dual-energy CT: Initial evaluation. *Radiology* **2011**, *261*, 516–524. [[CrossRef](#)] [[PubMed](#)]
11. Bongartz, T.; Glazebrook, K.N.; Kavros, S.J.; Murthy, N.S.; Merry, S.P.; Franz, W.B., 3rd; Michet, C.J.; Veetil, B.M.; Davis, J.M., 3rd; Mason, T.G., 2nd; et al. Dual-energy CT for the diagnosis of gout: An accuracy and diagnostic yield study. *Ann. Rheum. Dis.* **2015**, *74*, 1072–1077. [[CrossRef](#)]
12. Coupal, T.M.; Mallinson, P.I.; Gershony, S.L.; McLaughlin, P.D.; Munk, P.L.; Nicolaou, S.; Ouellette, H.A. Getting the Most From Your Dual-Energy Scanner: Recognizing, Reducing, and Eliminating Artifacts. *AJR Am. J. Roentgenol.* **2016**, *206*, 119–128. [[CrossRef](#)] [[PubMed](#)]
13. Schwabl, C.; Taljanovic, M.; Widmann, G.; Teh, J.; Klausner, A.S. Ultrasonography and dual-energy computed tomography: Impact for the detection of gouty deposits. *Ultrasonography* **2021**, *40*, 197–206. [[CrossRef](#)] [[PubMed](#)]
14. Desai, M.A.; Peterson, J.J.; Garner, H.W.; Kransdorf, M.J. Clinical utility of dual-energy CT for evaluation of tophaceous gout. *Radiographics* **2011**, *31*, 1365–1375; discussion 1376–1377. [[CrossRef](#)]
15. Girish, G.; Melville, D.M.; Kaeley, G.S.; Brandon, C.J.; Goyal, J.R.; Jacobson, J.A.; Jamadar, D.A. Imaging appearances in gout. *Arthritis* **2013**, *2013*, 673401. [[CrossRef](#)] [[PubMed](#)]
16. O'Connor, P.J. Crystal deposition disease and psoriatic arthritis. *Semin. Musculoskelet. Radiol.* **2013**, *17*, 74–79. [[CrossRef](#)] [[PubMed](#)]
17. Taljanovic, M.S.; Melville, D.M.; Gimber, L.H.; Scalcione, L.R.; Miller, M.D.; Kwok, C.K.; Klausner, A.S. High-Resolution US of Rheumatologic Diseases. *Radiographics* **2015**, *35*, 2026–2048. [[CrossRef](#)] [[PubMed](#)]
18. Teh, J.; McQueen, F.; Eshed, I.; Plagou, A.; Klausner, A. Advanced Imaging in the Diagnosis of Gout and Other Crystal Arthropathies. *Semin. Musculoskelet. Radiol.* **2018**, *22*, 225–236. [[CrossRef](#)]

19. Suh, Y.S.; Cheon, Y.H.; Kim, J.E.; Kim, J.M.; Kim, S.H.; Lee, W.S.; Yoo, W.H.; Lee, S.I.; Kim, H.O. Usefulness of plain radiography for assessing hypouricemic treatment response in patients with tophaceous gout. *Int. J. Rheum. Dis.* **2016**, *19*, 1183–1188. [[CrossRef](#)]
20. Ottaviani, S.; Gill, G.; Aubrun, A.; Palazzo, E.; Meyer, O.; Dieudé, P. Ultrasound in gout: A useful tool for following urate-lowering therapy. *Jt. Bone Spine* **2015**, *82*, 42–44. [[CrossRef](#)]
21. de Ávila Fernandes, E.; Kubota, E.S.; Sandim, G.B.; Mitraud, S.A.; Ferrari, A.J.; Fernandes, A.R. Ultrasound features of tophi in chronic tophaceous gout. *Skeletal. Radiol.* **2011**, *40*, 309–315. [[CrossRef](#)] [[PubMed](#)]
22. Abhishek, A.; Roddy, E.; Doherty, M. Gout—A guide for the general and acute physicians. *Clin. Med.* **2017**, *17*, 54–59. [[CrossRef](#)]
23. Dalbeth, N.; Merriman, T.R.; Stamp, L.K. Gout. *Lancet* **2016**, *388*, 2039–2052. [[CrossRef](#)]
24. Abdellatif, W.; Ding, J.; Khorshed, D.; Shojania, K.; Nicolaou, S. Unravelling the mysteries of gout by multimodality imaging. *Semin. Arthritis Rheum.* **2020**, *50*, S17–S23. [[CrossRef](#)]
25. Wright, S.A.; Filippucci, E.; McVeigh, C.; Grey, A.; McCarron, M.; Grassi, W.; Wright, G.D.; Taggart, A.J. High-resolution ultrasonography of the first metatarsal phalangeal joint in gout: A controlled study. *Ann. Rheum. Dis.* **2007**, *66*, 859–864. [[CrossRef](#)]
26. Thiele, R.G.; Schlesinger, N. Ultrasonography shows disappearance of monosodium urate crystal deposition on hyaline cartilage after sustained normouricemia is achieved. *Rheumatol. Int.* **2010**, *30*, 495–503. [[CrossRef](#)]
27. Das, S.; Goswami, R.P.; Ghosh, A.; Ghosh, P.; Lahiri, D.; Basu, K. Temporal evolution of urate crystal deposition over articular cartilage after successful urate-lowering therapy in patients with gout: An ultrasonographic perspective. *Mod. Rheumatol.* **2017**, *27*, 518–523. [[CrossRef](#)] [[PubMed](#)]
28. Rettenbacher, T.; Ennemoser, S.; Weirich, H.; Ulmer, H.; Hartig, F.; Klotz, W.; Herold, M. Diagnostic imaging of gout: Comparison of high-resolution US versus conventional X-ray. *Eur. Radiol.* **2008**, *18*, 621–630. [[CrossRef](#)] [[PubMed](#)]
29. Pattampaspong, N.; Vuthiwong, W.; Kanthawang, T.; Louthrenoo, W. Value of ultrasonography in the diagnosis of gout in patients presenting with acute arthritis. *Skeletal. Radiol.* **2017**, *46*, 759–767. [[CrossRef](#)]
30. Klauser, A.S.; Halpern, E.J.; Strobl, S.; Abd Ellah, M.M.H.; Gruber, J.; Bellmann-Weiler, R.; Auer, T.; Feuchtner, G.; Jäschke, W. Gout of hand and wrist: The value of US as compared with DECT. *Eur. Radiol.* **2018**, *28*, 4174–4181. [[CrossRef](#)]
31. Bayat, S.; Baraf, H.S.B.; Rech, J. Update on imaging in gout: Contrasting and comparing the role of dual-energy computed tomography to traditional diagnostic and monitoring techniques. *Clin. Exp. Rheumatol.* **2018**, *36* (Suppl. 114), 53–60. [[PubMed](#)]
32. Grainger, R.; Dalbeth, N.; Keen, H.; Durcan, L.; Lawrence Edwards, N.; Perez-Ruiz, F.; Diaz-Torne, C.; Singh, J.A.; Khanna, D.; Simon, L.S.; et al. Imaging as an Outcome Measure in Gout Studies: Report from the OMERACT Gout Working Group. *J. Rheumatol.* **2015**, *42*, 2460–2464. [[CrossRef](#)] [[PubMed](#)]
33. Zhang, T.; Yang, F.; Li, J.; Pan, Z. Gout of the axial joint—A patient level systemic review. *Semin. Arthritis Rheum.* **2019**, *48*, 649–657. [[CrossRef](#)]
34. Pillinger, M.H.; Mandell, B.F. Therapeutic approaches in the treatment of gout. *Semin. Arthritis Rheum.* **2020**, *50*, S24–S30. [[CrossRef](#)] [[PubMed](#)]
35. Singh, J.A.; Gaffo, A. Gout epidemiology and comorbidities. *Semin. Arthritis Rheum.* **2020**, *50*, S11–S16. [[CrossRef](#)] [[PubMed](#)]
36. Davies, J.; Riede, P.; van Langevelde, K.; Teh, J. Recent developments in advanced imaging in gout. *Ther. Adv. Musculoskelet. Dis.* **2019**, *11*, 1759720x19844429. [[CrossRef](#)] [[PubMed](#)]
37. Choi, H.K.; Atkinson, K.; Karlson, E.W.; Willett, W.; Curhan, G. Alcohol intake and risk of incident gout in men: A prospective study. *Lancet* **2004**, *363*, 1277–1281. [[CrossRef](#)]
38. Hak, A.E.; Curhan, G.C.; Grodstein, F.; Choi, H.K. Menopause, postmenopausal hormone use and risk of incident gout. *Ann. Rheum. Dis.* **2010**, *69*, 1305–1309. [[CrossRef](#)]
39. Bhole, V.; de Vera, M.; Rahman, M.M.; Krishnan, E.; Choi, H. Epidemiology of gout in women: Fifty-two-year followup of a prospective cohort. *Arthritis Rheum.* **2010**, *62*, 1069–1076. [[CrossRef](#)] [[PubMed](#)]
40. Zhu, L.; Wu, H.; Wu, X.; Sun, W.; Zhang, T.; Ye, L.; Wang, W.; Wang, J. Comparison Between Dual-Energy Computed Tomography and Ultrasound in the Diagnosis of Gout of Various Joints. *Acad. Radiol.* **2015**, *22*, 1497–1502. [[CrossRef](#)]
41. Choi, H.K.; Curhan, G. Independent impact of gout on mortality and risk for coronary heart disease. *Circulation* **2007**, *116*, 894–900. [[CrossRef](#)]
42. Choi, H.K.; De Vera, M.A.; Krishnan, E. Gout and the risk of type 2 diabetes among men with a high cardiovascular risk profile. *Rheumatology (Oxford)* **2008**, *47*, 1567–1570. [[CrossRef](#)] [[PubMed](#)]
43. Choi, H.K.; Ford, E.S.; Li, C.; Curhan, G. Prevalence of the metabolic syndrome in patients with gout: The Third National Health and Nutrition Examination Survey. *Arthritis Rheum.* **2007**, *57*, 109–115. [[CrossRef](#)]
44. Bardin, T.; Richette, P. Impact of comorbidities on gout and hyperuricaemia: An update on prevalence and treatment options. *BMC Med.* **2017**, *15*, 123. [[CrossRef](#)] [[PubMed](#)]
45. Klauser, A.S.; Halpern, E.J.; Strobl, S.; Gruber, J.; Feuchtner, G.; Bellmann-Weiler, R.; Weiss, G.; Stofferin, H.; Jäschke, W. Dual-Energy Computed Tomography Detection of Cardiovascular Monosodium Urate Deposits in Patients With Gout. *JAMA Cardiol.* **2019**, *4*, 1019–1028. [[CrossRef](#)] [[PubMed](#)]
46. Chou, H.; Chin, T.Y.; Peh, W.C. Dual-energy CT in gout—A review of current concepts and applications. *J. Med. Radiat. Sci.* **2017**, *64*, 41–51. [[CrossRef](#)]
47. Liu, F.; Dong, J.; Zhou, D.; Kang, Q.; Xiong, F. Gout is not associated with the risk of fracture: A meta-analysis. *J. Orthop. Surg. Res.* **2019**, *14*, 272. [[CrossRef](#)] [[PubMed](#)]

48. Towiwat, P.; Chhana, A.; Dalbeth, N. The anatomical pathology of gout: A systematic literature review. *BMC Musculoskelet. Disord.* **2019**, *20*, 140. [[CrossRef](#)] [[PubMed](#)]
49. Nicolaou, S.; Yong-Hing, C.J.; Galea-Soler, S.; Hou, D.J.; Louis, L.; Munk, P. Dual-energy CT as a potential new diagnostic tool in the management of gout in the acute setting. *AJR Am. J. Roentgenol.* **2010**, *194*, 1072–1078. [[CrossRef](#)] [[PubMed](#)]
50. Mallinson, P.I.; Reagan, A.C.; Coupal, T.; Munk, P.L.; Ouellette, H.; Nicolaou, S. The distribution of urate deposition within the extremities in gout: A review of 148 dual-energy CT cases. *Skeletal. Radiol.* **2014**, *43*, 277–281. [[CrossRef](#)] [[PubMed](#)]
51. Lee, S.K.; Jung, J.Y.; Jee, W.H.; Lee, J.J.; Park, S.H. Combining non-contrast and dual-energy CT improves diagnosis of early gout. *Eur. Radiol.* **2019**, *29*, 1267–1275. [[CrossRef](#)]
52. Dalbeth, N.; Kalluru, R.; Aati, O.; Horne, A.; Doyle, A.J.; McQueen, F.M. Tendon involvement in the feet of patients with gout: A dual-energy CT study. *Ann. Rheum. Dis.* **2013**, *72*, 1545–1548. [[CrossRef](#)] [[PubMed](#)]
53. Schumacher, H.R., Jr.; Becker, M.A.; Palo, W.A.; Streit, J.; MacDonald, P.A.; Joseph-Ridge, N. Tophaceous gout: Quantitative evaluation by direct physical measurement. *J. Rheumatol.* **2005**, *32*, 2368–2372.
54. Dalbeth, N.; Schauer, C.; Macdonald, P.; Perez-Ruiz, F.; Schumacher, H.R.; Hamburger, S.; Choi, H.K.; McQueen, F.M.; Doyle, A.; Taylor, W.J. Methods of tophus assessment in clinical trials of chronic gout: A systematic literature review and pictorial reference guide. *Ann. Rheum. Dis.* **2011**, *70*, 597–604. [[CrossRef](#)]
55. Ko, K.H.; Hsu, Y.C.; Lee, H.S.; Lee, C.H.; Huang, G.S. Tophaceous gout of the knee: Revisiting MRI patterns in 30 patients. *J. Clin. Rheumatol.* **2010**, *16*, 209–214. [[CrossRef](#)] [[PubMed](#)]
56. Dalbeth, N.; Pool, B.; Gamble, G.D.; Smith, T.; Callon, K.E.; McQueen, F.M.; Cornish, J. Cellular characterization of the gouty tophus: A quantitative analysis. *Arthritis Rheum.* **2010**, *62*, 1549–1556. [[CrossRef](#)] [[PubMed](#)]
57. Lee, Y.H.; Song, G.G. Diagnostic accuracy of ultrasound in patients with gout: A meta-analysis. *Semin. Arthritis Rheum.* **2018**, *47*, 703–709. [[CrossRef](#)] [[PubMed](#)]
58. Fields, T.R. The Challenges of Approaching and Managing Gout. *Rheum. Dis. Clin. N. Am.* **2019**, *45*, 145–157. [[CrossRef](#)]
59. Ogdie, A.; Taylor, W.J.; Neogi, T.; Fransen, J.; Jansen, T.L.; Schumacher, H.R.; Louthrenoo, W.; Vazquez-Mellado, J.; Eliseev, M.; McCarthy, G.; et al. Performance of Ultrasound in the Diagnosis of Gout in a Multicenter Study: Comparison With Monosodium Urate Monohydrate Crystal Analysis as the Gold Standard. *Arthritis Rheumatol.* **2017**, *69*, 429–438. [[CrossRef](#)]
60. Kravchenko, D.; Karakostas, P.; Kuetting, D.; Meyer, C.; Brossart, P.; Behning, C.; Schäfer, V.S. The role of dual energy computed tomography in the differentiation of acute gout flares and acute calcium pyrophosphate crystal arthritis. *Clin. Rheumatol.* **2021**. [[CrossRef](#)]
61. Bloch, C.; Hermann, G.; Yu, T.F. A radiologic reevaluation of gout: A study of 2,000 patients. *AJR Am. J. Roentgenol.* **1980**, *134*, 781–787. [[CrossRef](#)]
62. Glazebrook, K.N.; Kakar, S.; Ida, C.M.; Laurini, J.A.; Moder, K.G.; Leng, S. False-negative dual-energy computed tomography in a patient with acute gout. *J. Clin. Rheumatol.* **2012**, *18*, 138–141. [[CrossRef](#)]
63. Terslev, L.; Gutierrez, M.; Christensen, R.; Balint, P.V.; Bruyn, G.A.; Delle Sedie, A.; Filippucci, E.; Garrido, J.; Hammer, H.B.; Iagnocco, A.; et al. Assessing Elementary Lesions in Gout by Ultrasound: Results of an OMERACT Patient-based Agreement and Reliability Exercise. *J. Rheumatol.* **2015**, *42*, 2149–2154. [[CrossRef](#)]
64. Christiansen, S.N.; Filippou, G.; Scirè, C.A.; Balint, P.V.; Bruyn, G.A.; Dalbeth, N.; DeJaco, C.; Sedie, A.D.; Filippucci, E.; Hammer, H.B.; et al. Consensus-based semi-quantitative ultrasound scoring system for gout lesions: Results of an OMERACT Delphi process and web-reliability exercise. *Semin. Arthritis Rheum.* **2021**, *51*, 644–649. [[CrossRef](#)] [[PubMed](#)]
65. Grassi, W.; Meenagh, G.; Pascual, E.; Filippucci, E. "Crystal clear"-sonographic assessment of gout and calcium pyrophosphate deposition disease. *Semin. Arthritis Rheum.* **2006**, *36*, 197–202. [[CrossRef](#)] [[PubMed](#)]
66. Howard, R.G.; Pillinger, M.H.; Gyftopoulos, S.; Thiele, R.G.; Swearingen, C.J.; Samuels, J. Reproducibility of musculoskeletal ultrasound for determining monosodium urate deposition: Concordance between readers. *Arthritis Care Res. (Hoboken)* **2011**, *63*, 1456–1462. [[CrossRef](#)] [[PubMed](#)]
67. Thiele, R.G. Role of ultrasound and other advanced imaging in the diagnosis and management of gout. *Curr. Rheumatol. Rep.* **2011**, *13*, 146–153. [[CrossRef](#)]
68. Filippucci, E.; Riveros, M.G.; Georgescu, D.; Salaffi, F.; Grassi, W. Hyaline cartilage involvement in patients with gout and calcium pyrophosphate deposition disease. An ultrasound study. *Osteoarthr. Cartil.* **2009**, *17*, 178–181. [[CrossRef](#)]
69. Pineda, C.; Amezcua-Guerra, L.M.; Solano, C.; Rodriguez-Henríquez, P.; Hernández-Díaz, C.; Vargas, A.; Hofmann, F.; Gutiérrez, M. Joint and tendon subclinical involvement suggestive of gouty arthritis in asymptomatic hyperuricemia: An ultrasound controlled study. *Arthritis Res. Ther.* **2011**, *13*, R4. [[CrossRef](#)]
70. Wakefield, R.J.; Balint, P.V.; Szkudlarek, M.; Filippucci, E.; Backhaus, M.; D'Agostino, M.A.; Sanchez, E.N.; Iagnocco, A.; Schmidt, W.A.; Bruyn, G.A.; et al. Musculoskeletal ultrasound including definitions for ultrasonographic pathology. *J. Rheumatol.* **2005**, *32*, 2485–2487.
71. Carter, J.D.; Kedar, R.P.; Anderson, S.R.; Osorio, A.H.; Albritton, N.L.; Gnanashanmugam, S.; Valeriano, J.; Vasey, F.B.; Ricca, L.R. An analysis of MRI and ultrasound imaging in patients with gout who have normal plain radiographs. *Rheumatology (Oxford)* **2009**, *48*, 1442–1446. [[CrossRef](#)] [[PubMed](#)]
72. Taljanovic, M.S.; Gimber, L.H.; Becker, G.W.; Latt, L.D.; Klauser, A.S.; Melville, D.M.; Gao, L.; Witte, R.S. Shear-Wave Elastography: Basic Physics and Musculoskeletal Applications. *Radiographics* **2017**, *37*, 855–870. [[CrossRef](#)]

73. Tang, Y.; Yan, F.; Yang, Y.; Xiang, X.; Wang, L.; Zhang, L.; Qiu, L. Value of Shear Wave Elastography in the Diagnosis of Gouty and Non-Gouty Arthritis. *Ultrasound Med. Biol.* **2017**, *43*, 884–892. [[CrossRef](#)]
74. Wang, Q.; Guo, L.H.; Li, X.L.; Zhao, C.K.; Li, M.X.; Wang, L.; Liu, X.Y.; Xu, H.X. Differentiating the acute phase of gout from the intercritical phase with ultrasound and quantitative shear wave elastography. *Eur. Radiol.* **2018**, *28*, 5316–5327. [[CrossRef](#)] [[PubMed](#)]
75. Mallinson, P.I.; Coupal, T.M.; McLaughlin, P.D.; Nicolaou, S.; Munk, P.L.; Ouellette, H.A. Dual-Energy CT for the Musculoskeletal System. *Radiology* **2016**, *281*, 690–707. [[CrossRef](#)] [[PubMed](#)]
76. Carotti, M.; Salaffi, F.; Filippucci, E.; Aringhieri, G.; Bruno, F.; Giovine, S.; Gentili, F.; Floridi, C.; Borgheresi, A.; De Filippo, M.; et al. Clinical utility of Dual Energy Computed Tomography in gout: Current concepts and applications. *Acta Biomed.* **2020**, *91*, 116–124. [[CrossRef](#)]
77. Gamala, M.; Jacobs, J.W.G.; van Laar, J.M. The diagnostic performance of dual energy CT for diagnosing gout: A systematic literature review and meta-analysis. *Rheumatology (Oxford)* **2019**, *58*, 2117–2121. [[CrossRef](#)]
78. De Vulder, N.; Chen, M.; Huysse, W.; Herregods, N.; Verstraete, K.; Jans, L. Case Series: Dual-Energy CT in Extra-Articular Manifestations of Gout: Main Teaching Point: Dual-energy CT is a valuable asset in the detection of extra-articular manifestations of gout. *J. Belg. Soc. Radiol.* **2020**, *104*, 27. [[CrossRef](#)]
79. Wang, J.X.; Ng, B.; Bak, H.; Spencer, D.; Manolios, N.; Wong, P.K.K. The utility of dual energy computed tomography in the management of axial gout: Case reports and literature review. *BMC Rheumatol.* **2020**, *4*, 22. [[CrossRef](#)]
80. Marty-Ané, A.; Norberciak, L.; Andrès, M.; Houvenagel, E.; Ducoulombier, V.; Legrand, J.; Budzik, J.F.; Pascart, T. Crystal deposition measured with dual-energy computed tomography: Association with mortality and cardiovascular risks in gout. *Rheumatology (Oxford)* **2021**, *60*, 4855–4860. [[CrossRef](#)]
81. Popovich, I.; Dalbeth, N.; Doyle, A.; Reeves, Q. McQueen FM: Exploring cartilage damage in gout using 3-T MRI: Distribution and associations with joint inflammation and tophus deposition. *Skelet. Radiol.* **2014**, *43*, 917–924. [[CrossRef](#)] [[PubMed](#)]
82. McQueen, F.M.; Doyle, A.; Reeves, Q.; Gao, A.; Tsai, A.; Gamble, G.D.; Curteis, B.; Williams, M.; Dalbeth, N. Bone erosions in patients with chronic gouty arthropathy are associated with tophi but not bone oedema or synovitis: New insights from a 3 T MRI study. *Rheumatology (Oxford)* **2014**, *53*, 95–103. [[CrossRef](#)] [[PubMed](#)]
83. Fernandes, A.; Faria, M.T.; Oliveira, A.; Vieira, T.; Pereira, J. Bone scintigraphy in tophaceous gout. *Eur. J. Nucl. Med. Mol. Imaging* **2016**, *43*, 1387–1388. [[CrossRef](#)] [[PubMed](#)]
84. Goshen, E.; Schwartz, A.; Zwas, S.T. Chronic tophaceous gout: Scintigraphic findings on bone scan. *Clin. Nucl. Med.* **2000**, *25*, 146–147. [[CrossRef](#)]
85. Emsen, B.; Fitoussi, A.; Chalaye, J.; Adam, C.; Itti, E. FDG PET/CT of Cervical Gout with Spinal Cord Compression. *Clin. Nucl. Med.* **2020**, *45*, e29–e31. [[CrossRef](#)]
86. Ito, K.; Minamimoto, R.; Morooka, M.; Kubota, K. A case of gouty arthritis to tophi on 18F-FDG PET/CT imaging. *Clin. Nucl. Med.* **2012**, *37*, 614–617. [[CrossRef](#)]
87. Qiu, L.; Chen, Y.; Huang, Z.; Cai, L.; Zhang, L. Widespread gouty tophi on 18F-FDG PET/CT imaging. *Clin. Nucl. Med.* **2014**, *39*, 579–581. [[CrossRef](#)]
88. Vicente, J.S.; Gómez, A.L.; Moreno, R.L.; Torre, J.R.I.; Bernardo, L.G.; Madrid, J.I.R. Lumbar Gout Tophus Mimicking Epidural Abscess with Magnetic Resonance Imaging, Bone, and Gallium Scans. *Indian J. Nucl. Med.* **2018**, *33*, 158–160. [[CrossRef](#)]
89. Schlesinger, N.; Norquist, J.M.; Watson, D.J. Serum urate during acute gout. *J. Rheumatol.* **2009**, *36*, 1287–1289. [[CrossRef](#)]
90. Swan, A.; Amer, H.; Dieppe, P. The value of synovial fluid assays in the diagnosis of joint disease: A literature survey. *Ann. Rheum. Dis.* **2002**, *61*, 493–498. [[CrossRef](#)]
91. Janssens, H.J.; Janssen, M.; van de Lisdonk, E.H.; van Riel, P.L.; van Weel, C. Use of oral prednisolone or naproxen for the treatment of gout arthritis: A double-blind, randomised equivalence trial. *Lancet* **2008**, *371*, 1854–1860. [[CrossRef](#)]
92. Man, C.Y.; Cheung, I.T.; Cameron, P.A.; Rainer, T.H. Comparison of oral prednisolone/paracetamol and oral indomethacin/paracetamol combination therapy in the treatment of acute goutlike arthritis: A double-blind, randomized, controlled trial. *Ann. Emerg. Med.* **2007**, *49*, 670–677. [[CrossRef](#)] [[PubMed](#)]
93. Rainer, T.H.; Cheng, C.H.; Janssens, H.J.; Man, C.Y.; Tam, L.S.; Choi, Y.F.; Yau, W.H.; Lee, K.H.; Graham, C.A. Oral Prednisolone in the Treatment of Acute Gout: A Pragmatic, Multicenter, Double-Blind, Randomized Trial. *Ann. Intern. Med.* **2016**, *164*, 464–471. [[CrossRef](#)] [[PubMed](#)]
94. Wechalekar, M.D.; Vinik, O.; Schlesinger, N.; Buchbinder, R. Intra-articular glucocorticoids for acute gout. *Cochrane Database Syst. Rev.* **2013**. [[CrossRef](#)]
95. Zeng, L.; Qasim, A.; Neogi, T.; Fitzgerald, J.D.; Dalbeth, N.; Mikuls, T.R.; Guyatt, G.H.; Brignardello-Petersen, R. Efficacy and Safety of Pharmacologic Interventions in Patients Experiencing a Gout Flare: A Systematic Review and Network Meta-Analysis. *Arthritis Care Res. (Hoboken)* **2021**, *73*, 755–764. [[CrossRef](#)] [[PubMed](#)]
96. Sutaria, S.; Katbamna, R.; Underwood, M. Effectiveness of interventions for the treatment of acute and prevention of recurrent gout—a systematic review. *Rheumatology (Oxford)* **2006**, *45*, 1422–1431. [[CrossRef](#)]
97. Schumacher, H.R., Jr.; Boice, J.A.; Daikh, D.I.; Mukhopadhyay, S.; Malmstrom, K.; Ng, J.; Tate, G.A.; Molina, J. Randomised double blind trial of etoricoxib and indometacin in treatment of acute gouty arthritis. *BMJ* **2002**, *324*, 1488–1492. [[CrossRef](#)]
98. Schumacher, H.R.; Berger, M.F.; Li-Yu, J.; Perez-Ruiz, F.; Burgos-Vargas, R.; Li, C. Efficacy and tolerability of celecoxib in the treatment of acute gouty arthritis: A randomized controlled trial. *J. Rheumatol.* **2012**, *39*, 1859–1866. [[CrossRef](#)]

99. van Durme, C.M.; Wechalekar, M.D.; Buchbinder, R.; Schlesinger, N.; van der Heijde, D.; Landewe, R.B. Non-steroidal anti-inflammatory drugs for acute gout. *Cochrane Database Syst. Rev.* **2014**, CD010120. [[CrossRef](#)]
100. Terkeltaub, R.A.; Furst, D.E.; Bennett, K.; Kook, K.A.; Crockett, R.S.; Davis, M.W. High versus low dosing of oral colchicine for early acute gout flare: Twenty-four-hour outcome of the first multicenter, randomized, double-blind, placebo-controlled, parallel-group, dose-comparison colchicine study. *Arthritis Rheum.* **2010**, *62*, 1060–1068. [[CrossRef](#)]
101. Terkeltaub, R.A. Colchicine update: 2008. *Semin. Arthritis Rheum.* **2009**, *38*, 411–419. [[CrossRef](#)] [[PubMed](#)]
102. Liew, J.W.; Gardner, G.C. Use of Anakinra in Hospitalized Patients with Crystal-associated Arthritis. *J. Rheumatol.* **2019**, *46*, 1345–1349. [[CrossRef](#)] [[PubMed](#)]
103. Saag, K.G.; Khanna, P.P.; Keenan, R.T.; Ohlman, S.; Osterling Koskinen, L.; Sparve, E.; Akerblad, A.C.; Wiken, M.; So, A.; Pillinger, M.H.; et al. A Randomized, Phase II Study Evaluating the Efficacy and Safety of Anakinra in the Treatment of Gout Flares. *Arthritis Rheumatol.* **2021**, *73*, 1533–1542. [[CrossRef](#)]
104. FitzGerald, J.D.; Dalbeth, N.; Mikuls, T.; Brignardello-Petersen, R.; Guyatt, G.; Abeles, A.M.; Gelber, A.C.; Harrold, L.R.; Khanna, D.; King, C.; et al. 2020 American College of Rheumatology Guideline for the Management of Gout. *Arthritis Rheumatol.* **2020**, *72*, 879–895. [[CrossRef](#)] [[PubMed](#)]
105. Borstad, G.C.; Bryant, L.R.; Abel, M.P.; Scroggie, D.A.; Harris, M.D.; Alloway, J.A. Colchicine for prophylaxis of acute flares when initiating allopurinol for chronic gouty arthritis. *J. Rheumatol.* **2004**, *31*, 2429–2432.
106. Hershfield, M.S.; Callaghan, J.T.; Tassaneeyakul, W.; Mushiroda, T.; Thorn, C.F.; Klein, T.E.; Lee, M.T. Clinical Pharmacogenetics Implementation Consortium guidelines for human leukocyte antigen-B genotype and allopurinol dosing. *Clin. Pharmacol. Ther.* **2013**, *93*, 153–158. [[CrossRef](#)] [[PubMed](#)]
107. Becker, M.A.; Schumacher, H.R., Jr.; Wortmann, R.L.; MacDonald, P.A.; Eustace, D.; Palo, W.A.; Streit, J.; Joseph-Ridge, N. Febuxostat compared with allopurinol in patients with hyperuricemia and gout. *N. Engl. J. Med.* **2005**, *353*, 2450–2461. [[CrossRef](#)] [[PubMed](#)]
108. Becker, M.A.; Schumacher, H.R.; Espinoza, L.R.; Wells, A.F.; MacDonald, P.; Lloyd, E.; Lademacher, C. The urate-lowering efficacy and safety of febuxostat in the treatment of the hyperuricemia of gout: The CONFIRMS trial. *Arthritis Res. Ther.* **2010**, *12*, R63. [[CrossRef](#)] [[PubMed](#)]
109. White, W.B.; Saag, K.G.; Becker, M.A.; Borer, J.S.; Gorelick, P.B.; Whelton, A.; Hunt, B.; Castillo, M.; Gunawardhana, L.; Investigators, C. Cardiovascular Safety of Febuxostat or Allopurinol in Patients with Gout. *N. Engl. J. Med.* **2018**, *378*, 1200–1210. [[CrossRef](#)] [[PubMed](#)]
110. Khanna, D.; FitzGerald, J.D.; Khanna, P.P.; Bae, S.; Singh, M.K.; Neogi, T.; Pillinger, M.H.; Merill, J.; Lee, S.; Prakash, S.; et al. 2012 American College of Rheumatology guidelines for management of gout. Part 1: Systematic nonpharmacologic and pharmacologic therapeutic approaches to hyperuricemia. *Arthritis Care Res. (Hoboken)* **2012**, *64*, 1431–1446. [[CrossRef](#)]
111. Sundy, J.S.; Baraf, H.S.; Yood, R.A.; Edwards, N.L.; Gutierrez-Urena, S.R.; Treadwell, E.L.; Vazquez-Mellado, J.; White, W.B.; Lipsky, P.E.; Horowitz, Z.; et al. Efficacy and tolerability of pegloticase for the treatment of chronic gout in patients refractory to conventional treatment: Two randomized controlled trials. *JAMA* **2011**, *306*, 711–720. [[CrossRef](#)]
112. Baraf, H.S.; Yood, R.A.; Ottery, F.D.; Sundy, J.S.; Becker, M.A. Infusion-related reactions with pegloticase, a recombinant uricase for the treatment of chronic gout refractory to conventional therapy. *J. Clin. Rheumatol.* **2014**, *20*, 427–432. [[CrossRef](#)]
113. Tang, C.Y.; Fung, B. The last defence? Surgical aspects of gouty arthritis of hand and wrist. *Hong Kong Med. J.* **2011**, *17*, 480–486. [[PubMed](#)]
114. Capobianco, C.M. Surgical treatment approaches to second metatarsophalangeal joint pathology. *Clin. Podiatr. Med. Surg.* **2012**, *29*, 443–449. [[CrossRef](#)]
115. Caliozna, L.; Medetti, M.; Bina, V.; Brancato, A.M.; Castelli, A.; Jannelli, E.; Ivone, A.; Gastaldi, G.; Annunziata, S.; Mosconi, M.; et al. Pulsed Electromagnetic Fields in Bone Healing: Molecular Pathways and Clinical Applications. *Int. J. Mol. Sci.* **2021**, *22*, 7403. [[CrossRef](#)] [[PubMed](#)]
116. Ouyang, J.; Zhang, B.; Kuang, L.; Yang, P.; Du, X.; Qi, H.; Su, N.; Jin, M.; Yang, J.; Xie, Y.; et al. Pulsed Electromagnetic Field Inhibits Synovitis via Enhancing the Efferocytosis of Macrophages. *Biomed. Res. Int.* **2020**, *2020*, 4307385. [[CrossRef](#)] [[PubMed](#)]
117. Ross, C.L.; Ang, D.C.; Almeida-Porada, G. Targeting Mesenchymal Stromal Cells/Pericytes (MSCs) With Pulsed Electromagnetic Field (PEMF) Has the Potential to Treat Rheumatoid Arthritis. *Front. Immunol.* **2019**, *10*, 266. [[CrossRef](#)] [[PubMed](#)]
118. Garner, H.W.; Wessell, D.E. Current status of ultrasound and dual-energy computed tomography in the evaluation of gout. *Rheumatol. Int.* **2018**, *38*, 1339–1344. [[CrossRef](#)] [[PubMed](#)]
119. Dalbeth, N.; Frampton, C.; Fung, M.; Baumgartner, S.; Nicolaou, S.; Choi, H.K. Concurrent validity of provisional remission criteria for gout: A dual-energy CT study. *Arthritis Res. Ther.* **2019**, *21*, 150. [[CrossRef](#)]
120. Schumacher, H.R.; Taylor, W.; Edwards, L.; Grainger, R.; Schlesinger, N.; Dalbeth, N.; Sivera, F.; Singh, J.; Evans, R.; Waltrip, R.W.; et al. Outcome domains for studies of acute and chronic gout. *J. Rheumatol.* **2009**, *36*, 2342–2345. [[CrossRef](#)] [[PubMed](#)]
121. Perez-Ruiz, F.; Martin, I.; Canteli, B. Ultrasonographic measurement of tophi as an outcome measure for chronic gout. *J. Rheumatol.* **2007**, *34*, 1888–1893. [[PubMed](#)]
122. Peiteado, D.; Villalba, A.; Martín-Mola, E.; Balsa, A.; De Miguel, E. Ultrasound sensitivity to changes in gout: A longitudinal study after two years of treatment. *Clin. Exp. Rheumatol.* **2017**, *35*, 746–751. [[PubMed](#)]

123. Ebstein, E.; Forien, M.; Norkuviene, E.; Richette, P.; Mouterde, G.; Daien, C.; Ea, H.K.; Brière, C.; Lioté, F.; Petraitis, M.; et al. Ultrasound evaluation in follow-up of urate-lowering therapy in gout: The USEFUL study. *Rheumatology (Oxford)* **2019**, *58*, 410–417. [[CrossRef](#)] [[PubMed](#)]
124. Cipolletta, E.; Di Battista, J.; Di Carlo, M.; Di Matteo, A.; Salaffi, F.; Grassi, W.; Filippucci, E. Sonographic estimation of monosodium urate burden predicts the fulfillment of the 2016 remission criteria for gout: A 12-month study. *Arthritis Res. Ther.* **2021**, *23*, 185. [[CrossRef](#)]
125. Christiansen, S.N.; Østergaard, M.; Slot, O.; Keen, H.; Bruyn, G.A.W.; D’Agostino, M.A.; Terslev, L. Assessing the sensitivity to change of the OMERACT ultrasound structural gout lesions during urate-lowering therapy. *RMD Open* **2020**, *6*. [[CrossRef](#)] [[PubMed](#)]
126. Hammer, H.B.; Karoliussen, L.; Terslev, L.; Haavardsholm, E.A.; Kvien, T.K.; Uhlig, T. Ultrasound shows rapid reduction of crystal depositions during a treat-to-target approach in gout patients: 12-month results from the NOR-Gout study. *Ann. Rheum. Dis.* **2020**, *79*, 1500–1505. [[CrossRef](#)]
127. Ebstein, E.; Forien, M.; Norkuviene, E.; Richette, P.; Mouterde, G.; Daien, C.; Ea, H.K.; Brière, C.; Lioté, F.; Petraitis, M.; et al. UltraSound evaluation in follow-up of urate-lowering therapy in gout phase 2 (USEFUL-2): Duration of flare prophylaxis. *Jt. Bone Spine* **2020**, *87*, 647–651. [[CrossRef](#)] [[PubMed](#)]
128. Dalbeth, N.; Nicolaou, S.; Baumgartner, S.; Hu, J.; Fung, M.; Choi, H.K. Presence of monosodium urate crystal deposition by dual-energy CT in patients with gout treated with allopurinol. *Ann. Rheum. Dis.* **2018**, *77*, 364–370. [[CrossRef](#)] [[PubMed](#)]
129. Uhlig, T.; Eskild, T.; Karoliussen, L.F.; Sexton, J.; Kvien, T.K.; Haavardsholm, E.A.; Dalbeth, N.; Hammer, H.B. Two-year reduction of dual-energy CT urate depositions during a treat-to-target strategy in gout in the NOR-Gout longitudinal study. *Rheumatology (Oxford)* **2021**. [[CrossRef](#)]
130. Dalbeth, N.; Billington, K.; Doyle, A.; Frampton, C.; Tan, P.; Aati, O.; Allan, J.; Drake, J.; Horne, A.; Stamp, L.K. Effects of Allopurinol Dose Escalation on Bone Erosion and Urate Volume in Gout: A Dual-Energy Computed Tomography Imaging Study Within a Randomized, Controlled Trial. *Arthritis Rheumatol.* **2019**, *71*, 1739–1746. [[CrossRef](#)]



Review

Imaging and Treatment of Posttraumatic Ankle and Hindfoot Osteoarthritis

Tetyana Gorbachova ^{1,*}, Yulia V. Melenevsky ², L. Daniel Latt ³, Jennifer S. Weaver ⁴ and Mihra S. Taljanovic ^{5,6}

¹ Einstein Medical Center, Department of Radiology, Sidney Kimmel Medical College, Thomas Jefferson University, Philadelphia, PA 19141, USA

² Department of Radiology, UAB Medical Center, University of Alabama at Birmingham, Birmingham, AL 35249, USA; ymelenevsky@uabmc.edu

³ Department of Orthopaedic Surgery, University of Arizona, Tucson, AZ 85724, USA; dlatt@ortho.arizona.edu

⁴ Department of Radiology, University of New Mexico, Albuquerque, NM 87131, USA; jsweaver@salud.unm.edu

⁵ Department of Radiology, University of New Mexico Health Sciences, Albuquerque, NM 87131, USA; mihrat@radiology.arizona.edu

⁶ Departments of Medical Imaging and Orthopaedic Surgery, University of Arizona, Tucson, AZ 85724, USA

* Correspondence: GorbachT@einstein.edu

Abstract: Posttraumatic osteoarthritis of the ankle and hindfoot is a common and frequently debilitating disorder. 70% to 90% of ankle osteoarthritis is related to prior trauma that encompasses a spectrum of disorders including fractures and ligamentous injuries that either disrupt the articular surface or result in instability of the joint. In addition to clinical evaluation, imaging plays a substantial role in the treatment planning of posttraumatic ankle and hindfoot osteoarthritis. Imaging evaluation must be tailored to specific clinical scenarios and includes weight bearing radiography that utilizes standard and specialty views, computed tomography which can be performed with a standard or a weight bearing technique, magnetic resonance imaging, and ultrasound evaluation. This review article aims to familiarize the reader with treatment rationale, to provide a brief review of surgical techniques and to illustrate expected imaging appearances of common operative procedures performed in the setting of posttraumatic ankle and hindfoot osteoarthritis, such as joint-preserving procedures, ankle fusion, subtalar fusion, tibiotalarcalcaneal fusion and ankle arthroplasty. Pre-operative findings will be discussed along with the expected postoperative appearance of various procedures in order to improve detection of their complications on imaging and to provide optimal patient care.

Keywords: ankle and hindfoot osteoarthritis; ankle arthroplasty; subtalar fusion; tibiotalarcalcaneal fusion

Citation: Gorbachova, T.; Melenevsky, Y.V.; Latt, L.D.; Weaver, J.S.; Taljanovic, M.S. Imaging and Treatment of Posttraumatic Ankle and Hindfoot Osteoarthritis. *J. Clin. Med.* **2021**, *10*, 5848. <https://doi.org/10.3390/jcm10245848>

Academic Editor: Mitsuhiro Takeno

Received: 22 November 2021

Accepted: 10 December 2021

Published: 13 December 2021

Publisher's Note: MDPI stays neutral with regard to jurisdictional claims in published maps and institutional affiliations.



Copyright: © 2021 by the authors. Licensee MDPI, Basel, Switzerland. This article is an open access article distributed under the terms and conditions of the Creative Commons Attribution (CC BY) license (<https://creativecommons.org/licenses/by/4.0/>).

1. Introduction

Osteoarthritis of the ankle and hindfoot is a common and frequently debilitating disorder. Although joint deterioration may result from a variety of disease processes, such as developmental, inflammatory and neoplastic conditions, 70% to 90% of ankle osteoarthritis is related to prior trauma [1,2]. Posttraumatic osteoarthritis (PTOA) of the ankle and hindfoot may be generated by a spectrum of disorders including fractures and ligamentous injuries that either disrupt the articular surface or result in instability of the joint. In addition to clinical evaluation, imaging plays a substantial role in the treatment planning of posttraumatic ankle and hindfoot osteoarthritis. This review article aims to familiarize the reader with treatment rationale, to provide a brief review of surgical techniques and to illustrate the expected imaging appearance of common operative procedures performed in the setting of the posttraumatic ankle and foot osteoarthritis, such as osteotomies, fusion procedures, and ankle arthroplasty.

2. Anatomic Considerations

The ankle or talocrural joint is a synovial joint formed by the trochlear surface of the talus, the inferior articular surface of the tibia, and the articular facets of the medial and lateral malleoli [3]. The bones are connected by a fibrous capsule lined by synovium and reinforced medially and laterally by collateral ligamentous complexes. The distal tibiofibular joint is a fibrous joint, united by the syndesmotic ligamentous complex that includes the interosseous ligament and the anterior and posterior tibiofibular ligaments. The subtalar joint, also referred to as the posterior subtalar or posterior talocalcaneal joint, is a synovium-lined articulation between the posterior calcaneal facet of the talus and the posterior talar facet of the calcaneus [3]. Ligamentous structures stabilizing the posterior subtalar joint include the talocalcaneal ligaments as well as components of the medial and lateral ligamentous complexes of the ankle, such as the superficial deltoid ligament medially and the calcaneofibular ligament laterally. The subtalar joint may communicate with the ankle joint in approximately 10 to 20% of persons [3,4]. This anatomic communication may provide a pathway for the spread of pathological processes, such as infection or inflammation, as well as therapeutic injections between these two joints. In addition, physiologic communication may exist between the ankle joint and tendon sheaths of the flexor hallucis longus or the flexor digitorum longus, or both in approximately 20% of patients. The anterior subtalar joint, also referred to as the talocalcaneonavicular joint, is separated from the posterior subtalar joint by the tarsal canal and sinus tarsi. The anterior subtalar joint is a synovium lined joint that encompasses articulation between the talar head and posterior surface of the navicular bone and articulations between the anterior and middle facets of the calcaneus and plantar aspect of the talar head [3]. Some variations in joint communications may exist, which may lead to a distinction of a separate middle subtalar joint.

3. Spectrum of Traumatic Disorders and Clinical Presentation

PTOA may result from cartilage damage sustained at the time of injury or chronic cartilage overloading that is caused by articular incongruity and instability [5]. Intraarticular fractures, such as tibial plafond fractures, may directly disrupt the articular surface, whereas extraarticular fractures may produce deformities resulting in abnormal joint mechanics, and avulsion fractures that involve supporting capsuloligamentous structures may lead to joint instability. In the absence of a fracture, a ligamentous disruption during ankle sprain may have a profound effect on the joint biomechanics causing malalignment and instability that lead to abnormal loading and rapid development of secondary degenerative arthritis. Classic studies demonstrated that even 1 mm of lateral displacement of the talus on the tibia reduces the tibiotalar contact area by 42 percent [6]. In addition, it has been shown that up to 95% of severe ankle sprains have concomitant chondral injuries [7]. Although chronic abnormal loading and residual incongruity contribute to joint degeneration, it is the extent of injury to the articular cartilage during initial trauma that is believed to be the major predisposing factor in the development of PTOA of the ankle [1]. PTOA of the subtalar joint may result from subtalar dislocations, talar and calcaneal fractures, and fracture-dislocations. Fundamentally, anatomic reconstruction of joint congruity is essential for functional recovery after intraarticular fractures; however, despite adequate management, subtalar arthritis may develop as a result of primary cartilage damage at the time of injury [6].

The onset of clinical symptoms of pain and dysfunction may occur years or decades after the original injury [1,8]. Patients present with ankle and hindfoot joint pain that is worse with activity or weight bearing, and instability, stiffness, or swelling that is initially relieved by rest. The onset of symptoms is usually insidious with slow progression over time. Ankle PTOA is a potentially debilitating disorder that may significantly impact a patient's mobility and quality of life. Compared to osteoarthritis of other joints, patients with PTOA of the ankle are an average of 14 years younger at the time of diagnosis and

progress more rapidly to end-stage disease, resulting in increased duration of pain and loss of function [1,8].

4. Imaging Evaluation

Imaging assessment of PTOA of the ankle and foot begins with radiography. Osteoarthritis is depicted by usually asymmetric joint space narrowing, osteophyte formation, subchondral bone sclerosis and cyst-like changes [9]. Chronic posttraumatic osseous deformities and malalignment may also be evident. Standard radiographic views include weight bearing anteroposterior (AP), mortise, and lateral views of the ankle [10]. Additional radiographic views are employed to visualize the posterior subtalar joint [11,12]. Broaden views are obtained to depict various parts of the subtalar joint on lateral projection using 10 degrees beam increments. The Harris-Beath view, or axial calcaneal projection, can demonstrate the posterior subtalar joint, the middle facets of the anterior subtalar joint and the sustentaculum, which allows assessment of calcaneal deformities in the axial plane. Hindfoot alignment evaluation is performed to detect varus or valgus malalignment and consists of either the long axial view or the hindfoot alignment view [13,14]. Compared to radiographs, computed tomography (CT) provides a superior assessment of the articular surfaces of the ankle joint and, in particular, the subtalar joint, depicting articular surface deformity, degenerative changes and joint incongruity [11]. Reformations in the coronal and sagittal planes can be reconstructed with different obliquities. Weight-bearing CT (WBCT) of the foot and ankle is an emerging technology that is increasingly being used by orthopedic surgeons for diagnostic and preoperative planning purposes. In contrast to standard CT scans, WBCT scans demonstrate the alignment of the bones and joints during loading and are superior in the characterization of posttraumatic deformities and instability [15] (Figure 1). Similar to CT, magnetic resonance imaging (MRI) provides multiplanar imaging that allows a better depiction of the complex anatomy of the ankle and subtalar joints. CT is also the study of choice for pre-operative planning for a total ankle arthroplasty. Scanning is obtained from the knee to the ankle and three-dimensional reconstructions are used to create patient specific instrumentation (PSI) for a total ankle arthroplasty. MRI also provides the unique ability to identify ligamentous injury, subchondral marrow abnormalities and cartilage lesions [16]. In the setting of osteoarthritis, ultrasound examination helps assess the joints for the presence of effusion and synovitis and can be used to target therapeutic intraarticular injections. It must be emphasized that radiographic evaluation remains the first and principal imaging modality in the setting of advanced osteoarthritis. Moreover, obtaining weight bearing radiographs is essential for both initial assessment and postoperative evaluation.



Figure 1. (a–d). A 25-year-old female with posttraumatic osteoarthritis of the right tibiotalar and subtalar joints. AP (a) and lateral (b) weight bearing radiographs and coronal (c) and sagittal (d) reformatted weight bearing CT images of the right ankle show an ununited medial malleolus fracture (arrowheads) and severe osteoarthritis of the tibiotalar (arrows) and subtalar joints (dashed arrows) with asymmetric joint space narrowing, subchondral sclerosis and small cyst-like changes. In (b) note the external fixator pin track in the calcaneal tuberosity. In (c,d) note a platform underneath of the foot (open arrowheads) with the CT images acquired in a cone-beam CT scanner dedicated to extremity imaging that allows the assessment of the alignment. Case courtesy of Imran Omar MD, Chicago, IL.

5. Treatment

5.1. Non-Operative Treatment

Currently, no effective treatments are available to prevent the progression of PTOA and evidence indicates that therapeutic interventions must occur early in order to modify the course of disease [1]. Nonoperative treatment of PTOA of the ankle includes bracing and intraarticular injections. Brace treatment of ankle arthritis is aimed at limiting motion and reducing axial loading [17]. Therapeutic joint injections most commonly are performed with corticosteroids or anesthetics [18]. Injections of the ankle and subtalar joints can be successfully performed under ultrasound or fluoroscopic guidance. Corticosteroids are used to provide short- to medium-term pain relief. The clinical duration of effect is considered to be inversely proportional to the solubility of the injected steroid. Intraarticular injections may serve both as therapeutic and diagnostic procedures [19,20]. Injection of

local anesthetic, while giving very short-term pain relief, may assist in determining the patient's source of pain in the presence of multiple confounding factors. In addition to confirming the placement of the needle during fluoroscopically guided joint injection, intraarticular administration of contrast may demonstrate the presence of communication between the ankle joint and the subtalar joint. Such communication results in medications being delivered to both joints and needs to be considered when interpreting symptom relief and when planning further surgical procedures, such as ankle fusion or subtalar fusion.

5.2. Operative Treatment

Several surgical options are available for patients with different stages of ankle PTOA and can be broadly categorized as joint-preserving and joint-nonpreserving procedures.

5.2.1. Joint-Preserving Procedures

Joint-preserving procedures include arthroscopy or arthrotomy with debridement, distraction arthroplasty, osteochondral ankle joint resurfacing, and corrective osteotomies.

Open or arthroscopic joint debridement with removal of loose bodies, synovectomy, and resection of osteophytes may provide temporary relief of symptoms and is performed with variable success rates in patients with early osteoarthritis.

Distraction arthroplasty, or arthrodiastasis, is a technique where distraction force is applied to the joint for approximately 12–17 weeks using rigid external fixation by an Ilizarov apparatus or an anatomically located hinge to allow for a range of motion exercises. Current literature suggests that ankle joint distraction arthroplasty is a viable alternative treatment option in patients younger than 45 years with posttraumatic ankle osteoarthritis and preserved hindfoot motion. These procedures have been shown to reduce pain and improve mobility in patients with advanced osteoarthritis and delay the need for arthroplasty or fusion [21–23]. The therapeutic effect is considered to be due to the change in the metabolism of proteoglycans and the improvement of intra-articular inflammation [24]. Pain relief is generally incomplete. In patients with persistent pain and progressive ankle osteoarthritis, further therapeutic options can be later pursued [25].

Supramalleolar osteotomy is a realignment procedure reserved for eccentric cartilage loss secondary to excessive varus or valgus malalignment of the tibiotalar joint. Abnormal alignment results in focal increased pressure at the talar dome and tibial plafond, leading to asymmetric cartilage loss. Supramalleolar osteotomies are indicated for patients with at least 50% preservation of joint space [26]. The terms “closing” or “opening” in regard to osteotomies refer to either resecting or adding a wedge of bone, respectively, in order to correct the deformity.

Medial closing wedge osteotomy is used to correct valgus ankle deformity. A wedge-shaped fragment is resected from the medial distal tibial metadiaphysis, and stabilizing plate and screws are applied. Pre-existing shortening of the fibula due to malunion may affect tibiotalar joint alignment, necessitating a corrective lengthening osteotomy of the fibula [27] (Figure 2).

In patients with remaining valgus position of the calcaneus and abduction deformity of the mid- and forefoot, the deformity may be corrected by lateral lengthening calcaneal osteotomy [28].

Varus deformity of the tibiotalar joint can be corrected by medial opening wedge osteotomy or lateral closing wedge osteotomy. The medial opening wedge osteotomy is indicated in cases with a varus deformity less than 10° [26]. In patients with varus deformity of more than 10°, medial opening wedge osteotomy correction may be restricted by the fibula. This can be overcome by performing a lateral approach osteotomy of the fibula when a block of bone is removed. Subsequently, tibial lateral closing wedge osteotomy is performed [29].

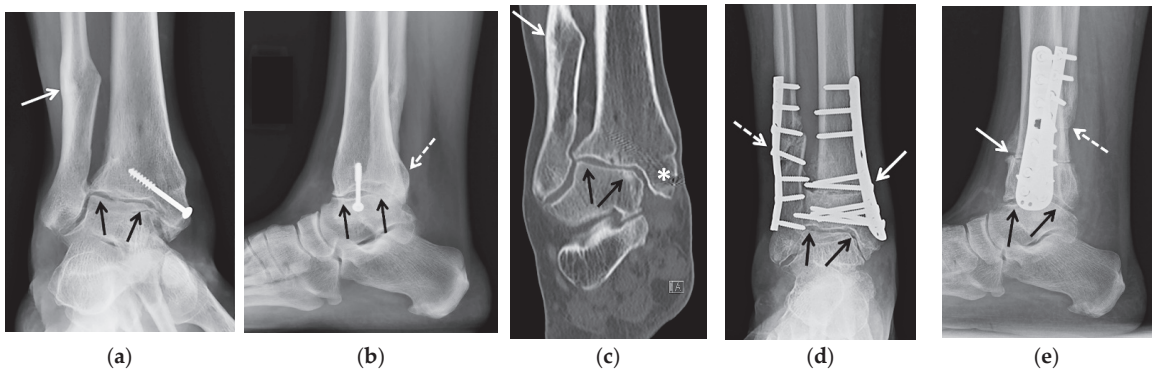


Figure 2. (a–e) A 47-year-old female with a history of remote trimalleolar right ankle fractures and posttraumatic tibiotalar joint osteoarthritis, treated with tibial wedge opening osteotomy and oblique fibular lengthening osteotomy. (a) Mortise and (b) lateral weight-bearing radiographs and (c) coronal reformatted CT image of the right ankle show a healed posttraumatic deformity of the medial malleolus with tibial valgus malunion transfixed by an interfragmentary screw (white asterisk in (c)) and healed posttraumatic deformities of the fibula (white arrow) and of the posterior malleolus (dashed white arrow). Note the asymmetric narrowing of the tibiotalar joint consistent with advanced posttraumatic osteoarthritis (black arrows). (d) Mortise and (e) lateral 3 months postoperative weight-bearing radiographs show improved alignment of the distal tibia (white arrow) and fibula (dashed white arrow) status post osteotomies with decreased tibiotalar joint space narrowing (black arrows). Osteotomy sites demonstrate partial union at 3 months, a normal finding.

5.2.2. Arthrodesis

Ankle arthrodesis is a well-documented surgical treatment of end-stage ankle arthritis. It has been a preferred treatment of ankle arthritis because of its predictable outcomes. Besides PTOA, indications for primary ankle arthrodesis include osteonecrosis of the talus, symptomatic osteochondral lesions of the talus, neuroarthropathy, and failed total ankle arthroplasties. The goals of ankle arthrodesis are to decrease pain, improve function, and provide stability and alignment to allow the patients to return to their functional activity. When the pain originates within the ankle joint, a successful arthrodesis usually eliminates it, and pain relief is more reliable with fusion than with most other techniques. Short-term results and complication rates have been markedly improved by modern techniques of limited periosteal stripping, rigid internal fixation, and meticulous attention to alignment and position. Secondary operations, other than occasional hardware removals, are rarely needed [17]. The patient’s age, weight, compliance, comorbidities, and expectations are taken into account when considering arthrodesis.

Over 30 various ankle arthrodesis techniques have been developed since the first description by Albert in 1879. Ankle arthrodesis is commonly performed via an open approach, however, arthroscopic ankle arthrodesis, while limited to minimal angular deformities, has become increasingly popular during the past decade due to the advantage of minimizing significant soft tissue stripping. The classic open procedure described in 1948 involves resection of the distal fibula approximately 2 cm proximal to the ankle joint, which is used for autologous graft material [30]. Articular cartilage of the distal tibia and talar dome is removed to the vascular bone. The intervening gap is closed, ensuring the optimal plantigrade position of the foot. A fibular onlay graft is applied to the lateral aspect of the talus and tibia and stabilized by screws. The fibular graft can be split longitudinally and applied to both the anterior and lateral surfaces of the talus and tibia [31]. This technique has evolved for several decades and included the using lateral malleolus as a graft source, a change in the number of implants used in tibiotalar stabilization, and a variation in the direction of screw insertion. Additionally, anterior, posterior and medial transmaleolar approaches have been described [32]. Currently, an anatomic ankle fusion with fibular-sparing technique is widely utilized as it offers several advantages. An intact fibula allows

increased surface area for union, preservation of the peroneal groove, prevention of valgus malalignment and lateral translation in cases of non-union and facilitates the possibility of conversion to a total ankle arthroplasty in the future [33]. The most frequent complications after tibiotalar and tibiotalocalcaneal arthrodesis involve nonunion, malunion, infection, and delayed wound healing. Additional complications include neurovascular injuries, adjacent hindfoot joint arthroses or laxity, malalignment, chronic edema, stress fractures, painful scars, and calluses [34].

Tibiotalocalcaneal arthrodesis is an effective salvage procedure used for the treatment of conditions that affect both the ankle and subtalar joints. Indications include failed tibiotalar arthrodesis, extensive osteonecrosis of the talus, failed total ankle arthroplasty, Charcot arthropathy, and gross instability presenting as flail ankle. This type of fusion is usually accomplished by retrograde intramedullary nail placement [35] (Figure 3). Compression at the site of arthrodesis may be lost due to bone resorption or settling. In order to improve healing by maintaining compression at the fusion sites, new techniques, such as the placement of internal pseudoelastic elements, have been implemented [36]. Limb shortening due to structural bone loss in tibiotalocalcaneal arthrodesis can negatively impact the patient's gait and weight-bearing. Structural bone deficit of the talus and ankle and hindfoot malalignment, often seen in end-stage degenerative joint disease, present complex reconstruction challenges that may necessitate the use of structural allograft [37]. A structural femoral head allograft (FHA) can be successfully used to maintain the height of the limb and correct the deformity during tibiotalar fusion [38] (Figure 4).

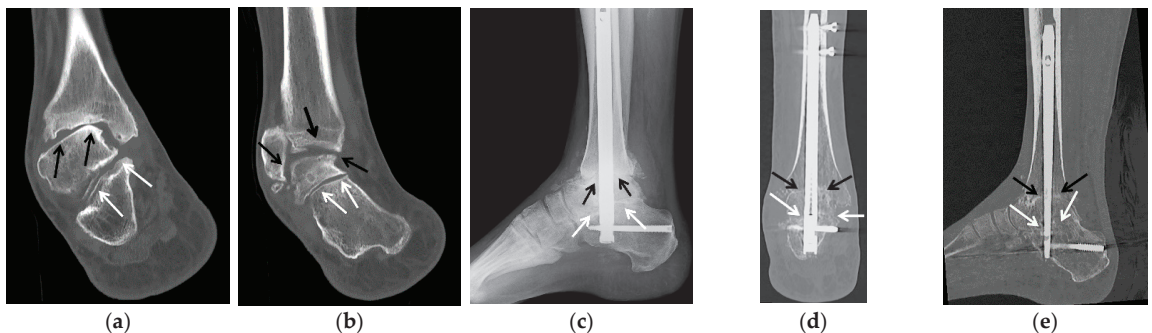


Figure 3. (a–e) A 58-year-old male with tibiotalar and subtalar osteoarthritis with varus alignment treated with tibiotalocalcaneal arthrodesis with intramedullary nail and iliac crest bone marrow aspirate. (a,b) Coronal reformatted preoperative CT images of the right ankle show advanced osteoarthritis of the tibiotalar (black arrows) and posterior subtalar (white arrows) joints with associated varus deformity. (c) Six weeks postoperative lateral weight-bearing radiograph shows a retrograde tibiotalocalcaneal intramedullary nail with interlocking screws in the calcaneus and distal tibial diaphysis transfixing the subtalar (white arrows) and tibiotalar (black arrows) joints with associated bone graft material. (d) Coronal and (e) sagittal reformatted CT images obtained 2.5 months after surgery show markedly improved alignment with progressive fusion across the subtalar (white arrows) and tibiotalar (black arrows) joints.

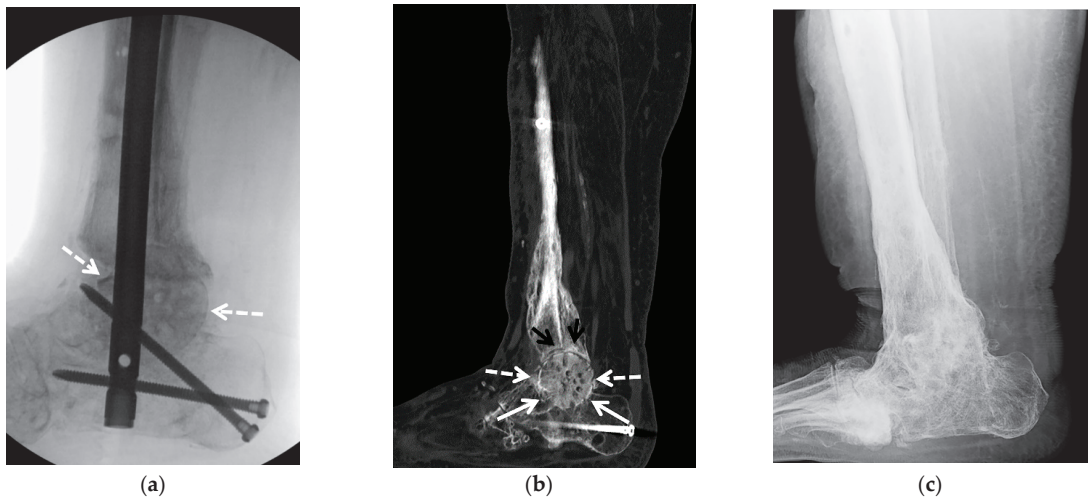


Figure 4. (a–c). A 58-year-old male with a complex medical history including diabetes mellitus, infected right Charcot midfoot and hindfoot as well as advanced secondary osteoarthritis, treated with staged fusion: first external fixation with antibiotic spacer and intravenous antibiotics followed by tibiototalcalcaneal fusion with a structural femoral head allograft. (a) Fluoroscopic lateral intraoperative image of the right ankle shows a retrograde tibiototalcalcaneal intramedullary nail with two distal screws in the calcaneus and across the posterior calcaneal facet, and a structural femoral head allograft placed at the talar dome bone void and resection site (white arrows). (b) Sagittal reformatted CT image obtained 3.5 months after surgery shows the structural femoral head allograft (dashed white arrows) replacing the talar dome, between the calcaneus (white arrows), talar head and tibial plafond (black arrows). Partially visualized is tibiototalcalcaneal fixation hardware. (c) Seven months postoperative lateral weight-bearing radiograph status post hardware removal shows complete solid bony fusion across the subtalar and tibiototal joints with complete incorporation of the structural femoral head allograft.

Subtalar arthrodesis may be performed as a primary procedure for subtalar arthrosis, usually secondary to calcaneal fracture, rheumatoid arthritis, primary osteoarthritis, or a non-resectable talocalcaneal coalition. Advantages of this procedure include preservation of hindfoot motion and lower risk of arthritis in adjacent joints [39]. During the procedure, cartilage and subchondral bone are removed from the talar and calcaneal articular surfaces; hindfoot alignment can be corrected by using wedge resection or graft application. One or two large caliber cannulated screws are placed to traverse the talocalcaneal articulations (Figure 5). Subtalar fusion may be paired with talonavicular fusion in a so-called double hindfoot arthrodesis. This procedure leaves the calcaneofibular joint free which is believed to act as a “force-dissipating” factor during ambulation [38] (Figure 6).

Triple arthrodesis is a fusion of the talocalcaneal, talonavicular, and calcaneocuboid joints (Figure 7). This procedure is reserved for cases when available conservative measures have failed, and a more limited surgical procedure will not provide appropriate pain relief and reduction of the deformity. The indications for triple arthrodesis include severe subtalar, talonavicular and calcaneocuboid degenerative disease, sequelae of talar neck fractures with subtalar joint involvement, posttraumatic hindfoot instability, and non-resectable calcaneonavicular or talocalcaneal coalition. Triple arthrodesis can be used to treat painful deformities due to inflammatory arthritides, neurogenic, and neuromuscular disorders. Triple arthrodesis is used for the treatment of fixed hindfoot deformity in the setting of adult-acquired flatfoot deformity (AAFFD, stage 3) [40]. The subtalar joint is fixated through the use of either one or two partially threaded cancellous screws. The talonavicular and calcaneocuboid joints are fixated using a combination of screws, staples, or plates [41].

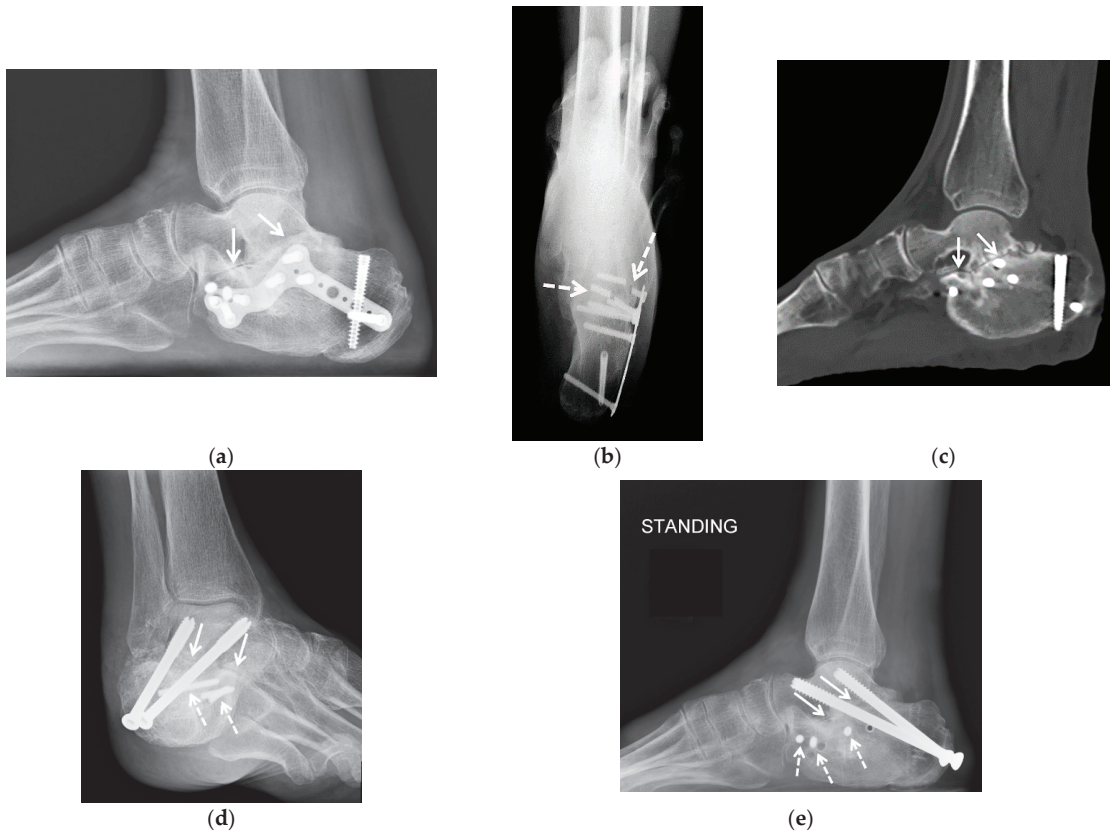


Figure 5. (a–c) A 67-year-old female with a history of remote comminuted right calcaneus fracture treated with plate and screws fixation with subsequent hardware fracture and subtalar osteoarthritis with subfibular impingement treated with calcaneal hardware removal, calcaneal exosteotomy and subtalar arthrodesis with cellular allograft. (a) Lateral weight-bearing radiograph of the right foot shows a healed calcaneus fracture status post plate and screws fixation. Note marked asymmetric narrowing of the subtalar joint consistent with advanced posttraumatic osteoarthritis (white arrows). (b) On the axial Harris weight-bearing radiograph note fracture of multiple fixation screws (dashed white arrows). (c) Sagittal reformatted CT image shows advanced posttraumatic osteoarthritis of the subtalar joint with asymmetric joint space narrowing, scattered subchondral sclerosis and cyst-like changes. (d) Broden and (e) lateral radiographs obtained 2.5 months after subtalar arthrodesis show interval removal of the calcaneal plate and multiple screws with three broken screw fragments remaining (white dashed arrows). Note two retrograde partially threaded cannulated screws transfixing the subtalar joint (white arrows) with early fusion about the fixation screws.

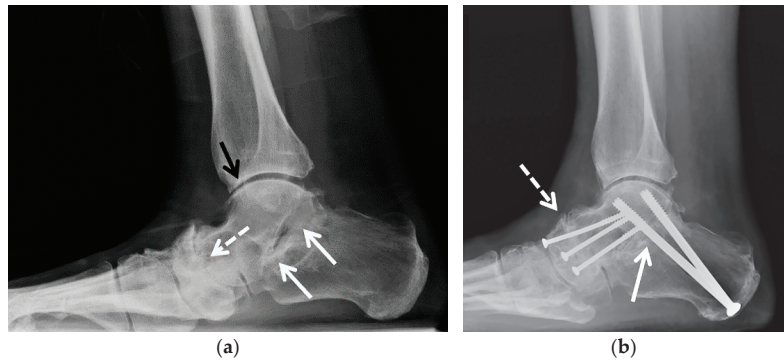


Figure 6. (a,b) A 72-year-old male with pes planus and severe talonavicular greater than subtalar osteoarthritis was treated with double hindfoot arthrodesis. (a) Preoperative weight-bearing lateral radiograph of the right foot shows severe osteoarthritis of the talonavicular (dashed white arrow) greater than subtalar joints (white arrows) and mild osteoarthritis of the tibiotalar joint (black arrow). (b) Weight-bearing lateral radiograph obtained 3 weeks after surgery shows three smaller partially threaded cannulated screws transfixing the talonavicular joint (dashed white arrow) and two larger, partially threaded cannulated screws transfixing the posterior subtalar joint (white arrow). Note the significant improvement of hindfoot alignment.



Figure 7. (a,b) A 64-year-old female with a history of traumatic right talonavicular dislocation several months prior presented with continued pain, pes planus with plantar valgus and equinus contracture and posttraumatic osteoarthritis, subsequently treated with triple arthrodesis. (a) Lateral weight-bearing radiograph of the right foot shows pes planus with dorsal subluxation of the talonavicular joint and superimposed advanced osteoarthritis (dashed white arrow). Note the associated mild asymmetric narrowing of the subtalar (white arrows) and calcaneocuboid joints (black arrow). (b) Postoperative weight-bearing lateral radiograph shows interval triple arthrodesis with two Herbert screws transfixing the posterior subtalar joint (white arrow), three partially threaded cannulated screws transfixing the talonavicular joint (dashed white arrow) and a short plate with two screws transfixing the calcaneocuboid joint (black arrow) with solid bony bridging across the arthrodesis sites.

Complications can occur with these various surgical procedures, as with any operative intervention, including edema, hematoma, seroma, dehiscence, ulceration, infection, and nerve damage. Specific complications of the osteotomy procedures and arthrodesis include nonunion, delayed union, malunion, and graft failure. With successful arthrodesis procedures in the long term, when movement at the joint is eliminated, accelerated secondary osteoarthritis of the neighboring joints often develops because of increased motion [39,42]. General principles of postoperative imaging evaluation include assessment of position and hardware integrity, graft incorporation, the adequate fusion of the joint with gradual obliteration of the joint space, presence of bone loss and zones of avascular sclerotic bone. All of these parameters are principally evaluated with serial weight bearing

radiography and additionally with CT. Nuclear medicine studies including single photon emission computed tomography (SPECT) scan with technetium and Indium-111 tagged white blood cells serve to determine the extent and activity of nonunion, infection, and osteonecrosis. In cases of suspected infection, a bone biopsy for cultures may be needed before a definitive procedure.

5.2.3. Ankle Arthroplasty

Traditionally, ankle arthrodesis has been a primary surgical option for patients with PTOA who have failed conservative treatment. However, ankle arthrodesis produces gait dysfunction and increased stress on the neighboring joints that frequently leads to accelerated osteoarthritis in these joints. Total ankle arthroplasty (TAA) represents an alternative to arthrodesis offering an advantage of preservation or improvement of mobility of the tibiotalar joint while reducing pain. Historically, ankle arthroplasty has not been as successful as replacement of other joints and early TAA designs had unacceptably high rates of failure. Newer generation designs combined with improved surgical technique and level of training among the surgeons have demonstrated substantially improved results that lead to a gradual increase in the utilization of TAA in the treatment of PTOA [43–45]. However, the rates of complications and failure with TAA remain greater than those seen in total knee and hip arthroplasty [46]. The most common indication for TAA is the treatment of advanced ankle arthropathy, failed prior ankle surgery, and ankle arthropathy with prior hindfoot or midfoot fusion for whom preserved functional range of motion is desired [47]. Appropriate patient selection is very important for a good clinical outcome of ankle arthroplasty [45,48]. Ideally, TAA is to be performed in middle-aged to older patients without significant comorbidities, with normal to low body mass index (BMI), adequate tibial and talar bone stock, stable and well-aligned hindfoot, and no lower extremity neurovascular impairment [45]. In the past decade indications for TAA have expanded and now include the presence of correctable deformities and less restrictive age and BMI criteria. TAA is contraindicated in the presence of active bone or soft tissue infection, neurovascular compromise, inadequate soft tissue support and poor bone stock. Designs of ankle prostheses have evolved towards improving osteointegration, decreasing the extent of bony resection and decreasing the degree of constraint allowing rotation and sliding motions in addition to flexion and extension (Figure 8). Two general categories of TAA implants are currently in use: two-component design, also referred to as “fixed bearing” (Figure 9), and three-component design, referred to as “mobile bearing” [43,49]. A polyethylene (PE) spacer is locked to the tibial base plate in a two-component prosthesis and is freely mobile in a three-component design. Prostheses are further distinguished by the composition and configuration of the metallic component, and the surgical approach for insertion, which may necessitate fibular osteotomy and syndesmotic fixation.

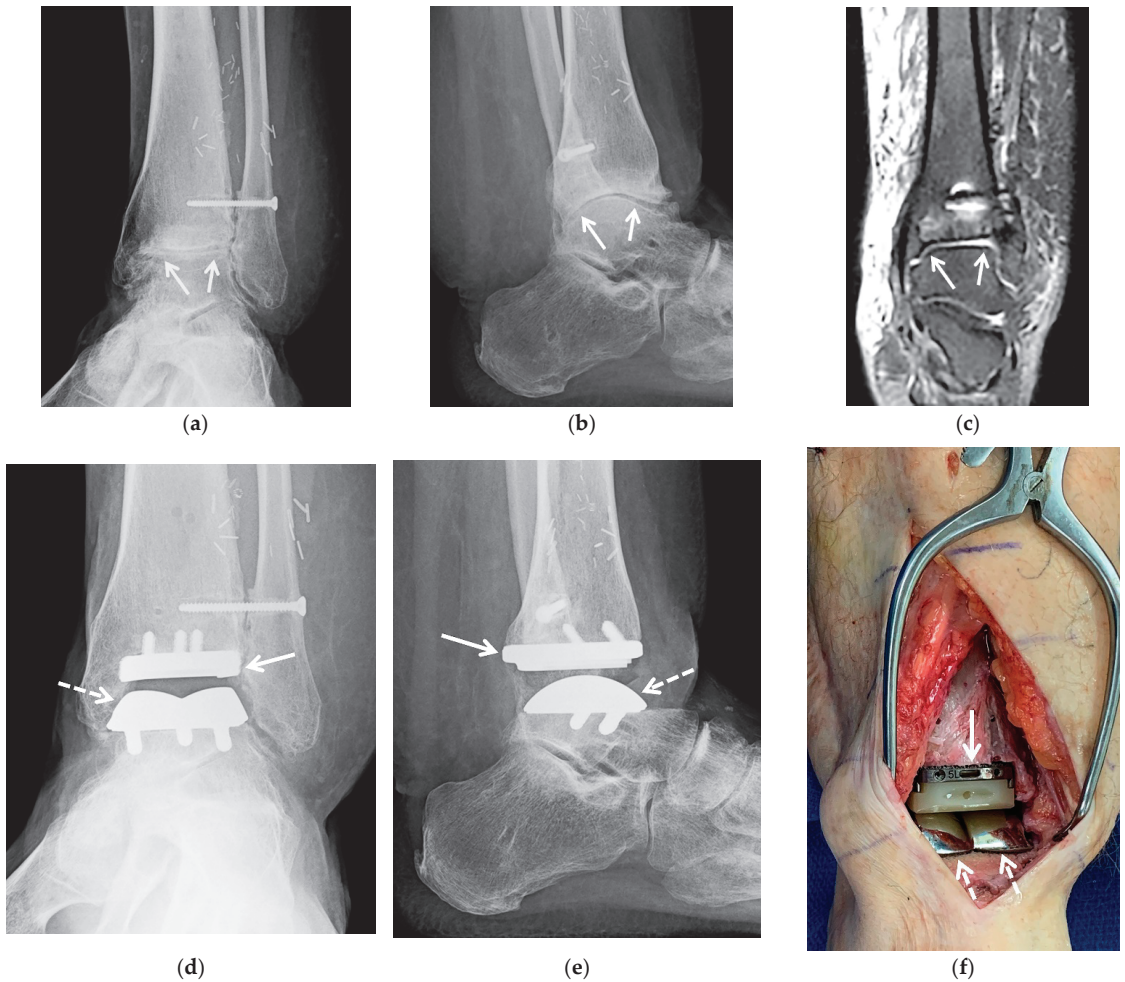


Figure 8. (a–f) A 36-year-old male with posttraumatic osteoarthritis of the left tibiotalar joint and equinus contracture resulting from open distal tibia fracture treated with open reduction internal fixation and free flap, with previous hardware removal, subsequently treated with ankle arthroplasty and gastrocnemius resection. (a) Mortise and (b) lateral weight-bearing radiographs of the left ankle show marked asymmetric narrowing of the tibiotalar joint (white arrows) with marginal osteophytes and intraarticular bodies consistent with severe osteoarthritis. Note tracts in the calcaneus and talus related to removed surgical hardware and retained laterally placed screw transfixing the distal tibiofibular syndesmosis. Numerous vascular clips overly the soft tissues of the lower leg. (c) Coronal fluid sensitive MR image shows asymmetric narrowing of the tibiotalar joint (white arrows). (d) Mortise and (e) lateral postoperative radiographs show interval placement of total ankle arthroplasty (Wright Medical Infinity with an Inbone talus). Note well seated tibial (white arrow) and talar (dashed white arrow) prosthesis components. (f) The intraoperative image shows tibial (white arrow) and talar components (dashed white arrow) in place.

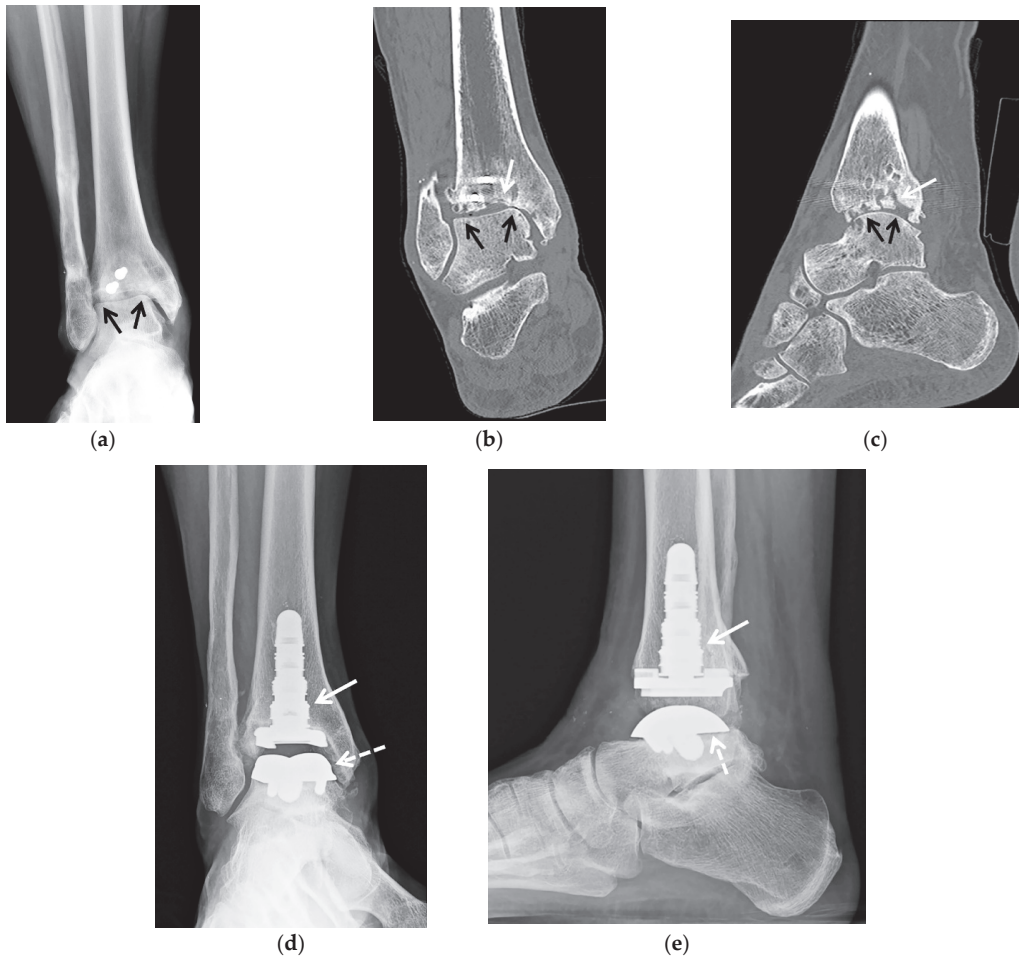


Figure 9. (a–e) A 57-year-old female with a history of remote open reduction and surgical fixation of the right ankle fractures, revision posterior malleolus 2 years prior and posttraumatic osteoarthritis with 2 cm devitalized bone at the central tibial plafond; patient subsequently treated with hardware removal and total ankle arthroplasty (Wright Medical with Inbone tibia and talus). (a) Mortise radiograph and (b) coronal and (c) sagittal reformatted CT images of the right ankle show asymmetric narrowing of the tibiotalar joint (black arrows) consistent with advanced osteoarthritis. In (a,b) note two retained screws in the distal tibia. In (b,c) note marked irregularity of the tibial plafond with scattered foci of sclerosis corresponding to devitalized bone (white arrow). (d) Mortise and (e) lateral postoperative weight-bearing radiographs show total ankle arthroplasty with well seated tibial (white arrow) and talar components (white arrowhead).

The overall complication rate in TAA has been reported as high as 20%. The most common reason for implant failure is aseptic loosening, followed by persistent pain and periprosthetic infection [48]. Overall TAA complications may be categorized based on several parameters, such as level of risk of development of implant failure or based on the time of occurrence [50,51]. Depending on the time since surgery, complications may be categorized as intraoperative, early postoperative, or delayed [47,51]. Early postoperative complications include infection, delayed wound healing, medial malleolar stress fracture and distal tibial or fibular fractures. Late complications consist of periprosthetic fracture, aseptic loosening, expansile osteolysis, impingement, polyethylene spacer wear and migration, subsidence, syndesmotic nonunion, heterotopic ossification, osteoarthritis,

tis in neighboring joints, and chronic regional pain syndrome. Imaging evaluation of TAA includes several modalities, such as radiography, CT, MRI, and nuclear medicine studies, with serial weight bearing radiographs being the mainstay of the imaging follow-up. Imaging surveillance may detect early findings of aseptic loosening or infection by demonstrating subtle abnormalities, such as subsidence, early osteolysis, and angular deformities [47].

6. Conclusions

Posttraumatic osteoarthritis of the ankle and hindfoot is a common and frequently debilitating disorder that compromises quality of life. Several non-operative treatments and surgical options may be considered with respect to the individual patient's therapy goals. In addition to clinical evaluation, imaging plays important role in treatment planning, monitoring treatment results and early diagnosis of surgical complications. Weight bearing radiographs are essential for both initial assessment and postoperative evaluation.

Author Contributions: Conceptualization, T.G., Y.V.M., L.D.L., M.S.T.; writing—original draft preparation, T.G. and Y.V.M.; writing—review and editing, all authors; supervision, T.G. and M.S.T. All authors have read and agreed to the published version of the manuscript.

Funding: This research received no external funding.

Institutional Review Board Statement: The study was conducted according to the guidelines of the Declaration of Helsinki and approved by the Institutional Review Board of University of Arizona (2107072004, 8 September 2021).

Informed Consent Statement: Patient consent was waived by the Institutional Review Board due to anonymous nature of the medical images used for review.

Conflicts of Interest: The authors declare no conflict of interest.

References

1. Delco, M.L.; Kennedy, J.G.; Bonassar, L.J.; Fortier, L.A. Post-traumatic osteoarthritis of the ankle: A distinct clinical entity requiring new research approaches. *J. Orthop. Res.* **2017**, *35*, 440–453. [[CrossRef](#)]
2. Barg, A.; Pagenstert, G.I.; Hügle, T.; Gloyer, M.; Wiewiorski, M.; Henninger, H.B.; Valderrabano, V. Ankle Osteoarthritis: Etiology, Diagnostics, and Classification. *Foot Ankle Clin.* **2013**, *18*, 411–426. [[CrossRef](#)]
3. Resnick, D.; Kang, H.S.; Pretterklieber, M.L. *Internal Derangements of Joints*; Saunders/Elsevier: Philadelphia, PA, USA, 2007.
4. Haller, J.; Resnick, D.; Sartoris, D.; Mitchell, M.; Howard, B.; Gilula, L. Arthrography, tenography, and bursography of the ankle and foot. *Clin. Podiatr. Med. Surg.* **1988**, *5*, 893–908. [[PubMed](#)]
5. McKinley, T.O.; Rudert, M.J.; Koos, D.C.; Brown, T.D. Incongruity versus Instability in the Etiology of Posttraumatic Arthritis. *Clin. Orthop. Relat. Res.* **2004**, *423*, 44–51. [[CrossRef](#)] [[PubMed](#)]
6. Ramsey, P.; Hamilton, W. Changes in tibiotalar area of contact caused by lateral talar shift. *J. Bone Jt. Surg.-Am. Vol.* **1976**, *58*, 356–357. [[CrossRef](#)]
7. Taga, I.; Shino, K.; Inoue, M.; Nakata, K.; Maeda, A.; Henry, J.H. Articular cartilage lesions in ankles with lateral ligament injury. *Am. J. Sports Med.* **1993**, *21*, 120–127. [[CrossRef](#)] [[PubMed](#)]
8. Brown, T.D.; Johnston, R.C.; Saltzman, C.L.; Marsh, J.L.; Buckwalter, J.A. Posttraumatic Osteoarthritis: A First Estimate of Incidence, Prevalence, and Burden of Disease. *J. Orthop. Trauma* **2006**, *20*, 739–744. [[CrossRef](#)]
9. Gorbachova, T.; Amber, I.; Beckmann, N.M.; Bennett, D.L.; Chang, E.Y.; Davis, L.; Gonzalez, F.M.; Hansford, B.G.; Howe, B.M.; Lenchik, L.; et al. Nomenclature of Subchondral Nonneoplastic Bone Lesions. *Am. J. Roentgenol.* **2019**, *213*, 963–982. [[CrossRef](#)]
10. Melenevsky, Y.; Mackey, R.A.; Abrahams, R.B.; Thomson, N.B. Talar Fractures and Dislocations: A Radiologist's Guide to Timely Diagnosis and Classification. *Radiographics* **2015**, *35*, 765–779. [[CrossRef](#)]
11. Janzen, D.L.; Connell, D.G.; Munk, P.L.; Buckley, R.E.; Meek, R.N.; Schechter, M. Intraarticular fractures of the calcaneus: Value of CT findings in determining prognosis. *Am. J. Roentgenol.* **1992**, *158*, 1271–1274. [[CrossRef](#)]
12. Lopez-Ben, R. Imaging of the Subtalar Joint. *Foot Ankle Clin.* **2015**, *20*, 223–241. [[CrossRef](#)] [[PubMed](#)]
13. Buck, F.M.; Hoffmann, A.; Mamisch-Saupe, N.; Espinosa, N.; Resnick, N.; Hodler, J. Hindfoot Alignment Measurements: Rotation-Stability of Measurement Techniques on Hindfoot Alignment View and Long Axial View Radiographs. *Am. J. Roentgenol.* **2011**, *197*, 578–582. [[CrossRef](#)]
14. Reilingh, M.L.; Beimers, L.; Tuijthof, G.J.M.; Stufkens, S.A.S.; Maas, M.; Van Dijk, C.N. Measuring hindfoot alignment radiographically: The long axial view is more reliable than the hindfoot alignment view. *Skelet. Radiol.* **2010**, *39*, 1103–1108. [[CrossRef](#)]

15. Conti, M.S.; Ellis, S.J. Weight-bearing CT Scans in Foot and Ankle Surgery. *J. Am. Acad. Orthop. Surg.* **2020**, *28*, e595–e603. [[CrossRef](#)]
16. Gorbachova, T. Magnetic resonance imaging of the ankle and foot. *Pol. J. Radiol.* **2020**, *85*, 532–549. [[CrossRef](#)]
17. Coughlin, M.J.; Mann, R.A.; Saltzman, C.L. *Mann's Surgery of the Foot and Ankle*; Mosby: St. Louis, MI, USA, 2013.
18. Rastogi, A.K.; Davis, K.W.; Ross, A.; Rosas, H.G. Fundamentals of Joint Injection. *Am. J. Roentgenol.* **2016**, *207*, 484–494. [[CrossRef](#)] [[PubMed](#)]
19. Khoury, N.J.; El-Khoury, G.Y.; Saltzman, C.L.; Brandser, E.A. Intraarticular foot and ankle injections to identify source of pain before arthrodesis. *Am. J. Roentgenol.* **1996**, *167*, 669–673. [[CrossRef](#)]
20. Hansford, B.G.; Mills, M.K.; Hanrahan, C.J.; Yablon, C.M. Pearls and pitfalls of fluoroscopic-guided foot and ankle injections: What the radiologist needs to know. *Skelet. Radiol.* **2019**, *48*, 1661–1674. [[CrossRef](#)] [[PubMed](#)]
21. Van Valburg, A.; Van Roermund, P.; Lammens, J.; Van Melkebeek, J.; Verbout, A.; Lafeber, E.; Bijlsma, J. Can Ilizarov joint distraction delay the need for an arthrodesis of the ankle? A preliminary report. *J. Bone Jt. Surgery. Br. Vol.* **1995**, *77-B*, 720–725. [[CrossRef](#)]
22. Saltzman, C.L.; Hillis, S.L.; Stolley, M.P.; Anderson, D.D.; Amendola, A. Motion versus fixed distraction of the joint in the treatment of ankle osteoarthritis: A prospective randomized controlled trial. *J. Bone Jt. Surg.-Am. Vol.* **2012**, *94*, 961–970. [[CrossRef](#)]
23. Paley, D.; Lamm, B.M.; Purohit, R.M.; Specht, S.C. Distraction Arthroplasty of the Ankle—How Far Can You Stretch the Indications? *Foot Ankle Clin.* **2008**, *13*, 471–484. [[CrossRef](#)]
24. Van Valburg, A.; Van Roermund, P.; Marijnissen, A.; Wenting, M.; Verbout, A.; Lafeber, F.; Bijlsma, J. Joint distraction in treatment of osteoarthritis (II): Effects on cartilage in a canine model. *Osteoarthr. Cartil.* **2000**, *8*, 1–8. [[CrossRef](#)]
25. Barg, A.; Amendola, A.; Beaman, D.N.; Saltzman, C.L. Ankle Joint Distraction Arthroplasty: Why and How? *Foot Ankle Clin.* **2013**, *18*, 459–470. [[CrossRef](#)]
26. Barg, A.; Pagenstert, G.I.; Horisberger, M.; Paul, J.; Gloyer, M.; Henninger, H.B.; Valderrabano, V. Supramalleolar osteotomies for degenerative joint disease of the ankle joint: Indication, technique and results. *Int. Orthop.* **2013**, *37*, 1683–1695. [[CrossRef](#)]
27. Weber, B.G.; Simpson, L.A. Corrective lengthening osteotomy of the fibula. *Clin. Orthop. Relat. Res.* **1985**, *199*, 61–67. [[CrossRef](#)]
28. Hintermann, B.; Valderrabano, V.; Kundert, H.-P. Lengthening of the Lateral Column and Reconstruction of the Medial Soft Tissue for Treatment of Acquired Flatfoot Deformity Associated with Insufficiency of the Posterior Tibial Tendon. *Foot Ankle Int.* **1999**, *20*, 622–629. [[CrossRef](#)] [[PubMed](#)]
29. Knupp, M.; Stufkens, S.A.; Pagenstert, G.I.; Hintermann, B.; Valderrabano, V. Supramalleolar Osteotomy for Tibiotalar Varus Malalignment. *Tech. Foot Ankle Surg.* **2009**, *8*, 17–23. [[CrossRef](#)]
30. Adams, J.C. Arthrodesis of the ankle joint; experiences with the transfibular approach. *J. Bone Jt. Surgery. Br. Vol.* **1948**, *30-B*, 506–511. [[CrossRef](#)]
31. Horwitz, T. The use of the transfibular approach in arthrodesis of the ankle joint. *Am. J. Surg.* **1942**, *55*, 550–552. [[CrossRef](#)]
32. Napiontek, M.; Jaszczak, T. Ankle arthrodesis from lateral transfibular approach: Analysis of treatment results of 23 feet treated by the modified Mann's technique. *Eur. J. Orthop. Surg. Traumatol.* **2015**, *25*, 1195–1199. [[CrossRef](#)] [[PubMed](#)]
33. Smith, J.T.; Chiodo, C.P.; Singh, S.K.; Wilson, M.G. Open Ankle Arthrodesis with a Fibular-Sparing Technique. *Foot Ankle Int.* **2013**, *34*, 557–562. [[CrossRef](#)] [[PubMed](#)]
34. Cooper, P.S. Complications of Ankle and Tibiotalocalcaneal Arthrodesis. *Clin. Orthop. Relat. Res.* **2001**, *391*, 33–44. [[CrossRef](#)]
35. Burks, J.B. Tibiotalocalcaneal Arthrodesis. *Clin. Podiatr. Med. Surg.* **2012**, *29*, 529–545. [[CrossRef](#)] [[PubMed](#)]
36. Latt, L.D.; Smith, K.E.; Dupont, K.M. Revision Tibiotalocalcaneal Arthrodesis with a Pseudoelastic Intramedullary Nail: A Case Study. *Foot Ankle Spec.* **2017**, *10*, 75–81. [[CrossRef](#)] [[PubMed](#)]
37. Neufeld, S.K.; Uribe, J.; Myerson, M.S. Use of structural allograft to compensate for bone loss in arthrodesis of the foot and ankle. *Foot Ankle Clin.* **2002**, *7*, 1–17. [[CrossRef](#)]
38. De Wachter, J.; Knupp, M.; Beat, H. Double-Hindfoot Arthrodesis through a Single Medial Approach. *Tech. Foot Ankle Surg.* **2007**, *6*, 237–242. [[CrossRef](#)]
39. López, R.; Singh, T.; Banga, S.; Hasan, N. Subtalar Joint Arthrodesis. *Clin. Podiatr. Med. Surg.* **2012**, *29*, 67–75. [[CrossRef](#)]
40. Flores, D.V.; Gómez, C.M.; Hernando, M.F.; Davis, M.A.; Pathria, M.N. Adult Acquired Flatfoot Deformity: Anatomy, Biomechanics, Staging, and Imaging Findings. *Radiographics* **2019**, *39*, 1437–1460. [[CrossRef](#)] [[PubMed](#)]
41. D'Angelantonio, A.M.; Schick, F.A.; Arjomandi, N. Triple Arthrodesis. *Clin. Podiatr. Med. Surg.* **2012**, *29*, 91–102. [[CrossRef](#)]
42. Coester, L.M.; Saltzman, C.L.; Leupold, J.; Pontarelli, W. Long-Term Results Following Ankle Arthrodesis for Post-Traumatic Arthritis. *J. Bone Jt. Surg.-Am. Vol.* **2001**, *83*, 219–228. [[CrossRef](#)]
43. Gougoulas, N.; Maffulli, N. History of Total Ankle Replacement. *Clin. Podiatr. Med. Surg.* **2013**, *30*, 1–20. [[CrossRef](#)]
44. Rybalko, D.; Schwarzman, G.; Moretti, V. Recent National Trends and Outcomes in Total Ankle Arthroplasty in the United States. *J. Foot Ankle Surg.* **2018**, *57*, 1092–1095. [[CrossRef](#)] [[PubMed](#)]
45. Neufeld, S.K.; Lee, T.H. Total ankle arthroplasty: Indications, results, and biomechanical rationale. *Am. J. Orthop.* **2000**, *29*, 593–602.
46. Sadoghi, P.; Liebensteiner, M.; Agreiter, M.; Leithner, A.; Böhler, N.; Labek, G. Revision Surgery After Total Joint Arthroplasty: A Complication-Based Analysis Using Worldwide Arthroplasty Registers. *J. Arthroplast.* **2013**, *28*, 1329–1332. [[CrossRef](#)] [[PubMed](#)]

47. Omar, I.M.; Abboud, S.F.; Youngner, J.M. Imaging of Total Ankle Arthroplasty: Normal Imaging Findings and Hardware Complications. *Semin. Musculoskelet. Radiol.* **2019**, *23*, 177–194. [[CrossRef](#)]
48. Lawton, C.D.; Butler, B.A.; Dekker, R.G.; Prescott, A.; Kadakia, A.R. Total ankle arthroplasty versus ankle arthrodesis—A comparison of outcomes over the last decade. *J. Orthop. Surg. Res.* **2017**, *12*, 1–10. [[CrossRef](#)]
49. Guyer, A.J.; Richardson, E.G. Current Concepts Review: Total Ankle Arthroplasty. *Foot Ankle Int.* **2008**, *29*, 256–264. [[CrossRef](#)]
50. Glazebrook, M.A.; Arsenaault, K.; Dunbar, M. Evidence-Based Classification of Complications in Total Ankle Arthroplasty. *Foot Ankle Int.* **2009**, *30*, 945–949. [[CrossRef](#)] [[PubMed](#)]
51. Bestic, J.M.; Peterson, J.J.; DeOrio, J.K.; Bancroft, L.; Berquist, T.H.; Kransdorf, M.J. Postoperative Evaluation of the Total Ankle Arthroplasty. *Am. J. Roentgenol.* **2008**, *190*, 1112–1123. [[CrossRef](#)] [[PubMed](#)]



Review

Elbow Stiffness Imaging: A Practical Diagnostic and Pretherapeutic Approach

Charles Lombard, Pedro Teixeira, Edouard Germain, Gauthier Dodin, Mathias Louis, Alain Blum and Romain Gillet *

Guilloz Imaging Department, Central Hospital, University Hospital Center of Nancy, 54035 Nancy, France; c.lombard@chru-nancy.fr (C.L.); p.teixeira@chru-nancy.fr (P.T.); e.germain@chru-nancy.fr (E.G.); gauthier-dodin@orange.fr (G.D.); m.louis@chru-nancy.fr (M.L.); alain.blum@gmail.com (A.B.)

* Correspondence: romain_gillet3@hotmail.com; Tel.: +33-3-83-85-21-61; Fax: +33-3-83-85-97-25

Abstract: Loss of elbow motion can lead to disability in everyday gestures, recreational activities, and work. Unfortunately, the elbow joint is particularly prone to stiffness because of its complex anatomy and biomechanics. The etiology of elbow stiffness is varied and must be diagnosed accurately in order to allow optimal treatment, which may be challenging for surgeons and physiotherapists. Its treatment can be either conservative, arthroscopic or surgical, with a trend for arthroscopic procedures when conservative treatment fails. There is no consensus on the optimal imaging workup for elbow joint stiffness, which may have an impact on patient management. This article reviews the current classification systems of elbow stiffness and the various imaging techniques used for diagnosis. Report checklists and clarifications on the role of each imaging method, as well as the imaging findings of normal and stiff elbows, are presented, leading to a proposed diagnostic algorithm. The main concern in imaging is to determine the cause of elbow stiffness, as many concomitant abnormalities might be present depending on the clinical scenario.

Keywords: elbow stiffness; MRI; CT; 4D-CT; elbow osteoarthritis

Citation: Lombard, C.; Teixeira, P.; Germain, E.; Dodin, G.; Louis, M.; Blum, A.; Gillet, R. Elbow Stiffness Imaging: A Practical Diagnostic and Pretherapeutic Approach. *J. Clin. Med.* **2021**, *10*, 5348. <https://doi.org/10.3390/jcm10225348>

Academic Editors:
Iwona Sudol-Szopińska and
Miha Taljanovic

Received: 31 October 2021
Accepted: 15 November 2021
Published: 17 November 2021

Publisher's Note: MDPI stays neutral with regard to jurisdictional claims in published maps and institutional affiliations.



Copyright: © 2021 by the authors. Licensee MDPI, Basel, Switzerland. This article is an open access article distributed under the terms and conditions of the Creative Commons Attribution (CC BY) license (<https://creativecommons.org/licenses/by/4.0/>).

1. Introduction

The elbow joint is a complex hinge-type synovial joint with an important role in the mobilization of the upper limb, linking the hand, wrist, and shoulder. The elbow allows precise hand positioning and serves as a forearm fulcrum maximizing grip strength [1]. Loss of elbow motion can lead to disability in everyday gestures, recreational activities, or work [1]. Unfortunately, the elbow joint is particularly prone to stiffness because of its complex anatomy and biomechanics [2,3]. Post-traumatic changes in the elbow's peri-articular tissues predispose to capsular calcification and ossification [4–6]. Fractures around the elbow, even if non-displaced and adequately treated, may require sustained immobilization due to difficulties in obtaining a stable osteosynthesis, which may also contribute to joint stiffness [6]. Histologically, elbow joint stiffness is thought to result from post-traumatic capsular thickening with disorganized collagen fibers, altered cytokine levels, and elevated myofibroblasts [7].

The etiology of elbow stiffness is varied and must be diagnosed accurately in order to allow the best therapeutic management, which may represent a challenge for surgeons and physiotherapists. Its treatment can be either conservative (e.g., physiotherapy and splinting), arthroscopic (e.g., most frequently: anterior capsular resection, cleansing the humeral fossae, osteophyte and loose bodies ablation) or surgical (e.g., open elbow arthrolysis and prosthetic joint replacement) [8,9]. Although a well-defined therapeutic algorithm has not yet been proposed, the frequency of postsurgical complications has led to favor arthroscopic procedures when conservative treatment fails [8,9].

There is also no consensus on the optimal imaging workup for elbow joint stiffness, which may have an impact on patient management. Radiographs and CT scan allow a

good analysis of osseous structures and joint spaces, while CT arthrography improves loose body detection and cartilage assessment. Although MRI excels in demonstrating capsular and periarticular soft tissue anomalies, its role in elbow stiffness workup is not well defined. In this article, after a key anatomical and biomechanical review, the different etiologies of elbow stiffness are reviewed, and a practical diagnostic and pretherapeutic imaging approach is proposed.

2. Anatomy and Biomechanics

The elbow encompasses three joints within a single articular capsule: humeroradial, humeroulnar, and proximal radioulnar. The distal humerus presents two condyles: the trochlea, medially, which articulates with the greater sigmoid notch of the proximal ulna, and the capitellum, laterally, which articulates with the radial head. The trochlea and the capitellum are anteverted by 30° , and they have a 5° medial rotation and a 6° valgus with respect to the humeral long axis. Anteriorly, radial and coronoid fossae lodge the radial head and coronoid process, respectively, during elbow flexion. Posteriorly, the olecranon fossa lodges the olecranon during extension. The radial head articulates medially with the radial notch of the ulna allowing forearm pronosupination.

The two humeral epicondyles harbor the insertions of various ligaments and tendons. The ulnar collateral ligaments and flexor–pronator tendon group insert onto the more prominent medial epicondyle while the lateral collateral ligament and extensor–supinator tendon group insert onto the less prominent lateral epicondyle [1].

Stability, mobility, and alignment are essential prerequisites for elbow function [3]. The maximal elbow flexion–extension range is from 0° to 150° with 75° forearm pronation and an 85° supination [1]. However, the minimal functional range of motion needed for daily living tasks is 30 – 130° of flexion–extension with 50° of pronosupination [10]. Tasks such as using a cell phone or a keyboard require at least 142° of flexion–extension and 65° of pronation [11]. Elbow stiffness is defined by a flexion–extension range from 30 to 120° or a forearm pronosupination inferior to 45° . Stiffness in flexion is less tolerated than in extension. Loss of supination is more devastating than the loss of pronation, which may be partially compensated by shoulder abduction [4,12]. Patient activity should also be taken into account, as athletes, musicians, and manual workers may require a greater superior limb range of motion than the general population.

The two main mechanisms that contribute to elbow stiffness are blocks, corresponding to compressive resistance in the direction of the motion, and tethers, corresponding to tensile resistance in the opposite direction of the motion [13]. Anterior tethers and posterior blocks can cause extension deficit, while posterior tethers and anterior blocks may lead to a flexion deficit (Table 1). According to Sun et al., tethers can be found alone, but blocks are often associated with tethers [13].

Table 1. Flexion–extension stiffness etiologies.

Extension Dysfunction	
<i>Anterior Tether</i>	<i>Posterior Block</i>
Thickened anterior capsule	Entrapped synovium
Contracture or HO of the anterior band of the medial collateral ligament	Osteophytes of the olecranon process or fossa
Contracture or HO of the flexor muscle/tendon	Loose bodies in the olecranon fossa
Anterior scarred skin	Posterior elbow ho
Posterior articular osteochondral lesion	
Flexion Dysfunction	
<i>Posterior Tether</i>	<i>Anterior Block</i>
Thickened posterior capsule	Entrapped synovium
Contracture or HO of the posterior band of the medial collateral ligament	Osteophytes of the coronoid process or fossa
Triceps contracture or HO	Loose bodies in the coronoid fossa
Posterior scarred skin	Anterior elbow ho
Anterior articular osteochondral lesion	

HO: heterotopic ossification.

3. Clinical Presentation

Acute or repeated trauma remains the most frequent cause of elbow stiffness, followed by osteoarthritis (OA). Elbow pain is usually mechanical in origin and appears in extreme degrees of motion limitation. Spontaneous elbow pain is unusual. In such cases, an infection should be considered and lead to prompt patient management (e.g., blood work, articular puncture/lavage, and antibiotics if septic arthritis is confirmed).

Several classifications of elbow stiffness have been proposed according to the structures involved, anatomic location, mechanism of injury, or severity of motion loss [2,3]. One of the most relevant classification systems from an imaging and clinical perspective is the one described by Morey et al., which divides elbow pathology into extra-articular; intra-articular, or mixed (the most frequent pattern) [4]. More recently, Sun et al. proposed a motion-based classification system. Elbow flexion–extension dysfunction is divided into four categories—tethers alone, tethers with blocks, articular malformation, or bony ankyloses, while forearm pronosupination dysfunction is divided into three—contracture alone, radial head malunion/nonunion, or proximal radioulnar bony ankyloses [13].

3.1. Extra-Articular Elbow Stiffness

Extra-articular elbow stiffness may be related to periarticular tissue pathology (e.g., articular capsule, muscles, ligaments, and skin), heterotopic ossifications, extra-articular bone malalignment or a combination of these. Extra-articular stiffness is frequently posttraumatic, in particular dislocations and complex elbow fractures, although simple nondisplaced radial head fracture or elbow subluxation could lead to stiffness especially after prolonged immobilization. Increased cast immobilization time, alcohol abuse, and prior joint surgery are also considered risk factors [12].

The diagnosis of skin involvement (usually treated by skin plasty), whether it is a large scar or burn, is clinical and does not necessarily require imaging, unless other associated lesions are suspected, in particular heterotopic ossifications (HO), in the setting of neurogenic paraosteopathy [13,14]. The latter consists of the formation of mature bone lamellae in soft tissues, which should be differentiated from capsular or ligamentous calcifications or ossifications (Figure 1). Periarticular HO occurs after direct elbow traumatism (up to 3% in simple dislocation and 20% in fracture–dislocation) and may affect elbow flexion–extension but also lead to a forearm pronosupination deficit due to radioulnar

synostosis formation [15] (Figure 2). HO risk factors include local burn, concomitant head or spinal injury, prolonged immobilization, and delays before surgery [16]. There is no consensus on HO treatment, which can be conservative or surgical. Botulinum toxin injections have been shown to be efficient [17]. Radiation therapy has also been proposed for HO prevention [16,17]. Joint capsule contractures can be secondary to trauma, arthritis (whether inflammatory, septic, or secondary to repetitive hemarthrosis in hemophilia), and surgery. The anterior capsule seems to be more frequently thickened than the posterior, explaining the preferential loss of extension rather than flexion (Figure 3). Other soft tissues such as muscle and ligaments can also be involved. Finally, bone malalignment can lead to stiffness especially in cases of extra-articular elbow fracture malunion or congenital anomalies (e.g., congenital dislocation of the radial head or arthrogryposis). Treatment is usually surgical [13].

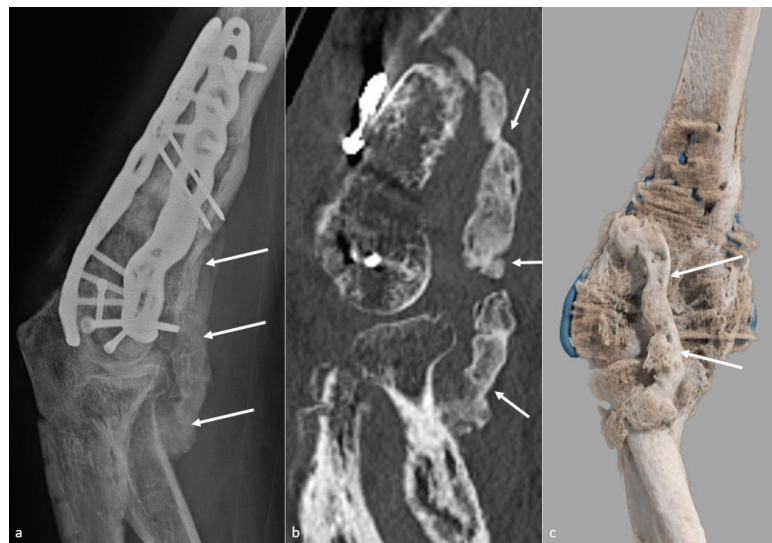


Figure 1. Heterotopic ossification forming a bony bridge between the humerus and the radial neck. Heterotopic ossification (white arrow), leading to severe loss of flexion in a 54-year-old man who suffered from a complex fracture–dislocation, shown (a) on a profile view radiograph, (b) a sagittal CT-scan reformat, and (c) a global illumination 3D reformat.

3.2. Intra-Articular Stiffness

The mechanisms of Intra-articular stiffness are multiple and can be combined. The most frequent are chondropathy (whether of posttraumatic origin, related to osteochondritis or as part of an OA), primary or secondary synovial chondromatosis, posttraumatic joint surface incongruence, and intra-articular adhesions. Proximal radioulnar joint arthritis, an incongruent radial head (Figure 4), or adhesions between the radial head and the annular ligament may lead to pronosupination deficits.

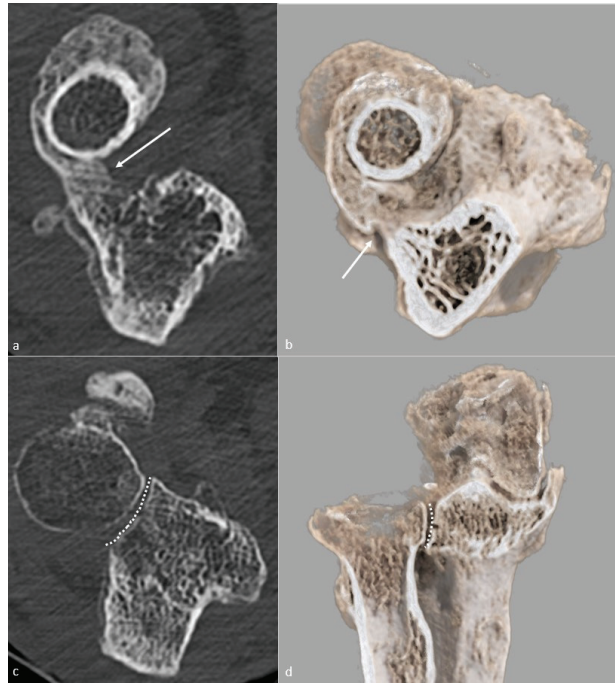


Figure 2. Proximal radioulnar synostosis. Proximal radioulnar synostosis (white arrow), leading to complete loss of forearm rotation in the same patient than in Figure 1, is shown on (a) an axial CT-scan view and (b) a global illumination 3D reformat. Note that the proximal radioulnar joint space (dotted line) can be considered normal and is shown (c) on an axial CT-scan view and (d) a global illumination 3D reformat.

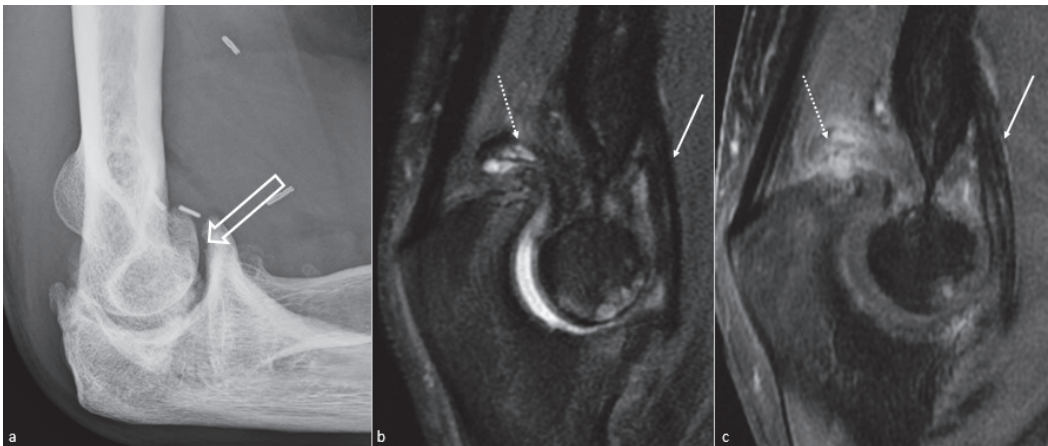


Figure 3. Anterior capsular thickening. (a) Profile view radiograph shows posttraumatic humeroulnar arthrosis (big white arrow), in a 45-year-old woman who suffered from a humeral fracture and presented an extension deficit. (b) Sagittal fat saturated T2-weighted images and (c) fat saturated T1-weighted gadolinium-enhanced images show anterior capsular fibrous thickening (white arrow). Additionally, note the posterior recess synovitis (dotted arrow), with a notable enhancement in (c), whereas no capsular thickening is seen, which also participates in the extension deficit.

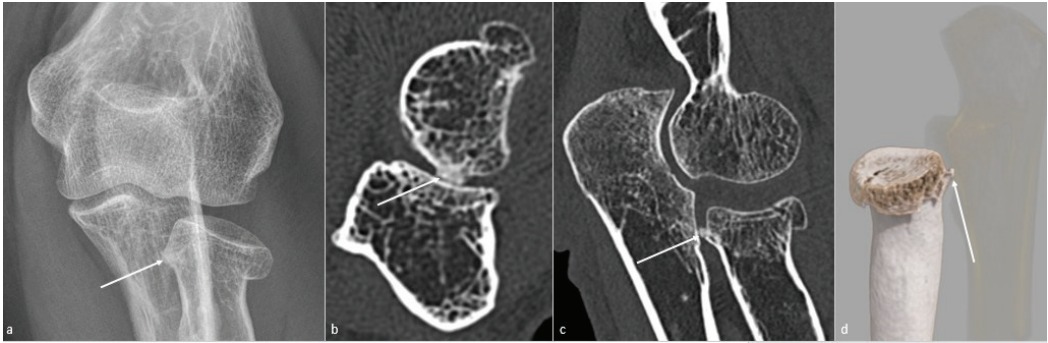


Figure 4. Posttraumatic radial head vicious bone callus. A vicious posttraumatic radial head bone callus (white arrow), causing forearm rotation dysfunction in a 47-year-old woman, is poorly defined on (a) an anteroposterior radiograph. The callus and its particular location are better seen on (b) an axial and (c) sagittal CT-scan reformat, and clearly defined on (d) a global illumination 3D reformat (ulna is voluntarily shown transparent).

OA remains one of the main causes of intra-articular stiffness. It is more often secondary to a traumatic injury, regardless of its severity; however, it can rarely be primitive, especially in manual laborers, weight lifters, and throwing athletes [18]. Distal humeral fracture and elbow fracture–dislocations are more prone to lead to OA than olecranon or radial head fractures [19]. In OA, the first mechanism of stiffness is mechanical impingement related to osteophytes at the extremes of flexion and extension (Figure 5) rather than cartilage surface damage. These osteophytes typically appear in the early stages of osteoarthritis and will classically develop on the tips of the olecranon and the coronoid or fill the coronoid and olecranon fossa (Figure 6) [5]. As for extra-articular causes, treatment is usually surgical or arthroscopic [13]. A total elbow arthroplasty is an option for joint ankyloses or advanced arthropathy [20].

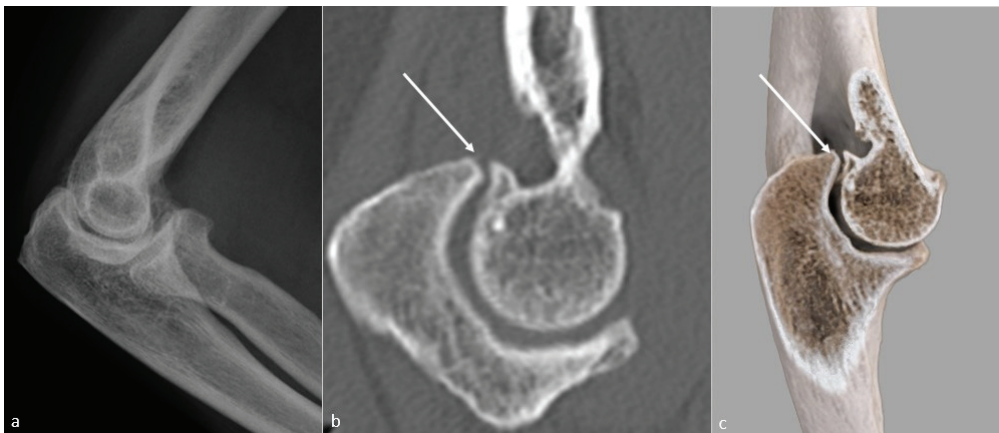


Figure 5. Loss of extension secondary to a bony osteophytic impingement. A bone block secondary to a trochlear osteophyte (white arrow) in a 51-year-old man, manual worker, is shown on (a) a profile view radiograph (not depicted), (b) a sagittal CT-scan reformat, and (c) a global illumination 3D reformat.



Figure 6. Olecranon fossa osteophytic filling. Osteophytic filling (white arrow) of the olecranon fossa (white dotted line) is shown on (a) a profile radiograph and (b) a sagittal CT-scan in a 26-year-old man who suffered from a humeral fracture and presents extension dysfunction when its corresponding normal aspect is shown in (e,f). The filling is also seen on (c) an extension global illumination 3D reformat and (d) in flexion (white arrows), when the normal aspect is shown in (g,h) (dotted white star).

4. Imaging Assessment of Elbow Stiffness

The aim of imaging is threefold: confirm the etiology of stiffness, determine which anatomic elements are involved, and allow optimal treatment planning (procedures and arthroscopic or surgical approaches). Therefore, the following elements should be evaluated in the standard imaging workup:

- Remaining bone stock;
- Bone alignment;
- Articular congruency;
- OA location and severity;
- Presence of osteophytes: presence and repercussions (impact on articular mobility and relation to neurovascular structures);
- Loose bodies (embedded in the synovial membrane or free);
- Presence of surgical implants (articular protrusion?);
- Soft tissue pathology.

5. Imaging Workup

5.1. Conventional Radiographs

The initial assessment of a stiff elbow should always begin with standard radiographs, with at least anteroposterior (AP) and lateral views. For the AP view, the patient is positioned with the elbow in full extension and the forearm in supination. It allows optimal visualization of the medial and lateral epicondyles, the radiocapitellar joint, and the coronal bones alignment. In case of inability to fully extend the elbow due to contracture, two anteroposterior views should be performed—one perpendicular to the distal humerus and one perpendicular to the proximal radius and ulna. CT is an option if those views cannot

be obtained. For the lateral view, the patient is positioned with the elbow in 90° flexion and the forearm in a neutral position, allowing a good assessment of the humeroulnar joint, coronoid, and olecranon. Humeral anteversion (30°) and articular congruency can also be checked with this view.

Additional oblique views can be performed according to the clinical suspicion. The medial oblique view consists of an AP view with a 45° medial rotation of the arm and forearm, improving the visualization of the trochlea, olecranon, and coronoid processes. The lateral oblique view is obtained with a 45° lateral rotation of the arm and forearm, improving the visualization of the radiocapitellar joint, medial epicondyle, radioulnar joint, and coronoid process. The radial head view consists of a lateral view with a 45° cranial angulation of the incident beam with respect to the humerus, allowing better visualization of the radial head and radiocapitellar joint. CT is gradually replacing these complementary radiographic views, which may be an advantage in the author’s opinion.

One must keep in mind that non-ossified articular loose bodies (i.e., cartilaginous) and soft tissues cannot be seen on standard radiographs and that filling of the olecranon and coronoid fossa can indicate the presence of osteophytes, which are better depicted on CT (Table 2).

Table 2. Radiographic checklist.

Items to be Checked on Radiographs	
<i>Anteroposterior view</i>	<i>Profile</i>
Malunion	Malunion
Malalignment in the frontal plane	Malalignment
Loose bodies	Loose bodies (olecranon and coronoid fossae)
Joint space narrowing	Radial head subluxation or dislocation
Periarticular calcification	Drop sign * (instability?)
Heterotopic ossification	Heterotopic ossification
Osteophytes (radial head)	Capsular ossification (anterior +++)
	Osteophytes (olecranon and coronoid +++)
	Olecranon, coronoid, or radial fossae osteophytic filling

*: The drop sign corresponds to an irregular humeroulnar joint space, superior to 3 mm in width [21].

5.2. Ultrasonography

Ultrasonography can be recommended for the evaluation of ligamentous, tendinous, nerve pathologies, and synovitis (Table 3). It is not the method of choice for the evaluation of loose bodies and osteochondral traumatic lesions and should only be used for this purpose when other imaging methods are not available [22]. The ulnar nerve deserves special attention, as it is often involved in traumatic or degenerative processes. Additionally, a “stretching” neuropathy can occur after treatment when the patient recovers normal motion. Radial and median nerves are less susceptible to injury but can be affected by scar formation, heterotopic ossification, or iatrogenic injury [3]. As their pathology can lead to instability, collateral ligaments should be checked if signs of instability are clinically present [23].

Table 3. Ultrasonographic checklist.

Ulnar neuropathy +++
Heterotopic ossification vasculonervous relations, if present
Cartilaginous lesions
Joint effusion and synovitis
Loose bodies (and their mobility)
Ligamentous pathology in case of instability
Osteophytes' location

5.3. CT and CT Arthrography

CT is superior to radiographs in identifying and characterizing the osseous causes of elbow stiffness [24]. It allows a better assessment of osteophytes, which are almost always present in OA patients at the trochleo-ulnar compartment (e.g., anterior coronoid area and medial part of the trochleo-ulnar joint) and in about 25% of the cases at the radiocapitellar compartment (e.g., both at the anterior and posterior portions). It also allows a precise joint space delineation, which permits the diagnostic of severe OA, defined by any degree of joint space narrowing by Kwak et al. [25]. Late elbow OA has been shown to present worse clinical and radiologic outcomes when treated by arthroscopic osteocapsular arthroplasty with respect to early OA. Severe OA is also a contraindication to isolated contracture release procedures, and in these cases, elbow arthroplasty should be considered [7]. The number and location of ossified intra-articular osteochondromas, the location and anatomic relations of HO (including their relations to neurovascular structures), and also study of complex fractures are facilitated by CT. A 3D volume rendering or preferably global illumination reconstructions should be performed to provide the surgeon with the cartography and relations of the ossified pathologic processes necessary for optimal surgical planning.

CT-arthrography is minimally invasive and allows an optimal evaluation of the cartilage articular surface (Figure 7), and is recommended prior to treatment of elbow osteoarthritis [26]. If such cartilaginous lesions are present, osteophytes treatment alone may not totally improve elbow function, and pain may remain after surgical management [5]. Outcomes after arthroscopic treatment are better when no cartilaginous lesion is observed, but current classification systems cannot be used as prognostic factors before treatment [5]. Finally, signs of impingement (osteophytes and filling of fossa) are more common than cartilaginous lesions and could be considered as a pre-arthritis stage.

CT arthrography should be preceded by a non-contrast acquisition to detect calcified loose bodies that by be obscured by the intra-articular iodinated contrast. As regards the evaluation of intra-articular osteochondromas, CT has two main purposes—location and mobility assessment (e.g., mobile after arthrography or not) (Figure 8). CT arthrography is particularly useful for the identification of non-ossified intra-articular loose bodies (e.g., cartilage fragments). Patients with loose bodies and no cartilaginous lesions on CT-arthrography have been shown to be good candidates for arthroscopic treatment of OA [26]. Moreover, CT-arthrography can also lead to capsular retraction diagnosis if the articular capacity is reduced to around 6 ± 3 mL. An intra-articular corticosteroid injection can be coupled with CT arthrography, serving as a diagnostic and therapeutic test (e.g., reduction of capsular inflammation).

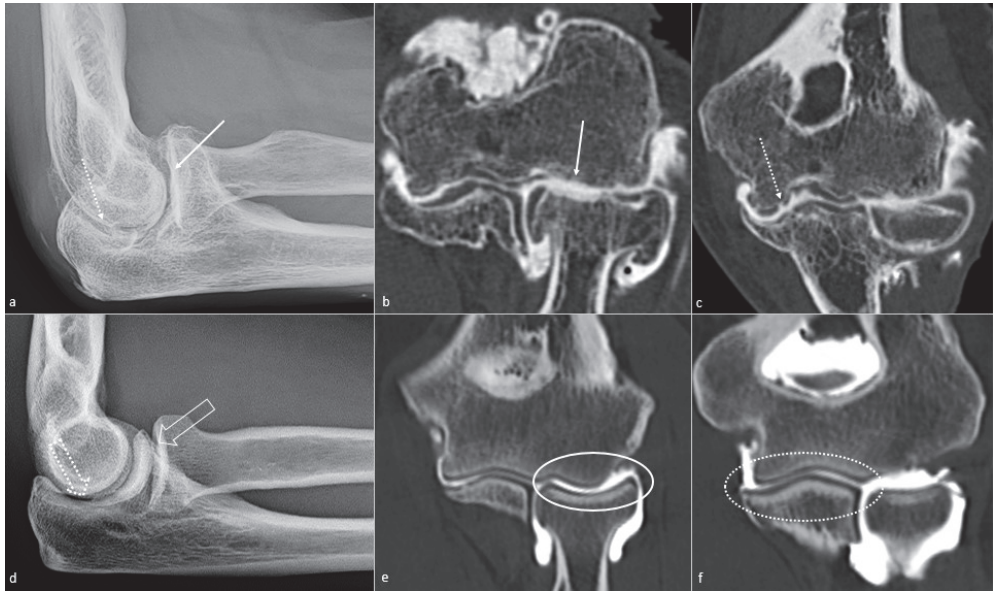


Figure 7. Elbow osteoarthritis. Elbow osteoarthritis in a 57-year-old man suffering from posttraumatic stiffness since she was 12 years old is seen on (a) a profile radiograph, with humeroradial (white arrow) and humeroulnar (dotted white arrow) joint space narrowing; humeroradial chondrolysis is depicted on (b) a frontal CT-arthrography view (white arrow), and humeroulnar cartilaginous erosions are shown on (c) a frontal CT-arthrography view (dotted white arrow). Normal corresponding aspects are shown in (d) a profile radiograph, (e) a frontal CT-arthrography view of the humeroradial joint (white circle) and (f) a frontal CT-arthrography view of the humeroulnar joint (dotted white circle).

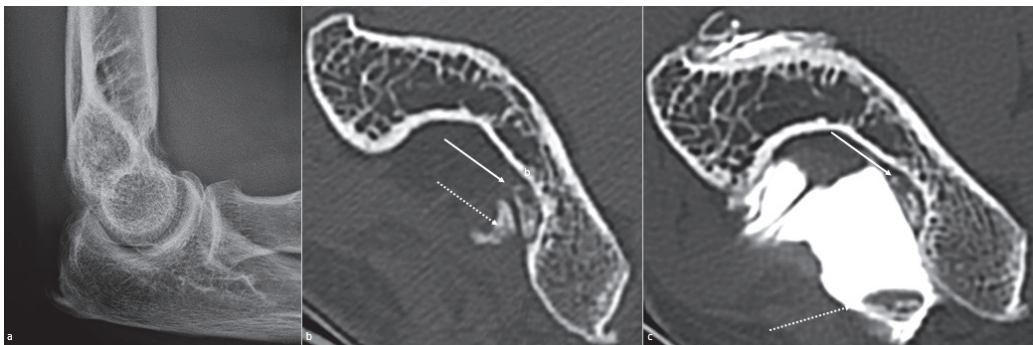


Figure 8. Articular loose bodies. Olecranon loose bodies are shown, not depicted on (a) a profile radiograph but well seen on (b) an axial CT-scan view (arrows). (c) CT arthrography allows identifying a free loose body (dotted white arrow) and a synovial-embedded one (white arrow), in a 57-year-old woman presenting osteoarthritis secondary to a radial head fracture.

A CT and CT-arthrography checklist is presented in Table 4.

Table 4. CT and CT-arthrography checklist.

Loss of flexion	CT/CT-Arthrography
	<i>Posterior tethers/anterior blocks</i>
	HO
	Anterior synovitis
	Loose bodies
	Osteophytes/fibrosis in the radial or coronoid fossa
	Osteophytes around the coronoid
	Joint space narrowing
Loss of extension	CT/CT-Arthrography
	<i>Posterior blocks/anterior tethers</i>
	HO
	Posterior synovitis
	Free bodies
	Osteophytes/fibrosis in the olecranon fossa
	Osteophytes around the olecranon
Joint space narrowing	
Forearm rotation dysfunction	CT
	Proximal radioulnar bony ankylosis
	Malunion or nonunion of the radial head
	Posttraumatic sequelae of the radial head
Any stiffness	CT-Arthrography
	Humeroulnar joint cartilaginous lesion (absent/mild/moderate/severe)
	Humeroradial joint cartilaginous lesion (absent/mild/moderate/severe)

HO: heterotopic ossification.

5.4. MR Imaging

MRI has a limited role in the assessment of elbow stiffness and may not be required [27]. Its main interest is soft-tissue evaluation, especially searching for capsular and/or ligament thickening, as the loss of soft tissue elasticity is thought to be the result of bleeding, edema, granulation tissue formation, and fibrosis, which may translate to a low signal intensity (e.g., in both T1 and T2 weighted images) capsular thickening on MRI (Figure 3). Depending on the amount of joint fluid, intra-articular adhesences can also be seen as tissue bands connecting the joint capsule to osseous structures. Non-fat-saturated T1 weighted sequences are also useful to identify fibrotic changes in the intra-articular fat-pads (e.g., low signal intensity bands and peripheral thickening). MRI should be performed when CT arthrography does not provide a clear explanation for joint stiffness or when soft tissue involvement is suspected (e.g., synovitis, ligament dysfunction, neuropathies) [13]. Moreover, intra-articular space-occupying lesions such as cystic ganglia may not be identified on CT and may cause neuropathies or induce elbow stiffness when located at the anterior joint compartment [28]. Neuropathies around the elbow constitute another MRI indication. For instance, the ulnar nerve is superficially located and susceptible to trauma and impingement due to degenerative joint changes [29]. Unexplained atraumatic elbow contracture with negative radiographs may be at times related to elbow benign and malignant soft tissues tumors that should be evaluated on MRI [30] (Figure 9). A particular situation should be noted: when the patient’s primary complaint after trauma is pain

rather than stiffness without osseous lesions on radiographs or CT, type 1 complex regional pain syndrome should be considered and ruled out, as those patients may not respond to conventional therapeutic strategies [7]. MR arthrography is also an option, allowing a combined evaluation of capsular and periarticular soft tissues, cartilage articular surface, and intra-articular loose bodies.

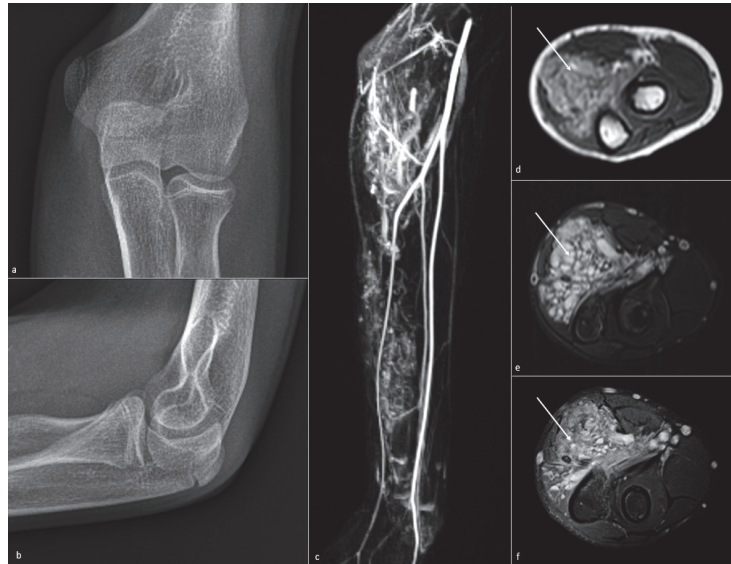


Figure 9. Vascular malformation of the forearm. Vascular malformation of the forearm causing elbow stiffness in a 12-year-old boy. (a,b) No phleboliths or bony anomalies are visible on radiographs. (c) Angio-MR sequence, (d) axial T1-weighted, (e) T2-weighted fat-saturated, and (f) T1-weighted gadolinium-enhanced fat-saturated show a fatty and heterogeneous lesion (white arrow), with high vascular enhancement, in the anterior forearm compartment.

An MRI diagnostic checklist is presented in Table 5.

Table 5. MRI checklist.

Loss of Flexion
<i>Anterior tethers/posterior blocks</i>
Capsular scarring (lateral and medial ligament complex)
Brachialis scar
HO
Anterior synovitis (consider IV contrast media if needed)
Loose bodies
Osteophytes in the radial or coronoid fossa
Osteophytes around the coronoid
Joint space narrowing
Loss of extension
<i>Posterior blocks/anterior tethers</i>
Capsular scarring (lateral and medial ligament complex)

Table 5. Cont.

Triceps scar
HO
Posterior synovitis
Loose bodies
Osteophytes in the olecranon fossa
Osteophytes around the olecranon
Joint space narrowing
Forearm rotation dysfunction
<i>Not initially indicated</i>
Chondropathy of the radial head
Annular ligament scar
Radioulnar synostosis
Any stiffness
Humeroulnar joint impingement (absent/partial/severe)
Humeroradial joint impingement (absent/partial/severe)
Soft tissue lesion
Ulnar nerve injury

HO: heterotopic ossification.

5.5. Dynamic and Kinematic CT

Dynamic CT should be performed in the preoperative evaluation of patients with elbow stiffness caused by bone lesions, intra-articular loose bodies, and periarticular ossifications/calcifications, particularly when multiple anomalies are present. Indeed, multifactorial joint blocks are frequent in clinical practice, and identifying the origin of the impingement with static imaging methods can be difficult (Figure 10). In this context, step-and-shoot acquisitions in maximal flexion and maximal extension may be helpful when dynamic CT is not available. Similarly, acquisitions in full pronation, neutral position, and full supination can be used for the evaluation of pronosupination deficits.

Wide-area detector scanner models allow the acquisition of kinematic 4-D datasets of the elbow during motion, by repeating low-dose acquisitions for about 7–8 s with a high temporal resolution (e.g., inter volume delays as low as 0.27 s). This method has been used for the evaluation of dynamic pathologic processes in various joints and can be used for the evaluation of the elbow during flexion–extension and pronosupination maneuvers [29–35]. Elbow kinematic CT can be seen as a problem-solving tool recommended for the evaluation of bony impingement when acquisitions in the extremes of joint position are not sufficient to clearly determine the nature of the impingement.

5.6. Rationale for Determining the Optimal Imaging Workup and Diagnostic Algorithm

Medical history, physical examination, and initial imaging workup with conventional radiography and ultrasonography usually allows differentiating between intra- or extra-articular origin of elbow stiffness but are rarely sufficient if surgical treatment is being considered (arthrolysis, interposition arthroplasties, and prosthetic replacements) [6]. Non-surgical treatment would be more effective in case of the absence of advanced joint derangements usually identified on conventional radiographs and ultrasound [6]. Additionally, both Kay’s and Morreys’ classification systems include soft tissue and bony anatomy, underscoring the need for a proper analysis of both articular and periarticular anatomy, which may require CT-arthrography or MRI. Thus, based on the presented information a diagnostic algorithm is proposed (Figure 11).

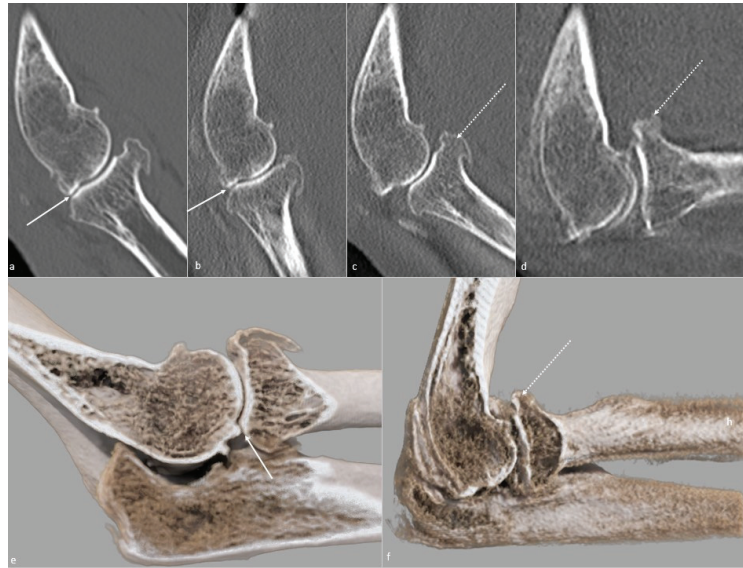


Figure 10. Osteophytic bone block on 4D cinematic CT. (a–d) Images obtained from a 4D-CT-scan, from maximal extension to maximal flexion, in a case of posttraumatic flexion–extension loss in a 56-year-old woman who suffered from a complex fracture–dislocation years ago. Posterior radial-head and capitellar osteophytes (white arrow) cause an extension bone block, whereas the anterior osteophytes (dotted white arrow) do not contact, suggesting a capsulous cause to the loss of flexion. Those osteophytes are better depicted on (e) a global illumination 3D reformat in extension and (f) flexion, also clarifying their anatomic relationships.

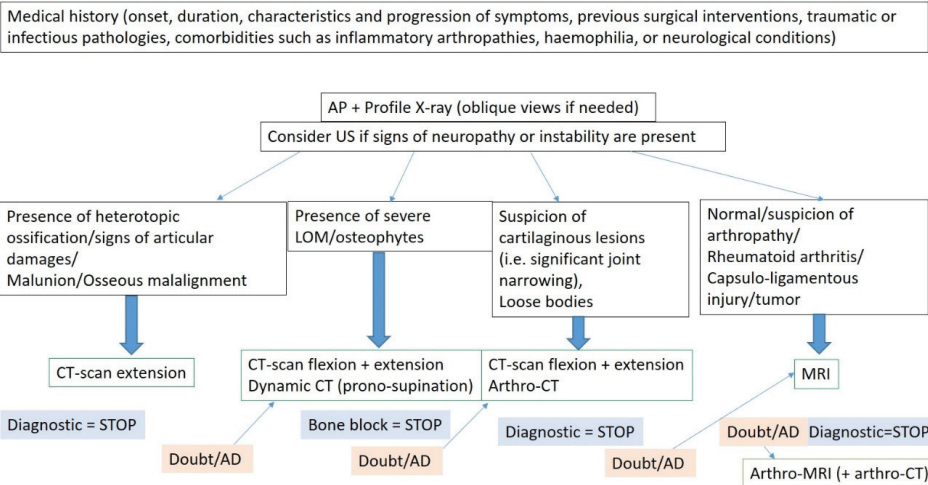


Figure 11. Diagnostic imaging studies prescription proposal. AD: alternative diagnosis; AP: anteroposterior; US: ultrasonography; LOM: loss of motion. The term doubt refers to an unsure diagnosis or a possible alternative diagnosis, requiring other imaging tests.

6. Conclusions

Although the etiology of elbow stiffness is multifactorial, it is most frequently caused by an association of tethers and/or blocks, essentially secondary to trauma and OA. Elbow stiffness can involve multiple intra-articular or extra-articular structures, such as capsular, and periarticular soft tissues and the imaging workup is paramount for optimal patient management. In addition to medical history and physical examination, radiographs and CT (ideally with acquisitions in the extremes of joint motion) represent the cornerstone of the imaging workup, illustrating and characterizing bony impingement. CT-arthrography is an effective tool in the preoperative setting allowing an optimal evaluation of the cartilage articular surface. Finally, MRI can be recommended when conventional radiographs and CT are inconclusive, especially if patients with atraumatic joint stiffness searching for a soft-tissue origin for joint stiffness.

Author Contributions: Conceptualization, C.L. and R.G.; methodology, P.T.; software, A.B.; validation, C.L., R.G. and P.T.; formal analysis, A.B.; investigation, E.G., G.D. and M.L.; resources, A.B.; data curation, P.T.; writing—original draft preparation, C.L.; writing—review and editing, R.G.; visualization, P.T.; supervision, R.G.; project administration, P.T. All authors have read and agreed to the published version of the manuscript.

Funding: This research received no external funding.

Conflicts of Interest: The authors declare no conflict of interest.

References

1. Fornalski, S.; Gupta, R.; Lee, T.Q. Anatomy and Biomechanics of the Elbow Joint. *Tech. Hand Up. Extrem. Surg.* **2003**, *7*, 168–178. [[CrossRef](#)]
2. Masci, G.; Cazzato, G.; Milano, G.; Ciolli, G.; Malerba, G.; Perisano, C.; Greco, T.; Osvaldo, P.; Maccauro, G.; Liuzza, F. The Stiff Elbow: Current Concepts. *Orthop. Rev.* **2020**, *12*, 8661. [[CrossRef](#)] [[PubMed](#)]
3. Adolfsson, L. Post-Traumatic Stiff Elbow. *EFORT Open Rev.* **2018**, *3*, 210–216. [[CrossRef](#)]
4. Morrey, B.F. The Posttraumatic Stiff Elbow. *Clin. Orthop.* **2005**, *431*, 26–35.
5. Lenoir, H.; Carlier, Y.; Ferrand, M.; Vidil, A.; Desmoineaux, P. Can Preoperative Imaging Predict the Outcomes after Arthroscopic Release for Elbow Arthritis? *Orthop. Traumatol. Surg. Res.* **2019**, *105*, S229–S234. [[CrossRef](#)] [[PubMed](#)]
6. Patiño, J.M.; Saenz, V.P. Stiff Elbow. In *StatPearls*; StatPearls Publishing: Treasure Island, FL, USA, 2020.
7. Gauger, E.M.; Rhee, P.C. Surgical Management of the Posttraumatic Stiff Elbow: A Step-Wise Algorithm for Open Osteocapsular Release. *Tech. Hand Up. Extrem. Surg.* **2018**, *22*, 127–133. [[CrossRef](#)] [[PubMed](#)]
8. Kodde, I.F.; van Rijn, J.; van den Bekerom, M.P.J.; Eygendaal, D. Surgical Treatment of Post-Traumatic Elbow Stiffness: A Systematic Review. *J. Shoulder Elb. Surg.* **2013**, *22*, 574–580. [[CrossRef](#)]
9. Pederzini, L.A.; Nicoletta, F.; Tosi, M.; Prandini, M.; Tripoli, E.; Cossio, A. Elbow Arthroscopy in Stiff Elbow. *Knee Surg. Sports Traumatol. Arthrosc.* **2014**, *22*, 467–473. [[CrossRef](#)]
10. Morrey, B.F.; Askew, L.J.; Chao, E.Y. A Biomechanical Study of Normal Functional Elbow Motion. *J. Bone Joint Surg. Am.* **1981**, *63*, 872–877. [[CrossRef](#)]
11. Sardelli, M.; Tashjian, R.Z.; MacWilliams, B.A. Functional Elbow Range of Motion for Contemporary Tasks. *J. Bone Joint Surg. Am.* **2011**, *93*, 471–477. [[CrossRef](#)]
12. Qian, Y.; Yu, S.; Shi, Y.; Huang, H.; Fan, C. Risk Factors for the Occurrence and Progression of Posttraumatic Elbow Stiffness: A Case-Control Study of 688 Cases. *Front. Med.* **2020**, *7*, 604056. [[CrossRef](#)]
13. Sun, Z.; Li, J.; Cui, H.; Ruan, H.; Wang, W.; Fan, C. A New Pathologic Classification for Elbow Stiffness Based on Our Experience in 216 Patients. *J. Shoulder Elb. Surg.* **2020**, *29*, e75–e86. [[CrossRef](#)]
14. Manske, M.C.; Hanel, D.P. Postburn Contractures of the Elbow and Heterotopic Ossification. *Hand Clin.* **2017**, *33*, 375–388. [[CrossRef](#)]
15. Nandi, S.; Maschke, S.; Evans, P.J.; Lawton, J.N. The Stiff Elbow. *HAND* **2009**, *4*, 368–379. [[CrossRef](#)] [[PubMed](#)]
16. Mittal, R. Posttraumatic Stiff Elbow. *Indian J. Orthop.* **2017**, *51*, 4–13. [[CrossRef](#)]
17. Freibott, C.E.; Bäcker, H.C.; Shoap, S.C.; Tedesco, L.J.; Galle, S.E.; Rosenwasser, M.P. Treatment Methods for Post-Traumatic Elbow Stiffness Caused by Heterotopic Ossification. *J. Shoulder Elb. Surg.* **2020**, *29*, 1380–1386. [[CrossRef](#)]
18. Papatheodorou, L.K.; Baratz, M.E.; Sotereanos, D.G. Elbow Arthritis: Current Concepts. *J. Hand Surg.* **2013**, *38*, 605–613. [[CrossRef](#)] [[PubMed](#)]
19. Guittou, T.G.; Zurakowski, D.; van Dijk, N.C.; Ring, D. Incidence and Risk Factors for the Development of Radiographic Arthrosis after Traumatic Elbow Injuries. *J. Hand Surg.* **2010**, *35*, 1976–1980.
20. D’Ambrosi, R.; Formiconi, F.; Ursino, N.; Rubino, M. Treatment of Complete Ankylosed Elbow with Total Arthroplasty. *BMJ Case Rep.* **2019**, *12*, e231123. [[CrossRef](#)] [[PubMed](#)]

21. Schaeffeler, C.; Waldt, S.; Woertler, K. Traumatic Instability of the Elbow—Anatomy, Pathomechanisms and Presentation on Imaging. *Eur. Radiol.* **2013**, *23*, 2582–2593. [[PubMed](#)]
22. Klauser, A.S.; Tagliafico, A.; Allen, G.M.; Boutry, N.; Campbell, R.; Court-Payen, M.; Grainger, A.; Guerini, H.; McNally, E.; O'Connor, P.J.; et al. Clinical Indications for Musculoskeletal Ultrasound: A Delphi-Based Consensus Paper of the European Society of Musculoskeletal Radiology. *Eur. Radiol.* **2012**, *22*, 1140–1148. [[CrossRef](#)]
23. Brandão, A.T.; Amaro, E.; Francisco, M.J.; Tanaka, R.M.; Santos, D.D.C.B.; Miranda, F.C.; Rahal, A.; Rosemberg, L.A. Ultrasonography and Magnetic Resonance Imaging of Elbow Ligaments: A Comparative Study. *Einstein São Paulo* **2019**, *17*, eAO4579. [[CrossRef](#)]
24. Zubler, V.; Saupe, N.; Jost, B.; Pfirmann, C.W.A.; Hodler, J.; Zanetti, M. Elbow Stiffness: Effectiveness of Conventional Radiography and CT to Explain Osseous Causes. *AJR Am. J. Roentgenol.* **2010**, *194*, W515–W520. [[CrossRef](#)] [[PubMed](#)]
25. Kwak, J.-M.; Kim, H.; Sun, Y.; Kholinne, E.; Koh, K.H.; Jeon, I.-H. Arthroscopic Osteocapsular Arthroplasty for Advanced-Stage Primary Osteoarthritis of the Elbow Using a Computed Tomography–Based Classification. *J. Shoulder Elb. Surg.* **2020**, *29*, 989–995. [[CrossRef](#)] [[PubMed](#)]
26. Carlier, Y.; Lenoir, H.; Rouleau, D.M.; Mansat, P.; Vidil, A.; Ferrand, M.; Bleton, R.; Herrisson, O.; Salabi, V.; Duparc, F.; et al. Arthroscopic Debridement for Osteoarthritis of the Elbow: Results and Analysis of Predictive Factors. *Orthop. Traumatol. Surg. Res.* **2019**, *105*, S221–S227. [[CrossRef](#)] [[PubMed](#)]
27. Everding, N.G.; Maschke, S.D.; Hoyen, H.A.; Evans, P.J. Prevention and Treatment of Elbow Stiffness: A 5-Year Update. *J. Hand Surg.* **2013**, *38*, 2496–2507. [[CrossRef](#)]
28. Goyal, N.; Luchetti, T.J.; Blank, A.T.; Cohen, M.S. Atraumatic, Progressive, and Painful Elbow Contracture From a Ganglion Cyst. *J. Hand Surg.* **2021**, *46*, 345.e1–e345.e3. [[CrossRef](#)] [[PubMed](#)]
29. Abou Arab, W.; Rauch, A.; Chawki, M.B.; Dap, F.; Dautel, G.; Blum, A.; Gondim Teixeira, P.A. Scapholunate Instability: Improved Detection with Semi-Automated Kinematic CT Analysis during Stress Maneuvers. *Eur. Radiol.* **2018**, *28*, 4397–4406. [[CrossRef](#)]
30. Athlani, L.; Rouizi, K.; Granero, J.; Hossu, G.; Blum, A.; Dautel, G.; Gondim Teixeira, P.A. Assessment of Scapholunate Instability with Dynamic Computed Tomography. *J. Hand Surg. Eur. Vol.* **2020**, *45*, 375–382. [[CrossRef](#)]
31. Gondim Teixeira, P.A.; Formery, A.-S.; Balazuc, G.; Lux, G.; Loiret, I.; Hossu, G.; Blum, A. Comparison between Subtalar Joint Quantitative Kinematic 4-D CT Parameters in Healthy Volunteers and Patients with Joint Stiffness or Chronic Ankle Instability: A Preliminary Study. *Eur. J. Radiol.* **2019**, *114*, 76–84. [[CrossRef](#)]
32. Gondim Teixeira, P.A.; Formery, A.-S.; Jacquot, A.; Lux, G.; Loiret, I.; Perez, M.; Blum, A. Quantitative Analysis of Subtalar Joint Motion With 4D CT: Proof of Concept With Cadaveric and Healthy Subject Evaluation. *AJR Am. J. Roentgenol.* **2017**, *208*, 150–158. [[CrossRef](#)] [[PubMed](#)]
33. Teixeira, P.A.G.; Gervaise, A.; Louis, M.; Raymond, A.; Formery, A.-S.; Lecocq, S.; Blum, A. Musculoskeletal Wide-Detector CT Kinematic Evaluation: From Motion to Image. *Semin. Musculoskelet. Radiol.* **2015**, *19*, 456–462. [[PubMed](#)]
34. Teixeira, P.A.G.; Blanc, J.-B.; Rauch, A.; Arab, W.A.; Hossu, G.; Athlani, L.; Blum, A. Evaluation of Dorsal Subluxation of the Scaphoid in Patients with Scapholunate Ligament Tears: A 4D CT Study. *AJR Am. J. Roentgenol.* **2020**, *216*, 1–9. [[CrossRef](#)] [[PubMed](#)]
35. Blum, A.; Gillet, R.; Rauch, A.; Urbaneja, A.; Biouichi, H.; Dodin, G.; Germain, E.; Lombard, C.; Jaquet, P.; Louis, M.; et al. 3D Reconstructions, 4D Imaging and Postprocessing with CT in Musculoskeletal Disorders: Past, Present and Future. *Diagn. Interv. Imaging* **2020**, *100*, 693–705. [[CrossRef](#)] [[PubMed](#)]

MDPI
St. Alban-Anlage 66
4052 Basel
Switzerland
www.mdpi.com

Journal of Clinical Medicine Editorial Office
E-mail: jcm@mdpi.com
www.mdpi.com/journal/jcm



Disclaimer/Publisher's Note: The statements, opinions and data contained in all publications are solely those of the individual author(s) and contributor(s) and not of MDPI and/or the editor(s). MDPI and/or the editor(s) disclaim responsibility for any injury to people or property resulting from any ideas, methods, instructions or products referred to in the content.



Academic Open
Access Publishing

[mdpi.com](https://www.mdpi.com)

ISBN 978-3-0365-8877-3